Holm Altenbach · Alexander H.-D. Cheng ·
Xiao-Wei Gao · Andrii Kostikov ·
Wladyslaw Kryllowicz · Piotr Lampart ·
Viktor Popov · Andrii Rusanov ·
Stavros Syngellakis   *Editors*

Advances in Mechanical and Power Engineering

Selected Papers from The International
Conference on Advanced Mechanical
and Power Engineering (CAMPE 2021),
October 18–21, 2021

Springer

Lecture Notes in Mechanical Engineering

Holm Altenbach · Alexander H.-D. Cheng ·
Xiao-Wei Gao · Andrii Kostikov ·
Wladyslaw Kryllowicz ·
Piotr Lampart · Viktor Popov ·
Andrii Rusanov · Stavros Syngellakis
Editors

Advances in Mechanical and Power Engineering

Selected Papers from The International
Conference on Advanced Mechanical
and Power Engineering (CAMPE 2021),
October 18–21, 2021

Springer

Editors
Holm Altenbach
Fakultät für Maschinenbau, G10/58
Otto-von-Guericke-Universität
Magdeburg, Germany

Alexander H.-D. Cheng
School of Engineering
University of Mississippi
Oxford, MS, USA

Xiao-Wei Gao
School of Aeronautics and Astronautics
Dalian University of Technology
Dalian, China

Andrii Kostikov
A. Pidhornyi Institute of Mechanical
Engineering Problems of the National
Academy of Sciences of Ukraine
Kharkiv, Ukraine

Wladyslaw Kryllowicz
Institute of Fluid-Flow Machinery
Lodz University of Technology
Lodz, Poland

Piotr Lampart
The Szewalski Institute of fluid-flow
machinery of Polish Academy of Sciences
Gdansk, Poland

Viktor Popov
Ascend Technologies Limited
Eastleigh, UK

Andrii Rusanov
A. Pidhornyi Institute of Mechanical
Engineering Problems of the National
Academy of Sciences of Ukraine
Kharkiv, Ukraine

Stavros Syngellakis
Wessex Institute of Technology
Southampton, UK

Preface

This volume of Lecture Notes in Mechanical Engineering gathers selected papers presented at the 14th International Conference on Advanced Mechanical and Power Engineering (CAMPE-2021), held online from Kharkiv, Ukraine, on October 18–21, 2021. Between 1972–2022, XXI CAMPE Editions were carried out. The first 7 conferences did not include international authors (1972–1993), and the other 14 conferences held in 1994–2021 were international events. CAMPE-2021 was organized by the National Academy of Sciences of Ukraine, the A. Pidhornyi Institute of Mechanical Engineering Problems of the National Academy of Sciences of Ukraine, the Engineering Academy of Ukraine, and the Joint Stock Company «Ukrainian Energy Machines».

The aim of the conference was to present the latest achievements in mechanical and power engineering and to provide an occasion for discussion and exchange of views and opinions. The conference covered the following topics:

– Development and Improvement of Numerical Methods of Calculation of Fluid Flow and/or Heat Transfer
– Numerical Analysis of Fluid Flow and/or Heat Transfer in Power Equipment
– Identification and Optimization of Fluid Flow and/or Heat Transfer in Power Equipment
– Profiling of Flow Parts of Turbomachines
– Development of Thermal Circuits and Improvement of Thermodynamic Characteristics of Power Equipment
– Efficient Fuel Combustion
– Renewable Energy Sources
– Resource-Saving and Energy-Efficient Technologies
– Energy Storage
– Environmental Safety Issues of Power Engineering
– Hydrogen Technologies
– Theoretical and Applied Mechanics
– Mechanical Structures and Stress Analysis
– Engineering Design

- Materials Engineering
- Nanotechnology and Microengineering
- Methods and Technologies for Additive Manufacturing
- Engine Technology
- Aerospace Technology and Astronautics

The organizers received 85 contributions from 264 authors and 26 countries around the world.

After a thorough peer-review process carried out in collaboration between the conference committee and the Springer series editors, 37 papers were accepted for publication in this book, prepared by authors from 19 countries (acceptance rate around 42%).

We would like to thank the members of the International Program Committee for their hard work during the review process. Their involvement and commitment were crucial for both the success of CAMPE-2021 and for the realization of this book.

The book "Advances in Mechanical and Power Engineering" has been organized in three parts, according to the main topic covered by the respective contributions:

1. Fluid Mechanics and Heat Transfer in Power Engineering.
2. Energy Saving Technologies and Environmental Safety.
3. Dynamics and Strength of Power Equipment.

The first part "Fluid Mechanics and Heat Transfer in Power Engineering" covers recent developments of advanced computational and analytical methods for applications in mechanical engineering, turbomachinery, heat and power engineering. It reports on both theoretical and experimental research, and the use of modern computer technology and effective mathematical methods for the analysis of fluid mechanics and heat transfer problems, as well as for the identification and optimization of fluid flow. It highlights new strategies for implementing intelligent solutions at the purpose of improving compressor and turbine stages and effective methods for profiling flow parts of turbomachines.

The second part "Energy Saving Technologies and Environmental Safety" presents some comparative analysis of computational methods adopted for renovation projects in mechanical engineering, such as those relating to the development of thermal circuits, and the improvement of thermodynamic characteristics of power equipment. The works belonging to this part are also devoted to methods for ensuring ecological and human safety and for reducing material costs and environmental pollution. New advancements in energy saving technologies, renewable energy sources, topical issues in environmental safety, resource-saving and hydrogen technologies are presented.

The third part "Dynamics and Strength of Power Equipment" reports on recent developments in mathematical models and methods to simulating the dynamics characteristics and durability of machines and engineering designs applications. It describes advanced mathematical models for simulating the behavior of power equipment under static and dynamic loads and for making qualitative predictions on

reliability and durability. It also covers topics related to stress-strain state, stability, structure optimization, and dynamic processes of mechanical systems and objects. It shows applications in nanotechnology, microengineering, engine and aerospace technologies, astronautics, materials engineering, and additive manufacturing.

We would like to take this opportunity to thank authors for their contributions, members of Program Committee, and invited external reviewers for their efforts and expertise in contribution to reviewing, without which it would be impossible to maintain the high standards of peer-reviewed papers.

We appreciate the partnership with Springer, EasyChair, StrikePlagiarism, and our sponsor Joint Stock Company «Ukrainian Energy Machines» for the essential support during the preparation of CAMPE-2021.

Thank you very much to CAMPE-2021 Team. Their involvement and hard work were crucial to the success of CAMPE-2021 conference.

May 2022

Holm Altenbach
Alexander Cheng
Xiao-Wei Gao
Andrii Kostikov
Wladyslaw Kryllowicz
Piotr Lampart
Viktor Popov
Andrii Rusanov
Stavros Syngellakis

Organization

Honorary Chairs

Olexandr Kyrylenko	National Academy of Sciences of Ukraine, Kyiv, Ukraine
Victor Subotin	Joint Stock Company «Ukrainian Energy Machines», Kharkiv, Ukraine
Igor Kravchenko	SE Ivchenko-Progress, Zaporizhzhia, Ukraine
Anatolii Boiko	National Technical University «Kharkiv Polytechnic Institute», Kharkiv, Ukraine
Yurii Matsevity	A. Pidhornyi Institute of Mechanical Engineering Problems of the National Academy of Sciences of Ukraine, Kharkiv, Ukraine
Oleksandr Shubenko	A. Pidhornyi Institute of Mechanical Engineering Problems of the National Academy of Sciences of Ukraine, Kharkiv, Ukraine
Anatolii Tarelin	A. Pidhornyi Institute of Mechanical Engineering Problems of the National Academy of Sciences of Ukraine, Kharkiv, Ukraine

General Chair

Andrii Rusanov	A. Pidhornyi Institute of Mechanical Engineering Problems of the National Academy of Sciences of Ukraine, Kharkiv, Ukraine

Co-chair

Andrii Kostikov	A. Pidhornyi Institute of Mechanical Engineering Problems of the National Academy of Sciences of Ukraine, Kharkiv, Ukraine

Steering Committee

Svitlana Alyokhina	A. Pidhornyi Institute of Mechanical Engineering Problems of the National Academy of Sciences of Ukraine, Kharkiv, Ukraine
Vitaliy Goman	A. Pidhornyi Institute of Mechanical Engineering Problems of the National Academy of Sciences of Ukraine, Kharkiv, Ukraine
Denis Kriutchenko	A. Pidhornyi Institute of Mechanical Engineering Problems of the National Academy of Sciences of Ukraine, Kharkiv, Ukraine
Sergii Misiura	A. Pidhornyi Institute of Mechanical Engineering Problems of the National Academy of Sciences of Ukraine, Kharkiv, Ukraine
Tetiana Protasova	A. Pidhornyi Institute of Mechanical Engineering Problems of the National Academy of Sciences of Ukraine, Kharkiv, Ukraine
Andrii Shpak	A. Pidhornyi Institute of Mechanical Engineering Problems of the National Academy of Sciences of Ukraine, Kharkiv, Ukraine
Natalia Smetankina	A. Pidhornyi Institute of Mechanical Engineering Problems of the National Academy of Sciences of Ukraine, Kharkiv, Ukraine
Anna Vorontsova	A. Pidhornyi Institute of Mechanical Engineering Problems of the National Academy of Sciences of Ukraine, Kharkiv, Ukraine
Mykola Zipunnikov	A. Pidhornyi Institute of Mechanical Engineering Problems of the National Academy of Sciences of Ukraine, Kharkiv, Ukraine

Program Committee

Almeida Júnior, José Humberto Santos	Queen's University Belfast, UK
Holm Altenbach	Otto-von-Guericke Magdeburg University, Magdeburg, Germany
Svitlana Alyokhina	A. Pidhornyi Institute of Mechanical Engineering Problems of the National Academy of Sciences of Ukraine, Kharkiv, Ukraine
Andrii Avramenko	A. Pidhornyi Institute of Mechanical Engineering Problems of the National Academy of Sciences of Ukraine, Kharkiv, Ukraine
Kostiantyn Avramov	A. Pidhornyi Institute of Mechanical Engineering Problems of the National Academy of Sciences of Ukraine, Kharkiv, Ukraine

Ivan Breslavsky	McGill University, Montreal, Quebec, Canada
Alexander Cheng	University of Mississippi, Brevard, USA
Olga Chernousenko	National Technical University of Ukraine «Igor Sikorsky Kyiv Polytechnic Institute»
Neelam Choudhary	Bennett University, Greater Noida, India
Ney Augusto Dumont	Pontifical Catholic University of Rio de Janeiro, Brazil
Xiao-Wei Gao	Dalian University of Technology, Dalian, China
Oleksandr Grygorenko	Taras Shevchenko National University of Kyiv, Ukraine
Vitalii Ivanov	Sumy State University, Sumy, Ukraine
Mohammed Kaabar	Washington State University, Pullman, WA, USA
Andreas Karageorghis	University of Cyprus, Cyprus
Andrii Kondratiev	O.M. Beketov National University of Urban Economy, Kharkiv, Ukraine
Oleg Kravchenko	A. Pidhornyi Institute of Mechanical Engineering Problems of the National Academy of Sciences of Ukraine, Kharkiv, Ukraine
Wladyslaw Kryllowicz	Lodz University of Technology, Lodz, Poland
Piotr Lampart	Robert Szewalski Institute of fluid-flow machinery of Polish Academy of Sciences, Gdańsk, Poland
Oleksiy Larin	National Technical University «Kharkiv Polytechnic Institute», Kharkiv, Ukraine
Mathias Legrand	McGill University, Montreal, Quebec, Canada
Yevgen Levchenko	Joint Stock Company «Ukrainian Energy Machines», Kharkiv, Ukraine
Mykhaylo Lototskyy	University of the Western Cape, Bellville, South Africa
Martin Luxa	Institute of Thermomechanics Academy of Sciences of the Czech Republic, Praha, Czech Republic
Gennadiy Lvov	National Technical University «Kharkiv Polytechnic Institute», Kharkiv, Ukraine
Kyrylo Maksymenko-Sheiko	A. Pidhornyi Institute of Mechanical Engineering Problems of the National Academy of Sciences of Ukraine, Kharkiv, Ukraine
José-Antonio Marmolejo-Saucedo	Universidad Panamericana, Ciudad de Mexico, Mexico
Gennadii Martynenko	National Technical University «Kharkiv Polytechnic Institute», Kharkiv, Ukraine
Sergiy Plankovskyy	O.M. Beketov National University of Urban Economy, Kharkiv, Ukraine

Viktor Popov	Ascend Technologies Ltd, Wessex House, Hampshire, UK
Robertas Poškas	Lithuanian Energy Institute, Kaunas, Lithuania
Jure Ravnik	University of Maribor, Slovenia
Tetiana Romanova	A. Pidhornyi Institute of Mechanical Engineering Problems of the National Academy of Sciences of Ukraine, Kharkiv, Ukraine
Stavros Syngellakis	Wessex Institute (WIT), Ashurst, Southampton, UK
Vladimir Sladek	Institute of Construction and Architecture, Slovak Academy of Sciences, Bratislava, Slovak Republic
Natalia Smetankina	A. Pidhornyi Institute of Mechanical Engineering Problems of the National Academy of Sciences of Ukraine, Kharkiv, Ukraine
Victor Solovey	A. Pidhornyi Institute of Mechanical Engineering Problems of the National Academy of Sciences of Ukraine, Kharkiv, Ukraine
Yurii Stoyan	A. Pidhornyi Institute of Mechanical Engineering Problems of the National Academy of Sciences of Ukraine, Kharkiv, Ukraine
Olena Strelnikova	A. Pidhornyi Institute of Mechanical Engineering Problems of the National Academy of Sciences of Ukraine, Kharkiv, Ukraine
Antonio Tadeu	University of Coimbra, Portugal
Ihor Yanchevskii	National Technical University of Ukraine «Igor Sikorsky Kyiv Polytechnic Institute»

Invited External Reviewers

Humberto Almeida	Queen's University Belfast, UK
Ney Augusto Dumont	Pontifical Catholic University of Rio de Janeiro, Brazil
Neelam Choudhary	Bennett University, Greater Noida, India
Mohammed Kaabar	Washington State University, Pullman, WA, USA
Kirill Kabalyk	Lodz University of Technology, Lodz, Poland
Piotr Klonowicz	Robert Szewalski Institute of fluid-flow machinery of Polish Academy of Sciences, Gdańsk, Poland
Wladyslaw Kryllowicz	Lodz University of Technology, Lodz, Poland
Piotr Lampart	Robert Szewalski Institute of fluid-flow machinery of Polish Academy of Sciences, Gdańsk, Poland

Mykhaylo Lototskyy	University of the Western Cape, Bellville, South Africa
Minavar Mir-Salim-Zade	Institute of Mathematics and Mechanics of NAS of Azerbaijan
Chitaranjan Pany	VSSC, Trivandrum, Kerala, India
David Simurda	Institute of Thermomechanics of the Czech Academy of Sciences, Czechia
Artur Szymanski	Cranfield University, Cranfield, UK
Lukasz Witanowski	Robert Szewalski Institute of fluid-flow machinery of Polish Academy of Sciences, Gdańsk, Poland

Contents

Fluid Mechanics and Heat Transfer in Power Engineering

Influence of Compressibility in Fluid - Structure Interaction Problems for Fluid-Filled Reservoirs

Neelam Choundhary[1] , Olga Usatova[2] , Denis Kriutchenko[2],
and Elena Strelnikova[2,3(✉)]

[1] Bennet University, Plot No. 9-11, Techzone II, Greater Noida 201310, Uttar Pradesh, India
[2] A. Podgorny Institute of Mechanical Engineering Problems NASU, Pozharsky, St. 2/10,
Kharkiv 61046, Ukraine
elena15@gmx.com
[3] V.N. Karazin Kharkiv National University, Svobody Sq., 4, Kharkov 61022, Ukraine

Abstract. The objective of this paper is to develop an effective numerical method for analyzing vibrations of fluid-filled elastic shells of revolution. The novelty of the proposed method consists in elaborating the unified approach for high accuracy evaluation of own frequencies and modes of empty and fluid-filled elastic shells, and compressible liquid sloshing in rigid reservoirs. The system of differential equations is obtained to describe compressibility effects in the acoustic approximation. Numerical simulation is based on coupled finite and boundary element methods involving singular integral equations; the integral presentations are corresponded to the Helmholtz equation. All unknown functions are presented as Fourie's series. This has allowed to obtain finally the one-dimensional integral equations. The eigenvalue problems for vibration analysis of reservoirs with compressible liquid are formulated, and the iterative method is proposed for their numerical solution. Accuracy and reliability of the proposed methods are ascertained. Numerical results demonstrate the mutual influence of compressibility, elasticity, and liquid sloshing. It is shown that compressibility effects are especially significant at high wave numbers. For sufficiently thin elastic shells, the lowest frequencies of vibration are obtained namely at the high harmonics. In such cases, the neglect of compressibility can lead to the incorrect resonance detuning.

Keywords: Elastic shell · Vibration · Compressibility · Sloshing · Helmholtz's equation · Boundary and finite element methods

1 Introduction

Fluid–structure interaction (FSI) problems are studied by many researchers during last decades. At simulations, elements of mechanical engineering structures are often considered as thin shells, partially filled with liquids. Therefore, the strength analysis of such structures should be carried out in coupled formulations, taking into account the interaction of two media.

In this paper, an effective method is proposed for estimating own frequencies of liquid-filled shells. The effects of elasticity of shell walls, compressibility of liquids, and free surface sloshing are studied and their mutual influence is analyzed.

FSI is one of the main problems in many engineering applications such as turbine engineering [1, 2], chemical industry [3], transport [4], spacecraft designs [5, 6] with analysis of strength [7] and vibration [8] characteristics of fuel tanks, etc.

Free vibrations of liquids and their suppression in rigid shells and shell structures are well studied. In [9, 10] the baffles are considered as slosh suppression devices in rigid cylindrical shells. Forced liquid vibrations in rigid containers are studied in [11]. In [12, 13] it was shown that viscosity and compressibility of liquids have a big impact on dynamical characteristics of structure elements under intensive impulsive loading. Sloshing problems in rigid containers in nonlinear formulations are considered in [5, 14]. Review in [15] indicates that the elasticity influence of the tank walls can be significant in the vibration analysis. Thus, the problem of vibrations of liquid-filled shells is far from its full solution. The dynamic characteristics of shells with liquid should be determined taking into account the mutual influence of various factors.

2 Methodology

2.1 Basic Relations

The objective of this contribution is to study vibrations of an elastic shell filled with a liquid. The shell of revolution, partially filled with the compressible liquid, is considered. The Cartesian coordinate system Oxyz is connected with the shell (Fig. 1). Below there are the basic relations that describe coupled shell-fluid interaction.
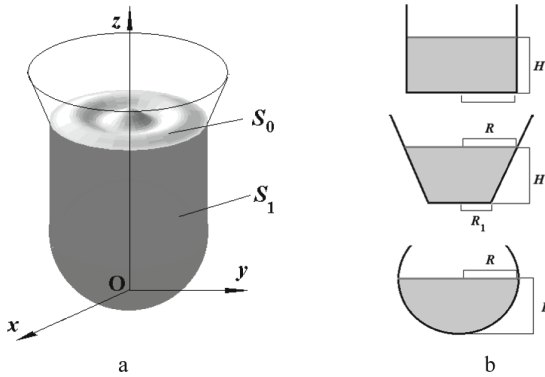
Fig. 1. Fluid-filled shell of revolution and drafts of cylindrical, conical, and spherical shells

Suppose that the liquid is an inviscid and compressible one. The equations of motion of the shell with the liquid are following [11]:

$$\mathbf{L}(\mathbf{U}) + \mathbf{M}(\ddot{\mathbf{U}}) = \mathbf{P}. \tag{1}$$

Here vectors $\mathbf{U}$ and $\mathbf{P}$ are the shell displacements and a liquid pressure on the wetted surface S_1, operators $\mathbf{L}$ and $\mathbf{M}$ are stiffness and mass matrices. Notice that the vector $\mathbf{P}$ is directed along the normal $\mathbf{n}$ to the wetted shell walls if the ideal liquid is considered.

To define the unknown pressure, we use the mass and momentum conservation laws

$$\frac{\partial \rho}{\partial t} = -\mathrm{div}(\rho \mathbf{V}_f) + Q, \ \rho \frac{d\mathbf{V}_f}{dt} = \rho \mathbf{b} + \mathrm{div}(\sigma_f), \tag{2}$$

where $\mathbf{V}_f$ is the liquid velocity, ρ is the liquid density, Q is for mass sources, vector $\mathbf{b}$ is volume forces, σ_f is the stress tensor.

To determine the components of the stress tensor σ_f, the following hypothesis is used:

$$\sigma_f = -p\mathbf{I} + \mathbf{T}; \quad \mathbf{T} = 2\mu \left(\dot{\mathbf{S}} - \frac{1}{3}\mathrm{div}(\mathbf{V}_f)\mathbf{I} \right).$$

Here $\dot{\mathbf{S}}$ is the strain-rate deviator, $\mathbf{I}$ is the unit tensor, and μ is the liquid viscosity coefficient. Let $p = |\mathbf{P}|$. Using the equations of state $p = p(\rho)$, $\frac{\partial p}{\partial \rho} = c^2$, and supposing $\mathbf{b} = 0$, one can obtain the acoustic approximation of Eqs. (2) as

$$\mathrm{div}\mathbf{V}_f = -\frac{1}{\rho_0 c^2}\frac{\partial p}{\partial t} + \frac{Q}{\rho_0}, \ \frac{\partial \mathbf{V}_f}{\partial t} = -\frac{1}{\rho_0}\nabla p + \frac{\mu}{3\rho_0}\nabla \mathrm{div}\mathbf{V}_f + \frac{\mu}{\rho_0}\Delta \mathbf{V}_f. \tag{3}$$

Here ρ_0 is the average value of the liquid density at linearization, c is the speed of sound. Considering divergence from the second equation in (3) with $Q = 0$, we have

$$\mathrm{div}\left(\frac{1}{\rho_0}\nabla p \right) - \frac{1}{\rho_0 c^2}\frac{\partial^2 p}{\partial t^2} + \mathrm{div}\left[\frac{4\mu}{3\rho_0}\nabla \left(\frac{1}{\rho_0 c^2}\frac{\partial p}{\partial t} \right) \right] = 0.$$

Then the following differential equation is obtained

$$\frac{1}{\rho_0 c^2}\frac{\partial^2 p}{\partial t^2} = \frac{1}{\rho_0}\mathrm{div}(\nabla p) + \frac{4\mu}{3\rho_0^2 c^2}\mathrm{div}\left[\nabla \left(\frac{\partial p}{\partial t} \right) \right] = 0. \tag{4}$$

It follows from Eq. (4) that viscosity contributes significantly less than compressibility. So, to define the pressure of the ideal compressible liquid we receive

$$\frac{1}{c^2}\frac{\partial^2 p}{\partial t^2} - \mathrm{div}(\nabla p) = 0. \tag{5}$$

The second equation in (3) without mass sources Q takes the form

$$\frac{\partial \mathbf{V}_f}{\partial t} = -\frac{1}{\rho_0}\nabla p. \tag{6}$$

Equation (5) in the fluid domain bounded by surfaces $S = S_1 \cup S_0$, is used to calculate the pressure p. So, it is necessary to apply boundary conditions. The non-penetration condition is satisfied at the shell inner wetted surface S_1, so $(\dot{\mathbf{U}}, \mathbf{n}) = (\mathbf{V}_f, \mathbf{n})$, where $\mathbf{n}$ is the unit outward normal to the surface S_1. It follows from Eqs. (3), (6) that

$$(\nabla p, \mathbf{n}) = -\rho_0 (\ddot{\mathbf{U}}, \mathbf{n})\big|_{S_1}. \tag{7}$$

At the free surface S_0, kinematic and dynamic conditions are set according to [11].

From the dynamic condition we have $p = \rho_0 g\zeta$. Here $\zeta = \zeta(x, y, t)$ is an unknown time-dependent function of the free surface elevation. According to the kinematic conditions, the following approximate equations are received at the free surface:

$$\frac{\partial \zeta}{\partial t} = (\mathbf{V}_f, \mathbf{n}), \quad \frac{\partial^2 \zeta}{\partial t^2} = \left(\frac{\partial \mathbf{V}_f}{\partial t}, \mathbf{n}\right) = \left(-\frac{1}{\rho_0}\nabla p, \mathbf{n}\right).$$

So, at the free surface S_0 we have

$$\zeta = \frac{p}{\rho_0 g}, \quad \left.\frac{\partial p}{\partial \mathbf{n}}\right|_{S_0} = -\frac{1}{g}\frac{\partial^2 p}{\partial t^2}. \tag{8}$$

Thus, the motion of the coupled "shell-fluid" system is described by the next system of differential equations with unknown functions $\mathbf{U}$ and p:

$$\mathbf{L}(\mathbf{U}) + \mathbf{M}(\ddot{\mathbf{U}}) = \rho\mathbf{n}, \tag{9}$$

$$\frac{1}{c^2}\frac{\partial^2 p}{\partial t^2} - \operatorname{div}(\nabla p) = 0, \quad (\nabla p, \mathbf{n})|_{S_1} = -\rho_0(\ddot{\mathbf{U}}, \mathbf{n}), \quad (\nabla p, \mathbf{n})|_{S_0} = -\frac{1}{g}\frac{\partial^2 p}{\partial t^2}. \tag{10}$$

Boundary value problem (9)-(10) is completed by conditions of the shell fixation, and initial conditions assuming that the sloshing motion starts from the state of rest.

2.2 Eigenvalue Problems for Shells Partially Filled with Compressible Liquid

Consider harmonic oscillations and suppose that

$$p(x, y, z, t) = \exp(i\omega t)\varphi(x, y, z), \quad \mathbf{U}(x, y, z, t) = \exp(i\omega t)\mathbf{u}(x, y, z), \tag{11}$$

Then for the function $\varphi(x, y, z)$, the Helmholtz equation is received as $\frac{\omega^2 \varphi}{c^2} + \nabla^2\varphi = 0$.

Represent this function as the sum $\varphi = \varphi_1 + \varphi_2$ of two auxiliary functions. Next, the following boundary value problems are formulated tor unknown functions φ_1 and φ_2.

The function φ_1 describes the compressible liquid sloshing in the rigid shell, so

$$\frac{\omega^2 \varphi_1}{c^2} + \nabla^2\varphi_1 = 0, \quad (\nabla\varphi_1, \mathbf{n}) = 0|_{S_1}, \quad (\nabla\varphi_1, \mathbf{n}) = -\left.\frac{\omega^2 \varphi_1}{g}\right|_{S_0}. \tag{12}$$

The function φ_2 describes vibrations process in the fluid-filled shell with elastic walls but without sloshing

$$\frac{\omega^2 \varphi_2}{c^2} + \nabla^2\varphi_2 = 0, \quad (\nabla\varphi_2, \mathbf{n}) = -\omega^2(\mathbf{u}, \mathbf{n})\Big|_{S_1}, \quad \varphi_2 = 0|_{S_0}. \tag{13}$$

Using Eqs. (9), (11), the coupled problem to study vibrations of elastic shells partially filled with compressible liquids is formulated as the system of differential equations and boundary conditions (12), (13) and the following equations

$$\mathbf{L}(\mathbf{u}) - \omega^2 \mathbf{M}(\mathbf{u}) = (\varphi_1 + \varphi_2)\mathbf{n}. \tag{14}$$

So, it is necessary to define functions $\varphi_1, \varphi_2, \mathbf{u}$ and frequencies ω from Eqs. (12)-(14). These equations represent the eigenvalue problem.

Let Ω be the domain occupied by the liquid, with boundaries $S = S_1 \cup S_0$, Fig. 1a). As it is assumed beforehand, Ω is the body of revolution, so the cylindrical coordinates system ρ, θ, z is introduced. Note that the free liquid surface in reservoirs may evolve in many different modes. These modes are usually defined by their wave numbers m and mode numbers n corresponded to each wave number. As in [11], all the unknown functions are presented as Fourie's series, namely:

$$\mathbf{u} = \sum_{m=0}^{\infty} \cos m\theta \sum_{n=0}^{\infty} \mathbf{u}^{mn}, \quad \varphi_i = \sum_{m=0}^{\infty} \cos m\theta \sum_{n=0}^{\infty} \varphi_i^{mn}, i = 1, 2. \tag{15}$$

According to [5, 11], Eqs. (15) allow us to obtain finally the one-dimensional integral equations for evaluating the pressure for each m and n.

We begin with eigenvalue problem (12) considering the rigid shell with the compressible liquid. For numerical simulation the boundary element method (BEM) [11] is implemented by using the fundamental solution $G(\mathbf{P}, \mathbf{P}_0)$ of the Helmholtz equation as in [16].

So, the integral equation for determining the function φ_1 is following

$$2\pi \varphi_1(\mathbf{P}_0) = \frac{\omega^2}{g} \iint_{S_0} \varphi_1(\mathbf{P}) G(\mathbf{P}, \mathbf{P}_0) dS - \iint_{S} \varphi_1(\mathbf{P}) \frac{\partial}{\partial \mathbf{n}} G(\mathbf{P}, \mathbf{P}_0) dS, \tag{16}$$

where $G(\mathbf{P}, \mathbf{P}_0) = \frac{\exp(ikr)}{r}, r = |\mathbf{P} - \mathbf{P}_0|, k = \frac{\omega}{c}, \mathbf{P} = (\rho, \theta, z), \mathbf{P}_0 = (\rho_0, \theta_0, z_0)$.

The integral operators on a surface S with a generatrix Γ are introduced as in [11]

$$\mathbf{A}(\sigma, \mathbf{S})p(\mathbf{P}) = \iint_{S} p(\mathbf{P}) G(\mathbf{P}, \mathbf{P}_0) dS = \int_{\Gamma} p(r, z)\Psi(\mathbf{P}, \mathbf{P}_0) d\Gamma, \quad \mathbf{P}_0 \in \sigma, \tag{17}$$

$$\mathbf{B}(\sigma, \mathbf{S})p(\mathbf{P}) = \iint_{S} p(\mathbf{P}) \frac{\partial}{\partial \mathbf{n}} G(\mathbf{P}, \mathbf{P}_0) dS = \int_{\Gamma} p(r, z)\Theta(\mathbf{P}, \mathbf{P}_0) d\Gamma, \mathbf{P} \in S, \tag{18}$$

where kernels $\Theta(\mathbf{P}, \mathbf{P}_0)$ and $\Psi(\mathbf{P}, \mathbf{P}_0)$ have logarithmical singularities.

Let $\{\xi_k\}_{k=1}^{N_1+N_0}$ be nodes of finite-boundary element net, N_0 is the number of the nodes on the free surface, N_1 corresponds to nodes of the shell wetted walls, and $N = N_1 + N_0$. Introducing the following vectors of the unknown function φ_1^{mn} values of in these nodes as $\{\varphi_{10}^{mn}\} = \{\varphi_1^{mn}(\xi_j)\}_{j=1}^{N_0}, \{\varphi_{11}^{mn}\} = \{\varphi_1^{mn}(\xi_j)\}_{j=N_0+1}^{N}$, we receive the eigenvalue problem for evaluation the own modes and frequencies of the liquid in the rigid shell

$$\mathbf{A}_0(k)\{\varphi_{10}^{mn}\} = \frac{\omega^2}{g} \mathbf{B}_0(k)\{\varphi_{10}^{mn}\}, \tag{19}$$

where $\mathbf{A}_0 = 2\pi\mathbf{I} + \mathbf{B}(S_0, S_1)\mathbf{C}^{-1}\mathbf{B}(S_1, S_0)$, $\mathbf{C} = 2\pi\mathbf{I} + \mathbf{B}(S_1, S_1)$, $\mathbf{B}_0 = \mathbf{A}(S_0, S_0) + \mathbf{B}(S_0, S_1)\mathbf{C}^{-1}\mathbf{A}(S_1, S_0)$. For determining the values of pressure $\{\varphi_{11}^{mn}\}$ on the wetted surface S_1 we have

$$\{\varphi_{11}^{mn}\} = \mathbf{C}^{-1}[\mathbf{B}(S_1, S_0) - \frac{\omega^2}{g}\mathbf{A}(S_1, S_0)]\{\varphi_{10}^{mn}\}. \tag{20}$$

The numerical solution of Eqs. (19) is based on reduced BEM [11]. The surface integrals (17)-(18) are reduced to one-dimensional ones, and for their evaluation the effective method is in use [17]. The difficulty of BEM implementation consists in necessity to solve singular integral equations with unknown kernels, i.e. with an unknown coefficient $k = \frac{\omega}{c}$. So, the iterative method for numerical treatment of Eqs. (19) is proposed. As first approximation we consider $k = 0$ that corresponds to incompressible liquid. Herein the values of frequencies ω_n^m and modes are received for each wave number m. Then for each m and n at the next iteration, the value $k = \frac{\omega_n^m}{c}$ is calculated. The process continues until $|\omega_n^{m\ (i)} - \omega_n^{m\ (i+1)}| > \varepsilon$ on adjacent iterations, with ε as the given accuracy. The proposed method allows us to obtain the own modes and frequencies of vibrations for both incompressible and compressible liquids in rigid shells. This problem is also the auxiliary one for coupled problem (12)-(14).

Next, consider eigenvalue problems for elastic shells with compressible liquid.

Vibrations of elastic shells, partially filled with compressible liquid, without sloshing, are described by the following equations

$$\mathbf{L}(\mathbf{u}) - \omega^2\mathbf{M}(\mathbf{u}) = \varphi_2, \frac{\omega^2\varphi_2}{c^2} + \nabla^2\varphi_2 = 0, \ (\nabla\varphi_2, \mathbf{n}) = -\omega^2(\mathbf{u}, \mathbf{n})\Big|_{S_1}, \ \varphi_2 = 0|_{S_0}. \tag{21}$$

Introducing vectors of values of the unknown functions in the nodes $\{\xi_k\}_{k=1}^{N_1+N_0}$ as $\{\mathbf{u}^{mn}\} = \{\mathbf{u}^{mn}(\xi_j)\}_{j=1}^{N_1}$, $\{\varphi_{21}^{mn}\} = \{\varphi_2^{mn}(\xi_j)\}_{j=N_0+1}^{N}$ and using the integral presentation for Helmholtz' equation as in [16], we receive

$$\{\varphi_{21}^{mn}\} = \omega^2\mathbf{H}\{\mathbf{u}^{mn}\}, \mathbf{H} = \mathbf{H}_1^{-1}\mathbf{H}_2. \tag{22}$$

$$\mathbf{H}_1 = 2\pi\mathbf{I} + \mathbf{B}^{-1}(S_1, S_1)\mathbf{A}(S_1, S_0)\mathbf{A}^{-1}(S_0, S_0)\mathbf{B}(S_0, S_1),$$

$$\mathbf{H}_2 = \mathbf{B}^{-1}(S_1, S_1)\mathbf{A}(S_1, S_0) - \mathbf{A}(S_1, S_0)\mathbf{A}^{-1}(S_0, S_0)\mathbf{A}(S_0, S_1).$$

With applying (22), the first equation in (21) takes the form

$$\mathbf{L}\{\mathbf{u}^{mn}\} - \omega^2[\mathbf{M} + \mathbf{H}]\{\mathbf{u}^{mn}\} = 0. \tag{23}$$

So, we obtain the eigenvalue problem for evaluating the vibration modes $\{\mathbf{u}^{mn}\}$ and frequencies ω^{mn} of the elastic shell, with added liquid masses, but without sloshing.

Finally, the coupled eigenvalue problem for elastic shells partially filled with compressible liquid including sloshing effects is described by Eqs. (12)-(14). For pressure $\{\varphi_{11}^{mn}\}$ we have Eq. (20), and pressure $\{\varphi_{21}^{mn}\}$ is received from Eq. (22). So, Eq. (14) takes

the form $\mathbf{L}\{\mathbf{u}^{mn}\} - \omega^2[\mathbf{M} + \mathbf{H}]\{\mathbf{u}^{mn}\} = \mathbf{C}^{-1}[\mathbf{B}(S_1, S_0) + \frac{\omega^2}{g}\mathbf{A}(S_1, S_0)]\{\varphi_{10}^{mn}\}$. Then this equation is rewritten as follows

$$\tilde{\mathbf{L}}\{\mathbf{f}^{mn}\} - \omega^2\tilde{\mathbf{M}}\{\mathbf{f}^{mn}\} = 0, \tag{24}$$

where extended matrices are introduced

$$\tilde{\mathbf{L}} = \begin{pmatrix} \mathbf{L} & 0 \\ 0 & \mathbf{C}^{-1}\mathbf{B}(S_1, S_0) \end{pmatrix}, \tilde{\mathbf{M}} = \begin{pmatrix} \mathbf{M} + \mathbf{H} & 0 \\ 0 & \mathbf{C}^{-1}\frac{1}{g}\mathbf{A}(S_1, S_0) \end{pmatrix}, \{\mathbf{f}^{mn}\} = \begin{Bmatrix} \{\mathbf{u}^{mn}\} \\ \{\varphi_{10}^{mn}\} \end{Bmatrix}.$$

So, the eigenvalue problem is formulated in more general formulation.

3 Results and Discussion

3.1 Numerical Simulation of Liquid Vibrations in Rigid Shells

Modes and frequencies of free liquid vibrations for rigid conical, spherical and cylindrical rigid shells (Fig. 1b) are evaluated by solving eigenvalue problem (12) using proposed BEM for its numerical implementation. It is supposed that $R = 1$ m, $H = 1$ m, for all shells under consideration, and $R_1 = 0.5$ m for truncated conical shell.

First, the required number of boundary elements along shell meridians and radii of the free surface is determined as $N = 240$ to achieve accuracy $\varepsilon = 10^{-4}$. Table 1 below provides the numerical values of the natural frequencies of liquid sloshing for $m = 0,1$ for different shells, and comparison with known analytical and numerical data.

Table 1. Frequency parameter χ_{0k}^2/g for different shells

M	n	Conical shell	Spherical shell		Cylindrical shell	
		Present study	Present study	Numerical results [15]	Present study	Analytical results [15]
0	1	3.4665	3.7454	3.7451	3.8281	3.8281
	2	6.6810	6.9767	6.9763	7.0160	7.0159
	3	9.8453	10.1479	10.1474	10.1732	10.1734
1	1	1.3052	1.5603	1.5601	1.7501	1.7501
	2	4.9255	5.2759	5.2755	5.3392	5.3293
	3	8.1411	8.5060	8.5044	8.5362	8.5366

For slosh frequencies in the rigid cylindrical shell, the analytical solution [15] is used

$$\frac{\omega_{mn}^2}{g} = \frac{\mu_{mn}}{R}\tanh\left(\mu_{mn}\frac{H}{R}\right), n = 1, 2, .., \varphi_{2mn} = J_m\left(\frac{\mu_n}{R}r\right)\cosh\left(\frac{\mu_n}{R}z\right)\cosh^{-1}\left(\frac{\mu_n}{R}H\right). \tag{25}$$

Here values μ_n are roots of the equation $J'_m(x) = 0$, where $J_m(x)$ is the Bessel function of the first kind ω_{mn}, φ_{2mn} are liquid sloshing frequencies and modes. The numerical solution is obtained by using the proposed BEM and compared with analytical solution (25). The numerical data of [15] for spherical shells are also used for comparison. Noted, that for $m = 0,1$ the difference between frequencies for compressible and incompressible liquids is quite small. But with increasing the wave number the difference became more notable. For instance, in Table 2 there are natural frequencies $_{6n}$ for compressible and incompressible liquids compared with the numerical data of [15, 18].

Table 2. Natural frequencies of compressible and incompressible liquids, $_{6n}$, Hz

n	Compressible liquid		Incompressible liquid	
	Present study	Results of [18]	Present study	Results of [15]
1	1.363	1.365	1.363	1.363
2	1.707	1.707	1.707	1.707
3	1.947	1.948	2.152	2.152

The results of Table 2 demonstrate that compressibility reduces the natural frequencies for high wave numbers. The iteration process for receiving the frequencies of sloshing, including compressibility influence, is convergent in 3–4 iterations.

3.2   Numerical Simulation of Elastic Shell Vibrations Coupled with Liquid Sloshing

We have studied coupled vibrations of the "elastic shell - incompressible fluid" system and estimated the parameters at which the effect of wall elasticity cannot be neglected. At simulations, the circular cylindrical elastic shell, partially filled with the liquid, has been considered, with geometrical and mechanical parameters of [11]. We supposed that the shell bottom is elastic, and the shell is clamped along the bottom contour. Equations (24) have been used for numerical implementation. Some lowest frequencies of coupled vibrations of fluid-filled cylindrical shells with different thickness h are presented in Table 3.

Results of Table 3 demonstrate that the lowest frequencies of the elastic shells decrease with decreasing the shell thickness. So, for very thin elastic shell, the lowest coupled frequency will be much smaller than the fundamental liquid frequency. In such cases, the effect of wall elasticity is very significant. This also does not allow to consider separately the spectra of frequencies of the shell and liquid sloshing.

The vibration modes corresponding to frequencies ω_{11}, ω_{01}, $\omega_{0,26}$, and $\omega_{0,34}$, are shown in Fig. 2a)-Fig. 2d).

The different nature of the vibration is expressed by the vector $\{\mathbf{f}^{mn}\}$ in Eq. (24) that determines the dominant modes. Finite element method is used for evaluation of matrices $\mathbf{L}$ and $\mathbf{M}$, as in [7, 11].

Table 3. Frequencies of fluid-filled elastic cylindrical shells

M	n	h/R = 0.01	h/R = 0.0015	Type of dominate vibration modes
1	1	0.6422	0.6422	liquid sloshing
0	1	0.97441	0.9744	liquid sloshing
0	10	5.5213	0.8644	bottom vibration
0	26	43.8628	7.0645	wall vibration
0	34	210.0076	41.1698	vibration of wall and free surface

| a | b | c | d |
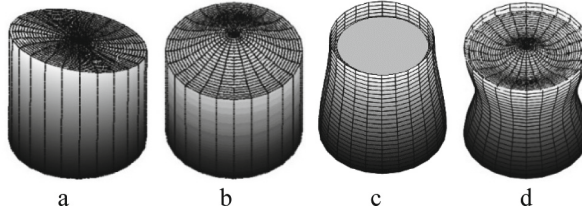
Fig. 2. Modes of vibrations of "elastic shell - incompressible fluid" system

The compressibility effects are not essential at these wave numbers. But the fixation conditions can lead to a significant change in frequencies. Thus, it was shown in [19] that the lowest vibration frequencies of elastic shells with rigid bottoms were obtained at the 6th -7th harmonics. Namely for such harmonics, as shown above, the effect of compressibility leads to notable changing in the frequency characteristics.

As advantages of the proposed method, it should be mentioned the possibility to estimate: frequencies of empty shell ($p = 0$ in Eqs. (9); sloshing frequencies, when the only Eq. (12) is under consideration; frequencies of fluid-filled shell without including free surface effects, when Eqs. (13) and (14) are solved; frequencies of elastic shells including sloshing from Eqs. (12)-(14), and also the possibility to estimate the abovementioned frequencies for both compressible and incompressible liquids. The importance of the proposed method consists in possibility to analyze the dominating vibration modes. Among them there are sloshing dominating modes, structure dominating modes with added liquid masses, coupled modes, combining the structure and the fluid vibrations. The disadvantages are linear formulation constraints due to the acoustic approximation, neglect of damping and viscosity.

4   Conclusion and Future Research

The approach based on the boundary and finite element methods is proposed to study the frequencies and modes of vibrations of fluid-filled elastic shells of revolution. The eigenvalue problems are formulated for rigid shells with compressible liquid, for elastic shells partially filled with compressible liquid with and without including sloshing effects. The singular integral equations are received by using the fundamental solution of

the Helmholtz equation. Accuracy and reliability of the proposed method are ascertained. The effects of compressibility are estimated. It was demonstrated that with increasing the wave number, starting from the 6th harmonic, these effects became notable, and neglection of compressibility for these wave numbers can lead to incorrect resonance detuning. It has been established that the effect of wall elasticity is significant at relative shell thicknesses less than 0.001. At the next stage, the developed methodology will be generalized for studying nonlinear vibrations.
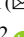
References

1. Rusanov, A., Shubenko, A., Senetskyi, O., Babenko, O., Rusanov, R.: Heating modes and design optimization of cogeneration steam turbines of powerful units of combined heat and power plant. Energetika **65**(1), 39–50 (2019). https://doi.org/10.6001/energetika.v65i1.3974
2. Misura, S., Smetankina, N., Misiura, Ie.: Optimal design of the cyclically symmetrical structure under static load. Integrated Computer Technologies in Mechanical Engineering-2020. Springer, Cham, pp. 256–266 (2020). https://doi.org/10.1007/978-3-030-66717-7_21
3. Shirsendu, M., Mukherjee, S., Ghosh, A., Bandyopadhyay, D.: Industrial & Engineering Chemistry Research **58**(16), 6756–6766 (2019). https://doi.org/10.1021/acs.iecr.8b06345
4. Valsamos, G., Casadei, F., Solomos, G., Larcher, M.: Risk assessment of blast events in a transport infrastructure by fluid- structure interaction analysis. Safety Science **118**, 887–897 (2019). https://doi.org/10.1016/j.ssci.2019.06.014
5. Strelnikova, E., Kriutchenko, D., Gnitko, V., Degtyarev, K.: Boundary element method in nonlinear sloshing analysis for shells of revolution under longitudinal excitations. Engineering Analysis with Boundary Elements **111**, 78–87 (2020). https://doi.org/10.1016/j.enganabound.2019.10.008
6. Zhang, C., Zhang, Q., Zhu, Z., Yao, D., Yang, P., Zong, Y., Chen, S.: Numerical simulation of thermal–structural behaviour of liquid helium tank during filling process. Fusion Engineering and Design **173**, 112798 (2021). https://doi.org/10.1016/j.fusengdes.2021.112798
7. Gontarovskyi, P., Smetankina, N., Garmash, N., Melezhyk, I.: Improvement of computational methods for estimating the stress-strain state of fuel tanks of launch vehicles in 3D formulation. Integrated Computer Technologies in Mechanical Engineering-2020, 188. Springer, Cham 609–619 (2021). https://doi.org/10.1007/978-3-030-66717-7_52
8. Zaitsev, B.P., Protasova, T.V., Smetankina, N.V., Klymenko, D.V., Larionov, I.F., Akimov, D.V.: Oscillations of the payload fairing body of the cyclone-4M launch vehicle during separation. Strength Mater. **52**(6), 849–863 (2020). https://doi.org/10.1007/s11223-021-00239-5
9. Behshad, A., Shekari, M.: A boundary element study for evaluation of the effects of the rigid baffles on liquid sloshing in rigid containers. International Journal of Maritime Technology **10**, 45–54 (2018). https://doi.org/10.29252/ijmt.10.45
10. Tao, K., Zhou, X., Ren, H.: A novel improved coupled dynamic solid boundary treatment for 2D fluid sloshing simulation. J. Mar. Sci. Eng. **9**, 1395 (2021)
11. Strelnikova, E., Choudhary, N., Kriutchenko, D., Gnitko, V., Tonkonozhenko, A.: Liquid vibrations in circular cylindrical tanks with and without baffles under horizontal and vertical excitations, Engineering Analysis with Boundary Elements **120**, 13–27 (2020). https://doi.org/10.1016/j.enganabound.2020.07.024

12. Spina, L., Förster, A., Kronbichler, C., Wall, W.A.: On the role of (weak) compressibility for fluid-structure interaction solvers. Int J Numer Meth Fluids. **92**, 129–147 (2020). https://doi.org/10.1002/fld.4776

13. Ravnik, J., Tibaut, J.: Boundary-domain integral method for vorticity transport equation with variable viscosity. t, Int. J. Comp. Meth. and Exp. Meas. **6**(6), 1087–1096 (2018). https://doi.org/10.2495/CMEM-V6-N6-1087-1096

14. Liu, Z., Wei, G., Wang, Z., Qiao, J.: The meshfree analysis of geometrically nonlinear problem based on radial basis reproducing kernel particle method. Int. Journal of Applied Mechanics **12**(4), 2050044 (2020). https://doi.org/10.1142/S1758825120500441

15. Raynovskyy, I.A., Timokha, A.N.: Sloshing in Upright Circular Containers: Theory, Analytical Solutions, and Applications. CRC Press/Taylor & Francis Group, p. 170 (2020)

16. Ravnik, J., Tibuat, J.: Fast boundary-domain integral method for unsteady convection-diffusion equation with variable diffusivity using the modified Helmholtz fundamental solution. Numer Algor. **82**, 1441–1466 (2019). https://doi.org/10.1007/s11075-019-00664-3

17. Karaiev, A., Strelnikova, E.: Singular integrals in axisymmetric problems of elastostatics. International Journal of Modeling, Simulation, and Scientific Computing **11**(1), 2050003 (2020). https://doi.org/10.1142/S1793962320500038

18. Liu, P., Bai-Jian Tang, B.-J., Kaewunruen, S.: Vibration-induced pressures on a cylindrical structure surface in compressible fluid. Appl. Sci. **9**, 1403 (2019)

19. Ghasemi, A.R., Meskini, M.: Free vibration analysis of porous laminated rotating circular cylindrical shells. Journal of Vibration and Control **25**(18), 2494–2508 (2019). https://doi.org/10.1177/1077546319858227

Modeling of Aeroelastic Instability of Fan Blades

Vitaly Gnesin[1] , Yuriy Bykov[1(✉)] , Lyubov Kolodyazhnaya[1] ,
Viacheslav Donchenko[2] , and Oleksii Petrov[2]

[1] A. Pidgorny Institute of Mechanical Engineering Problems of the National Academy of
Sciences of Ukraine, 2/10 Pozharskogo St., Kharkiv 61046, Ukraine
`bykow@ipmach.kharkov.ua`
[2] SE Ivchenko-Progress, 2 Ivanova St., Zaporizhzhia, Ukraine

Abstract. The flutter of fan rotor blades is one of the main problems facing
designers of modern aircraft engines. To predict the flutter of fan blades, various
simplified methods were previously used, which were based on the experience of
designing and fine-tuning engines, on the processing of a large number of tests
performed. Another method for predicting aeroelastic instability is the frequency
method, in which the motion of the blades is described by harmonic functions in
time with a constant phase angle between the blades. In this work, a numerical
method is used to predict flutter, which is based on solving a coupled problem
of unsteady aerodynamics and the dynamics of oscillating blades in an unsteady
spatial viscous gas flow. Based on the solution of the aeroelastic problem, a study of
the aeroelastic behavior of the fan blade row in a viscous gas flow has been carried
out. Numerical modeling is implemented using an explicit monotone finite-volume
difference scheme of the 2nd accuracy order of Godunov-Kolgan, generalized for
an arbitrary deformable computational mesh. To describe the motion (vibrations)
of the blades, a modal approach was used taking into account the first five natural
modes of vibrations. The results of aeroelastic characteristics calculations and
aerodamping coefficients of the fan blades for harmonic and coupled oscillations
at different inter-blade phase angles are presented.

Keywords: Aircraft engine · Aeroelastic problem · Flutter · Viscous gas ·
Natural mode

1 Introduction

Among the problems of aeroelastic nature, the most common are resonant vibrations,
flutter, and self-oscillations of the rotor blades of turbomachines (turbines, compressors,
fans, etc.). Flutter is one of the most dangerous phenomena of aeroelasticity due to its
disastrous consequences. Most of the modern research is devoted to the problem of flutter
of the last stages of steam turbines [1–4], blades of wind turbines [5], and radial turbines
[6]. The problem of the aeroelastic behavior of fans and compressor rotors of aircraft
engines is especially actual [7–10]. The supersonic flow, flow stall, surge in compressors
complicates the prediction of the onset of the aeroelastic blade vibration [11–14].

Methods of mathematical modeling of aeroelasticity in blade rows can be divided into two approaches – modeling of oscillations in the frequency and time domains. For the frequency approach, linearization of motion equations in time is usually used, which makes it difficult to simulate oscillations with large amplitude, but can significantly reduce the cost of calculation [2, 15]. Some improvements of this method and taking into account some nonlinear dependencies make it possible to obtain a satisfactory result [6, 7, 12]; methods for solving the coupled problem have also been proposed [16]. Another approach – modeling in the time domain – makes it possible to completely reproduce non-stationary phenomena in a turbomachine, however, it requires other simplifications to reduce the cost of calculation [17]. The most popular methods are modeling inviscid flows or limiting the motion of the blades to several modes, frequencies, or phases of oscillations [10]. Quite often used is the energy method, which consists in determining the work of aerodynamic forces for given oscillations of the blades [4]. To simplify the blade motion equations, the modal method is also used [13, 18]. For some objects, in particular, for the axial-radial compressor of a helicopter engine, modeling in the frequency domain turns out to be more efficient [14].

The need to simulate transient aeroelastic processes, especially in partial modes, requires the development of numerical methods for solving the coupled problem of unsteady aerodynamics and elastic oscillations of blades in a three-dimensional viscous gas flow. The purpose of this article is to numerically simulate the aeroelastic oscillations of the fan blades of an aircraft engine using the developed method [18] for solving the coupled problem to identify the instability boundaries of the blade oscillations.

2 Aeroelastic Problem Statement

A three-dimensional flow of viscous gas through a rotating blade row of the fan blades is considered, the oscillations of which are described using a modal approach.

The blade row is an axial fan impeller consisting of 24 blades.

A three-dimensional transonic flow of a viscous gas through the blade row is considered in the physical domain, including an impeller rotating at a constant angular velocity ω, in a Cartesian coordinate system, and is described by the complete system of Reynolds-averaged Navier–Stokes's equations, represented in differential form of conservation laws [18].

$$\begin{cases} \frac{\partial \rho}{\partial t} + \nabla(\rho \boldsymbol{v}) = 0 \\ \frac{\partial \rho \boldsymbol{v}}{\partial t} + \nabla(\rho \boldsymbol{v}) - \nabla \Pi = 0 \\ \frac{\partial \rho E_t}{\partial t} + \nabla(\rho E_t \boldsymbol{v}) - \nabla(\Pi \boldsymbol{v}) + \nabla \boldsymbol{q} = 0 \end{cases} \quad (1)$$

In the Eq. (1) ρ denotes density; E_t – specific total energy; Π – stress tensor; $\boldsymbol{q}$ – heat flux; $\boldsymbol{v} = \boldsymbol{i}u + \boldsymbol{j}v + \boldsymbol{k}w$ – velocity vector.

As flow Eqs. (1) closure, an algebraic turbulence model is used, based on the original two-layer model of Cebeci-Smith and modified by Baldwin and Lomax [19].

The boundary conditions are determined by waves arriving at the boundaries with fixed values of the flow parameters (in the inlet section – total pressure p_0, total temperature T_0 and flow angles in the tangential and meridional sections β, γ; at the outlet boundary – static pressure p_2).

On the "solid" walls of the computational domain, the following are specified:

- the condition of "no-slip" $v = v_w$, where v_w is the speed of wall movement in the considered coordinate system;
- heat flux q_w (for an adiabatic wall $q_w = 0$);
- relation for pressure at the wall obtained by projection on the normal to the wall of the momentum conservation equation $\frac{\partial p}{\partial n} = \mathrm{grad}_n \tau$.

The discrete form of Eqs. (1) was obtained using the Godunov-Kolgan difference scheme of the 2nd order of accuracy in coordinates and time, generalized to the case of an arbitrary spatial deformable computational mesh [20]. The mesh size for the aerodynamic calculation containing 24 blades is 5,088,000 cells.

The dynamic model of oscillating blades in a linear formulation is described by a matrix equation using the modal approach [21].

The numerical solution of the problem of integrating a coupled system of equations of aerodynamics and dynamics of oscillating blades consists in the parallel solution at each time step of aerodynamic and dynamic problems with exchange of the calculation results for each of the problems at previous iteration as input data for the next iteration. Instantaneous aerodynamic loads obtained from the solution of the aerodynamic problem at the previous time layer are used as input data in the dynamic problem; in the aerodynamic problem, the new position and vibration velocities of blades obtained from solution of the dynamic problem are taken as boundary conditions.

3   Results and Discussion

A numerical study was carried out for a blade row, which is an axial fan impeller consisting of 24 blades (Fig. 1). Due to copyright restrictions, detailed drawings of the fan blade are not shown.

Fig. 1. Blade row of axial fan impeller.

Calculations of aeroelastic characteristics of the blade row were performed for the mode:

– total inlet pressure = 100,426 ÷ 100,530 Pa;
– total inlet temperature = 288 K;
– flow angles in the circumferential (α) and radial (γ) directions are given;
– the static pressure at the outlet behind the fan was assumed to be variable along the radius (Fig. 2);
– rotational speed of the blade row = 3610 rpm.

Vibrations of the rotor blades were determined taking into account the first five natural modes of vibrations (Table 1) without taking into account mechanical damping.

Table 1. Fan blade natural frequencies

Natural form number	1	2	3	4	5
Frequency, ν_i, Hz	91	212	393	454	635

Figure 2 shows the graphs of the spanwise distribution of total pressure p_0 at the inlet in the absolute coordinate system, total pressure p_{0w} in the rotating coordinate system, and static pressure p_2 at the outlet behind the blade row.
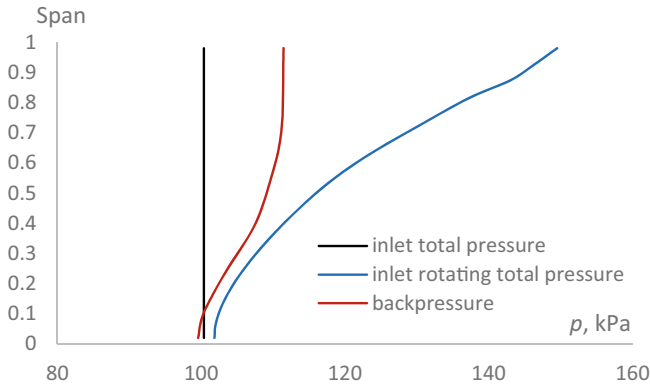
Fig. 2. Spanwise inlet distribution of total pressure in the absolute and rotating coordinate system, and static backpressure

A calculation of airflow through rotating fan blade row with given harmonic law of blades oscillations was carried out. The aerodynamic calculation is performed until reaching of periodic unsteadiness of the flow with a frequency equal to the blade oscillation frequency.

The criterion of resistance to flutter is the expression for the coefficient of aerodynamic damping ($D > 0$, $W < 0$), which is equal to the coefficient of work W, taken with a minus sign, performed by the aerodynamic load during one period of oscillation. If the value of W is positive, then flutter will occur, otherwise, it will not.

The influence of the inter-blade phase angle (IBPA) of the blade oscillations on the aerodamping coefficient, taking into account the first five natural modes of oscillations, is shown in Fig. 3.
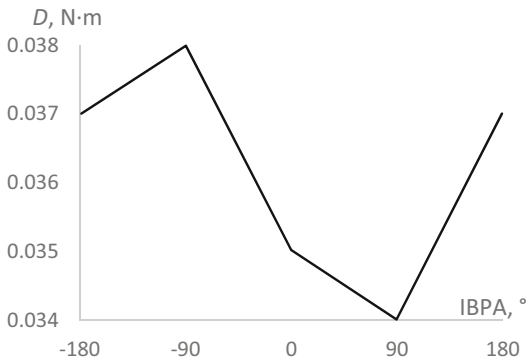
Fig. 3. Dependence of the aerodamping coefficient averaged over the blade height on the IBPA for 1–5 natural modes

For all IBPAs, the aerodamping coefficient is $D > 0$ ($W < 0$), which corresponds to the dissipation of oscillating blade energy into the main stream. The maximum aerodamping takes place at oscillations with a phase shift IBPA = –90°, the minimum value at IBPA = + 90°.

Further, the calculation of coupled oscillations for 8 periods is carried out. In this work, the calculation of aeroelastic characteristics of the fan blades is presented for IBPA = + 90°.

Figure 4 shows graphs of unsteady aerodynamic forces acting in the circumferential direction (F_y) on the peripheral layer of the blades (Fig. 4, a), in the axial direction (F_z) (Fig. 4, c), aerodynamic moment (M) (Fig. 4, e) and their amplitude-frequency characteristics (Fig. 4, b, d, f). On the amplitude-frequency characteristics, A_0 denotes mean amplitude value, and A/A_0 denotes dimensionless values of the force or moment amplitude respectively.

As follows from the graphs, unsteady components of aerodynamic loads decrease in the transient process, and the aerodynamic loads converge to the loads corresponding to stationary mode.

The displacements of the blade peripheral section in the circumferential, axial directions and rotation relative to the center of gravity for IBPA = + 90° are shown in Fig. 5 for two periods of harmonic oscillations and eight periods of coupled oscillations. On Fig. 5 A0 denotes mean displacement amplitude, and A/A_0 denotes dimensionless values of the displacement amplitude.

The greatest contribution to unsteady components of oscillations in the circumferential direction is made by the frequency close to the 1st natural form frequency (~90 Hz), in the axial direction – the frequency close to the 1st natural frequency (~90 Hz) and to the 2nd natural frequency (~200 Hz).

Only the first two natural modes of vibration make a significant contribution to the motion of the blades. Vibrations of the blades in the first and second modes are approaching a stable vibration mode with constant amplitude and frequency.
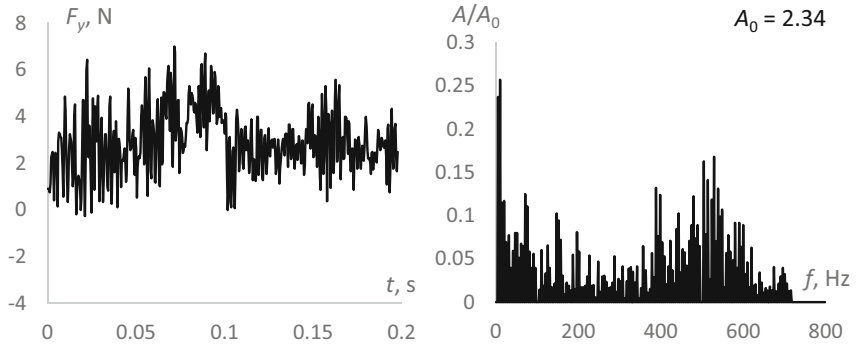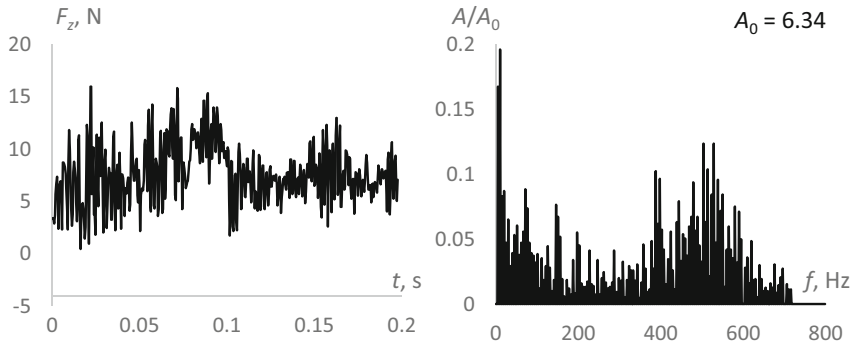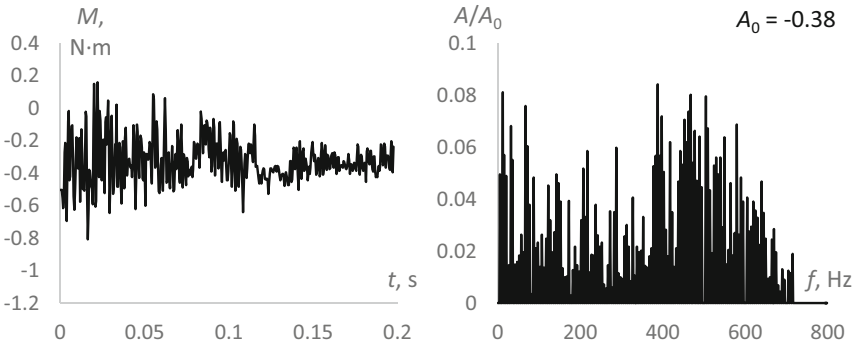
Fig. 4. Unsteady loads acting on the peripheral section of the blade against time and frequency: a) in the circumferential direction; b) in the axial direction; c) aerodynamic torque relative to the center of gravity
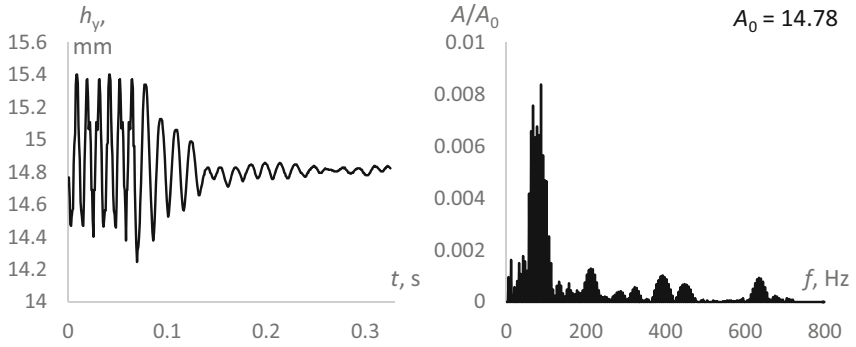
a
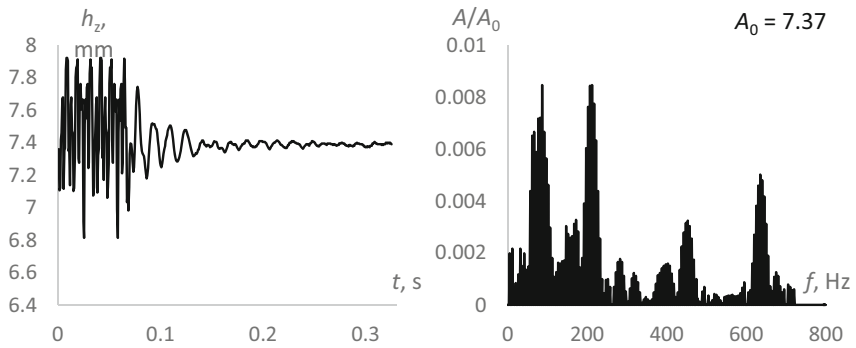
b
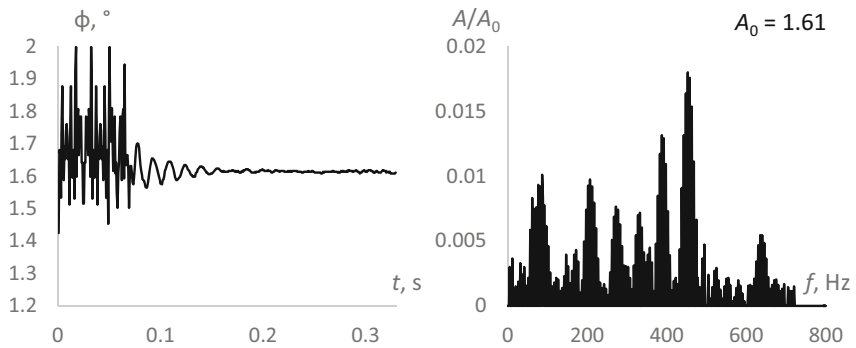
c

Fig. 5. Displacement of the peripheral section of the fan blade against time and frequency: a) in the circumferential direction; b) in the axial direction; c) torsion angle relative to the center of gravity

4   Conclusion

A numerical analysis of aeroelastic characteristics of the fan blade row for the given operating mode was carried out using a mathematical model for solving the coupled problem of unsteady aerodynamics and dynamics of elastic vibrations.

With harmonic oscillations of the blades according to given law, taking into account interaction of the first five natural modes of oscillations, there is "positive aerodamping" ($W < 0, D > 0$), i.e., removal of energy from the oscillating blade into the main stream.

The numerical analysis of coupled vibrations showed that only the first two natural modes of vibrations make a significant contribution to the motion of the blades. Blade oscillations in the first and second modes are approaching to a stable vibration mode with constant amplitude and frequency and undergoing aerodamping for the 3–5 natural modes.

References

1. Rzadkowski, R., Surwilo, J., Kubitz, L., Szymaniak, M.: Unsteady forces in LP last stage 380 MW steam turbine rotating and non-vibrating rotor blades with exhaust hood. J. Vibr. Eng. Technol. **6**(5), 357–368 (2018)
2. Petrie-Repar, P., Fuhrer, C., Grübel, M., Vogt, D.: Two-dimensional steam turbine flutter test case. In: ISUAAAT2014, The 14th International Symposium on Unsteady Aerodynamics, Aeroacoustics and Aeroelasticity of Turbomachines, 8th–11th September 2015, Stockholm, Sweden, pp. 33–43. Curran Associates Inc. N.Y. (2015)
3. Drewczyński, M., Rzadkowski, R., Maurin, A., Marszałek, P.: Free vibration of a mistuned steam turbine last stage Bladed Disc. In: Proceedings of ASME TURBO EXPO 2015, June 15–19, Montreal, Canada, GT 2015–26011, ASME, N.Y. (2015)
4. Sun, T., Petrie-Repar, P., Vogt, D.M., Hou, A.: Detached-eddy simulation applied to aeroelastic stability analysis in a last-stage steam turbine blade. ASME. J. Turbomach. **141**(9), 091002-1−11 (2019)
5. Sabale, A.K., Gopal, N.K.V.: Nonlinear aeroelastic analysis of large wind turbines under turbulent wind conditions. AIAA Journal **57**(10), 4416–4432 (2019)
6. Kovachev, N., Waldherr, C.U., Mayer, J.F., Vogt, D.M.: Prediction of aerodynamically induced blade vibrations in a radial turbine rotor using the nonlinear harmonic approach. ASME. J. Eng. Gas Turbines Power **141**(2), 021007-1−10 (2019)
7. Romera, D., Corral, R.: Nonlinear stability analysis of a generic fan with distorted inflow using passage-spectral method. ASME. J. Turbomach. **143**(6), 061001-1−9 (2021)
8. Stapelfeldt, S., Vahdati, M.: Improving the flutter margin of an unstable fan blade. ASME. J. Turbomach. **141**(7), 071006-1−9 (2019)
9. Dong, X., Zhang, Y., Zhang, Z., Lu, X., Zhang, Y.: Effect of tip clearance on the aeroelastic stability of a wide-chord fan rotor. ASME. J. Eng. Gas Turbines Power **142**(9), 091010-1−11 (2020)
10. Vahdati, M., Cumpsty, N.: Aeroelastic instability in transonic fans. ASME. J. Eng. Gas Turbines Power **138**(2), 022604–1−14 (2018)
11. Hanschke, B., Kühhorn, A., Schrape, S., Giersch, T.: Consequences of borescope blending repairs on modern high pressure compressor blisk aeroelasticity. ASME. J. Turbomach **141**(2), 021002–1−7 (2019)
12. Besem, F.M., Kielb, R.E.: Influence of the tip clearance on a compressor blade aerodynamic damping. Journal of Propulsion and Power **33**(1), 227–233 (2017)

13. Gan, J., Im, H., Zha, G.: Stall flutter simulation of a transonic axial compressor stage using a fully coupled fluid-structure interaction. In: 55th AIAA Aerospace Sciences Meeting, AIAA 2017-0783, pp. 1–28 (2017)
14. Vallon, A., Herran, M., Ficat-Andrieu, V., Detandt, Y.: Numerical investigations of flutter phenomenon in compressor stages of helicopter engines. In: 2018 AIAA/CEAS Aeroacoustics Conference, AIAA 2018–4091, pp. 1–9 (2018)
15. Corral, R., Greco, M., Vega, A.: Tip-shroud labyrinth seal effect on the flutter stability of turbine rotor blades. ASME. J. Turbomach. **141**(10), 101006−1−10 (2019)
16. Huang, H., Liu, W., Petrie-Repar, P., Wang, D.: An efficient aeroelastic eigenvalue method for analyzing coupled-mode flutter in turbomachinery. ASME. J. Turbomach. **143**(2), 021010−1−12 (2021)
17. Ojha, V., Fidkowski, K.J., Cesnik, C.E.S.: Adaptive high-order fluid-structure interaction simulations with reduced mesh-motion errors. AIAA Journal **59**(6), 2084–2101 (2021)
18. Rzadkowski, R., Gnesin, V., Kolodyazhnaya, L.: Aeroelastic behaviour of three and half stage compressor rotor blades with foreign object in engine inlet. In: Proceedings of the Twelve International Conference on Vibration Engineering and Technology of Machinery (VETOMAC-XII), Warsaw, Poland, 7–9 (September 2016). Wydawnictwo Instytutu Technicznego Wojsk Lotniczych, Warszawa, pp. 303–319 (2016)
19. Baldwin, B., Lomax, L.: Thin layer approximation and algebraic model for separated turbulent flow. AIAA Paper **78–0257**, 1–8 (1978)
20. Rzadkowski, R., Kubitz, L., Gnesin, V., Kolodyazhnaya, L.: Flutter of long blades in a steam turbine. J. Vibr. Eng. Technol. **6**, 289–296 (2018)
21. Rzadkowski, R., Gnesin, V., Kolodyazhnaya, L., Kubitz, L.: Aeroelastic behaviour of a 3.5 stage aircraft compressor rotor blades following a bird strike. J. Vibr. Eng. Technol. (6), 281−287 (2018)

Experimental Studies of Pump-Turbine Flow Part Models at Heads of 80–120 m

Oleg Khoryev , Pavlo Korotaiev , Yevgen Agibalov , Yuriy Bykov(✉) ,
and Kyrylo Maksymenko-Sheiko

A. Pidgorny Institute of Mechanical Engineering Problems of the National Academy of Sciences
of Ukraine, 2/10 Pozharskogo St., Kharkiv 61046, Ukraine
`bykow@ipmach.kharkov.ua`

Abstract. Further development of hydropower as a source of renewable energy
is an important factor for the world economy. As the hydro potential of large rivers
in Ukraine is almost exhausted, one of the relevant ways to increase hydropower
production is to complete the construction of existing and design new hydropower
and pumped storage plants. In IMEP of NASU, with the help of modern numer-
ical methods, two variants of the radial-axial pump-turbine runners of different
specific speeds for heads of 80–120 m were designed, which meet the conditions
of promising PSPs of Ukraine. The aim of the work was to obtain and analyze
the energy characteristics in the turbine and pump modes of the two developed
variants of the pump-turbine runners and evaluate the possibility of their applica-
tion at promising PSPs of Ukraine. An experimental study was conducted at the
hydrodynamic stand and energy characteristics were determined in a wide range
of operation. The blade elements of the models for the experimental study were
made of PLA plastic on a 3D printer. Experimental studies have confirmed the
high theoretical energy performance of the developed flow parts. The best charac-
teristics in both turbine and pump modes are obtained on the model with a higher
specific speed. Based on the results of the research, a conclusion was made on the
compliance of the obtained characteristics of the models with the requirements
for the development of pump-turbines to the parameters of promising PSPs of
Ukraine.

Keywords: Pump-turbine · Runner · Hydrodynamic test stand · Experimental
studies · Energy characteristics

1 Introduction

Nowadays, the world's hydropower provides about 20% of total electricity genera-
tion, which is the largest contribution to the energy system among renewable energy
sources. Further development of hydropower, namely – construction and modernization
of hydraulic power plants (HPP) and PSPs – is an important factor for the world economy
for the following reasons [1–6]:

– these energy sources are renewable;

– support of other renewable sources: solar and wind stations;
– the guarantee of the stability of energy production and prices;
– providing consumers with water from reservoirs, reducing the risks of floods and droughts;
– providing stability and reliability of energy systems;
– contribution to the fight against climate change by preventing greenhouse gas emissions, which helps to slow global warming. Improving air quality, as HPPs and PSPs do not produce toxic by-products at all and do not emit pollutants into the air, thus reducing the amount of acid rain and smog;
– contribution to the development of infrastructure and economy;
– the guarantee of clean and cheap energy "for today" and "for tomorrow", as the average service life of HPPs is 50–100 years. At the same time, the stations can be easily modernized, introducing the latest technologies and spending minimal funds on their operation and maintenance in the future.

In the energy systems of developed countries, the share of HPPs and PSPs in the total capacity has been increased to at least 15–20%, which ensures the operation of steam and nuclear turbines at modes close to nominal. At the same time, in 2021, the volume of energy production at HPPs (including HPPs at the "green" tariff) in Ukraine is forecast to be at the level of 5.287 billion kWh, taking into account the low water content of the river in recent years. PSPs power generation is defined at 1.7 billion kWh, which is about 5% of the total [7].

As the hydro potential of large rivers in Ukraine is almost exhausted, one of the current areas of the hydropower production increase is the completion of the Dniester (head $H = 165$ m) and Tashlyk ($H = 125$ m) PSPs, which began in the last century, as well as the construction of a new Kaniv PSP ($H_{max} = 113$ m) [8, 9].

Specialists of "Ukrhydroproject" PRJSC are developing projects for the construction of promising PSPs of Ukraine, including Chervonooskilska ($H = 84$ m), Lomachynska ($H = 125$ m), Pechenizhska ($H = 80$ m) and others [10]. Thus, an extremely relevant and important task is the development of pump-turbines flow parts (FP) for a heads range of 80–120 m.

2   Analysis of Literature Sources and Problem Statement

A review of recent publications has identified the following technical directions to increase efficiency and expand the range of pump-turbines [11]:

– application of asynchronous motor-generator with variable adjustable rotation speed – up to $\pm$ 30% of synchronous – for hydraulic units [12–14];
– application of runners with intermediate shortened blades – splitters – in Francis pump-turbines [15–18]. In IMEP, experimental and numerical studies of the influence of splitters geometrical parameters on energy characteristics of the pump-turbine at heads up to 200 m in the turbine and pump modes are carried out [19, 20];
– air intake under the runner to reduce the level of pressure pulsations and improve cavitation;

– one of the most promising areas is the design of new runners with an increased number of blades and their significant spatial shape [21, 22].

Based on the literature review, the latter direction was chosen as the main one for the design, numerical and experimental study of the pump-turbines flow parts at heads of 80–120 m, which meet the conditions of promising PSPs of Ukraine.

In IMEP, with the help of modern numerical methods [23, 24], two options of the pump-turbine flow part of different specific speeds are designed: the first option of the increased specific speed (such pump-turbines have not been developed so far) and the usual one.

Today, numerical and experimental methods are used to study the working process in hydraulic machinery flow parts. Numerical methods have the following advantages: require less time and money, provide detailed information on the structure of the flow in any cross-section of the flow part elements. However, it should be noted that experimental studies on modern hydrodynamic test stands provide more reliable data on energy, cavitation, pulsation, and other characteristics of models in a wide range of operation.

The purpose of this paper was to obtain and analyze the energy characteristics in the turbine and pump modes of two Francis pump-turbines flowpath designs of different specific speeds and evaluate the possibility of their application at promising PSPs of Ukraine.

The flow parts differed primarily in the geometric parameters of the runner: the runner of higher specific speed received the number ORO5247M, the second one – ORO5248. Table 1 shows a comparison of the geometric parameters of the two runner options.

Table 1. Comparison of geometric parameters of the ORO5247M and ORO5248 runners.

Parameters	ORO5247M	ORO5248
Guide vane height, b_0/D_1	0,25	0,20
Number of blades, z	9	7
The guide vane shaft diameter, D_0/D_1	0,85	0,85
The angle of coverage of the peripheral section, φ, °	77,5	84,1
The leaning angle of the pressure edge in the circular direction, γ, °	40	30

Previously, a numerical study of the flow in designed flow parts of viscous incompressible fluid was carried out [24], a picture of the flow in the characteristic flow part cross-sections was obtained and the calculated energy characteristics in a wide range of modes were determined. The results of the numerical study predicted a high level of performance of the flow parts.

3   Description and Characteristics of the Hydrodynamic Test Stand

Experimental studies of the pump-turbine flow part model were performed on the hydrodynamic test stand ECS-30.

This stand is designed to perform research work on the study of the processes in hydraulic machines (hydraulic turbines, pumps, pump-turbines, micro HPPs), conduct research, and obtain experimental characteristics of hydraulic machinery models [25]. In terms of its parameters and equipment, the ECS-30 stand is a unique structure that has no analogs in Ukraine and received the status of "national heritage" in 2007.

Extensive operational capabilities of the stand control system ensure ease of installation and stability of test modes. The automated system of measurements and mathematical processing of operating mode parameters allows obtaining the characteristics of hydroturbine models with a high level of reliability while ensuring compliance with the modeling criteria provided by the international standard IEC 60193 [26], as well as other requirements for acceptance tests. Table 2 shows the compliance of the stand measurement parameters with the requirements of the IEC 60193 standard.

Table 2. Comparison of measurement error of model hydroturbine parameters with IEC 60193 requirements.

Parameter	Measurement error	
	IEC 60193 requirements, %	Achieved value at the ECS-30 stand, %
Rotation speed	± 0,075	± 0,03
Head	± 0,100	± 0,10
Torque	± 0,100	± 0,10
Mass flow rate	± 0,200	± 0,20
Model efficiency	± 0,250	± 0,25

The main parameters of the experimental equipment of the ECS-30 test stand: diameter of the runner model of 300–400 mm; heads up to 30 m in turbine and pump modes; flow rate up to 0.500 m^3/s, supply up to 0.700 m^3/s; power of DC motors of circulating pumps up to 160 kW; power of the balancing motor-generator of 200 kW.

The pump-turbine flow parts models consist of a spiral case (SC), stay vanes, guide vanes, a runner with a diameter of $D_1 = 350$ mm, and a draft tube (DT).

SC has round meridional sections, which were calculated according to the law of constant circular velocity, the coverage angle $\varphi_{сп} = 360°$, the velocity coefficient in the input section $К = 0.97$.

Stay vanes consist of 20 columns, including a stay vane tongue. Profile of columns have a slight positive curvature. Radial guide vane consists of 20 blades of positive curvature, height $b_0 = 0.25D_1$. The guide vane shaft diameter $D_0 = 1.2D_1$.

The parameters of the runner are given above, in Table 1.

The draft tube is made with an elbow of KU-3RO type, overall dimensions: height $h = 3.15D_1$, length $l = 4.5D_1$.

In order to significantly reduce the cost of the model unit manufacturing and reduce the time of research, the most complex and time-consuming elements in production – spiral case and blades of the runner – were made by 3D-printing technology from PLA plastic. The advantages of this material are its non-toxicity (natural raw materials in

PLA plastic allow to use it for various purposes without endangering human health), size stability, absence of necessity to heat the platform when printing, surface smoothness, it being ideal for moving models, etc. [27]. Blades were printed with a layer thickness of 0.1 mm, then, to achieve satisfactory smoothness, the surface of the model has been polished and varnished. Preliminary calculations for strength have shown that the study of runner models with blades made of PLA plastic can be carried out at heads up to 20 m. Figure 1 shows a picture of the SC and model unit runner. During the research, SC was placed in a metal box filled with water to reduce the pressure acting on the walls of the spiral.
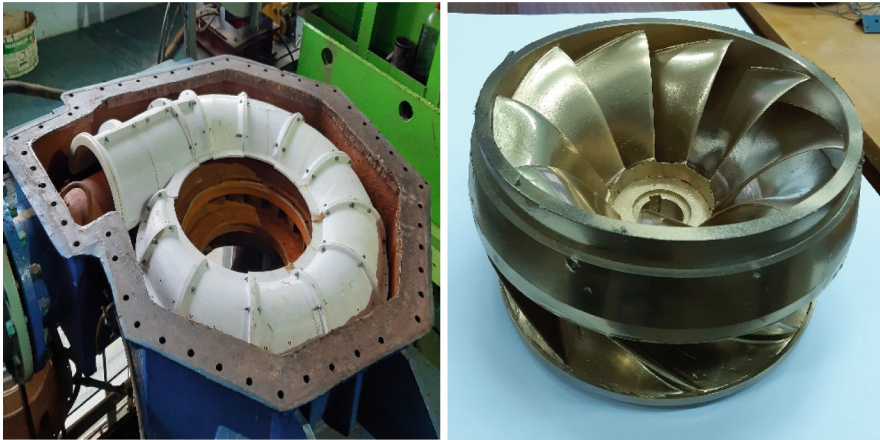
Fig. 1. Spiral case and pump-turbine runner model.

In the turbine mode, the study was conducted at the head of $H = 6$ m, guide vane openings from 10 to 42 mm with a step of 2 mm. In the pump mode, the study was conducted at the runner rotation speed of 800 min^{-1}, with openings from 12 to 34 mm with a step of 2 mm.

4   Results of Experimental Study

4.1   Turbine Mode

The working characteristics and hill charts of the pump-turbine flow part models with runners ORO5247M and ORO5248 (Fig. 2 and Fig. 3, respectively) are constructed.

An important difference in the characteristics of the ORO5247M flow part is the location of the power limitation line in the area of high flow rates, which allows to reliably operate the unit in a wide range of operation and, accordingly, generate more power. The maximum value of efficiency in the turbine mode was obtained when the guide vane opening was $a_0 = 20$ mm, the reduced flow rate was $Q_I{'} = 0.570$ m^3/s and the reduced rotation speed was $n_I{'} = 80.5$ min^{-1}. A fairly high level of efficiency in a wide range of costs and rotation speeds should be noted. Thus, the efficiency isoline,
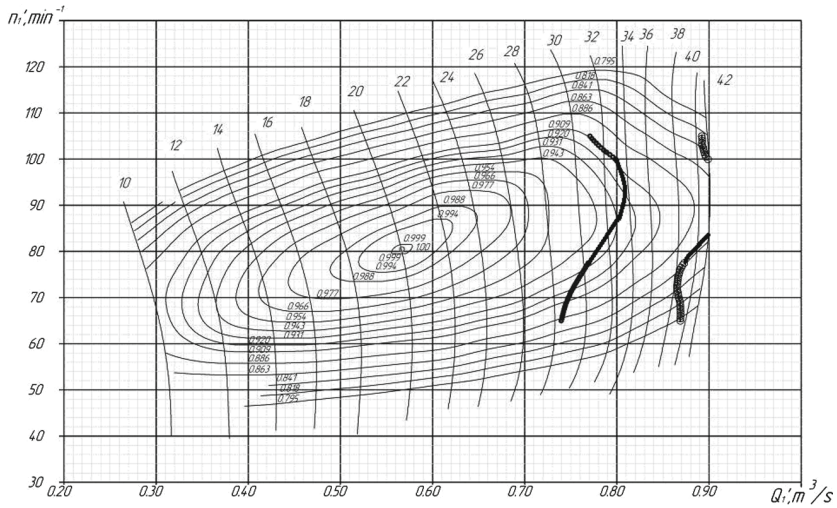
Fig. 2. Hill chart of the flow part model ORO5247M.
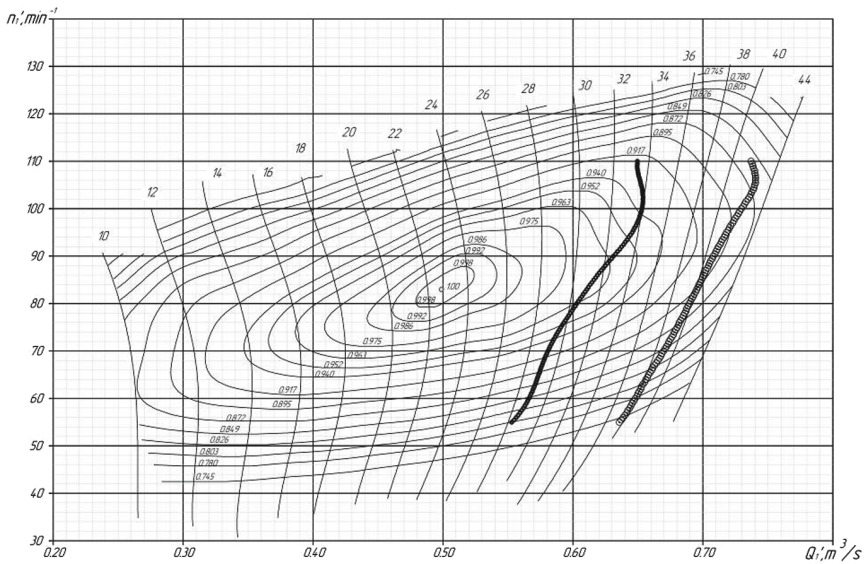
Fig. 3. Hill chart of the flow part model ORO5248.

corresponding to 0.994 of the maximum efficiency, extended in the flow rate range from
0.520 to 0.620 m^3/s at the rotation speed of 76 to 87 min^{-1}.

The optimum of the flow part with ORO5248 runner in turbine mode was obtained
when guide vane opening was $a_0 = 23$ mm, the reduced flow rate was $Q_I' = 0.500$ m^3/s
and the reduced rotation speed was $n_I' = 83$ min^{-1}. It should be noted that the value of
the maximum efficiency of this flow part was almost 0.85% lower than in ORO5247M,

obtained at a higher value of the guide vane opening, at a lower by 0.070 m³/s flow rate and higher by 2.5 min⁻¹ rotation speed.

4.2 Pump Mode

In the ORO5247M flow part with small values of guide vane openings (12, 16 mm) the maximum efficiency was obtained at a flow rate of approximately 0.460 m³/s, but there is a surge at such supplies, as well as head failure, which leads to unstable operation of the unit. At the increase of guide vane opening to 18 mm, the operation point with the maximum efficiency shifted to the right on the characteristic to $Q_\mathrm{I}' = 0.520$ m³/s where the surge is absent.

Figure 4 shows the energy and head characteristics of the flow part model ORO5247M in the pump mode at the values of guide vane opening close to optimal. Interesting results were obtained with the guide vane openings of 20 and 22 mm, where a slight difference in the guide vane opening leads to a significant change in the type of characteristics: at $a_0 = 20$ mm the maximum efficiency corresponds to the supply of $Q_\mathrm{I}' = 0.560$ m³/s, while at $a_0 = 22$ mm it already is $Q_\mathrm{I}' = 0.720$ m³/s. In the supply range of $Q_\mathrm{I}' = 0.450\ldots0.650$ m³/s, the efficiency at $a_0 = 20$ mm exceeds the same indicator at $a_0 = 22$ mm up to 5%.
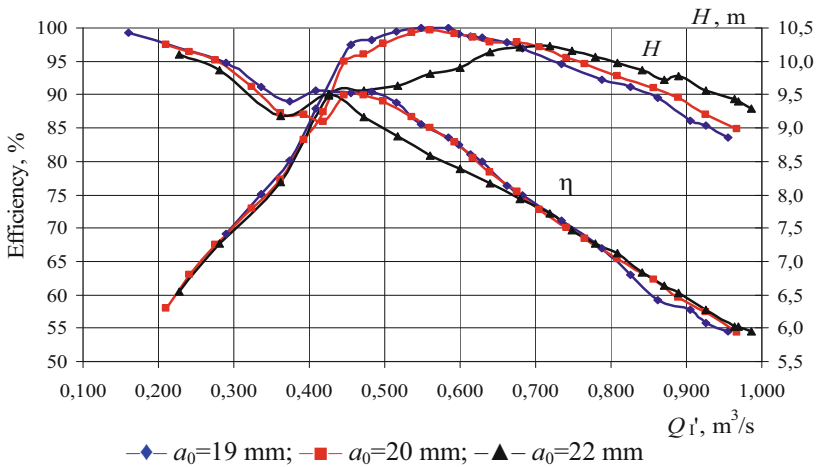
Fig. 4. Dependence of relative efficiency and heads on supply of the ORO5247M flow part

Studies of the model at a rotation speed of 600 min⁻¹ gave similar results. Additionally, studies were performed at $a_0 = 19$ mm, at which the maximum efficiency was obtained in the pump mode, which corresponded to the supply of $Q_\mathrm{I}' = 0.550$ m³/s.

At higher values of the guide vane opening the supply corresponding to the modes with the maximum efficiency is shifted to the right of the characteristic, and the value of these efficiencies decreases.

In the ORO5248 flow part (Fig. 5), the best characteristics were obtained with the guide vane openings from 19 to 21 mm. The maximum value of efficiency was obtained

at $a_0 = 21$ mm when supply was $Q_I{'} = 0.455$ m^3/s. At the opening of 22 mm the maximum efficiency sharply shifts to the right to values of supply of 0.700 m^3/s, thus the value of head in the range of supply of 0.420…0.700 m^3/s considerably falls. The value of the maximum efficiency of the flow part with ORO5248 runner is 0.2% lower than with ORO5247M.
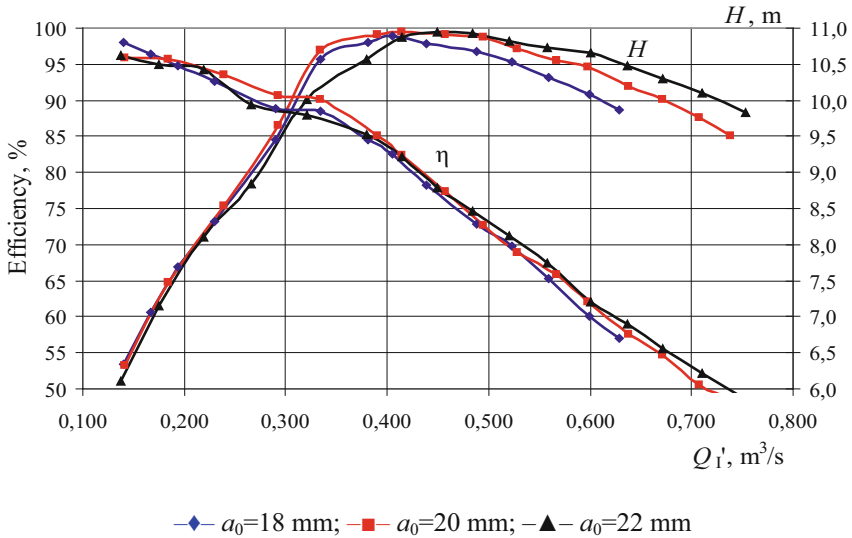
Fig. 5. Dependence of relative efficiency and heads on supply of the ORO5248 flow part

5   Conclusion

Two options of flow part models of Francis pump-turbines with heads of 80–120 m, which differed by runners of different specific speeds, were designed, numerically and experimentally studied.

Experimental studies conducted at the hydrodynamic test stand confirmed the high energy performance of the developed flow parts. The best characteristics in both turbine and pump modes were obtained on the model with high specific speed. Conducted numerical investigation of the flow parts verified their energy characteristics.

According to the results of the experimental study, the use of the pump-turbine flow part with the high specific speed ORO5247M runner is recommended for the PSPs of Ukraine with heads of 80–120 m.

References

1. ITAIPU Homepage: https://www.itaipu.gov.br/en/energy/10-reasons-promoting-hydroelectri city. Last accessed 14 July 2021

2. Vennemann, P., Thiel, L., Funke, H.C.: Pumped storage plants in the future power supply system. VGB PowerTech **1–2**, 44–49 (2010)
3. Ruppert, L., et al.: An analysis of different pumped storage schemes from a technological and economic perspective. Energy **141**, 368–379 (2017)
4. Bessa, R., et al.: Role of pump hydro in electric power systems. J. Phys. Conf. Ser. **813**, 012002 (2017)
5. Nishiwaki, Y.: A proposal to realize sustainable development of large hydropower project. Soc. Soc. Manag. Syst. Internet J. **5**(1), 1–10 (2009)
6. Fischer-Aupperle, B.: Current opportunities for hydro power in China. HyPower **16**, 24–27 (2007)
7. UHE Homepage: https://uhe.gov.ua/media_tsentr/novyny?field_rik_dogovoru_target_id= All&field_misac_dogovoru_target_id=All&field_rubrika_novini_target_id=All&page=1. Last accessed 14 July 2021
8. Lynnyk, A., Khaitov, V.: Up-to-date level and main trends in development of hydraulic turbine construction in Ukraine. Journal of mechanical engineering **1**(13), 11–18 (2010)
9. DSNEWS Homepage: https://www.dsnews.ua/economics/bez-vody-nikak-pochemu-pri-dvi zhenii-v-evropu-u-gaes-net-31082017100000. Last accessed 14 July 2021
10. IPMACH Homepage: https://ipmach.kharkov.ua/wp-content/uploads/2019/10/Abstracts-of-section-2-of-UE-2019.pdf. Last accessed 14 July 2021
11. Nowicki, P., Sallaberger, M., Bachmann, P.: Modern design of pump-turbines. In: 2009 IEEE Electrical Power & Energy Conference (EPEC), Montreal, pp. 1–7. IEEE (2009)
12. Kubo, T., Osada, O., Tojo, H., Shiozaki, T., Suzumura, T., Watanabe, T.: Design and Manufacturing of The World's Largest 475 MVA/460 MW Adjustable Speed Generator-Motor for Pumped Storage Hydro Electric Power Plant. 2014 CIGRE session, A1_113_2014, pp. 1–7 (2014)
13. Kuwabara, T., et al.: Design and dynamic response characteristics of 400 MW adjustable speed pumped storage unit for Ohkawachi power station. IEEE Trans. Energy Convers. **11**(2), 376–384 (1996)
14. Von Nessen-Lapp, W., Novicki, P.: 4×265 MW pumpenturbine in germany: spezial mechanical design features and variable speed operation. In: 22nd IAHR Symposium of Hydraulic Machinery and System, 1–11 (2004)
15. Taguchi, T., Umeda, N., Tezuka, K.: Runner for pumped storage power plant. In: XXI IAHR Symposium of Hydraulic Machinery and System, pp. 1–9 (2002)
16. Yun, J., Wei, X., Wang, Q., Cui, J., Li, F.: Experimental study of the effect of splitter blades on the performance characteristics of francis turbines. Energies **12**, 1676 (2019)
17. Hou, Y., Li, R., Zhang, J.: Research on the length ratio of splitter blades for ultra-high head Francis runners. Procedia Eng. **31**, 92–96 (2012)
18. Jia, Y., et al.: Experimental study of the effect of splitter blades on the performance characteristics of Francis turbines. Energies **12**(9), 1676 (2019)
19. Rusanov, A., Khoryev, O., Agibalov, Y., Bykov, Y., Korotaiev, P.: Experimental research of francis pump-turbines with splitters in a pump mode. In: 2020 IEEE KhPI Week on Advanced Technology (KhPIWeek), pp. 183–187. IEEE (2020)
20. Rusanov, A., Khoryev, O., Agibalov, Y., Bykov, Y., Korotaiev, P.: Numerical and experimental research of radial-axial pump-turbine models with splitters in turbine mode. In: Proceedings of Integrated Computer Technologies in Mechanical Engineering – 2020, pp. 427–439. Springer International Publishing (2021)
21. Cepa, Z.: On experience following from unit 4 upgrading at Dalesice pumped storage power plant, pp. 99–109. Conf. on Hydraulic turbomachines un hydropower and other industrial application, Kliczkow Castle (2005)
22. Brekke, H.: Design, Performance and Maintenance of Francis Turbines. Global Journal of Research in Engineering: Mechanical and Mechanics Engineering **13**, 28–40 (2013)

23. Rusanov, A.V., et al.: Naukovo-tekhnichni osnovy modeliuvannia i proektuvannia pro-tochnykh chastyn enerhetychnykh turboustanovok. Podgorny Institute for Mechanical Engineering Problems, Kharkiv (2019)
24. Rusanov, A., Khoryev, O., Dedkov, V.: The runner design of the radial-axial pump-turbine for the conditions of Kaniv PSPP. Bulletin of NTU «KhPI». Series: Hydraulic machines and hydraulic units **17**, 4–8 (2019)
25. Veremeenko, I.S., Gladyishev, S.V., Dedkov, V.N.: Modernization of energy cavitation stands of the laboratory of hydromachines of IPMash of NAS of Ukraine. J. Mech. Eng. **13**, 3–12 (2010)
26. IEC 60193:2019. Hydraulic turbines, storage pumps and pump-turbines – Model acceptance tests. International Electrotechnical Commission, Geneva (2019)
27. 3DToday Homepage: https://3dtoday.ru/wiki/PLA_plastic. Last accessed 14 July 2021

Turboexpander Unit Use for Efficiency Increase of Gas Compressor Station

Aleksandr Shubenko[1], Mikola Babak[1], Oleksandr Senetskyi[1,2(✉)],
Volodymyr Sarapin[3], and Yana Forkun[2]

[1] A. Pidhornyi Institute of Mechanical Engineering Problems NAS of Ukraine, Kharkiv, Ukraine
aleksandr-seneckij@ukr.net
[2] Beketov National University of Urban Economy in Kharkiv, O. M, Kharkiv, Ukraine
[3] MIRAI INTEX S.R.O., Brno, Czech Republic

Abstract. The purpose and principle of operation of a gas-pumping unit with a gas-turbine drive are described using the example of GTC-10i of compressor station "Pervomayskaya". The possibility of efficient use of fuel gas overpressure energy by a turboexpander is considered. A technical solution for use of a turboexpander unit for increasing energy-economic and environmental indices of compressor station is proposed. The fact that the use of mechanical energy of the expander for additional compression and cooling of the atmospheric air flow in front of the compressor of a gas turbine engine will increase the efficiency of the gas pumping unit is shown. Results of the simulation of thermodynamic processes in elements of existing and proposed schemes by software package "Thermal Schemes" (product of A. N. Podgorny Institute of Problems of Mechanical Engineering NAS Ukraine) are shown. The comparative analysis of energy consumption and environmental indicators of the considered schemes is carried out. The economic feasibility and prospects of introducing the proposed technical solution in modern conditions are proved.

Keywords: Compressor station · Natural gas · Gas turbine engine · Turboexpander unit · Energy efficiency · Energy saving

1 Introduction

An important role in issues of increasing environmental safety is allotted using of resource and energy saving technologies. Energy saving measures allows to weaken the anthropogenic load on the environment, reduce the volume and rate of depletion of underground sources of fossil fuels and also preventing environmental damage associated with their extraction, processing, transportation, use and further disposal of waste. The use of these technologies in such an important complex of the country's economy as the gas transmission system is an actual task.

Gas compressor stations (GCS) are an integral part of the gas transmission system. Since the natural gas (NG) pressure in pipelines gradually decreases during long-distance transportation, it becomes necessary to periodically compress it. Gas turbine engines

(GTE) are used to drive booster compressors at the most of GCS in Ukraine (64%), using 8 – 10% of the transported NG volume for their own needs (about 4.5 billion m^3 per year). The combustion products of these engines are significant sources of air pollution [1].

One of the promising ways to solve the issue of improving the economic and environmental performance of GCS with a gas turbine drive is the use of turboexpander units (TEU) for utilizing the excess fuel gas pressure.

2 Problem Statement

Turboexpander units (TEU) instead of a throttling valve allows to convert the potential energy of the compressed NG pressure into the kinetic energy of the flow and then into the mechanical energy of the rotor, which in turns moves an electric generator or compressor. The expansion of the gas flow in the turboexpander is accompanied by a decrease in its temperature. Thus, TEU allows to produce electricity and cold using the power potential of the gas flow [2–5].

Sufficient experience has already been accumulated in world practice in the development and implementation of TEU in nodes for reducing NG pressure at gas distribution stations (GDS) [5–7], in boiler houses and thermal power plants [8, 9]. There is also an accumulated experience in using TEU at GCS to reduce pressure of fuel gas before it is fed into the gas turbine engine with the electricity generation for its own needs [10, 11]. This technical solution allows to achieve partial independence of the station from external power supply but doesn't solve the issue of improving the environmental performance of GCS.

3 Research Aim and Tasks

The aim of this work is to develop a technical solution for the use of TEU at the purpose of improving the energetic, economic and environmental performance of GCS.

The following tasks were solved to achieve this goal:

– the principles of operation of a gas compressor unit (GCU) with a gas turbine drive were analyzed (on the example of the compressor station "Pervomayskaya", Kharkiv region, Ukraine) and a solution was proposed for the use of TEU;
– thermodynamic processes of the original and proposed schemes were simulated, indicators of energy consumption and volumes of emissions into the atmosphere were compared;
– the economic feasibility of introducing the proposed solution was assessed.

4 Research Materials and Methods

To accomplish the assigned tasks, the materials of the main GCU technical characteristics of GCS "Pervomayskaya" UMG "Kharkivtransgaz" were used, as well as the following research methods:

– modeling of thermodynamic processes in elements of GCS technological scheme [12, 13];
– ecological and economic calculation of the feasibility of implementing the proposed TS.

5 Research Results

The solution of the problem was considered on the example of GCS "Pervomayskaya" with GCU of GTC-10i type (Table 1) with a capacity of 10 MW (7 units), which are completed the gas turbine engine of MS3142 type (Table 2).

Table 1. Technical characteristics of GTC-10i GCU

Characteristic	Value
Climatic performance	«C.1»
Nominal productivity, mln m^3/day	17.6
Inlet pressure, MPa	5.1
Outlet pressure, MPa	7.55
Pressure ratio (outlet to inlet)	1.48
Gas turbine engine	MS3142
Nominal power at the engine coupling (in stationary conditions), MW	10.0
Nominal rotor speed of the power turbine engine, rpm	6500
Efficiency (in stationary conditions),%	31.8
Compressor type	RF2BB30
Unit weight (dry) in the scope of delivery, kg	110000

A simplistic technological scheme of GCU with GTE is shown in Fig. 1.

The operation principle of this traditional scheme: atmospheric air is compressed in the compressor (C) and supplied to the combustion chamber (CC). At the same time, the fuel NG is supplied to CC, which is taken from the low-pressure line. The gas pressure is throttled by a control tap (Regulating Tap, RT). In the combustion chamber NG is combusted. The air is additionally mixed with the combustion products to decrease their temperature to the value allowed by the mode of turbine operation. In the first turbine (T), which drives the compressor, there is a partial expansion of the combustion products. In the second turbine (power, PT), the combustion products expand to atmospheric pressure. This turbine serves as a drive for a booster compressor (BC), which increases the gas pressure in the line.

As can be seen from the technological scheme, the potential energy of the fuel NG is irretrievably lost in RT. The gas for compression at GCS "Pervomayskaya" is taken from a low-pressure line with a pressure of 5.1 MPa and throttled to 0.729 MPa. Another disadvantage of GTE operation is the dependence of its efficiency on the outside

Table 2. Engine characteristics of MS3142

Characteristic	Value
Nominal power, MW	10
NG flow rate at 100% load, m^3/h	4295
Efficiency, %	27.1
Compressor pressure ratio	17.5
Working fluid flow rate through the engine, kg/s	52.0
Output shaft/generator speed, rpm	7100/6500
Gas temperature at engine outlet, °C	520
Fuel gas pressure, MPa	1.5
Oil flow rate, kg/h	0.6
Weight, kg	61800
Resource before overhaul/appointed, h	16 000/100 000
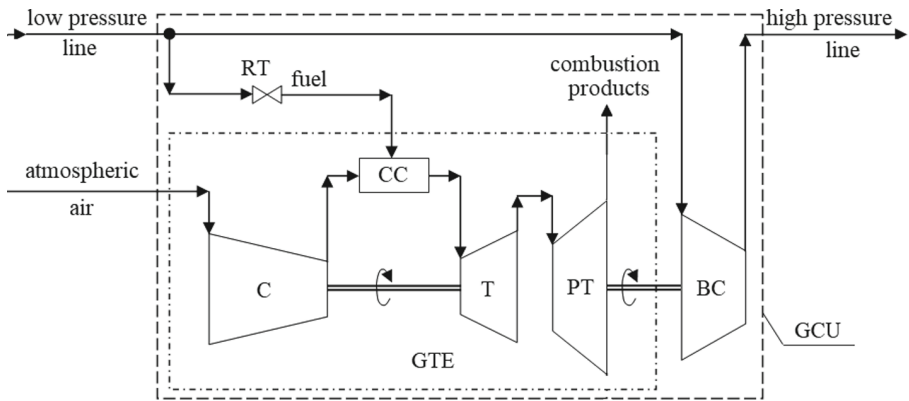
Fig. 1. Technological Scheme of GCU GCS: RT – regulating tap; C – compressor; CC – combustion chamber; T – turbine; PT – power turbine; BC – booster compressor.

air temperature. With an increase in the air temperature at the compressor inlet, its power consumption increases, this leads to an increase in the consumption of the fuel NG and a decrease in the engine efficiency. For example, with an increase in the temperature from 20 °C to 30 °C, the volume of the fuel gas consumption increases by 4%, which, accordingly, leads to a proportional increase in the volume of emissions of combustion products.

To improve the fuel-economic and environmental performance of GCS "Pervomayskaya", we will consider a proposal to improve the process flow diagram of GTC-10i GCU. Our proposal consists in using the potential energy of the fuel NG by installing a TEU instead of regulating tap. Thus, a turboexpander and a compressor were located on the same shaft (see Fig. 2). TEU is using the mechanical work of the turboexpander

to increase the air pressure at the inlet to GTE compressor. The gas expansion in the turboexpander leads to a decrease in its temperature. This makes it possible to cool the atmospheric air at the inlet to GTE compressor. The use of the potential energy of the fuel NG to pressurize the flow of atmospheric air, pre-cooled by the same gas, leads to an increase of GTE efficiency.
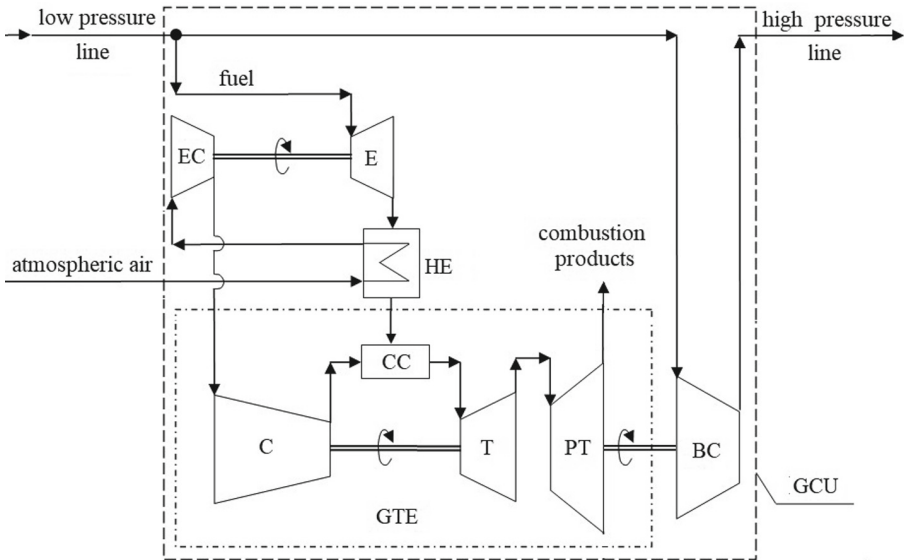
Fig. 2. The proposed technological scheme of GCU GCS: EC – expander compressor; E – expander; HE – heat exchanger.

In accordance with this scheme, the atmospheric air is cooled in a heat exchanger (HE), partially compressed in expander compressor (EC) and then finally compressed in C of GTE and supplied to CC. After the overpressure in the turboexpander has been triggered and heated in the HE from the atmospheric air, NG taken from the low-pressure line is also fed into this chamber. Then everything is as in the previous scheme.

To calculate technological schemes and determine the volumes of formation and emissions of natural gas (NG) combustion products during the operation of GTC-10i GCU at GCS "Pervomayskaya", the "Thermal Scheme" software complex developed at A. Pidhornyi Institute of Mechanical Engineering Problems NAS of Ukraine (Kharkiv) [14] was used. This software allows to simulate thermal schemes considering the thermodynamic properties of multicomponent working mediums. The following natural gas composition was taken (values are in % mol): CH_4 – 92; C_2H_6 – 3.9; C_3H_8 – 1.0; C_4H_{10} – 0.4; C_5H_{12} – 0.3; N_2 – 1.5; and CO_2 – 0.1. The results of calculating the characteristics of the previously presented technological schemes for one GTC-10i GCU are given in Table 3.

The economic assessment and efficiency of the proposed technological schemes was carried out further using data from only one, the least favorable operating mode of GCS (outside air temperature + 25 °C, see Table 3). An increase in the outside air temperature

adversely affects GTE operation. The operation of the station in other, more favorable modes may only improve the characteristics presented below. Seasonal changes in the operating mode of GCS are regulated by the number of included GPUs.

Table 3. Thermodynamic calculations results of technological schemes with atmospheric air parameters: the pressure is 0.101325 MPa and the temperature is 25 °C

Characteristics			Value for different schemes	
			scheme on Fig. 1	scheme on Fig. 2
Air temperature before compression in the compressor, °C			25	24.3
Inlet air pressure:		GTE compressor, MPa	0.101325	0.10389
		combustion chamber, MPa	0.729	0.72954
Gas pressure:		inlet to BC, MPa	5.1	
		outlet to BC, MPa	7.55	
Gas temperature at the outlet of BC, °C			66.6	
Flow rates:	NG which is transported, kg/s (st. m^3/h)		147.87 (733 333)	
	air, kg/s (st. m^3/h)		52.00 (155366)	50.03(149480)
	fuel NG	kg/s (st. m^3/h)	0.873(4329)	0.840(4166)
		thousand tons/year (mln st.m^3/year)	27.53(37.926)	26.49(36.493)
	combustion products	kg/s (st. m^3/h)	52.87(155521)	50.87(149630)
		mln tons/year (mln st.m^3/year)	1.667(1362.4)	1.604(1310.7)
	including	CO$_2$	kg/s (st. m^3/h)	2.38(4656)	2.29(4480)
			thousand tons/year (mln st.m^3/year)	75.055(40.78)	72.217(39.24)
		NO$_x$	kg/s (st. m^3/h)	0.0125(35.41)	0.0109(30.88)
			thousand tons/year (mln st.m^3/year)	0.394(0.31)	0.343(0.2705)
Excess power of GTE, kW			10 000	
GCU efficiency, %			25.45	26.45

At assessing the values of NG combustion products emissions, it was taken into account that GTEs are characterized by a high fuel combustion efficiency, which is usually 0.95 – 0.99 in the entire range of operating loads and 0.98 – 0.99 in the design mode [15]. Natural gas (NG) is considered one of the most environmentally friendly fuels, as it doesn't contain ash and sulfur compounds. The chemical reaction of its

complete combustion can be expressed by equation:

$$C_nH_m + \left(n + \frac{m}{4}\right)O_2 \rightarrow nCO_2 + \frac{m}{2}H_2O, \tag{1}$$
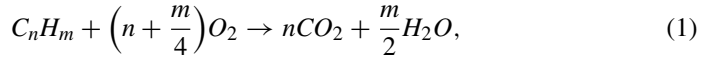
where n is the number of carbon atoms, m is the hydrogen in a hydrocarbon molecule.

Under conditions of high-temperature fuel combustion, air nitrogen becomes reactive with forming nitrogen oxides (NO_x): "thermal", "fast" and fuel (according to the Ya. B. Zeldovich theory [16]). The determining factors in the formation of nitrogen oxides are the temperature and residence time of the fuel-air mixture in the combustion zone.

Comparison of the thermodynamic calculations results showed that the implementation of the proposed technical solution, using the example of one GTC-10i GCU of GCS "Pervomayskaya", will annually save about 1,433 thousand m^3 of fuel NG and reduce the annual emissions of its combustion products on 52 tons of NO_x and 2838 tons of CO_2.

For determine the feasibility of implementing the proposed TS at this GCS, its simple payback period was calculated τ_{pp}:

$$\tau_{pp} = \frac{CC}{A}, \tag{2}$$

where CC is the total capital costs for the purchase, assembling and commissioning of new equipment, UAH; A is the annual savings from implementation, UAH/year.

Measures for modernization of GCS, including capital costs for assembling and commissioning of new equipment, as a rule, are taken at the rate of ~ 15% of its cost (C_{eq}) [17]. According to preliminary estimates, the cost of one TEU with 132 kW nominal capacity, for example, produced by PrJSC "Turbogaz" amount is $C_{eq} = 12$ million UAH [18]. Considering the costs of installation and commissioning, the capital costs for one unit will be $K = 1.15 \cdot C_{eq} = 1.15 \cdot 12 = 13.8$ million UAH.

The annual income from the implementation consists of savings on fuel (A_{NG}) and the amount of the environmental tax (A_{ET}):

$$A = A_{NG} + A_{ET} = (V_0 - V_M) \cdot C_{NG} + \sum_{i=1}^{n}((M_{i0} - M_{iM}) \cdot T_{Ri}), \tag{3}$$

where V_0, V_M are the annual fuel gas consumption, respectively, before and after modernization, thousand m^3/year (see, Table 3); $C_{NG} = 1280$ UAH/thousand m^3 is the price of NG for operators of the gas distribution network for production and technological costs, normalized losses and their own needs. This price corresponds to the price list of NJSC "Naftogaz of Ukraine" prior to the adoption of the resolution [19], according to which C_{NG} is determined by each network operator. For a preliminary estimate of A, we will use the previously indicated value of C_{NG}, since, in the new resolution, on the average, it is likely that this price has increased; M_{i0}, M_{iM} are the annual volumes of emissions of i-th combustion product, respectively, before and after modernization, t/year (see, Table 3); T_{Ri} is the tax rates in the current year for a ton of i-th substance, UAH/t (according to the Tax Code of Ukraine [20] as of 2021 $T_{RCO_2} = 0.41$ UAH/t, $T_{RNO_x} = 2451.84$ UAH/t).

The annual savings from the implementation of the proposed technical solution (scheme 2) will be:

$A = (37926 - 36493) \cdot 12180 + (75055 - 72217) \cdot 0.41 + (394 - 343) \cdot 2451.84 = 17580147.42$ UAH/year = 17.58 million UAH/year.

Its simple payback period is $\tau_{pp} = \frac{13.8}{17.58} \approx 0.78 \text{(years)} \approx 10 \text{(months)}$.

6   Conclusions

GCS "Pervomayskaya" (Kharkiv region, Ukraine) provides compression of transit natural gas in main gas pipelines by operation of seven GTC-10i GCU (with nominal power 10 MW), which are equipped with gas turbine drives model MS3142. Each GCU in the process of its operation annually combusts ~ 37.926 million m^3 (27.53 thousand tons) of natural gas and is a source of constant influence on the atmospheric air with an annual emission of 394 tons of NO_x and 75.055 thousand tons of CO_2.

The works [2–5] discussed the need to introduce a turboexpander unit, but did not considered the possibility of replacing the control valve with a turboexpander unit. In order to improve the energetic, economic and environmental indicators of GCS, an energy saving technical solution is proposed, which consists in using the potential energy of the natural gas at installing TEU instead of a throttle valve. The compressor, using the mechanical operation of the turboexpander, raises the air pressure at the inlet to GTE compressor. The cold formed during gas expansion in the turboexpander is used for cooling the atmospheric air at the inlet to GTE compressor.

Modeling of thermodynamic processes of the original and proposed schemes using the example of one GTC-10i GCU showed that the use of TEU will increase its efficiency, while annually saving 1,433 thousand m^3 of the fuel NG and, accordingly, reduce harmful NO_x emissions on 52 tons and CO_2 on 2838 tons, if it compared to existing approaches [10, 11]. Subject to annual operation of six GCUs of GCS "Pervomayskaya" (+ 1 GCU in reserve), the proposed solution will save almost 8.6 million m^3 of NG and reduce station NO_x emissions on 312 tons and CO_2 on 17028 tons.

The results of the ecological and economic efficiency research of the proposed solution may depict the perspectives for its realization. With a total capital expenditures of 13.8 million UAH, based on one GCU, the annual economies from the inculcation of TEU will amount to ~ 17.5 million UAH at the expense of decrease in the fuel NG flow rate and 126.2 thousand UAH at the expense of decrease in the amount of environmental tax. Its simple payback period is ~ 10 months.

The example considered here (GCS "Pervomayskaya") also suggests the possibility of using TEU at other stations equipped with gas turbine drives. First of all, on those, which are characterized by a greater value of ΔP and power of GTE. The widespread implementation of the proposed solution may make it possible to save millions of cubic meters of natural gas annually, and to significantly reduce air pollution, which is in line with the state policy in the field of energy saving and ecology.

References

1. Corporate Annual Environmental Report: Kiev, NJSC "Naftogaz of Ukraine" 36 (2019). https://www.naftogaz.com/files/Activities/Grupa-Naftogaz-Oxorona-dovkillya-2019.pdf. Last accessed 20 August 2021

2. Stepanets, A.A.: Energy-saving turboexpander units. Moscow, Subsoil business center, 258 (1999)

3. Epifanova, V.I.: Compressor and expansion turbomachines of radial type. Moscow, MVTU im. N.I. Bauman 376 (1998)

4. Barnes, Ryan N.: Essays on the Economics of Energy and Transportation. Utah, Utah State University, p. 131 (2017). https://digitalcommons.usu.edu/cgi/viewcontent.cgi?article=6699&context=etd. Last accessed 20 August 2021

5. Shubenko, A.L., Sarapin, V.P., Senetskyi, O.V., Sarapina, M.V.: Energy saving at the gas distribution station during the joint operation of the turboexpander and air climate system, 20, pp. 15–19. Bulletin of the National Technical University "HPI", Series: Hydraulic machines and hydraulic units (2016)

6. Osipov, S., Zlyvko, O., Bychkov, N., Kharlamova, D., Zaryankin, A.: Increasing the efficiency of using the natural gas potential energy in turbo-expander units for power generation. In: AIP Conference Proceedings 2323, 060007, pp. 060007-1–060007-6 (Published Online: 08 March 2021). https://doi.org/10.1063/5.0043465. Last accessed 20 August 2021

7. Zatsepin, S.S., Kuptsov, S.M.: Application of turboexpander units at gas distribution stations. Territory "OIL" **12**, 50–53 (2016)

8. Kulichikhin, V.V.: Fulity of use of expander-generator sets at thermal power plants. Safety and Reliability of Power Industry **11**(2), 161–166 (2018)

9. Kulichikhin, V.V.: Practice of operation of expander-generator units at Mosenergo CHPPs. Historical overview. Safety and Reliability of Power Industry **10**(2), 159–166 (2017)

10. Plan of the gas transportation system development: Operator of the gas transmission system of the Limited Liability Company "OPERATOR OF THE GAS TRANSMISSION SYSTEM OF UKRAINE" for 2021–2030. Kiev, LLC "Operator of the gas transmission system of Ukraine" 107 (2020). https://tsoua.com/wp-content/uploads/2020/10/TYNDP-2021-2030-TSO-4.1.pdf?fbclid=IwAR38itV8gJUj3MX1ekS33FosXDY5sEQapc8I25M91by9DX7eH3LYsGVWGgw. Last accessed 20 August 2021

11. Sheludko, L.P., Gulina, S.A., Biryuk, V.V.: Energy gas turboexpander installation for compressor shops of main gas pipelines. Izvestiya Samarskogo nauchnogo tsentra RAS, **2**(4), 929–934 (2015)

12. Gorpinko, Yu.I., Senetskyi, O.V., Sarapin, V.P., Shubenko, O.L., Malyarenko, V.A.: Double contour thermodynamic cycle with unidirectional heat transfer between the refrigeration and energy cycle. Problemele Energeticii Regionale **3**(44), 51–64 (2019)

13. Inozemtsev, A.A., Nikhamkin, M.A., Sandratsky, V.L.: Gas turbine engines. Fundamentals of designing aircraft engines and power plants. Moscow, Mechanical engineering 208 (2007)

14. Shubenko, A.L., Sarapin, V.P.: Peculiarities of using the Thermal Scheme software for calculating thermal circuits. Visnyk Nats. tech. HPI University. Coll. Science. ave. ser. Power and heat engineering processes and equipment. Kharkiv, NTU "KhPI" **13**(1289), 4–8 (2018)

15. Kanilo, P.M., Khristich, V.A.: Energy and environmental characteristics of gas turbine engines using hydrocarbon fuels and hydrogen. Kiev, Scientific Opinion 256 (1987)

16. Zeldovich, Ya.B., Sadovnikov, P.Ya., Frank-Kamenetsky, D.A.: Oxidation of nitrogen during combustion. Leningrad. Izdatelstvo AN SSSR 147 (1947)

17. Bondarenko, G.A., Kirik, G.V.: Compressor stations: a textbook. Sumy, Sumy State University, p. 385 (2016)

18. Elaboration and production of turboexpander equipment: https://turbogaz.com.ua/en/. Last accessed 07 June 2021
19. Resolution of the National Commission for Regulation of Economic Competition dated 06.11.2020 No 2033 "On approval of the Methodology for determining the size of regulatory and production-technological losses/costs of natural gas in the distribution of natural gas and changes to some regulations of the National Commission for Regulation of Economic Competition". Verkhovna Rada of Ukraine (2021). https://zakon.rada.gov.ua/laws/show/v2033874-20#Text. Last accessed 07 June 2021
20. Tax Code of Ukraine dated 02.12.2010. No 2755-VI. Verkhovna Rada of Ukraine. Official publishing house. Kyiv: Information of the Verkhovna Rada of Ukraine, No 13–14, No 15–16, No 17, p. 112 (2011)

Thermodynamic Analysis and Optimization of the Cycle of a CHP Plant Power Unit Operating with Ultra-supercritical Steam Parameters

Victoria Tarasova[(✉)] , Andrii Kostikov , and Mikhail Kuznetsov

A. Pidgorny Institute of Mechanical Engineering Problems of National Academy of Science of Ukraine, Pozharskogo 2/10, Kharkiv 61046, Ukraine
tarasova@ipmach.kharkov.ua

Abstract. The actual problem of modern power engineering both in Ukraine and around the world is the transfer of existing energy generating capacity of combined heat and power plants (CHPP) to operate with ultra-supercritical steam parameters. Reconstruction of CHPP power units can extend the service life of existing steam generators, improve environmental and economic performance. But increasing the ranges of operating modes due to the introduction of new technologies and types of power equipment requires a radical revision of approaches to the quality of design of thermal circuits. The purpose of the study was to create a method for optimizing the CHPP power units operating with ultra-supercritical steam parameters, taking into account losses from the irreversibility of thermodynamic processes in their main elements. The topological-exergetic model of the CHPP power unit with intermediate superheating of steam, operating with ultra-supercritical steam parameters, was formed. Thermodynamic and exergy analysis of the CHPP power unit operation with variation of superheated steam parameters were performed. The method for optimizing the operating modes of the CHPP power unit operating with ultra-supercritical steam parameters was developed. As a result of multivariate calculations, the optimal operating parameters were found, at which the maximum efficiency of the CHPP power unit with the minimum values of the exergy destruction in its main elements is observed. This makes it possible to determine the rational limit for further increasing the parameters of the superheated steam.

Keywords: Combined heat and power plant · Energy efficiency · Exergy analysis · Optimization · Resource use efficiency · Ultra-supercritical steam parameters

1 Introduction

The actual problem of modern power engineering both in Ukraine and around the world is the transfer of existing energy generating capacity of combined heat and power plants (CHPP) to operate with ultra-supercritical steam parameters. Reconstruction of CHPP

power units can extend the service life of existing steam generators, improve environmental and economic performance. Currently, the typical range of steam supercritical parameters is from 240 bar to 285 bar of pressure at temperatures from 540 °C to 596 °C.

Today, the global thermal power industry has already taken real steps towards a massive transition to power units operating with ultra-supercritical steam parameters (30 MPa/600 °C, and even up to 35 MPa/650 °C). In the literature there are reports of work on the design of power units operating at an initial steam temperature of more than 700 °C [1].

But increasing the ranges of operating modes due to the introduction of new technologies and types of power equipment requires a radical revision of approaches to the quality of the thermal circuits design [2–5]. It is known that huge funds are spent on the development of CHPPs, so in modern economic conditions it is necessary to develop and improve advanced methods of analysis and decision-making in the design of thermal circuits of energy systems [6–12].

The actual task is the design search for the optimal value of ultra-supercritical parameters of superheated steam, corresponding to energy, environmental and economic requirements.

The purpose of this research can be formulated as the creation of a method for optimizing CHPP power units operating with ultra-supercritical steam parameters, taking into account losses from the irreversibility of thermodynamic processes in their main elements.

2 Literature Analysis and Problem Statement

When analyzing the feasibility of reconstructing the CHPP thermal circuit, it is necessary to take into account that the operation of the equipment being replaced is determined by the efficiency of not only the main, but also the auxiliary elements of the power unit. Power units consist of a large number of elements, the dependencies between which are always complex. In this case, not only the parameters inside the power unit are important, but also the analysis of all possible types of interaction of energy flows at the boundaries of the system.

One of the effective methods for analysing thermal schemes is the exergy method [6–8], the basis of which is the assessment of the state of the energy-technological system as a whole and its individual elements using a generalized thermodynamic characteristic (exergy), which provides the final target effect.

Using the exergy method, it is possible to comprehensively solve such problems as the thermoeconomic optimization of the power unit or its subsystems, the determination of rational operating modes, and the distribution of exergy costs between the power unit elements.

As is known [9], in any energy conversion system there is always an element (or set of elements), the change in thermodynamic losses in which most affects the efficiency of the system as a whole. Using the exergy approach to design, it is possible to choose variable factors, the change of which decisively affects the efficiency of the system. This solves the problem of finding a "bottleneck" in the system, where the increase in costs per unit exergy is particularly sharp. This makes it possible to significantly narrow

the range of variation of the parameters in the search for rational technical solutions for the reconstruction of the thermal circuit elements, which creates the preconditions for the construction of evolutionary algorithms for the synthesis of energy conversion systems. Here arises the important task of choosing a strategy for the development of the production power system.

Currently, various methods of designing complex technical systems based on the exergy approach are being introduced into engineering practice [6, 7]. They can be grouped into two classes: algebraic and numerical methods. All of them are based on the use of thermoeconomic models or topological-exergetic models, which are formed from a complex set of linear equations to determine the exergetic product of each element of the system. Among the algebraic methods are: the theory of exergetic cost, the theory of average costs and the modified productive structural analysis. Numerical methods include thermoeconomic functional analysis and engineering functional analysis. A thorough analysis of the literature on the application of exergy methods for the analysis of thermal power plants was performed in [10]. This paper compares various approaches to the so-called 4-E modeling (energy, exergy, economics and ecology), which includes methods and algorithms for exergy analysis of energy conversion systems, methods for modeling the relationships between exergy and economic flows and their costs in the power unit and its elements.

A purely thermodynamic analysis of the supercritical Rankine cycle with single and double intermediate overheating for a modern steam power plant with a capacity of 1,200 MW was performed in [11]. Variational calculations were used to determine the exergy destruction in each element, and it was shown that an increase in temperature has a greater effect on an increase in the power plant electrical efficiency than an increase in pressure. Thus, with superheated steam parameters of 325 bar/700 °C, the efficiency of the single/double intermediate overheating cycle is 46.45%/49.40%, and at 350 bar/650 °C this efficiency is 45.40%/47.92%. However, the authors did not consider the influence of the intermediate superheated steam parameters, and did not determine the limits in which an increase in the parameters of the superheated steam still has a rational meaning.

Research in [12] is devoted to the energy and exergy evaluation of a 220 MW supercritical thermal power plant. The authors performed the component based exergy analysis and calculated the exergy destruction in the main elements of the power plant. It is determined that the total exergy that was destroyed in the power plant was 400.015 MW. The maximum values of exergy destruction (87%) take place in the boiler. At the same time, the exergy destruction in three turbines is in total 9%, and in the condenser it is only 2%. The authors tried to reduce the losses of exergy in the boiler, but at the same time they did not study the influence of the irreversibility of thermodynamic processes in other elements on the exergy destruction in the boiler.

It should be noted that in all studies, the parameters of superheated steam were set selectively without any system, which does not allow determining the general trend in the change in efficiency when varying the parameters. In addition, an unsolved problem is the determination of the limit to which a further increase in the superheated steam parameters is thermodynamically expedient.

Therefore, the research tasks are:

1. Formation of a topological-exergetic model of a CHPP power unit with intermediate superheating of steam, operating with ultra-supercritical steam parameters.
2. Performing a thermodynamic and exergy analysis of the CHPP power unit operation with variation of superheated steam parameters.
3. Development of a method for optimizing the operating modes of the CHPP power unit operating with ultra-supercritical steam parameters, taking into account losses from the irreversibility of thermodynamic processes in its main elements.

When performing these research tasks, the modern methods of applied thermodynamics will be used, including the structural theory of thermoeconomics. This theory was developed by representatives of the Spanish school of applied thermodynamics [13].

3   Thermodynamic and Exergetic Model of a CHPP Power Unit Operating with Ultra-supercritical Steam Parameters

Figure 1 shows the thermal diagram of a CHPP power unit with intermediate superheating of steam.

BOIL – boiler; HPT – high-pressure turbine; LPT – low-pressure turbine;
EG – electric generator; COND – condenser; IHE – intermediate heat
exchanger; CONDP – condenser pump; FWP – feed water pump
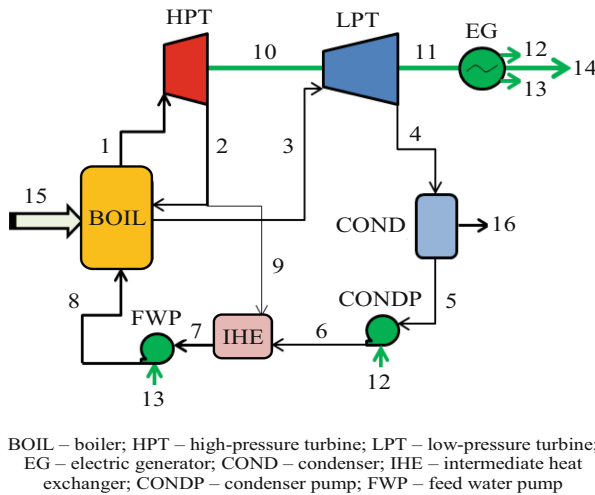
Fig. 1. Thermal diagram of a CHPP power unit with intermediate superheating of steam.

The equations of the thermodynamic model of a CHPP power unit with intermediate superheating of steam for its main blocks are presented in [14].

The indexation of exergy flows is shown in Fig. 1. The i-th flow of exergy ($i = 1 \ldots 9$) is determined by the equation

$$E_i = G_i(h_i - h_0 - [(T_0 + 273.15)(s_i - s_0)]),$$

where G is the mass flow rate; h_0, s_0 are the enthalpy and entropy of the working fluid at ambient pressure and ambient temperature, which are taken equal to $P_0 = 1.013$ bar and $T_0 = 20\,°C$.

Exergy flows from the 10-th to the 14-th can be written as: $E_{10} = N_{HPT}$, where N_{HPT} is the high-pressure turbine power; $E_{11} = N_{LPT}$, where N_{LPT} is the low-pressure turbine power; $E_{12} = N_{condp}$, where N_{condp} is the condenser pump power; $E_{13} = N_{FWP}$, where N_{FWP} is the feed water pump power; $E_{14} = N_{CHPP}$, where N_{CHPP} is the electric power of the CHPP power unit. The 15-th exergy flow E_{15} is equal to the heat output of the boiler Q_{boil}, and the entropy $s_{15} = 0$.

The exergy flow from the condenser can be written as

$$E_{16} = Q_{cond}\left[1 - \left(\frac{T_0 + 273.15}{T_5 + 273.15}\right)\right],$$

where Q_{cond} is the heat output of the condenser.

For a detailed exergy analysis, it is necessary to form a topological-exergetic model [15] of a CHPP power unit by dividing the exergy flows according to a qualitative attribute into "fuel" or "product" of an element, using the LIFO-principle of exergy flow decomposition [13, 15]. The model is formed as a complex of interrelated exergy flows of elements, in each of which the process of energy conversion (electrical, mechanical, thermal) is carried out. Energy conversion is estimated by the amount of decrease ("fuel") or increase ("product") of exergy flow in the power unit elements. Using the topological-exergetic model of the power unit, a relationship is established between the efficiency of the system and the exergetic efficiency of its elements. A detailed algorithm for the formation of a topological-exergetic model of the production structure of a power plant is given by us in [15].

Table 1 shows expressions for determining the exergy destruction in each element of the CHPP power unit and the distribution of exergy flows according to the qualitative attribute "fuel" or "product".

Table 1. Distribution of exergy flows in the elements of the CHPP power unit for "fuel" or "product" and their destruction.

No	Element	"Fuel"	"Product"	Exergy destruction, E_{Dk}
0	Environment	$E_{14} + E_{16}$	E_1	–
1	Boiler	E_{15}	$(E_1 - E_8) + (E_3 - E_2)$	$E_{D\,boil} = E_{15} + E_2 + E_8 - E_1 - E_3$
2	High-pressure turbine	$E_1 - E_2 - E_9$	E_{10}	$E_{D\,HPT} = E_1 - E_2 - E_9 - E_{10}$
3	Low-pressure turbine	$E_3 - E_4$	E_{11}	$E_{D\,LPT} = E_3 - E_4 - E_{11}$

(*continued*)

Table 1. (*continued*)

No	Element	"Fuel"	"Product"	Exergy destruction, E_{Dk}
4	Condenser pump	E_{12}	E_6–E_5	$E_{D\,condp} = E_{12} + E_5 - E_6$
5	Intermediate heat exchanger	E_9	E_7–E_6	$E_{D\,IHE} = E_6 + E_9 - E_7$
6	Feed water pump	E_{13}	E_8–E_7	$E_{D\,FWP} = E_{13} + E_7 - E_8$
7	Electric generator	$E_{10} + E_{11}$	$E_{12} + E_{13} + E_{14}$	$E_{D\,EG} = E_{10} + E_{11} - E_{14} - E_{12} - E_{13}$
8	Condenser	E_4–E_5	E_{16}	$E_{D\,cond} = E_4 - E_5 - E_{16}$

4 Determination of the CHPP Power Unit Efficiency with Varying Temperature and Pressure of Superheated Steam

Thermodynamic analysis of the cycle of the CHPP power unit operating with ultra-supercritical steam parameters, as well as its exergy analysis and optimization were performed. The following parameters were set as variables: the temperature of superheated steam was sequentially taken equal to 540 °C, 650 °C, and 700 °C, and its pressure was 24 MPa, 30 MPa, and 35 MPa. The following parameters were taken as fixed: pressure and temperature of steam in the low-pressure turbine inlet $T_3 = 540$ °C, $P_3 = 3.6$ MPa; steam pressure and temperature in the low-pressure turbine outlet $T_4 = 26.68$ °C, $P_4 = 0.0035$ MPa; temperature and pressure of feed water at the boiler inlet $T_8 = 249.9$ °C, $P_8 = 24.5$ MPa.

Also, the following parameters were taken as fixed: thermal efficiency of the boiler $\eta_{boil} = 0.93$; isentropic efficiency of the high-pressure turbine $\eta_{HPT} = 0.9$; isentropic efficiency of the low-pressure turbine $\eta_{LPT} = 0.9$; efficiency of the electric generator $\eta_{EG} = 0.98$. The efficiency of the pumps was taken equal to 0.85. For all calculations, the mass flow rate of superheated steam was set the same and equal to $G_1 = 266.7$ kg/s. It should also be noted that the relative degree of steam dryness at the low-pressure turbine outlet ($x_4 = 95\%$) was also taken as a fixed parameter.

Table 2 shows the cycle parameters of the CHPP power unit with intermediate superheating of steam at varying temperatures and pressures of superheated steam.

Variant *i* (see Table 2) was analyzed, for which the highest CHPP power unit efficiency is observed (Fig. 2). For this, the parameters of the corresponding reference cycle with avoidable exergy costs were found, namely: thermal efficiency of the boiler $\eta_{boil} = 0.99$; isentropic efficiency of the high-pressure turbine $\eta_{HPT} = 0.99$; isentropic efficiency of the low-pressure turbine $\eta_{LPT} = 0.99$; efficiency of the electric generator $\eta_{EG} = 1$; boiler pressure losses $\Delta P_{boil} = 0$; pressure losses in the superheater of the boiler $\Delta P_{SH} = 0$. The efficiency of the pumps was taken equal to 0.99.

Table 2. Cycle parameters of the CHPP power unit.

Parameter	Variant								
	a	b	c	d	e	f	g	h	i
T_1, °C	590	650	700	590	650	700	590	650	700
P_1, MPa	24	24	24	30	30	30	35	35	35
T_2, °C	311.0	357.5	397.1	281.2	325.4	363.6	261.7	303.8	340.8
P_2, MPa	3.8	3.8	3.8	3.8	3.8	3.8	3.8	3.8	3.8

Figure 2 shows the change in the CHPP power unit efficiency when changing T_1 and P_1.

Table 3 shows the values of exergy destruction in each element of the CHPP power unit, both complete exergy destruction and its component parts. In addition, Table 3 shows the avoidable (exogenous $E_{Dk}{}^{EX}$ and endogenous $E_{Dk}{}^{EN}$) and unavoidable $E_{Dk}{}^{UN}$ parts of exergy destruction in each k-th element, related to the complete destruction E_{Dk} in the each k-th element in percent. It should be noted that 82.57% of the total exergy destruction in the CHPP power unit ($E_{Dtot} = 427.77$ MW) corresponds to the exergy destruction in the boiler, 5.60% – in the low-pressure turbine, 6.82% – in the intermediate heat exchanger, and the rest (5.01%) corresponds to other elements.
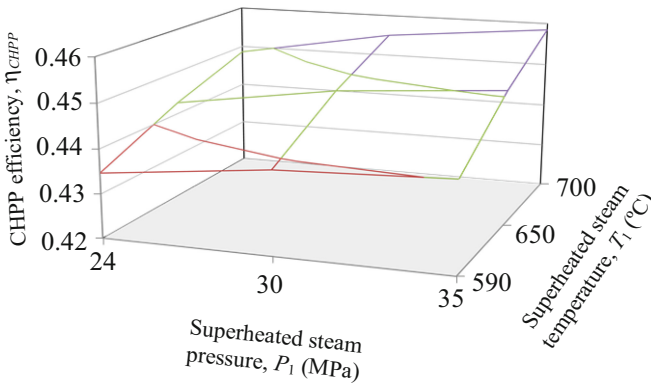
Fig. 2. CHPP power unit efficiency when changing T_1 and P_1.

From the Table 3 it can be seen that most of the exergy destruction in the boiler corresponds to unavoidable destruction ($E_{Dk}{}^{UN} = 83.60\%$), the endogenous component $E_{Dk}{}^{EN}$ of avoidable destruction (associated with the imperfection of the boiler itself) is 6.31%, and the exogenous component $E_{Dk}{}^{EX}$ of avoidable destruction (associated with the imperfection of other elements) is 10.09%.

Calculations show that most of the exogenous part of exergy destruction in the boiler is associated with irreversible thermodynamic processes in the low-pressure turbine, and a smaller, but also important part, with irreversibility in the high-pressure turbine and

Table 3. Exergy destruction in each element of the CHPP power unit (variant *i*).

Element	E_{Dk}, MW	$E_{Dk}EN$, MW	$E_{Dk}EX$, MW	$E_{Dk}{}^{UN}$, MW	$E_{Dk}{}^{EN}$, %	$E_{Dk}{}^{EX}$, %	$E_{Dk}{}^{UN}$, %
Boiler	353.18	22.28	35.64	295.27	6.31	10.09	83.60
High-pressure turbine	9.01	8.08	0.10	0.84	89.64	1.06	9.30
Low-pressure turbine	23.95	20.87	1.00	2.09	87.13	4.16	8.71
Condenser pump	0.12	0.09	0.02	0.01	77.31	18.00	4.69
Intermediate heat exchanger	29.20	1.20	3.40	24.60	4.11	11.63	84.26
Feed water pump	1.00	0.76	0.19	0.05	76.31	18.58	5.11
Electric generator	7.87	7.80	0.07	0.00	99.15	0.85	0.00
Condenser	3.42	1.97	0.18	1.28	57.48	5.12	37.40

losses in the electric generator. Thus, if we improve these elements, or find the optimal modes of their operation, it is possible to reduce the exergy destruction in the boiler, and therefore in the entire CHPP power unit.

5   Optimization of the Cycle of the CHPP Power Unit

To determine the optimal value of pressure P_1, up to which the efficiency of the CHPP power unit is still increasing, its cycle was optimized as follows.

It should be noted that in Table 1 the "product" of the condenser is the irreversible losses of exergy to the environment. Therefore, the electric power of the CHPP power unit can be represented by the exergy balance equation

$$N_{CHPP} = Q_{boil} - E_{Dtot} - E_{16},\qquad(1)$$

where E_{Dtot} is the total exergy destruction in all elements of the CHPP power unit.

Equation (1) can be represented as:

$$\eta_{CHPP} = \frac{N_{CHPP}}{Q_{boil}} = 1 - e_{Dtot} - e_{16},\qquad(2)$$

where $e_{Dtot} = E_{Dtot}/Q_{boil}$ is the relative total exergy destruction in the CHPP power unit; $e_{16} = E_{16}/Q_{boil}$ is the relative exergy costs in the condenser.

We will consider (2) as a function that depends on the pressure P_1. To find the optimal value of P_1, which provides the maximum value of the CHPP power unit efficiency, we use the necessary extremum condition:

$$\frac{\partial \eta_{CHPP}}{\partial P_1} = -\frac{\partial e_{Dtot}}{\partial P_1} - \frac{\partial e_{16}}{\partial P_1} = 0.$$

For convenience, we will write

$$f = \left(-\frac{\partial e_{Dtot}}{\partial P_1} - \frac{\partial e_{16}}{\partial P_1} \right).$$

To determine the optimal superheated steam pressure P_{1opt}, we plot the dependences $f(P_1)$ for each temperature T_1 under consideration (Fig. 3). The optimal value of P_{1opt} is located at the intersection of f with the abscissa axis.

6   Results and Discussion

Figure 3 shows that at $T_1 = 590\ ^\circ C$ $P_{1opt}^{(590)} = 38$ MPa, and at $T_1 = 700\ ^\circ C$ $P_{1opt}^{(700)}$ is almost 45 MPa. For each temperature T_1, until the pressure P_1 reaches the P_{1opt} value, the CHPP power unit efficiency η_{CHPP} will increase, and with a further increase in pressure P_1, η_{CHPP} will gradually decrease.
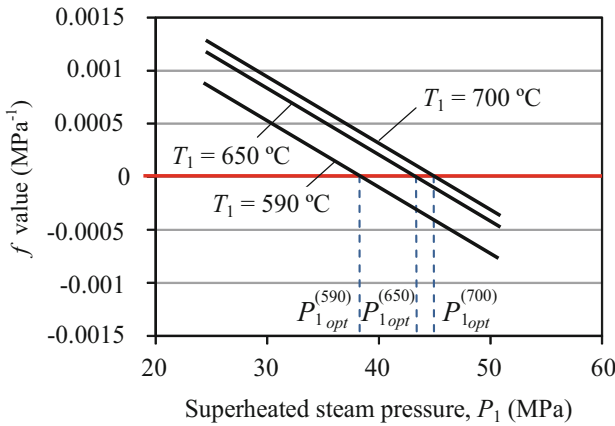
Fig. 3. Dependence of f value on P_1.

Thus, variant g (see Table 2) at $T_1 = 590\ ^\circ C$ and $P_1 = 35$ MPa is the closest to the optimal one, at which there are the minimum relative total exergy destruction in the CHPP power unit and the minimum relative costs of exergy, which is lost from the condenser to the environment. Further improvement of this variant will not significantly affect the energy efficiency of the CHPP power unit.

As for variant i at $T_1 = 700\ ^\circ C$ and $P_1 = 35$ MPa, a further increase in pressure P_1 will only improve the energy performance of this variant.

If you choose from variants $a - c$ at $P_1 = 24$ MPa, then preference should be given to variant c with highest efficiency, namely, at $T_1 = 700\ ^\circ C$ (see Fig. 2).

The obtained results do not contradict the data of other authors [5, 7, 8], but when choosing the best variant, such restrictions arise as the real technical capabilities of mechanical engineering and the cost of equipment. Therefore, further research will be devoted to the thermoeconomic analysis and optimization of the CHPP power unit operating with ultra-supercritical steam parameters.

7   Conclusions

1. The topological-exergetic model of the CHPP power unit with intermediate superheating of steam, operating with ultra-supercritical steam parameters, was formed.
2. Thermodynamic and exergy analysis of the CHPP power unit operation with varying parameters of superheated steam were performed. The values of exergy destruction in each element of the CHPP power unit, both complete exergy destruction and its component parts, were obtained. It has been shown that most (more than 80%) of the total exergy destruction in the CHPP power unit corresponds to the exergy destruction in the boiler. Most of the exogenous part of exergy destruction in the boiler is associated with irreversible thermodynamic processes in the low-pressure turbine, and a smaller, but also important part, with irreversibility in the high-pressure turbine and losses in the electric generator.
3. The method for optimizing the operating modes of the CHPP power unit operating with ultra-supercritical steam parameters was developed. As a result of multivariate calculations, the optimal operating parameters were found, at which the maximum efficiency of the CHPP power unit with the minimum values of the exergy destruction in its main elements is observed. This makes it possible to determine the rational limit for further increasing the parameters of the superheated steam.
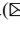
References

1. Basu, S., Debnath, A.K.: Power plant instrumentation and control handbook. A guide to thermal power plants. 2nd edn. Academic Press (2019)
2. Yang, M., Zhou, Yl., Wang, D., Han, J., Yan, Y.: Thermodynamic cycle analysis and optimization to improve efficiency in a 700 °C ultra-supercritical double reheat system. J. Therm. Anal. Calorim. **141**, 83–94 (2020)
3. Rocha, D.H.D., Silva, R.J.: Exergoenvironmental analysis of a ultra-supercritical coal-fired power plant. J. Clean. Prod. **231**, 671–682 (2019)
4. Nikam, K.C., Kumar, R., Jilte, R.: Exergy and exergo-environmental analysis of a 660 MW supercritical coal-fired power plant. J. Therm. Anal. Calorim. **145**, 1005–1018 (2021)
5. Zhao, Z., et al.: Exergy analysis of the turbine system in a 1000 MW double reheat ultra-supercritical power plant. Energy **119**, 540–548 (2017)
6. Pattanayak, L., Sahu, J.N., Mohanty, P.: Combined cycle power plant performance evaluation using exergy and energy analysis. Environ. Prog. Sustainable Energy **36**(4), 1180–1186 (2017)
7. Kumar, A., Nikam, K.C., Behura, A.K.: An exergy analysis of a 250 MW thermal power plant. Renew. Energy Res. Appl. **1**(2), 197–204 (2020)
8. Uysal, C., Kurt, H., Kwak, H.-Y.: Exergetic and thermoeconomic analyses of a coal-fired power plant. Int. J. Therm. Sciences **117**, 106–120 (2017)
9. Wang, L., Fu, P., Yang, Z., Lin, T.-E., Yang, Y., Tsatsaronis, G.: Advanced exergoeconomic evaluation of large-scale coal-fired power plant. J. Energy Eng. **146**(1), 04019032 (2020)
10. Kumar, R.: A critical review on energy, exergy, exergoeconomic and economic (4-E) analysis of thermal power plants. Eng. Science and Technology, an Int. J. **20**(1), pp. 283–292 (2017)
11. Peyyala, N.R., Govindarajulu, K.: Thermodynamic analysis of 1200 MW coal based supercritical thermal power plant with single and double reheating. Int. J. Eng. Sciences & Research Technol. **3**, 677–684 (2017)

12. Eke, M.N., Onyejekwe, D.C., Iloeje, O.C., Ezekwe, C.I., Akpan, P.U.: Energy and exergy evaluation of a 220 MW thermal power plant. Nigerian J. Technol. **37**(1), 115–123 (2018)
13. Torres, C., Valero, A.: The exergy cost theory revisited. Energies **14**(6), 1594 (2021)
14. Rusanov, A.V., Kostikov, A.O., Shubenko, O.L., Kharlampidi, D., Tarasova, V.O., Senetskyi, O.V.: Highly efficient cogeneration power plant with deep regeneration based on air Braiton cycle. J. Mechanical Engineering **22**(4), 12–23 (2019)
15. Kharlampidi, D., Tarasova, V., Kuznetsov, M., Voytenko, E.: Thermodynamic analysis of air-compression refrigerating machine based on the exergy cost theory. Eastern-European J. Enterprise Technologies **5**(8), 30–38 (2017)

Advanced Computer Technologies in the New Flow Part Development for Reactive Type HPC Steam Turbine of T-100 Series

Andrii Rusanov , Marina Chugay , and Roman Rusanov[✉]

A. Pidhornyi Institute of Mechanical Engineering Problems of the NAS of Ukraine, Pozharskogo 2/10, Kharkiv 61046, Ukraine
roman_rusanov@ipmach.kharkov.ua

Abstract. The paper is devoted to designing the new high-pressure cylinder (HPC) flow part of T-100 series heating turbines based on numerical simulation of gas dynamic characteristics using the in-house IPMFlow software package. The new flow part is designed with reactive-type stages. The comprehensive methodology, which is implemented in IPMFlow package, includes methods of various type of complexity: gas dynamic calculations with taking into account thermodynamic properties of the real steam (IAPWS-95 equations) and methods for designing blade profiles geometry based on a fixed finite number of parameters. At the final step, calculating end-to-end of the HPC with 18 stages was performed. The calculations are performed using the parallel computing technology. It is shown the substantial increasing in power and efficiency of the developed HPC. Such increase was reached due to using the monotonic meridional contours and stages of reactive type with advanced smooth blade profiles.

Keywords: Steam turbine · Reactive type blading · Flow part · High-pressure cylinder · Spatial flow · Computational research

1 Introduction

In July 2021, the European Commission released the "Fit for 55" package of proposals to change the EU's policies about climate, energy, etc. to reduce the greenhouse gas emissions by 55% by 2030, compared to 1990 [1]. The main direction of meeting these requirements is the transition to clean "green" fuels with a simultaneous decrease in the use of hydrocarbons [2], including the almost complete rejection of "dirty" coal-fired thermal power plants (TPP) [3]. Another way to satisfy "Fit for 55" package of proposals consists in increasing the efficiency of power generating equipment at combined heat and power plants (CHPP) and TPPs. This way provides decreasing the unit coal-fired fuels consumption for generated electricity, and reducing the harmful emissions [4].

The efficiency of TPPs and CHPPs facilities, namely power generating equipment, can also be improved, so that it will be possible to improve the gas dynamic characteristics of the flow parts of steam turbines. This is important for Ukraine and post-soviet countries because actually all the equipment at most existing power units of TPPs almost

completely exhausted its estimated and residual resource [5]. They need to be replaced with new ones [6], or require complete reconstruction [7]. In world practice of turbine building, it is accepted that the flow part of powerful steam turbines consists of three cylinders: of high, intermediate and low pressure [8]. The most problematic of them are HPCs. Almost all the HPCs of steam turbines that are part of TPPs and CHPPs, which are operated in Ukraine and post-soviet countries, are made with impulse-type stages [9]. Stages of such type allow to trigger large thermal drops (compared to reactive), therefore, their number is smaller, which helps to reduce the production price of the turbine. One of the main differences of reactive-type stages is the fact that the flow velocity is higher and such stages require significantly improved seals [10]. Recent investigations concern with numerical simulations of gas dynamic characteristics for improvement and modifications of the turbomachine flow parts, are carried out using the 3D CFD methods [11, 12]. These research works indicate the significant advantages of the reactive-type stages in efficiency compared with the impulse-type ones [13].

It should be noted that the T-100 series turbines with an impulse-type HPC are the most widespread steam turbines. On the territory of Ukraine, 6 turbines of the T-100 series have been installed and are in operation, and there are more than 300 of them all over the world.

The article presents a new design of the reactive-type HPC flow part of the T-100 series turbine. The main purpose to develop the new flow part is adjustment within the overall the existing turbine dimensions. New turbine was developed using the in-house IPMFlow software package. The comprehensive methodology, which is implemented in IPMFlow package, includes methods of various type of complexity: gas dynamic calculations with taking into account the real thermodynamic properties of steam, as well as methods for designing of the blade profiles geometry. It is shown that due to using the monotonic meridional contours and reactive-type stages with smooth blade profiles, substantial increase of power and efficiency is obtained in the developed HPC.

2 Method for Gas Dynamic Calculation and Profiling of Axial Reactive-Type Flow Parts

Numerical simulating the 3D steam flow and designing the new flow part of the steam turbine are accomplished with the in-house IPMFlow software package. This in-house package is the result of development and generalization of earlier in-house Computer Codes FlowER and FlowER-U [14]. The IPMFlow software package is based on the next mathematical model [15]:

- the numerical implementation of the unsteady Reynolds-averaged Navier-Stokes equations;
- the implicit quasi-monotonic ENO method of high accuracy;
- the Menter k-ω shear stress transport turbulence two-equation model;
- the method of analytical approximation-interpolation to IAPWS-95 equations taking into account the steam thermodynamic properties [16].

The numerical simulation was accomplished using IPMFlow software package. The sufficient reliability of results is demonstrated both by qualitative flow specifics, and

by quite accurate quantitative estimations of the dynamical characteristics of isolated turbine stage as well as the whole turbomachine.

For reducing and accelerating the computation time in the IPMFlow software package, the advanced parallel computing technology is introduced [17]. Its main features are following:

– usage for shared RAM computers only,
– applicability for any operating system (considering each parallel process as the executable module).
– in one parallel process, at least one blade row should be considered (minimal geometric object);
– the total processes number should not exceed the number of rows of turbine blades.
– the total number of processes may be unequal to the cores number.
– the computational acceleration depends almost linearly on the total number of processes.

For instance, using the parallel computations of the 18-stages flow part with 9 processes at 8 cores led to the computational time acceleration by 7.1 while maximum possible acceleration is 8.

For describing the axial blade row geometry, the method of analytical profiling [18] is used. Here the blade is determined by the set of flat profiles defined by 4th and 5th order curves. As the initial data, the finite number of parameters is used. These parameters commonly accepted in turbine engineering are following: number of blades, width of profile, inflow and effective outflow angles, etc. The method allows to obtain full three-dimensional geometric characteristics of a wide range of axial turbines flow parts in a short time. That makes it qualified and efficient in gas dynamic design, modification, and improvement of turbomachines.

3   Research Object

The latest modifications of the T-100 series turbines, namely T-110/120–130, is considered in this research. The nozzle steam distribution system with a two-stage Curtis control stage is used in this turbine [19]. HPC consists of a control stage and 8 impulse-type pressure stages (Fig. 1).

The lowest efficiency in the control stage is 67.9%, the efficiency of the pressure stages is 89.5–90%, and HPC's efficiency as a whole is 84.5%. The initial flow part total capacity is 46.3 MW. All these data were obtained from simulations and described in [20]. Calculations were performed without taking into account losses in blade-shaft and blades-casing clearances.
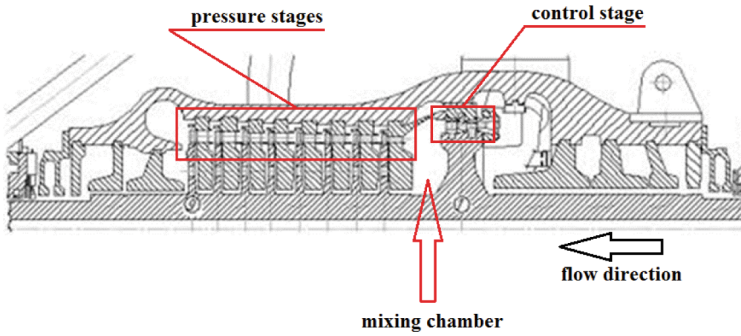
Fig. 1. Mid-meridional section of the flow part of HPC of T-110/120–130 series turbine [20].

4   Results and Discussion

The main outcome of the research is development of the new HPC flow part. The elaborated unit has essential advantages, such as fitting into the existing dimensions, possibility of installation on the existing fundaments of the original one. The boundary conditions involved for the gas dynamic design are satisfied for the initial HPC, namely, behind the control valves at the HPC inlet, the total pressure and temperature are 12.8 MPa and 555 °C, respectively, static outlet pressure is 3.3 MPa, and mass flow is 133.06 kg/s.

The developed HPC flow part has 18 cylindrical stages: control stage and 17 reactive-type stages. All stages are designed with constant cross-sections. To reduce the losses, the control compartment of the new HPC was designed without a mixing chamber [21]. Instead of the abovementioned mixing chamber, the axial distance between the first stage rotor and second stage stator was increased. To provide the optimal loading of the new flow part stages, their number and thermal drops distribution are chosen so as to provide an approximate equality of the value u/c0 to 0.7 (with an exception for the control stage) [22]. The outflow angle from the stage is chosen to ensure proximity to the axial direction. The design of meridional contours with the stages position in them (Fig. 2) is carried out on the basis of the data obtained using approximate methods. These data include number of stages, mid-diameters, thermal drops, and heights of stages. The next step in the design was manual and separate creation and calculations of the stages. At the final step, end-to-end computations of the entire HPC and its refinement were carried out. The final HPC's flow part view was obtained by considering, on the average, 5–7 options for each stage separately, and 3 options of HPC entirely. End-to-end HPC computations of all 18 stages were accomplished on h-type difference grids with boundary layer thickness corresponding to $y + < 5$, and the total cell number of about 15 million (about 450 thousand for each row). Calculations were performed without taking into account the losses in blade-shaft and blades-casing clearances.
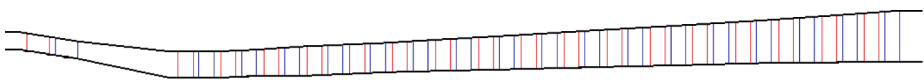
Fig. 2. The new HPC mid-meridional section of (red line – stator blades, blue line – rotor blades).

Figure 2 demonstrates the smoothness of the meridional contours and absence of overlaps. This helps to avoid the emergence of circulation zones (flow separation) in places of the sharp shape changing in the meridional contours [23].

Figs. 3, 4 and 5 show the isolines, and Figs. 6, 7 and 8 demonstrate the diagrams of static pressure distribution in the mid-tangential sections on the blade surfaces.

a   b
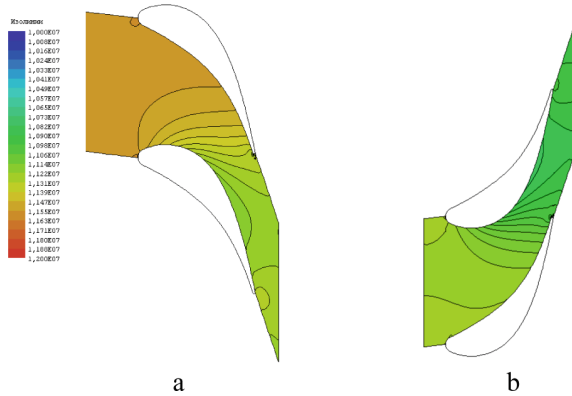
Fig. 3. Static pressure isolines in 2nd stage along the middle tangential section: a – stator, b – rotor

a   b
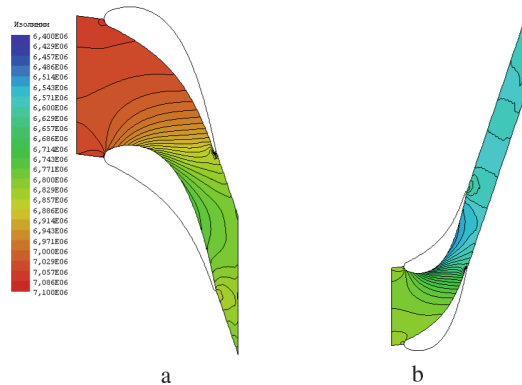
Fig. 4. Static pressure isolines of 10th stage along middle tangential sections: a – stator, b – rotor.

It can be seen from the results obtained (Figs. 3, 4, 5, 6, 7 and 8) that smoothing the profiles by 4th and 5th order curves led to the fairly monotonic static pressure distribution on the blades. Such picture of the flow can be observed in each row of the designed flow part. This indicates the high level of the flow part gas dynamic perfection that is confirmed by the integral characteristics presented in Table 1.

Table 2 demonstrates the gas dynamic characteristics of the initial and new HPCs. So, the first (control) stage efficiency is higher than 91%, and the rest of the stages are in the range of 92–94%. The total elaborated HPC flow part efficiency is 93.5%, and its power of nominal mode is 51.2 MW. The efficiency and power of the offered flow part compared with the initial one increase by 9.0% and 4.9 MW, respectively.

a   b
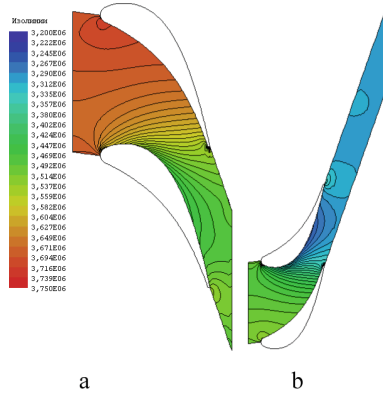
Fig. 5. Static pressure isolines in 18th stage along middle tangential sections: a – stator, b – rotor.

a   b
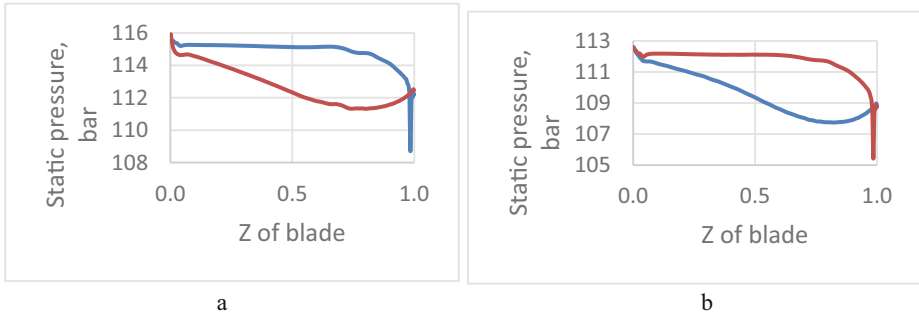
Fig. 6. Static pressure at the blade surfaces along middle tangential sections of the 2nd stage: a – stator, b – rotor, Z – axial dimensionless coordinate (0 – leading edge, 1 – trailing edge).

a   b
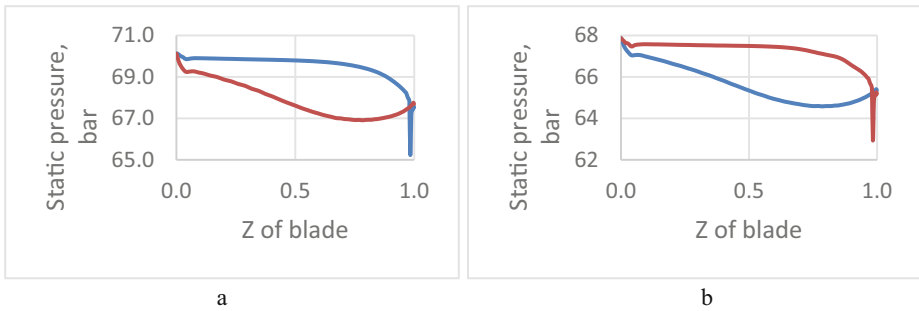
Fig. 7. Static pressure at blade surfaces along middle tangential sections of the 10$^{\text{th}}$ stage: a – stator, b – rotor, Z – axial dimensionless coordinate (0 – leading edge, 1 – trailing edge).

a   b
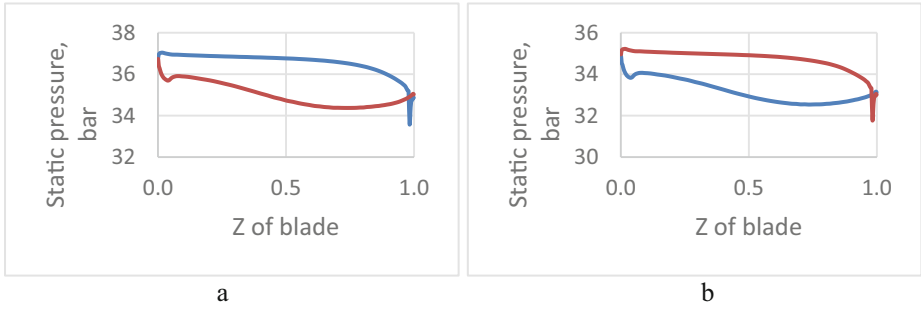
Fig. 8. Static pressure at the blade surfaces along middle tangential sections of the 18th stage: a – stator, b – rotor, Z – axial dimensionless coordinate (0 – leading edge, 1 – trailing edge).

Table 1. The main integral characteristics by stages for new high pressure cylinder flow part.

No of stage	Efficiency, %	Reactivity degree, %	Power, MW
1	91.26	0.225	4.31
2	92.25	0.519	2.43
3	92.53	0.499	2.40
4	92.51	0.476	2.49
5	92.55	0.479	2.43
6	92.82	0.502	2.52
7	92.88	0.494	2.53
8	93.01	0.49	2.56
9	93.15	0.49	2.57
10	93.02	0.488	2.61
11	93.67	0.494	2.64
12	93.86	0.5	2.67
13	94.02	0.49	2.70
14	93.80	0.488	2.72
15	94.17	0.501	3.14
16	93.96	0.481	3.39
17	94.05	0.48	3.50
18	93.83	0.484	3.65

Table 2. Integral characteristics of the old and new high pressure cylinder flow parts.

	Mass flow, kg/s	Power, MW	Efficiency, %
Original HPC	133.06	46.3	84.5
New HPC	133.06	51.2	93.5
Difference	+0.0	+4.9	+9.0

5   Conclusions

The 3D geometry and computational models of the new HPC flow part of T-110/120–130 series steam turbine have been developed based on the variational principles of 3D turbulent steam flows. Numerical simulation was accomplished using methods and solvers for gas dynamic calculations and design of flow parts originated and evolved at IPMach NAS of Ukraine.

The results and computational analysis are presented for the final version of the new HPC flow part of the T-110/120–130 series steam turbine. The proposed HPC flow part contains 18 stages (the control and 17 reactive-type) compared with 9 stages of the initial design.

The developed HPC flow part total efficiency is 93.5%, and its power is 51.2 MW at the nominal mode that is by 9.0% and 4.9 MW higher than those of the original turbine.

The total efficiency of the offered HPC flow part is 93.5%, whereas its power of nominal mode is 51.2 MW that demonstrate increasing the efficiency and power of the offered flow part compared to the initial one by 9.0% and 4.9 MW, respectively.

The technique developed in this paper and obtained experience will be successfully applied in elaboration of new and improvement of existing HPC flow parts in different large steam turbines in operation, or can be implemented at thermal power and combined heat and power plants both in the Ukraine and other countries.

References

1. European Electricity Review 6-month update H1-2021. Ember (2021)
2. Directive 2004/8/ec of the European parliament and of the council of 11 February 2004 on the promotion of cogeneration based on a useful heat demand in the internal energy market and amending Directive 92/42/EEC: Official Journal of the European Union (2004)
3. Alparslan, U.: Turkey, Ukraine and Western Balkan countries compete for top spot in coal power air pollution in Europe. Ember research (2021)
4. Assessing the effectiveness of EU policy on large combustion plants in reducing air pollutant emissions. European Environment Agency, Report No 7/2019. Luxemb. Publ. Off. Eur. Union (2019)

5. Chernousenko, O.Yu., Peshko, V.A.: Estimating the Low-Cycle Fatigue, Damageability and the Residual Life of the Rotor of High Pressure Turbine T-100/120–130 unit No 1 used by PJSC "Kharkiv CHPP-5". Visnyk NTU «KhPI», Series: Enerhetychni ta teplotekhnichni protsesy y ustatkuvannia **10**(1232), 29–37 (2017). (in Russian)

6. Mikhailov, V.E., Smolkin, Y.V., Sukhorukov, Y.G.: The main directions for improving the efficiency of the power equipment of a CHPP. Therm. Eng. **68**(1), 54–58 (2021). https://doi.org/10.1134/S0040601520120046

7. Shibaev, T.L.: A review of trends in development of cogeneration steam turbine units. Therm. Eng. **67**, 903–908 (2020)

8. R.A. Chaplin: Thermal Power Plants, vol. III, Steam Turbine Components and Systems. EOLSS (2009)

9. Bazeev, E.T., et al.: Energy: history, present and future, Book. 3: Development of heat and hydropower. In: Klimenko, V.M., Landau, Yu. O., Sigal. I. Ya. (eds.) Science (2013). (in Ukrainian)

10. Wolf, R., Romanov, K.: Steam Turbines: Siemens Reactive Blading – designed for highest efficiency and minimal performance degradation. Siemens AG, 19 p. (2014)

11. ANSYS-Fluent Homepage. http://www.ansys.com/Products/Fluids/ANSYS-Fluent

12. NUMECA Homepage. https://www.numeca.com/en_eu/turbomachinery

13. Haller, B., D'Ovidio, A., Henson, J., Beevers, A., Gupta, A.: Development of improved reaction technology blading (RTB LAR) for large steam turbines. In: Proceedings of the ASME 2019 Power Conference. Salt Lake City, Utah, USA (2019)

14. Yershov, S., Rusanov, A., Gardzilewicz, A., Lampart,, P.: Calculations of 3D viscous compressible turbomachinery flows, In: Proceedings of the 2nd Symposium on Compter Technologies for Fluid/Thermal/Chemical Systems with Industrial Applications, ASME PVP Division Conference, Vol. 397.2, pp. 143–154., Boston, USA (1999)

15. Menter, F.R.: Two-equation eddy viscosity turbulence models for engineering applications. AIAA J. **32**(8), 1598–1605 (1994)

16. Rusanov, A.V., Lampart, P., Pashchenko, N.V., Rusanov, R.A.: Modelling 3D steam turbine flow using thermodynamic properties of steam IAPWS-95. Polish Maritime Res. **23**(1), 61–67 (2016)

17. Fischer, P.F., Venugopal, M.: A commercial CFD application on a shared memory multiprocessor using MPI, In: Ecer, A., Periaux, J., Satdfuka, N., Taylor, S. (eds.) Parallel Computational Fluid Dynamics, pp. 231–238. North-Holland (1996)

18. Rusanov, A., Rusanov, R., Lampart, P.: Designing and updating the flow part of axial and radial-axial turbines through mathematical modeling. Open Eng. **5**, 399–410 (2015). https://doi.org/10.1515/eng-2015-0047

19. Achille, M., Cardarelli, S., Pantano, F., Zito M.: Design and CFD analysis of a curtis turbine stage, ECOS 2016. In: Proceedings of the 29th International Conference on Efficiency, Cost, Optimisation, Simulation and Environmental Impact of Energy Systems, Portorož, Slovenia, 19–23 June 2016

20. Goloshumova, V.N., Brodov, Y., Mikhailov, A.G.: Directions of perfection of design high-pressure cylinder of cogeneration steam turbine family T-100-130. Bull. South Ural State University, Series: Energetic **15**(4), 5–12 (2015). (in Russian)

21. Zaryankin, A.E., Lavyrev, I.P., Cherkasov, M.A.: Nozzle steam distribution with a remote mixing chamber. Therm. Eng. **67**(9), 655–659 (2020)

22. Nguyen, K., Laskin, A.: Influence of u/C0 ratio on unsteady loads and efficiency level of axial turbine stage. Sci. Educ. Bauman **6**, 56–66 (2015). (in Russian)

23. Rusanov, A., Rusanov, R.: The influence of stator-rotor interspace overlap of meridional contours on the efficiency of high-pressure steam turbine stages. Arch. Thermodyn. **42**(1), 97–114 (2021)

Energy Saving Technologies and Environmental Safety

Using Pneumo-Hydrovortex Nozzles
for Effective Combustion of Liquid Boiler Fuels

Oleg Kravchenko(✉) , Vitalii Homan , Iryna Suvorova , and Igor Baranov

A. Pidhornyi Institute of Mechanical Engineering Problems of NAS of Ukraine, Kharkiv,
Ukraine
krav@ipmach.kharkov.ua

Abstract. The research aim is to manage an effective and ecological combustion of liquid fuels, including composite ones, in power plant boilers by using refined pneumo-mechanical nozzles, in which air is the atomizing medium. The main distinction of the developed pneumo-hydrovortex nozzles from existing pneumo-mechanical ones is that the dispersed liquid is fed using the film technique with a flow swirl. Numerical simulation and physical modeling methods were used to refine the standard design of the pneumo-hydrovortex nozzle. Without degrading dispersion quality, this enabled to reduce the flow velocity of the atomized fuel and increase significantly the flame cone angle. Preliminary tests of the quality of atomizing a model liquid were performed using plastic pneumo-hydrovortex nozzles obtained with 3D printers. Industrial tests of the new type pneumo-hydrovortex nozzle demonstrated that its application for hydrocarbon fuel combustion could reduce toxic emissions into the atmosphere with flue gases and offer a saving of energy resources during heat and electric power production.

Keywords: Reducing toxic emissions · Combustion process intensification · Atomization devices · Liquid stream dispersion

1 Introduction

The energy and environmental indicators of the power-plant boilers operation depend directly on the fuel combustion quality. During liquid fuel combustion even a minor loss of atomization quality can lead to an increased consumption of energy resources; an increased amount of toxic atmospheric emissions in flue gases; contamination of boiler heat exchange surfaces, and so forth [1]. Improving the performance of power installations with simultaneous improvement of their environmental performance calls for developing the new types of burners. The emergence in the energy market of new kinds of liquid composite boiler fuels in the form of emulsions and suspensions, differing in their physical-chemical and rheological properties from conventional hydrocarbons, including greater viscosity and the presence of a solid dispersion phase also implies the need to upgrade burners. Hence, the development of new atomization devices for effective flame combustion of liquid fuels is a topical problem [2].

Mechanical, steam-mechanical and pneumatic nozzles are used most often to atomize liquid boiler fuel.

The dispersion of combusted fuel with mechanical nozzles requires substantial pressures at the nozzle inlet. These nozzles have a small adjustment range and are sensitive to fuel quality. A significant increase in the adjustment range can be achieved by using steam-mechanical nozzles. However, at certain operating conditions steam consumption can be up to 0.3 kg per kilogram of fuel. This involves substantial energy expenditures to manage effective combustion. In addition, the problem of nozzle contamination is not fully eliminated [3].

The research aim is to manage an effective and ecological combustion of liquid fuels, including composite ones, in power-plant boilers without an extensive upgrading of burners by using refined pneumo-mechanical nozzles, in which air is the atomizing medium. Pneumo-mechanical nozzles ensure high dispersion and atomization quality. In spite of that partial mixing of combustion mixture components (air oxygen and combustible matter) occurs prior to the initiation of the combustion reaction (inside the nozzles), the combustion process per se in this case is that of the diffusion type [4]. This is because the amount of air fed to the nozzle is insufficient for complete fuel combustion. Therefore, the bulk of secondary air is fed directly into the combustion zone.

Since during diffusion combustion the rate of oxidation of the burnt fuel depends on the intensity of the process of mixing with the secondary air, managing an effective formation of a fuel-air mixture is pivotal. Thus, managing effective combustion of liquid fuel requires not only its quality atomization but also a thorough mixing of its fine droplets with air. With quality atomization, the specific surface of contact of hydrocarbon fuel droplets with secondary air can increase to over 2,500 times to accelerate substantially the heating and evaporation of the combusted energy resource.

2 Literature Reviews

Numerical simulation techniques are used commonly to develop new devices [5]. A computational research was conducted in different approaches to simulating laminar diffusion combustion. Paper [6] considers the classical Burke-Schurmann problem in application to building a mathematical model of a diffusion flame above a fuel film. However, to ensure complete fuel combustion in a small volume and better mixing with the oxidiser (secondary air), it is required to provide turbulence of the injected flow of combusted liquid in the furnace volume. Hence, the fuel is dispersed most often with a swirl of the atomized flow, and burners use special flame tubes whose design features enable to increase a fuel-air mixture formation effectiveness [7].

Paper [8] presents the results of research in the processes of liquid fuels dispersion with account of the Ohnesorge number (Oh) of the Sauter mean droplet diameter. It is shown that the majority of combustible liquids are burnt in the gas phase because the heating of these substances above the surface of the droplets forms a steam space, from which the combusted fuel particles flow into the zone for mixing with air oxygen [9].

Papers [1, 10–14] describe in details the results of experimental research in the dispersion of liquid droplets in the atomized nozzle flame using compressed air. Fuel dispersion with compressed air significantly increases the combustible liquid evaporation rate. This is because the oxidizer is fed directly into the atomized flame core and a partially prepared fuel-air mixture flows into the furnace volume.

Atomization with pneumo-mechanical nozzles using compressed air as an atomizing medium intensifies the processes of fuel droplets ignition and evaporation. Due to this, the fuel is ignited at earlier stages, the heating and evaporation rate of fuel droplets increases, and the flame length shortens.

The above advantages of pneumo-mechanical nozzles during the atomization of liquid fuels, including composite ones (emulsions and suspensions), allows drawing a conclusion that one of the ways of increasing the efficiency of existing power-plant boilers with minimal upgrading is to replace in-service nozzles with devices using compressed air as an atomizing medium.

3 Research Methodologies

IPMash NAS of Ukraine has developed and built a number of pneumo-hydrovortex nozzles for atomizing liquids by using compressed air as an atomizing medium [15]. They were developed using numerical simulation and physical modelling methods. Computer simulation of fluid dynamics for nozzles was performed using the structural *R*-functions method. The mathematical models were built based on the Navier-Stokes system of equations reduced to a nonlinear fourth-order partial differential equation for the stream function and Poisson's equation for static pressure [15].

The main distinction of the developed pneumo-hydrovortex nozzles from existing pneumo-mechanical ones is that the dispersed liquid feeding uses the film technique with a flow swirl. When the atomizing medium (air) is fed tangentially with a high speed into the nozzle, intense vortex formation takes place in its mixing chamber with occurrence of local zones with reduced pressure. This ensures an effective dispersion of the liquid and better quality mixing of the high-viscosity fuel with the oxidizer. Also, note that due to the film tangential compressed air feed to the atomizing path, the abrasive wear of its inner surfaces, including the orifice part is reduced. The latter is especially significant for atomizing suspension fuels. Preliminary tests of the quality of atomizing a model liquid were performed using plastic pneumo-hydrovortex nozzles manufactured by 3D printers. Figures 1 and 2 are clearly displaying the vortex character of the nozzle stream. 3D printing significantly reduces the cost of developed devices and speeds up the process of their experimental research. It also shortens the process of refining and making production prototypes.

The results of commercial pneumo-hydrovortex nozzles performance quality pilot-scale tests demonstrated their high effectiveness for combustion of a wide range of non-standard low-reactivity fuels. The substantial energy and environmental indicators improvement was achieved as compared to those of commonly used nozzles.
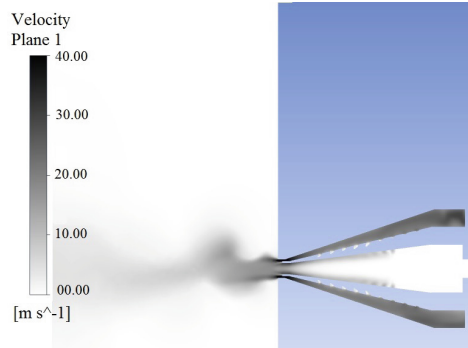
Fig. 1. Simulating the dispersed liquid flow by means of a pneumo-hydrovortex nozzle

Fig. 2. Model liquid atomization with a pneumo-hydrovortex nozzle made by 3D printing

The developed nozzles passed the tests successfully. They are used for combustion of high-viscosity composite fuels based on oil tanker crude oil slops, high ash content waste of coal preparation plants, highly watered sewage from municipal water treatment plants and other kinds of waste of various origins.

Table 1 shows the results of comparative experimental research in the environmental indicators of combustion of hydrocarbon fuel (fuel oil) for different atomization devices—the developed pneumo-hydrovortex nozzle and a mechanical rotatory one.

Table 1. Environmental indicators of the processes of fuel oil combustion for different types of nozzles

Nozzle type	CO, ppm	CO_2, %	NO_x, ppm	SO_x, ppm
Pneumo-hydrovortex	12	11.1	91	132
Rotatory	33	8.4	97	136

According to the results (Table 1), using pneumo-hydrovortex nozzles reduces the amount of toxic emissions into the atmosphere in flue gases during the combustion of hydrocarbon energy carriers. The result of higher quality fuel dispersion and mixing in the developed devices is the combustion with a lower excess air factor to consequently reduce NO_x emissions.

Experimental research in the combustion of non-standard alternative low-reactivity fuel mixtures containing a significant amount of moisture and solid impurities has confirmed not only the possibility of using the developed nozzles but also the high efficiency of combustion processes.

In particular, experimental research in the processes of combustion of composite fuels based on fuel oil with addition of alcoholic beverage production waste as the aqueous phase (AP) was conducted. The composite fuel of the given type was produced using the energy-technological research complex shown in [15]. Tests demonstrated the inadaptability of standard commercial nozzles and burners due to the unsatisfactory dispersion of high-viscosity fuel mixtures and the loss of flame caused by their clogging. Hence, the results of combustion of a composite fuel are given only for the pneumo-hydrovortex nozzle.

The basic physico-chemical and rheological properties of the combusted composite fuel are shown in Table 2.

Table 2. Physico-chemical and rheological properties of researched composite fuels

Fuel	Moisture content, %	Ash content, %	Specific combustion heat, MJ/kg	Viscosity, mPa·s
Fuel oil + 20% AP	19.7	0.18	33.4	264
Fuel oil + 25% AP	24.4	0.22	32.5	276
Fuel oil + 30% AP	29.1	0.26	31.7	329
Fuel oil + 35% AP	33.9	0.32	31.1	436
Fuel oil + 40% AP	38.8	0.38	29.2	524

During the research of the composite fuel combustion processes (Table 2), the focus was on the combustion environmental indicators because the task was to assess the possibility of using waste of given origin in the composition of fuel emulsions during their flame utilisation. The results of analysing the composition of flue gases during composite fuel combustion are given in Table 3.

Table 3. Results of analysing the composition of flue gases during composite fuel combustion

Fuel	Excess air factor, α	CO,ppm	CO_2, %	NO_x, ppm	SO_x, ppm
Fuel oil + 20% AP	1.22	19	11.8	69	94
Fuel oil + 25% AP	1.24	20	11.6	76	95
Fuel oil + 30% AP	1.27	24	11.5	75	96
Fuel oil + 35% AP	1.29	27	11.4	78	96
Fuel oil + 40% AP	1.31	32	11.2	84	98

An analysis of the results of experimental research allows making a conclusion that using pneumo-hydrovortex nozzles can ensure high-quality and environmentally safe combustion of low-reactivity high-viscosity composite fuels. Their use can significantly increase the efficiency of power-plant boilers during combustion of both conventional fuel oil and fuel-water emulsions without a substantial upgrading of power equipment.

4   Results and Discussion

According to IEA data [16], currently about 38% of electric power in the world is produced by coal-fired thermal power plants. The boiler units at these plants are started up and brought to predesigned thermal operating conditions by combustion of natural gas or fuel oil. When fuel oil is used as the start-up fuel, mechanical or steam-mechanical nozzles are used in the majority of cases. The drawbacks of these nozzles were described earlier in this paper.

The developed pneumo-hydrovortex nozzles are considered as an alternative to these nozzles. As demonstrated above, pneumo-hydrovortex nozzles ensure not only high-quality dispersion of the burnt fuel but also a resistance to clogging, including the case when suspension fuels are used.

Depending on the purpose and design of the power-plant boiler, a number of requirements are imposed on the fuel flame: the flame length and pattern, its temperature, radiation capability, the atomized fuel stream discharge velocity (largely affects combustion stability), heat transfer to heated surfaces, and other parameters. Proceeding from these requirements, the design of a nozzle for atomizing the combusted liquid fuel should ensure not only the specified dispersion of the droplets but also the required flame pattern with the specified atomized stream discharge velocity.

The developed designs of pneumo-hydrovortex nozzle ensure ultradispersion atomizing with a flame cone angle within 20–90° and the atomized fuel stream discharge velocity of 20–30 m/s.

Nozzles that provide a small cone angle and a long flame are most often used in very long furnace units. For instance, cyclone primary furnaces with a length of 8–10 m are provided for burning water-coal suspensions in industrial power-plant boilers. The combustion chambers of these primary furnaces are lined with refractory materials to create the required thermal stress level. The big length of the primary furnaces is due to the low moisture evaporation rate from the surface of coal particles and their

complete combustion. Such primary furnaces cannot use nozzles with big flame cone angles because the contact of fuel droplets with the refractory lining of the walls leads to the formation of solid deposits of unburnt fuel.

For power-plant boilers with a big furnace volume, when the fuel flow rate reaches 500–2,000 kg/h and more, secondary air is supplied by force-flow fans with low heads. In this case, the atomized flame cone angle should be 75–90°. At smaller angles, the quality of atomized fuel mixing with the secondary air degrades, combustion efficiency drops, toxic atmosphere emissions (incl. CO) grow, and the unburnt fuel contacts the heat exchange and other boiler surfaces to form solid deposits that degrade heat transfer and the operation of the boiler unit as a whole.

Industrial pilot-scale tests were conducted for pneumo-hydrovortex nozzles developed by IPMash NAS of Ukraine. These pneumo-hydrovortex nozzles are intended for burning fuel oil during starting up and bringing to design thermal operating conditions of a 200 MW pulverised coal-fired power-plant boiler. The need to replace standard mechanical nozzles was due to the low quality of fuel oil combustion, and big chemical and mechanical underburns.

The first stage of this research used a hydraulic test bench to conduct preliminary tests of the quality of atomization of a model liquid (water) and determine the cone angle. Nozzles with a design fuel flow rate of 1,500 kg/h and various flame cone angles were tested. Air with a pressure of 5 bar was fed to the nozzle for atomization. The fuel feed pressure was 7 bar.

Figures 3 and 4 show photographs of water atomization with cone angles of 20° and 90°.

Fig. 3. Water atomization with a cone angle of 20°

Visual monitoring of the operation of the nozzles suggested that the atomization process was steady in the hydro-gas-dynamic sense and that the dispersion quality was high (no films, and compact and homogeneous filling of the flame).

Both nozzles were tested in a power-plant boiler during its start up. The developed nozzles were installed in place of standard mechanical ones. Nozzles with the flame cone angle of 20° failed to ensure steady fuel oil combustion and their operation was characterised by short-time fuel ignition with subsequent flame loss. This is attributed to high discharge velocities of the atomized stream and a small flame cone angle, failing to ensure quality fuel mixing with the secondary air. Thereat, the amount of primary air

Fig. 4. Water atomization with a cone angle of 90°

fed for atomizing (less than 8% of the required volume) is insufficient for stabilising combustion, thus resulting in flame loss and extinction.

Using nozzles with a flame cone angle of 90° resulted in a substantial decrease in the discharge velocity of the atomized flame with the same flow rate parameters.

From the moment of firing and further during boiler operation, we observed steady fuel combustion with a bright-yellow flame. There was no evidence of the formation of "black" smoke – one of the principal indicators of fuel underburning. Figure 5 illustrates the process of fuel oil combustion in the furnace of a power-plant boiler using a pneumo-hydrovortex nozzle with a cone angle of 90°.

Fig. 5. Fuel oil combustion in the furnace of a power-plant boiler using a pneumo-hydrovortex nozzle

At the same time, we monitored the operation of standard mechanical nozzles. As distinct to fuel combustion in a boiler with a pneumo-hydrovortex nozzle, the flame colour has a pink hue when mechanical nozzles are used (indicative of low combustion temperatures), and a big amount of black smoke was seen.

To determine the basic energy and environmental indicators of using pneumo-hydrovortex nozzles when fuel oil is combusted, it is planned to conduct industrial pilot-scale tests on a power-plant boiler with replacement of all mechanical atomizing devices.

Such tests will allow determining the amount of toxic atmospheric emissions in the flue gases, as well as the amount of fuel consumed for bringing the boiler unit to design thermal operating conditions. According to tentative estimates, using pneumo-hydrovortex nozzles instead of mechanical ones for fuel oil combustion, when a pulverised-coal boiler will be brought to steady-state operating conditions, will provide fuel oil savings of 3–4%. This will also result in a substantial reduction of CO and NO_x in the flue gases. Further, this will open the prospects of expanding the fuel base due to using composite fuels.

5   Results and Discussion

The operating efficiency and environmental indicators of power installations when liquid fuels are combusted depend on both fuel atomization quality and the quality of their mixing with the oxidiser.

Since there are several types of nozzles as per the criterion of dispersion, a multi-faceted approach is needed to install them in power-plant boilers. It must account for the following: the basic characteristics of the combusted fuels; the equipment design and the technical prospects of its revamping (managing the use of an atomizing agent, and the possibility of providing auxiliary systems for preparing and feeding compressed air, and so forth); and the energy, environmental and economic requirements to the thermal energy process.

By the example of fuel oil combustion, the paper has shown the environmental advantages of using pneumo-hydrovortex nozzles over rotary ones. Pneumo-hydrovortex nozzles ensure high-quality fuel dispersion and intensify the processes of evaporation and ignition of fuel droplets. Subsequent comparative tests in composite fuel combustion showed that the suggested type of nozzles is optimal. They ensure quality dispersion of viscous watered composite fuel based on fuel oil and alcoholic beverage production waste. In this case, the environmental combustion indicators confirmed process efficiency.

Industrial pilot-stage tests conducted on a 200 MW fuel oil-fired boiler also confirmed the possibility of increasing the efficiency of combustion of hydrocarbon fuels in power plant equipment without its extensive upgrading by using pneumo-hydrovortex nozzles.

The pneumo-hydrovortex nozzles developed by IPMash NAS of Ukraine are a unique type of devices for atomizing liquids and fuels of different origin including high-viscosity highly watered ones, as well as those with solid impurities. Apart from the fuel-and-energy complex, these types of atomizing devices can be used in the food industry, fire-fighting systems, for dust suppression, in the production of nano powders and in many other industries.

6   Conclusions

Experiments have proved the possibility of essentially increasing the efficiency of the processes of combustion of hydrocarbon liquid fuel in power-plant boilers by using new types of pneumo-hydrovortex nozzles. It was shown that the developed devices ensure quality atomization of composite fuels and substantially reduce the amount of

hazardous emissions with flue gases. A comparison of the environmental indicators of the processes of combustion of fuel based on fuel oil and alcoholic beverage production waste has shown that using pneumo-hydrovortex nozzles is an optimal solution enabling a quality dispersion of viscous watered composite fuel.

During the research, the design of pneumo-hydrovortex nozzles was refined. This helped achieve the specified (required) flame cone angles and velocity of discharge of the atomized liquid. This makes it possible to use nozzles of such type in industrial power-plant high-capacity boiler units without a substantial upgrading of the equipment in place to improve the energy and environmental indicators of producing thermal and electric power.

According to the results of preliminary theoretical research, using pneumo-hydrovortex nozzles instead of mechanical ones for burning fuel oil, when bringing the pulverised-coal firing boiler to its specified operating conditions, fuel oil savings can be 3–4%, and the amount of CO and NO_x in the flue gases can be significantly reduced. Further, this opens the prospects of extending the fuel base by using composite fuels.

The developed pneumo-hydrovortex nozzle can be used with success not only in the power industry, but also in other industries requiring quality atomization of liquids, including suspensions.

References

1. Kalghatgi, G.: Development of fuel/engine systems—the way forward to sustainable transport. Engineering **5**, 510–518 (2019)
2. Suvorova, I., Kravchenko, O., Baranov, I., Goman, V.: Innovative technologies for utilization and disinfection of waste to ensure sustainable development of civilization. Eur. J. Sustain. Dev. **7**(4), 423–434 (2018). https://doi.org/10.14207/ejsd.2018.v7n4p423
3. Anufriev, I.S., Alekseenko, S.V., Kopyev, E.P., Sharypov, O.V.: Combustion of substandard liquid hydrocarbons in atmosphere burners with steam gasification. J. Eng. Thermophys. **28**(3), 324–331 (2019). https://doi.org/10.1134/S1810232819030032
4. Guryanov, A.I., Evdokimov, O.A., Veretennikov, S.V., Guryanova, M.M.: Experimental investigation of premixed air–fuel mixtures and of the combustion specifics of diffusion fuel jets. Int. J. Energ. Clean Environ. **18**(4), 335–348 (2017). https://doi.org/10.1615/InterJEnerClean Env.2018021223
5. Dovgyallo, A.I., Kudinov, V.A., Shestakova, D.A.: Working cycle analysis of the inter-nal combustion engine with heat regeneration. In: International Conference on Mechanical, System and Control Engineering, ICMSC 2017, IEEE Catalog Number: CFP17K79-ART, pp. 36–39 (2017). ISBN: 978-1-5090-6530-1
6. Belousov, V.N., Smorodin, S.N., Tsimbal, V.D.: Fuel and combustion processes in thermal power plants: textbook/HSE SPbGUPTD.-SPb, Part 2, 152 p. (2020). ISBN 978-5-91646-211-6
7. Sviridenkov, A.A., Toktaliev, P.D., Tretyakov, V.V.: Numerical simulation of heat and mass transfer, mixture formation in combustion chamber of gas turbine engine. Math. Model. **XL**, 127–139 (2017)
8. Ghahremani, A.R., Saidi, M.H., Hajinezhad, A., Mozafari, A.A.: Experimental investigation of spray characteristics of a modified bio-diesel in a direct injection combustion chamber. Exp. Therm. Fluid Sci. **81**, 445–453 (2017). https://doi.org/10.1016/j.expthermflusci.2016.09.010

9. Mobasheri, R., Seddiq, M., Peng, Z.: Separate and combined effects of hydrogen and nitrogen additions on diesel engine combustion. Int. J. Hydrogen Energy **43**(3), 1875–1893 (2018). https://doi.org/10.1016/j.ijhydene.2017.11.070
10. Zhuravskiy, G.I.: Oil sludge fuel. Phys. Eng. J. **92**(4), 971–978 (2019)
11. Mobasheri, R., Aitouche, A., Peng, Z., Li, X.: A numerical study of the effects of oxy-fuel combustion under homogeneous charge compression ignition regime. Int. J. Engine Res. **23**, 649–660 (2022). https://doi.org/10.1177/1468087421993359
12. Li, X., et al.: A feasibility study of implementation of oxy-fuel combustion on a practical diesel engine at the economical oxygen-fuel ratios by computer simulation. Adv. Mech. Eng. **12**(12), 1–13 (2020). https://doi.org/10.1177/1687814020980182
13. Wang, C., et al.: Experimental study on the deposited fuel film and microscopic spray characteristics of spray impinging on viscous oil film. Fuel (2020)
14. Jokela, T., Kim, B., Gao, B., Peng, Z.: A review of fuel cell technology for commercial vehicle applications. Int. J. Heavy Veh. Syst. **28**, 650–678 (2020)
15. Kravchenko, O., Suvorova, I., Baranov, I., Goman, V.: Hydrocavitational activation in the technologies of production and combustion of composite fuels. Eastern-Eur. J. Enterp. Technol. **4**(5 (88)), 33–42 (2017)
16. International Energy Agency: World gross electricity production, by source. https://www.iea.org/data-and-statistics/charts/world-gross-electricity-production-by-source-2018 (2018)

Integrated Energy Technologies When Using Natural Gas in Utility Heat Power Engineering

Victor Solovey[✉] and Andrii Rusanov

A. Pidhornyi Institute of Mechanical Engineering Problems of the NAS of Ukraine,
Pozharskogo 2/10, Kharkiv 61046, Ukraine
`solovey_v_v@ukr.net`

Abstract. An analysis of the technical capabilities and prospects for increasing the efficiency of natural gas usage in the energy supply system of Ukraine is presented in this article. An assessment of the prospects for increasing electricity production without reducing the volume of heat generation on the basis of a more complete use of the energy potential of fuel gas in combined cycle gas turbines is given. It is shown that the retrofitting of the existing heat generating systems based on CHP and water boilers with gas turbine superstructures will increase the nominal capacity of power generating equipment in the energy system of Ukraine by 17–20% without building additional power plants. Additional generation of electricity in combined cycle gas turbines will allow to displace up to 20% of coal from power generation, which will significantly reduce specific CO_2 emissions. Comprehensive implementation of the considered scientific and technical measures in the creation of specialized heat and power equipment for steam turbine plants will provide an increase in the efficiency of power generation by 35–40% with relatively small investment. The aim of this paper is to assess the possible scale of additional electricity production during the reconstruction of existing power facilities.

Keywords: Gas · Combined cycle gas turbine · Cogeneration technologies · Energy efficiency

1 Introduction

Despite the relatively high potential of the Ukrainian energy sector (it ranks sixth in Europe in terms of generated electricity capacity), the technical condition of the equipment installed at power plants raises reasonable concerns. A significant part (up to 80%) of the equipment is obsolete and has an operating time exceeding the design resource by 150–170 thousand hours. The utilization rate of the nominal capacity of Ukrainian TPPs is 31%, while in the world this indicator is 45% on average. This might be due to frequent shutdowns of power units for repair work, technological downtime and operation at variable modes to cover peak loads. As a result, such important technical and economic indicators of their operation as efficiency and reliability deteriorate [1, 2]. Annual electricity production in the country is at the level of 150–160 billion kW·h,

which corresponds to a specific energy consumption per capita of 3200 kW·h. This is almost 6 times less than in Norway and 3 times less than in the United States. Due to the reduction in the number of able-bodied people in Ukraine, the growth of the gross domestic product (GDP) can be ensured only with an increase in labor productivity, which requires an increase in the power supply, at least to 0.32–0.34 kW·h/USD of GDP. This will create the energy foundation for a gradual increase in this indicator to the level reached in industrialized countries. According to the updated Energy Strategy [3], it is planned to achieve the specific indicator of fuel consumption for electricity generation at the level of 347–350 g of conventional fuel/1 kW·h in Ukraine only by 2035, while in the EU countries it is already 280–300 g of conventional fuel/1 kW·h.

About 73% of the total numbers of the Ukrainian thermal power plants operate burning the coal as a fuel affecting a negative impact on the environment. Such impact involves emission of more than 50% of nitrogen oxides, more than 60% of sulfur oxides and 30% of particulate matter in the total number of atmospheric pollutants. As a result, according to the environmental indicators, the Ukrainian TPPs do not meet the European standards either in terms of specific or gross emissions.

Compared to other types of fossil fuels, when burning natural gas, combustion products contain significantly less harmful substances, including nitrogen oxides, with almost complete absence of sulfur dioxide, ash and dust [4]. Nowadays, the steam turbine power units with an electrical efficiency of less than 36% constitute 85% of the thermal power generation capacities. Consequently, 64% of the fuel energy is released into the environment. World experience shows that it is much more efficient to use the fuel in cogeneration systems, primarily in combined cycle gas turbines (CCGT), in which the efficiency in the production of electricity has already reached 50% and can be increased to 60–65% in the near future [5–7].

Due to the high consumer qualities of natural gas, the world now has a tendency to increase its use for energy and technological needs. The special literature names this tendency as a "gas pause". The natural gas becomes a symbol of the modern stage of power engineering development. Therefore, the natural gas considered as a potential opportunity to meet the demand of modern society in energy without leading to catastrophic consequences for the environment [8–10].

Ukraine has got one of the most powerful gas transmission systems in the Europe. Its property is the developed system of the gas transmission pipelines, the total length of which is about 33 thousand km, about 40% of which are the unique high-pressure pipelines (5.5 and 7.5 MPa) with diameter of 1020–1420 mm. The system involves 80 compressor stations. The total nominal capacity of gas- pumping units at these stations is about 5.4 million kW. The system involves also 12 large underground storage facilities providing storage of the accumulated gas volume of 35.5 billion m^3 that is the particular important part of the system. To improve the efficiency of management and operation of the gas transmission system, it is advisable to combine all elements of the gas infrastructure within the framework of a consortium. At the same time, the production, transportation, distribution and storage of natural gas will be carried out at a qualitatively new level ensuring the integrated management of the gas power generation system.

The aim of this paper is to analyze methods for increasing the use of the energy potential of natural gas in the heat and power sector by means of the gas turbine super-structure to existing power generating plants and to assess the possible scale of additional electricity production during the reconstruction of existing power facilities.

2   Methodology

The climatic features of Ukraine are such that there are practically no industrial, municipal and agricultural enterprises in the country that would not consume heat for heating, hot water supply and technological needs.

Analysis of the structure of the heat generation system indicates that the bulk of heat supply is carried out by boiler houses, the number of which is close to 26 thousand with the volume of heat supply to consumers at the level of $33 \cdot 10^6$ Gcal/year, in which the exergy potential of the fuel is implemented in less than 20% [11]. The structure of the heat supply system in Ukraine is shown in Fig. 1.
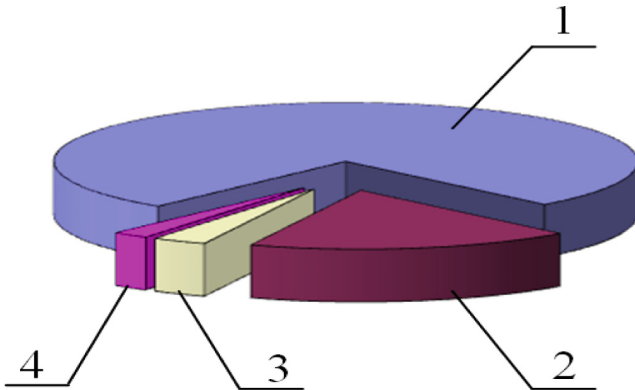
Fig. 1. Structure of the heat supply system in Ukraine: 1 – boiler houses -74%; 2 – CHP - 21%; 3 – thermal secondary energy resources – 4%; 4 – electric heating – 1%.

Taking into account that the technical condition of the main equipment of the boiler plants is characterized by wear of more than 70%, from economic point of view, it is expedient to reconstruct only 60–65% of their total number. The rest boiler plants should be completely replaced. Involvement in to the program of cogeneration modernization of the most technically advanced water boilers will give the possibility for putting into operation the equipment to generate 3.6–3.8 million kW of electric power additionally. Since the district boiler houses are close to the consumer, energy losses in heating mains are reduced, which, with centralized heat supply, averagely is 15–17%. In addition, they already have gas facilities and can be transferred to work on a cogeneration power supply scheme quite simply and in a short time. In this case, due to the generation of additional electrical power in cogeneration plants, it becomes possible to transfer a part of the population's needs for cooking and heating to a much more efficient and safe energy carrier—electricity [12]. Electric stoves are 3.5–4 times more economical in comparison

with gas burners. The use of electricity and modern air conditioning systems operating according to a heat pump scheme provides a reduction in energy consumption (by at least 1.7–2.5 times) for premises heating in the autumn-winter period and their cooling in the summer season. It is also advisable to carry out a phased transfer of hot water supply to electric heating, which increases the efficiency of its generation and reduces losses during transportation and use. As a result, more than a threefold reduction in gas consumption for these purposes can be provided.

CHP plants are no less promising objects for the implementation of the gas turbine superstructure. In Ukraine, there are about 250 CHP plants in operation with a total heat production of $30 \div 35 \cdot 10^6$ Gcal per year. More than 200 of them are departmental industrial heat-and-power plants with heating turbines, in which the consumption of natural gas makes up to 58% of the total volume of used energy carriers. Improvement of their technical and economic indicators can be achieved by energy symbiosis of gas turbine and steam turbine power generation cycles [7, 13]. Integration of the gas turbine unit and steam turbine plant cycles leads to a significant increase in the efficiency of the combined cycle gas turbines (CCGT), which depends on the efficiency of the steam and gas cycles and the ratio of heat volumes used in each of these plants [7].

There are the restrictions for implementing the gas superstructure to the existing power plants. They are associated with the need to ensure the flow and temperature parameters of the existing equipment operation. In particular, the restrictions concern the steam generator of the steam turbine plants. There are the restrictions for implementing the gas superstructure to the existing power plants. They are associated with the need to ensure the flow and temperature parameters of the existing equipment operation. In particular, the restrictions concern the steam generator of the steam turbine plant to ensure the generated steam parameters meeting the requirement for the steam turbine actuating medium. Since a part of the gas fuel energy in the case of the superstructure is used in the gas turbine unit for the production of work then it is necessary to introduce additional energy to maintain the volume of its supply to the steam turbine cycle. From a thermodynamic point of view, the most effective is the supply of an additional volume of gas to the combustion chamber of the gas turbine unit. However, in this option, the temperature of the exhaust gases usually does not exceed 500 °C, which is lower than the temperature required for the operation of the steam generator. Therefore, it is necessary to heat them up to the rated temperature. It is possible to exclude additional heat input into the steam generator by implementing a process close to isothermal in the gas turbine. In practice, this can be implemented in a specially developed gas turbine design with sequential heat input during gas expansion in the flow part. In [14], theoretical aspects of multistage heat supply to the working fluid in the gas turbine unit are considered, and in [7], technical solutions that ensure their implementation are given. The use of new constructional heat-resistant materials based on the so-called viscous ceramics and nickel-manganese steels or chromium alloys allows to increase the operating temperature of turbine blades by 200–500° and, as a result, increase the cycle efficiency. New technical and technological capabilities make it possible to abandon traditional designs for staged heat supply with external combustion chambers and open up prospects for using the interdisk space of a turbine as intermediate annular combustion chambers. In this case, through the cooling system of the blade row, it is possible to introduce the fuel along the

circumference into the interdisk space, turning it into a combustion chamber with a high degree of turbulization. As a result of effective mixing, a uniform flame front, supported by the high-temperature surfaces of the flow part, is formed. To stabilize combustion, these elements must have a cermet coating with catalytic properties to intensify the fuel oxidation process [15]. Such heat supply brings the expansion process closer to isothermal, in which all the additionally supplied heat is converted into work. In this case, the temperature of the gases at the outlet of the turbine will be higher, to a greater extent meeting the needs of the operation of the steam generator. The use of the thermal potential of the gas turbine unit exhaust gases in the combined cycle steam turbine part makes it possible to limit the compression ratio to $\pi_{\kappa} \leq 15$, which simplifies the compressor design and minimizes the volume of additionally compressed gas in the gas turbine unit cycle.

To increase the efficiency of the gas turbine unit by reducing the amount of combustion air and, therefore, the work expended on its compression, it is advisable to inject superheated water or wet steam with a low degree of dryness x > 0.6 to bring the gas temperature to a technically acceptable level [7]. The use of water in the liquid phase will significantly reduce its consumption compared to steam cooling. However, this requires the development of a special design of the gas cooler to prevent the ingress of droplet moisture into the flow part of the gas turbine. Technically, this can be done by installing a ceramic nozzle with low hydraulic resistance at the outlet of the combustion chamber. When the gas turbine unit operates in an open scheme, regardless of whether water is used in the liquid or vapor phase, its replenishment is required. In the known designs, to compensate for water losses at the outlet of the steam generator, a contact gas-liquid heat exchanger is installed (by analogy with the "Aquarius" system) to capture steam from the combustion products [16]. The high content of steam in the combustion products allows to obtain the required volume of recycled water for the operation of the gas cooling system even with its partial condensation (at the level of 70–80%).

3   Results and Discussion

To create a project for modernizing a thermal power plant, it needs to determine the data influencing strongly on the choice of the technological scheme and on the operating parameters of the main structural elements on the integral energy characteristics namely at the stage of technical proposal developing. To create a project for modernizing a thermal power plant, it needs to determine the data influencing strongly on the choice of the technological scheme and on the operating parameters of the main structural elements on the integral energy characteristics. It needs to have such data at the stage of technical proposal developing.

The dependence of the efficiency of the steam-gas unit on the efficiency of the gas turbine unit and steam turbine plant, taking into account the additionally supplied heat, can be determined by the equation

$$\eta_{CCP} = \frac{(1 + \eta_{GTU}) \cdot \eta_{CCP} - \eta_{STP}}{1 + \eta_{GTU} + \eta_{GTU}^2}, \tag{1}$$

η_{GTU} is the gas turbine unit efficiency; ηCCP is the steam-gas plant efficiency; η_{STP} is the steam turbine plant.

The range of change in the efficiency of the steam and gas parts developed by the energy industry was set in the calculations. Figure 2 shows a graphical interpretation of the efficiency indicator of the CCGT unit for electricity generation for various combinations of integrated cycles.
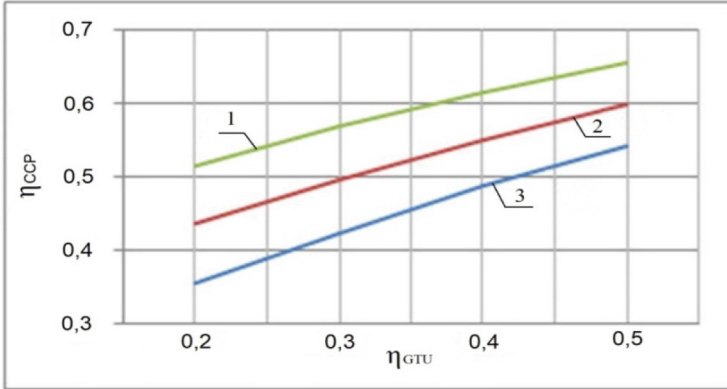
Fig. 2. Dependence of the integral efficiency of the CCGT plant on the values of the efficiency of the gas turbine unit and steam turbine plant: 1—0.4; 2—0.3; 3—0.2.

The analysis of the obtained results shows that even with moderate indicators of the thermodynamic efficiency of the elements integrated into the combined scheme of the steam gas unit this unit provides the level of efficiency, which is unattainable by other currently known megawatt power plants. The small specific volume of the gas turbine part (0.6–0.7 m^3/kW) makes it possible to place the gas turbine units and steam turbine plants during modernization in the premises occupied by the existing steam turbine power units. This makes it possible to use the production areas of existing power plants to accommodate additional equipment, which reduces financial costs during the reconstruction of power facilities [17]. When cogeneration modernization of the existing power equipment through the use of the existing construction and technical base, the cost of a unit of additionally installed power generating capacity does not exceed $ 250–450 per kW. Such projects have a relatively short commissioning time and are characterized by lower unit capital costs compared to newly built plants (Table 1), which reduces the return on investment to 3–3.5 years [3].

The planned rates of increase in electricity production are significantly higher in comparison with the rates of increase in heat supply. Therefore, priority should be given to the electrical component modernization. Without claiming the absolute accuracy of the analysis results, in view of the high and difficult-to-predict dynamics of changes in the domestic energy market, Fig. 3 shows the ratio between the volumes of additionally used gas (the darker part of the histogram) and the increase in electricity production due to the introduction of combined cycle technologies during the modernization of existing power supply enterprises.

The given data indicates that due to the introduction of steam and gas power generation at existing facilities, the volume of electricity production can be increased by

Table 1. Technical and economic indicators of the modern power generation systems

Parameter	Plant type				
	CCGT (combined cycle gas turbines)	GTU (gas turbine unit)	TPP (thermal power plant)	Nuclear power plant	Fuel cells
Power generation efficiency, %	50–65	30–40	25–36	30–35	45–70
Cost of kW of nominal capacity, thousand USD	0.6–1.0	1.1–1.6	1.0–1.7	2.0–3.0	2.5–4.5
CO_2 emissions at equal power, %	50	75	100	0	0
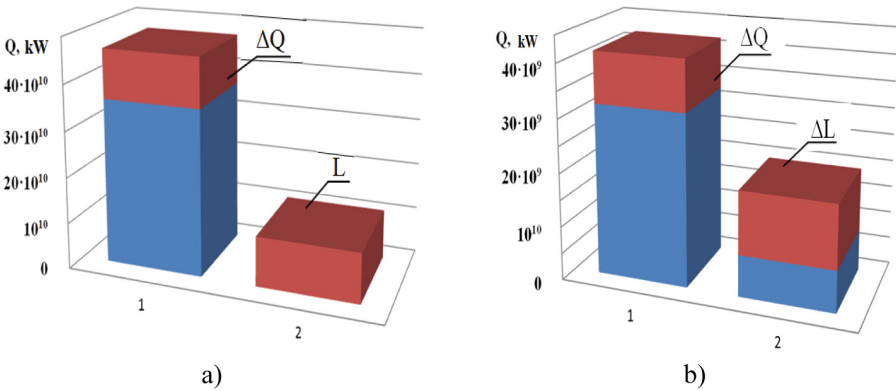
Fig. 3. The potential for increasing electricity production under increasing during cogeneration based on the steam and gas technologies at: a) water boiler plants; b) CHP.

27–35%, which will provide coal substitution in the volume of $8{,}6 \cdot 10^6$ tons of conventional fuel. The environmental effect of this measure will ensure a reduction in emissions of carbon dioxide, sulfur oxides and ash in proportion to the decrease in the volume of used coal. Another no less important argument in favor of the reconstruction of heat and power equipment using steam and gas technologies is its higher thermodynamic efficiency, which contributes to the reduction of thermal pollution and CO_2 emissions into the atmosphere. The problem of CO_2 emission into environment is especially acute in Ukraine due to the fact that the further increase in power generating capacities by the traditional way is constrained by the lack of water resources for cooling the equipment of TPPs and NPPs where the water consumption is, respectively, 30 and 50 m^3/s under generating power of 10^3 MW. The introduction of the steam and gas technologies to

existing facilities does not require the attraction of additional volumes of process water. That is a significant factor when choosing a strategy for modernization of the domestic power industry.

The results of the analysis of the efficiency of additional fuel usage efficiency in the CCGT unit testify in favor of the cogeneration reconstruction [18]. This indicator reflects the ratio of the difference of works taking place during the steam-gas and steam turbine cycles and additionally supplied heat in the combined cycle and can be estimated by the formula

$$K = \frac{l_{CCP} - l_{STP}}{\Delta Q}, \tag{2}$$

where $lCCP$ is the work at CCGT cycle; $lSTP$ is the work at the basic steam turbine cycle, ΔQ – additional heat introduced during the combined cycle; $\Delta Q = QCCP\text{-}Qbas$.

By expanding the values of these quantities, we get

$$K = \frac{(1 + \eta_{GTU}) \cdot \eta_{CCP} - \eta_{STP}}{\eta_{GTU} + \eta_{GTU}^2}. \tag{3}$$

Analyzing the K change in the range of real values of the efficiency of the gas turbine unit and CCGT we can see that the energy of the additional fuel is almost completely transformed into work.

Thus, a significant increase in the technical and economic indicators of the use of natural gas can be achieved due to the following innovative technical solutions:

– providing for water cooling of the gases before the gas turbine input;
– providing for the actuating medium expansion process with heat supply in the flow part of the gas turbine;
– implementing the contact technologies to remove moisture from combustion products;
– improving the gas dynamic characteristics of steam and gas turbines;
– optimizing the thermal schemes of the steam gas power generating systems [19, 20].

The comprehensive implementation the above mentioned scientific and technical measures for creating the specialized heat-and-power engineering equipment for the steam turbine plants will result in increasing the efficiency of power generation by 35–40% under a relatively small investment.

The total volume of investments required to implement the initial stage of the program for innovative modernization of the power supply equipment in the amount of 25–30% of the total nominal capacity will amount to $ 2.5–3.0 billion. To compare commissioning of the new equipment of similar capacity will require more than $ 30 billion and much longer terms of its implementation.

4   Conclusions

The article describes the ways of the power generating enterprises modernization to be done by introducing the cogeneration steam and gas technologies in conditions of the

limited financial capabilities of the modern economy to achieve the indicators of the efficiency of electricity and heat production declared in the Energy Strategy of Ukraine.

Analysis of the CCGT main elements operation feature under integration of the CCGT into energy-technological cogeneration systems showed that the chemical energy of the additional fuel is converted into work with a transformation ratio close to unity. Assessment of the increase in the efficiency of electric energy production is given depending on the ratio of the energy indicators of the gas turbine superstructure and the basic steam turbine plant.

It was analyzed the methods for improving the thermodynamic processes by heat generation in the gas turbine unit flow parts. Such approach gives the possibility for providing the gas expansion process closer to isothermal, providing a higher degree of energy transformation and an increase in the temperature of gases transferred to the steam turbine flow part, which reduces the consumption of natural gas for their additional heating.

It is shown that the retrofitting of existing heat generating systems based on CHP and water boiler plants with gas turbine superstructures will increase the installed capacity of power generating equipment in the Ukrainian energy system by 17–20% without building additional power plants.

The considered option of increasing the efficiency of natural gas use is an important step to realize the policy of coal substitution and transition to the low-carbon technologies reducing the emissions of CO_2 and other harmful substances in proportion to the reduction in coal consumption. Additional generation of electricity in CCGT will give the possibility for displacing up to 20% of coal from power generation process, which will reduce the specific CO_2 emissions by more than 2.0 times.

The experience of reconstruction of the power supply enterprises can be used for introducing the cogeneration technologies in to industrial boiler and power technology schemes of the enterprises that consume natural gas to provide thermal processes. Gas consumption for these needs is 1.5 times higher than its consumption in the energy sector and, therefore, the effect of cogeneration modernization will be even more significant.

References

1. Shevchenko, A.A., Zipunnikov, M.M., Kotenko, A.L.: Adaptation of the high-pressure electrolyzer in the conditions of joint operation with TPP and NPP power-generating units. Naukovyi visnyk Natsionalnoho Hirnychoho Universytetu **6**, 76–82 (2020)
2. Kulyk, M.M., Nechaeva, T.P., Zghurovets, O.V.: Prospects and problems of the development of the unified energy system of Ukraine in the conditions of its accession to the energy system of the European Union and hypertrophied use of wind and solar power plants in its composition. Probl. Gen. Energy **4**(59), 4–12 (2019)

3. Khalatov, A.A., Fialko, N.M., Tymchenko, M.P.: Energy security of Ukraine: the threat of long-term energy resources depletion: thermophysics and thermal. Power Eng. **42**(3), 5–22 (2020)
4. Aminov, R.Z., Bairamov, A.N., Garievskii, M.V.: Assessment of the performance of a nuclear-hydrogen power generation system. Therm. Eng. **66**(3), 196–209 (2019)
5. Aminov, R.Z., Bairamov, A.N., Garievskii, M.V.: Estimating the system efficiency of the multifunctional hydrogen complex at nuclear power plants. Int. J. Hydrogen Energy **45**(29), 14614–14624 (2020)
6. Matsevityiy, Y., Ganchin, V.V.: To the Solution of Geometric Inverse Heat Conduction Problems. J. Mech Eng. **24**(4), 6–12 (2021)
7. Karakurt, S.A., Güneş, Ü.: Performance analysis of a steam turbine power plant at part load conditions. J. Therm. Eng. **3**(2), 1121–1128 (2017)
8. Vnukova, N.V., Matskevich, G.E.: Efficiency of using natural resources in Ukraine in the context of the concept of sustainable development. Ecol. Saf. Balanced Use Resour. **2**(16), 148–153 (2017)
9. Shevchenko, A., Zipunnikov, M., Kotenko, A., Vorobiova, I., Semykin, V.: Study of the influence of operating conditions on high pressure electrolyzer efficiency. J. Mech. Eng. **22**(4), 53–60 (2019)
10. Solovey, V., Kozak, L., Shevchenko, A., Zipunnikov, M., Campbell, R., Seamon, F.: Hydrogen technology of energy storage making use of wind power potential. J. Mech. Eng. **20**(1), 62–68 (2017)
11. Rusanov, A., Solovei, V., Zipunnikov, M., Shevchenko, A.: Thermogasdynamics of Physical and Energy Processes in Alternative Technologies: Monograph. PC "Technology Center," Kharkiv, Ukraine (2018). https://doi.org/10.15587/978-617-7319-18-3
12. Khalatov, A.A.: Ukraine's energy security: has the margin of safety been preserved. Thermophys. Therm. Power Eng. **39**(2), 12–17 (2017)
13. Arakelyan, E.K., et al.: Features of steam turbine stages operation in low-flow modes when modeling hydrodynamic processes in the turbine in steamless and motor modes. Procedia Comput. Sci. **170**, 935–940 (2020)
14. Shubenko, A.L., Goloshchapov, V.N., Senetska, D.O.: The operation of the last stage of steam turbine at low-flow rate modes. Energetika **66**(1), 58–67 (2020)
15. Shubenko, O., Babak, M., Senetskyi, O., Senetskaya, D.: Development of methods for calculating the nonequilibrium phase transformations during the condensation of supercooled steam in the turbine flow path. Mat. Sci.: Non-Equilib. Phase Transformations **4**(2), 69–72 (2018)
16. Kim, S.-J., Suh, J.-W., Choi, Y.-S., Park, J., Park, N.-H., Kim, J.-H.: Inter-blade vortex and vortex rope characteristics of a pumpturbine in turbine mode under low flow rate conditions. Water **11**(12), 2554 (2019)
17. Khalatov, A.A., Kovalenko, G.V., Meyris, A.J.: Using of tubular heat exchange surface with dimples in the gas turbine regenerators. Thermophys. Therm. Power Eng. **39**(5), 70–77 (2017)
18. Khalatov, A.A., Kovalenko, A.S., Reznik, S.B.: Features of organization of film cooling of high temperature gas turbines blades. Thermophys. Therm. Power Eng. **39**(4), 11–20 (2017)
19. Rusanov, A., Shubenko, A., Senetskyi, O., Babenko, O., Rusanov, R.: Heating modes and design optimization of cogeneration steam turbines of powerful units of combined heat and power plant. Energetika **65**(1), 39–50 (2019)
20. Wang, W., Sun, Y., Jing, S., Zhang, W., Cui, C.: Improved boiler-turbine coordinated control of CHP units with heat accumulators by introducing heat source regulation. Energies **11**, 2815 (2018)

The System for Planning Cost-Efficient and Resource-Saving Operating Modes of TPP

Olga Chernousenko ⓘ, Vitalii Peshko⁽✉⁾ ⓘ, and Dmitro Rindyuk ⓘ

Igor Sikorsky Kyiv Polytechnic Institute, 37 Peremohy Avenue, Kyiv 03056, Ukraine
vapeshko@gmail.com

Abstract. Thermal power plants are often operated in the semi-peak and peak part of the electrical load schedule of the power system. It is known that frequent operation of power equipment in variable modes leads to a deterioration of economic indicators and accelerated exhaustion of residual resource. The paper proposes a system for planning rational modes of operation of equipment of power plants. The optimal distribution of the regime parameters of the power unit during the year is investigated, namely the operating time, the number of starts and the proportion of starts from different thermal states. The target functions of the research are the specific consumption of equivalent fuel per 1 kWh of energy produced and the residual resource of the power unit. When calculating the cost-efficiency of the power plant, it was decided to bring all types of heat, electricity and fuel losses to the similar losses of equivalent fuel. To calculate the residual life of the power unit, the Palmgren-Miner hypothesis was used to estimate the damage of the equipment during exploitation under different operating modes. The proposed system was tested on the example of a real power unit with a capacity of 200 MW. Equipment start-up modes were investigated on the basis of start-up schedules provided by the generating company. The research results showed that using the proposed system for planning rational operating modes it is possible to achieve a reduction of the specific consumption of equivalent fuel by 16% and an increase in the individual resource of the power unit by 21%.

Keywords: Rationalization · Operating modes · Power unit · Thermal power plant · Fuel losses · Efficiency · Durability · Residual resource

1 Introduction

Thermal power plants (TPP) are used as semi-peak and peak capacities in the power systems of many countries around the world. This is due to the availability of cheaper energy produced at nuclear power plants, the availability of cleaner energy obtained from non-traditional energy sources, the insufficient supply of highly maneuverable capacities etc. [1] The reasons for this work vary from country to country. However, the common consequence is that equipment designed to operate in stationary modes is operated in frequent variable modes.

The operation of any power equipment on non-stationary modes is always accompanied by deterioration of economy, environmental friendliness and reliability. This

deterioration will be the more intense, the longer the duration of the variable mode and the more it differs from the nominal [2].

At the same time, the authors of [3] noted a significant impact of equipment start-up modes on the rate of accumulation of damage in the main metal, which can lead to premature failure and catastrophic consequences.

Thermal power plants in many countries around the world (especially China, USA, Ukraine, Russia) are characterized by a significant exhaustion of individual resource of its equipment. Therefore, the above circumstances significantly exacerbate the issue of rational planning of the strategy of operation of TPP units.

A significant amount of scientific and applied research proves the effectiveness of predictive optimization in addressing the rational use of energy resources and reducing the negative impact of the energy sector on the environment [4, 5]. The authors of [5] showed that by optimizing the daily composition of generating equipment in the Chinese power system, it is possible to decrease material input and global warming potential by 29%, and to decrease water deprivation by 19%. The paper took into account the full cycle of energy production from the energy source to the consumer supply.

A common research is to increase the efficiency of power plants by optimizing their modes of operation [6, 7]. Thermal power plant operating on the organic Rankine cycle with a heat pump was investigated in [6]. Typical operating modes and different types of coolants for the cycle are studied. Mathematical optimization of the main thermodynamic and technological parameters of TPP was performed on the basis of exergy analysis of energy production. The optimal working parameters of the system provide a 28% higher electrical efficiency.

The paper [7] is devoted to the study of rational modes of operation of the TPP power unit with a capacity of 300 MW. The authors investigated 7 different modes of operation of equipment from the fully basic (7000 h per year) to the mode with daily stops for 7 h during periods of night reduction in consumption. According to the results of calculations, an increase in the cost of electricity for the selected modes is investigated. The authors' calculation of turbine resource indicators deserves special attention. This calculation is performed using the concept of equivalent exhaustion of the resource for different methods of operation. The data obtained by the authors are of great interest to generating companies.

At the same time, the calculations of the resource indicators of the equipment performed by the authors [7] are significantly simplified, as they do not take into account all the specifics of cyclic damage to the equipment during start-up. A detailed model of low-cycle fatigue of the secondary superheater of the boiler is presented in [3]. The calculations take into account the main mechanisms of destruction, as well as the effects of oxidation, corrosion and welding. When conducting a study of the optimal modes of operation of the secondary superheater, it is possible to significantly simplify the calculations of cyclic damage. For this purpose, the authors performed an analytical representation of the experimental Coffin-Manson curve for X7CrNiTi steel at a symmetrical load cycle and constant temperature.

A similar study was performed by the authors [8]. On the basis of the modified Steinhart-Hart equation, the analytical adaptation of the fatigue curve of steel 25Cr1Mo1V at variable temperatures was performed. This analytical dependence has

become a component of the system for estimating and forecasting the rational resource-saving modes of TPP operation. This system allows to set the distribution of the operating parameters of the unit, which will provide the least accumulation of damage during variable operating modes.

Given the above, it can be argued that research aimed at developing a system of rationalization of the operating modes of a single unit to ensure cost-efficiency and resource-saving is relevant. Such a system will allow generating companies to more effectively plan the strategy of operation of their equipment. Effective planning will significantly reduce the cost of generated electricity and prevent premature failure of the main power equipment of thermal power plants.

2 Rationalization of Operating Modes of TPP Power Units to Reduce Energy Losses During Operation

2.1 Loss of Fuel, Heat and Electricity During the Start-Up of TPP Power Unit

Rationalization of TPP operation modes in order to minimize fuel consumption requires the establishment of the value and range of changes in energy losses for typical start-up and stationary modes of operation.

The key problem in determining the value of these losses is that the total heat consumption at start-up mode always consists of the heat consumption itself, the consumption of electrical energy to drive the motors of the mechanisms and fuel consumption.

Thus, when estimating the fuel loss during start-up ΔB_i, it is necessary to take into account not only the overconsumption of natural fuel, but also the equivalent overconsumption of fuel, which compensates existing heat and electricity losses:

$$\Delta B_i = \Delta B_i^f + \Delta B_i^h + \Delta B_i^e + \Delta B_i^u \qquad (1)$$

where ΔB_i^f, ΔB_i^h, ΔB_i^e – fuel, heat from an external source and electricity for own needs used on the i stage of start-up or cooling and reduced to the equivalent fuel (calorific value of 1 kg of equivalent fuel is equal to 29.3 MJ);

ΔB_i^u – the amount of fuel that is equivalent to the useful electricity supplied to the power grid during cooling, loading and stabilization.

It is convenient to divide the starting cycle of the power unit into several stages: down-time of power unit, stage of preparation for start-up, ignition of the boiler and exploitation before the rotor rotation, acceleration of the turbine to idle frequency, electrical load of the turbine to rated power, stabilization of thermal state.

For each of the above six steps, the main components of fuel losses from the Eq. (1) are determined. Specific methods for calculating start-up losses are usually approved by the regulatory documents of the energy sector of the vast majority of countries [9].

In this study it was used the methodology presented in the normative document "RD 34.09.106–94. Method for Calculation of Loss of Fuel, Electric Power and Steam During Startup of Power Units with Power of 160–1200 MW" (Ukraine).

Start-up operating modes of TPP power units are classified depending on the metal temperature before start-up. The determining temperature is usually the temperature of the metal of the first stage, or the flanges in the area of the steam outlet, or the steam inlet pipes.

In this paper, it is proposed to consider the following start-up modes of power units: start-up from cold state of metal (CS) at a temperature $> 150\,^\circ\text{C}$, start-up from uncooled state of metal (US) at a temperature 200–300 $^\circ\text{C}$ and start-up from hot state of metal (HS) at a temperature 410–460 $^\circ\text{C}$.

2.2 Development of a System for Planning Rational Modes of Operation of TPP Power Units Aimed at Minimizing Fuel Consumption

After establishing the value of energy losses during the operation of the power unit at start-up and stationary modes of operation, it is advisable to develop a system for planning a rational strategy for the operation of thermal power plant. The main stage in the development of such a system is the formulation and solution of the optimization problem. This task is to determine the distribution of technological and operating parameters of the unit, providing minimal energy losses.

The specific consumption of equivalent fuel b_{eq} is proposed as a target function of the optimization problem. It is quite complex and easy to analyze indicator of the efficiency of electricity generation.

$$b_{eq}(\vec{x}) \rightarrow \min_{\vec{x}\in\overline{X}} b_{eq}(\vec{x}) \tag{2}$$

The solution to the set optimization problem is $\vec{x}^{opt} \in \overline{X}$, that $b_{eq}(\vec{x}^{opt}) \le b_{eq}(\vec{x})$ for all $\vec{x} \in \overline{X}$. In other words:

$$b_{eq}(\vec{x}^{opt}) = \min_{\vec{x}\in\overline{X}} b_{eq}(\vec{x}) \tag{3}$$

$$N_{Xmin} \le |\overline{X}| \le N_{Xmax} \tag{4}$$

where $\vec{x}$ is vector of the operating parameters that affect b_{eq}; $\overline{X}$ is the area of the existence of $\vec{x}$; N_{Xmin}, N_{Xmax} are the boundaries of the existence of vector $\vec{x}$.

For the intended problem, the main components of the vector $\vec{x}$ (optimization factors) are offered:

1) unit operation time during the year $t_{min} \le t_i \le t_{max}$;
2) the total number of start-ups from different thermal states for 1 year $n_{min} \le n_j \le n_{max}$;
3) the percentage of cold start-ups from the total number $CS_{min} \le CS_k \le CS_{max}$;
4) the percentage of hot start-ups from the total number $HS_{min} \le HS_l \le HS_{max}$.

The percentage of start-ups from the uncooled state of the metal is determined by the percentages of start-ups from other thermal states $US_{k,l} = 1 - (CS_k + HS_l)$.

Given the above, the following equation is obtained to calculate the average annual specific consumption of equivalent fuel at the TPP:

$$b_{eqi.j,k,l} = \frac{B_1 \cdot t_i + \Delta B_{CS} \cdot n_j \cdot CS_k + \Delta B_{HS} \cdot n_j \cdot HS_l + \Delta B_{US} \cdot n_j \cdot (1 - (CS_k + HS_l))}{N \cdot (t_i - \Sigma t_{TS}) + E_{CS} \cdot n_j \cdot CS_k + E_{HS} \cdot n_j \cdot HS_l + E_{US} \cdot n_j \cdot (1 - (CS_k + HS_l))} \tag{5}$$

where B_1 – absolute consumption of equivalent fuel consumed for 1 h of operation of the power unit at rated load; ΔB_{CS}, ΔB_{HS}, ΔB_{US} – overconsumption of equivalent fuel at each type of start-up, calculated by Eq. (1); N – rated power of the power unit rated power of the power unit; E_{CS}, E_{HS}, E_{US} – the amount of energy supplied to the network during each type of start-up; t_i, n_j – term of operation and number of start-ups during the year; CS_k, HS_l – percentage of start-ups from cold and hot state of metal; Σt_{TS} – the total time spent on all start-up modes.

Thus, the numerator of Eq. (5) presents the sum of all equivalent fuel consumed for all modes of operation. This value consists of the nominal consumption during the operating time t_i and the amount of fuel overconsumption at each type of start-up. The denominator shows the total amount of energy generated during the nominal and all start-up modes.

According to the nature of operation in the power system during the year, we can recognize two diametrically opposed strategies for the operation of the power unit: completely basic mode of operation and completely peak mode.

With a completely peak mode, the operating time of the unit goes to its minimum value $t_i \rightarrow t_{min}$. Conversely the number of starts goes to its maximum value $n_j \rightarrow n_{max}$. At the same time, due to the peak mode and a significant number of starts during the year, the metal of the turbine will most likely not have time to cool to a temperature below 150 °C (start-up from a cold state). Thus, the percentage of hot and uncooled start-ups will prevail in the share ratio $CS_k \rightarrow CS_{min}$.

With a completely basic mode of operation, the situation with the considered parameters will be opposite: the operating time of the power unit goes to its maximum value $t_i \rightarrow t_{max}$, the number of starts goes to its minimum value $n_j \rightarrow n_{min}$. At the same time, the percentage of cold start-ups will prevail in the share ratio $CS_k \rightarrow CS_{max}$.

Between these two opposite exploitation strategies of the power unit there are thousands of variations with different combinations of variables $t_i, n_j, .., HS_l$, among which there is an optimal mode surrounded by rational ones.

Given the above, the equation for calculating the average annual specific consumption of equivalent fuel eq. (5) can be represented as:

$$b_{eqi.j} = \frac{B_1 \cdot t_i + n_i \left[CS_i \cdot \Delta B_{CS} + CS_i \cdot HS_j \cdot \Delta B_{HS} + CS_i \cdot (1 - HS_j) \cdot \Delta B_{US} \right]}{N \cdot [t_i - \Sigma t_{i,j}^{TS}] + n_i [CS_i \cdot E_{CS} + CS_i \cdot HS_j \cdot E_{HS} + CS_i \cdot (1 - HS_j) \cdot E_{US}]} \tag{6}$$

$$\Sigma t_{i,j}^{TS} = n_i \left[CS_i \cdot t_{CS} + CS_i \cdot HS_j \cdot t_{HS} + CS_i \cdot (1 - HS_j) \cdot t_{US} \right] \tag{7}$$

$$n_i = (n_{min} - n_{max}) \frac{t_i - t_{min}}{t_{max} - t_{min}} + n_{max} \tag{8}$$

$$CS_i = (CS_{max} - CS_{min}) \frac{t_i - t_{min}}{t_{max} - t_{min}} + CS_{min} \tag{9}$$

where t_{CS}, t_{HS}, t_{US} – start-up time from cold, hot and uncooled states, respectively.

Based on the above, a system of planning rational modes of operation of TPP units was created. As an example, the results of using the system in relation to a specific power unit with a capacity of 200 MW with a TP-100 power boiler and a K-200–130 steam turbine are presented. The main operating parameters of the power unit are set using the start-up map developed by the manufacturer. The amount of electricity generated for each start-up E_{CS}, E_{HS}, E_{US} is calculated by integrating the electric power curve of the turbogenerator presented in the start-up graphs.

The results of the calculations are presented in Fig. 1. The boundaries of change of operating factors are chosen as follows: power unit usage time $t_i = 2000$–6500 h; annual number of start-ups $n_i = 25$–75; percentage of start-ups from the cold state $CS_i = 10$–90%; percentage of hot start-ups in the range of hot and uncooled start-ups $GS_j = 0$–100%.
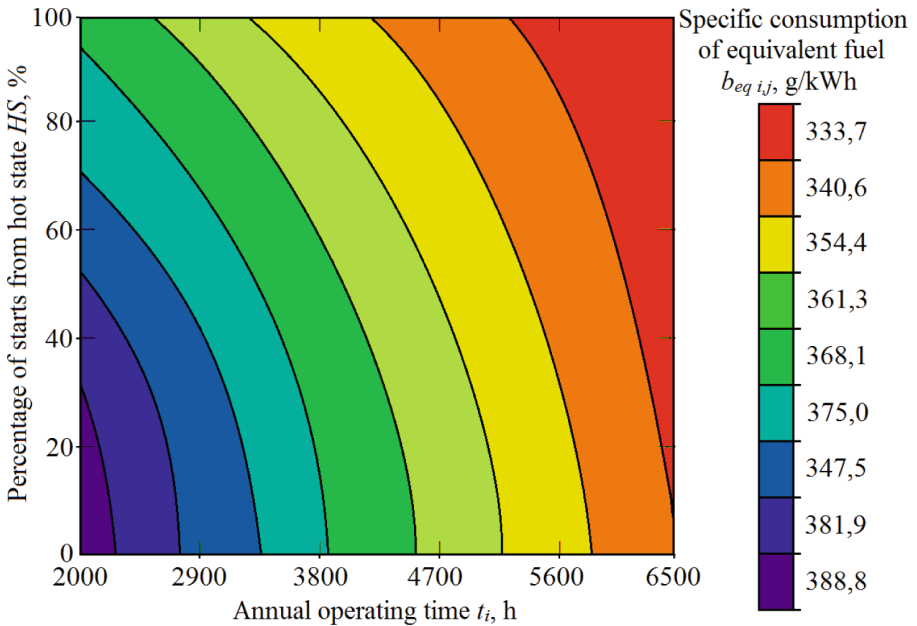
Fig. 1. The chart of specific consumption of equivalent fuel depending on operating parameters for 200 MW power unit

Analyzing the obtained results (Fig. 1), it can be noted that the rational distribution of the operating parameters of the 200 MW power unit, which are able to minimize the consumption of equivalent fuel is:

1) annual operating time of the power unit $t_i = 5500$–6500 h;
2) annual number of start-ups $n_i = 25$–36;
3) percentage of start-ups from the cold state $CS_i = 72$–90%, from the hot state –$HS_j = 10$–28%, from the uncooled state – $US_{i,j} = 0$–18%.

When operating in this range of parameters, the consumption of equivalent fuel is about 334–340 g/kWh. The difference between the most rational and irrational regimes is 16,5% (overconsumption 55 g/kWh).

The obtained results are expected – the optimal mode for the given boundaries of optimization parameters is the mode which is as close as possible to completely basic, at which there are no overconsumption of fuel during start-ups. The consumption of equivalent fuel in completely basic mode is $b_{eq}{}^{bas} = 323{,}3$ g/kWh. However, it is clear that the 200 MW unit cannot be operated in the completely basic mode of operation, both due to the operating conditions of the power system and due to accidental circumstances that could lead to an emergency shutdown of the equipment.

In addition, it should be noted that obtained values of the specific consumption of conventional fuel are somewhat optimistic, as they are calculated for the conditions of strict execution of start-up load schedules, instructions of exploitation and the absence of incorrect actions of operating personnel.

3   Ensuring the Long-Term Operation of TPP Units by Rationalization Operating Modes

The residual resource of the power unit determines the allowable residual operating time of the equipment before the transition to the limit state. The residual operating time of a power unit is often determined by the allowable service life of its turbine [7] and can be calculated:

$$G = \frac{1 - D'_{st} - D'_c}{D''_{fc}} \tag{10}$$

where D'_{st}, D'_{st} are the static and cyclic damage accumulated in the metal of turbine at the time of estimating residual resource; D''_{fc} – forecasted average annual damage for the next period of operation.

The calculation of damage indicators is a separate complex task, that requires a significant set of studies, performed by the authors earlier and presented in [8].

To ensure a high residual resource of the main equipment, it is proposed to rationalize the modes of operation of the power unit according to a similar approach presented above. Taking into account the Palmgren-Miner hypothesis, the residual resource of the power unit can be represented as:

$$G_{i,j} = \frac{\left(1 - D'_{st} - D'_c\right) \cdot \chi}{\frac{t_i}{[T]} + n_i\left(\frac{CS_i}{[N_{CS}]} + \frac{CS_i \cdot HS_j}{[N_{HS}]} + \frac{CS_i \cdot (1 - HS_j)}{[N_{US}]}\right)} \tag{11}$$

where χ – average annual operating time of the power unit according to the technical audit; $[T]$ – allowable operating time of the metal at rated loads and maximum

temperatures, determined by experimental curves of long-term strength of steel; $[N_{CS}]$, $[N_{HS}]$, $[N_{US}]$ – allowable number of start-up cycles from cold, hot and uncooled states, determined by the curves of low-cycle fatigue of Coffin-Manson [8].

Demonstration of practical use of the developed system of planning of rational operating modes of TPP power units is offered to be presented on the example of power unit № 15 of Luhansk TPP (Ukraine). Resource indicators of this unit were calculated by the authors earlier. As of 01.01.2020, this power unit has an operating time of 308 000 h with 1467 start-ups from different thermal states.

The results of rationalization of the operating modes of this power unit in order to ensure resource-saving are presented in Fig. 2.
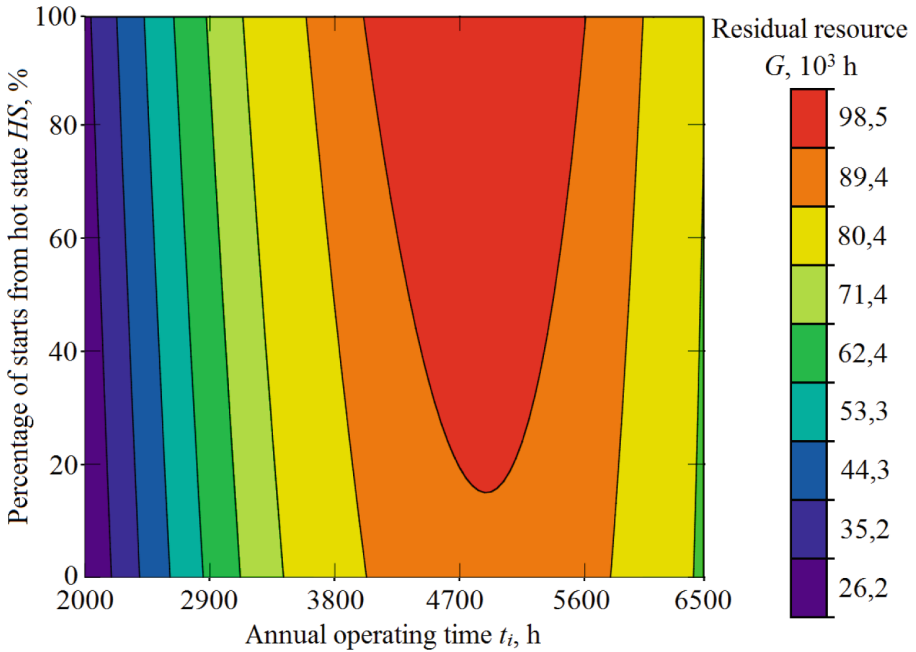
Fig. 2. The chart of residual resource of the 15th power unit of Luhansk TPP (Ukraine) depending on operating parameters

Analyzing the obtained results (Fig. 2), it should be noted that the rational distribution of the regime parameters of the 15th power unit of Luhansk TPP, which demonstrates the highest values of the residual resource is:

1) annual operating time of the power unit $t_i = 4200$–5300 h;
2) annual number of start-ups $n_i = 38$–49;
3) percentage of start-ups from the cold state $CS_i = 51$–68%, from the hot state $-HS_j = 20$–49%, from the uncooled state $- US_{i,j} = 0$–29%.

The residual resource of the power unit is about 90–98 thousand hours when operating in this range of regime parameters.

The most rational mode of operation in comparison with irrational increases an individual resource by 21.6%. If we consider the application of this system to a new power unit, it is possible to achieve much higher growth rates of individual resource (up to 50%).

4   Discussion of Research Results

Considering the results of the application of the developed rationalization systems, it can be noted that the optimal distribution of the operating parameters for minimizing fuel consumption and maximizing the residual resource do not match. The task is to find a compromise solution that can to some extent satisfy the generating company. Therefore, as rational, we can distinguish the following distribution of the operating parameters:

1) annual operating time of the power unit $t_i = 4800$–5800 h;
2) annual number of start-ups $n_i = 33$–44;
3) percentage of start-ups from the cold state $CS_i = 60$–77%, from the hot state $-HS_j = 20$–40%, from the uncooled state $- US_{i,j} = 0$–20%.

When operating in this range of operating parameters, the residual resource of the unit is about 87–97 thousand h at a fuel consumption of 335–346 g/kWh. This proves the effectiveness of the proposed system for planning cost-effective and resource-saving operation of thermal power plants.

In the future, the authors will improve the proposed system of planning rational modes of operation of TPP units, by bringing several target functions to a single one. This indicator can be considered the economic profit of TPP from direct savings of fuel, heat and electricity, as well as the profit from extended service life, reduction of repair costs, etc. At the same time, if we take into account the profit from the direct sale of electricity to suppliers of the power system, the value of the results increases significantly.

In summary, it can be noted that the usage of developed system for rationalization of the operating parameters of power units for energy generating companies is a very promising and relevant tool to improve the efficiency of TPP operation.

5   Conclusions

The system for planning cost-efficient and resource-saving operating modes of TPP is developed in the work. The concept of this work is to analyze thousands of possible exploitation modes of power equipment, among which are those that provide extreme values of the selected target functions. Operating modes are determined by operating parameters, such as the annual operating time of the unit, the annual number of start-ups and the percentage of start-ups by several thermal conditions.

The developed system of planning of rational operating modes allows to increase efficiency of exploitation of thermal power plants to 16.5%. This is achieved by reducing fuel consumption when working in irrational modes of operation. In the proposed system there is an opportunity to change the boundaries of the studied parameters.

From the point of view of resource saving when using the developed system, it is possible to significantly reduce the negative impact of irrational modes of operation on the rate of accumulation of damage in the main equipment and prevent its premature failure. As a result, the individual resource of the power unit can be increased to 21.6%.

References

1. Zhao, X., Peng, B., Elahi, E., Zheng, C., Wan, A.: Optimization of Chinese coal-fired power plants for cleaner production using Bayesian network. J. Clean. Prod. **273**, 122837 (2020). https://doi.org/10.1016/j.jclepro.2020.122837
2. Milovanović, Z.N., Papić, L.R., Milovanović, S.Z., Janičić Milovanović, V.Z., Dumonjić-Milovanović, S.R., Branković, D.L.: Planning methods for production systems development in the energy sector and energy efficiency. In: Ram, M., Pham, H. (eds.) Advances in Reliability Analysis and its Applications. SSRE, pp. 95–148. Springer, Cham (2020). https://doi.org/10.1007/978-3-030-31375-3_3
3. Stoppato, A., Mirandola, A., Meneghetti, G., Lo Casto, E.: On the operation strategy of steam power plants working at variable load: technical and economic issues. Energy **37**(1), 228–236 (2012). https://doi.org/10.1016/j.energy.2011.11.042
4. Mayanti, B., Songok, J., Helo, P.: Multi-objective optimization to improve energy, economic and environmental life cycle assessment in waste-to-energy plant. Waste Manage. **127**, 147–157 (2021). https://doi.org/10.1016/j.wasman.2021.04.042
5. Ding, N., Pan, J., Liu, J., Yang, J.: An optimization method for energy structures based on life cycle assessment and its application to the power grid in China. J. Environ. Manage. **238**, 18–24 (2019). https://doi.org/10.1016/j.jenvman.2019.02.072
6. Pan, M., et al.: Thermodynamic, exergoeconomic and multi-objective optimization analysis of new ORC and heat pump system for waste heat recovery in waste-to-energy combined heat and power plant. Energy Convers. Manage. **222**, 113200 (2020). https://doi.org/10.1016/j.enconman.2020.113200
7. Aminov, R., Shkret, A., Garievskii, M.: Estimation of lifespan and economy parameters of steam-turbine power units in thermal power plants using varying regimes. Therm. Eng. **63**, 551–557 (2016). https://doi.org/10.1134/S0040601516080012
8. Chernousenko, O., Rindyuk, D., Peshko, V., Chernov, O., Goryazhenko, V.: Development of a system for estimating and forecasting the rational resource-saving operating modes of TPP. Eastern-Eur. J. Enterp. Technol. **3**(8), 14–23 (2020). https://doi.org/10.15587/1729-4061.2020.204505
9. ISO 50045:2019: Technical Guidelines for the Evaluation of Energy Savings of Thermal Power Plants. International Organization for Standardization, Geneva, Switzerland. https://www.iso.org/standard/67849.html (2019)

Assessment of Quality Criteria of Shot Blasting Cleaning of the Inner Surfaces of Chemically Resistant Containers

Oleksii Goryk[1]([✉]) [iD], Stanislav Koval'chuk[1] [iD], Oleksandr Brykun[1] [iD], and Sergii Aksonov[2]

[1] Poltava State Agrarian University, Skovorody Str. 1/3, Poltava 36003, Ukraine
oleksii.goruk@pdaa.edu.ua

[2] ProFermer, Volkersdorfer Street 2, 27419 Sittensen, Germany

Abstract. Long-term practice shows that even the best protective anti-corrosion coatings cannot protect a poorly cleaned steel surface from destruction. The resistance of protective non-metallic coatings (glassy, ceramic, polymer, glass-crystalline, rubber), which, in terms of chemical resistance, noticeably surpass the known stainless steels and special alloys, depends on the criteria of purity and roughness of the metal surface on which it will be applied. Among the mechanical cleaning methods, the priority is abrasive-jet, which provides the required level of surface cleanliness and uniform roughness of the specified parameters. Existing regulatory quality criteria for treated surfaces do not always provide a complete answer to questions related to the strength of adhesion to them of protective non-metallic coatings. This is especially true for cleaning and coating the inner surfaces of large hollow bodies of biological, chemical, food and other devices, where the resistance of the protective layer is crucial. The purpose of this work is to substantiate the need to supplement such products with the generally accepted regulatory requirements for the condition of surfaces prepared for the application of corrosion-resistant non-metallic coatings. These requirements relate to the technological interval between the process beginning of shot blasting of the product and the process beginning of applying the soil layer to the cleaned surface, the uniformity of surface roughness according to specified geometric parameters and measures of the surface charging by fragments of a technical shot.

Keywords: Shot blasting cleaning · Quality criteria · Technological interval

1 Introduction

Many technological processes in various industries are carried out in an aggressive working environment at elevated temperatures (up to 300 °C) and pressure (up to 20 atm). Such technological processes take place in closed capacitive devices, which are made of structural materials with high resistance to aggressive environments, namely: stainless steels; nickel-chromium-molybdenum alloys such as Hastelloy, Remanit; carbon steels clad with an acid-resistant layer of another metal or alloy; carbon-graphite composite materials and others [1].

The research aim of this work is to substantiate the need to take into account special specific requirements for the quality of preparation of the inner surfaces of chemically resistant housing of devices for applying anti-corrosion non-metallic coating on them. This will significantly increase the reliability and efficiency of expensive large-sized container products for biological, chemical and food purposes and others.

In order to improve the quality of surface preparation for the manufacture of parts and assemblies, a promising direction is the use of low-cost low-carbon steels, on the surface of which, at the stage of semi-finished products, protective non-metallic coatings (glassy, ceramic, polymer, glass-crystalline, rubber) are applied, which are noticeably superior in chemical resistance to well-known stainless steels and special alloys [2, 3]. This method of manufacture is justified since it saves expensive metals: nickel, molybdenum, titanium and others. In addition, capacitive devices with a protective non-metallic coating have an increased service life; allow obtaining sufficiently clean processed products that are not contaminated with metal sludge. However, the resistance of protective non-metallic coatings requires very careful surface preparation [4].

The most effective, environmentally acceptable and economically profitable mechanical way to form the necessary criteria for the quality of the treated surface is shot blasting, which is carried out without the use of lubricants and coolants, and waste products are harmless and relatively easy to remove and dispose of [5]. Compared to hazardous electrochemical and electrophysical methods of cleaning metal surfaces, shot blasting is a less energy-intensive process. Unlike chemical and physical methods, shot blasting does not lead to metal saturation with hydrogen, which has a positive effect on the stability of the protective coating [6].

Despite the availability of normative documentation on the research and standardization of quality criteria for the cleaned surfaces: visual assessment of surface cleanliness [7], tests to assess surface finish [8], the characteristics of the roughness or profile of the surface [9], there is a need to supplement some criteria for shot blasting of the surfaces of metal corrosion-resistant products cavities, which is of great technological importance. Indicators for assessing the quality of preparation of steel surfaces of such products for protective anti-corrosion coatings, given in international standards and technical literature, clearly do not sufficiently take into account the specific features of the shot blasting technology.

2 Methodology

The research concerned large-scale equipment for the chemical, petrochemical, microbiological, medical and food industries, the cavities of which are prepared for the application of durable protective non-metallic coatings. Such products are mainly made of low-carbon steels. The strength of adhesion of non-metallic coatings to the treated surface directly depends on the quality criteria of its processing.

To study the quality criteria of the treated surfaces, flat disk samples with a diameter of 80 mm were made from the material of the product. Shot blasting was carried out in a special protective chamber equipped with a shot blasting device with a capacity of $3...10 \, m^3/h$. The attack speed of the pellets with a diameter of 0.8, 1.0 and 1.4 mm was $v = 40...120 \, m/s$, the angle of attack $\alpha = 15...90°$.

Before shot blasting, the experimental disk samples were prepared according to the technology adopted in chemical engineering [10]. They were subjected to heat treatment in the mode of normalization annealing in a chamber electric furnace with a protective atmosphere. To do this, the samples were placed in furnaces so that their surfaces did not touch each other, heated to a temperature of $850 \pm 20\,°C$ at a rate of $300\,°C/h$, and kept at this temperature for 30 min.

On the basis of the measurements, the surface roughness was determined and shot debris charging of the treated surface on the manufactured sections of size $40 \times 20 \times 5$ mm was studied using an electron microscope.

3   Results

We will substantiate certain specific requirements for the condition of the surfaces of capacitive products cleaned with shot-air jet before applying stable non-metallic protective coatings on them.

3.1   Time Interval

The activated metal surface, after shot blasting, begins to interact intensively with the surrounding atmosphere. This primarily concerns water vapor and oxygen in the air.

The interaction of the cleaned surface of a steel product with oxygen proceeds in several stages [11]: physical adsorption of oxygen molecules, accompanied in many cases by dissociation $O_2 \rightarrow O + O$; chemisorption of oxygen atoms; formation of metal oxide nuclei in certain areas of the surface; formation of phase oxides and increasing the continuity of the oxide film. Completion of these stages depends on the properties and structure of the steel surface, while the heat of oxygen adsorption is an important characteristic.

The adsorbed film serves as the basis for the formation of a phase oxide film, the formation rate of which depends on the chemical activity of the metal. Most oxide films have an ionic structure; their crystal lattice consists of charged metal and oxygen ions with an interpolar bond. However, there is an imperfection in the structure of real oxidative phases: uneven distribution of ions in the crystal lattice, free empty spaces (holes), dislocations, distortions, etc. In places of transition from the oxide phase to the metal, there is an intermediate zone with a thickness of several atomic layers, which is a distorted part of the metal lattice on the one hand and the oxide part on the other. Due to the presence of such an intermediate layer (interlayer) oxide films have a high strength of adhesion to the metal.

Chemisorbed oxygen significantly changes the physical and chemical properties of the surface of the metal product, which is very important for the processes of interaction of the metal with the soil layer of the protective non-metallic coating. In this regard, it can be expected that not metal oxides, but the treatment of the metal surface with active oxygen before applying the soil layer will be effective for increasing the adhesion strength of the soil with the metal. In the real conditions of machine-building production of large-sized capacitive devices, hours pass between the beginning of shot blasting

cleaning and the beginning of applying the soil layer on the cleaned surface. This is primarily due to the removal of metal dust and drying of the treated surface.

In the time interval between the operations of cleaning and applying a protective coating, the activated surface of the steel product is intensively oxidized, which negatively affects the adhesion strength of the soil layer to the metal base. Therefore, the time between these operations is limited to a certain interval. After this period of stay of the cleaned capacitive devices in the workshop conditions, their surfaces become unsuitable for applying a soil protective layer on them from the point of view of the reliability of the contact adhesion.

The quality of steel surfaces cleaned by shot blasting is divided by experts in the field of enameling of cavities of chemical devices according to the time interval (TI) between the operations of their cleaning and coating into four groups of suitability, based on the strength of the soil-metal contact: TI2, the interval is 2 h; TI4—4 h; TI6—6 h; TI8—8 h.

The study of the adhesion strength of glass-enamel coatings with steel 08 confirms the proportional dependence of the adhesion strength of the soil-metal contact on the time interval. That is, the eight hour interval is the limit in terms of the suitability of the cleaned surface for applying a non-metallic protective coating to it.

The practice of manufacturing large-sized chemical containers shows that the proposed classification of surface quality of steel products after shot blasting, depending on the time interval of exposure in an atmosphere of free air, is justified and aimed at the strength of the anti-corrosion coating. Therefore, this time indicator should be considered one of the important quality criteria and should be monitored when developing a technological chart for cleaning the inner surfaces of large containers that require significant cleaning time. And, if necessary, a short-term additional operation of surface activation should be provided.

3.2 Roughness Parameters

Between the thickness of the dry baked soil layer and the surface roughness of the steel product, which is estimated by the parameter R_z [12]—the height of the profile roughness at ten points, the ratio is:

$$aR_z = \delta, \tag{1}$$

where $a \approx 2.0$ is a coefficient of proportionality, the meaning of which is that the soil layer should fill all the depressions of the profile and cover with some margin the highest protrus ions of microroughnesses R_{max}.

There is a relationship between the average step of the surface profile roughness S_m and the parameter R_z:

$$S_m = bR_z, \tag{2}$$

where b is the coefficient of proportionality, which for low-carbon steel products processed at attack speeds $v = 80...125$ m/s, and was 8 at the angle of attack $\alpha = 70°$ and ~12 at $\alpha = 45°$.

Roughness parameters R_z and S_m, as a reflection of the dimensions of the trace—height ($h \approx R_z$) and length ($l \approx S_m$), depending on the technological modes of cleaning (attack speed, angle of attack and shot size) can be determined by viscoelastic [13] and elasticplastic models [14] of impact interaction between a shot and a fixed metal barrier.

It is known that the quality of the protective non-metallic coating depends on the uniformity of the distribution of the material along the height of the surface profile. In this regard, for the surfaces of the products cleaned by an abrasive-air stream it is recommended to adhere to a certain ratio between a step of roughnesses S_m and height of microroughnesses R_z. It is established that the ratio S_m/R_z to ensure uniform roughness varies between 9...10 at optimal angles of attack, which is achieved by changing the technological modes, among which the determining factor is the angle of attack. Therefore, when assessing the quality of treated surfaces, along with the specified parameters of roughness [9], the ensuring of its uniformity, which is not discussed in the current standards, should also be taken into account.

The ratio $S_m/R_z \approx l/h$ decreases with increasing angle of attack, remaining practically independent of the diameter of the shot. This fact made it possible to construct a family of curves of dependences l/h on the angle of attack α at different speeds of attack (see Fig. 1).
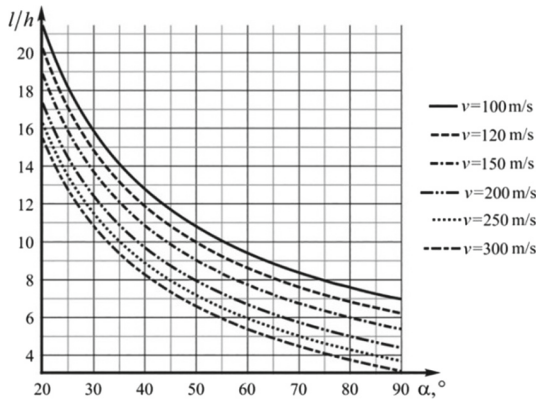
Fig. 1. Graphs of the ratio l/h.

These graphs make it easy to determine the angle of attack at the initial speed of the attacking shot to ensure the quality criterion of the cleaned surface by the uniformity of roughness, based on the ratio $\theta = S_m/R_z \approx l/h$. Having set the necessary indicator θ of uniform roughness, we determine the corresponding angle of attack at a given technological speed of attack of the shots and vice versa. For example, within the range of variation of the uniform roughness index $\theta = 9...10$, the optimal angle of attack at $v = 100...300$ m/s ranges from 65° to 32°.

This approach makes it possible to control one of the important quality criteria of the cleaned metal surfaces of products from the point of view of uniform roughness of the specified parameters with specific initial data of the shot blasting process according to the

graphs (see Fig. 1), while balancing the technological parameters to achieve maximum productivity.

3.3 Charging of the Treated Surface

Impacting wear is the predominant type of wear of technical shot when cleaning metal products [15]. Attacking shots hit a stationary work surface at speeds $v \geq 80$ m/s. This leads to the splitting of the shots, chipping of their protruding tops, rounding of the cutting edges of the shots, etc. The bulk of the grinding products ricochet or turn into metal dust, but some of the fragments of the shots penetrate into the surface layer of the processed product and often turn out to be wrapped in the surface layer by other shots, which subject the surface layer to severe plastic deformation. Such saturation of the surface layer with fragments of shots is called charging.

Technical steel crushed shot of standard quality differs in chemical composition from low-carbon steels primarily in carbon content $C - 0.8...1.2\%$, because it must be stronger and harder than carbon steel after appropriate heat treatment in order to have the expected durability n, calculated in hundreds of cycles.

Therefore, the electrode potentials embedded in the surface layer of the fragments of the shot differ from the electrode potential of low-carbon steel product. Without presenting any danger at the stage of application and formation of a protective non-metallic coating on the surface of the capacitive devices, fragments of the shot manifest themselves later in the operation of the capacitive device. They become foci of electrochemical corrosion, which destroy the protective non-metallic coating inside. One such defect can bring out of order a capacitive device with a working volume of tens of cubic meters.

Unfortunately, currently most machine builders do not pay attention to the charging degree of the treated surface of low-carbon steel products, on the surface of which protective non-metallic coatings are applied. This, in addition to capacitive devices, should also include parts of load-bearing structures made of low-carbon steels of trucks, agricultural vehicles, lifting and transport equipment, etc., the free surfaces of which are protected from the chemical effects of the environment with paint and varnish coatings.

The quantitative degree of charging was established on the basis of the analysis of the microstructure, which was studied by electron microscopy [16] of the surface layer of the cleaned product. Thus, the quantitative composition and the volume fraction of stuck shot fragments in a certain volume of the surface layer with a thickness $\delta = 0.1$ mm were established experimentally on a microsection behind the known methods of stereometric metallography.

The number of sections of shot fragments per unit area of a thin section was determined by the Jeffries method. For this, a square was selected in the plane of the thin section, the natural area of which is equal to 1 mm^2, and counted the number of cuts of charged shot fragments according to the formula:

$$n_{ch} = z + 0.5\omega + 0.25u, \tag{3}$$

where n_{ch} is the total number of units of shot fragments; z is the number of whole units within a square contour; ω is the number of units crossed by straight contour lines; u is the number of angular units.

The number of shot fragments in 1 mm^3 of the surface layer volume was determined by the Shailo-Shvarts-Saltykov formula:

$$N_{ch} = (a_k n_k - a_{k-1} n_{k-1} - \ldots - a_1 k_1)/\Delta, \tag{4}$$

where Δ is the breakdown price, which is equal to the quotient of dividing the maximum diameter of the fragments by the number of groups (monodisperse systems); a—coefficients, the values of which depend on the number of groups; n is the number of sections of shot fragments of a certain size group k per unit area of the section.

Figures 2–3 show graphs of the indicator dependence of the charging degree N_{ch} on the speed v and angle of attack α of the treated surface.
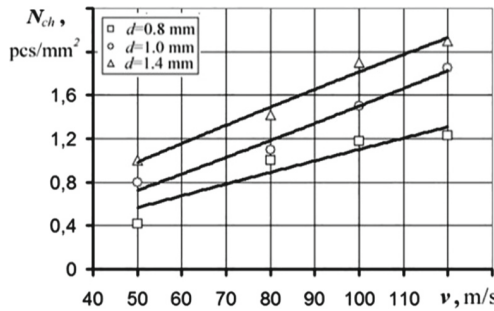
Fig. 2. Dependences of the charging degree N_{ch} on the speed of attack v.

The charging of the surface by fragments of the shot gradually increases with increasing angle of attack and reaches a maximum value regardless of the diameter of the shot and the attack speed at $\alpha \to 90°$. With a decrease in the diameter of the shot, the maximum value of the charging indicator decreases slightly. Thus, if for $d = 1.4$ mm at the angle of attack $\alpha = 90°$ the charging rate is $N_{ch} \approx 2.2 \, \text{pcs/mm}^2$, then for $d = 0.8$ mm—$N_{ch} \approx 1.1 \, \text{pcs/mm}^2$ (see Fig. 3).

Metallographic studies have established that the geometric dimensions of the shot fragments along the diameter of the sphere described around them vary over a wide range—from several to tens of micrometers. The ratio of small to large fragments is approximately 5:1. About 20% of small shot fragments were completely immersed in the surface layer. They were found only on the sections of experimental samples.

Let's connect the charging degree with the technological parameters of cleaning. Provided that when hitting the surface, n_{fr} fragments are separated from the shot, then the total number of formed fragments N_{fr}, and which can potentially charge the treated surface, will be proportional to the shot number $N_{sh} = t B_{sh}/m_{sh}$ with the mass m_{sh}, that during the time t at mass supply of a shot through a shot-jet nozzle B_{sh} attack the surface

$$N_{fr} = n_{fr} t B_{sh}/m_{sh}. \tag{5}$$

Number of fragments n_{fr}, separated from the shot fraction 1.0 mm at the attack speed close to 100 m/s, according to our observations, it varies within 4…8 pieces. Number of
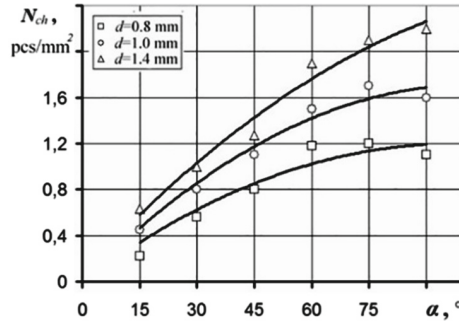
Fig. 3. Dependences of the charging degree N_{ch} on the angle of attack α.

shot fragments N_{ch}, charging the surface area of 1 m^2, will be a certain part of the total number of fragments formed N_{fr}, which is determined by the charging coefficient k_{ch}. Then:

$$N_{ch} = k_{ch} n_{fr} t B_{sh} / m_{sh}. \tag{6}$$

The coefficient k_{ch}, with constant physical and mechanical properties of the contacting bodies, is a function of the attack speed v, angle of attack α, particle size distribution of the fraction d_{sh}, the mass of one shot m_{sh}, as well as the duration t of the shot action on the treated surface. Studies show that the charging of the treated surface with fragments of shot after removal of the defective layer takes on a stable character and does not depend on the duration t of the jet in the future. For the constant course of the phenomenon of charging, if the number of stuck fragments is equal to the number of removed ones, it is advisable to assume that the coefficient k_{ch} will be proportional to the work on the plastic deformation of the product, the value of which is determined by the main technological modes—attack speed, angle of attack and the shot mass

$$k_{ch} = \zeta m_{sh} (v \sin \alpha)^2 (1 - k_r^2), \tag{7}$$

where $\zeta \approx 0.1$ is the coefficient of proportionality, which is experimentally refined for specific conditions; k_r is a shot rate recovery coefficient v with the angle of attack α, determined by known techniques.

Substituting eq. (7) into eq. (6) and replacing the time t of cleaning of 1 m^2 the surface with the inverse value of the surface productivity $t = 1/Q_f$ with a completely removed defect layer, we find the number of fragments N_{ch} (pcs/m^2) that charge the treated surface

$$N_{ch} = \zeta (v \sin \alpha)^2 (1 - k_r^2) n_{fr} B_{sh} / Q_f. \tag{8}$$

The mass of shot fragments, which probably charges the surface of the product of low-carbon steel per unit time, can be predicted as follows:

$$M_{ch} = \mu B_{sh} / (Q_f n), \tag{9}$$

depending on the share of the technical shot (μ), which charges the treated surface, the durability of the technical shot n in cycles and already known technological parameters.

For products made of low-carbon steels that have undergone normalizing annealing, when using standard chipped technical steel shot, the coefficient μ is insignificant ≤ 0.01.

Quantitative eq. (8) and mass eq. (9) measures of charging of the surface layer, as well as the ratio of small and large fragments, make it possible to pre-determine the conditional size (mass) of large fragments, as future foci of corrosion ignition.

4   Conclusions

It can be argued that the reliability and durability of metal products, especially capacitive chemically resistant devices, directly depend on the quality of surface preparation of the product cavities for applying a stable non-metallic coating on them, is of decisive importance for the integrity and strength of the soil-metal contact.

The quality of shot blasting cleaning of steel surfaces under the protective non-metallic coating should be assessed, in addition to the generally accepted scale of cleanliness, also by such additional criteria as: time interval between the shot blasting process of the product and the process of applying the soil layer to the cleaned surface; uniformity of surface roughness according to the specified geometrical parameters; the charging degree of the surface by fragments of technical shot and the limit values of their size.

These quality criteria for shot blasting of metal surfaces require further deep theoretical and experimental study and addition to the current standards.

References

1. Talbot, D.E.J., Talbot, J.D.R.: Corrosion Science and Technology, 3rd edn. CRC Press (2018)
2. Kubler, R., Berveiller, S., Bouscaud, D., Guiheux, R., Patoor, E., Puydt, Q.: Shot peening of TRIP780 steel: experimental analysis and numerical simulation. J. Mater. Process. Technol. **270**, 182–194 (2019)
3. Shiryaev, A.A., Trofimov, V.N., Karmanov, V.V., Vindokurov, D.V.: Influence of ultrasonic shot blasting parameters on the physicomechanical properties of the surface layer of samples from 08PS and 12Kh18N10T steels. In: 28th Russian Conference on Mathematical Modelling in Natural Sciences (2020)
4. Rajput, A., Ak, M., Kim, S.J., Noh, S.H., Park, J.H., Paik, J.K.: Effects of the surface preparation on the life of epoxy coating in steel ship plates: an experimental study. Ships Offshore Struct. **14**(sup1), 199–206 (2019). https://doi.org/10.1080/17445302.2019.1565072
5. Polyanskii, S.N., Butakov, S.V., Olkov, I.S., Aleksandrov, V.A.: Repair of turbine components by abrasive-jet machining. J. Mach. Manuf. Reliab. **50**(1), 72–78 (2021). https://doi.org/10.3103/S1052618821010143
6. Li, J., Du, A., Fan, Y., Zhao, X., Ma, R., Wu, J.: Effect of shot-blasting pretreatment on microstructures of hot-dip galvanized coating. Surf. Coat. Technol. **364**, 218–224 (2019)
7. ISO 8501-1:2007 Preparation of steel substrates before application of paints and related products – Visual assessment of surface cleanliness – Part 1: Rust grades and preparation grades of uncoated steel substrates and of steel substrates after overall removal of previous coatings (2007)
8. ISO 8502-3:2017 Preparation of steel substrates before application of paints and related products – Tests for the assessment of surface cleanliness – Part 3: Assessment of dust on steel surfaces prepared for painting (pressure-sensitive tape method) (2017)

9. ISO 8503-1:2012 Preparation of steel substrates before application of paints and related products – Surface roughness characteristics of blast-cleaned steel substrates – Part 1: Specifications and definitions for ISO surface profile comparators for the assessment of abrasive blast-cleaned surfaces (2012)

10. Bachar, A., et al.: Effect of thermal treatment on the property of enamel coating on steel substrate. J. Mater. Env. Sci. **8**, 3884–3891 (2017)

11. Montemore, M.M., Spronsen, M.A., Madix, R.J., Friend, C.M.: O_2 activation by metal surfaces: implications for bonding and reactivity on heterogeneous catalysts. Chem. Rev. **118**(5), 2816–2862 (2017)

12. ISO 4287:1997 Geometrical Product Specifications (GPS) – Surface Texture: Profile Method – Terms, Definitions And Surface Texture Parameters (1997)

13. Goryk, A., Koval'chuk, S., Brykun, O., Chernyak, R.: Viscoelastic resistance of the surface layer of steel products to shock attack of a spherical pellet. Key Eng. Mater. **864**, 217–227 (2020). https://doi.org/10.4028/www.scientific.net/KEM.864.217

14. Gorik, A.V., Zinkovskii, A.P., Chernyak, R.E., Brikun, A.N.: Elastoplastic deformation of the surface layer of machinery constructions on shot blasting. Strength Mater. **48**(5), 650–657 (2016). https://doi.org/10.1007/s11223-016-9808-6

15. Zdansky, O., Kriz, A., Simecek, J.: Correlation between blasting wear resistance and impact test on Hadfield steel. In: 26th International Conference on Metallurgy and Materials, pp. 629–634. METAL, Brno (2017)

16. Egerton, R.F.: Physical Principles of Electron Microscopy: an Introduction to TEM, SEM and AEM. Springer International Publishing, Cham (2016). https://doi.org/10.1007/978-3-319-39877-8

Numerical Simulations of Mixture Formation to Ensuring the Quality of Thermal Deburring

Sergiy Plankovskyy[1] , Olga Shypul[2] , Yevgen Tsegelnyk[1(✉)] ,
Sergiy Zaklinskyy[2] , and Olha Bezkorovaina[3]

[1] O. M. Beketov National University of Urban Economy in Kharkiv, 17 Marshala Bazhanova
Street, Kharkiv 61002, Ukraine
y.tsegelnyk@kname.edu.ua
[2] National Aerospace University "Kharkiv Aviation Institute", 17 Chkalova Street,
Kharkiv 61070, Ukraine
[3] Progresstech Ukraine LLC, 3 Sholudenka Street, Kyiv 04116, Ukraine

Abstract. The paper refers to the issues of ensuring the quality of Thermal Energy Method (TEM) processing of complex-shaped parts. The required energy of TEM processing depends on the accuracy of the fuel mixture, bearing in mind its component composition, stability and homogeneity. To gain further insight into mixture formation near structural elements of complex-shaped parts a sphere with blind holes having different length-to-diameter ratios were considered. To investigate the effect of the mixture formation in the chamber a numerical simulation for two strategies of filling was conducted, particularly a sequential filling of the chamber with the mixture components and filling the chamber with a prepared mixture of a given composition. A criterion based on the fuel mass fraction distribution was used to assess the quality of the fuel mixture with the possibility of the quality assessment in the individual subareas. The state of the mixture while mutual diffusion of its components and mixing with the residual velocity of gas movement was simulated and the required value of the holding time was determined. Obtained results show that the heterogeneity of the fuel mixture effects significantly the distribution and magnitude of the acting heat fluxes. It is proved that to ensure the degree of the mixture homogeneity required for accurate TEM processing, it is preferable to fill the chamber with the prepared mixture.

Keywords: Numerical simulation · Impulse Thermal Energy Method · Component composition · Homogeneity of fuel mixture

1 Introduction

A development vector of high-precision mechanisms engineering including 3D printing technologies increases requirements to reliability and resource, mainly due to an industrial cleanliness of surfaces and quality of edge treatment [1–3]. Now abrasive technologies are widely used for edge finishing and surface cleaning including various flow abrasive processes [4], and washing, increasingly ultrasonic [5], in spite of the use

of abrasives can lead to secondary contamination of surfaces. The use of such technologies is dangerous in the production of high-precision mechanisms due to the remnants of micro-abrasive particles can lead to increased wear or even jamming of friction pairs. An alternative may be deformation-free edge processing methods [6], such, for example, as electrochemical [7], electroerosive [8], laser [9], but taking into account they do not provide combined edge finishing and surface cleaning at the moment. The only united difficulty for all mentioned technologies is absent automated high control accuracy and special methods for calculating processing modes with predictable accuracy [10, 11].

Having unique advantages from this perspective the Thermal Energy Method (TEM) [12, 13] is successfully implemented along with classic finishing technologies [14, 15] and is promising for use in additive manufacturing for cleaning from particles of non-sintered powder [16]. For processing by TEM the parts are located in a closed chamber filled with the fuel gas mixture and ignited by a spark, thereby the treating occurs due to the interaction of the part material and the combustion products [17]. In the case of a time-controlled exhaust of gases from the chamber, inherent the Impulse Thermal Energy Method (ITEM) [18, 19] the processing time can be tenths of a second. With such a short treatment time, especially for precision parts manufacturing to provide uniform processing accuracy, it is necessary to ensure the quality of the initial fuel mixture composition and homogeneity. This becomes particularly important when internal cavities of complex-shaped parts need to be cleaned. In the works devoted to TEM processing, the issues of calculating specific heat fluxes [20], determining the initial pressure and processing time according to the given edge characteristics [18], the optimal layout of parts in the chamber [21–23], the issue of creating and control multicomponent gas mixtures were considered. However, there was not studied enough the problem of ensuring the quality of the fuel mixture including its component composition and homogeneity for required accuracy TEM processing. Thus, the study of this paper focuses to fill the gap mentioned above. It is almost impossible to determine experimentally the composition of the mixture in the internal cavities of the workpieces after the chamber has been filled. In order to solve this problem and highlight hard-to-reach areas, the study was carried out by numerical simulating.

2 Mixture Formation Problem Formulation for TEM

The single-phase multicomponent flow will be taken as a model to describe the process of mixture formation in the chamber of the TEM installation. The equations for calculating the composition of the mixture are applied in the following form:

$$\frac{\partial \rho}{\partial t} + \operatorname{div}(\rho \vec{u}) = 0, \tag{1}$$

$$\rho \frac{\mathrm{d}\vec{u}}{\mathrm{d}t} = \operatorname{div} P + \vec{f}, \tag{2}$$

$$\rho \frac{\mathrm{d}e}{\mathrm{d}t} = \operatorname{div}(\lambda \operatorname{grad} T) + P \cdot grad\ \vec{u}, \tag{3}$$

$$\rho \frac{\partial c_i}{\partial t} = -\operatorname{div} \vec{\mathbf{I}}_i, \quad i = 1, ..., N - 1, \tag{4}$$

where $\rho(\rho_i)$ is the density of the mixture and its species i; c_i is the mass fraction of species i; $\vec{u}$ is the velocity vector; P is the stress tensor; $\vec{\mathbf{I}}_i = \rho_i \vec{w}_i$ is diffusion flow vector; T is the temperature of the gas; λ is the coefficient of thermal conductivity of the gas; e is the internal energy of the gas.

When determining the diffusion flow vector, the effects of thermo- and barodiffusion were not taken into account in the model, and therefore the diffusion rate in (4) was given by Fick's law [24]:

$$\vec{w}_i = -D_i \operatorname{grad} c_i, \tag{5}$$

where D_i is the diffusion coefficient of species i in the mixture of N components.

In this case, the action of bulk forces $\vec{f}$ (of the gravity) is taken into account to ensure the possibility of stratification of the fuel mixture from components of different densities. When calculating the density and gas constant mixture, standard mixing rules are being used:

$$1/\rho = \sum_{i=1}^{N} c_i/\rho_i, \ \mathfrak{R} = \sum_{i=1}^{N} c_i \mathfrak{R}_i. \tag{6}$$

The model (1)–(6) was closed by the equations of the SST turbulence model [25]. This choice was justified by the ability to take into account the peculiarities of the flow, both in the volume of the chamber and near the wall areas, especially to analyze the mixture composition into the part cavities.

We applied a criterion based on the distribution functions of the mass fraction of fuel to assess the quality of the fuel mixture. For this, the range between the minimum and maximum values of the mass fraction $c_{\min}^{fuel}$ and $c_{\max}^{fuel}$ was divided into N intervals. As group frequencies we used the value of the relative volume of the chamber $\overline{V}_k^{ch}$, in which the value of the mass fraction of combustible gas is between the values of c_{k-1}^{fuel} and c_k^{fuel}. The degree of homogeneity of the mixture was assessed by the function determining the mathematical expectation of the mass fraction of fuel:

$$Ec^{fuel} = \sum_N \overline{V}_k^{ch} c_k^{fuel},$$

and its standard deviation:

$$Sc^{fuel} = \sqrt{\frac{\sum_N \left(c_k^{fuel} - Ec^{fuel}\right)^2}{N}}.$$

The mixture meets the requirements of the TEM processing under the condition that

$$[c^{fuel}] - \delta \cdot [c^{fuel}] \leq Ec^{fuel} - Sc^{fuel} \cup Ec^{fuel} + Sc^{fuel} \leq [c^{fuel}] + \delta \cdot [c^{fuel}], \tag{7}$$

where $[c^{fuel}]$ is a specified value of mass fraction of fuel (as a rule it corresponds to a stoichiometric ratio for ITEM); δ is a set permissible deviation of the mass fraction of fuel.

The peculiarity of the criterion (7) is that the assessment of the quality of the fuel mixture is carried out not on average in the chamber but in the specific sub-areas – such as the internal cavities of parts of complex shape, canals of blind holes, etc.

The mass flow at the inlet of the chamber and no-slip condition on the wall were used in the simulation as boundary conditions. As the initial conditions, the velocity, temperature and pressure so as mass fraction of the mixture components were set at the inlet of the chamber. Based on the operating sets of the TEM machine, it is assumed that before filling air presents with atmospheric pressure in the chamber.

The mixture composition in the chamber with the workpiece located into was determined by the numerical simulation. To assess the features of the mixture formation near specific sub-areas, the spherical part with the canals of blind holes with a diameter d of 2 and 4 mm and a length-to-diameter ratio $l/d = 2; 3; 4; 5$ had been considered (Fig. 1).
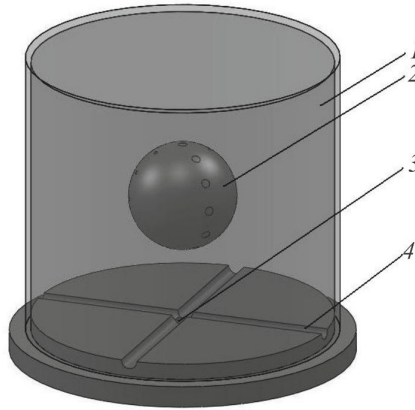
Fig. 1. A chamber with a part: *1* is the chamber body; *2* is the part; *3* is a hole for the mixture supply; *4* is a groove.

In order to exclude the influence on the result of factors associated with the location, holes of the same diameter with the same l/d ratio are located in the same diametrical plane with an equal pitch. The influence of holes geometry on the homogeneity of the mixture into its cavities was estimated by averaging the component mass fraction for all holes of the same size.

The simulation of filling the chamber with a methane-oxygen mixture with the values of $[c^{fuel}] = 0.2$, $\delta = 0.03$ was conducted for two mixture formation strategies:

- sequential filling of the chamber with the components of the mixture, assuming feeding a fuel and an oxidizing agent to a predetermined mass; then holding for 0.1 s;
- filling the chamber with a previously prepared mixture of a given composition, assuming feeding the mixture up to a given mass; then holding for 0.1 s.

3 Numerical Simulation Results

The problem (1)–(7) was solved using the commercial code Ansys CFX in the form of a chain of tasks, switching between which was carried out when the specified conditions for the mass of the gas supplied to the chamber were reached. The condition of the solution interruption was evaluated by the achievement of the specified holding time at the end of filling. The criterion (7) assessed the quality of the fuel mixture. For each group of holes, the distribution of the methane mass fraction, as well as the values of its mathematical expectation and standard deviation, were calculated.

When the successive filling in the cavities of blind holes, a significant non-identical in the methane mass fraction to the stoichiometric value was observed. Figure 2 shows an assessing the quality of the fuel mixture in the cavities of the blind holes with different l/d ratios for this filling strategy. Obviously, the composition of the mixture does not meet the requirements for criterion (7) for a given value $\delta = 0.03$.

That is why one may conclude that with the sequential filling of the chamber, it is practically impossible to provide stable processing conditions for all surfaces and edges of parts with cavities of complex shape.

Filling the chamber according to second strategy, namely with the prepared mixture, the distribution of the methane mass fraction into the internal cavities of the holes is completely different (Fig. 3). The mixture composition is almost homogeneous and the mass fraction values correspond to the flammability limits. However, the mixture composition also does not meet criterion (7) during the holding time of 0.1 s. In order to determine the required value of the holding time, an additional simulation was conducted for this case. The mixture formation by mutual diffusion of the components and mixing with the residual velocity of gas movement was simulated.
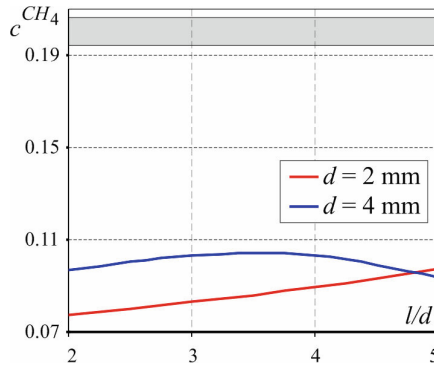
Fig. 2. Dependence of the methane mass fraction on the l/d ratio with the sequential filling.

Figure 4 presents the mathematical expectation of the methane mass fraction into the holes cavities depending on the holding time. The simulation results highlight the needed holding time near 1 s.

Moreover, the relationship between the mixture composition after filling and the heat flux after its combustion was estimated by simulating combustion and heat transfer using
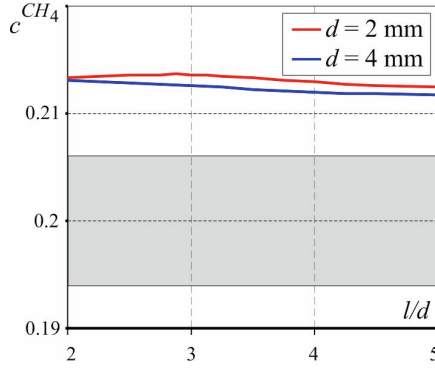
Fig. 3. Dependence of methane mass fraction on the *l/d* ratio when filling the chamber with the finished mixture.
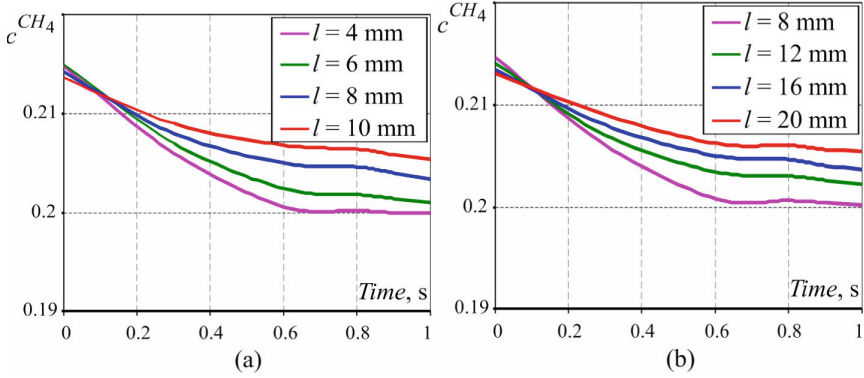
Fig. 4. The mathematical expectation of the methane mass fraction over the holding time for the holes with a diameter of 2 mm (a); the holes with a diameter of 4 mm (b).

the model described in [18] and the Pearson correlation coefficient were calculated. The mixture composition as well as the initial values of the gas velocity and temperature before ignition corresponded to the conditions of the end of the filling process. To calculate the correlation coefficient a point cloud was built on the surfaces of holes with the same diameter. The values of the methane mass fraction and the value of the specific heat flux at the end of combustion at these points formed samples for correlation analysis. The sample size was 800 points for each group of holes.

The Pearson correlation coefficient was determined as:

$$r_{xy} = \sum_{i=1}^{n} (c^{CH_{4_i}} - \bar{c}^{CH_4})(q_i - \bar{q}) / \sqrt{\sum_{i=1}^{n} (c^{CH_{4_i}} - \bar{c}^{CH_4})^2 \sum_{i=1}^{n} (q_i - \bar{q})^2},$$

where $c^{CH_4} = (c^{CH_{4_1}}, ..., c^{CH_{4_n}})$, $q = (q_1, ..., q_n)$ are the sampling for mass fraction and heat flux at points by groups of holes; $\bar{c}^{CH_4}, \bar{q}$ are the average values of samples.

The study found a significant difference in the correlations between samples for groups of holes with various sizes. For holes with a small length-to-diameter ratio (l/d = 2; 3), there is hardly ever the correlation between the samples in terms of the heat flux and the mass fraction of methane after filling. Because of the depth of the shallow hole, the amount of heat flux is more influenced by the stirring of the mixture during the propagation of the flame front. But for the deep holes (l/d = 3; 4) a nearly linear dependence was established between the samples. Figure 5 shows a diagram of the distribution of samples for a group of holes with a diameter of 2 mm and a depth of 8 mm. For samples corresponding to groups of holes with l/d = 3; 4 Pearson's correlation coefficient was within 0.7622…0.8266 with a standard error of 0.0004.
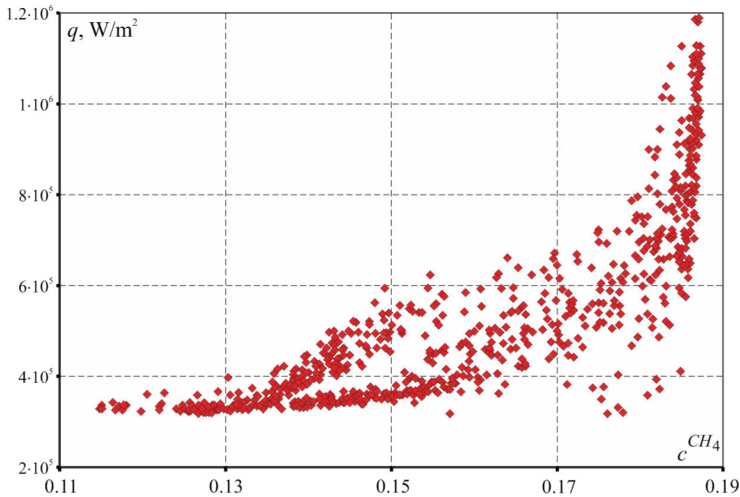
Fig. 5. Distribution of heat flux and mass fraction of methane for the group of holes with a diameter of 2 mm and length of 8 mm.

Thus, the fuel mixture composition is an important factor that should be taken into account for the processing of the part with deep holes by TEM method.

In addition, it was simulated the mixture formation process in the TEM chamber with located into it the GTE unit to check the correctness of the recommendations of the filling strategy choice. The GTE unit has a complex-shaped body with a lot of through, intersecting and blind holes (Fig. 6). Based on the GTE unit's operability the most important for it is the high-quality cleaning of the internal cavities, therefore, the main attention in assessing the degree of homogeneity of the fuel mixture was focused on the internal volumes. Therefore, when building the computational grid, the internal volume of the body was selected in a separate subarea.

The simulation was conducted for the described above two strategies: the sequential filling and the filling with the prepared mixture. As in previous experiments, it is observed considerable scatter of the values of methane mass fraction during the sequential filling. Herewith areas form with a mass fraction of methane below the ignition limit (Fig. 7a).
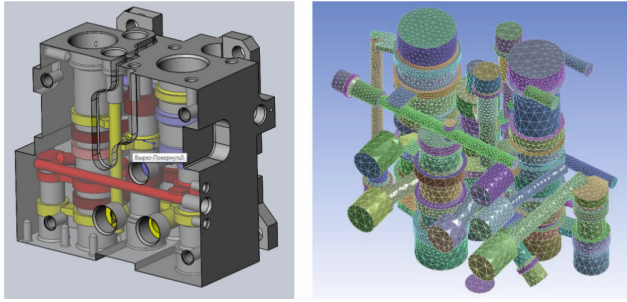
Fig. 6. Model of the GTE unit body and the computational grid for its internal volume.

When filling with prepared mixture, its composition in the internal volumes is almost homogeneous and is everywhere within the ignition (Fig. 7b).
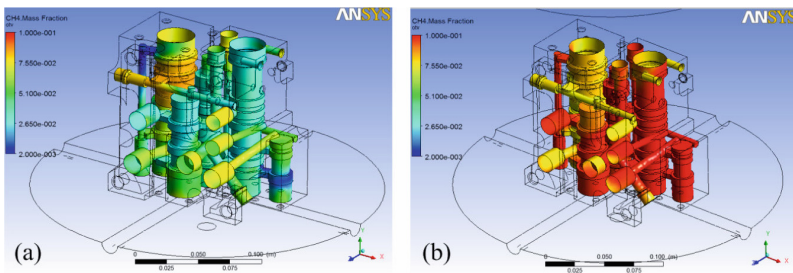
Fig. 7. The distribution of the methane mass fraction into internal cavities of the GTE unit body: (a) the sequential filling; (b) filling with the prepared mixture.

Studying the process of mixture formation estimates that the mixture quality, particularly its homogeneity, have to be assured for accurate complex-shaped parts processing by TEM method.

4   Conclusions

The heterogeneity of the fuel mixture has a significant effect on the distribution and magnitude of heat fluxes that occur on the inner surfaces of the parts cavities. To ensure the proper degree of the mixture homogeneity required for accurate TEM processing, it is preferable to fill the chamber with the prepared mixture. The setting of the mixture holding time in terms of ensuring its uniform composition may base on the results of modelling the formation of the mixture by mutual diffusion of components and mixing with a residual velocity of gases taking into account the influence of gravity to assess the possibility of stratification. In most practical cases, the holding time of the mixture should be set in the range of 0.8…1 s.

References

1. Schellekens, P., et al.: Design for precision: current status and trends. CIRP Ann. **47**(2), 557–586 (1998). https://doi.org/10.1016/S0007-8506(07)63243-0

2. Pavlenko, D., Dvirnyk, Y., Przysowa, R.: Advanced materials and technologies for compressor blades of small turbofan engines. Aerospace **8**(1), 1 (2021). https://doi.org/10.3390/aerospace8010001

3. Vambol, O., Kondratiev, A., Purhina, S., Shevtsova, M.: Determining the parameters for a 3D-printing process using the fused deposition modeling in order to manufacture an article with the required structural parameters. Eastern-European Journal of Enterprise Technologies **2**(1–110), 70–80 (2021). https://doi.org/10.15587/1729-4061.2021.227075

4. Petare, A.C., Jain, N.K.: A critical review of past research and advances in abrasive flow finishing process. The Int. J. Adva. Manuf. Technol. **97**(1–4), 741–782 (2018). https://doi.org/10.1007/s00170-018-1928-7

5. Fuchs, F.J.: Ultrasonic cleaning and washing of surfaces. In: Gallego-Juárez, J.A., Graff, K.F. (eds.) Power Ultrasonics: Applications of High-Intensity Ultrasound, pp. 577–609. Woodhead Publishing, Cambridge (2015). https://doi.org/10.1016/B978-1-78242-028-6.00019-3

6. Zhong, Z.-W.: Advanced polishing, grinding and finishing processes for various manufacturing applications: A review. Mater. Manuf. Processes **35**(12), 1279–1303 (2020). https://doi.org/10.1080/10426914.2020.1772481

7. Ruszaj, A., Gawlik, J., Skoczypiec, S.: Electrochemical machining – special equipment and applications in aircraft industry. Management and Production Engineering Review **7**(2), 34–41 (2016). https://doi.org/10.1515/mper-2016-0015

8. Khafizov, I.I., Nurullin, I.G.: Improving the quality of surfaces of products obtained by electroerosion treatment. IOP Conference Series: Materials Science and Engineering **915**(1), 012027 (2020). https://doi.org/10.1088/1757-899X/915/1/012027

9. Cerwenka, G., et al.: In-depth characterization of the scanner-based selective laser deburring process. J. Laser Appl. **30**(3), 032510 (2018). https://doi.org/10.2351/1.5040642

10. Korohodskyi, V., et al.: Determining the characteristics for the rational adjusting of an fuel-air mixture composition in a two-stroke engine with internal carburation. Eastern-European Journal of Enterprise Technologies **2**(5–104), 39–52 (2020). https://doi.org/10.15587/1729-4061.2020.200766

11. Plankovskyy, S., et al.: Simulation of surface heating for arbitrary shape's moving bodies/sources by using R-functions. Acta Polytechnica **56**(6), 472–477 (2016). https://doi.org/10.14311/AP.2016.56.0472

12. Gillespie, L.K.: Deburring and edge finishing handbook. Society of Manufacturing Engineers, Dearborn (1999)

13. Struckmann, J., Kieser, A.: Thermal Deburring. ATL Anlagentechnik Luhden GmbH (2020)

14. Fritz, A., et al.: Experimental analysis of thermal energy deburring process by design of experiment. In: Proceedings of the ASME 2012 International Mechanical Engineering Congress and Exposition, vol. 3, pp. 2035–2041. ASME, New York (2012). https://doi.org/10.1115/IMECE2012-88411

15. Jin, S.Y., Pramanik, A., Basak, A.K., Prakash, C., Shankar, S., Debnath, S.: Burr formation and its treatments—a review. The International Journal of Advanced Manufacturing Technology **107**(5–6), 2189–2210 (2020). https://doi.org/10.1007/s00170-020-05203-2

16. Sibanda, P.S., Carr, P., Ryan, M., Bigot, S.: State of the art in surface finish of metal additive manufactured parts. In: Jin, Y., Price, M. (eds.) Advances in Manufacturing Technology XXXIII, Advances in Transdisciplinary Engineering, vol. 9, pp. 221–225. IOS Press, Amsterdam (2019). https://doi.org/10.3233/ATDE190039

17. Lamikiz, A., Ukar, E., Tabernero, I., Martinez, S.: Thermal advanced machining processes. In: Davim, J.P. (eds.) Modern Machining Technology, pp. 335–372. Woodhead Publishing, Oxford (2011). https://doi.org/10.1533/9780857094940.335

18. Plankovskyy, S., et al.: Advanced thermal energy method for finishing precision parts. In: Gupta, K., Pramanik, A. (eds.) Advanced Machining and Finishing, pp. 527–575. Elsevier, Amsterdam (2021). https://doi.org/10.1016/B978-0-12-817452-4.00014-2

19. Plankovskyy, S., Shypul, O., Tsegelnyk, Y., Pankratov, A., Romanova, T.: Amplification of Heat Transfer by Shock Waves for Thermal Energy Method. In: Nechyporuk, M., Pavlikov, V., Kritskiy, D. (eds.) ICTM 2020. LNNS, vol. 188, pp. 577–587. Springer, Cham (2021). https://doi.org/10.1007/978-3-030-66717-7_49

20. Plankovskyy, S., et al.: Determination of detonable gas mixture heat fluxes at thermal deburring. Acta Polytechnica **59**(2), 162–169 (2019). https://doi.org/10.14311/AP.2019.59.0162

21. Romanova, T., et al.: Sparsest packing of two-dimensional objects. Int. J. Prod. Res. **59**(13), 3900–3915 (2021). https://doi.org/10.1080/00207543.2020.1755471

22. Romanova, T., et al.: Sparsest balanced packing of irregular 3D objects in a cylindrical container. Eur. J. Oper. Res. **291**(1), 84–100 (2021). https://doi.org/10.1016/j.ejor.2020.09.021

23. Plankovskyy, S., Shypul, O., Tsegelnyk, Y., Pankratov, A., Romanova, T., Litvinchev, I.: Circular Layout in Thermal Deburring. In: Shkarlet, S., Morozov, A., Palagin, A. (eds.) MODS 2020. AISC, vol. 1265, pp. 111–120. Springer, Cham (2021). https://doi.org/10.1007/978-3-030-58124-4_11

24. Arias-Zugasti, M., Garcia-Ybarra, P.L., Castillo, J.L.: Efficient calculation of multicomponent diffusion fluxes based on kinetic theory. Combust. Flame **163**, 540–556 (2016). https://doi.org/10.1016/j.combustflame.2015.10.033

25. Huang, H., et al.: Modeling and computation of turbulent slot jet impingement heat transfer using RANS method with special emphasis on the developed SST turbulence model. Int. J. Heat Mass Transf. **126**, 589–602 (2018). https://doi.org/10.1016/j.ijheatmasstransfer.2018.05.121

Structure and Wear-Resistance of Hardened Thin-Blade Knives with PVD Coating

Tamara Skoblo[1] , Svitlana Romaniuk[1,3(✉)] , Efim Belkin[1] , Igor Garkusha[2] ,
and Anton Taran[2]

[1] State Biotechnology University, 44, Alchevskih Street, Kharkiv 61002, Ukraine
`romaniuk.khntusg@gmail.com`
[2] Institute of Plasma Physics, National Science Center "Kharkov Institute of Physics and Technology", 1, Akademicheskaya St., Kharkiv 61108, Ukraine
[3] National Centre for Nuclear Research, 7, Andrzeja Soltana, 05-400 Otwock, Poland

Abstract. A new technological process for hardening thin-walled knives 0.64 mm thick with a cutting edge of 0.1 mm used in the confectionery industry is proposed. For their hardening, the ion-plasma method of applying a nanostructured TiN multilayer coating was used. Statistical studies of the operational stability of such a tool in industrial production during crushing nuts have been carried out. By analyzing the results obtained, it was found that their operational durability varies over a wide range from 10 to 210 shifts. At the same time, the surface hardening coating with a thickness of 3.3 μm does not completely wear out. The main reasons for the failure of such a tool in operation are the insufficient quality of the metal products and processed products, which contribute to pore and crack formation, intensification of diffusion processes and the formation of zones of inhomogeneous distribution of phase components. Using modern methods, structural changes that occur during operation and affect the wear resistance of a thin-walled tool hardened with a nanostructured TiN coating are studied. The proposed integrated approach to quality control of the cutting tool in operation made it possible to identify changes in structure formation, the level of emerging stresses and degradation of the metal by the anisotropy of properties. Timely quality control of the tool made it possible to prevent the use in operation of knives with a large number of defects in the structure or an increased level of residual stresses.

Keywords: Nanostructured coating · Thin-walled tool · Service life · Inhomogeneity · Diffusion of components · Defects

1 Introduction

The main condition for increasing the wear resistance of products is the quality and properties of their working surfaces. If in the field of traditional industries there are well-established, well-studied and substantiated methods for hardening such products in various industries, then with the development of science in mechanical engineering and electronics, new areas using nanotechnologies are attracting special attention [1, 2].

The operational stability of the tool can be improved by using certain types of processing that provide wear resistance [3, 4], durability [5], corrosion resistance [6], depending on the material and operating conditions. One of the promising methods of hardening is the technology of vacuum-arc ion-plasma coating deposition [7, 8]. In the production process, the most common methods of ion-plasma deposition are magnetron sputtering [9] and vacuum-arc deposition [10, 11]. The characteristics and properties of the hardened layer depend on the material and the method of its application to the working surface. Taking this into account, an attempt was made to strengthen such a tool with nanostructured coatings with a composition of CrN and WC [12]. The wear resistance of hardening knives increased only from 11 to 45 shifts, which did not significantly ensure the economic efficiency of this process due to the high cost of consumables. A cheaper nanostructured coating that provides high hardness is TiN [13]. However, the technological process of applying such a composition is accompanied by a higher temperature. This requires additional modern experimental research methods and the development of new theoretical approaches to determine effective coatings when hardening a thin-walled tool.

The existing variety of control methods makes it possible to conduct comparative studies and effectively apply them to solve certain previously unresolved problems. One of the methods of non-destructive testing, which makes it possible to detect defects and determine the properties of a thin surface layer, is testing using image process [14]. Since most materials have a heterogeneous structure, appropriate modeling methods are needed [15]. For a more detailed study of the structure of materials, research is carried out at the micro- and nano-level. For simply inhomogeneous materials with a regular lattice, a general concept of multiscale modeling is used, called the periodic unit cell [16]. In the case of heterogeneous materials with a random microstructure, it is possible to use the optical-mathematical method to reveal the variability of the phase composition [17]. The fractal approach [18] is successfully used for the theoretical analysis of the influence of the structure on the physical and mechanical properties, which from a physical point of view describes the compactness of filling the space with the object of study.

Directly in the hardening of thin-walled tools in mechanical engineering, the number of developments is very limited, which is associated with differences in certain operating conditions, as well as with a more complex individual approach to improve consumer properties, the need for multi-stage scientific research to achieve effective properties and structure of the metal. An unresolved and urgent task is to conduct comprehensive studies on the timely detection of the anisotropy of the properties of thin-walled knives associated with the presence of a large number of defects in the structure or an increased level of residual stresses, with an assessment of the formed heterogeneity of the structure formation of the hardened working layer.

The aim of this work is to study the structural changes that occur during operation and affect the wear resistance of a thin-walled tool hardened with a nanostructured TiN coating.

2 Methodology

Statistical studies were carried out on 50 thin-walled knives installed on Model CD-A Dicer equipment, Urschel Laboratories, Incorporated. To increase their operational

stability, hardening with a TiN coating was carried out. Coating was carried out on a Bulat-6 installation with the manufacture of special devices developed at the Institute of Plasma Physics of the NSC KIPT (Kharkov). The TiN coating was applied by the vacuum-arc method using an RF-discharge. To prevent overheating of the thin-walled tool, pauses with multiple time parameters for the formation of each layer were used. Total time TiN coating deposition was 15 min at the cyclic mode of sedimentation (5 min deposition with 3 min pauses (cycle 3)). The quality of the hardened knives and their wear resistance were evaluated under production conditions.

The paper proposes a new integrated approach to experimental and theoretical studies using modern and new methods and developments for a detailed study of structure formation and assessment of tool quality. To identify the degree of defectiveness of the tool with an assessment of the stress state and anisotropy coefficient K, a patented approach [17] was used using the magnetic method of non-destructive testing (according to the coercive force Hc). The areas of the cutting tool (Fig. 1) were magnetized with a transducer to magnetic saturation, and then demagnetized and a measured coercive force was determined from the measured current compensation of the residual induction in the closed circuit.
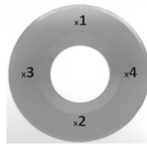
Fig. 1. Cutting tool with measuring zones

With the help of EDS and X-ray diffraction analyzes, structure formation was experimentally investigated, changes in the elemental composition of TiN hardening coatings were determined, and formed defects were revealed during operation.

To carry out theoretical studies, we used new developed approaches for mathematical description of the degree of inhomogeneity of the surface working layer of the tool. Such studies are based on a statistical analysis of the pixels of digitized metallographic images obtained on optical (XDS-3 MET) and scanning (JEOL JSM-6390LV) microscopes. Each pixel of the structure image has a specific value from 0 to 255, corresponding to a conditional color (from black to white). By their distribution and ratio, the processes of structure formation of materials are revealed, such as changes in density, inhomogeneities, diffusion of chemical components, etc. Taking into account the objectives of the research, a large number of dependencies have been developed for schemes consisting of various combinations of pixels. In this research work, the index of the degree of inhomogeneity of the TiN nanostructured coating was theoretically estimated from the anisotropy of the distribution of components. The studies were carried out according to dependence (1) with an assessment in the horizontal and vertical directions.

$$H = \frac{n \prod_{i=1}^{n} p_i}{\sum p_i^n} \tag{1}$$

where p_i is the variability index (the probability of color matching in the selected interval), i is the pixel number of the structure image, n is the number of dots (pixels).

A comparative analysis was carried out using a mathematical method using a different number of dots (pixels) of the structure image and the degree of heterogeneity of different TiN coverage zones was evaluated. In the process of statistical analysis, we considered images of the structure obtained with an optical microscope at magnifications of 200 and 500 times, hardened by the coating of the tool after operation. To select an effective interval for the analysis of the inhomogeneity of the structure formation of coatings, which makes it possible to obtain the most stable results, we studied a different number of points. Based on the identified local deviations in the degree of heterogeneity of structure formation, intervals corresponding to 2,3,4,5,6 and 7 points are proposed. A similar calculation was made for 10, 20, 30 and 35, 40 points of structure analysis with the determination of its heterogeneity. To detect zones with minimum and maximum inhomogeneity, the obtained values (100%) were distributed over 19 intervals with a definition from the largest, which was 1/19 of the share, to the minimum anisotropy index - 19/19 (i.e. K $\rightarrow$ 1.0).

3   Results

To assess the structural state of knives and damage after operation, at the first stage, a non-destructive magnetic method was used by coercive force and visual assessment of the friction surface, as well as optical microscopy.

The state of the knives in this case was judged by four estimates of its base (corresponding to the areas of origin and development of cracks), which were located in zones equidistant from each other. Table 1 shows the results of evaluating the coercive force and operational durability of thin-walled circular knives (50 pcs) after various periods of operation.

The performed analysis of the friction surface showed a large spread in the indications of the operational durability of knives (from 10 to 210 shifts). The main causes of failures during visual inspection of such knives are: damage (were identified in tool No. 1, 4,7,9,10,12,14–16,22,28,30,31,33,34,42), cracks (in knives no. Cutting edge (No. 21). Almost all tested knives retained the hardening coating. The exception is a knife that has served 210 shifts, which did not have a coating on the cutting edge. However, there were no visible defects on this instrument.

The revealed damage of knives is largely related to the quality of the processed products (with increased hardness, moisture content of nuts and the presence of abrasive - solid inclusions in the raw material). During the operation of hardened knives, a violation of flatness was detected only in one case. Of the entire tested batch, only 10 knives were taken out of service of the set without damage to the main part (only the blade) and they served a different number of shifts 27–33, 41–51, 210, which confirms one of the main reasons for the knives to go out of service, noted above.

The assessment of the state of the knives after operation was carried out in the same areas as the visual analysis, using the magnetic method according to the coercive force Hc, based on the available experience [7]. It was planned to identify degradation zones in the metal, as well as local stresses in the knives after operation. The results

Table 1. Indicators of operational durability and the level of coercive force of knives hardened with a nanostructured TiN multilayer coating

Knife designation	Durability indicators, shifts	Hc, A/cm				Knife designation	Durability indicators,shifts	Hc, A/cm			
		1	2	3	4			1	2	3	4
1	10	27.4	20.3	19.5	20.7	26	34	19.5	19.5	20.6	21.1
2	10	19.2	19.1	23.7	30.2	27	36	21.9	21.2	19.6	20.0
3	10	20.2	19.4	20.6	20.6	28	36	41.1	19.7	18.8	20.4
4	11	40.1	20.2	19.2	20.2	29	36	18.9	19.8	22.0	22.2
5	11	23.8	20.1	21.0	22.1	30	36	24.1	18.9	20.6	19.9
6	11	27.1	19.5	20.4	19.9	31	37	20.8	19.7	23.3	22.0
7	11	40.9	19.8	19.6	20.3	32	37	21.1	19.1	20.0	24.0
8	20	23.4	20.2	21.2	20.0	33	37	29.8	18.6	18.8	18.5
9	20	40.5	18.8	19.3	18.6	34	38	41.6	19.7	23.1	19.3
10	20	41.8	19.0	18.3	18.7	35	40	23.0	20.5	23.5	19.5
11	20	24.0	19.6	23.9	20.3	36	40	25.4	20.2	21.5	21.6
12	20	37.0	19.3	18.5	18.5	37	40	21.6	20.3	21.8	21.5
13	20	19.8	19.9	20.3	21.2	38	41	40.8	21.5	21.7	21.0
14	20	39.2	20.0	19.4	20.5	39	46	25.5	20.8	20.0	22.5
15	20	21.0	19.1	27.1	21.2	40	51	20.8	21.2	20.8	20.1
16	20	24.4	20.5	19.5	20.7	41	55	20.2	19.7	19.3	18.6
17	23	20.7	20.6	21.9	22.4	42	55	33.7	19.1	18.5	18.7
18	23	21.4	19.4	21.4	21.0	43	55	22.8	19.9	21.2	19.6
19	23	27.4	20.9	22.2	22.1	44	59	23.5	21.1	20.2	21.1
20	23	20.9	19.9	20.3	20.0	45	59	18.5	21.0	23.8	22.4
21	23	24.2	23.0	24.4	22.7	46	59	23.4	19.4	19.8	19.8
22	23	21.5	17.5	16.9	19.5	47	59	23.9	20.8	20.7	19.6
23	23	20.5	20.2	21.5	27.6	48	59	22.5	20.8	19.4	19.8
24	30	20.9	20.6	21.0	19.9	49	59	21.7	20.1	24.6	19.8
25	33	32.6	18.9	18.5	19.3	50	210	18.9	19.4	20.8	19.8

of measurements of tested knives in production are shown in Table 1. It can be seen from the obtained data that the readings of the coercive force on such knives vary over a wide range from 16.9 to 41.8 A/cm. At the same time, in hotel knives, the difference in readings reached 50%. Knives, on which, after operation, visualization did not reveal defects (damage, local deformations) differed in closer coercive force readings (with anisotropy coefficients $K \rightarrow 1.0$), which, on average, varied from 18.8 to 21.1 A / cm. The difference did not exceed 2.3A/cm and the proportion of such knives was 36%.

Lower resistance of knives was revealed at indicators $K < 1.0$ or $K > 1.1$. In the presence of defects ($K > 1.2$), the scatter of readings varied over a wider range from 16.9 to 41.1 A/cm, and the average deviations of the values for these measurements

amounted to a significantly larger scatter of readings up to 24.4 A/cm. Based on the results obtained, it can be concluded that only this characteristic cannot objectively separate the degradation of the knife structure that occurs during operation, as well as the presence of damage and local deformations in them.

To clarify the nature of the destruction and degradation of the coating metal, we additionally used an integrated approach in research, according to the methods of optical and electron microscopy, thermionic emission, and the optical-mathematical description of structural changes on the friction surface.

Therefore, at the second stage, images of the structure of the friction surface of tools that differed in service life were analyzed comparatively.

From a comparative analysis it follows that all the options considered are characterized by the structurization of the friction surface, and to a greater extent it manifests itself in a knife that has worked 10 shifts and to a lesser extent for - 210, which may be the result of significant wear of the latter.

In all analyzed cases, with additional computer magnification, very small cracks (tears) are visible, which form both along and across the friction bands, and they are especially clearly visible on light bands. Such damage (Fig. 2,a,b) is more typical for knives, which are distinguished by a high level of coercive force index up to 30–40.8 A/cm compared to the rest 16.9–24 A/cm. Based on this, it can be concluded that a significant increase in local stresses in the knives contributes to the formation of microtears and damage.

a   b   c
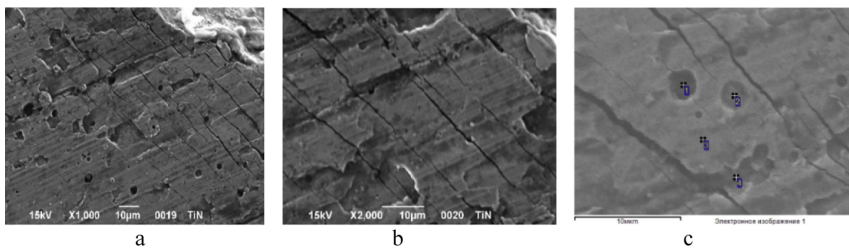
Fig. 2. Microcracks (a, b) in the zone of fatigue damage and Defects on the hardened friction surface of the knife after 10 shifts of operation (c)

Local structural changes and the formation of defects on the friction surface were determined comparatively after 10 and 210 shifts in operation. Cracks, tears and pores were found in knives with lower service life (Fig. 2,c).

In the damaged areas, there is an increased concentration of carbon up to 16.64% (Table 2), which diffuses from the base metal of the knife, and oxygen up to 31.22%, and the appearance of a number of components in a small amount is determined by the deposition of processed raw materials.

The pores contain different proportions of titanium and nitrogen, which indicates that they belong to the droplet phase. Previous studies have shown that, along the boundaries, the droplet phase containing titanium is saturated with nitrogen in the form of a TiN film covering it, which, under local deformations under friction conditions, is partially (along

the boundaries) destroyed and increases the accumulation of oxygen, carbon and other components in such pores.

Table 2. EDS analysis of the working surface of a hardened knife after 10 shifts of operation (measurement zones, see Fig. 2,c)

Spectrum	C	N	O	Al	Si	Ca	Ti	Fe	Total
1	16.64	5.16	31.22	0.17	0.28	3.50	41.96	1.07	100.00
2	8.85	24.84	11.14				54.11	1.06	100.00
3	4.85	31.85					62.40	0.90	100.00
4	11.33	16.55	11.37		0.19		60.56		100.00

Due to the fact that such a droplet phase is destroyed to varying degrees, the concentration of components in these zones can also change significantly.

It has been established by thermionic emission that the main components of the coating N and Ti are absent in the damage zones of the knife (microcracks) (Fig. 3). This fact can be associated not only with the zone of development of fatigue stresses (according to the nature of their location), but also with significant wear of the thickness of the hardened layer under operating conditions.
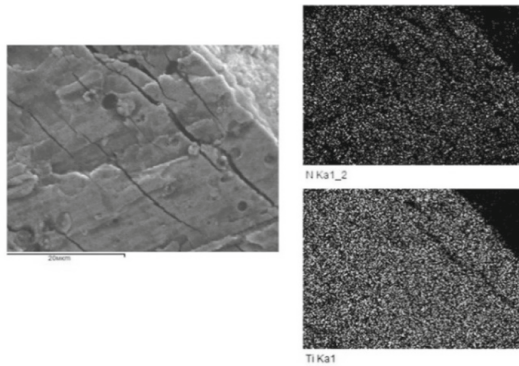
Fig. 3. Distribution of components on the working surface of a hardened knife after 10 shifts of operation. Thermionic emission

In the knife, which was operated for 210 shifts, the defects listed above were not detected, however, the zones of tension (energy release) and the drop phase are more clearly manifested, which do not contain nitrogen and are characterized by a reduced proportion of titanium in the pores and are significantly saturated with carbon, which may indicate their different degree of heterogeneity preceding destruction. According to the revealed intensive diffusion of carbon, the degree of inhomogeneous distribution of nitrogen and titanium (Fig. 4), one can judge not only the degree of degradation of the working surface, but also its significant wear.

The assessment of the degree of heterogeneity of the structure of the hardened layer, which significantly affects the degradation phenomena during operation, was studied on the basis of the developed integrated approach that combined experimental and theoretical studies. Correlations were established between the degree of structural heterogeneity and the durability of a tool hardened with a TiN coating, and the influence of the stability of its components during operation was determined to correct the parameters of the deposition process.
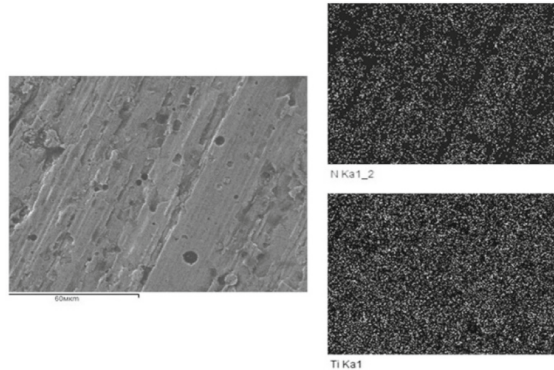
Fig. 4. Distribution of components on the working surface of a hardened knife after 210 shifts of operation. Thermionic emission

As a result of the calculation of regression dependences of coating wear on one, two, three and four parameters characterizing the degree of structure inhomogeneity for 2, 3, 4, 5, 6 and 7 points (pixels) of images, it was found that the correlation coefficients for each parameter of structure inhomogeneity are not exceeded 0.50. With an increase in the number of parameters under consideration, an increase in the correlation coefficients up to 0.777 is observed. With an increase in the number of analyzed points (10, 20, 30) during statistical processing of metallographic images of the TiN reinforcing coating, the correlation coefficient was 0.816. A further increase in the number of considered points (30, 40) led to a decrease in the correlation coefficient. Thus, the most reliable estimates for determining the degree of durability of a tool hardened with a TiN coating are achieved according to an analysis of 10–30 pixels. As a result of the analysis of the obtained dependencies, taking into account the parameters characterizing different degrees of inhomogeneity, it was found that the maximum contribution to the tool life is made by the structure anisotropy coefficient ($K \to 1.0$).

The revealed degree of heterogeneity of the structure of the TiN nanocoating on the working surface of the hardened cutting tool after 10 and 210 operation shifts (when analyzed by 10–30 pixels) is qualitatively shown in Fig. 5.

In the knife, which was taken out of service after 10 shifts of use, it was distinguished by maximum inhomogeneity intervals from 2/19 to 12/19, which is associated with intensive structuring of the friction surface, a clear identification of compression and rarefaction bands. In the intervals 13/19–19/19, structurization is insignificantly expressed and differs in a more uniform distribution of phases (Fig. 5a).

An analysis of the degree of knife heterogeneity after 210 shifts of operation showed that it is significantly higher in the intervals 2/19–7/19, and in the rest it manifests itself to a lesser extent, which can be explained by more significant wear of the hardened working surface (Fig. 5b).

a   b
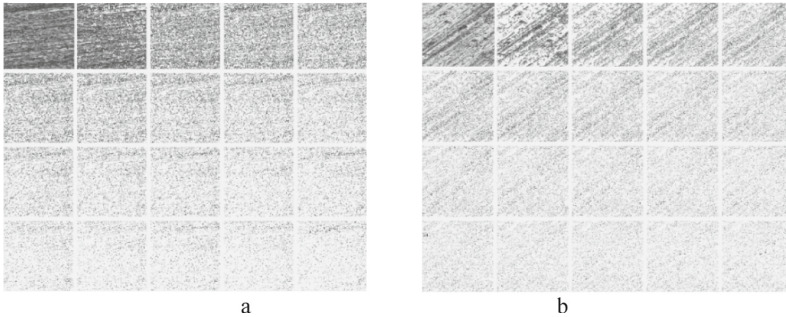
Fig. 5. Inhomogeneity of the distribution of phases on the working surface of the hardened knife after 10 (a) and 210 (b) shifts of operation. The first photo on the left is the original photo, and then the analyzed intervals for the inhomogeneity of the phase distribution are shown in the same order in the first, second, third and fourth rows

The developed approach for identifying the degree of heterogeneity during hardening and operation makes it possible to reliably evaluate this indicator in coatings and explain significant deviations in physical and mechanical properties, non-destructive testing indicators during the entire life of the tool.

4   Conclusion

Fifty knives with nanostructured TiN coating were investigated under operation conditions. TiN hardened coating applied onto one side of the knife increased the tool durability by 210 times. It was found that hardened knives with multilayer TiN coatings provided a self-sharpening effect. The deposition process is economically viable, and it prevents tools' failure and cracking.

Various techniques including the methods of nondestructive quality testing, optical and scanning electron microscopy, as well as the optical-mathematical method of describing structural changes (degree of phase nonuniformity) during durability friction have been applied.

References

1. Yuan, Z., et al.: Damage evolution behavior of TiN/Ti multilayer coatings under high-speed impact conditions. Surf. Coat. Technol. **426**, 127807 (2021)
2. Müller, K., et al.: Review on the processing and properties of polymer nanocomposites and nanocoatings and their applications in the packaging. Automotive and Solar Energy Fields. Nanomaterials **7**(74), 1–47 (2017)

3. Lepicka, M., et al.: Effect of mechanical properties of substrate and coating on wear performance of TiN-or DLC-coated 316LVM stainless steel. Wear **38**, 262–270 (2017)
4. Uddin, G., et al.: Experimental study of tribological and mechanical properties of TiN coating on AISI 52100 bearing steel. Adv. Mech. Eng. **10**(9), 1–10 (2018)
5. Skoblo, T., et al.: Study of degradation mechanism of metal-cutting tools and their hardening by ZrN PVD coatings. Problems of atomic science and technology **6**(118), 300–303 (2018)
6. Lou, J., et al.: Comparative investigation on corrosion resistance of stainless steels coated with titanium nitride, nitrogen titanium carbide and titanium-diamond-like carbon films. Coatings **11**, 1543 (2021)
7. Geyao, L., Yang, D., Wanglin, C., Chenngyoung, W.: Development and application of physical vapor deposited coatings for medical devices: a review. Procedia CIRP **89**, 250–262 (2020)
8. Maksakova, O., et al.: The influence of deposition conditions and bilayer thickness on physical-mechanical properties of CA-PVD multilayer ZrN/CrN coatings. Mater. Charact. **140**, 189–196 (2018)
9. Chelvanathan, P., et al.: Effects of RF magnetron sputtering deposition process parameters on the properties of molybdenum thin films. Thin Solid Films **638**, 213–219 (2017)
10. Kuprin, A., et al.: Deposition of TiN-based coatings using vacuum arc plasma in increased negative substrate bias voltage. Problems of atomic science and technology **5**(123), 154–160 (2019)
11. Romashchenko, E., Girka, I., Bizyukov, A.: Effect of background gas pressure on macroparticles in cathodic arc plasma deposition. IEEE Trans. Plasma Sci. **47**, 1494–1499 (2019)
12. Skoblo, T., A. et al.: Surface morphology and mechanical properties of vacuum-arc evaporated CrN and TiN coatings on cutting tool. Journal of Advanced Microscopy Research. **13**(4), 477–481 (2018)
13. Andreev, A., Kostyk, G., Sysoiev, I., Minaiev, N.: Properties of composite vacuum-arc coatings of the TiN-Ti/TiON structure. Problems of atomic science and technology **1**(113), 127–133 (2018)
14. Perumal, P., et al.: Investigation of TiN coating uniformity and its corrosion behaviour using image process. Materials Research Express **6**(4), 046411 (2019)
15. Sereda, B., Belokon, Y., Sereda, D., Kruglyak, I.: Modeling of processes for the production of bassed TiAl and NiAl in the conditions of SHS for aerospace applications. Mater. Sci. Technol. **1**, 137–142 (2019)
16. Zrůbeka, L., et al.: Image synthesis of metal foam micro-structure with the use of wang tiles. Acta Polytechnica CTU Proceedings **15**, 142–147 (2018)
17. Skoblo, T., et al.: Strengthening method for thin-walled knives with multi-layer nanocoatings and quality assessment by non-destructive method. J. Adv. Microsc. Res. **13**(3), 333–338 (2018)
18. Vakhrusheva, V., Volchuk, V., Hruzin, N., Tiutieriev, I.: Fractal model of estimating quality of cold worked fuel cladding tubes. Problems of Atomic Science and Technology **135**(5), 57–63 (2021)

Modeling of Degradation Processes of Cast Iron Carbide Phase of Mill Rolls at Operation

Tamara Skoblo ⓘ, Oksana Klochko(✉) ⓘ, Oleg Trishevskij ⓘ, Efim Belkin ⓘ, and Evgeniya Deryabkina ⓘ

State Biotechnological University, 44, Alchevskih Street, Kharkiv 61002, Ukraine
`klochko.hntysh@gmail.com`

Abstract. In metallurgy, chromium-nickel cast iron is used in making the working layers of double-layer mill rolls. The main distinctive feature of chromium-nickel cast iron is the presence of large inclusions of carbide phase in its structure. This characteristic determines the high ruggedness of the contact surface touching hot rolled metal, and ensures wear resistance of the working tool. Operational degradation and wear of the products surfaces leads to destruction of the carbides crystalline structures; the latter contributes to reduce in hardness and quality of the working layer. The aim of our present study is to investigate the defect conditions in chromium-nickel cast iron and their influence on the development of degradation processes at high temperatures and at presence of the local deformations. We evaluate damageability and degradation of cast iron using the method of optical-mathematical analysis of microstructure images, which comprises scientific novelty of the present work. These values are estimated via modeling the diffusion processes and variability of the dislocation structure in the largest inclusions of the Me_3C carbide phase. Based on the results obtained and to underline the practical value of our study, we propose a number of technological solutions that help hinder and eliminate the degradation phenomena described above, thus stabilizing the carbide phase properties and hardening the mill rolls.

Keywords: Chromium-nickel cast iron · Carbide phase degradation · Diffusion · Dislocation structure · Phase composition variability

1 Introduction

Chromium-nickel and high-chromium cast irons are widely used in metallurgy in production of sheet and broadband mill rolls [1]. The main distinctive feature of chromium-nickel cast iron is the presence of large inclusions of carbide phase in its structure [2]; this characteristic determines the ruggedness of the contact surface [3] and ensures wear resistance of the working tool [4]. Degradation, wear and destruction of the carbide phase result in the decrease of hardness and quality of the working layer [5, 6], which leads to necessity of the mill roll to be reground. At the same time, the number of regrinds is quite limited since the alloyed cast irons are present only in the working layers produced via centrifugal casting, while the core, roll necks and wobblers are made by batch casting

of gray cast iron. Such producing technology of the rolling tools occurs to be the most effective, since it excludes collar chipping and neck breakage, while also possessing a number of disadvantages (on instance, thin and patchy working layer at both upper and lower parts of the roller body which may occur when casting the rolls at a vertical centrifugal machine, especially for mill rolls with 3000 mm and 3600 mm maximum width of flat product) [7].

In recent years, such cast iron has also been used for the working layer when casting rolls with cast streams by the centrifugal method and insert rings. This provides uniform hardness and wear resistance along the perimeter of the entire caliber [1].

Below, we conduct a detailed analysis of the nucleation of defects and their influence both on the onset of degradation processes development at high temperatures and local deformations in chromium-nickel cast iron. The damageability and degradation of such cast iron has been estimated using data on the diffusion processes progressing and variability of the dislocation structures situated inside the largest inclusions of the carbide phase. Influence of ordering on the formation of new phases (subgrains and walls) and their interactions has been analyzed as well. Although dislocation structure has been earlier identified in the carbide phase [8, 9], the experimental evaluation of its role in diffusion processes became possible only now on account of an optical-mathematical method for structural changes evaluation first described in [10, 11].

The aim of this study is to reveal the role of variability of the dislocation structure when exposed to deformation and heat on the development of diffusion processes leading to destabilization of the carbide phase and, hence, formation of new phases.

2 Methodology

The relative rate of sublimation of various structural components of multiphase and multicomponent alloys during vacuum etching is hardly discussed in literature. In this regard, empirical approach has been used for revealing the modes of vacuum etching. The latter allows one to identify dislocations along the pits at a range of temperatures and deformations values [12], thus ensuring the transfer of matter through gaseous medium. In the process of vacuum etching, both surface and volume diffusions occur, as well as selective sublimation of atoms which contribute to a certain surface topography [13]. Depending on the processing parameters, state of the sample surface and the phase type, one of the above factors may become of the major importance.

In order to identify the fine structure of the carbide phase of chromium-nickel cast iron, the parameters inside the chamber have been set to 13.3×10^{-3} Pa at 200 °C–600 °C (both parameters correspond to operating conditions of the rolls), which are optimal for residual pressure and local deformation. The processing time depended on the chemical composition of the material and the structural changes identified.

Chromium-nickel cast iron blocks (1.8% Cr and 4.2% Ni, 30 × 40 × 80 mm) with rigidly fixed ends have been used as research samples. Heating has been performed in the middle of the sample. In this zone, stresses and local deformation (occurring due to difference in values of linear expansion at the interface between the heated and cold parts) have been observed during different etching periods via an increase in the density of dislocations, their mutual interactions and slip.

The issues related to the influence of defects on the metal quality are a subject of many studies. Some of them are dedicated to identification of non-metallic inclusions with the help of standardized mathematical approaches (e.g., contour-structural color shades method [14, 15]).

In [16], proportions of ferrite and pearlite, as well as the sizes of non-metallic inclusions [17] have been determined via identified conventional colors of the metallographic images, using a specially developed computer software. In [18], authors present mathematical models for both quality control of the lattice curvature formation inside a degradation structure and estimation of the fatigue processes development.

Since the above approaches are aimed at solving some of the specific problems, they are not designed for explaining the causes and phenomena associated with the variability of phase and chemical compositions that take place during development of the diffusion processes. The latter occur over the operation of understable carbide phases of products under high temperatures and deformations.

Below, we present our results of both experimental and theoretical modeling, and evaluation of degradation phenomena in the carbide phase, that determine the operating durability of rolls. We here use a special approach that allows one outline the dislocation structure variability and identify the carbide phase degradation [19].

Images of the micro structures have been obtained using JEOL JSM-6390LV scanning electron microscope (SEM) in the reflected electron (BSE) mode. Data analysis has been carried out via a method of optical-structural machine analysis, which determines statistical characteristics of a micro structure from distribution and density of the pixels in an image. Each pixel coordinate of a digital image is being assigned to a certain value, which corresponds to a conventional color (hereinafter simply a color). An approach of the discussed method is based on the analysis of structure formation processes (energy dissipation, diffusion transfer, density change) via hydrodynamic analogies, which characterize the phase variability [20]. An entire range obtained via digital processing (0–255 gray tones) is divided into 16 discrete ranges of grey undertones [19, 21]: 0 corresponds to graphite, 1–9 correspond to ferrite (values vary by the carbon saturation of defects, in increasing order), 10 corresponds to bainite, and 11–15 are carbides MeC, Me_xC_y and Me_3C, respectively. The phase variability has been estimated using images of microstructures in the.pgm digital format. Each image has been divided into 3 × 3 pixel fragments.

The emergence of dislocations and their local variability have been determined from local heterogeneity in the carbide phase. Function of the energy dissipation power M and stress function S has been used as criteria of diffusion processes, changes in the dislocation structure and density:

$$M = divC(x, y) \cdot \Delta C(x, y), \tag{1}$$

$$S = divC(x, y) - \Delta C(x, y) \tag{2}$$

where $divC(x, y)$ is the divergence; $\Delta C(x, y)$ is the Laplacian; $C(x, y)$ is the function of pixel coordinates of a metallographic image, x and y are pixel coordinates. In the finite-difference representation, $C(x, y)$ s a matrix $C_{i,j}$:

$$C_{i,j} = \begin{pmatrix} c_{i-1,j-1} & c_{i-1,j} & c_{i-1,j+1} \\ c_{i,j-1} & c_{i,j} & c_{i,j+1} \\ c_{i+1,j-1} & c_{i+1,j} & c_{i+1,j+1} \end{pmatrix} \tag{3}$$

where pixel is taken as a coordinate relative to the central element; $c_{i,j}$ is a color (i and j denote rows and columns, respectively).

$C_{i,j}$ matrix has been processed via sequential scanning of each pixel as a central element of a given fragment. As described in [17], variability of the dislocation structure phase composition at a specific position of a selected image fragment corresponds to the ratio of the number of coincidences of the central pixel color with the colors of the surrounding pixels to the total number of all pixels inside the considered fragment.

3   Results

Analysis of the collected data shows that defects in the crystal structure are the main contributors to development of an instability in the carbide phase structure of chromium-nickel cast iron. Diffusion of components is associated with nucleation, interaction and mobility of such defects. Development of local inhomogeneity in carbide phase during operation has also been noted.

Degradation process is limited to local changes in the distribution of components and phases with a significant structural perfection provided.
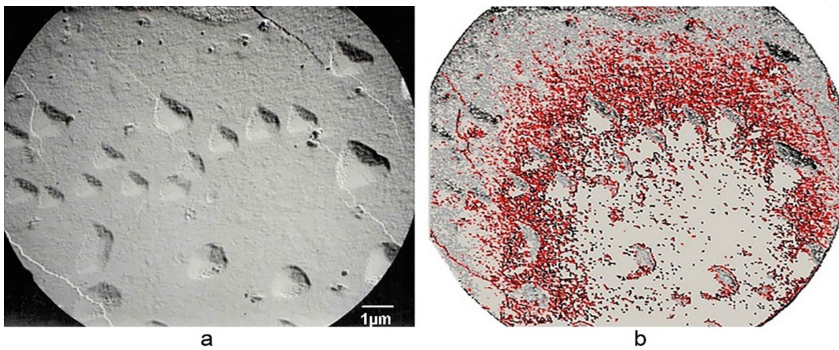
Fig. 1. Local deformation at the boundary of the polygonal dislocation wall with new defects, where (a) SEM image of the dislocation wall, ×10000; (b) density of the new defects around the dislocation wall (shown in red), from the stress function S.

At the initial stages of degradation phenomena, we note the formation of a sub-structure in the carbide phase in the form of dislocation walls. Subsequently, these substructures become concentrators of local stresses, and, hence, some of new defects appear around them (Fig. 1). There is a variety of phase combinations that are already present at this time: ferrite saturated with carbon (colors 8 and 9), bainite (up to 1.3%, color 10), MeC and Me_xC_y carbides (1.35%, colors 11 and 12). No movement of defects is noted around the dislocation walls at this stage (Fig. 1).

In case of the defects mobility increase, the intensity of diffusion processes also rises significantly. This process is being accompanied by emergence of new phases inside the deformation bands of defects; interaction between defects appears as well. A more intense phase emergence is observed inside the deformation bands, associated with jump-like behavior of local deformation emergence, which characterizes the advancement of defects. New point defects appearing both inside deformation bands and at their boundaries are a good evidence of the jump-like nature of the above process (Fig. 2). Below, we analyze such structure using an optical-mathematical method through stress function and functions of energy dissipation power (Fig. 2, (b) and (c)).
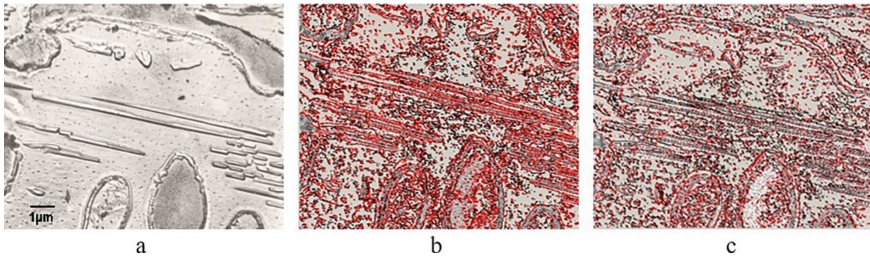
Fig. 2. Analysis of structural changes in chromium-nickel cast iron in dislocation glide: (a) SEM photograph of the micro structure, ×10000, (b) estimation via the stress function S and (c) estimation via the energy dissipation function M.

Data visualization and analysis reveals a noticeable decrease of stresses due to the dislocation glide: as seen in Fig. 2, the number of nonzero values of the functions decreases, including those that exceed a threshold value (255, shown in red).

For a more detailed analysis of the formation phases in the same SEM image and according to the described method, we have estimated the quantitative ratio of phases to their interaction (Fig. 3, Table 1). As it occurs, the identified ferrite phases do not exceed 4.63% in total. They are released in the result of mutual interaction, i.e., interaction takes place between the phases with different degree of carbon saturation (combinations of color intervals 7, 8; and 8, 9; and 7, 8, 9).

At the same time, we have identified interactions between carbon-saturated ferrite (color 9) and bainite (color 10), as well as between ferrite, bainite, and non-stoichiometric carbides (colors 11 and 12), with total share of 7.85%. A particularly strong change in the initial carbide phase composition has been observed during exposure to temperature and stresses: a significant amount of carbides of nonstoichiometric composition (up to 40.5%) with colors 12, 13, and 14 appear under such conditions. Separately for carbides of colors 13 and 14, their share has reached 5.07% (or even 23.51% if interconnection with Me_3C is present).
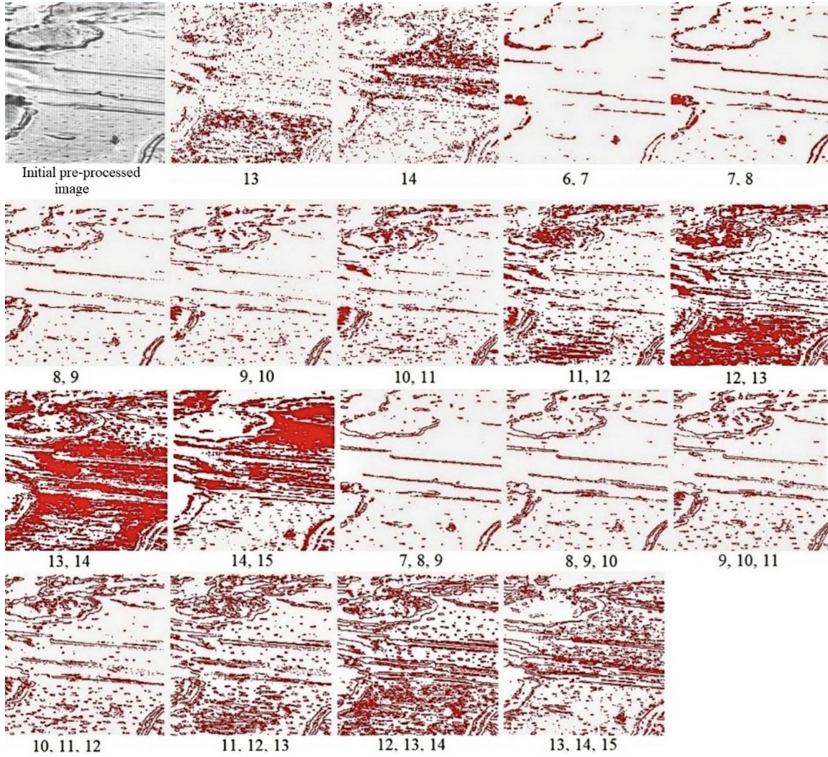
Fig. 3. Characteristics of the qualitative and quantitative ratio of phases at carbide phase degradation, $\times 10000$

There is a possibility of occurrence of the stress relieving processes in dislocation glide and interaction. To establish this, we compare the assessments of the revealed structural changes obtained from structure analysis with the optical-mathematical method (see Fig. 2). We show that the process of energy dissipation during glide and interaction of dislocations takes place, but its role is significantly reduced due to the appearance of new defects and cementite degradation within glide bands and near their boundaries, which causes additional stresses.

Table 1. Phase formation as a result of carbide phase degradation

Combinations of the intervals of conditional colors

Variant No	Identified combinations					% of cases	Variant No	Identified combinations					% of cases
1	13	0	0	0	0	1,83	10	13	14	0	0	0	22,84
2	14	0	0	0	0	3,25	11	14	15	0	0	0	20,47
3	6	7	0	0	0	1,51	12	7	8	9	0	0	1,03
4	7	8	0	0	0	2,02	13	8	9	10	0	0	1,19
5	8	9	0	0	0	1,58	14	9	10	11	0	0	1,45
6	9	10	0	0	0	1,74	15	10	11	12	0	0	1,98
7	10	11	0	0	0	2,68	16	11	12	13	0	0	3,117
8	11	12	0	0	0	5,57	17	12	13	14	0	0	4,267
9	12	13	0	0	0	13,38	18	13	14	15	0	0	3,042

4 Conclusion

Analysis of the degradation processes development in heating and local deformation shows a substantial destabilization of Me_3C carbide phase. Degradation phenomena in the carbide phase are determined by development of defects in the crystal structure and substructure, increase in the dislocations density, their interaction and glide. Such processes are accompanied by local deformation, diffusion of carbon and iron, formation of new phase types and their interaction, as well as energy dissipation.

At the same time, to control the processes of inhibition or exclusion of such degradation phenomena, new technological solutions are required for the production and hardening of mill rolls that would stabilize the carbide phase properties. Additional alloying and modification of metal can have a positive effect, providing crushing of the carbide phase, increasing the hardness with a sufficient total fraction of this phase, as well as adjusting the cobbing parameters and the cooling system of the operation at the mill.

References

1. Kiss, I.: Cast iron rolls – an overview on the proper hardness assured by the manufacturing process. Tech. J. **13**(2), 92–99 (2019). https://doi.org/10.31803/tg-20180516131304
2. Keough, J.R., Hayrynen, K.L.: Heat treatment of high-alloy white cast irons. In: Stefanescu, D.M. (eds.) Cast Iron Science and Technology, vol. 1A. ASM International (2017). https://doi.org/10.31399/asm.hb.v01a.a0006305
3. Skoblo, T.S., et al.: Heat treatment of two-layer alloyed-iron rollers. Steel Transl. **43**, 603–606 (2013). https://doi.org/10.3103/S096709121309012X

4. Medyński, D., Samociuk, B., Janus, A., Chęcmanowski, J.: Effect of Cr, Mo and Al on microstructure, abrasive wear and corrosion resistance of Ni-Mn-Cu cast iron. Materials **12**(21), 3500 (2019). https://doi.org/10.3390/ma12213500

5. Rizov, B.L.: Some results from the investigation of effects of heat treatment on properties of ni-hard cast irons. Int. J. Eng. Res. Dev. **13**(2), 30–35 (2017)

6. Ngqase, M., Pan, X.: An overview on types of white cast irons and high chromium white cast irons. J. Phys. Conf. Ser. **1495**, 12023 (2020). https://doi.org/10.1088/1742-6596/1495/1/012023

7. Vdovin, K.N., Gorlenko, D.A., Zavalishchin, A.N., Kuryaev, D.V.: Effect of production process on the structure and properties of the functional layer of forming rolls from cast iron LPKhND-71. Met. Sci. Heat Treat. **62**(3–4), 247–252 (2020). https://doi.org/10.1007/s11041-020-00543-y

8. Yasuda, Y., Ohashi, T.: Crystal plasticity analysis considering dislocations' behavior in ferrite/cementite lamellar structure. ISIJ Int. **57**(3), 573–580 (2017). https://doi.org/10.2355/isijinternational.ISIJINT-2016-612

9. Mironova, T., Proidak, S.: Peculiarities of alloying effect on the eutectic cementite behavior under hot rolling. New Trends in Production Engineering **2**(2), 289–300 (2019). https://doi.org/10.2478/ntpe-2019-0093

10. Fernández, M.G., de Castro, Y., Álvarez, M., Moreno-Labella, J.J., Panizo-Laiz, M., del Río, B.: Color-metallographic characterization of alloyed white cast irons Ni-Hard type. Metals **10**(6), 728 (2020). https://doi.org/10.3390/met10060728

11. Nayak, U.P., et al.: Image processing using open source tools and their implementation in the analysis of complex microstructures. Pract. Metallogr. **58**(8), 484–506 (2021). https://doi.org/10.1515/pm-2021-0039

12. Lu, Y., et al.: Relative mobility of screw versus edge dislocations controls the ductile-to-brittle transition in metals. Proceedings of the National Academy of Sciences Sep 2021, **118**(37) e2110596118 (2021). https://doi.org/10.1073/pnas.2110596118

13. Li, N., et al.: Quantification of dislocation nucleation stress in TiN through high-resolution *in situ* indentation experiments and first principles calculations. Sci. Rep. **5**, 15813 (2015). https://doi.org/10.1038/srep15813

14. Ivanyts'kyi, Y.L., Kun', P.S., Lenkovs'kyi, T.M, Mol'kov, Y.V., Shtayura, S.T: The choice of spacing in measuring displacements for the evaluation of strains by the method of optical-digital image correlation. Mater. Sci. **53**(6), 849–854 (2018). https://doi.org/10.1007/s11003-018-0144-9

15. Wang, Y., Karasev, A., Jönsson, P.G.: Comparison of nonmetallic inclusion characteristics in metal samples using 2D and 3D methods. Steel Res. Int. **91**(7), 1900669 (2020). https://doi.org/10.1002/srin.201900669

16. Duwe, S., Tonn, B.: The effect of seven etching solutions used for the differentiated visualization of complex microstructures in low-alloyed cast iron. Pract. Metallogr. **58**(8), 507–538 (2021). https://doi.org/10.1515/pm-2021-0040

17. Skoblo, T.S., Sidashenko, O.I., Saichuk, O.V., Klochko, O.Y., Levkin, D.A.: Influence of stresses on structural changes in gray cast iron. Mater. Sci. **56**(3), 347–358 (2020). https://doi.org/10.1007/s11003-020-00436-8

18. Panin, V.E., et al.: The role of lattice curvature in structural degradation of the metal surface layer of a rail under long-term operation. Dokl. Phys. **65**, 376–378 (2020). https://doi.org/10.1134/S1028335820100043

19. Skoblo, T.S., et al.: Signs of degradation of carbide phases in chromium-nickel cast iron at the operating temperatures of forming rolls. Mater. Sci. **56**(6), 771–778 (2021). https://doi.org/10.1007/s11003-021-00494-6

20. Yousefi, M.H.N., Najafabadi, S.H.G., Tohidi, E.: A new spectral integral equation method for solving two-dimensional unsteady advection-diffusion equations via Chebyshev polynomials. Eng. Comput. **36**(7), 2327–2368 (2019). https://doi.org/10.1108/EC-02-2018-0063
21. Romaniuk, S.P.: New comprehensive approach to mathematical modeling of metallographic images of tool structures. J. Mech. Eng. **22**(4), 67–73 (2019). https://doi.org/10.15407/pmach2019.04.067

Application of Artificial Neural Network (ANN) for Calculations of Pressure–Concentration–Temperature (PCT) Diagrams in Hydrogen – Metal Hydride Systems

Ziphezinhle Khethiwe Simelane[1] , Andrei Kolesnikov[1(✉)] ,
and Mykhaylo Lototskyy[2]

[1] Department of Chemical and Metallurgical Engineering, Tshwane University of Technology,
Pretoria 0183, South Africa
kolesnikova@tut.ac.za

[2] HySA Systems Competence Center, South African Institute for Advanced Materials
Chemistry, University of Western Cape, Bellville 7535, South Africa

Abstract. MATLAB Neural Network (NN) toolbox was used to obtain relations between pressure, temperature, and concentration in a metal hydride. In previous simulations of heat and mass transfer in metal hydride containers PCT calculations based on semi-empirical models and first principles models took significant time. The advantage of using NN to predict PCT curve instead of traditional models is the shorter computational time. The integration of MATLAB Neural Network Toolbox and COMSOL software allows to speed up simulations.

Keywords: Clean energy · Hydrogen · Metal hydrides · PCT diagrams · Modelling

1 Introduction

Metal hydride (MH) materials are widely used in environment-friendly fuel cell energy technologies and related fields [1, 2] for hydrogen and energy storage [3], hydrogen compression [4] and purification [5], as well as in many other applications which utilize hydrogen and require efficient processes of its handling [6].

The MH technologies are based on the reversible heat-driven interaction of gaseous hydrogen (H_2) with hydride-forming metal or alloy (M) to yield metal hydride (MH_x):

$$M(s) + x/2\,H_2(g) \rightleftarrows MH_x(s) + Q \tag{1}$$
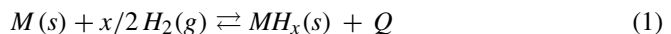
where notations *(s)* and *(g)* relate to solid and gas phases, respectively, and Q is a heat effect approximately equal to the negated reaction enthalpy, $-\Delta H$.

According to reaction (1), metal hydrides exhibit the exothermic effect during H_2 absorption (direct reaction), and endothermic effect during H_2 desorption (reverse reaction). The heat effect $Q > 0$ ($\Delta Ha < 0$) varies between approximately 20 and 70 kJ (mol

$H_2)^{-1}$. At equilibrium, hydrogen concentration in the solid metal hydride is determined by the relation between hydrogen pressure in gas phase (P), hydrogen concentration in the solid (C) and temperature (T). The relation between these three parameters can be presented in graphical format as a set of pressure – composition isotherms. Alternatively, the relation is expressed as some equation:

$$P = P(C, T) \, or \, C = C(P, T) \, or \, T = T(C, P) \tag{2}$$

A family of pressure – composition isotherms (see example in Fig. 1) composes the PCT diagram. The equilibrium pressure on the pressure – composition isotherm is approximately constant (plateau region) in wide range of hydrogen concentrations. The existence of plateau region is due to the co-existence of α-solid solution of H atoms in the parent metal/alloy and β-hydride.

The value of the plateau pressure linearly depends on the reciprocal absolute temperature, according to well-known van't Hoff equation:

$$\ln\left(\frac{P}{P_0}\right) = -\frac{\Delta S}{R} + \frac{\Delta H}{RT} \tag{3}$$

where $P_0 = 1$ atm $= 101.325$ kPa is a standard reference pressure, ΔS and ΔH are the entropy and enthalpy changes of the hydride formation and R is the universal gas constant.
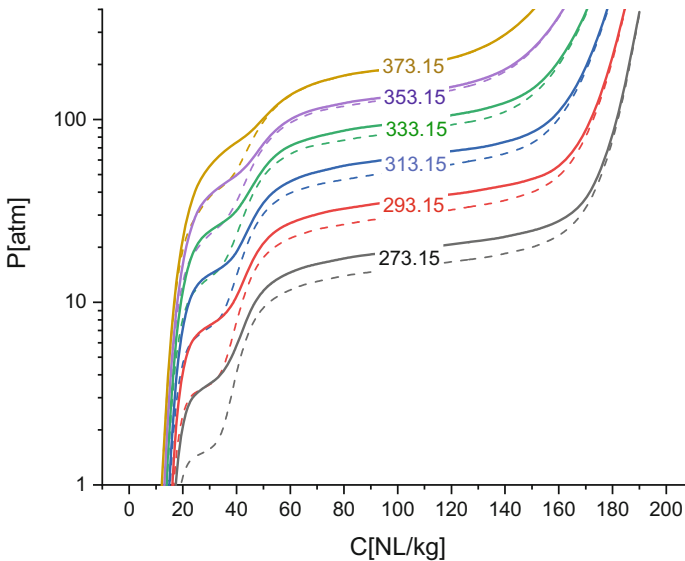
Fig. 1. Hydrogen absorption (solid lines) and desorption (dashed lines) isotherms (the temperatures in K are shown as curve labels) for the mixture of AB_2 (90 wt%) and AB_5 (10 wt%) intermetallic alloys used for H_2 storage on-board fuel cell forklift and H_2 compression for its refueling [7]. The curves were plotted using Lototskyy model [8] where the model parameters were obtained by the fitting of experimental PCT data for the AB_2 and AB_5 components.

Because of simplicity of Eq. (3), it cannot accurately reflect the isotherms behavior outside of plateau region The PCT diagram in the whole concentration region (including concentrations below and above the plateau region) has much more complicated behavior (Fig. 1). An overview of the PCT models reported in the literature can be found in ref. [8].

Low rate of heat transfer in metal hydride powder bed slows down approach to thermodynamics equilibrium even though most of the MH materials used in hydrogen storage and compression applications are characterized by fast kinetics of both direct and reverse processes of reaction (1). The reason of low heat transfer rate in MH bed is low effective thermal conductivity of MH beds (as a rule, below 1 W m^{-1} K^{-1}). The low MH effective thermal conductivity limits the amount of heat supplied to the MH material during absorption and amount of heat removed from it during desorption. Therefore, in real operation of MH storage tanks the pressure – temperature operating conditions deviate from the equilibrium ones.

Thus, optimizing heat transfer in MH reactors for H$_2$ storage and compression is a critical problem to be solved during system development.

Modeling and simulation of heat and mass transfer in MH reactors is a powerful and important tool for the solution of this problem. Though a simplified approach for the estimation of charge/discharge time of a porous hydrogen storage bed starting from its thermal properties and characteristic dimension has been recently suggested [9], its accuracy is very poor (about order of magnitude), and more precise modeling (see, e.g. [10–15] and many other works) requires solution of partial differential equations (PDEs) for energy and momentum conservation, as well as non-linear ordinary differential equations (ODEs) for hydrogen adsorption/desorption rate. In turn, solution of the kinetic ODEs requires the information about PCT data for the used MH, i.e., solution of Eq. (2) in respect to equilibrium concentration, hydrogen pressure or temperature. The numerical solution of the PDEs coupled with solution of highly non-linear ODEs and the PCT equation should be performed at any point of fine spatial and time grid. To achieve reasonable accuracy, the discretization in space and time should be sufficiently fine, resulting in a grid with large number of nodes and small time step. Therefore, the solution procedure becomes long, and computation time can reach 3–7 days.

Conventionally [10–15], the equilibrium pressure is calculated by the application of van't Hoff Eq. (3) with additional empirically derived terms accounting for plateau slope, absorption/desorption hysteresis and other features of the pressure – composition isotherm. Application of this approach requires reasonably short computation time, but it gives unacceptably high errors when the pressure – temperature conditions become out of the available experimental PCT limits used for the determination of the empirical coefficients. Moreover, it does not work in the case of isotherms which have several plateau segments.

Application of more accurate PCT models based on statistical and/or thermodynamic prerequisites (e.g., Lototskyy model [8]) gives realistic extrapolations and can model the multi-segment PCT diagrams, for example, in the cases when a mixture of several MH materials is used. However, it is even more time consuming because of combination of numerous iteration procedures and calculation of convolution integrals.

As an alternative faster method to calculate the PCT model, the mathematical technique called Artificial Neural Network (ANN) could be used. Though recently ANN, or more generally, machine learning methods have been suggested for the prediction of metal hydrides for hydrogen storage [16, 17], their application for the modelling of PCT diagrams has not been reported so far.

In this paper, the original Lototskyy model was used to pre-calculate a set of points for different concentrations, pressures, and temperatures for the certain metal hydride. Using the calculated dataset, the ANN (i.e., a mathematical algorithm) was developed to predict PCT diagram in any form of Eq. (2). Incorporation of ANN into COMSOL solver allows faster solution of PDEs describing heat and mass transfer in MH reactor.

The main purpose of this paper is development of ANN for the fast prediction of the PCT diagram in the system "H_2 gas – mixture of AB_2- and AB_5-type metal hydrides" used for H_2 storage on-board fuel cell forklift and H_2 compression for its refueling [7] (see Fig. 1).

2 Methodology

2.1 General Algorithm

Neural networks (NN) have been used extensively in recent years to model a wide range of physical and chemical phenomena in engineering as well as some non-engineering applications. Selection of neural networks to solve some engineering problems is justified in cases when first-principle (mechanistic) models are too complicated or time-consuming to solve in real time [18].

The idea of numerical algorithm called "neural network" was taken from the research on human brain operation. Human brain consists of structural elements called neurons connected by organic links. The information propagates through this biological neural network as electrical impulses in parallel, thus making fast computations.

Typical NN consists of several layers as shown in Fig. 2. The first layer (called input layer) receives incoming data and after processing passes it to several hidden layers. After processing in hidden layers, the processed data propagate further to last (output) layer.

Information is processed using simple summation with weights and multiplication by sigmoidal function (see Fig. 3). The weights are unique for each node in network. The weights are unknown parameters. And they are estimated in training period, to allow the NN predictions to fit to experimental data from the studied process.

Once the network is trained (meaning all weights are known), the NN undergoes validation. For this process, different large set of experimental data from the same process is used. If NN predictions are not close the experimental data, changes in the network structure must be made. Training/validation process is repeated for the modified network. The whole process (training/validation/network structure modification) is repeated until satisfactory matching to experimental data is achieved.

2.2 Building Neural Networks

The general procedure how neural networks are built is well-documented and typically consists of five basics steps [21]:
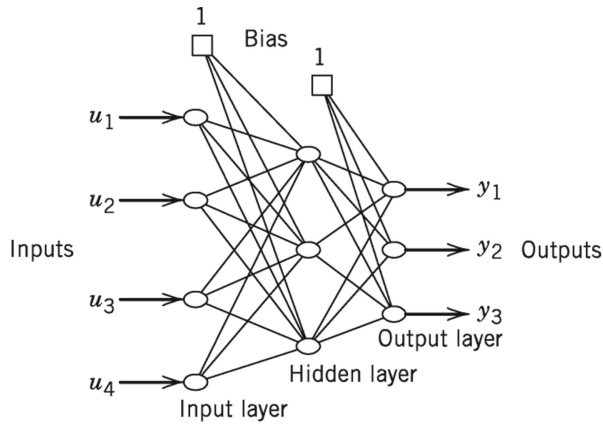
Fig. 2. Architecture of typical artificial neural network with 3 layers.

u_i = Input signals
W_{ij} = Weights
y_j = Output signal

$$I_j = \sum_{j=1}^{n} W_{ij}u_i$$

$$y_j = \frac{1 - e^{-I_j}}{1 + e^{-I_j}}$$
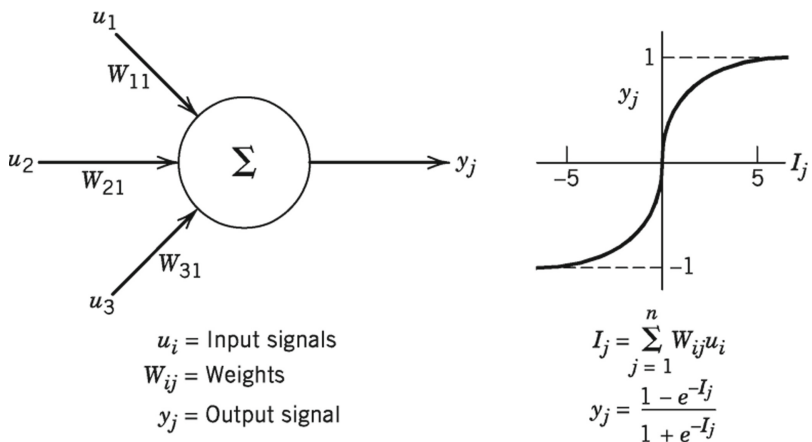
Fig. 3. Signal propagation for a neuron [20].

1. **Running experiment and recording measured signals (data).** This is the first step in designing NN development.
2. **Initial pre-processing of raw data.** The step is required to filter data from errors(noise), (2) to bring data to common scale and (3) to perform randomization in order to eliminate possible data shift (bias) in some experimental series.
3. **Network construction.** Initial guessed structure of the network is laid down at this step. Designer must specify the number of hidden layers, number of nodes in each layer, initial values of weights, the signal propagation function (usually sigmoidal) and other functions for network training.
4. **Network training.** To achieve matching between NN predictions and experimental data, the weights are continuously modified (using some optimization algorithm, for example, minimization of least squares) until the NN calculated outputs become close to the measured experimental data.

5. **Network validation.** The validation procedure is evaluation of the developed ANN ability to quantitatively predict the modelled process behavior by using different large data set from the same process [22].

2.3 Data Sources

The source datasets (partially reproduced in Fig. 1) included PCT data, $P = P(C,T)$ calculated using model [8], with model parameters (65 in total) obtained by the separate fitting of the experimental PCT diagrams taken for the AB_2 ($T = 248.15–348.15$ K, $P = 0.01–20$ MPa, goodness of fit corresponded to the relative mean-square error $R_f = 0.28\%$) and AB_5 ($T = 283.35–393.15$ K, $P = 0.01–15$ MPa, $R_f = 0.13\%$) used as an additive to the main AB_2 material for the improvement of its activation performance. The fractions of plateau segments which corresponded to the mixture components were corrected in accordance with their content in the mixture (90 wt% AB_2 + 10 wt% AB_5). Each dataset (absorption and desorption) contained 407 points where the values of the equilibrium H_2 pressures (P) were calculated in the ranges of arguments $T = 273.15–373.15$ K (step 10 K), $C = 10–190$ NL(H_2) kg(alloy)$^{-1}$ (step 5 NL kg^{-1}).

Of the total 407 points in the absorption or desorption dataset, 285 (70%) were used for training, 61 (15%) for validation and the remaining 61 (15%) for testing.

2.4 ANN Development

The NN training was executed by minimization of squared deviations of predicted data from experimental values. The NN weights were adjusted by Marquardt algorithm. The MATLAB code was written to generate the best fit of the NN weights.

The minimization criteria used in training and were the Mean Square Error (*MSE*) and goodness of fit (R^2) [23]:

$$MSE(y) = \frac{\sum_i n\left(y_{ann,i} - y_{exp,i}\right)^2}{n} \tag{4}$$

$$R = \sqrt{1 - \frac{\sum_{i-1} n\left(y_{exp,i} - y_{pred,i}\right)^2}{\sum_{i-1} n\left(y_{exp,i} - \dot{x}\right)^2}} \tag{5}$$

where n is number of experimentally measured values, $y_{ann,\,i}$ is output value predicted by NN, $y_{exp,\,i}$ is experimentally measured value.

Training was performed until stopping criteria were satisfied, i.e. the number of iterations and the error tolerance, respectively. Therefore, the training stopped when the relative error or the maximum number of training sessions (epochs) was reached [24].

3 Results

3.1 ANN Training, Validation and Test

Figure 4 shows interface of MATLAB software used for the building, validation, and testing of the PCT model built.
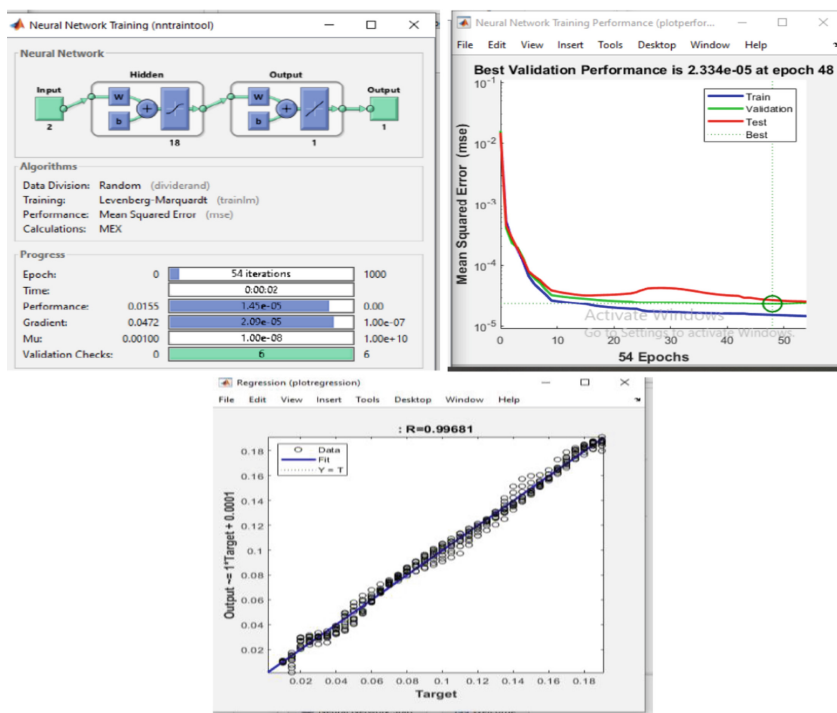
Fig. 4. Top left – structural arrangement of a double-hidden layer configuration of ANN model; top right – summary of the training, validation, and test results; bottom – example of the post-training regression analysis.

A satisfactory fit was obtained for configuration ANN [2-14-1-1] (14 hidden neurons) and further improved for ANN [2-18-1-1] (18 hidden neurons).

Training was stopped after 6 validation checks were reached which means that the network performances upon the validation set increased more than maximum validation failures, which occurred after 54 iterations.

A summary of the ANN performance is presented in Table 1. It is seen that the ANN model adequately reproduces time consuming PCT modelling results [8] and is able to calculate one of three parameters (equilibrium pressure, concentration and temperature) depending on the values of the two others. The results practically coincide with the input data (Fig. 1), with maximum deviations of 4 NL kg^{-1}, (high concentration region), 0.28 atm (low pressure region) and 1.07 K (high temperature region), for the concentration, pressure and temperature, respectively.

Further improvement of the ANN predictive capability can be achieved by the increase of the number of the hidden neurons, training vectors and the input values, as well as by trying different training algorithms. Certainly, for each new MH material the initial network weights and biases must be reset to new values (experimental or pre-fitted PCT data) and followed by the new training.

Presently, the ANN PCT model is incorporated in Computational Fluid Dynamics (CFD) software for the modelling of heat and mass transfer in MH reactors being developed by the authors [12, 13, 25]. Depending on the grid fineness, the PCT calculation times in the simulations using modified software is 2.5–5 times faster than previous ones [12, 25].

Table 1. Summary of the ANN performance.

Step	Number of samples	Modeled dependence and performances					
		$C(P, T)$		$\text{Log}_{10}[P(C, T)]$		$T(C, P)$	
		MSE	R	MSE	R	MSE	R
Training	285	$1.521 \cdot 10^{-5}$	0.9974	$8.268 \cdot 10^{-4}$	0.9995	$7.294 \cdot 10^{-1}$	0.9996
Validation	61	$2.234 \cdot 10^{-5}$	0.9948	$1.406 \cdot 10^{-3}$	0.9994	$7.589 \cdot 10^{-1}$	0.9996
Test	61	$2.729 \cdot 10^{-5}$	0.9954	$1.614 \cdot 10^{-3}$	0.9987	1.492	0.9993

4 Conclusions

The Neural Networks (NN) were developed to link pressure, temperature, and concentration variables (PCT curves) in simulations of heat and mass transfer in a metal hydride container using COMSOL software. MATLAB NN Toolbox was used for the neural network development. The NN training was done using PCT data sets, pre-calculated by Lototskyy algorithm [8]. The increase in number of hidden neurons allows to improve accuracy of the PCT curve representation. The incorporation of the developed neural network in the heat and mass transfer model allowed to significantly increase speed of COMSOL simulations.

References

1. Abe, J.O., Popoola, A.P.I., Ajenifuja, E., Popoola, O.M.: Hydrogen energy, economy, and storage: review and recommendation. Int. J. Hydrog. Energy **44**, 15072–15086 (2019)
2. Gambini, M., Stilo, T., Vellini, M.: Hydrogen storage systems for fuel cells: comparison between high and low-temperature metal hydrides. Int. J. Hydrog. Energy **44**, 15118–15134 (2019)
3. Hirscher, M., et al.: Materials for hydrogen-based energy storage – past, recent progress and future outlook. J. Alloys Compd. **827**, 153548 (2020)

4. Bellosta von Colbe, J., et al.: Application of hydrides in hydrogen storage and compression: achievements, outlook and perspectives. Int. J. Hydrog. Energy **44**, 7780–7808 (2019)

5. Jinsheng, X., Tong, L., Yang, T., Bénard, P., Chahine, R.: Lumped parameter simulation of hydrogen storage and purification systems using metal hydrides. Int. J. Hydrog. Energy **42**, 3698–3707 (2017)

6. Bhuiya, M.M.H., Kumar, A., Kim, K.J.: Metal hydrides in engineering systems, processes, and devices: a review of non-storage applications. Int. J. Hydrog. Energy **40**, 2231–2247 (2015)

7. Lototskyy, M.V., et al.: Metal hydride hydrogen storage and supply systems for electric forklift with low-temperature proton exchange membrane fuel cell power module. Int. J. Hydrog. Energy **41**, 13831–13842 (2016)

8. Lototskyy, M.V.: New model of phase equilibria in metal – hydrogen systems: features and software. Int. J. Hydrog. Energy **41**, 2739–2761 (2016)

9. Wang, C.-S., Brinkerhoff, J.: Is there a general time scale for hydrogen storage with metal hydrides or activated carbon? Int. J. Hydrog. Energy **46**, 12031–12034 (2021)

10. Mohammadshahi, S.S., Gray, M.A.E., Webb, C.J.: A review of mathematical modelling of metalhydride systems for hydrogen storage applications. Int. J. Hydrog. Energy **41**, 3470–3484 (2016)

11. Askri, F., Jemni, A., de Rango, P., Marty, P., Nasrallah, S.B.: Heat and mass transfer during hydriding. In: Aloui, F., Dincer, I. (eds.) Exergy for A Better Environment and Improved Sustainability 1. GET, pp. 489–507. Springer, Cham (2018). https://doi.org/10.1007/978-3-319-62572-0_33

12. Satya Sekhar, B., Lototskyy, M., Kolesnikov, A., Moropeng, M.L., Tarasov, B.P., Pollet, B.G.: Performance analysis of cylindrical metal hydride beds with various heat exchange options. J. Alloy. Compd. **645**, S89–S95 (2015)

13. Minko, K.B., Bocharnikov, M.S., Yanenko, Y., Lototskyy, M.V., Kolesnikov, A., Tarasov, B.P.: Numerical and experimental study of heat-and-mass transfer processes in two-stage metal hydride hydrogen compressor. Int. J. Hydrog. Energy **43**, 21874–21885 (2018)

14. Chandra, S., Sharma, P., Muthukumar, P., Tatiparti, S.S.V.: Modeling and numerical simulation of a 5 kg LaNi$_5$-based hydrogen storage reactor with internal conical fins. Int. J. Hydrog. Energy **45**, 8794–8809 (2020)

15. Chibani, A., Merouani, S., Bougriou, C., Hamadi, L.: Heat and mass transfer during the storage of hydrogen in LaNi$_5$-based metal hydride: 2D simulation results for a large scale, multi-pipes fixed-bed reactor. Int. J. Heat Mass Transf. **147**, 118939 (2020)

16. Rahnama, A., Zepon, G., Sridhar, S.: Machine learning based prediction of metal hydrides for hydrogen storage, part I: prediction of hydrogen weight percent. Int. J. Hydrog. Energy **44**, 7337–7344 (2019)

17. Rahnama, A., Zepon, G., Sridhar, S.: Machine learning based prediction of metal hydrides for hydrogen storage, part II: prediction of material class. Int. J. Hydrog. Energy **44**, 7345–7353 (2019)

18. Himmelblau, D.M.: Accounts of experience in the application of artificial neural networks in chemical engineering. Ind. Eng. Chem. Res. **47**, 5782 (2008)

19. Haykin, S.S.: Neural Networks and Learning Machines, 3rd edn. Prentice-Hall, Upper Saddle River, NJ (2009)

20. Edgar, T.F., Himmeblau, D.M., Lasdon, L.S.: Optimization of Chemical Processes, 2nd edn. McGraw-Hill, New York (2001)

21. Tymvios, F., Michaelides, S., Skouteli, C.: Estimation of surface solar radiation with artificial neural networks. In: Badescu, V. (ed.) Modeling Solar Radiation at the Earth Surface, pp. 221–256. Springer, Germany (2008). ISBN 978-3-540-77454-9

22. Maitha, H., Al Shamisi, A.A.H., Hejase, H.A.N.: Using MATLAB to develop artificial neural network models for predicting global solar radiation in Al Ain City – UAE, Engineering Education and Research Using MATLAB. In: Assi, A.H. (ed.) IntechOpen (2011). https://doi.org/10.5772/25213. Available from: https://www.intechopen.com/chapters/21382
23. Khoshjavan, S.: Artificial neural network modeling of gold dissolution in cyanide media. J. Cent. South Univ. Technol. **18**, 1976–1984 (2011)
24. Abidoye, L.K., Mahdi, H.L.: ANN-derived equation and ITS application in the prediction of dielectric properties of pure and impure CO_2. J. Clean. Prod. **175**, 123–132 (2018)
25. Moropeng, M.L., Kolesnikov, A., Lototskyy, M., Mavhungu, A.: Numerical investigation of heat and mass transfer during hydrogen sorption in a mixture of AB_2 – AB_5 metal hydride for hydrogen storage. Chem. Prod. Process. Model. **16**(1), 41–53 (2021)

Thermal Stability, Cyclic Durability and Hydrogen Resistance of Cast Nickel-Cobalt Alloys for Gas Turbine Blades

Lyubomir Ivaskevich[1(✉)] ⓘ, Alexander Balitskii[1] ⓘ, Iuliia Kvasnytska[2] ⓘ,
Kateryna Kvasnytska[2] ⓘ, and Heorhiy Myalnitsa[3] ⓘ

[1] Ukrainian National Academy of Sciences, Karpenko Physicomechanical Institute, Lviv,
Ukraine
lyubom538@gmail.com

[2] Ukrainian National Academy Sciences, Physico-Technological Institute of Metals and Alloys,
Kiev, Ukraine

[3] "Zorya–Mashproekt" Scientific and Production Complex of Gas-Turbine Building, Mykolaiv,
Ukraine

Abstract. Phase-structural stability, short-term and long-term strength, low- and high-cycle fatigue and hydrogen embrittlement of cast heat-resistant nickel-cobalt SM-88, SM-90 and SM-104 alloys have been studied. It was found that after exposure for 5000 h at temperatures of 1073 and 1123 K in all alloys there was a carbide reaction MC $\rightarrow$ $M_{23}C_6$, and a brittle σ-phase was not formed. With increasing temperature and duration of exposure, the yield strengths decrease significantly, the plasticity characteristics of alloys SM-90 and SM-104 change insignificantly, and plasticity of SM-88 alloys has decrease. In the 0–15 MP range of hydrogen gaseous pressures, its influence on the relative elongation, reduce of area and low-cycle durability of alloys increases, and further increase of hydrogen pressure to 30 MPa does not cause a further decrease in these characteristics. The SM-90 alloy single-crystal has the highest values of fatigue, long-term strength and hydrogen resistance. This alloy can be recommended for the manufacture of gas turbine blades running on hydrogen-containing fuel.

Keywords: Superalloys blade · Hydrogen energy · Fatigue strength

1 Introduction

The service life of a gas turbine engine depends on the reliability of the turbine blades [1, 2], which are operated in extreme conditions – in aggressive environments (corrosive, hydrogen-containing [3–5]) at high temperatures and static, cyclic and vibration loads [6–8]. In review [6] was discuss the potential materials challenges of gas turbines fuelled with hydrogen, provide an updated overview of the most promising alloys for this application. Turbine blades are produced of cast heat-resistant nickel and nickel-cobalt alloys with admixtures of chromium and refractory and phase-forming metals guaranteeing high levels of heat and corrosion resistances [4, 5, 8, 9]. In view of the large number of

alloying elements, complex long-term loads, and the presence of corrosive and hydrogen-containing substances in the fuel, it is actual to study the high-temperature mechanical properties, structural stability of these materials, as well their hydrogen embrittlement [2, 10, 11].

The aim of the work is to study the effect of static and cyclic loads, aging for 5000 h at operating temperatures and hydrogen gas on changes the structure and mechanical properties obtained by vacuum-induction melting of cast nickel heat-resistant alloys Ni57Cr16Co11W6Ti4Al4Mo2Hf (SM-88), Ni57Cr16Co12W6Ti4Al3Mo2Hf (SM-90), and Ni59Cr21Co10W4Ti3Al3MoLa (SM-104).

2 Materials and Testing Method

The investigated alloys are characterized by the presence of chromium, refractory (hafnium, molybdenum and tungsten) elements, and intermetallic forming (aluminum and titanium) elements (Table 1) and, hence, by the high levels of high-temperature strength and heat and corrosion resistances [3, 5, 8, 9, 12]. The amount of the γ'-phase in the SM-104 alloy constitutes 36–37 wt.%, while its amounts in the other two alloys are close to 40–42 wt.%. In addition, chromium, molybdenum, and tungsten carbides (mainly MC and M23C6) and borides are formed in the studied alloys in the course of thermal treatment (holding for 3 h at 1433 K, cooling in air, holding for 4 h at 1333 K, cooling in air, aging at 1123 K for 16 h and cooling in air). Their high corrosion resistance is attained as a result of alloying with chromium (15.5, 15.6, and 21.2 wt.%) and the optimal ratio of the contents of titanium and aluminum Ti/Al $\geq$ 0.7 [3–6]. All alloys contain rare-earth metals improving the structure of the boundaries of grains, decelerating the grain-boundary sliding, and neutralizing the action of harmful admixtures [5–10].

Table 1. Chemical composition of the investigated alloys.

Alloy	Content of elements, wt.%											
	C	Cr	Co	W	Mo	Al	Ti	Nb	Hf	B	Ce	Zr
SM-88	0,9	15,6	10,2	5,9	2,0	3,8	4,2	0,2	0,2	0,07	0,015	0,05
SM-90	0,12	15,5	10,5	5,7	2,3	3,0	4,4	0,3	0,3	0,01	0,015	0,03
SM-104	0,13	21,2	11,5	3,6	0,7	2,8	3,2	0,3	La 0,02	0,015	–	0,03

Short-term stretching (static tensile tests) was carried out at a speed of 0.1 mm/min (by displacement rate $V_d = 6.7 \times 10^{-5}$ s^{-1}) in the air and gaseous hydrogen under the pressure 0–30 MPa on standard cylindrical specimens with working part diameter 5 mm. This type of sample was used to determine the long-term strength and high-cycle durability submitted to cyclic loading on scheme "pure bending with rotation" at fixed strain amplitude with 50 Hz frequency at temperature 1073 K. The low-cycle life (number of cycles to fracture, N) under stiff pure pulsating bending was determined over a pressure up to 30 MPa at an amplitude of 1.6% with a frequency of 0.5 Hz on ground flat specimens with a $3 \times 6 \times 20$ mm test portion.

The X-ray phase diffraction analysis of the alloys was performed and the lattice constants of the phases were determined by using a DRON-3M installation in the CuKα-radiation ($\lambda = 0.154187$ nm).

3 Results and Discussion

3.1 Thermal Stability, High-Cycle Fatigue and Long-Term Strength of Alloys in Air

Aging of the SM-88 alloy at 1073 K leads to some increase in the tensile strength σ_u and decrease in the yield strength $\sigma_{0.2}$, relative elongation the δ and reduction of area ψ (Table 2). As a result of exposure to higher temperatures, all strength characteristics are reduced, but the deterioration of the properties is insignificant except for significant softening of the alloy SM-104 after aging at 1123 K. This material with increased chromium content has the highest corrosion resistance and was developed for nozzle blades of gas turbine engines [5].

The stability of the mechanical properties of alloys correlates with the results of X-ray diffraction analysis. It is established that in the process of heat treatment they form intermetallic, carbide and boride phases with a complex structure. As a result of aging of alloys in the temperature range 1073–1123 K the total number of secondary phases increases, coagulation of intermetallics occurs, and tetragonal densely packed σ-phase, the presence of which leads to dangerous brittle fractures [4–7], under these conditions aging does not stand out.

In all alloys with increasing aging time there is a dissolution of MC carbide and the formation of new particles of carbide $M_{23}C_6$, and the reaction rate of MC → $M_{23}C_6$ increases with increasing temperature, is highest in alloy SM-104, lowest – in alloy SM-88. This transformation changes the morphological structure of the alloy and leads to a decrease in the chromium content in the matrix phase, which impairs its corrosion resistance [3–6].

Table 2. Influence of long aging on the strength and plasticity of alloys.

Alloy	Aging and test temperature, K	Aging time, h	Mechanical properties			
			$\sigma_{0,2}$ MPa	σ_u MPa	δ %	ψ %
SM-90	1073	0	810	990	8.9	19.5
		5000	816	958	9.2	15.4
	1123	5000	636	785	9.0	20.1
SM-88	1073	0	750	960	8.5	19.5
		5000	742	1032	4.9	14.8
	1123	5000	579	718	3.7	8.8
SM-104	1073	0	683	786	7.8	19.6
		5000	580	729	8.2	9.8
	1123	5000	442	579	8.3	18.5

The ability to withstand prolonged static, cyclic and thermal loads is important characteristics of the blades [13, 14]. Macroscopic studies of the fracture surface of the blade have shown that that destruction often occurs by the mechanism of fatigue [13]. The fatigue of alloys was investigated under load by the method of symmetric alternating bending of samples [15]. The values of the fatigue limits of the alloys were determined on the basis of tests of 2×10^7 cycles at temperature 1073 K. Presented in Fig. 1 the results show the advantage of the single-crystal alloy SM-90 is especially noticeable at high load bases and the lowest level of fatigue strength of specimens of the alloy SM-104.
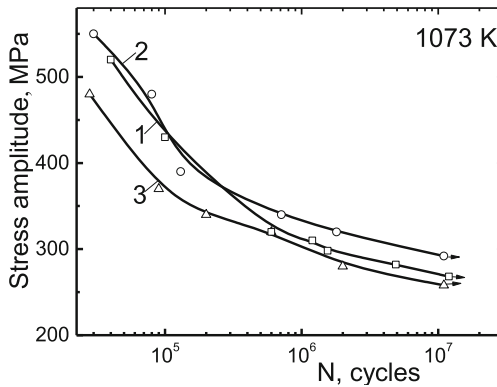
Fig. 1. Curves of high-cycle fatigue at symmetrical alternating bending of specimens from SM-88 (1), SM-90 (2) and SM-104 (3) alloys at a temperature of 1073 K.

The long-term strength curves of alloys at temperatures of 973, 1073, and 1173 K, show that the values of long-term strength for all load bases decrease in the order of SM-90 > SM-88 > SM-104 (see Fig. 2).
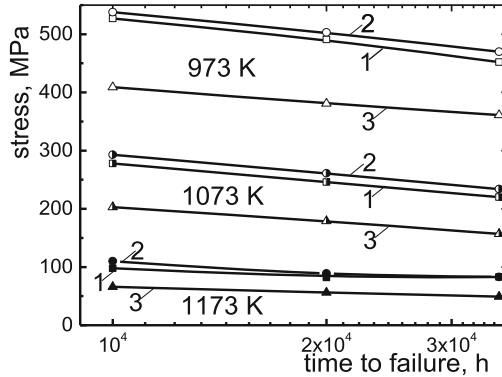
Fig. 2. Long-term strength of specimens from SM-88(1), SM-90 (2) and SM-104 (3) alloys at temperatures of 973, 1073 and 1173 K.

The low heat resistance of the SM-104 alloy is due to the lower content of molybdenum, tungsten, titanium and aluminum (Table 1), and, as a consequence, less reinforcing intermetallic γ'-phase. The highest values of short-term and long-term strength in the single-crystal alloy SM-90 (see Fig. 2, Table 1, 2) with minimal sensitivity to hydrogen embrittlement among the studied alloys (see Fig. 3).

3.2 Influence of Hydrogen on the Strength, Plasticity and Low-Cycle Durability of Alloys

It is known literature data on the positive effect of cobalt and hafnium on the corrosion and hydrogen strength of heat-resistant nickel alloy, as well as the weakening of hydrogen embrittlement of austenitic dispersion hardening steels and alloys with decreasing carbon content [16–18]. Therefore we compared the effect of hydrogen on two alloys modifications. The first (CCI) – industrial alloys with the chemical composition given in Table 1. The second (CCII) – with a reduced concentration of carbon and increased content of cobalt and hafnium. The carbon content in the alloy SM-88 is reduced to 0.05 wt. %, cobalt and hafnium increased in accordance with 11 and 0.3 wt. %. Similar indicators in the alloy SM-90 are 0.8 (C), 11.3 (Co) and 0.6 (Hf), in the alloy SM-104 0.09 (C) and 11.9 wt. % (Co), hafnium – missing.

Alloys with chemical composition II are more plastic in an inert environment and hydrogen and more resistant to hydrogen embrittlement. The strength characteristics of the specimens with both chemical compositions differ insignificantly (Table 3).

An important test parameter when considering materials for the use in hydrogen is his pressure [15–21]. The effect of hydrogen pressure on plasticity and low-cycle durability was studied on samples from CCII at a rate of cylindrical samples short-term loading

Table 3. Mechanical properties of SM-88, SM-90 and SM-104 alloys in air and hydrogen at a pressure of 30 MPa and room temperature.

Alloy	Test environment	σ_u, MPa	$\sigma_{0,2}$, MPa	δ, %	ψ, %
SM-88, CCI	Air	976	921	2,1	7,5
	Hydrogen	920	890	0,5	1
SM-88, CCII	Air	960	890	5	8
	Hydrogen	910	860	2	2
SM-90, CCI	Air	922	867	2,9	7
	Hydrogen	890	860	2	3
SM-90, CCII	Air	970	860	13	16
	Hydrogen	840	800	6	8
SM-104, CCI	Air	889	747	2,9	8
	Hydrogen	780	750	1	2
SM-104, CCII	Air	870	760	8	12
	Hydrogen	780	750	3	4

0.1 mm/min and the bending amplitude of flat samples 1.6%. It is established that the graphs of dependences of low-cycle durability (N) and plasticity characteristics (δ and ψ) (see Fig. 3) of alloys on hydrogen pressure consist of two regions. In the first (in the pressure range 0–15 MPa) N, δ and ψ decrease sharply, in the second – the negative effect of hydrogen is almost stabilized, and further increase in hydrogen pressure does not cause additional deterioration of properties. Thus, there is the pressure at which the degradation of materials by hydrogen reaches its limit. The average number of cycles to failure under zero bending of alloys SM-88, SM-90 and SM-104 according to the results of five tests is 404, 904 and 604 in air and 77, 177 and 98 in hydrogen at maximum embrittlement.

Similar pressure dependences are also established for ferritic iron [19], low-carbon [20, 21], heat treatable (CrMo, CrMn) [21] martensitic [22] and austenitic stainless [21] steels and 05Cr19Ni55, Ni56Cr17Mo6Nb4, Ni51Cr9Mo3Nb2AlTi alloys in deformable, cast and powder modification [11, 16, 23] and others nickel alloys [24]. Thus, in this (see Fig. 3) and previous works, the presence of the limit of hydrogen embrittlement, the minimum value of performance characteristics (plasticity, low life cycle and fracture toughness), which do not decrease with further increase in hydrogen gas pressure and absorbed hydrogen content, was established. Such limiting small values of mechanical properties depend on the load speed and in the case of martensitic aging steels [22] and high-nickel alloys (over 55 wt.% Ni) [16, 23] are achieved at hydrogen pressures above 10 and 30 MPa, respectively, and stable dispersion-strengthened austenitic steels and alloys (20–55 wt.% Ni) at a pre-absorbed hydrogen content of 15–30 ppm [16, 23]. For the investigated alloys SM-88, SM-90 and SM-104 at a tensile rate $V_d = 6.7 \times 10^{-5}$ s^{-1},
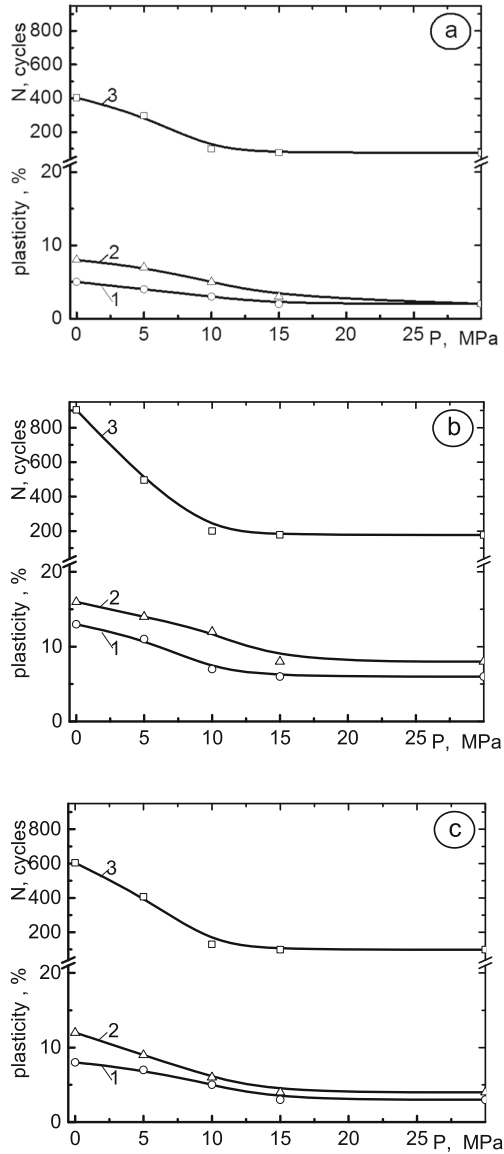
Fig. 3. Dependences of relative elongation δ (1), reduce of area ψ (2) and number of cycles N before fracture (3) of specimens from cast alloys SM-88 (a), SM-90 (b) and SM-104 (c) from hydrogen pressure at 293 K

frequency and amplitude of cyclic bending of 0.5 Hz and 1.6%, this critical pressure value is equal to 15 MPa (see Fig. 3).

This pattern is due to the fact that the interaction of hydrogen gas with metals includes stages of adsorption (physical and chemical), dissociation of hydrogen molecules, its

penetration into the metal (diffusion, including in the stress field, transfer of moving dislocations), accumulation at the crack tip, movement together with (in front) a crack [16–20]. Depending on the load conditions [16, 21, 22], chemical composition [17, 18, 24] and structure of the material [16, 23, 24], each of these stages has a decisive influence on the kinetics and degree of hydrogen embrittlement.

At static and low cycle load the highest resistance to hydrogen embrittlement was found in the single-crystal alloy SM-90. This alloy retains high strength and plasticity in air and hydrogen over a wide range of temperatures [5]. Thus, SM-90 alloy can be recommended for the manufacture of gas turbine blades running on hydrogen-containing fuel.

4   Conclusion

Phase-structural stability, short-term and long-term strength, low- and high-cycle fatigue and hydrogen embrittlement of cast heat-resistant nickel-cobalt superalloys have been studied.

With increasing temperature and duration of exposure, the yield strengths decrease significantly, the plasticity characteristics of alloys SM-90 and SM-104 change insignificantly, and plasticity of SM-88 alloys has decrease.

In the 0–15 MPa hydrogen gaseous pressures range its influence on the relative elongation, reduce of area and low-cycle durability of alloys increases, and further increase of hydrogen pressure to 30 MPa does not cause a further decrease in these characteristics.

The SM-90 alloy single-crystal has the highest values of fatigue, long-term strength and hydrogen resistance.

References

1. Hollander, D., Kulawinski, D., Weidner, A., Thiele, M., Gampe, U.: Small-scale specimen testing for fatigue life assessment of service-exposed industrial gas turbine blades. Int. J. Fatigue **92**(1), 262–271 (2016)
2. Bancalari, E., Chan, P., Diakunchak, I.S.: Advanced hydrogen gas turbine development program. In: ASME Turbo Expo 2007: Power for Land, Sea, and Air. Paper No: GT2007-27869, pp. 977–987. Montreal, Canada, May 14–17 (2007)
3. Rajabinezhad, M., Bahrami, A., Mousavinia, M., Seyedi, S.J., Taheri, P.: Corrosion-fatigue failure of gas-turbine blades in an oil and gas production plant. Materials **13**(4), 900 (2020)
4. Glotka, O.A.: Distribution of alloying elements in carbides of refractory nickel alloys under the conditions of equiaxial crystallization. Mater. Sci. **56**(5), 714–721 (2021)
5. Balyts'kyi, O.I., Kvasnytska, Y.H., Ivaskevych, L.M., Mialnitsa, H.P.: Corrosion and hydrogen resistance of heat resistance blade nickel-cobalt alloys. Mater. Sci. **54**(2), 230–239 (2018)
6. Stefan, E., Talic, B., Larring, Y., Gruber, A., Peters, T.A.: Materials challenges in hydrogen-fuelled gas turbines. Int. Mater. Rev. **67**(5), 461–486 (2021). https://doi.org/10.1080/09506608.2021.1981706
7. Šmíd, M., Horník, V., Kunz, L., Hrbáček, K., Hutař, P.: High cycle fatigue data transferability of MAR-M 247 superalloy from separately cast specimens to real gas turbine blade. Metals **10**(11), 1–16 (2020)
8. Wu, X., Makineni, S.K., Liebscher, C.H., Dehm, G., Mianroodi, J.R.: Unveiling the Re effect in Ni-based single crystal Superalloys. Nat. Commun. **11**, 389 (2020)

9. Hlotka, A.A, Haiduk, S.V.: Prediction of the thermodynamic processes of phase separation in single-crystal refractory alloys based on nickel. Mater. Sci. **55**(6), 878–883 (2020). https://doi.org/10.1007/s11003-020-00382-5

10. Zhang, Z., Obasi, G., Morana, R., Preuss, M.: In-situ observation of hydrogen induced crack initiation in a nickel-based superalloy. Scr. Mater. **140**, 40–44 (2017)

11. Tkachev, V.I., Ivaskevich, L.M., Levina, I.M.: Distinctive features of hydrogen degradation of heat-resistant alloys based on nickel. Mater. Sci. **33**(4), 524–531 (1997)

12. Amouyal, Y., Seidman, D.N.: The role of hafnium in the formation of misoriented defects in Ni-based superalloys: an atom-probe tomographic study. Acta Mater. **59**(9), 3321–3333 (2011)

13. Fallah Sheykhlari, A., Khani Moghanaki, S., Moattari, M., Shafiei, A., Amirjan, M.: On the failure behavior of fifth stage gas turbine blade. Eng. Fail. Anal. **116**, 104766 (2020)

14. Rayapati, S.: Gas turbine blade failure scenario due to thermal loads in case of Nickel based super alloys. Mater. Today Proc. **46**, 8119–8126 (2021)

15. Panasyuk, V.V., Dmytrakh, I.M., Toth, L., Bilyi, O.L., Syrotyuk, A.M.: A method for the assessment of the serviceability and fracture hazard for structural elements with cracklike defects. Mater. Sci. **49**(5), 565–576 (2014)

16. Balitskii, A.I., Ivaskevich, L.M.: Assessment of hydrogen embrittlement in high-alloy chromium-nickel steels and alloys in hydrogen at high pressures and temperatures. Strength Mater. **50**(6), 880–887 (2018)

17. Dadfarnia, M., Nagao, A., Wang, S., Martin, M.L., Somerday, B.P., Sofronis, P.: Recent advances on hydrogen embrittlement of structural materials. Int. J. Fract. **196**(1–2), 223–243 (2015). https://doi.org/10.1007/s10704-015-0068-4

18. Lee, A.: Hydrogen embrittlement of nickel, cobalt and iron-based superalloys. The problem, its characterization and effects on particular alloy classes. In: Gangloff, R.P., Somerday, B.P. (eds.) Gaseous Hydrogen Embrittlement of Materials in Energy Technologies, vol. 1, pp. 624–667. Woodhead Publ. Ltd., Oxford, Cambridge, Philadelphia, New Delhi (2012)

19. Ogawa, Y., Umakoshi, K., Nakamura, M., Takakuwa, O., Matsunaga, H.: Hydrogen-assisted, intergranular, fatigue crack-growth in ferritic iron: influences of hydrogen-gas pressure and temperature variation. Int. J. Fatigue **140**, 105806 (2020)

20. Yamabe, J., Yoshikawa, M., Matsunaga, H., Matsuoka, S.: Effects of hydrogen pressure, test frequency and test temperature on fatigue crack growth properties of low-carbon steel in gaseous hydrogen. Procedia Struct. Integrity **2**, 525–532 (2016)

21. Michler, T., Wackermann, K., Schweizer, F.: Review and assessment of the effect of hydrogen gas pressure on the embrittlement of steels in gaseous hydrogen environment. Metals **11**(4), 637 (2021)

22. Balytskyi, O.I., Ivaskevich, L.M., Mochylskii, V.M.: Mechanical properties of martensitic steels in gaseous hydrogen. Strength Mater. **44**(1), 64–73 (2012)

23. Balitskii, A., Ivaskevich, L., Mochulskyi, V., Eliasz, J., Skolozdra, O.: Influence of high pressure and high temperature hydrogen on fracture toughness of Ni-containing steels and alloys. Arch. Mech. Eng. **61**(1), 129–138 (2014)

24. Lu, X., Mab, Y., Wang, D.: On the hydrogen embrittlement behavior of nickel-based alloys: alloys 718 and 725. Mater. Sci. Eng. A **792**, 139785 (2020)

Dynamics and Strength of Power Equipment

Study of Reduction of Strength of Composite Plates with Delamination

Andrii Kondratiev[1]([✉]) [iD], Lina Smovziuk[2] [iD], Maryna Shevtsova[2] [iD],
Anton Tsaritsynskyi[2] [iD], and Tetyana Nabokina[2] [iD]

[1] O.M. Beketov National University of Urban Economy in Kharkiv, Marshal Bazhanov. 17,
Kharkiv 61002, Ukraine
andrii.kondratiev@kname.edu.ua

[2] National Aerospace University "Kharkiv Aviation Institute", Chkalova, 17, Kharkiv 61070,
Ukraine

Abstract. Different types of damages may appear and accumulate in the structures made of laminated composites during their production and operation. The most common and serious damages are defects such as discontinuities, i.e. delaminations. The negative impact of such defects on the properties of weakened structures causes significant deterioration of their strength and necessitates the development and improvement of the methods for assessment of the residual strength of such structures. The authors of this paper have developed the method for assessment of strength of the composite plate with the delamination damage. The method allows us to determine the degree of stress concentration in the area of stepwise change in thickness, and identify the most dangerous point where the failure of the structure may begin. It is shown that for the rectangular plate the difference in the strength reduction caused by rectangular and elliptical delamination is from 1 to 3.5% at the different ratios of the defect size. The necessity of taking into account the delamination length when determining the permissible sizes of defects is substantiated. Independence of the strength reduction factor on the geometric dimensions of the plate at the constant relative values of the area and depth of delamination is confirmed. The necessity of consideration of the ratios of sides of the plate weakened by delamination for the development of effective repair methods is shown.

Keywords: Discontinuity · Concentration · Layer-by-layer analysis

1 Introduction

The use of the polymeric composite materials (PCM) in various industries offers a wide range of possibilities both for improvement of existing structures used for the variety of purposes, and for development of new design solutions and processes [1, 2]. The fundamental importance of replacing the traditional structural materials with PCM lies in the fact that instead of metals with the same properties in all directions it is possible to use new materials with the properties, which differ depending on the filler orientation [3]. In spite of high physical and mechanical characteristics (PhMC) of multilayer composites,

their use requires consideration of specific features inherent to them, eg. Probable hidden defects such as material discontinuities along the interfaces of individual layers [4, 5]. Interlaminar defects in structural elements made of PCM associated with imperfections of their manufacturing technology, as well as complex interactions of components, result in decrease in strength of such elements [6]. Delaminations as local violations of the joint action of individual layers are the most common defects in the structures made of multilayer composites [7]. The basis for their occurrence is the layered structure of the PCM itself. Given high cost of PCM, repair of products made of them should be considered relevant [8]. The development of modern technologies for the repair of PCM parts is highly demanded by the leading companies [9]. Choice of the method for repair of such defects in the panel structure directly depends on the degree of impact on its bearing capacity [10]. For example, depending on the dimensions, configuration and location of the delamination in the thickness and area of the panel, installation of the repair patch can be either unnecessary or insufficient measure. Therefore, the need for use of the reinforcement patch is to be justified by the results of assessment of the residual bearing capacity of the panel weakened by delamination.

The purpose of this paper is to study the influence of the delamination parameters and inherent characteristics of the defective structure on its residual strength.

2 Literature Review

The analytical model for studying the stress-strain behavior (SSB) during buckling of composite plates with the rectangular delamination has been developed in [11]. The proposed model allowed investigating the global, local and mixed response to bending of delaminated composite plates. The impact of size of the delamination, its location and various angles of orientation of the PCM fibers on the response of buckling of the composite plates weakened by delamination was studied using numerical examples. In modeling the delamination in [12] it is assumed that interlaminar stresses in the laminated composite are similar to stresses in the adhesive joint. However, there are no reliable mathematical models of the composite material discontinuity defects constructed in that way. The presence of local and boundary effects caused by delamination stipulates certain conditions for the solvability of the classical boundary-value problems and variability of calculations in the process of problem solving. The paper [13] offers the modified approach to analytical modeling of the effect of delamination on the SSB of the weakened composite panel. The traditional approach to determination of the total potential energy has been extended by introducing the modified functional. This functional similar to the total potential energy can take into account the total mechanical coupling of the layers at various ratios of the external actions. Parametric study of the change in the ratio of the delamination size to the depth of its location has been conducted. The method for predicting the SSB of composite plates weakened by delamination is described in [14]. This method is based on the new pattern of laminate splitting for better consistency of the displacement near the delamination boundary. Using the example of compressed multilayer plate with the interlaminar through-thickness delamination, the problems of fracture process were solved in [15]. The studies have shown that for the adequate solution of the problems under consideration, it is advisable to use the numerical models

based on the finite element method. The refined finite element model for assessing the effect of delamination on the strength of the composite panel without significant simplifications and idealization of the damage is developed in [16]. Compressive strength and interlaminar rupture strength are shown as key parameters influencing the residual strength of the damaged panel as a whole. The effects of interlaminar strength, delamination area and depth of its location on the residual strength of the damaged panel are studied in [17]. The paper [18] deals with the development of three-dimensional model of the composite panel damage. The model considers the physical mechanisms of fiber and matrix failure under tension and compression, when the delaminated panel is in three-dimensional stress state. The features of interlaminar damage and the effect of the delamination area on the residual strength of the panel are discussed. The most adequate assessment of the bearing capacity of composite structures with the technological defects concerned can be given using the experimental studies. The impact of the size and location of delamination on the mechanical properties of the laminated composites in buckling is experimentally investigated in [19, 20]. The paper [19] determines the critical delamination size for the composite materials with the various delamination dimensions. The negative impact of the delamination on the mechanical properties of the panel, which is proportional to the delamination location is evaluated. Composite panels with different reinforcement patterns in [20] were artificially delaminated and subjected to the compression test in the fixture, which allowed the local sub-laminate and global modes of the panel buckling to interact. Compared to the panels without delamination, interaction of the modes of buckling reduces the panel buckling strain by up to 29%.

3   Research Methodology

The paper deals only with the defects, which cause the reduction of strength of the product, thereby affecting its overall bearing capacity. It occurs when the material in the damaged area is not capable of perceiving and transmitting the applied loads [19, 20]. Within the framework of this assumption, a computational model of the plate with stepwise variable thickness was used for the determination of the panel SSB [21]. We considered the flat rectangular plate with the specified delamination comprising k orthotropic layers. It was assumed that the coordinate plane (x, y) coincides with the lower surface of the plate, and the coordinate axis z is directed upwards (Fig. 1). The delamination actually being of arbitrary shape was approximated by the rectangle (or ellipse) with the area equal to that of the real delamination.
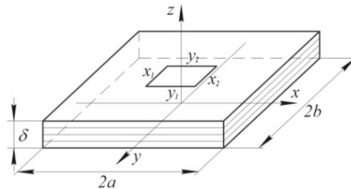
Fig. 1. Geometrical parameters of the plate and delamination.

Since significant transverse shear deformations may occur in the adhesive layer providing the joint action of the structure and the reinforcing patch, an assumption has been made on fulfillment of the straight-line hypothesis within each individual layer. The joint deformation of skin layers is ensured by fulfilling the condition of continuity of movements on their interfaces. To reduce three-dimensional problem of the theory of elasticity to two-dimensional one and construct a solution using the Ritz-Timoshenko method, displacements of the points of the layer interface surfaces were defined as the functions

$$u_i(x, y) = (y^2 - b^2)(u_{1,i} + u_{2,i}x + u_{3,i}y + u_{4,i}x^2 + u_{5,i}xy + \ldots + u_{st,i}y^{st});$$
$$v_i(x, y) = (x^2 - a^2)(v_{1,i} + v_{2,i}x + v_{3,i}y + v_{4,i}x^2 + v_{5,i}xy + \ldots + v_{st,i}y^{st}); \quad (1)$$
$$\omega(x, y) = (x^2 - a^2)(y^2 - b^2)(\omega_1 + \omega_2 x + \omega_3 y + \omega_4 x^2 + \omega_5 xy + \ldots + \omega_{st}y^{st}),$$

where st – degree of the polynomial determining the plate displacement; $u_{i,j}$, $v_{i,j}$, ω_i – unknown coefficients to be determined. The convergence was satisfactory with $st = 8$ for the case of asymmetric delamination location and 4 for symmetric one. The error in determining the deflection, normal and shear stresses did not exceed 0.5%.

According to the assumption, tangential displacement of the points u_x^i and u_y^i of the i-th layer are distributed linearly over its thickness and are determined as follows:

$$u_x^i = u_i + (u_{i+1} - u_i)(z - z_i)/\delta_i; u_y^i = v_i + (v_{i+1} - v_i)(z - z_i)/\delta_i. \quad (2)$$

The displacement u_z^i remains constant for all layers of the plate considering the assumption of no compression and is equal to ω.

Stresses and strains of the i-th layer are interrelated using the generalized Hooke's law with regard to the presence of only one plane of elastic symmetry parallel to the middle surface of the skin for each layer and neglecting smallness of the transverse stresses σ_z.

Stepwise change of the panel thickness or local change of its PhMC was modeled by defining the coefficients of stiffness matrix b_{ij} of the relevant layers with the use of special functions. To switch from the design model of undamaged plate to the model of the plate with a delamination, auxiliary function F has been introduced to simulate the defect:

$$F = 1 - H(x - x_1)H(x - x_2)H(y - y_1)H(y - y_2) \quad (3)$$

where x_1, x_2, y_1, y_2 – coordinates of boundaries along x and y axes of the stepwise change in the plate thickness in the i-th layer (Fig. 1); H – Heaviside function.

For the SSB determination, the energy approach was used, according to which the functional of the panel total deformation energy is equal to the sum of deformation energies of the individual layers, taking into account the action of external forces

$$U = A + \frac{1}{2} \sum_{i=1}^{k} \iint_S \int_{z_i}^{z_{i+1}} \left\{ \sigma^i \varepsilon^i \right\} A_1 A_2 \, dx \, dy \, dz, \quad (4)$$

where A – total action of external forces on the panel; z_i and z_{i+1} – coordinates of the surfaces bounding the i-th layer; k – number of layers in the panel.

After obtaining an approximate solution in the displacements based on the Lagrange variation principle, stresses and strains can be finally determined at any point of the structure under study.

To assess the degree of impact of the defect on strength of the structure, we used the strength reduction factor:

$$K = \sigma_{eq}^{delam}/\sigma_{eq}^{0}, \tag{5}$$

where σ_{eq}^{delam} and σ_{eq}^{0} – maximum values of the relative equivalent stresses in the panel with a defect and undamaged panel, respectively.

For determination of the relative equivalent stress in the laminated composite panel, the Von Mises-Hill energy criterion of strength was chosen:

$$\sigma_{eq} = \sqrt{\frac{\sigma_x^2}{F_x^2} - \frac{\sigma_x\sigma_y}{F_xF_y} + \frac{\sigma_y^2}{F_y^2} + \frac{\tau_{xy}^2}{F_{xy}^2} + \frac{\tau_{xz}^2}{F_{xz}^2} + \frac{\tau_{yz}^2}{F_{yz}^2}}, \tag{6}$$

where σ_x, σ_y, τ_{xy}, τ_{xz}, τ_{yz} – normal and tangential effective stresses, F_x, F_y, F_{xy}, F_{xz}, F_{yz} – PCM ultimate strength values.

The developed mathematical model used to calculate the SSB of the defective structure considers the panel as a set of interconnected orthotropic layers with arbitrary PhMC. The strength criterion (6) in this setting should be written separately for each layer. In this case, the ultimate bearing capacity of the panel as a whole will be defined as the initiation of a fracture of any of its layers.

When we use the proposed method for SSB determination, the normal stresses σ_x, σ_y and tangential stress τ_{xy} within the layer vary according to the linear law, and the transverse shear stresses τ_{xz} and τ_{yz} are constant. Therefore, the equivalent stresses in the i-th layer are maximal at the interfaces of layers z_i and z_{i+1}. Consequently, maximum value of the relative equivalent stresses σ_{eq}^{max} for the panel as a whole is equal to maximum value of the equivalent stress values σ_{eq}^{i}, calculated at the most loaded point of the i-th layer ($i = 1\ldots k$).

Using the described approach, we studied the influence of individual delamination parameters on the strength of the flat rectangular panel fixed along the contour. This panel was made of UT-900-2.5 woven carbon fiber composite based on EDT-69N binder with the characteristics given further: ultimate tensile strength along the grain –917 MPa; ultimate tensile strength across the grain – 881 MPa; modulus of elasticity along the grain – 69 GPa; modulus of elasticity across the grain – 67 GPa; ultimate compressive strength along the grain – 55 MPa; ultimate compressive strength across the grain – 50 MPa; ultimate shear strength in the laying plane – 75 MPa; shear modulus in the laying plane – 5.5 GPa; Poisson's ratio – 0.32; layup pattern – $[0°/90°/0°/90°]_S$.

The panel is under the action of the uniformly distributed lateral load. In the process of the plate calculations, conditions for its edges' fixing correspond to the boundary conditions of free bearing. The fixing conditions as a set of static and geometric boundary conditions are written at $x = \pm a$ as follows: $\omega = 0$, $v = 0$, $\theta_y = 0$, $N_x = 0$, $M_x = 0$; at $x = \pm b$: $\omega = 0$, $u = 0$, $\theta_x = 0$, $N_y = 0$, $M_y = 0$.

We assessed the decrease in strength of the structure with a defect when the shape, location, dimensions, depth of delamination and dimensions of the panel were changed.

4   Results and Discussion

According to study of [15, 21] for the laminated panel under action of tensile and compressive loads, surface delaminations of the rectangular and elliptical shape are the most common. This classification is also true for the action of the transverse load, since the outer layers of the panel under bending are in stretched/compressed state. Based on this, we studied the impact of the defect shape on the reduction of safety factor of the considered rectangular panel (Fig. 2).

The analysis of results allowed us to conclude that for the rectangular panel under study the difference in strength reduction caused by the delamination of rectangular and elliptical shape is from 1 to 3.5% at the different ratios of defect size.

Delamination dimensions and depth are the most important characteristics of a defect. Studies have shown that for a given shape and area of the delamination, a certain critical ratio of the delamination dimensions a_1/b_1 (sides for a rectangle and axes for an ellipse) was found. This led to maximum decrease in strength at $S_{delam} = const$.
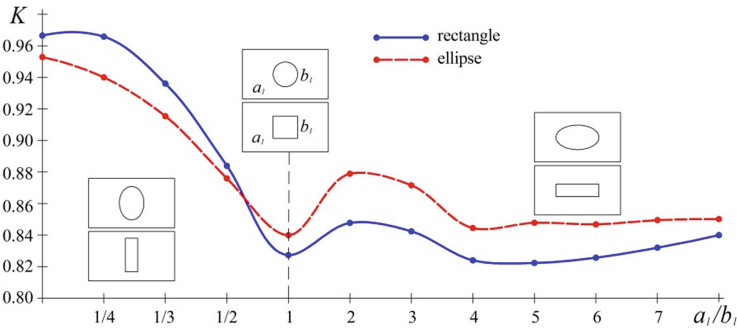
Fig. 2. Dependence of the strength reduction factor on the ratio of delamination sides for rectangular panels.

Therefore, when determining the admissible parameters of a defect, both the area and critical length of the defect are taken into account at $a_1/b_1 \rightarrow K_{min}$.

The impact of the defect size was studied on the example of $140 \times 70 \times 1.8$ mm flat rectangular panel. Under the assumption about exclusion of the material in the defect zone, it is suggested that the applied external load is redistributed between undamaged layers of the panel. Therefore, maximum delamination depth was taken equal to half the thickness of the plate with no damage. The dependences of the strength reduction factor $K(l)$ on the delamination length were plotted for the relative areas $\overline{S} = 0.01$ and 0.09 and different defect depths $\overline{\delta}$ (Fig. 3). Here and elsewhere $\overline{S} = S_{delam}/S_0$; $\overline{\delta} = \delta_{delam}/\delta_0$.

Using the constructed graphs, we determined the values of the critical delamination length l_{cr} and corresponding minimum strength reduction factors K for each combination of ($\overline{S} - \overline{\delta}$), as shown in Fig. 4.

Location (along with dimensions) is one of important parameters of the delamination. The impact of this factor on the strength reduction factor of the damaged structure was studied using the example of $100 \times 100 \times 1.8$ mm square panel with the layup pattern
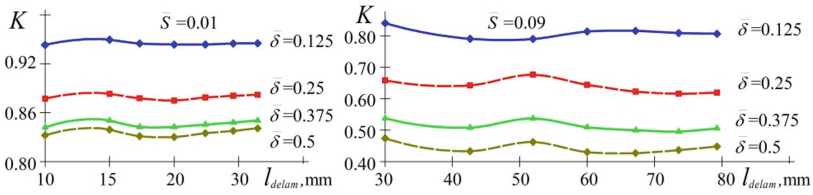
Fig. 3. Dependence of the strength reduction factor on the delamination length at different values of $\bar{S}$ and $\bar{\delta}$.
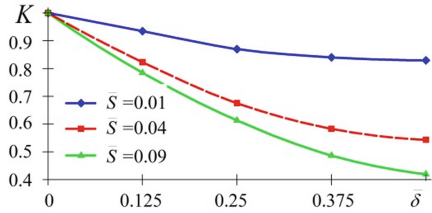
Fig. 4. Dependence of the strength reduction factor on the relative delamination length for the rectangular plate ($a = 2b$).

of $[0°/90°/0°/90°]_S$. In our case, it was square-shaped delamination of the relative area and depth equal to 0.04 and 0.125, respectively.

In order to take into account the impact of the delamination location on the bearing capacity of the panel with a defect, we introduced a correction factor $\gamma = K_{(0,0)}/K_{max}$, where K_{max} – maximum strength reduction factor obtained after changing the position of the delamination center; $K_{(0,0)}$ – strength reduction factor for the case when delamination is in the center of the panel. Numerical results of calculations are shown in Fig. 5 as a dependence of the coefficient γ on the position of the delamination center.
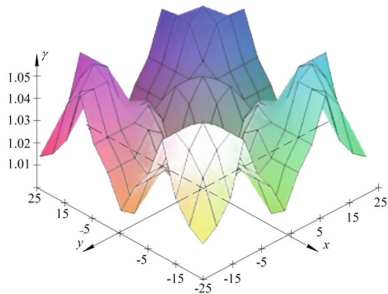
Fig. 5. Dependence of the coefficient γ on the coordinates of the position of the delamination center for square panel under study.

Coefficient γ for the square panel under study, taking into account the delamination location, is 1.06.

As is shown above, change in the shape of the delamination has a significant impact on the residual strength of the panel with a defect. Figure 6 represents the dependences of the strength reduction factor K and the relative critical delamination length $\bar{l}_{cr}$ for the ratio of panel sides *A/B*.
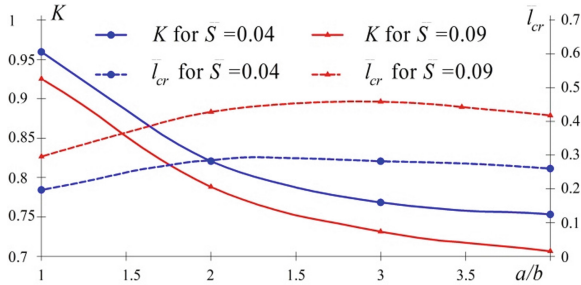
Fig. 6. Dependence of the strength reduction factor and the critical size of the defect on the ratio of the panel side lengths.

The results obtained demonstrate that the structure is more sensitive to the defect when the panel length is increased.

Since the curves of the strength reduction factor tend to asymptote as the *A/B* value increases, certain critical elongation of the panel can be determined, above which the strength reduction factor remains constant. According to results shown in Fig. 6, the critical ratio of sidesє dimensions is equal to 4 for the rectangular panels of UT-900-2.5 carbon fiber composite based on the EDT-69N binder. As a consequence, parameters of the defect which satisfy the permissible decrease in strength in the panel of critical length are acceptable for panels with any ratio of sides made of the material under study. In contrast to the classical theory of laminated plates [11, 13], the proposed model gives an opportunity to simplify three-dimensional problem by setting the displacement field on interfaces of the layers and their linear interpolation over the plate thickness, taking into account the transverse shear deformations. Unlike the papers [12, 15, 16], where the transverse shear was considered in whatever way, the proposed model allowed modelling the structure of step-variable thickness. The proposed mathematical model is characterized by the certain field of applicability, where the accuracy of results corresponds to the required one. Based on the comparison of results with the literature data [19, 21], the error of the theoretical determination of deflection does not exceed 3%, and that of stresses – 8%. It corresponds to sufficiently high accuracy of the description of stress-strain behavior of a multilayer plate.

5   Conclusions

In accordance with the assigned purpose, a new method has been developed for assessment of strength of the composite plate with the delamination damage. The method allows us to determine the degree of stress concentration in the area of stepwise change in thickness, and identify the most dangerous point where the failure of the structure may

begin. The impact of elliptical and rectangular defects on the strength reduction factor has been analyzed. The need to consider the ratio of the panel sides in the development of effective standards for the acceptance of composite structures has been shown. The proposed method can be successfully used to solve practical problems such as determination of the stress–strain behavior of a damaged structure or structure after repair, specification of the permissible delamination dimensions, and defining the parameters of the bonded repair process.

References

1. Rodichev, Y.M., Smetankina, N.V., Shupikov, O.M., Ugrimov, S.V.: Stress-strain assessment for laminated aircraft cockpit windows at static and dynamic loads. Strength Mater. **50**(6), 868–873 (2019). https://doi.org/10.1007/s11223-019-00033-4

2. Fomin, O., Gorbunov, M., Gerlici, J., Vatulia, G., Lovska, A., Kravchenko, K.: Research into the strength of an open wagon with double sidewalls filled with aluminium foam. Materials **14**(12), 3420 (2021). https://doi.org/10.3390/ma14123420

3. Kondratiev, A.: Improving the mass efficiency of a composite launch vehicle head fairing with a sandwich structure. East.-Eur. J. Enterp. Technol. **6**(7(102)), 6–18 (2019). https://doi.org/10.15587/1729-4061.2019.184551

4. Kombarov, V., Kryzhyvets, Y., Biletskyi, I., Tsegelnyk, Y., Aksonov, Y., Piddubna, L.: Numerical control of fiberglass pipe bends manufacturing. In: IEEE 2nd KhPI Week on Advanced Technology, pp. 357–362 (2021). https://doi.org/10.1109/KhPIWeek53812.2021.9570068

5. Kondratiev, A., Slivinsky, M.: Method for determining the thickness of a binder layer at its non-uniform mass transfer inside the channel of a honeycomb filler made from polymeric paper. East.-Eur. J. Enterp. Technol. **6**(5(96)), 42–48 (2018). https://doi.org/10.15587/1729-4061.2018.150387

6. Kostyk, K., Hatala, M., Kostyk, V., Ivanov, V., Pavlenko, I., Duplakova, D.: Simulation of diffusion processes in chemical and thermal processing of machine parts. Processes **9**(4), 698 (2021). https://doi.org/10.3390/pr9040698

7. Deng, B., Shi, Y., Yu, T., Zhao, P.: Influence mechanism and optimization analysis of technological parameters for the composite prepreg tape winding process. Polymers **12**(8), 1843 (2020). https://doi.org/10.3390/polym12081843

8. Otrosh, Y., Kovalov, A., Semkiv, O., Rudeshko, I., Diven, V.: Methodology remaining lifetime determination of the building structures. MATEC Web Conf. **230**, 02023 (2018). https://doi.org/10.1051/matecconf/201823002023

9. Fomin, O., Lovska, A., Kučera, P., Píštěk, V.: Substantiation of improvements for the bearing structure of an open car to provide a higher security during rail/sea transportation. J. Mar. Sci. Eng. **9**(8), 873 (2021). https://doi.org/10.3390/jmse9080873

10. Archer, E., McIlhagger, A.: 15 – Repair of damaged aerospace composite structures. In: Woodhead Publishing Series in Composites Science and Engineering, Polymer Composites in the Aerospace Industry, pp. 441–459. Woodhead Publishing (2020). https://doi.org/10.1016/B978-0-08-102679-3.00015-0

11. Chen, X., Wu, Z., Nie, G., Weaver, P.: Buckling analysis of variable angle tow composite plates with a through-the-width or an embedded rectangular delamination. Int. J. Solids Struct. **138**, 166–180 (2018). https://doi.org/10.1016/j.ijsolstr.2018.01.010

12. Barakhov, K., Dvoretska, D., Poliakov, O.: One-dimensional axisymmetric model of the stress state of the adhesive joint. In: Nechyporuk, M., Pavlikov, V., Kritskiy, D. (eds.) ICTM 2020. LNNS, vol. 188, pp. 310–319. Springer, Cham (2021). https://doi.org/10.1007/978-3-030-66717-7_26

13. Köllner, A.: Predicting buckling-driven delamination propagation in composite laminates: an analytical modelling approach. Compos. Struct. **266**, 113776 (2021). https://doi.org/10.1016/j.compstruct.2021.113776

14. Shabanijafroudi, N., Ganesan, R.: A new methodology for buckling, postbuckling and delamination growth behavior of composite laminates with delamination. Compos. Struct. **268**, 113951 (2021). https://doi.org/10.1016/j.compstruct.2021.113951

15. Chermoshentseva, A., Pokrovskiy. A., Bokhoeva, L.: The behavior of delaminations in composite materials – experimental results. In: IOP Conference Series: Materials Science and Engineering, vol. 116, p. 012005 (2016). https://doi.org/10.1088/1757-899X/116/1/012005

16. Abir, M.R., Tay, T.E., Ridga, M., Lee, H.P.: Modelling damage growth in composites subjected to impact and compression after impact. Compos. Struct. **168**, 13–25 (2017). https://doi.org/10.1016/j.compstruct.2017.02.018

17. Sun, X.C., Hallet, S.R.: Failure mechanisms and damage evolution of laminated composites under compression after impact (CAI): experimental and numerical study. Compos. Part A **104**, 41–59 (2018). https://doi.org/10.1016/j.compositesa.2017.10.026

18. Liu, H., Falzon, B.G., Tan, W.: Predicting the compression-after-impact (CAI) strength of damage-tolerant hybrid unidirectional/woven carbon-fibre reinforced composite laminates. Compos. Part A: Appl. Sci. Manuf. **105**, 189–202 (2018). https://doi.org/10.1016/j.compositesa.2017.11.021

19. Ipek, G., Arman, Y., Celik, A.: The effect of delamination size and location to buckling behavior of composite materials. Compos. Part B **155**, 69–76 (2018). https://doi.org/10.1016/j.compositesb.2018.08.009

20. Rhead, A.T., Butler, R., Hunt, G.W.: Compressive strength of composite laminates with delamination-induced interaction of panel and sublaminate buckling modes. Compos. Struct. **171**, 326–334 (2017). https://doi.org/10.1016/j.compstruct.2017.03.011

21. Kondratiev, A., Píštěk, V., Smovziuk, L., Shevtsova, M., Fomina, A., Kučera, P.: Stress–strain behaviour of reparable composite panel with step–variable thickness. Polymers **13**(21), 3830 (2021). https://doi.org/10.3390/polym13213830

Comparative Analysis of Numerical Methods for Solving Linear Equation Systems for Poisson's Equation

Svitlana Moiseienko[1] , Uliana Tuchyna[2] , Dmytro Redchyts[2(✉)] ,
Volodymyr Zaika[2] , and Inna Vygodner[1]

[1] Kherson National Technical University, Beryslavske Highway, 24, Kherson 73008, Ukraine
`4moiseenko@ukr.net`
[2] Institute of Transport Systems and Technologies of the NASU, Pysarzhevskoho Str., 5, Dnipro 49005, Ukraine
`Redchits_da@ua.fm`

Abstract. This paper reviews stationary and nonstationary iterative methods for solving large sparse systems of linear equations (SLE) for elliptic equations of mathematical physics. Nonstationary iterative methods for solving large sparse SLE are compared on the problem of electric potential distribution in a region. Original equation of electrostatics is discretized using the Finite Volume Method in curvilinear coordinates. The central difference scheme of the second order accuracy was involved to approximate the derivatives in equation of electrostatics. Approximation for original equation generates a symmetric positive definite matrix of large spectral radius. Among iterative methods variety this study considers Conjugate Gradient (CG) method, Generalized Minimal Residual (GMRES) method and Biconjugate Gradient (BiCG) method as the most popular nonlinear SLE solving methods. The ILU(0) decomposition is used as a preconditioner. A residual norm serves as a convergence criterion. It was assumed that the system of linear equations is solved if current residual norm is seven orders less than the initial one. GMRES method showed some good and stable convergence for solving systems of linear equations with sparse symmetric positive definite matrix. It was established that GMRES method for sparse matrices has high computing efficiency for solving elliptic problems.

Keywords: Numerical methods for solving the systems of linear algebraic equations · SLE · Equations of elliptic type · Krylov subspace · GMRES · CG · BiCG · MINRES · BiCGSTAB

1 Introduction

Mathematical physics equations of different types underlie the numerical simulation of physical processes. Discrete analogues of original differential equations require solving sparse systems of linear equations (SLE). These systems can be extremely large, for example like ones describing coupled tasks of computational aerodynamics, electrodynamics, heat transferring and solid mechanics [1, 20, 21]. Solving of SLE takes the

biggest part of computing equipment capacity, therefore a selection of optimal method for solving of linear equation systems is one of mathematical simulation key problems.

All methods applied for solving linear equations systems can be divided into two classes: direct and iterative methods [2–6]. By the term direct method, we mean a method that theoretically gives the exact value of all variables in a finite number of arithmetic operations (Cramer's rule). Iterative methods provide the solution as the limit of sequence of vectors obtained over the same mathematical procedure named as iterative process or successive approximation [7, 8].

The main arguments in favor of iterative methods are to reduce computer storage and processor time. Another iterative methods advantage is their convenience for modern computing equipment. As of solving large sparse system of linear equations, direct methods become ineffective due to round-off accumulation and dramatic number of mathematical operations. Iterative methods provide solution of SLE with a prescribed error. Their advantage over direct methods is their superiority in convergence speed and convenience of implementation in practice as well.

Generally, iterative methods are used for sparse SLE that arise due to finite-element, finite-different or finite-volume approximation of partial differential equations (equation systems). Iterative methods are often combined with preconditioning operators that increase the convergence speed of the method. The selection of preconditioning operator is a separate task. At the same time, iterative methods can be successfully implemented for solving some large dense SLEs.

The most effective and robust iterative methods for solving these systems of equations are so-called projection-based methods and especially those that are related to Krylov subspace. High level of robust distinguish them among all iterative methods. Studies [17, 18] describe iterative methods and focus on different forms of preconditioning. This paper gives a review of methods for solving SLE based on Krylov subspace. Numerical algorithms of iterative methods for SLE solving are described in [22, 23].

It should be noted that nowadays there are no universal methods working equally well for different classes of problems. Generally, the challenge is to select the most effective method for each problem.

This paper aims to compare SLE solving methods with respect to mathematical physics equations of elliptic type. First, we review the main stationary and nonstationary iterative methods in their historical evolution. The third part describes iterative methods advantages and disadvantages, influencing their efficiency for SLE solving, which correspond to considering class of problems. The fourth and fifth parts comprise the problem statement and discussion of obtained results according to assumed convergence criterion for the problem of electric potential distribution in specified region.

2 Iterative Methods for Solving Systems of Linear Algebraic Equations

Iterative methods are comprised of stationary and nonstationary methods [2, 3].

Stationary iterative method is a method that can be represented in a following simple form:

$$x^{k+1} = \mathbf{A}\,x^k + c, \tag{1}$$

where **A** and c are not dependent from iteration number k. Otherwise the method is nonstationary.

Stationary iterative methods have been used for a long time and are clear and easy for implementation, but commonly less effective in comparison to nonstationary methods. Nonstationary methods are relatively new and can be highly effective in terms of computing capacity [2, 3].

The rate of iterative method convergence substantially depends on matrix spectral radius. Thus, iterative methods generally comprise the second matrix that transforms matrix **A** into matrix of less spectral radius. This transformation matrix is called a preconditioning matrix. Good preconditioning enhances convergence of iterative method. Without preconditioning, the iterative method may not converge [3, 22, 23].

There are lots of iterative methods. Here we consider ones illustrating historical evolution of iterative methods for solving sparse systems of linear equations.

2.1 Stationary Methods

– The Jacobi method suppose the solution for each variable locally by the other variables; the solution for each variable is found once per iteration. It is clear and easy to implement, but slowly converging.
– The Gauss-Seidel method can be considered as the Jacobi method modification. The key idea consists in involving of new values of each variable as they are known, meanwhile in Jacobi method they remain unchanged until the next iteration.
– Successive Overrelaxation method (SOR) can be derived from the Gauss-Seidel method if add an extrapolation parameter ω. If ω is optimally selected, SOR may converge by an order of magnitude faster than Gauss-Seidel method.
– Symmetric Successive Overrelaxation method (SSOR). As itself it has no advantages over SOR, but can be applied as a preconditioner for nonstationary methods.

2.2 Nonstationary Methods

– Conjugate Gradient method (CG) is a method for defining function local minimum based on information about its value and gradient [3, 4].
– MINimum RESidual method (MINRES). This method is a computational alternative of CG method for a matrix with symmetric and positive indefinite coefficients [3, 18].
– Generalized Minimal RESidual method (GMRES). As an extension of MINRES, it also generates a sequence of orthogonal vectors with further solving them through a least-squares technique. However, in contrast to MINRES and GC it requires high storage capacity because the whole sequence is to be saved. Therefore, the generally used are "restarted" versions with limiting the computing and storage demand via the fixed number of vectors to be generated. The GMRES is applicable for general nonsymmetric matrices [2, 17].

- BiConjugate Gradient method (BiCG). This method provides two mutually orthogonal or "bi-orthogonal" sequences of conjugate gradient vectors. One of them is generated on basis of the system with original coefficient matrix $\mathbf{A}$ and other one – on $\mathbf{A^T}$. It takes limited storage. This method is applicable for symmetric matrices, but the convergence might be irregular. BiCG undertakes calculation of a matrix-vector product and a transpose product at each iteration [22].
- Chebyshev Iteration method. This method provides recursively defying of polynomials with coefficients selected to minimize the norm of residual in a min-max sense. For this case the coefficient matrices must be positive definite and the extremal eigenvalues are to be known. The advantage of this method consists in no inner multiplication [3].

3   Comparative Assessment of Iterative Methods for Solving Systems of Linear Algebraic Equations

SLE solving efficiency significantly depends on selection of iterative method. The advantages and disadvantages of iterative methods are considered below [3, 22, 23].

1. Jacobi method [2]

   - This method is easy for implementation, but if the matrix is not diagonally dominant, it is better to consider it as an introduction to iterative methods or as preconditioner for nonstationary methods.
   - Easy for paralleling.

2. Gauss-Seidel method [3]

   - The convergence is faster than with Jacobi method, but generally, it cannot compete with nonstationary methods.
   - It is applicable for diagonally dominant matrixes or symmetric positive definite matrixes.
   - Paralleling performance depends on coefficient matrix structure.
   - It is a particular case of SOR method, obtained by setting $\omega = 1$.

3. Successive Overrelaxation method [2, 3]

   - SOR provides an acceleration of the Gauss-Seidel method convergence ($\omega > 1$, upper relaxation); also SOR can provide the convergence in case when the Gauss-Seidel method is not converged ($0 < \omega < 1$, lower relaxation).
   - The convergence speed mainly depends on parameter ω; the optimum value of ω can be estimated on the spectral radius of Jacobi matrix.
   - Paralleling performance depends on structure of coefficient matrix.

4. Conjugate Gradient method [5]

   – CG is efficient when the system is symmetric positive definite.
   – The speed of convergence depends on a range of conditions.
   – Paralleling performance significantly depends on coefficients matrix and on preconditioner.

5. Generalized Minimal Residual method [17]

   – GMRES is efficient when the matrices are non symmetric.
   – GMRES minimizes the residual for fixed number of iterations, but the cost of these iterations grows.
   – In order to limit the growing of computational costs and number of steps per iteration GMRES should be restarted.
   – GMRES requires only matrix-vector products with matrix of coefficients.
   – The number of inner products rises linearly with the number of iterations up to the restart point. As for realization based on classical Gram-Schmidt process, inner products are independent, so together they indicate only one point of synchronization. More stable realization relies on using modified Gram-Schmidt orthogonalization and has one synchronization point per each inner product.

6. Biconjugate Gradient method [22]

   – BiCG method is applicable for non symmetric matrices.
   – BiCG method requires the matrix-vector product of matrix coefficients and transposed matrix.
   – Paralleling performance is similar to CG performance.

7. Chebyshev Iteration method [2, 3]

   – It is applicable for non symmetric matrices.
   – Computational structure is similar to CG method, but it does not comprise synchronization points.
   – Adaptive Chebyshev method can be combined with CG or GMRES methods.

Selecting the "best" method for a given class of problems is largely a matter of trial and error. Although among the variety of iterative methods, the most efficient are CG, GMRES and BiCG methods [2, 3].

4 Problem Statement

We will compare iterative methods for solving large sparse systems of linear equations in example by the problem of electric potential distribution in specified region [11, 12].

The equation of electric field excluding resultant density of space and surface charge represents the Laplace's equation

$$\nabla(\varepsilon_r \nabla \varphi) = 0, \tag{2}$$

where ε_r – relative dielectric permittivity, φ – electric potential. It is elliptic type equation.

As the initial conditions for Laplace's equation we set the null distribution of electric potential and as the boundary condition we used the voltage, applied to electrodes. To solve this equation we'll use corresponding values of relative dielectric permittivity for air and dielectric. The voltage $\varphi = 30$ kV is applied to exposed electrode and covered electrode is loaded by null potential. At external boundaries, we set the Neumann condition. The layout diagram of computational domain is given in Fig. 1.

Original equation of electrostatics was discretized using the Finite Volume Method in curvilinear coordinates [9, 10, 13–16]. The central difference scheme of the second order accuracy was involved to approximate the derivatives in equation of electrostatics.

Original Eq. (2) discretizing followed finding the solution for obtained system of linear equations using CG, GMRES and BiCG methods [19, 24].

5   Results and Discussion

The dielectric is represented by Macor ceramic material with relative dielectric permittivity ε_r and thickness d = 2.1 mm. Relative dielectric permittivity for air is $\varepsilon_r = 1.0$. Two cuprum lines represent electrodes. The exposed electrode length is equal to 5 mm, and the covered electrode length is equal to 25 mm. The origin of coordinate is located on the right edge of exposed electrode.

Multi-block structured grid describing computational domain geometry comprises 5 blocks of a total number of nodes equal to 17275 (see Fig. 2). The value of minimum step along the right edge of exposed electrode was selected equal to 10^{-5}.

The discretization of original equation gives a sparse matrix **A** where the total number of non-zero elements is 94663, including diagonal ones.

The Laplace's equation is a differential equation and elliptic in nature. Because it comprises variable coefficients (second derivatives coefficients) the special methods for solving, for example like fast Fourier transform, are inapplicable. Thus, the question is, what solver is better to use for obtained system of linear equations.

Approximation for Laplace's equation generates the symmetric positive definite matrix of large spectral radius. Hence, the matrix is ill-conditioned.

We'll compare CG, GMRES and BiCG methods as the most popular SLE solving nonlinear methods. The ILU(0) decomposition is used as a preconditioner. Direct methods for solving of SLE are not considered due to their initially poor convergence for this class of equations.

In result, we defined the distribution of electric potential in a region (see Fig. 3). For better illustrating and understanding we denoted obtained results to maximum value of voltage $\varphi = 30$ kV.

A residual norm serves as a convergence criterion. The system of linear equations is solved if current residual norm is seven orders less than the initial one.

Dependences of residual norm on number of iterations for CG, GMRES and BiCG methods are presented in Fig. 4. Obtained results show that CG method does not converge. Although BiCG methods converges but the speed of convergence and behavior put in doubt this method robustness. Only GMRES method showed good and stable convergence for solving of systems of linear equations. So this solver can be recommended as robust for solving SLE with symmetric positive definite matrix **A**.
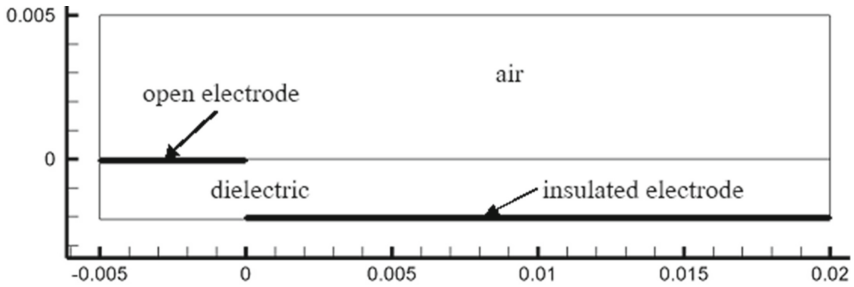
Fig. 1. Layout diagram
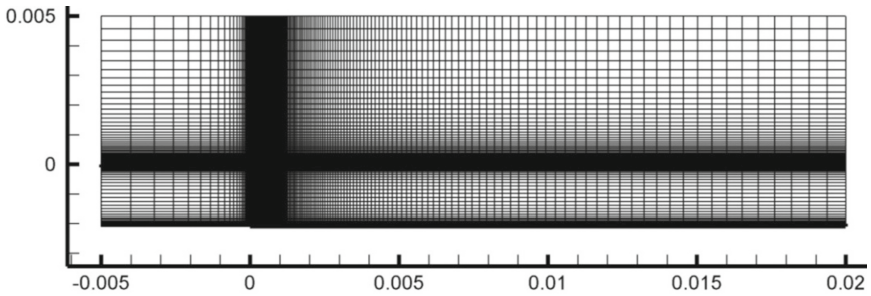
Fig. 2. Multi-block structured grid
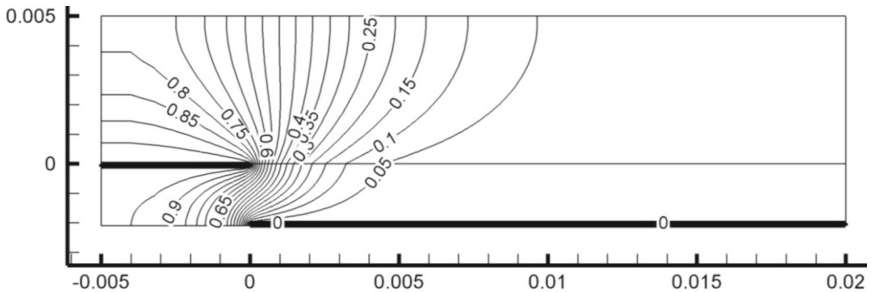
Fig. 3. Distribution of electric potential
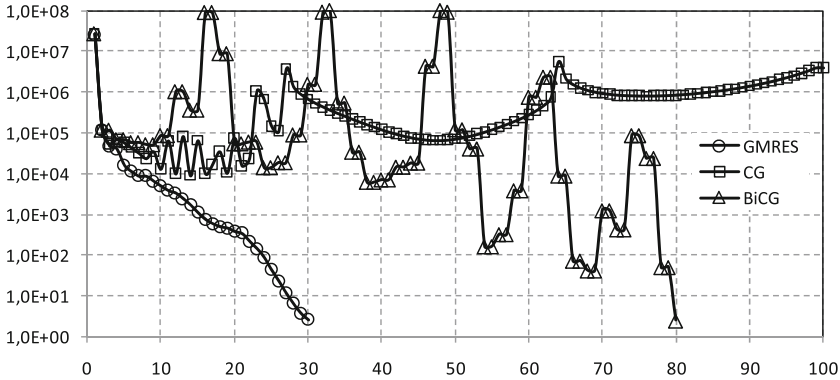
Fig. 4. Dependence of residual norm on the number of iterations

6 Conclusions

In this paper, we have reviewed stationary and nonstationary iterative methods for solving large sparse systems of linear equations for elliptic equations of mathematical physics. The study was conducted in example by the problem of electric potential distribution in specified region. The discretization of original equation of electrostatics with using the Finite Volume Method in curvilinear coordinates and approximation of the derivatives, involving the central difference scheme of the second order accuracy, have led to generation of symmetric positive definite matrix of large spectral radius. Therefore, taking into account advantages and disadvantages, the CG, GMRES and BiCG methods were selected as the most efficient and suitable for this study. They have been compared according to convergence criterion, so the system of linear equations was assumed solved when the current residual norm was seven orders less than the initial one. Among considered methods, only GMRES method ensured good and stable convergence for solving SLE with sparse symmetric positive definite matrix and highly effective for computing elliptic problems.

References

1. Anderson, J.: Computational Fluid Dynamics. McGraw-Hill Education, New York (1995)
2. Axelsson, O.: Iterative Solution Methods. Cambridge University Press, Cambridge (1994)
3. Barrett, R., Berry, M., Chan, T.: Templates for the Solution of Linear Systems: Building Blocks for Iterative Methods. SIAM, Philadelphia (1994)
4. Fletcher, R.: Conjugate gradient methods for indefinite systems. In: Watson, G.A. (ed.) Numerical Analysis. LNM, vol. 506, pp. 73–89. Springer, Heidelberg (1976). https://doi.org/10.1007/BFb0080116
5. Freund, R., Nachtigal, N.: Iterative solution of linear systems. In: Acta Numerica. Cambridge University Press, Cambridge (1992)
6. Golub, G., Van Loan, C.: Matrix Computations. The Johns Hopkins University Press, Baltimore (1996)
7. Lanczos, C., Res, J.: An iteration method for the solution of the eigenvalue problem of linear differential and integral operators. J. Res. Natl. Bur. Stand. **45**, 225–280 (1950)

8. Paige, C., Saunders, M.: Solution of sparse indefinite systems of linear equations. SIAM J. Numer. Anal. **12**, 617–629 (1975)
9. Prikhod'ko, A., Redtchits, D.: Numerical modeling of a viscous incompressible un-steady separated flow past a rotating cylinder. Fluid Dyn. **6**(44), 823–829 (2009)
10. Redchyts, D., Gourjii, A., Moiseienko, S., Bilousova, T.: Aerodynamics of the turbulent flow around a multi-element airfoil in cruse configuration and in takeoff and landing configuration. East.-Eur. J. Enterp. Technol. **9**(5), 36–41 (2019)
11. Redchyts, D., Moiseienko, S.: Numerical simulation of unsteady flows of cold plasma during plasma actuator operation. Space Sci. Technol. **27**(1), 85–96 (2021)
12. Redchyts, D., Shkvar, E., Moiseienko, S.: Control of Karman vortex street by using plasma actuators. Fluid Dyn. Mater. Process. **15**(5), 509–525 (2019)
13. Roe, P.: Characteristic-based schemes for the Euler equations. Annu. Rev. Fluid Mech. **18**, 337–365 (1986)
14. Roe, P.: Approximate Riemann schemes. J. Comput. Phys. **43**, 357–372 (1981)
15. Rogers, S., Kwak, D.: An upwind differencing scheme for the incompressible Navier-Strokes equations. Appl. Numer. Math. **8**(1), 43–64 (1991)
16. Rogers, S., Kwak, D.: Upwind differencing scheme for the time-accurate incompressible Navier-Stokes equations. AIAA J. **28**(2), 253–262 (1990)
17. Saad, Y.: GMRES a generalized minimal residual algorithm for solving non-symmetric linear systems. SIAM J. Sci. Statist. Comput. **7**, 856–869 (1986)
18. Saad, Y.: Iterative Methods for Sparse Linear Systems. PWS Publishing Company, Boston (1996)
19. Sonneveld, P.: CGS a fast Lanczos-type solver for non-symmetric linear systems. SIAM J. Sci. Statist. Comput. **10**, 36–52 (1989)
20. Spalart, P., Allmaras, P.: A one-equation turbulence model for aerodynamic flow. AIAA Paper **12**, 439–478 (1992)
21. Tannehill, J., Anderson, D., Pletcher, R.: Computational Fluid Mechanics and Heat Transfer, 2nd edn. Taylor & Francis, New York (1997)
22. Van der Vorst, H.: Bi-CGSTAB: a fast and smoothly converging-variant of Bi-CG for the solution of non-symmetric linear systems. SIAM J. Sci. Statist. Comput. **13**, 631–644 (1992)
23. Van der Vorst, H.: Iterative Methods for Large Linear Systems, Utrecht, The Netherlands (2002)
24. Weiss, R.: Error-minimizing Krylov subspace methods. SIAM J. Sci. Statist. Comput. **15**, 511–527 (1994)

Exact Analytical Solution of the Pure Bending Problem of a Multilayer Wedge-Shaped Console

Stanislav Koval'chuk[(✉)] [ID], Oleksii Goryk [ID], and Anatolii Antonets [ID]

Poltava State Agrarian University, Skovorody Str. 1/3, Poltava 36003, Ukraine
stanislav.kovalchuk@pdaa.edu.ua

Abstract. This paper has presented an exact analytical solution of the flat pure bending problem of a multilayer wedge-shaped console consisting of an arbitrary number of wedge-shaped rigidly connected layers. It is assumed that the console is deformed elastically, and its layers are made of orthotropic or isotropic homogeneous materials. The problem is solved by the methods of linear theory of elasticity using a continuous approach, in which the multilayer console is considered as a continuous body with variable in the transverse direction mechanical characteristics of the material. This has allowed to obtain generalized relations for the components of the stress-strain state immediately for the whole package of layers. The solution of the problem is reduced to the definition of an unknown continuous function of tangential stress distribution in cylindrical cross-sections of the console. The defining equation is obtained for this function, the main types of solutions for homogeneous orthotropic and isotropic layers are investigated. As a special case, a homogeneous orthotropic and isotropic wedge is studied, for which closed relations for stresses and displacements are obtained. The correspondence to the known solution for a homogeneous isotropic wedge is shown. The obtained solution can be directly used to predict strength and stiffness of multilayer beams of variable cross-section, to solve other bending problems of such elements, as well as to verify the accuracy of approximate calculation methods.

Keywords: Wedge · Multilayered structures · Bending

1 Introduction

Beams and wedge-shaped beams are quite common in various structures in modern construction and mechanical engineering, in particular for aircraft designs. Compared to beams of constant cross-section, wedge-shaped elements allow achieving significant savings in materials and weight of the structure. A much greater effect from the use of such elements can be achieved by replacing the homogeneous material composite multilayer structure. However, as in the case of constant cross-section beams, the heterogeneity of the structure of the composite wedge-shaped element significantly complicates the determination of its stress-strain state (SSS) due to insufficient development of analytical theories of such elements deformation.

The aim of this work is to construct an accurate analytical solution for the problem of flat pure bending of a multilayer wedge-shaped console, which consists of an arbitrary

number of orthotropic wedge-shaped layers under the condition of their absolutely rigid connection.

At present, we can note the active development of the direction the numerical calculation of variable cross-section beams [1, 2] and the direction of their analytical modeling. The latter direction is represented mainly by works in which analytical and semi-analytical deformation models of homogeneous and composite beams of variable cross-section are developed. Such models are built as approximate solutions to the corresponding problems. There are far fewer papers that provide accurate solutions to such elements.

In most recent works, the Timoshenko hypothesis is the basis for constructing analytical models of deformation. For example, in [3] a model of a homogeneous cantilever wedge-shaped beam bending under the action of an arbitrary load at the free end and an evenly distributed load on the longitudinal faces was constructed. A more general case of a homogeneous isotropic beam with an arbitrary change in the height of cross-sections is considered in [4], where a one-dimensional model of such elements bending based on the Timoshenko hypothesis is proposed. In [5], the model similar to [4] was constructed for the case of asymmetric section with respect to the main plane, as well as taking into account transverse compressive stresses. Using the Timoshenko hypothesis an analytical theory of a conical inflatable beam for the case of external moment was developed [6].

The Timoshenko's hypothesis was also used in the construction of deformation models of variable cross-section composite beams. In particular, the model presented in [4] was developed in [7] for the case of a multilayer beam with isotropic layers. In [8] a comparison with different methods of SSS determination for wedge-shaped I beams is given, where a significant error of stress values is shown when applying the calculated relations for prismatic beams.

In some works, the models of deformation of variable cross-section beams are built using elements of the classical model of homogeneous prismatic beams deformation. For example, in [9] the assumption about the validity of the Navier equation was applied to obtain analytical relations for stresses in straight homogeneous isotropic beams with an arbitrary change in the height of cross-sections along the length. This method was developed for a more general case of loading and changing the size of sections in [10]. In [11], a model of a three-layer wedge-shaped beam based on a layer-by-layer approach and the assumption that the deformation of the outer layers of constant thickness can be described using the classical bending model is proposed. And in [12] a similar approach has been used to develop a semi-analytical method for calculating multilayer beams with variable stiffness.

It is important to note that during the construction of these deformation models certain assumptions were made about the distribution of stresses and displacements, so their application does not allow establishing a complete and accurate representation of the SSS even for the simplest case of a symmetrical wedge-shaped beam of constant width. This can be achieved only by constructing an exact solution of the elasticity theory equations for the corresponding conditions of loading and fixing of the beam.

The well-known solution of Carothers and Inglis for isotropic wedge and the solution of Sergey Lehnitsky for orthotropic wedge give exact relations for the components of the stress state. Current studies [13] show the possibility of solving the pure bending

problem of an uncut isotropic and orthotropic wedge using the theory of a complex variable functions. However, the authors did not find a solution for the case of pure bending of a multilayer wedge-shaped console.

2   Methodology

Consider a narrow console of variable cross section, which is part of the wedge with an angle ψ at the apex O. The console consists of m wedge-shaped layers P_k of equal width b of different materials (see Fig. 1). We assume that the conditions of absolutely rigid connection between the beam layers are fulfilled.
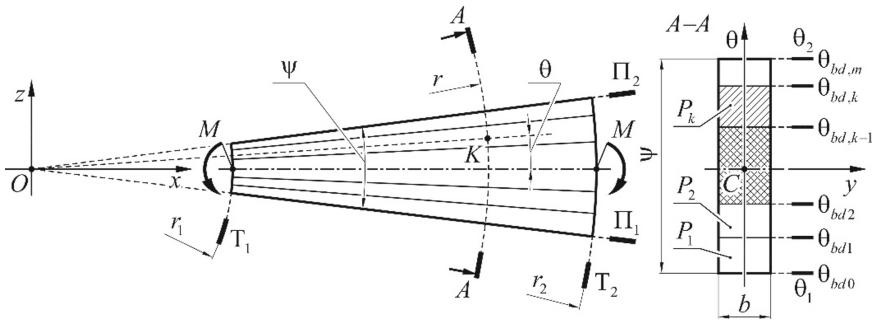
Fig. 1.   Scheme and structure of the cross section multilayer circular beam

The ends of the beam T_ς ($\varsigma = 1, 2$) are parts of coordinate cylindrical concentric surfaces with radii r_ς, and the longitudinal faces Π_ς belong to the coordinate planes that form angles θ_ς with a plane xOy.

The system of loads at the end T_1 has zero equivalent force and is reduced to the equivalent moment M (see Fig. 1), which puts the considered beam in the conditions of pure bending. At the end T_2 with the coordinate r_2, we consider the given kinematic and static conditions that simulate the rigid fixing of the console.

The elastic characteristics of the investigated beam, their products and relations in the system $r\theta y$ will be piecewise continuous functions $\mu_a^S = \mu_a^S(\theta)$ that can be analytically described using the Heaviside function $H(\theta)$:

$$\mu_a^S = \sum_{k=1}^{m} \left\{ S_a^{[k]} \left[H\left(\theta - \theta_{bd,k-1}\right) - H\left(\theta - \theta_{bd,k}\right) \right] \right\}, \tag{1}$$

where $S_a^{[k]}$ – mechanical characteristic value for the k-th layer; $\theta_{bd0} = \theta_1$, $\theta_{bd,m} = \theta_2$ – angular coordinates of longitudinal surfaces Π_ς.

Consider the construction of an analytical solution of the problem with the elastic work of the console's layers materials. In this case, we apply the continuous approach proposed in [14, 15] to determine the SSS of straight and circular multilayer beams. This approach will provide generalized relations describing the distribution of SSS components for the entire package of layers.

Given the accepted external loads and geometric parameters of the beam, it can be assumed that it is in the conditions of a generalized flat stress state. To solve our problem we use the equation of the plane problem of the elasticity linear theory in the polar coordinate system:

$$\frac{\partial \sigma_r}{\partial r} + \frac{1}{r}\frac{\partial \tau_{r\theta}}{\partial \theta} + \frac{\sigma_r - \sigma_\theta}{r} = 0; \qquad\qquad \frac{\partial \tau_{\theta r}}{\partial r} + \frac{1}{r}\frac{\partial \sigma_\theta}{\partial \theta} + \frac{2\tau_{\theta r}}{r} = 0, \quad (2)$$

$$\varepsilon_r = \frac{\sigma_r}{\mu_r^E} - \frac{\mu_{\theta r}^\nu \sigma_\theta}{\mu_\theta^E}; \qquad \varepsilon_\theta = \frac{\sigma_\theta}{\mu_\theta^E} - \frac{\mu_{r\theta}^\nu \sigma_r}{\mu_r^E}; \qquad \gamma_{r\theta} = \frac{1}{\mu_{r\theta}^G}\tau_{r\theta}, \quad (3)$$

$$\varepsilon_r = \frac{\partial u_r}{\partial r}; \qquad \varepsilon_\theta = \frac{1}{r}\left(\frac{\partial u_\theta}{\partial \theta} + u_r\right); \qquad \gamma_{r\theta} = \frac{1}{r}\left(\frac{\partial u_r}{\partial \theta} - u_\theta\right) + \frac{\partial u_\theta}{\partial r}. \quad (4)$$

The system of external loads on the longitudinal surfaces Π_ς and ends T_1 of the beam imposes on the components of the stress state such boundary conditions:

$$\sigma_\theta|_{\theta=\theta_\varsigma} = 0; \qquad\qquad \tau_{\theta r}|_{\theta=\theta_\varsigma} = 0, \quad (5)$$

$$\sigma_r|_{r=r_1} = -p_{r1}; \qquad\qquad \tau_{r\theta}|_{r=r_1} = -p_{\theta 1}. \quad (6)$$

The relationship of stresses in the cross sections of the console with the internal force factors caused by the load on T_1 gives the following integral conditions:

$$\int_{\theta_1}^{\theta_2}(\sigma_r\cos\theta)d\theta - \int_{\theta_1}^{\theta_2}(\tau_{r\theta}\sin\theta)d\theta = 0, \quad \int_{\theta_1}^{\theta_2}(\sigma_r\sin\theta)d\theta + \int_{\theta_1}^{\theta_2}(\tau_{r\theta}\cos\theta)d\theta = 0,$$

$$\int_{\theta_1}^{\theta_2}(\sigma_r\sin\theta)d\theta + \int_{\theta_1}^{\theta_2}(\tau_{r\theta}\cos\theta)d\theta - \int_{\theta_1}^{\theta_2}(\tau_{r\theta})d\theta = \frac{M}{br^2}. \quad (7)$$

The compatible solution of the second and third expressions (7) gives a relation:

$$\int_{\theta_1}^{\theta_2}\tau_{r\theta}d\theta = -\frac{M}{b}\frac{1}{r^2}. \quad (8)$$

The corresponding form of the solution (8) for tangential stresses $\tau_{r\theta}$:

$$\tau_{r\theta} = \frac{\Theta_{r\theta}^{\tau 1}}{r^2}, \quad (9)$$

where $\Theta_{r\theta}^{\tau 1} = \Theta_{r\theta}^{\tau 1}(\theta)$ – unknown tangential stress distribution function.

By substituting (9) for the second condition (5) and (8), we obtain the conditions for $\Theta_{r\theta}^{\tau 1}$:

$$\Theta_{r\theta}^{\tau 1}|_{\theta=\theta_\varsigma} = 0, \quad \int_{\theta_1}^{\theta_2}\Theta_{r\theta}^{\tau 1}d\theta = -\frac{M}{b}. \quad (10)$$

By solving the equilibrium Eq. (2) with respect to the functions of normal stresses taking into account (9), the first condition (5) and conditions (7) we obtain

$$\sigma_r = \frac{1}{r^2}\frac{d\Theta_{r\theta}^{\tau 1}}{d\theta}, \quad \sigma_\theta = 0. \tag{11}$$

It can be noted that the third and fourth conditions (6) must directly specify the distribution of functions $\Theta_{r\theta}^{\tau 1}$ and $\sigma_r|_{r=r_1}$. However, their use at this stage makes it impossible to satisfy the system of equations and conditions (2)–(7). Therefore, we will limit ourselves only to conditions (7), (10) and determine in which case the obtained solutions will satisfy the boundary conditions (6).

By solving the first and second expressions of the Cauchy relations (4) and substituting (3) and (11), we obtain solutions for displacements u_r i u_θ:

$$u_r = \frac{1}{\mu_r^E}\frac{d\Theta_{r\theta}^{\tau 1}}{d\theta}\left(\frac{1}{r_1} - \frac{1}{r}\right) + u_r|_{r=r_1},$$

$$u_\theta = \frac{1}{r}\int_{\theta_1}^{\theta}\left(\frac{1-\mu_{r\theta}^\nu}{\mu_r^E}\frac{d\Theta_{r\theta}^{\tau 1}}{d\theta}\right)d\theta - \frac{1}{r_1}\int_{\theta_1}^{\theta}\left(\frac{1}{\mu_r^E}\frac{d\Theta_{r\theta}^{\tau 1}}{d\theta}\right)d\theta - \int_{\theta_1}^{\theta}u_r|_{r=r_1}d\theta + u_\theta|_{\theta=\theta_1}. \tag{12}$$

By substituting expressions (12) to the third relation (4) and performing the transformation, we obtain the following condition:

$$r\frac{d}{dr}\left(\frac{u_\theta|_{\theta=\theta_1}}{r}\right) - \frac{1}{r^2}\left[\frac{d}{d\theta}\left(\frac{1}{\mu_r^E}\frac{d\Theta_{r\theta}^{\tau 1}}{d\theta}\right) + \frac{\Theta_{r\theta}^{\tau 1}}{\mu_{r\theta}^G} + 2\int_{\theta_1}^{\theta}\left(\frac{1-\mu_{r\theta}^\nu}{\mu_r^E}\frac{d\Theta_{r\theta}^{\tau 1}}{d\theta}\right)d\theta\right]$$

$$+ \frac{1}{r}\left[\frac{1}{r_1}\frac{d}{d\theta}\left(\frac{1}{\mu_r^E}\frac{d\Theta_{r\theta}^{\tau 1}}{d\theta}\right) + \frac{1}{r_1}\int_{\theta_1}^{\theta}\left(\frac{1}{\mu_r^E}\frac{d\Theta_{r\theta}^{\tau 1}}{d\theta}\right)d\theta + \frac{du_r|_{r=r_1}}{d\theta} + \int_{\theta_1}^{\theta}u_r|_{r=r_1}d\theta\right] = 0. \tag{13}$$

The components in square brackets in (13) depend only on the variable θ. Therefore, this condition can be fulfilled for all points of the beam, only if the expressions in square brackets are equal to some constant:

$$\frac{d}{d\theta}\left(\frac{1}{\mu_r^E}\frac{d\Theta_{r\theta}^{\tau 1}}{d\theta}\right) + \frac{\Theta_{r\theta}^{\tau 1}}{\mu_{r\theta}^G} + 2\int_{\theta_1}^{\theta}\left(\frac{1-\mu_{r\theta}^\nu}{\mu_r^E}\frac{d\Theta_{r\theta}^{\tau 1}}{d\theta}\right)d\theta = K_1, \tag{14}$$

$$\frac{du_r|_{r=r_1}}{d\theta} + \int_{\theta_1}^{\theta}u_r|_{r=r_1}d\theta + \frac{1}{r_1}\frac{d}{d\theta}\left(\frac{1}{\mu_r^E}\frac{d\Theta_{r\theta}^{\tau 1}}{d\theta}\right) + \frac{1}{r_1}\int_{\theta_1}^{\theta}\left(\frac{1}{\mu_r^E}\frac{d\Theta_{r\theta}^{\tau 1}}{d\theta}\right)d\theta = K_2. \tag{15}$$

Taking into account (14) and (15), condition (13) is transformed into the equation:

$$r\frac{d}{dr}\left(\frac{1}{r}u_\theta|_{\theta=\theta_1}\right) = \frac{1}{r^2}K_1 - \frac{1}{r}K_2. \tag{16}$$

Taking into account the homogeneous boundary conditions for function $\Theta_{r\theta}^{\tau 1}$ (10) and the linearity of Eq. (14) we can introduce a substitution:

$$\Theta_{r\theta}^{\tau 1} = K_1 \Theta_{r\theta}^{\tau}. \tag{17}$$

By substituting (17) to (14), we obtain

$$\frac{d}{d\theta}\left(\frac{1}{\mu_r^E}\frac{d\Theta_{r\theta}^{\tau}}{d\theta}\right) + \frac{\Theta_{r\theta}^{\tau}}{\mu_{r\theta}^G} + 2\int_{\theta_1}^{\theta}\left(\frac{1-\mu_{r\theta}^{\nu}}{\mu_r^E}\frac{d\Theta_{r\theta}^{\tau}}{d\theta}\right)d\theta = 1. \tag{18}$$

Conditions (10) after taking into account the replacement (17), give the boundary conditions for the function $\Theta_{r\theta}^{\tau}$ and value of the unknown constant:

$$\Theta_{r\theta}^{\tau}|_{\theta=\theta_\varsigma} = 0, \quad K_1 = -M \big/ \big(bB_0^{\tau}\big), \quad B_0^{\tau} = \int_{\theta_1}^{\theta_2} \Theta_{r\theta}^{\tau} d\theta. \tag{19}$$

After a single differentiation (18) and execution of transformations, we obtain

$$\frac{1}{\mu_r^E}\frac{d^3\Theta_{r\theta}^{\tau}}{d\theta^3} + \frac{d}{d\theta}\left(\frac{2}{\mu_r^E}\right)\frac{d^2\Theta_{r\theta}^{\tau}}{d\theta^2}$$

$$+\left(2\frac{1-\mu_{r\theta}^{\nu}}{\mu_r^E} + \frac{1}{\mu_{r\theta}^G} + \frac{d^2}{d\theta^2}\left(\frac{1}{\mu_r^E}\right)\right)\frac{d\Theta_{r\theta}^{\tau}}{d\theta} + \frac{d}{d\theta}\left(\frac{1}{\mu_{r\theta}^G}\right)\Theta_{r\theta}^{\tau} = 0. \tag{20}$$

The analytical solution (20) is possible for a single k-th homogeneous layer.

Within the k-th homogeneous orthotropic layer, when $\theta \in \big(\theta_{bd,k-1}, \theta_{bd,k}\big)$, mechanical characteristics $S_a^{[k]} = \text{const}$ and Eq. (20) will have a general solution

$$\Theta_{r\theta}^{\tau[k]} = C_1^{[k]} + C_2^{[k]}\sin\left(\beta^{\tau[k]}\theta\right) + C_3^{[k]}\cos\left(\beta^{\tau[k]}\theta\right), \tag{21}$$

where $\beta^{\tau[k]} = \sqrt{2 - 2\nu_{r\theta}^{[k]} + E_r^{[k]}\big/G_{r\theta}^{[k]}}$ – constant for the k-th orthotropic layer.

In the case of an isotropic layer: $E_r^{[k]} = E_\theta^{[k]} = E^{[k]}$, $\nu_{\theta r}^{[k]} = \nu_{r\theta}^{[k]} = \nu^{[k]}$, $G_{r\theta}^{[k]} = E^{[k]}\big/\big(2+2\nu^{[k]}\big)$, and constant $\beta^{\tau[k]} = 2$.

The function $\Theta_{r\theta}^{\tau}$ for the whole beam can be formed using solutions (21) similarly to the functions of elastic characteristics (1):

$$\Theta_{r\theta}^{\tau} = \sum_{k=1}^{m}\left\{\Theta_{r\theta}^{\tau[k]}\big[H\big(\theta - \theta_{bd,k-1}\big) - H\big(\theta - \theta_{bd,k}\big)\big]\right\}. \tag{22}$$

The expression obtained in (22) will include $3m$ unknown constants of integration $C_1^{[k]}$, $C_2^{[k]}$, $C_3^{[k]}$. To determine all unknown constant boundary conditions (19), it is sufficient only for the console consisting of a single layer.

Additional conditions for the multilayer console will be obtained from the condition of absolutely rigid connection of layers which will be carried out in case of:

$$\Theta_{r\theta}^{\tau[k]}|_{\theta=\theta_{bd,k}} = \Theta_{r\theta}^{\tau[k+1]}|_{\theta=\theta_{bd,k}}, \quad \frac{1}{E_r^{[k]}} \frac{d\Theta_{r\theta}^{\tau[k]}}{d\theta}|_{\theta=\theta_{bd,k}} = \frac{1}{E_r^{[k+1]}} \frac{d\Theta_{r\theta}^{\tau[k+1]}}{d\theta}|_{\theta=\theta_{bd,k}}. \tag{23}$$

Another condition for a function $\Theta_{r\theta}^{\tau}$ is dictated by the defining Eq. (18):

$$\frac{C_1^{[k]}}{G_{r\theta}^{[k]}} = 1 + 2\left[\int \left(\frac{1-v_{r\theta}^{[k]}}{E_r^{[k]}} \frac{d\Theta_{r\theta}^{\tau[k]}}{d\theta}\right)d\theta\right]|_{\theta=\theta_{bd,k-1}} - 2\sum_{i=1}^{k-1}\left[\int_{\theta_{bd,i-1}}^{\theta_{bd,i}} \left(\frac{1-v_{r\theta}^{[i]}}{E_r^{[i]}} \frac{d\Theta_{r\theta}^{\tau[i]}}{d\theta}\right)d\theta\right]. \tag{24}$$

The solution of Eq. (15) can be obtained by direct integration for the whole package of console layers. Taking into account (17) and (19) obtained:

$$u_r|_{r=r_1} = \frac{M}{br_1B_0^\tau} \frac{1}{\mu_r^E} \frac{d\Theta_{r\theta}^{\tau}}{d\theta} - \left[\frac{M}{bB_0^\tau}\left(\frac{1}{\mu_r^E} \frac{d\Theta_{r\theta}^{\tau}}{d\theta}\right)|_{\theta=\theta_1} - r_1u_r|_{r=r_1,\theta=\theta_1}\right]\frac{\sin(\theta_2-\theta)}{r_1\sin\psi}$$
$$- \left[\frac{M}{bB_0^\tau}\left(\frac{1}{\mu_r^E} \frac{d\Theta_{r\theta}^{\tau}}{d\theta}\right)|_{\theta=\theta_2} - r_1u_r|_{r=r_1,\theta=\theta_2}\right]\frac{\sin(\theta-\theta_1)}{r_1\sin\psi}. \tag{25}$$

By integrating Eq. (16), taking into account (17), (19) and (25) obtained:

$$u_\theta|_{\theta=\theta_1} = -\frac{M}{2bB_0^\tau}\left(\frac{r}{r_1^2} - \frac{1}{r}\right) + \cos\psi\left(r_1u_r|_{r=r_1,\theta=\theta_1} - \frac{M}{bB_0^\tau}\left(\frac{1}{\mu_r^E} \frac{d\Theta_{r\theta}^{\tau}}{d\theta}\right)|_{\theta=\theta_1}\right)\frac{r-r_1}{r_1^2\sin\psi}$$
$$- \left(r_1u_r|_{r=r_1,\theta=\theta_2} - \frac{M}{bB_0^\tau}\left(\frac{1}{\mu_r^E} \frac{d\Theta_{r\theta}^{\tau}}{d\theta}\right)|_{\theta=\theta_2}\right)\frac{r-r_1}{r_1^2\sin\psi} + \frac{u_\theta|_{\theta=\theta_1,r=r_1}}{r_1}r. \tag{26}$$

3 Results

Thus, the general solutions and conditions for determining the unknown integration constants for all the required functions of the problem are obtained, which makes it possible to record closed analytical expressions for all components SSS of the considered multilayer element. In particular, for stresses and displacements we have:

$$\tau_{r\theta} = -\frac{M}{bB_0^\tau}\frac{\Theta_{r\theta}^{\tau}}{r^2}, \quad \sigma_r = -\frac{M}{bB_0^\tau}\frac{1}{r^2}\frac{d\Theta_{r\theta}^{\tau}}{d\theta}, \quad \sigma_\theta = 0, \tag{27}$$

$$u_r = \frac{M}{bB_0^\tau}\frac{1}{r}\frac{1}{\mu_r^E}\frac{d\Theta_{r\theta}^{\tau}}{d\theta} - \left[\frac{M}{bB_0^\tau}\left(\frac{1}{\mu_r^E}\frac{d\Theta_{r\theta}^{\tau}}{d\theta}\right)|_{\theta=\theta_1} - r_1u_r|_{r=r_1,\theta=\theta_1}\right]\frac{\sin(\theta_2-\theta)}{r_1\sin\psi}$$
$$- \left[\frac{M}{bB_0^\tau}\left(\frac{1}{\mu_r^E}\frac{d\Theta_{r\theta}^{\tau}}{d\theta}\right)|_{\theta=\theta_2} - r_1u_r|_{r=r_1,\theta=\theta_2}\right]\frac{\sin(\theta-\theta_1)}{r_1\sin\psi}, \tag{28}$$

$$u_\theta = -\frac{M}{bB_0^\tau}\left[\frac{1}{r}\int_{\theta_1}^{\theta}\left(\frac{1-\mu_{r\theta}^\nu}{\mu_r^E}\frac{d\Theta_{r\theta}^\tau}{d\theta}\right)d\theta + \frac{1}{2}\left(\frac{r}{r_1^2}-\frac{1}{r}\right)\right]$$

$$+\left[\frac{M}{bB_0^\tau}\left(\frac{1}{\mu_r^E}\frac{d\Theta_{r\theta}^\tau}{d\theta}\right)|_{\theta=\theta_1} - r_1 u_r|_{r=r_1,\theta=\theta_1}\right]\frac{r_1\cos(\theta_2-\theta)-r\cos\psi}{r_1^2\sin\psi} \tag{29}$$

$$+\left[\frac{M}{bB_0^\tau}\left(\frac{1}{\mu_r^E}\frac{d\Theta_{r\theta}^\tau}{d\theta}\right)|_{\theta=\theta_2} - r_1 u_r|_{r=r_1,\theta=\theta_2}\right]\frac{r-r_1\cos(\theta-\theta_1)}{r_1^2\sin\psi} + \frac{u_\theta|_{\theta=\theta_1,r=r_1}}{r_1}r.$$

Stresses (27) satisfy static boundary conditions (5). However, conditions (6) at the end T_1 will be fulfilled only when the loads correspond to (27).

To model the fastening of the console (see Fig. 1) it is necessary to exclude the movement and rotation T_2, which is possible under conditions similar to [14]:

$$u_r|_{r=r_2,\,\theta=\theta_1} = 0, \quad u_r|_{r=r_2,\,\theta=\theta_2} = 0, \quad u_\theta|_{r=r_2,\,\theta=\theta_1} = 0. \tag{30}$$

Applying (28) and (29) under conditions (30) and solving the obtained equations with respect to the unknown constants of integration, we obtain

$$u_r|_{r=r_1,\theta=\theta_1} = \frac{M}{bB_0^\tau}\left(\frac{1}{\mu_r^E}\frac{d\Theta_{r\theta}^\tau}{d\theta}\right)|_{\theta=\theta_1}\frac{r_2-r_1}{r_2 r_1}, \quad u_r|_{r=r_1,\theta=\theta_2} = \frac{M}{bB_0^\tau}\left(\frac{1}{\mu_r^E}\frac{d\Theta_{r\theta}^\tau}{d\theta}\right)|_{\theta=\theta_2}\frac{r_2-r_1}{r_2 r_1},$$

$$u_\theta|_{\theta=\theta_1,r=r_1} = \frac{M}{bB_0^\tau}\frac{r_2-r_1}{r_2^2}\left(\frac{r_2+r_1}{2r_1} - \left(\frac{1}{\mu_r^E}\frac{d\Theta_{r\theta}^\tau}{d\theta}\right)|_{\theta=\theta_2}\frac{1}{\sin\psi} + \left(\frac{1}{\mu_r^E}\frac{d\Theta_{r\theta}^\tau}{d\theta}\right)|_{\theta=\theta_1}\frac{\cos\psi}{\sin\psi}\right). \tag{31}$$

Equations (33) give the values of displacements at the extreme points of the initial section of the wedge-shaped multilayer console. By using (33) it is possible to determine the amount of deflection of the lower fiber of the console.

For a homogeneous orthotropic console ($\theta_{1,2} = \mp\frac{1}{2}\psi$) consisting of a single layer after applying solution (21) under conditions (19), we have

$$\Theta_{r\theta}^\tau = \frac{E_r}{2(1-\nu_{r\theta})}\left(1 - \frac{\cos\beta^\tau\theta}{\cos\frac{1}{2}\beta^\tau\psi}\right), \quad \beta^\tau = \sqrt{2-2\nu_{r\theta}+\frac{E_r}{G_{r\theta}}}. \tag{32}$$

The ratios for stresses (27) and deflection $u_z|_{\theta=\theta_1,r=r_1} = u_\theta|_{\theta=\theta_1,r=r_1}\cos\theta_1 + u_r|_{\theta=\theta_1,r=r_1}\sin\theta_1$ of the truncated and not truncated ($\lim_{r_1\to 0} u_z|_{\theta=\theta_1,r=r_1}$) console, after substitution (32) will take the following form

$$\tau_{r\theta} = -\frac{M}{b}\frac{\beta^\tau\cos\left(\frac{1}{2}\beta^\tau\psi\right)-\beta^\tau\cos(\beta^\tau\theta)}{\psi\beta^\tau\cos\left(\frac{1}{2}\beta^\tau\psi\right)-2\sin\left(\frac{1}{2}\beta^\tau\psi\right)}\frac{1}{r^2}, \quad \sigma_\theta = 0,$$

$$\sigma_r = -\frac{M}{b}\frac{(\beta^\tau)^2\sin(\beta^\tau\theta)}{\psi\beta^\tau\cos\left(\frac{1}{2}\beta^\tau\psi\right)-2\sin\left(\frac{1}{2}\beta^\tau\psi\right)}\frac{1}{r^2},$$

$$u_z|_{\substack{\theta=\theta_1,\\r=r_1}} = \frac{M(r_2-r_1)(\beta^\tau)^2\cos\left(\frac{1}{2}\psi\right)}{br_2^2 E_r\left(\psi\beta^\tau - 2\text{tg}\left(\frac{1}{2}\beta^\tau\psi\right)\right)}\left[\frac{1-\nu_{r\theta}}{\beta^\tau}\frac{r_2+r_1}{r_1} - \frac{\text{tg}\left(\frac{1}{2}\beta^\tau\psi\right)}{\sin\psi}\right. \tag{33}$$

$$\left. -\text{tg}\left(\frac{1}{2}\beta^\tau\psi\right)\left(\frac{1}{\text{tg}\psi}-\frac{r_2}{r_1}\text{tg}\left(\frac{1}{2}\psi\right)\right)\right], \quad u_z|_{\substack{\theta=\theta_1,\\r=r_1}} = -\frac{M(\beta^\tau)^2\text{tg}\left(\frac{1}{2}\beta^\tau\psi\right)}{br_2 E_r\sin\left(\frac{1}{2}\psi\right)\left(\psi\beta^\tau - 2\text{tg}\left(\frac{1}{2}\beta^\tau\psi\right)\right)}.$$

The Eq. (33) make it possible to indirectly check the correctness of the constructed solution. By changing the direction of the external moment, denoting the values and rearranging the terms, expressions (33) can lead to the form of a known solution for an isotropic wedge-shaped console.

4   Conclusion

The problem of pure flat bending of a multilayer wedge-shaped console at absolutely rigid connection and elastic work of cylindrically orthotropic wedge-shaped layers is solved by methods of the elasticity theory.

The obtained result is an exact solution of the plane problem of the elasticity theory, provided that the load distribution, which is reduced to the equivalent moment, on the free end of the console corresponds to (27).

Relationships (27), (28) and (29) make it possible to predict with high accuracy the distribution of stresses and displacements for composite wedge-shaped multilayer beams, in particular, consoles of variable cross-section. At the same time, the obtained dependences are analytical, which allows to easily make changes to the original data in the calculation at the stage of variable design.

The combination of the obtained solution together with similar solutions for other types of loads opens the possibility of developing an applied method for solving a wide range of problems of strength, rigidity, optimal design of effective multilayer wedge-shaped elements.

References

1. Rajasekaran, S., Khaniki, H.: Bending, buckling and vibration of small-scale tapered beams. Int. J. Eng. Sci. **120**, 172–188 (2017)
2. Mercuri, V., Balduzzi, G., Asprone, D., Auricchio, F.: Structural analysis of non-prismatic beams: critical issues, accurate stress recovery, and analytical definition of the finite element (FE) stiffness matrix. Eng. Struct. **213**, 110252 (2020)
3. Wong, F., Gunawan, J., Agusta, K., Herryanto, H., Tanaya, L.: On the derivation of exact solutions of a tapered cantilever Timoshenko beam. Civ. Eng. Dimension **21**(2), 89–96 (2019)
4. Balduzzi, G., Aminbaghai, M., Sacco, E., Füssl, J., Eberhardsteiner, J., Auricchio, F.: Non-prismatic beams: a simple and effective Timoshenko-like model. Int. J. Solids Struct. **90**, 236–250 (2016)
5. Vilar, M., Hadjiloizi, D., Masjedi, P., Weaver, P.: Stress analysis of generally asymmetric non-prismatic beams subject to arbitrary loads. Eur. J. Mech. – A/Solids, **90**, 104284 (2021)
6. Chen, Z., Zhao, H., Li, X., Chen, J.: Deflection analysis of the airship structure based on the tapered inflatable beam. Aircr. Eng. Aerosp. Technol. **91**(4), 601–606 (2019)
7. Balduzzi, G., Aminbaghai, M., Auricchio, F., Füssl, J.: Planar Timoshenko-like model for multilayer non-prismatic beams. Int. J. Mech. Mater. Des. **14**(1), 51–70 (2017). https://doi.org/10.1007/s10999-016-9360-3
8. Balduzzi, G., Hochreiner, G., Fussl, J.: Stress recovery from one dimensional models for tapered bi-symmetric thin-walled I beams: deficiencies in modern engineering tools and procedures. Thin-Walled Struct. **119**, 934–945 (2017)
9. Bertolini, P., Eder, M., Taglialegne, L., Valvo, P.: Stresses in constant tapered beams with thin-walled rectangular and circular cross sections. Thin-Walled Struct. **137**, 527–540 (2019)

10. Bertolini, P., Taglialegne, L.: Analytical solution of the stresses in doubly tapered box girders. Eur. J. Mech. – A/Solids, **81**, 103969 (2020)
11. Ai, Q., Weaver, P.: Simplified analytical model for tapered sandwich beams using variable stiffness materials. J. Sandwich Struct. Mater. **19**(1), 3–25 (2017)
12. Masjedi, P., Weaver, P.: Variable stiffness composite beams subject to non-uniformly distributed loads: an analytical solution. Compos. Struct. **256**, 112975 (2021)
13. Wang, G., Jia, P., Suo, Y., Zhang, L., Zeng, L.: Elasticity solution of composite material wedge loaded with a concentrated moment. J. Mater. Sci. Chem. Eng. **7**, 77–85 (2019)
14. Koval'chuk, S., Goryk, A.: Elasticity theory solution of the problem on bending of a narrow multilayer cantilever with a circular axis by loads at its end. Mech. Compos. Mater. **54**(5), 605–620 (2018)
15. Koval'chuk, S., Gorik, A., Pavlikov, A., Antonets, A.: Solution to the task of elastic axial compression-tension of the composite multilayered cylindrical beam. Strength Mater. **51**(2), 240–251 (2019)

Application of the R-functions Method and Shell Theory of the Higher-Order to Study Free Vibration of Functionally Graded Shallow Shells

Lidiya Kurpa[1(✉)] and Tetyana Shmatko[2]

[1] Department of Applied Mathematics, National Polytechnic University "KhPI",
Kharkov 61002, Ukraine
`kurpalidia@gmail.com`

[2] Department of Higher Mathematics, National Polytechnic University "KhPI", Kharkov 61002,
Ukraine

Abstract. Free vibrations of shallow shells of an arbitrary shape are investigated. It is assumed that shell is fabricated of functionally graded materials. Mathematical model has been constructed on base of shear deformation shell theory of the higher-order (HSDT). Voigt's model is applied to define effective material properties of the structure. To study a shell with an arbitrary planform the R-functions theory combined with the variational Ritz method is used. The method proposed was confirmed by different tests realized by means of corresponding software created. Comparison was fulfilled for functionally graded shells of rectangular planform with various curvatures and boundary conditions. New results for shallow shells with complex planform are presented. The considered shell has four external cut-outs bounded by semicircles and one internal square cut-out. One of the examined variants is a cylindrical panel clamped on whole boundary with clamped internal cut-out. This object is fabricated of four types of functionally graded material. Effect of gradient index on natural frequency for all those materials is analyzed and shown in different pictures. Computational experiment shown that with increasing the gradient index value the natural frequencies are decreasing for all types of functionally graded materials. It is effect is observed due to decreasing of volume fraction of ceramics. Modes of vibration for cylindrical panel with complex form are presented. Analysis of the natural frequencies obtained in a framework of two theories (first and higher orders) was carried out in the paper.

Keywords: R-functions theory · Shallow shells · FGM · Higher-order shear deformation theory

1 Introduction

October 21, 2021 is the 95th anniversary of the greatest Ukrainian scientist, Academician of the National Academy of Sciences of Ukraine Vladimir Logvinovich Rvachev. He is an extraordinary scientist in the field of mathematics, mechanics and cybernetics, Laureate of the State Prize of Ukraine in the field of science and technology, Honoured Worker

of Science and Technology of Ukraine, Professor; Doctor of Physical and Mathematical Sciences. Rvachev V.L. is an author of the theory of the R-functions, which belongs to one of the greatest scientific discoveries of the twentieth century. Numerous applications of this theory are presented in the works of his students. The name of V.L. Rvachev is in many encyclopaedic reference books. A large number of publications are devoted to him and his scientific achievements. We want to devote our paper to our greatest teacher.

Early in many works [1, 2] the R-functions method was applied to linear and geometrically nonlinear dynamic problems of the laminated shallow shell with complex planform. Since 2014 the R-functions method has been applied to static and dynamic problems of plates and shallow shells fabricated of modern composite materials, so-called functionally graded materials (FGM's) [3–6]. This class of composite materials has significant advantages over multilayer composites due to continuous and smooth variation in properties in one or several directions. They restrain a sharp change in the mechanical properties of the layers and, as a consequence, prevent stress concentration, destruction and delamination of layers. In addition they are able to withstand high temperature environments. Due to these reasons, the study of the static and dynamic behavior of FGM structures draws an attention of many researchers. Calculation of FGM structures is among the most important problems of modern mechanics. A huge number of works devoted to this problem and, in particular, to vibration FGM's plates and shells is known [7–12]. To analyze the dynamic behavior of plates and shells many theories have been developed in last two decades. A recent review of the theories for the modeling and analysis of FG sandwich plates and shells has been presented in works [13, 14].

So far the main applications of the RFM have been connected with research buckling, linear and nonlinear vibrations of the functionally graded plates and shallow shells by means of classical or refined theory of the first order (FSDT). In this paper we apply the higher-order shear deformation shell theory (HSDT) to investigate free vibration of the FG shallow shells and plates with complex planform and different boundary condition. In these theories the shear correction factor is eliminated, but number of unknown functions is the same as in FSDT.

2   Mathematical Formulation of the Vibration Problems for Functionally Graded Plates and Shallow Shells in Framework of HSDT

Shallow shells and plates made of functionally graded materials (mixture of metal and ceramics) are considered.

A shell panel can have a complex shape. It can be clamped by different ways. We will apply the third order shear deformation theory (TSDT) of the shells [7–11]. The displacement field in the TSDT is defined by the following expressions:

$$
\begin{aligned}
u(x, y, z) &= u_0(x, y) + z\Phi_x - c_1 z^3\left(\Phi_x + \frac{\partial w}{\partial x}\right), \\
v(x, y, z) &= v_0(x, y) + z\Phi_y - c_1 z^3\left(\Phi_y + \frac{\partial w}{\partial y}\right), \\
w(x, y, z) &= w_0(x, y),
\end{aligned}
\tag{1}
$$
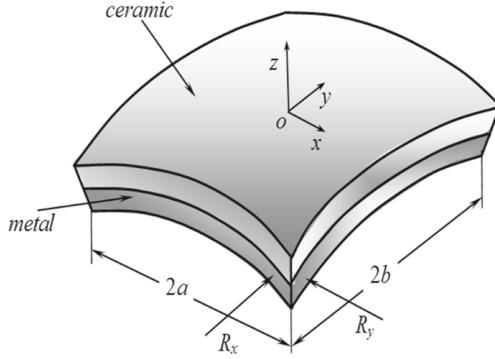
Fig. 1. FGM shallow shell

where $c_1 = 4/(3h^2)$, h is the shell thickness, functions Φ_x and Φ_y describe corresponding rotations around the OY-and OX-axes of the normal to midsurface of the shell.

The strain-displacement relations are defined as

$$\left\{\varepsilon^0\right\} = \left\{\varepsilon_{xx}^{(0)}, \varepsilon_{yy}^{(0)}, \gamma_{xy}^{(0)}\right\} = \left\{\frac{\partial u_0}{\partial x} + \frac{w_o}{R_1}, \quad \frac{\partial v_0}{\partial y} + \frac{w_o}{R_2}, \quad \frac{\partial v_0}{\partial x} + \frac{\partial u_0}{\partial y}\right\},$$

$$\left\{\varepsilon^0\right\} = \left\{\gamma_{yz}^{(0)}, \gamma_{xz}^{(0)}\right\} = \left\{\Phi_y + \frac{\partial w_0}{\partial y} - \frac{v_o}{R_2}, \quad \Phi_x + \frac{\partial w_0}{\partial x} - \frac{u_o}{R_1}\right\} \tag{2}$$

$$\left\{\varepsilon^{(1)}\right\} = \left\{\varepsilon_{xx}^{(1)}, \varepsilon_{yy}^{(1)}, \gamma_{xy}^{(1)}\right\} = \left\{\frac{\partial \Phi_x}{\partial x}, \quad \frac{\partial \Phi_y}{\partial y}, \quad \frac{\partial \Phi_y}{\partial x} + \frac{\partial \Phi_x}{\partial y}\right\},$$

$$\left\{\varepsilon^{(1)}\right\} = \left\{\gamma_{yz}^{(1)}, \gamma_{xz}^{(1)}\right\} = -c_1\left\{\Phi_y + \frac{\partial w_0}{\partial y} - \frac{v_o}{R_2}, \quad \Phi_x + \frac{\partial w_0}{\partial x} - \frac{u_o}{R_1}\right\} \tag{3}$$

$$\left\{\varepsilon^{(2)}\right\} = \left\{\varepsilon_{xx}^{(1)}, \varepsilon_{yy}^{(1)}, \gamma_{xy}^{(1)}\right\} = -c_2 \left\{ \begin{array}{l} \dfrac{\partial \Phi_x}{\partial x} + \dfrac{\partial^2 w_0}{\partial x^2} - \dfrac{1}{R_1}\dfrac{\partial u_0}{\partial x}; \quad \dfrac{\partial \Phi_y}{\partial y} + \dfrac{\partial^2 w_0}{\partial y^2} - \dfrac{1}{R_2}\dfrac{\partial v_0}{\partial y}; \\[2mm] \dfrac{\partial \Phi_y}{\partial x} + \dfrac{\partial \Phi_x}{\partial y} + 2\dfrac{\partial^2 w_0}{\partial x \partial y} - \dfrac{1}{R_2}\dfrac{\partial v_0}{\partial x} - \dfrac{1}{R_{12}}\dfrac{\partial u_0}{\partial y} \end{array} \right\}, \tag{4}$$

where $k_1 = 1/R_x$, $k_2 = 1/R_y$ are the principal curvatures of the shell along the coordinates x and y, $c_2 = 3c_1$.

Strain energy U and kinetic energy T are defined by expressions:

$$U = \int_\Omega \left(N_{xx}\varepsilon_{xx}^{(0)} + N_{yy}\varepsilon_{yy}^{(0)} + N_{xy}\gamma_{xy}^{(0)} + M_{xx}\varepsilon_{xx}^{(1)} + M_{yy}\varepsilon_{yy}^{(1)} + M_{xy}\gamma_{xy}^{(1)} + Q_x\gamma_{xz}^{(0)} + Q_y\gamma_{yz}^{(0)} - \right.$$

$$\left. - c_1\left(P_{xx}\varepsilon_{xx}^{(2)} + P_{yy}\varepsilon_{yy}^{(2)} + P_{xy}\gamma_{xy}^{(2)} +\right) - c_2\left(R_x\gamma_{xz}^{(0)} + R_y\gamma_{yz}^{(0)}\right)\right)\partial\Omega, \tag{5}$$

$$T = \int_\Omega \left(I_0\left(\left(\frac{\partial u_0}{\partial t}\right)^2 + \left(\frac{\partial v_0}{\partial t}\right)^2 + \left(\frac{\partial w_0}{\partial t}\right)^2\right) + I_1\left(\frac{\partial \Phi_x}{\partial t}\frac{\partial u_0}{\partial t} + \frac{\partial \Phi_y}{\partial t}\frac{\partial v_0}{\partial t}\right) + I_2\left(\left(\frac{\partial \Phi_x}{\partial t}\right)^2 + \left(\frac{\partial \Phi_y}{\partial t}\right)^2\right) - \right.$$

$$\left. c_1 I_3\left(\frac{\partial \gamma_{xz}^{(0)}}{\partial t}\frac{\partial u_0}{\partial t} + \frac{\partial \gamma_{yz}}{\partial t}\frac{\partial v_0}{\partial t}\right) - c_1 I_4\left(\frac{\partial \gamma_{xz}^{(0)}}{\partial t}\frac{\partial \Phi_x}{\partial t} + \frac{\partial \gamma_{yz}}{\partial t}\frac{\partial \Phi_y}{\partial t}\right) + c_1^2 I_6\left(\left(\frac{\partial \gamma_{xz}}{\partial t}\right)^2 + \left(\frac{\partial \gamma_{yz}}{\partial t}\right)^2\right)\right)d\Omega \tag{6}$$

where

$$
\begin{Bmatrix} \{N\} \\ \{M\} \\ \{P\} \end{Bmatrix} = \begin{bmatrix} [A] & [B] & [E] \\ [B] & [D] & [F] \\ [E] & [F] & [H] \end{bmatrix} \begin{Bmatrix} \varepsilon^{(0)} \\ \varepsilon^{(1)} \\ \varepsilon^{(2)} \end{Bmatrix} \quad \begin{Bmatrix} \{Q\} \\ \{R\} \end{Bmatrix} = \begin{bmatrix} [A] & [D] \\ [D] & [F] \end{bmatrix} \begin{Bmatrix} \gamma^{(0)} \\ \gamma^{(2)} \end{Bmatrix}, \quad (7)
$$

$$
\left(A_{ij}, B_{ij}D_{ij}, E_{ij}F_{ij}, H_{ij}\right) = \int_{-h/2}^{+h/2} Q_{ij}(z, T)\left(1, z, z^2, z^3, z^4, z^6\right)dz \quad i, j = 1, 2, 3 \quad (8)
$$

$$
\left(A_{ij}, D_{ij}, F_{ij}\right) = \int_{-h/2}^{+h/2} Q_{ij}(z, T)\left(1, z^2, z^4\right)dz, \quad i, j = 4, 5, \quad (9)
$$

$$
(I_1, I_2, I_3, I_4, I_5, I_7) = \int_{-h/2}^{+h/2} \rho(z)\left(1, z, z^2, z^3, z^4, z^6\right)dz, \quad (10)
$$

$$
Q_{11} = Q_{22} = \frac{E_{eff}(z, T)}{1 - v_f^2}, \quad Q_{12} = v_f Q_{11}, \quad Q_{13} = Q_{23} = 0; \quad Q_{33} = Q_{44} = Q_{55} = \frac{E_{eff}(z, T)}{2(1 + v_f)}. \quad (11)
$$

The effective material properties E_{eff} of the FGMs are calculated by Voigt's model [13, 14], provided that Poisson's ratio v is a constant. The Young modulus E_{eff} and density ρ of FG structure are defined as:

$$
E_{eff}(z, T) = (E_c(T) - E_m(T))V_c + E_m(T), \quad (12)
$$

$$
\rho(z) = (\rho_c - \rho_m)V_c + \rho_m, \quad V_c = \left(\frac{2z + h}{2h}\right)^p, \quad (13)
$$

In formulas (11–13) z is the distance between the current point and the shell mid-surface, the index p ($0 \le p < \infty$) denotes the volume fraction exponent of ceramics V_c which is connected with volume fraction of metal V_m by relation $V_c + V_m = 1$.

3 Solution Method

To investigate linear vibrations of the FGM shallow shells of complex planform with various boundary conditions the R-functions theory [15] combined with variational Ritz's method (RFM) is used. The total energy functional for FGM shallow shell is as follows

$$
J = T - U \quad (14)
$$

Assuming that the shell vibrates periodically, the vector of unknown functions can be presented as

$$
\begin{aligned}
\vec{U}\left(u(x, y, t), v(x, y, t), w(x, y, t), \psi_x(x, y, t), \psi_y(x, y, t)\right) = \\
= \vec{U}\left(u(x, y), v(x, y), w(x, y), \psi_x(x, y), \psi_y(x, y)\right) \sin \lambda t
\end{aligned} \quad (15)
$$

where λ is a vibration frequency. Using formulas (14) and (15) and Hamilton's principle, we get the variational statement of the problem

$$\delta J = 0, \tag{16}$$

where

$$J = U\left(u, v, w, \psi_x, \psi_y\right) - \lambda^2 T\left(u, v, w, \psi_x, \psi_y\right). \tag{17}$$

Variation (16) of the functional (17) is carried out on the set of functions that satisfy the given boundary conditions.

Now, expressions for U and T in formula (17) depend on (x, y) and the kinetic energy takes the following form

$$T = \int_{\Omega} \left(I_0\left(u_0^2 + v_0^2 + w_0^2\right) + I_1\left(\Phi_x u_0 + \Phi_y v_0\right) + I_2\left(\Phi_x^2 + \Phi_y^2\right) - c_1 I_3\left(\gamma_{xz}^{(0)} u_0 + \gamma_{yz}^{(0)} v_0\right) \right.$$

$$\left. - c_1 I_4\left(\gamma_{xz}^{(0)} \Phi_x + \gamma_{yz}^{(0)} \Phi_y\right) + c_1^2 I_6\left(\gamma_{xz}^2 + \gamma_{yz}^2\right) \right) d\Omega.$$

In this study, minimization of functional (17) is performed by using the Ritz method, belonging to a powerful tool in the vibration analysis of shells and plates. The accuracy and stability of the Ritz method depend essentially on the choice of admissible functions.

Suppose that admissible functions $\{u_i\}$, $\{v_i\}$, $\{w_i\}$, $\{\psi_{xi}\}$, $\{\psi_{yi}\}$ have been constructed. Then, according to the Ritz method, unknown functions $u(x, y)$, $v(x, y)$, $w(x, y)$, $\psi_x(x, y)$, $\psi_y(x, y)$ are presented as follows.

$$u = \sum_{i=1}^{N_1} a_i u_i, \; v = \sum_{i=N_1+1}^{N_2} a_i v_i, \; w = \sum_{i=N_2+1}^{N_3} a_i w_i, \; \psi_x = \sum_{i=N_3+1}^{N_4} a_i \psi_{xi}, \; \psi_y = \sum_{i=N_4+1}^{N_5} a_i \psi_{yi}, \tag{18}$$

Coefficients of this expansion $\{a_i\}$, $i = 1, ..., N_5$ in (18) are yielded by the Ritz system

$$\frac{\partial J}{\partial a_i} = 0, \quad i = 1, ..., N_5.$$

4   Numerical Results

4.1   Test Problem. Shells with Rectangular Shape of Plan

Material properties of the FG mixture applied in the study are presented in Table 1. The corresponding values are from [7–11].

Test. The natural frequency of FG square shallow shells with movable simply supported edges and different curvatures with dimensionless parameter $a/h = 5$ is analyzed. Aluminum and Alumina FG mixture Al/Al_2O_3 are considered as constituent materials. The task was solved in framework of two theories: FSDT with shear coefficient 5/6 and TSDT. The number of the admissible functions was chosen as $N_1 = N_2 = N_3 = N_4 = 15$, $N_5 = 28$. Comparison of the obtained results with ones of works [9] is shown in Table 2.

Table 1. Mechanical properties of the constituent materials

Material	E (GPA)	ν	ρ (kg/m^3)
Al	70	0.3	2707
Al_2O_3	389	0.3	3800
Si_3N_4	322.27	0.3	2370
$SUS304$	207.78	0.3	8166
ZrO_2	200	0.3	5700

Table 2. Comparison of the fundamental frequency parameters $a/h = 5$ of the square FG shallow shells with simply supported movable edges (Al/Al_2O_3, $a/h = 5$)

$a/h = 5$								
b/R_y	a/R_x	Method	$p = 0$	$p = 0.5$	$p = 1$	$p = 4$	$p = 10$	$p = \infty$
0	0	RFM(FSDT)	0.211	0.180	0.162	0.139	0.132	0.108
		RFM(TSDT)	0.208	0.177	0.161	0.136	0.129	0.110
		[9]	0.212	0.182	0.164	0.138	0.131	0.108
0.5	0.5	RFM(FSDT)	0.2297	0.1961	0.1774	0.1497	0.1408	0.1168
		RFM(TSDT)	0.2335	0.1999	0.1806	0.1517	0.1425	0.1194
		[9]	0.2301	0.2000	0.1819	0.1526	0.1420	0.1172
1	1	RFM(FSDT)	0.2753	0.2370	0.2149	0.1774	0.1641	0.1400
		RFM(TSDT)	0.2782	0.2402	0.2179	0.1794	0.1656	0.1421
		[9]	0.2735	0.2425	0.2233	0.1858	0.1688	0.1393
0	0.5	RFM(FSDT)	0.2141	0.1827	0.1649	0.1405	0.1329	0.1089
		RFM(TSDT)	0.2182	0.1862	0.1680	0.1424	0.1347	0.1117
		[9]	0.2153	0.1855	0.1678	0.1413	0.1328	0.1096
0	1	RFM(FSDT)	0.2235	0.1913	0.1730	0.1459	0.1371	0.1137
		RFM(TSDT)	0.2271	0.1946	0.1759	0.1477	0.1386	0.1162
		[9]	0.2239	0.1945	0.1769	0.1483	0.1380	0.1140
0.5	−0.5	RFM(FSDT)	0.2049	0.1751	0.1582	0.1354	0.1283	0.1040
		RFM(TSDT)	0.2090	0.1785	0.1611	0.1373	0.1300	0.1070
		[9]	0.2064	0.1770	0.1596	0.1346	0.1270	0.1051
1	−1	RFM(FSDT)	0.1908	0.1631	0.1475	0.1262	0.1194	0.0969
		RFM(TSDT)	0.1945	0.1662	0.1501	0.1279	0.1209	0.09956
		[9]	0.1920	0.1648	0.1487	0.1252	0.1181	0.0977

4.2   Shells with a Complex Planform

New results for shallow shells with a complex planform (Fig. 2) were obtained.

It is assumed that shell is clamped completely including the cut-out. Geometrical dimensions are following:

$$a_1/a = 0.2; \ a_1 = b_1; \ r/2a = 0.25; \ h/2a = 0.5; \ \frac{2a}{R_x} = 1; \ \frac{2a}{R_y} = 0.$$

We will analyse four kinds of FGMs:

$$(M_1; M_2; M_3; M_4) = (Al/Al_2O_4; \ Al/ZrO_2; \ Si_3N_4; \ /SUS304; \ ZrO_2/Ti - 6Al - 4V).$$

Solution structure [1, 2, 15] for shells with complete clamped boundary can be taken as:

$$w = \omega\Phi_1, \quad u = \omega\Phi_2, \quad v = \omega\Phi_3, \quad \psi_x = \omega\Phi_4, \quad \psi_y = \omega\Phi_5$$

where $\Phi_i, \ i = \overline{1,5}$ are indefinite components of the structure [1, 2, 15].
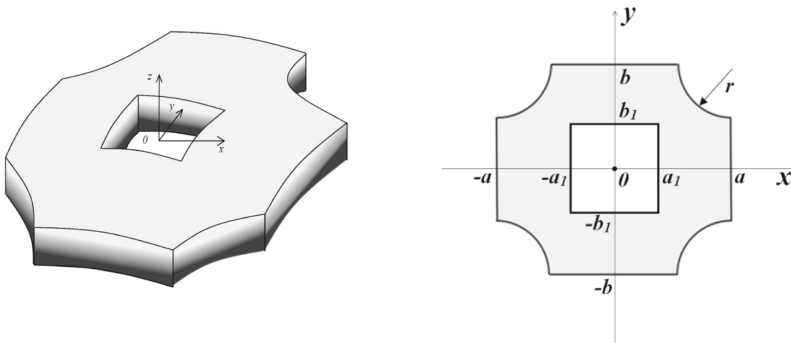
Fig. 2. Geometry of the FGM shallow shell and its plan shape

Indefinite components $\Phi_i, \ i = \overline{1,5}$ of the structure were expanded in a power series with account of problem symmetry.

To approximate indefinite component Φ_1 it was taken twenty eight terms of the polynomials series and remain indefinite components were approximated by fifteen terms. Function $\omega(x, y)$ is constructed by the R-functions theory and vanished on whole boundary.
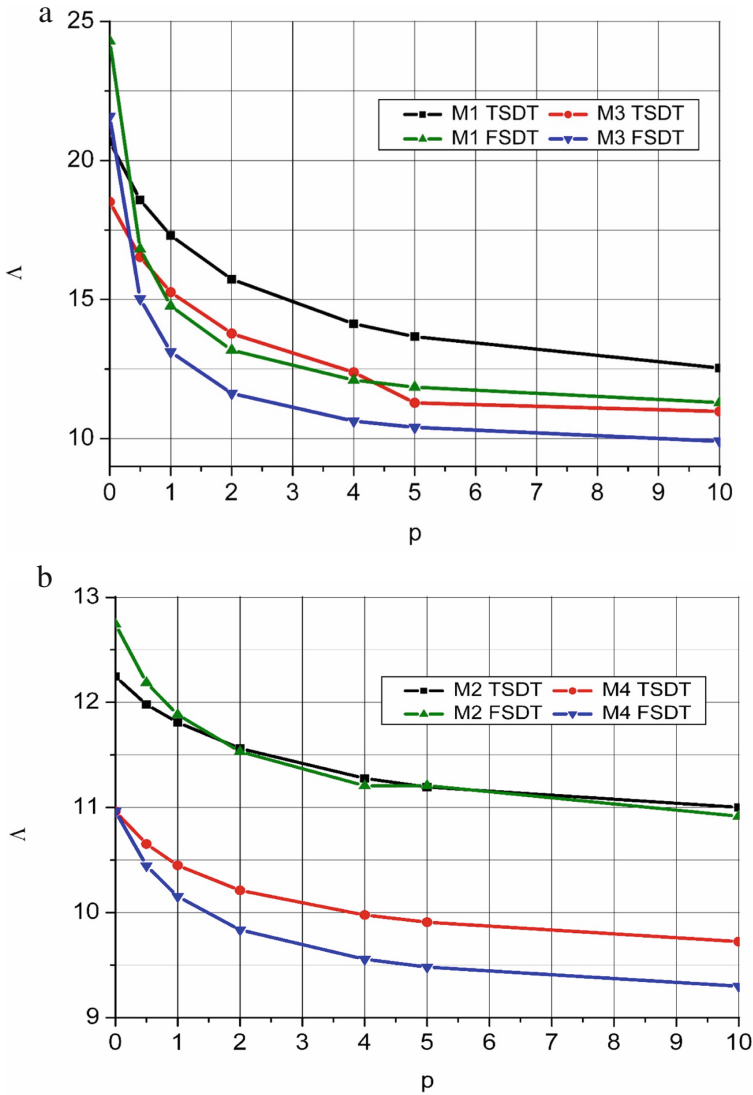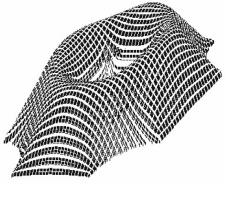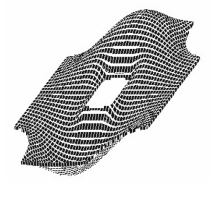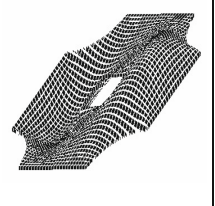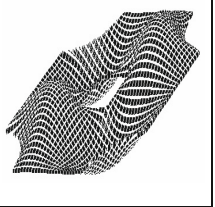
Fig. 3. a Effect of gradient index p on natural frequencies of shells made of M1 and M3. b Effect of gradient index p on natural frequencies of shells made of M2 and M4

Effect of the gradient index p on natural frequencies of cylindrical shells fabricated of the different materials is shown in Fig. 3a, b. The non-dimensional natural frequency parameters are defined as $\Lambda = \frac{\lambda}{h}\sqrt{\frac{\rho_m}{E_m}}$. Presented here results were obtained within the framework of two theories (FSDT (5/6) and TSDT). From Fig. 3a, b we can conclude, that it is necessary to use the higher-order shells theory for thick shells.

The modes of vibration for given cylindrical shells made of mixture M3 for gradient index $p = 2$ are presented in Table 3 $\left(p = 2;\ 2a/R_x = 1;\ 2a/R_y = 0;\ 2a/h = 0.5\right)$.

Table 3. Modes of vibration of the cylindrical shell, fabricated of M3 material

| (FSDT) $\Lambda_1 = 11.625$ | $\Lambda_2 = 12.825$ | $\Lambda_3 = 12.635$ | $\Lambda_4 = 15.953$ |
| (TSDT) $\Lambda_1 = 13.178$ | $\Lambda_2 = 13.994$ | $\Lambda_3 = 13.907$ | $\Lambda_4 = 17.608$ |

Notethat vibration modes obtained in framework of two theories are the same, but the natural frequencies differ from each other by 9–11.7%.

5   Conclusion

In this work, the R-functions method is used for the first time to study the free linear vibrations of functionally graded shallow shells with complex shape within the framework of the higher order deformation theory. Voight's model is used to calculate the effective material properties of FGM's. The corresponding software is created and applied for the test and solution of the new vibration problems for shallow shells. The comparisons of the results obtained within framework of FSDT and HSDT are carried out. Considered test problems confirm the validation of the proposed approach and developed software.

References

1. Kurpa, L., Shmatko, T., Awrejcewicz, J.: Vibration analysis of laminated functionally graded shallow shells with clamped cutout of the complex form by the Ritz method and the R-functions theory. Lat. Am. J. Solids Struct. **16**(1), e95 (2019)
2. Lidiya, K., Tetyana, S., Awrejcewicz, J.: Parametric Vibrations of Functionally Graded Sandwich Plates with Complex Forms. In: Lacarbonara, W., Balachandran, B., Ma, J., Tenreiro Machado, J.A., Stepan, G. (eds.) New Trends in Nonlinear Dynamics, pp. 69–77. Springer, Cham (2020). https://doi.org/10.1007/978-3-030-34724-6_8
3. Awrejcewicz, J., Kurpa, L., Shmatko, T.: Linear and nonlinear free vibration analysis of laminated functionally graded shallow shells with complex plan form and different boundary conditions. J. Non-linear Mech. **107**, 161–169 (2018)
4. Kurpa, L.V., Shmatko, T.V.: Buckling and free vibration analysis of functionally graded sandwich plates and shallow shells by the Ritz method and the R-functions theory. J. Mech. Eng. Sci. Part C **235**, 1–12 (2020)
5. Awrejcewicz, J., Kurpa, L., Shmatko, T: Application of the R-functions in free vibration analysis of FGM plates and shallow shells with temperature dependent properties. ZAMM - Journal of Applied Mathematics and Mechanics. Zeitschrift für Angewandte Mathematik und Mechanik, (2021) https://doi.org/10.1002/zamm.202000080
6. Kurpa, L.V., Shmatko, T.V.: Investigation of free vibrations and stability of functionally graded three-layer plates by using the R-functions theory and variational methods. J. Math. Sci. **249**(3), 496–520 (2020)

 7. Reddy, J.N., Liu, C.F.: A higher-order shear deformation theory of laminated elastic shells. Int. J. Eng. Sci **23**, 319–330 (1985)
 8. Reddy, J.N., Loy, C.T., Lam, K.Y.: Vibration of functionally graded cylindrical shells. Int. J. Mech. Sci. **41**, 309–324 (1999)
 9. Matsunaga, H.: Free vibration and stability of functionally graded shallow shells according to a 2D higher-order deformation theory. Compos. Struct. **84**, 132–146 (2008)
10. Shen, H.S.: Functionally Graded Materials of Plates and Shells. CRC Press, Florida (2009)
11. Neves, A.M.A., Ferreira, A.J.M., Carrera, E., Cinefra, M., Roque, C.M.C., Jorge, R.M.N., et al.: Free vibration analysis of functionally graded shells by a higher-order shear deformation theory and radial basis functions collocation accounting for through the thickness deformations. Eur. J. Mech. A/Solids **37**, 24–34 (2013)
12. Fazzolari, F.A., Carrera, E.: Refined hierarchical kinematics quasi-3D Ritz models for free vibration analysis of doubly curved FGM shells and sandwich shells with FGM core. J. Sound Vib. **333**, 1485–1508 (2014)
13. Thai, H.-T., Kim, S.-E.: A review of theories for the modeling and analysis of functionally graded plates and shells. Compos. Struct. **128**, 70–86 (2015)
14. Di Sciuva, M., Sorrenti, M.: Bending and free vibration analysis of functionally graded sandwich plates: an assessment of the refined Zigzag theory. J. of Sandwich Struct. Mater. **23**, 1–43 (2019)
15. Rvachev, V.L.: The R-functions Theory and Its Some Application. Naukova Dumka, Kiev (in Russian) (1982)

Spot Welded Joints of Steels Produced by Electric Arc and Laser Welding in Different Spatial Positions

Artemii Bernatskyi[(✉)] , Pavlo Goncharov , Mykola Sokolovskyi ,
Olha Goncharova , and Taras Nabok

E. O. Paton Electric Welding Institute of the National Academy of Sciences of Ukraine,
11 Kazymyr Malevych Street, Kyiv 03150, Ukraine
bernatskyi@paton.kiev.ua

Abstract. The research results on the application of the laser and electric arc welding technologies on AISI 316Ti/AISI 321 joints in the process of creation of a honeycomb thin-walled structure are presented. A comparative analysis of characteristics of spot welded joints of thin-sheet high-alloy steels produced by electric arc and laser welding in different spatial positions is carried out. Both technologies considered in this work are challenging to use in manufacture of shell structures of honeycomb panels with cellular filler. Over the course of this study the structure and the microhardness of the weld, as well as the heat-affected-zone were determined. As a result, it was established that the laser welding is more rational for use in mass production of large-sized structures due to the possibility to increase in the overall efficiency of the process, while the usage of argon-arc welding will be more rational if it is necessary to manufacture a large range of single parts or to manufacture small series of products.

Keywords: Argon-arc welding · Continuous wave laser welding · Welding of AISI 316Ti/AISI 321 joints · High-alloy steels · Honeycomb thin-walled structures · Thin-sheet panel

1 Introduction

The creation and development of modern structures of new technologies is associated with reduction of their mass [1]. In modern thin-sheet shell structures, the usage of multilayer shells, in which a high load-bearing capacity is achieved with a minimum loss of metal due to a rational distribution of it in the separate elements of a structure has become widespread [2]. Such structures have high strength and rigidity characteristics, good sound and thermal insulation properties with a relatively small mass [3]. A three-layered panel with cellular filler (also known as "honeycomb panel") is one of the types of honeycomb structures.

A honeycomb panel with cellular filler represents a composite three-layer welded structure, consisting of two load-bearing layers of thin-sheet metal and cellular filler located between them, as well as frame elements (edges, ends, cover plates, etc.) [4].

The load-bearing layers perceive loads (tension, compression, shear) and transverse bending moments in their respective planes. The filler, monolithically bonded to the load-bearing layers (linings), provides combined operation and stability of a three-layer structure and perceives transverse forces during its bending [5]. The manufacture of such panels requires production of a large quantity of welded spot joints. In this case, a series spot welding becomes necessary.

In welding industry, spot welding is one of the most widespread methods for manufacture of thin-sheet metal structures. It is used in creating products for construction purposes [6], power equipment [7], automotive engineering [8], railway cars [9], frame structures in rocket building [10], etc. [11]. Compared to continuous welding, spot welding provides minimal deformations of structures and allows for high accuracy manufacturing. The use of spot welding provides high efficiency and quality of performed works, while saving time and material resources thanks to reduction in straightening works, required because of their after-welding buckling, as well as decrease in electric power consumption.

The most widespread welding method is resistance spot welding [12]. However, it's usage in select cases is complicated. For example, it is not always possible to manufacture overlapped complex geometric shape joints with double-sided access while welding in flat position. It is also impossible to arrange the parts of said structures between the electrodes of resistance machines, which is necessary to provide sufficient pressure during welding. To weld large geometrically complex structures, a welding tool, capable of movement relative to the product during the manufacturing process is necessary. In other select cases, such as welding a one-sided spot joint of a thin-sheet, the usage of resistance spot welding causes difficulties due to the complexity in the constructive design of equipment required for resistance spot welding. The use of resistance welding with a single-sided current supply is limited by the low rigidity of joined parts as well as impossibility of using backing plates counteracting the pressure of electrodes. Also, resistance welding is complicated due to lack of possibility to perform this process on the side of lining. In this case, however, it is more expedient to use other welding methods of sequential welding to provide possibility to work on each side of a honeycomb structure: arc spot welding with non-consumable electrode in shielding gas [13]; electron beam welding [14]; laser welding [15].

The methods of arc spot welding (ASW) allow us to eliminate typical drawbacks of resistance spot welding machines [16]. Here, it is not necessary to use sizable forces when joining sheets of metal to have sufficient one-sided access to the product, and it is possible to perform welding in the presence of a regulated gap. Arc welding tool allows us to perform welding operations in all spatial positions at a considerable distance from the power source. The strength of the joints (static and fatigue), produced by arc spot welding, is comparable to the strength of the joints, produced by riveting or resistance spot welding, and in some cases is even higher [17]. Thus, the arc spot welding of a number of structures is the only possible and economically rational way to produce a welded spot joint. At the same time, the efficiency of arc spot welding is inferior to electron beam and laser welding methods [18].

The usage of laser spot welding (LSW) and electron beam spot welding methods in the manufacture of thin-walled multilayer shells envisages automation of the process,

which significantly reduces the impact of "human" factor and improves the end product quality [19]. However, laser and electron beam welding methods do not allow for the presence of a gap of more than 0.2 mm between the welded surfaces [20]. Therefore, the mentioned welding methods require usage of more complex additional technological equipment. The main drawbacks of electron beam welding method include: high cost of equipment as well as the need in specialized vacuum chambers, which greatly complicates the process and limits the widespread use of this welding method in manufacturing of thin-walled multilayer shells.

The aim of this work is a comparative analysis of structural features and mechanical characteristics of spot welded joints of thin-sheet high-alloy steels produced by electric arc and laser welding in different spatial positions.

2   Methodology

A characteristic feature of honeycomb structures is a very small thickness of applied metal (0.05–1.00 mm) and the presence of two outer thin-sheet linings, between which a third element – filler is located.

The filler is monolithically bonded to the linings and adds the necessary strength and rigidity to the structure. The filler is joined with the outer shell (upper sheet) and the inner frame ring (bottom sheet) by welding. The material for the outer and inner shell is an analogue of steel AISI 316Ti of 0.5–0.6 mm thickness. The cellular filler is made out of 0.2–0.3 mm thick AISI 321 steel sheets. The chemical composition of these steels is given in the Table 1 gives a summary of all heading levels.

Table 1.   Chemical composition of steels AISI 316Ti and AISI 321.

Steel grade	Composition of elements, %								
	C	Si	Mn	Cr	Ni	Mo	Ti	Nb	Fe
AISI 316Ti	≤0.03	≤0.1	≤0.1	10.0–11.0	9.0–10.5	1.8–2.3	0.7–1.1	≤0.15	Bal.
AISI 321	≤0.12	≤0.8	≤2.0	17.0–19.0	9.0–11.0	≤0.5	0.4–1.0	–	Bal.

In ASW, the inverter welding source "FRONIUS MW3000" as well as a specialized welding torch were used. The practicing of the argon-arc spot welding technology for a three-layer panel with cellular filler was carried out in the laboratory installation. The practicing of ASW technology was performed on 0.5 mm thick austenitic-ferrite AISI 316Ti steel, as well as on 0.2 mm thick austenitic AISI 321 steel specimens. The ASW was performed on the side of austenitic-ferrite class steel. The welding was carried out in flat and vertical positions ("on the wall"). In ASW of these specimens a tungsten 1.6 mm diameter WT-20 electrode was used. The protection of welding arc and welding zone was carried out by argon. The spot joints were welded with an arc of a constant power and with a pulsed arc, the power of which varied according to the cyclogram (see Fig. 1), which allowed us to reduce the heat input to welded joint, providing the optimal formation of weld geometry without forming hardened structures. The arc length

was 2 mm. The modes of pulsed argon-arc spot welding of specimens, performed at a frequency of 100 Hz with a smooth increment and a drop of welding current are given in the Table 2.
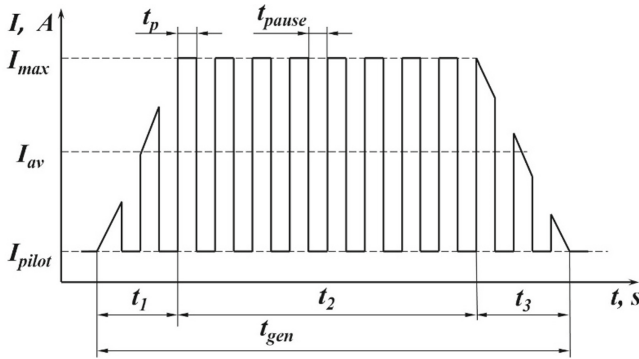
Fig. 1. Cyclogram of welding current at pulsed ASW: I_{max}, I_{av}, I_{pilot} – welding current of maximum, average values and pilot arc, respectively; t_{gen} – total welding time; t_1–t_3 – duration of rising of welding current, working welding current and its drop, respectively; t_p, t_{pause} – duration of welding current pulses and pause between them, respectively.

Table 2. Argon-arc spot welding modes.

No. of specimen	Welding current, A	Arc voltage, V	Welding time, s	Shielding gas consumption, l\min
1	40	12.6	2.0	12
2	50	13.3	2.0	12
3	44	15.6	2.3	13
4	50	13.0	1.8	12
5	60	13.4	1.6	13
6	70	13.3	1.6	13
7	80	15.5	1.6	13

Over the course of investigations, the Nd:YAG-laser "DY044" of the company "Rofin-Sinar" with radiation wavelength $\lambda = 1.06\,\mu m$ was used. By selecting the modes, a joint in the form of a spot of 4.0 mm diameter was produced, which corresponded to the size of a argon-arc weld spot. The process was conducted in argon shielding with the protection of melt pool and the back side of a joint. Quality and reliability of the produced joint were controlled by adjusting operating modes of the laser (continuous or pulsed), power of laser radiation, time of welding process, position of the lens focus relative to the parts being welded. The welding was carried out in flat and vertical position ("on the wall").

The metallographic examinations of specimens were performed using optical microscopy (using "Versamet" microscope) (Fig. 2 and Fig. 3), as well as scanning electron microscopy ("Philips" "SEM-515" microscope). The quantitative evaluation of element distribution in lines and separate zones was done using the energy dispersion analyzer of the "LINK" system.

3   Results

An overlapped welded joint in argon-arc spot-welding with non-consumable electrode was formed with a full penetration of an upper welded-on part and a full or partial penetration of a lower part with the formation of a weld spot nugget joined for the parts being welded. The use of electronic devices provided a rather accurate adjustment of arc burning time and strength of welding current. In this case, it is possible to regulate thermal energy emitted by welding arc within the wide ranges and to perform spot welding of a large thickness range (from 0.2 to 2.0 mm) without usage of filler metal.

The spot joints were welded for 1.6–2.3 s with 40–80 A of current, with blowing the joint zone by shielding gas. Reduction of temperature in the metal that surrounds the weld spot is facilitated by blowing the welding zone with argon as well as by removal of heat using a water-cooled supporting nozzle of welding tool. Thus, the correct choice of the optimal diameter of the weld spot is of great importance; not only to provide the required strength of the welded joint, but also being a necessary condition to achieve a high quality of spot weld joints. When changing spatial positions, a slight decrease in the dependence of the appearance of defects on the change in the technological parameters and conditions of argon-arc spot welding was observed. An increase of the feasibility of variation ranges of welding conditions, at which production of geometrically and mechanically satisfactory welded joints is possible, is observed to be from about $\pm 5\%$ to $\pm 10\%$. A typical microstructure of welded joint produced by argon-arc spot welding (general view) is presented in Fig. 2.a. The center of the weld has a grain size of 5–15 μm, the microhardness is in average 2420 MPa (Fig. 2.b).

At the top of the weld, where the AISI 321 was placed, the structure has a crystalline form with a microhardness of 1710 MPa. After a more detailed consideration of the "weld + AISI 321" interface, it was found that on the side of the weld both uniaxial structure with a 2530–2570 MPa microhardness, as well as crystallites with HV3 = 1940 MPa are observed. Similarly, crystallization on the side of the weld metal, as well as the cracks (up to 10%) were observed, microhardness near which reached 1060 MPa. At the same time, an activation zone with a depth of 15–20 μm with a microhardness of 2270 MPa at the interface was observed. Near the fusion line on the AISI 316Ti side, a fine-grained structure with a size of 5–10 μm and a microhardness of 2520 MPa is observed, followed by a decrease in the values of microhardness to 2320–2370 MPa at a depth of 100–200 μm from the joint line in the direction of base metal. In the base AISI 316Ti, the grain size is 5–20 μm with a microhardness of 2320–2420 MPa. The sharp gradients in the distribution of chemical elements were not observed. From the standpoint of proper geometry formation and a high level of mechanical characteristics, the optimal mode of argon-arc welding of spot joints was determined with such characteristics: welding current – 80 A; arc voltage – 15.5 V; welding time – 1.6 s; shielding gas consumption – 13 l/min.
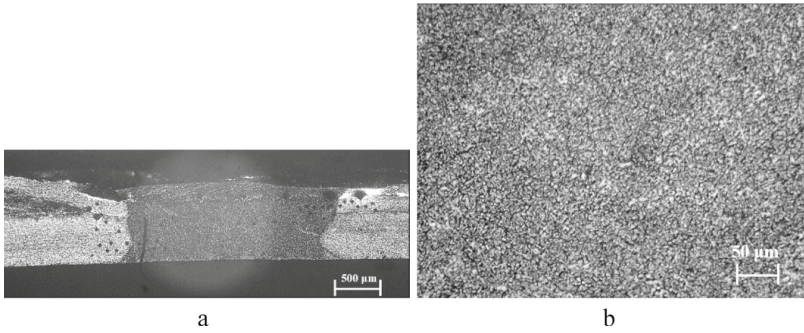
Fig. 2. Microstructure of welded joint produced by argon-arc spot welding (a) – general view; (b) – structure of weld metal on the fusion line.
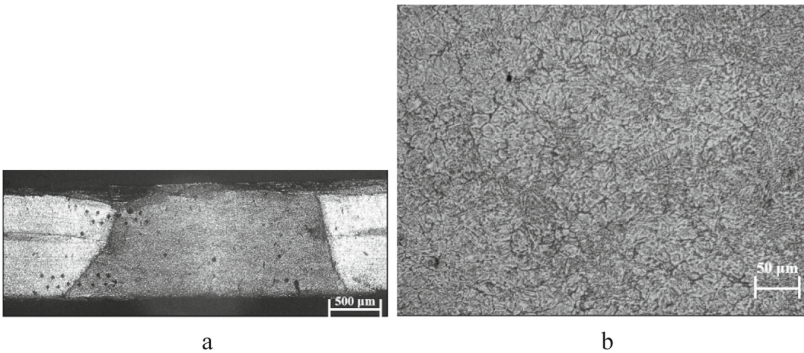
Fig. 3. Microstructure of welded joint produced by laser spot welding (a) – general view; (b) – structure of weld metal.

Experiments on laser welding of spot overlapped joints of 0.5 mm thick AISI 316Ti steel, as well as on 0.2 mm thick austenitic AISI 321 steel specimens were carried out in the laboratory stand based on the multicoordinate manipulator and the Nd:YAG DY044 laser. To improve the quality and efficiency of the laser welding process when manufacturing overlapped joints of heterogeneous stainless steels, following techniques were tried and practiced on the series of specimens: laser welding with a defocused beam; pulsed and continuous welding mode; use of different systems of gas shielding of a weld pool; as well as variation of the technological process parameters (laser radiation power, position of lens focus relative to welded surfaces, treatment rate, etc.). In order to determine the efficiency of each application, a series of studies was performed for each of the abovementioned methods. The performed studies allowed us to establish advantages and drawbacks of the aforementioned techniques. In the course of studies, the technological parameters varied in following ranges: laser radiation power P – from 200 W to 4000 W, defocusing value ΔF – from -40 to $+40$ mm, welding speed (movement of laser relative to the fixed adjusting clamp with the specimen) V – from 500 mm/min to 6000 mm/min. Gas protection of the weld pool was carried out at the consumption rate of Q 2–20 l/min using argon or helium.

It was established that the spot welded joints, optimal from the standpoint of weld geometry formation and the absence of defects in the form of cracks, lacks of penetration and burns, are formed during laser welding in a continuous generation mode in vertical spatial position; using such procedures as welding with non-focused beam (with displacement of lens focus relative to welded surfaces to $+20$ mm) and using argon protection at the consumption rate of 14 l/min. Optimal characteristics of the process are: power of laser radiation of 1500 W; treatment time of one spot of 0.5 s.

The change in the spatial position from flat to vertical allowed the authors to extend the ranges of variation of welding modes from about $\pm 5\%$ to $\pm 10\%$, at which it is possible to produce welded joint with satisfactory geometric and mechanical characteristics.

A special adjusting clamp was developed and manufactured for faster treatment of specimens (honeycomb panels with cellular filler). Its purpose is to clamp the specimen during laser welding. Thanks to its use, the efficiency for laser welding of 40 spot joints per a one setting and the percentage of rejection were determined.

A typical microstructure of a spot welded joint produced by laser welding is presented in Fig. 3.a. The center of the weld has a grain size of 20–50 µm, with an average microhardness of 2370 MPa (Fig. 3.b).

When studying the line of the "weld AISI 316Ti/AISI 321" joint, such results are observed. On the side of the weld, both in the interface with AISI 321 as well as with AISI 316Ti, the structure is mainly crystalline with h × l dimensions varying from 5 × 50 µm to 5 × 250 µm. The microhardness of the weld in the "weld AISI 321" interface is 2630 MPa. The grain size on the side of AISI 321 near the joint line is 5–15 µm with a microhardness of 2570 MPa. On the depth of 50–100 µm from the joint line the microhardness decreases to 2270–2420 MPa.

The results of mechanical tests of single spot welded joints produced by argon-arc and laser welding are given in Table 3. The comparison of the mechanical test results shows that the specimens welded by both methods meet the requirements for overlapped joints of high-alloy steel sheets of such thicknesses (shear force P). The shear force P for the specimens with a single spot joint produced using the technologies of laser and arc welding with non-consumable electrode at the optimal modes is 1.42 kN for both welding methods. The results of mechanical tests show that the specimens welded by spot laser welding have more stable values as compared to argon-arc spot welding using a non-consumable electrode. This can be explained by the relatively more complex stress-strain state of a spot welded joint produced by the argon-arc method.

Therefore, while further practicing technologies for manufacturing of honeycomb panels, the authors consider it expedient to perform comparative studies of the stress-strain state of the spot joints produced by the technology of laser and arc spot welding with non-consumable electrode.

Table 3. Results of mechanical tests.

No. of specimen	Shearing force of ASW (kN)	Shearing force of LSW (kN)
1	1.07	1.42
2	1.42	0.96
3	0.51	1.21
4	0.90	0.97
5	0.46	1.00
6	1.35	1.28

The percentage of welded spot joints defects (lacks of penetration, cracks, burns, etc.) during welding of honeycomb panels with cellular filler applying laser and argon-arc method is not higher than 0.5%.

Results, obtained in this study on the improvement of mechanical characteristics of AISI 316Ti and AISI 321 welded joints due to greater structural refinement favorably correlate with the results of a similar study, carried out by Kumar et al. [21]. In this study, authors have conducted a complex analysis (consisting of microstructural analysis, a hardness test as well as a tensile behavior test) of a selected AISI 304SS and AISI 316SS weld, aimed out to understand the metallurgical and mechanical behavior of the weld. The selection criteria in this work are based on the maximum and minimum strength achieved by the respective welds. It has been observed, that the current pulsation, base metal composition and variation in heat input have significant influence on control of the microstructural constituents (i.e. phase fraction, grain size etc.). This is also confirmed by results of a previous study by Du, Xin et al. [18]. Other studies, such as that conducted by Soltani and Tayebi [22], confirm the results of an earlier comparative study between arc spot welding (in this case – TIG welding) and laser spot welding of welds between AISI 304L and AISI 316L. It's results show that welding depth of TIG welding was higher than that of laser welding. Additionally, it was observed that by increasing voltage, the strength and toughness of samples decreased for both TIG and laser welding. However, this could be offset with increasing beam spot size in laser welding, which improved strength, toughness and hardness of the weld.

The relevance of these works is confirmed by conclusions made by Shehab et al. [23], which conclude that LSW is increasingly being seen as a high-speed substitute to resistance spot welding in many industries, especially when it comes to welding thin sheet metal parts.

As a result of investigations on laser and argon-arc spot welding of honeycomb panels with cellular filler, it was established that the process efficiency largely depends on the degree of its automation. At the same time, the efficiency of the technological process is significantly influenced by specific technological features of each process. The absence of the need in the additional mechanical clamping operation during the process of welding allowed the authors to drastically increase the overall rate of product treatment during laser welding compared to the arc welding process. At the same time, argon-arc spot welding requires less complex assembling technological equipment, which

reduces the cost of the process compared to laser welding, as well as allowing to carry out preparatory assembling operations significantly (2–3 times) faster. Thus, both of the technologies considered in this work are challenging to use in the manufacturing of shell structures (honeycomb panels) with cellular filler. The authors consider the usage of the laser welding process for production of large-sized structures to be more expedient, explaining their choice by the possibility to increase the overall treatment efficiency. However, when it is necessary to manufacture a large range of single parts or small series of small-sized products, the usage of argon-arc welding will be more expedient.

4   Conclusions

It was established that spot welded joints of steel of 0.5 mm thick austenitic-ferrite AISI 316Ti steel, as well as on 0.2 mm thick austenitic AISI 321 steel, optimal from the standpoint of weld geometry formation and the absence of defects in the form of cracks, lacks of penetration and burns, are formed during laser welding in a continuous generation mode in vertical spatial position while using such procedures as welding with non-focused beam (with displacement of lens focus relative to welded surfaces to +20 mm) and using argon protection at the consumption rate of 14 l/min. In this case, power of laser radiation should equal 1500 W with the treatment time of one spot is 0.5 s. The optimal mode of argon-arc welding of spot joints from the standpoint of proper geometry formation and a high level of mechanical characteristics, is determined to have following characteristics: welding current – 80 A; arc voltage – 15.5 V; welding time – 1.6 s; shielding gas consumption – 13 l/min.

The further direction of study is associated with the determination and comparison of stress-strain state of the welded spot joints produced applying the technologies of laser and arc spot welding with non-consumable electrode.

References

1. Zhang, D., Fei, Q., Zhang, P.: Drop-weight impact behavior of honeycomb sandwich panels under a spherical impactor. Compos. Struct. **168**, 633–645 (2017)
2. Xie, S., Jing, K., Zhou, H., Liu, X.: Mechanical properties of Nomex honeycomb sandwich panels under dynamic impact. Compos. Struct. **235**, 111814 (2020)
3. Mahmoudabadi, M.Z., Sadighi, M.: Experimental investigation on the energy absorption characteristics of honeycomb sandwich panels under quasi-static punch loading. Aerosp. Sci. Technol. **88**, 273–286 (2019)
4. Wei, A., Chang, B., Meng, F., Du, D., Han, Z.: Research on the weld position detection for the t-joints in web-core sandwich panels based on eddy current technology. Sensors **20**(9), 2691 (2020)
5. Petrushinets, L.V., Falchenko, Y.V., Fedorchuk, V.E., Shinkarenko, V.S.: Possibilities of manufacturing three-layer welded honeycomb panels from aluminium alloys. Paton Weld. J. **7**, 25–29 (2018)
6. Gavidel, S.Z.: Statistical approach to performance comparison of predictive algorithms: application in resistance spot welding. Wayne State University, Detroit (2018)
7. Klimenov, V.A., Slobodyan, M.S., Ivanov, Y.F., Kiselev, A.S., Matrenin, S.V., Vaulina, O.Y.: Structure and properties of Ti-Au fusion zone formed by spot welding. AIP Conf. Proc. **2310**(1), 020148 (2020)

8. Yu, J.: Adaptive resistance spot welding process that reduces the shunting effect for automotive high-strength steels. Metals **8**(10), 775 (2018)
9. Akkaş, N.: Effect of welding current and time on tensile-peel loading in resistance spot welding of SPA-H steel sheets used in railway vehicles. Acta Phys. Pol. A **132**(3), 549–552 (2017)
10. Sahoo, A., Tripathy, S.: Development in plasma arc welding process: a review. Mater. Today: Proc. **41**(2), 363–368 (2021)
11. Shen, Z., Ding, Y., Gerlich, A.P.: Advances in friction stir spot welding. Crit. Rev. Solid State Mater. Sci. **45**(6), 457–534 (2020)
12. Manladan, S.M., Yusof, F., Ramesh, S., Fadzil, M., Luo, Z., Ao, S.: A review on resistance spot welding of aluminum alloys. Int. J. Adv. Manuf. Technol. **90**(1), 605–634 (2017)
13. Wang, Y.: Research on arc spot welding of T12 steel. IOP Conf. Ser.: Earth Environ. Sci. **358**(5), 052020 (2019)
14. Gao, F., Yu, W., Song, D., Gao, Q., Guo, L., Liao, Z.: Fracture toughness of TA31 titanium alloy joints welded by electron beam welding under constrained condition. Mater. Sci. Eng.: A **772**, 138612 (2020)
15. Bernatskyi, A., Khaskin, V.: The history of the creation of lasers and analysis of the impact of their application in the material processing on the development of certain industries. Hist. Sci. Technol. **11**(1), 125–149 (2021)
16. Unnikrishnakurup, S., Rouquette, S., Soulié, F., Fras, G.: Estimation of heat flux parameters during static gas tungsten arc welding spot under argon shielding. Int. J. Therm. Sci. **114**, 205–212 (2017)
17. Chen, L., Suzuki, R.: Dissimilar metal joining process "element arc spot welding." Kobelco Technol. Rev. **36**, 41–49 (2018)
18. Abioye, T.E., Olugbade, T.O., Ogedengbe, T.I.: Welding of dissimilar metals using gas metal arc and laser welding techniques: a review. J. Emerg. Trends Eng. Appl. Sci. **8**(6), 225–228 (2017)
19. Du, X., Jin, X., Lv, H., Wang, S.: Experimental analysis of key parameters of laser ion welding of honeycomb plate heat exchanger. Therm. Sci. **23**(5), 2757–2764 (2019)
20. Poznyakov, V.D., et al.: Cold cracking resistance of butt joints in high-strength steels with different welding techniques. Strength Mater. **51**(6), 843–851 (2019)
21. Kumar, N., Mukherjee, M., Bandyopadhyay, A.: Comparative study of pulsed Nd:YAG laser welding of AISI 304 and AISI 316 stainless steels. Opt. Laser Technol. **88**, 24–39 (2017)
22. Soltani, H.M., Tayebi, M.: Comparative study of AISI 304L to AISI 316L stainless steels joints by TIG and Nd:YAG laser welding. J. Alloy. Compd. **767**, 112–121 (2018)
23. Shehab, A.A., et al.: CO_2 laser spot welding of thin sheets AISI 321 austenitic stainless steel. Arch. Mater. Sci. Eng. **106**(2), 68–77 (2020)

Determination of Composite's Bearing Strength in the Area of Circular Hole of Fastening Element

Oleksandr Dveirin[1] , Anton Tsaritsynskyi[2] , Tetyana Nabokina[2] ,
and Andrii Kondratiev[3](✉)

[1] ANTONOV COMPANY, Akademika Tupoleva. 1, Kyiv 03062, Ukraine
[2] National Aerospace University "Kharkiv Aviation Institute", Chkalova. 17, Kharkiv 61070, Ukraine
[3] O.M. Beketov National University of Urban Economy in Kharkiv, Marshal Bazhanov. 17, Kharkiv 61002, Ukraine
andrii.kondratiev@kname.edu.ua

Abstract. The system for experimental determination of the bearing strength of the composite parts in mechanical joints has been developed. The system includes fixation of the straight line fracture on the "load-displacement" diagram, as well as a special composite specimen, which is mounted in the original test device. The developed original specimen of the material in the form of a disk of circular or octagonal shape allows constructing the diagram of anisotropy of bearing strength with 4… 6 times decrease in the material consumption and reduction of the experiments' labor inputs 3… 4 times. The developed system greatly simplifies the experiments, since there is no need to measure the degree of ovalization of the hole in the process of loading. Processing and study of the results obtained in the course of the experiments showed that the difference in values of the ultimate bearing strength because of the anisotropy of properties of the material under study varied within 11… 60%. Basically, the minimum value of the ultimate bearing strength can be found in the direction of 45… 68°, closer to the upper limit of the specified range. Grouping of layers with longitudinal laying leads to the decrease in the ultimate strength of the material by 10…34%. Based on the results of the experiments, the engineering relationship was synthesized to predict the bearing strength of the wide range of structures of polymeric composite materials and diameters of fastening elements.

Keywords: Mechanical joint · Composite specimen · Package structure

1 Introduction

The wide application of polymeric composite materials (PCM) in the mechanical engineering is conditioned by the sharp decrease in metal consumption and, as a consequence, the weight of the product and increase in corrosion resistance and maintainability [1]. In its turn, it results in the significant reduction of the energy intensity of production and

improvement in its sustainability [2]. The use of PCM elements in the structures gives rise to new problems associated with their joining to each other and to metal structures [3, 4]. It is one of the most important questions in the designing of structures with the use of PCM. When determining the bearing capacity of mechanical joints of parts made of PCM, it is necessary to know a number of their mechanical characteristics, such as bearing, tensile, shear and interlaminar shear strength of the PCM. Starting of the accumulation of non-critical damage is most often preceded by the bearing of the hole wall in the place of its contact with the body of the fastening element. Bearing, or rather the point of transition from the collapsed material to uncollapsed one, initiates the failures such as breaking or shear of the part, or tear-out of material of the part [5]. Therefore, correct setting of the permissible level of collapse stresses is essential for ensuring of the bearing capacity and service life of the joint.

Research aim is to develop and test the methods and means for determining the bearing strength of laminated composites, taking into account anisotropy and lay-up sequence by thickness, on the basis of which the engineering design dependencies for the specific type of carbon fiber composite are to be synthesized.

2   Literature Review

Ultimate bearing strength is a conditional value for many reasons, including the area of collapse to which the bearing load refers, the law of distribution of the load within the bearing area, and recording of the moment of onset of the collapse. While the assumptions [6] have long been accepted regarding the first two factors, there are disagreements concerning the recording of the moment of onset of the collapse in accordance with the terminology proposed in the standard [7]. It is possible to use two approaches. The first one is the binding of the target values to any nominal value of the material. The second approach is to assess the collapse stresses on the basis of the onset of the collapse itself. The first approach is quite successfully used for the metal structures [8]. The generally accepted level of collapse stresses for metals in the mechanical joint is estimated as fractions of the yield strength or tensile strength. The yield point is used for the plastic materials, and the tensile strength is used for brittle ones. Most of the PCM based on thermosetting matrices are brittle materials [9, 10]. Then, by analogy with brittle materials, the ultimate tensile strength can be taken as the base value, but in PCM this value depends both on the structure of the package and on the load direction [11]. In view of this, the said approach is of little use for the composite products. The second approach, in principle, is suitable for the composites, but there is a certain arbitrariness in the assignment of the attribute of onset of the collapse. The use of residual ovalization of the hole as an attribute of onset of the collapse is the most widespread method. For example, achievement of 4% residual ovalization of the hole as the attribute of reaching the conditional ultimate bearing strength is assumed in [12]. The papers [7, 13] propose to take the achievement of 2% residual ovalization of the hole as the attribute of reaching the conditional ultimate bearing strength. Here it may be noted that we are talking about residual ovalization, that is, plastic deformation occurred in the material of the part (which is unacceptable in PCM), since microcracks arise at the place of bearing, and they can spread into the package and cause the further failure [5, 6]. Therefore, the first

argument against assignment of the residual ovalization as a criterion for assessing the collapse stresses is the material brittleness and impossibility to ensure the fitting of the bolt shank into the hole with the guaranteed tightness [5, 6]. The second argument is the fact that almost all design patterns of mechanical joints [14, 15] are based on the linear setting, i.e. presence of plastic deformations is not allowed. Then the subsequent assessment of the bearing capacity of the joint in terms of bearing should be based on the interpretation of the bearing strength as the beginning of nonlinearity on the "load-displacement" diagram [16].

To maintain continuity in the approaches to the calculations of mechanical joints, a number of papers use for the joints of parts made of PCM the same "conditional calculations" as for the metal parts. Approaches to assessment of the level of permissible stresses during collapse in these papers have been adjusted. The effect of the PCM thickness and its lay-up sequence on the bearing strength is studied experimentally in [17]. In addition, finite element analysis using two-dimensional failure criteria was carried out to assess the behavior of collapse progression. Multi-point collapse tests to determine the progression of damage in the area around the bolt holes at different loading stages are described in [18]. It is shown that combination of the loads results in the complex distribution of stresses along the contour of the hole. The development and verification of the numerical mesoscale model for predicting damage and failure of bolted joints in the laminated composites of the various configurations and geometries is represented in [19]. It is demonstrated that dimensions of the collapsed PCM layer depend on the magnitude, nature and time of action of the load. The paper [20] proposes the method for predicting the probabilistic failure of composite joints. This method takes into account the random nature of the local plastic deformation, which occurs under compression of the solids at the points of their contact. The paper [21] shows that bearing of the material begins when the stress intensity reaches a certain value close to its yield point. With the static effect of the load, it occurs simultaneously over the entire area of the contact; in case of non-static one, bearing covers the contact area gradually.

The issue of processing of the collapse test results is equally important. The known collapse test methods [7, 12, 13, 22] traditionally suggest to use rectangular plates to assess the bearing strength. It allows to easily assess the bearing strength in the longitudinal and transverse directions, as well as under the condition of balanced two-way reinforcement [0°/90°±45°], in the direction of ±45°. However, in the studies of the anisotropy of bearing strength, it is necessary to avoid the influence of edge effects, which makes the use of specimens in the form of rectangular plates impractical.

Consequently, on the basis of the above we can draw a conclusion about complexity and contradictory nature of the problem of experimental support. On the one hand, it is necessary to provide the most accurate description of the material behavior in the contact area, taking into account the most important factors acting in the real joint. On the other hand, when interpreting and analyzing the results, one should remain within the framework of the engineering methodology for calculations of the joint. The latter requirement restricts the use of finite element analysis of the areas of contact of the fastening element with a hole in the part [16].

3   Research Methodology

According to the performed review, when assessing the ultimate bearing strength it is necessary to take into account both the structure of the package (properties of initial components of the material, angles of arrangement of layers in the package, proportion and distribution of layers by thickness) and direction of load application relative to the axes of orthotropy of the package properties, as well as geometric parameters (hole diameter and package thickness). The most promising prototype of the specimen to carry out the necessary study is the disk specimen proposed in [14, 15]. On the basis of this prototype, the unified specimen has been developed (Fig. 1), allowing to measure the bearing strength in five directions (six measurement points in each), and the equipment required for tests (Fig. 2).
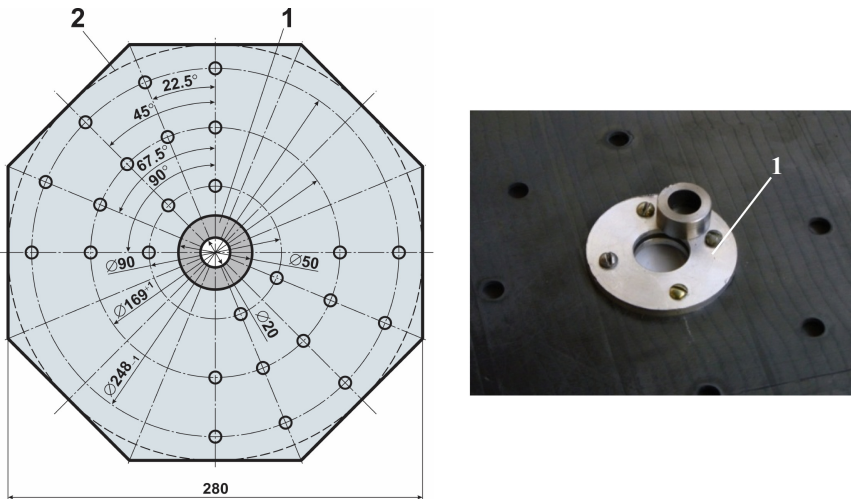
Fig. 1. Type specimen for collapse test with holes up to 8 mm in diameter: 1 – central reinforcement plate; 2 – contour of the specimen in the form of a circle.

Dimensions of the sample are selected in such a way that, while fulfilling the conditions for the specimen fixation in the equipment, the distance between the holes is not less than four diameters, which allows asserting that there is no mutual influence [14, 15]. This approach helped to complete the task with minimal material consumption.

When choosing the scheme of testing equipment, we took into account the requirements to provide the following: installation in the tensile testing machine without adapters; self-centering of the elements of equipment and specimen relative to the loading axis (which would allow to avoid bending of the equipment and specimen); possibility of quick and convenient readjustment of the specimen holder (in this case, the probability of errors during a series of tests is minimized). After analysis, it was decided to use for collapse tests of the PCM the variant of equipment (Fig. 2), which provided two shear planes of the pin. Swivel bearings were required to compensate for possible misalignment of holes in the arms. To ensure easy readjustment of the equipment, swivel

bearings are fitted with slip-fit bushings with the relevant internal bore diameters. The only inconvenience is the lack of mobility of the equipment links during repositioning of the pin.
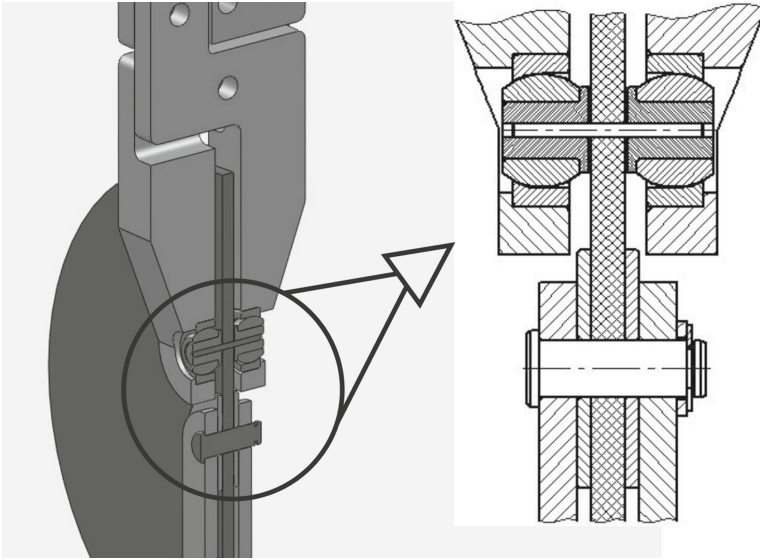
Fig. 2. Variant of equipment for collapse test of PCM package.

Material ELUR-008 P/5-211-BN with the properties shown in Table 1 was used for the manufacturing of specimens.

Table 1. Properties of unidirectional package based on ELUR-008 P/5–211-BN.

Parameter	Value	Parameter	Value
Monolayer thickness, mm	0.087	Ultimate tensile strength across the grain, MPa	21
Ultimate tensile strength along the grain, MPa	677	Ultimate compressive strength across the grain, MPa	210
Ultimate compressive strength along the grain, MPa	939	Modulus of elasticity across the grain, GPa	7
Modulus of elasticity along the grain, GPa	136	Ultimate shear strength in the laying plane, MPa	75
Poisson's ratio	0.32	Shear modulus in the laying plane, GPa	5.5

For studying of the effect of the package structure on the ultimate bearing strength, the most common variants of the package were taken, on the condition of different

proportion of layers with 0° lay-up pattern: No. 1 – $[0^{\circ}_{0.7}; \pm45^{\circ}_{0.2}; 90^{\circ}_{0.1}]$; No. 2 – $[0^{\circ}_{0.5}; \pm45^{\circ}_{0.4}; 90^{\circ}_{0.1}]$; No. 3 – $[0^{\circ}_{0.8}; \pm45^{\circ}_{0.2}]$; No. 4 – $[0^{\circ}_{0.3}; \pm45^{\circ}_{0.6}; 90^{\circ}_{0.1}]$. The layers in the package were line-symmetrical with regard to the median surface.

To construct the plan of experiments, the ranges of variation of the geometric parameters were taken: hole diameters 3, 4, 5, 6, 8 mm; specimen thicknesses 1.74, 3.48, 5.22, 6.96, 8.7 mm, corresponding to the package of 20, 40, 60, 80 and 100 layers. The comprehensive study of influence of the material structure for all variants of combinations of geometric parameters requires significant costs; therefore, the initial parameters were analyzed and the number of measurement points was reduced. Based on the above conditions, the list of specimens required for experiments was formed (Table 2).

Table 2. List of specimens for bearing experiments.

Specimen number	Structure number	Structure	Thickness, mm/number of monolayers	Diameter of the hole, mm	Specimen number	Structure number	Structure	Thickness, mm/number of monolayers	Diameter of the hole, mm
1	1	$[0^{\circ}_{0.7}; \pm45^{\circ}_{0.2}; 90^{\circ}_{0.1}]$	1.74/20	3, 4	11	1	$[0^{\circ}_{0.7}; \pm45^{\circ}_{0.2}; 90^{\circ}_{0.1}]$	5.22/60	4
2	2	$[0^{\circ}_{0.5}; \pm45^{\circ}_{0.4}; 90^{\circ}_{0.1}]$	1.74/20	3, 4	12	2	$[0^{\circ}_{0.5}; \pm45^{\circ}_{0.4}; 90^{\circ}_{0.1}]$	5.22/60	4
3	1	$[0^{\circ}_{0.7}; \pm45^{\circ}_{0.2}; 90^{\circ}_{0.1}]$	1.74/20	5	13	1	$[0^{\circ}_{0.7}; \pm45^{\circ}_{0.2}; 90^{\circ}_{0.1}]$	5.22/60	6
4	2	$[0^{\circ}_{0.5}; \pm45^{\circ}_{0.4}; 90^{\circ}_{0.1}]$	1.74/20	5	14	2	$[0^{\circ}_{0.5}; \pm45^{\circ}_{0.4}; 90^{\circ}_{0.1}]$	5.22/60	6
5	1	$[0^{\circ}_{0.7}; \pm45^{\circ}_{0.2}; 90^{\circ}_{0.1}]$	1.74/20	6	15	3	$[0^{\circ}_{0.8}; \pm45^{\circ}_{0.2}]$	5.22/60	6
6	2	$[0^{\circ}_{0.5}; \pm45^{\circ}_{0.4}; 90^{\circ}_{0.1}]$	1.74/20	6	16	4	$[0^{\circ}_{0.3}; \pm45^{\circ}_{0.6}; 90^{\circ}_{0.1}]$	5.22/60	6
7	1	$[0^{\circ}_{0.7}; \pm45^{\circ}_{0.2}; 90^{\circ}_{0.1}]$	1.74/20	8	17	1	$[0^{\circ}_{0.7}; \pm45^{\circ}_{0.2}; 90^{\circ}_{0.1}]$	6.96/80	4
8	2	$[0^{\circ}_{0.5}; \pm45^{\circ}_{0.4}; 90^{\circ}_{0.1}]$	1.74/20	8	18	2	$[0^{\circ}_{0.5}; \pm45^{\circ}_{0.4}; 90^{\circ}_{0.1}]$	6.96/80	4
9	1	$[0^{\circ}_{0.7}; \pm45^{\circ}_{0.2}; 90^{\circ}_{0.1}]$	3.48/40	4	19	1	$[0^{\circ}_{0.7}; \pm45^{\circ}_{0.2}; 90^{\circ}_{0.1}]$	8.7/100	3
10	2	$[0^{\circ}_{0.5}; \pm45^{\circ}_{0.4}; 90^{\circ}_{0.1}]$	3.48/40	4	20	2	$[0^{\circ}_{0.5}; \pm45^{\circ}_{0.4}; 90^{\circ}_{0.1}]$	8.7/100	3

According to Table 2, variants, which allowed covering almost all range of values of the parameters under study, were selected.

4   Results and Discussion

Specimens' test results were processed statistically with the determination of the arithmetic mean and the root-mean-square value; besides, the check according to the Chauvenet criterion was carried out [23]. The results of measurement are grouped by dimensionless parameters: the angle of deviation of the direction of the load application from the axis of orthotropy of the specimen φ, ratio of the specimen thickness to the diameter of the fastening element $\bar{\delta}$; ratio of bending modulus of the package to the modulus of elasticity of the monolayer in the direction of grain $\bar{E}$. . This minimum number of parameters will allow taking into account the mutual influence of anisotropy of properties, geometric parameters (thickness of the part and diameter of fastening element), as well as the structure of the package. The results obtained are shown in the graphs of Fig. 3.
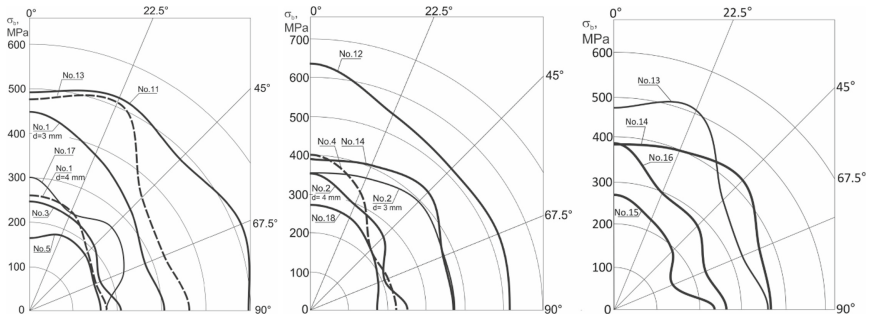
Fig. 3. Distribution of the conventional ultimate bearing strength for specimens: a – with the structure No. 1, b – with the structure No. 2 and c – with structures No. 1–No. 4.

Based on the obtained data, a dependence was synthesized to calculate the values of the conventional ultimate bearing strength. The expressions were assumed to have the structure below

$$\bar{\sigma}_b = f_1\left(\bar{\delta},\ \varphi\right) \cdot f_2\left(\bar{E},\ \varphi\right), \tag{1}$$

where $\bar{\sigma}_b$ is ultimate bearing strength, referred to the ultimate strength of PCM along the grain.

To obtain the coefficients of function (1), polynomials of the 3$^{\text{rd}}$ and 4$^{\text{th}}$ degree and approximation of functions by the least squares method were used.

The result is as follows:

$$
\begin{aligned}
\overline{\sigma}_b\left(\varphi,\ \overline{\delta},\ \overline{E}\right) = &((0.1511\varphi^3 + 0.025\varphi^2 - 0.8569\varphi + 0.1969)\overline{\delta}^3 \\
&+(-0.8867\varphi^3 + 0.8324\varphi^2 + 2.4594\varphi - 1.2611)\overline{\delta}^2 \\
&+(1.1182\varphi^3 - 1.4281\varphi^2 - 1.996\varphi + 2.594)\overline{\delta} \\
&+(-0.1737\varphi^3 + 0.1544\varphi^2 + 0.4967\varphi - 0.2505)) \\
&\times((442.27\varphi^4 - 1444.3\varphi^3 + 1436.4\varphi^2 - 375.22\varphi - 80.007)^3 \\
&+(-829.6\varphi^4 + 2715.9\varphi^3 - 2698.9\varphi^2 + 691.15\varphi + 146.32)^2 \\
&+(499.55\varphi^4 - 1638.5\varphi^3 + 1625.3\varphi^2 - 406.21\varphi - 86.4) \\
&+(-94.595\varphi^4 + 310.49\varphi^3 - 306.75\varphi^2 + 74.178\varphi + 17.254)).
\end{aligned}
\tag{2}
$$

Example of check of the accuracy of approximation for the package with structure No. 1 $[0^\circ{}_{0.7}; \pm45^\circ{}_{0.2}; 90^\circ{}_{0.1}]$ is given in Table 3. The discrepancy between the calculated and experimentally measured values of the ultimate bearing strength was calculated by the formula

$$
\Delta = \left(\frac{\overline{\sigma}_{b\,calc} - \overline{\sigma}_{b\,exp}}{\overline{\sigma}_{b\,exp}}\right)100\%.
$$

Table 3. Discrepancy between the calculated and measured values of the ultimate bearing strength for specimens with the package structure No. 1 $[0^\circ{}_{0.7}; \pm45^\circ{}_{0.2}; 90^\circ{}_{0.1}]$, Δ %.

Specimen No	$\overline{\delta}$	Specimen loading direction φ, °				
		0	22,5	45	67,5	90
5	0.29	−5.9	0.2	0.1	−8.9	−21.8
3	0.36	8.3	4.4	4.2	−6.2	−2.5
1	0.46	−17.9	−17.7	−29.2	−29.9	−43.7
1	0.59	14.6	7.9	8.6	8.4	−0.1
9	0.89	−5.1	−5.2	1.5	2.1	−12.3
13	0.91	−3.6	6.2	−18.8	−22.6	−27.1
11	1.37	2.2	2.4	−7.8	−3.2	−15.1
17	1.93	0.2	−4.7	2.4	−13.8	−15.6

Processing and study of the results obtained during the experiments showed the following. The difference in values of the ultimate bearing strength because of the anisotropy of properties of the investigated material varied within 11… 60%. Basically, the minimum value of the ultimate bearing strength can be found in the direction of 45…67.5°, closer to the upper limit of the specified range. It follows from the above that in case of calculations of mechanical joints loaded with normal, shear force and temperature field (with several fastening elements in series) the minimum value of the ultimate bearing strength should be used. When the direction of the force vector acting on the fastening elements is predetermined and guaranteed, the value of the ultimate bearing strength

in this direction can be used. The function of the influence of relative thickness of the part has a maximum at the value $\bar{\delta} = 0.8\ldots1.3$. It should be additionally checked, since at high values of the relative thickness the influence of bending of the bar on the bearing conditions may increase. Structure of the package affects the resistance of the part to bearing. As shown by the results given in Table 3, the ultimate bearing strength is directly related to the proportion of layers of two-way reinforcement (in this case $\pm45°$). It is recommended to provide a proportion of $\pm45°$ layers at 30% as a minimum. The layers with different laying angles should be evenly distributed over the thickness of the package. Grouping of layers with $0°$ lay-up pattern leads to the decrease in the ultimate strength of the material by $10\ldots34\%$. At the same time, rare types of failure were found such as a shear on four sides of the block with $0°$ pattern.

Thus the system for experimental determination of the bearing strength of composites has been developed, which unlike the papers [7, 12, 13], system is characterized by the fact that for determination of the bearing strength of the polymeric composite, the proposal is substantiated towards interpretation of this characteristic as the value of conventional stresses at which a straight line fracture is observed on the "load-displacement" diagram. As distinct from the classical theory [12, 13] it greatly simplifies the experiments, since there is no need to measure the degree of ovalization of the hole in the process of loading. It is of prime importance for low-diameter fastening elements and molded holes becoming more common in the composite structures. This confirms the conclusions of a number of papers, such as [6, 14]. In addition, study of the nature of the change in the "load-displacement" curve will allow more correct selection of the CM structures in the area of mechanical joint in the future [16].

The original material specimen in the form of circular or octagonal disk, fixed in the testing machine in the center with a fork, has been proposed and implemented in practice; it allowed to construct a diagram of the anisotropy of bearing strength with 4… 6 times decrease in material consumption and reduction of the experiments' labor inputs 3… 4 times compared to known collapse test methods [7, 12, 13, 22]. For loading of the fastening element, the test device characterized by self-aligning grips to compensate for errors and automatically adjustable force of the grip pressing to the disk specimen was developed and manufactured; such device allows both double-sided and one-sided (console) grip of the fastening element and is suitable for collapse tests of materials and shear tests from the hole to edge of the specimen.

5   Conclusions

According to the results of the experiments carried out for carbon fiber composite based on ELUR-0.08P tape and 5-211-BN binder, the engineering relationship was synthesized to predict the bearing strength of the wide range of PCM structures and diameters of fastening elements (3, 4, 5, 6 and 8 mm) which found practical application at the "Antonov" State Enterprise.

References

1. Hsissou, R., Seghiri, R., Benzekri, Z., Hilali, M., Rafik, M., Elharfi, A.: Polymer composite materials: a comprehensive review. Compos. Struct. **262**, 113640 (2021). https://doi.org/10.1016/j.compstruct.2021.113640

2. Hu, Z., Vambol, O., Sun, S.P.: A hybrid multilevel method for simultaneous optimization design of topology and discrete fiber orientation. Compos. Struct. **266**, 113791 (2021). https://doi.org/10.1016/j.compstruct.2021.113791

3. Fomin, O., Lovska, A.: Improvements in passenger car body for higher stability of train ferry Engineering Science and Technology. Int. J.-Jestech **23**(6), 1455–1465 (2020). https://doi.org/10.1016/j.jestch.2020.08.010

4. Smetankina, N., Ugrimov, S., Kravchenko, I., Ivchenko, D.: Simulating the process of a bird striking a rigid target. In: Ivanov, V., et al. (eds.) DSMIE 2019. LNME, pp. 711–721. Springer, Cham (2020). https://doi.org/10.1007/978-3-030-22365-6_71

5. Kostyk, K., Hatala, M., Kostyk, V., Ivanov, V., Pavlenko, I., Duplakova, D.: Simulation of diffusion processes in chemical and thermal processing of machine parts. Processes **9**(4), 698 (2021). https://doi.org/10.3390/pr9040698

6. Zhai, Y.N., Li, D.S., Li, X.Q., Wang, L.: An experimental study on the effect of joining interface condition on bearing response of single-lap, countersunk composite-aluminum bolted joints. Compos. Struct. **134**, 190–198 (2015). https://doi.org/10.1016/j.compstruct.2015.08.078

7. ASTM D5961/D5961M-17: Standard test method for bearing response of polymer matrix composite laminates. In, p. 31 (2017)

8. Kovalov, A., Otrosh, Y., Rybka, E., Kovalevska, T., Togobytska, V., Rolin, I.: Treatment of determination method for strength characteristics of reinforcing steel by using thread cutting method after temperature influence. In: Andronov, V. (ed.) International Scientific Applied Conference on Problems of Emergency Situations, PES 2020, 1006 MSF, pp. 179–184. Trans Tech Publications Ltd (2020). https://doi.org/10.4028/www.scientific.net/MSF.1006.179

9. Kombarov, V., Kryzhyvets, Y., Biletskyi, I., Tsegelnyk, Y., Aksonov, Y., Piddubna, L.: Numerical control of fiberglass pipe bends manufacturing. In: IEEE 2nd KhPI Week on Advanced Technology, pp. 357–362 (2021). https://doi.org/10.1109/KhPIWeek53812.2021.9570068

10. Kondratiev, A., Slivinsky, M.: Method for determining the thickness of a binder layer at its nonuniform mass transfer inside the channel of a honeycomb filler made from polymeric paper. Eastern-Eur. J. Enterpr. Technol. **6**(5–96), 42–75 (2018). https://doi.org/10.15587/1729-4061.2018.150387

11. Baran, I., Cinar, K., Ersoy, N., Akkerman, R., Hattel, J.H.: A review on the mechanical modeling of composite manufacturing processes. Arch. Comput. Methods Eng. **24**(2), 365–395 (2016). https://doi.org/10.1007/s11831-016-9167-2

12. Military Handbook - MIL-HDBK-17-1F: Composite Materials Handbook, vol. 1 - Polymer Matrix Composites Guidelines. U.S. Department of Defense (2002)

13. ASM handbook. Volume 21, Composites. ASM International. Handbook Committee, Knovel (Firm) (2001)

14. Beketova, G., Shevtsova, M., Symonov, V.: Static and fatigue characteristics of pinned metal-composite joints. Mech. Compos. Mater. **55**(5), 655–666 (2019). https://doi.org/10.1007/s11029-019-09842-9

15. Kondratiev, A.: Improving the mass efficiency of a composite launch vehicle head fairing with a sandwich structure. Eastern-Eur. J. Enterpr. Technol. **6**(7–102), 6–18 (2019). https://doi.org/10.15587/1729-4061.2019.184551

16. Dveirin, O.Z., Andreev, O.V., Kondrat'ev, A.V., Haidachuk, V.Y.: Stressed state in the vicinity of a hole in mechanical joint of composite parts. Int. Appl. Mech. **57**(2), 234–247 (2021). https://doi.org/10.1007/s10778-021-01076-4

17. Takamoto, K., et al.: Experimental and numerical studies of the open-hole compressive strength of thin-ply CFRP laminates. Compos. A Appl. Sci. Manuf. **145**, 10 (2021). https://doi.org/10.1016/j.compositesa.2021.106365

18. Cao, Y.J., et al.: Experimental investigation on bearing behavior and failure mechanism of double-lap thin-ply composite bolted joints. Compos. Struct. **261**, 14 (2021). https://doi.org/10.1016/j.compstruct.2021.113565

19. Zhuang, F.J., Arteiro, A., Furtado, C., Chen, P.H., Camanho, P.P.: Mesoscale modelling of damage in single- and double-shear composite bolted joints. Compos. Struct. **226**, 19 (2019). https://doi.org/10.1016/j.compstruct.2019.111210

20. Liu, F.R., Fang, Z.A., Zhao, L.B., Zhang, J.Y., Hu, N.: A failure-envelope-based method for the probabilistic failure prediction of composite multi-bolt double-lap joints. Compos. Part B-Eng. **172**, 593–602 (2019). https://doi.org/10.1016/j.compositesb.2019.05.034

21. Zhao, J.Q., Zhou, H.J., Sun, X.Y., Jing, Y.H.: Evaluation on compressive properties of composite laminates with a hole reinforced by metal plate. Compos. Struct. **258**, 9 (2021). https://doi.org/10.1016/j.compstruct.2020.113423

22. Shah, V.: Handbook of Plastics Testing and Failure Analysis, 3rd edn. Wiley, Hoboken (2007)

23. Bingham, N.H., Fry, J.M.: Regression: Linear Models in Statistics. Springer, London (2010). https://doi.org/10.1007/978-1-84882-969-5

Elastoplastic Thermo-mechanical Stressed State of Turbine Blades Locking Joints

Ihor Palkov[2] , Mykola Shulzhenko[3] , Konstantin Avramov[3,4,5(✉)] ,
and Ivan Breslavsky[1]

[1] McGill University, Montreal, QC, Canada
[2] Joint-Stock Company Turboatom, Kharkiv 61037, Ukraine
[3] National Academy of Science of Ukraine, Podgorny Institute for Mechanical Engineering,
Kharkiv, Ukraine
`kvavr@kharkov.ua`
[4] National Technical University "Kharkiv Polytechnic Institute", Kharkiv, Ukraine
[5] Department of Technical Systems, Kharkiv National University of Radio Electronics, Kharkiv,
Ukraine

Abstract. Thermo-mechanical stressed state of blades locking joints and the disk of the middle pressure first stage are analyzed. The integrity violation of the locking joints is observed after long-term turbine operations. The main objective of this paper is determination of the causes of the turbine unit fracture. The effect of contact interaction between bodies and plastic states on the unit strength is analyzed. The most stressed elements of the locking joints are determined from numerical simulations. The methodology of analysis of elastoplastic thermo-mechanical stressed state contact problem by using 3D model of locking joints is suggested. The computer model is verified by comparison the finite element results with experimental data and by the convergence analysis.

The significant temperature stresses are generated due to dependence of linear expansion coefficient on the temperature field. The maximal tensile stresses are observed close to the holes for the pins. The behavior of the contact stresses in the locking joint is analyzed by calculation of the elastoplastic thermo-mechanical stressed state using the commercial software ANSYS. The data of the stress-strain state calculations, which are obtained using plastic model with account of bilinear and multilinear approximations of the stress-strain curve, are close.

Keywords: Stress-strain state · Locking joints · Contacting bodies · Turbine blade

1 Introduction

Many efforts have been done to analyze thermo-mechanical stressed states of turbine units. The heat transfer and stress-strain state were analyzed numerically by the finite element method to obtain temperature field and stress distributions in [1]. The results showed that the maximum thermal stress occur in the vicinity of the cooling ducts where the temperature gradient is maximum. Methodology of prediction of thermo-mechanical

fatigue of stream turbine rotor is treated in [2]. The trained neural network model for estimating the turbine blade life cycle as a function of parameters, which affect the blade metal temperature and thermo-mechanical stresses, is developed in [3]. The computer model on the basis of the finite element method was developed in order to predict the creep behavior of high pressure turbine blades [4]. The paper [5] presents the thermo-mechanical analysis of a typical small gas turbine engine to study the blade tip clearance influenced by the deformation of turbine stage components during transient phases. The paper [6] presents an analysis of the fracture of the gas turbine 2nd stage blade. The effects of thermal barrier coating thickness on temperature and stress distribution over the blade body are investigated in [7]. The study [8] presents the analysis of non-stationary stresses and fatigue cracking in impulse steam turbine rotors. The research [9] investigates the effects of excessive damage as blades rupture in the high-pressure turbine. The methods of the structures dynamics are treated in [10–13].

The integrity of the blades locking joints of the middle pressure stage is destroyed after turbine long time operation (Fig. 1). The breakaway of the disk part close to locking joints is observed. As follows from the preliminary analysis of the fracture of the unit, bearing capacity of this unit was inadequate. Complex geometry of the structure, high operational temperatures, significant temperature gradient, contact interactions of the turbine elements have an influence on this breakaway.
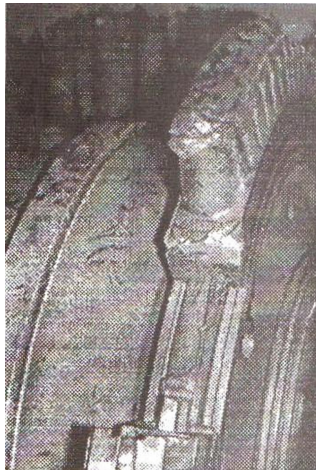

Fig. 1. Turbine disk close to blades after fracture

The accurate numerical calculations of the blades locking joints stress-strain states will be carried out to predict the cause of the fracture. The subsequent accounting of the different factors allows determining their influence on the stress-strain state of the locking joints. The stress-strain state of the structure is calculated by the finite element method, which is implemented in the commercial software ANSYS.

2   Methodology

The objective of this investigation is analysis of the stress-strain state of the locking joint of the middle pressure first stage blades. Elastoplastic thermo-mechanical stressed state is analyzed to predict the fracture of the locking joints. The temperature field is accounted to analyze the stress-strain state of the structure. The blades operate under the action of nonuniform temperature field due to the heat supply from gas flow. Therefore, the mechanical properties of the structure materials are changed. Moreover, the thermal expansions of the structural elements are unequal, which induces the temperature stresses. The combination of these stresses with mechanical ones, which generates by the external loads, can result the structure damage. The significant plastic strains occur and the structure is fractured. The temperature contact stresses are calculated in the locking joints accounting the heat transfer. The interactions of the contacting bodies are described by essentially nonlinear problem. The interactions of the temperature and mechanical strains are described by the boundary conditions in the bodies contact area with unknown parameters. The stress-strain state and the contact interactions between the bodies depend on the temperature fields. Moreover, this temperature fields depend on the contact interactions between the bodies too [14].

The model of contact layer with contact finite elements is used to describe the temperature contact interactions in the locking joints [14]. The mechanical interactions of the contacting bodies are determined by the value of the interpenetration. The main parameter of contact layer is contact stiffness C_n. The contact stresses are determined from the following equations:

$$\sigma_n = C_n\left(u_n^{(1)} - u_n^{(2)} - \delta_n\right),$$

where n is number of contact points; $u_n^{(1)}$, $u_n^{(2)}$ are displacements of the surfaces in the normal directions; δ_n is initial clearance between the contacting surfaces.

The ideal heat contact is assumed on the boundaries of the contacting bodies. The ideal heat contact is expressed by equality of temperatures and the heat flows on the contacting surfaces of two bodies [14]:

$$T_1\left(x_k, y_k, z_k, t\right) = T_2\left(x_k, y_k, z_k, t\right),$$

$$\lambda_1\left(\frac{\partial T}{\partial n}\right)_k = \lambda_2\left(\frac{\partial T}{\partial n}\right)_k,$$

where $\lambda_1(T)$, $\lambda_2(T)$ are heat conduction coefficients of the contacting bodies depending on the temperature fields T; $\left(x_k, y_k, z_k\right)$ are coordinates of contact surfaces points.

The problem of thermal conduction precedes the calculations of heat contact interactions between the bodies of the locking joints. The values of the contact stresses are calculated more exactly by iteration algorithm, which is implemented in the software ANSYS.

Finite element model has several domains of contact interactions: contacts domains of pins and disk; contacts areas of blade roots and shafts. Transfers of the forces between the bodies are observed in the contact areas. The concentration of the finite element mesh in contacts areas is done to achieve the convergence of the solution.

Theory of elasto-plastic stress-strain state is used to analyze the locking joints of the middle pressure first stage. Simple loading occurs in the locking joints. In this case, the theory of the elasto-plastic stress-strain state predicted accurately the experimental data [15–17]. The total strains consist of elastic, plastic and temperature strains [15]:

$$\varepsilon = \varepsilon_e + \varepsilon_p + \varepsilon_t,$$

where ε_e, ε_p, ε_t are elastic, plastic and temperature strains. Multilinear and bilinear approximations are used to describe the stress-strain curves of the blade materials. The slopes of the first sections of the stress-strain curves approximations are determined from elastic properties of the material [15].

The centrifugal forces for the rotor rotation with the angular velocity 314.16 rad/s are considered as the applied loads. The sector of the bladed dick with the corner angle *φ = 20°* is calculated numerically due to the structure symmetry. The symmetry conditions are set on the sides. The structure computer model with 371498 finite elements is used to calculate the stress-strain state of the locking joint (Fig. 2).
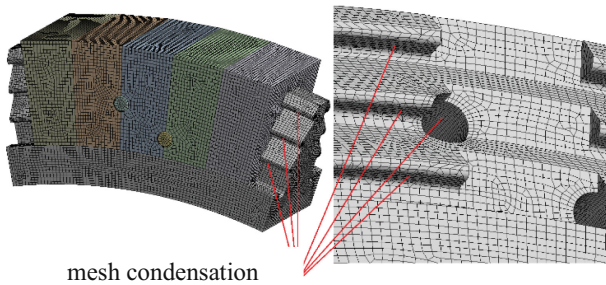

mesh condensation

Fig. 2. Finite element mesh of locking joint

The finite element *Solid226* with twenty nodes is used for mesh generation. This finite element has generalized coordinates to describe mechanical displacements and temperature fields. Thus, this element allows solving heat contact problem with account of plastic state. The optimal sizes of the finite elements are obtained by calculations of the locking joints stress-strain state. From the convergence analysis, it is obtained, that the optimal finite elements size is 3 mm. The mesh condensation is used in the contact area. The convergence is analyzed to choice the mesh in the contact area. From the convergence analysis, it is obtained, that the size of the finite elements is 1 mm.

3   Results of Numerical Simulations

The distributions of the radial stresses in the locking joints are obtained accounting thermoelastic behavior of material (Fig. 3). As follows from Fig. 3, the distributions of the radial stresses have very complex form. The areas of the material compressions alternate with the areas of the material expansions. Maximal compression stresses are equal to 50 MPa. Maximal tensile stresses are observed near the disk holes for pins. These stresses are equal to 1787 MPa. The maximal von Mises equivalent stresses are equal to 2800 MPa. Thus, the plastic state of the structure material can be observed.

As follows from the stress-strain state numerical calculations, the significant increase of the stresses are observed due to temperature field. Significant thermal stresses take place due to significant dependence of the linear expansion coefficient on the temperature field. The areas with maximal tension stresses are observed at the holes for pins and the fillets of locking joints. The tensile stresses in the holes exceed significantly the yield stress.

The effect of the temperature strains in the locking joints on the distribution of the contact pressure is analyzed by the solution of heat contact problem. The redistribution of the stresses between the contacting bodies in comparison with the stress-strain state of the structure without accounting the temperature field is observed.
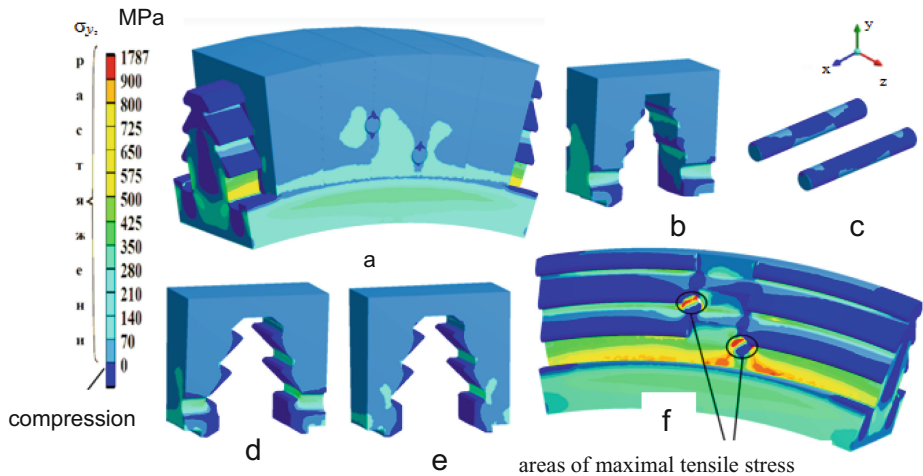

Fig. 3. The distributions of radial stresses: a. locking joint; b. locking blade; c. pins; d. disk
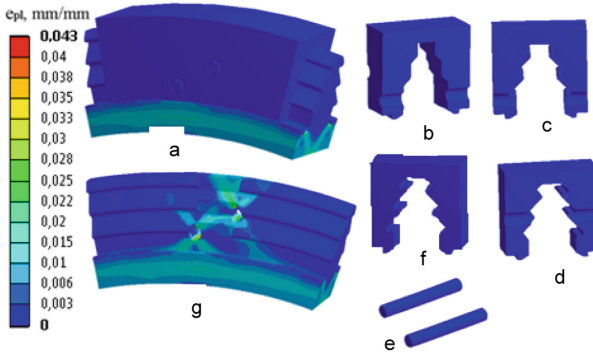
Fig. 4. Distributions of equivalent plastic strains, which are obtained using bilinear approximation of stress-strain curve: a. locking joint; b. locking blade; c. blade; e. pins; f. blade; g. disk
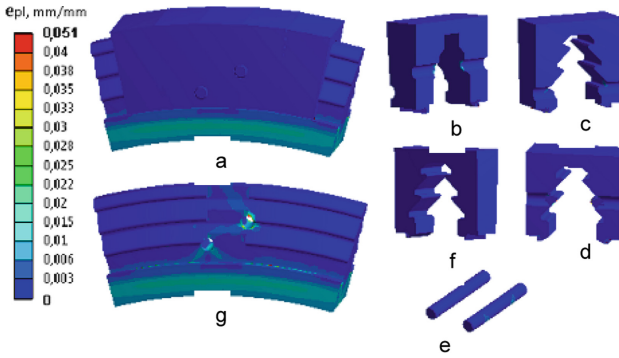

Fig. 5. Distributions of equivalent plastic strains, which are obtained using multilinear approximation of stress-strain curve: a. locking joint; b. locking blade; c. blade; e. pins; f. blade; g. disk

The distributions of the equivalent plastic strains in the blades locking joints are shown on Fig. 4 and Fig. 5. These data help to detect the areas of plastic deformations. Figure 4 and Fig. 5 show the distribution of equivalent plastic strains, which are obtained using bilinear and multilinear approximations of the stress-strain curve. One color scale is used to perform qualitative analysis of distribution of equivalent plastic strains in the locking joints. The patterns of equivalent plastic strains distributions at two types of stress-strain curve approximations are identically described the areas of maximal strains. Note, that the maximal values of strains are different in two cases. The maximal equivalent strains for the calculations with multilinear approximation are equal to 0.051 mm/mm and the maximal one at calculations with bilinear approximation are 0.043 mm/mm. The maximal plastic strains are observed at the hole in the disk for the pins (Fig. 4g, Fig. 5g). Note, that the von Mises equivalent stresses in this area are equal to 2800 MPa. The area between holes and area close to the locking joint have significant value of strains. In the rest part of the disk, the value of the plastic strains is not great; it

is equal to 0.002 mm/mm. Figure 6 shows the distribution of the von Mises equivalent stresses on the locking joints.
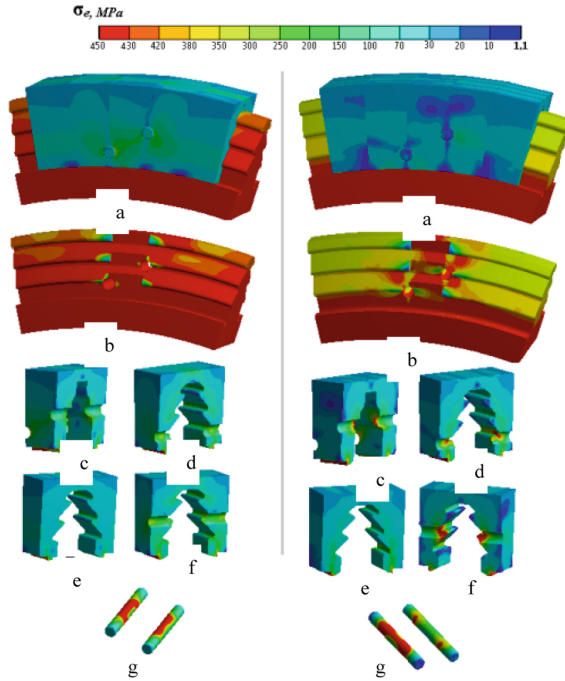

Fig. 6. The distribution of von Mises equivalent stresses in locking journals. The data, which are obtained using bilinear and multilinear approximations, are shown in left and right columns, respectively. a. locking joints; b. disk; c. locking blade; e. blade; g. pins

The obtained distributions of the von Mises equivalent stresses in the locking joints have complex form. This takes place due to stresses redistributions in the case of plastic deformations of the structure material. The structure areas with the values of the stresses close to the yield point $\sigma_T = 450$ MPa is observed near the holes for pins. The maximal equivalent stresses, which are obtained by using bilinear and multilinear approximations of the stress-strain curve, are equal to 448 MPa and 443 MPa, respectively. Thus, the numerical values of the maximal equivalent stresses for two cases are close. The difference in the distributions of the equivalent stresses in the locking joint for two types of stress-strain curves approximations is observed. The stressed state, which is calculated using bilinear approximation, has less drop of the von Mises equivalent stresses.

The maximal contact stresses are observed on the third pair of the blade bearing surface. The maximal stresses occur near holes for pins. Contact stresses have large gradient on all bearing surfaces. The maximal contact stress on the third bearing surfaces of the blades is equal to 200 MPa. The mean value of the contact stresses on the bearing surface is equal to 80 MPa.

4   Conclusions

The new methodology for analysis of the contact stress-strain state of the locking joint with account of elastoplastic thermo-mechanical state is suggested.

The maximal plastic strains are equal to 0.05 mm/mm. These strains are observed near the holes for pins.

The essential differences of the contact stresses on the bearing surfaces of the blades are observed. The maximal contact stresses are equal to 200 MPa. They are observed at the third bearing surface.

References

1. Vaferi, K., et al.: Thermo-mechanical simulation of ultrahigh temperature ceramic composites as alternative materials for gas turbine stator blades. Ceram. Int. **47**, 567–580 (2021)
2. Nesládek, M., Jurenka, J., Litvinov, M., Ruzicka, M., Mest'anek, P., Dzugan, J.: An assessment of thermo-mechanically induced fatigue damage of a stream turbine shaft. Procedia Struct. Integrity **7**, 190–197 (2017)
3. Sanaye, S., Hosseini, S.: Prediction of blade life cycle for an industrial gas turbine at off-design conditions by applying thermodynamics, turbo-machinery and artificial neural network models. Energy Rep. **6**, 1268–1285 (2020)
4. Branda, P., Infante, V., Deus, A.M.: Thermo-mechanical modeling of a high pressure turbine blade of an airplane gas turbine engine. Procedia Struct. Integrity **1**, 189–196 (2016)
5. Kumar, R., Kumar, V.S., Butt, M.M., Seikh, N.A., Khan, S.A., Afzal, A.: Thermo-mechanical analysis and estimation of turbine blade tip clearance of a small gas turbine engine under transient operating conditions. Appl. Therm. Eng. **179**, 115700 (2020)
6. Sławiński, D., Ziółkowski, P., Badur, J.: Thermal failure of a second rotor stage in heavy duty gas turbine. Eng. Fail. Anal. **115**, 104672 (2020)
7. Ziaei-Asl, A., Ramezanlou, M.T.: Thermo-mechanical behavior of gas turbine blade equipped with cooling ducts and protective coating with different thicknesses. Int. J. Mech. Sci. **150**, 656–664 (2019)
8. Banaszkiewicz, M.: Numerical investigations of crack initiation in impulse steam turbine rotors subject to thermo-mechanical fatigue. Appl. Therm. Eng. **138**, 761–773 (2018)
9. Eryilmaz, I., Guenchi, B., Pachidis, V.: Multi-blade shedding in turbines with different casing and blade tip architectures. Aerosp. Sci. Technol. **87**, 300–310 (2019)
10. Avramov, K.V., Borysiuk, O.V.: Nonlinear dynamics of one disk asymmetrical rotor supported by two journal bearings. Nonlinear Dyn. **67**, 1201–1219 (2012)
11. Avramov, K.V.: Nonlinear forced vibrations of a cylindrical shell with two internal resonances. Int. Appl. Mech. **42**, 169–175 (2006). https://doi.org/10.1007/s10778-006-0072-5
12. Avramov, K.V., Gendelman, O.V.: Interaction of elastic system with snap-through vibration absorber. Int. J. Non-Linear Mech. **44**, 81–89 (2009)
13. Breslavsky, I., Avramov, K.V., Mikhlin, Y., Kochurov, R.: Nonlinear modes of snap-through motions of shallow arch. J. Sound Vib. **311**, 297–313 (2008)
14. Shul'zhenko, N.G., Gontarovskii, P.P., Zaitsev, B.F.: Problems of thermal strength, vibration monitoring and life time of energetic equipment. LAP LAMBERT Academic Publishing GmbH & Co. KG, Saarbrücken (2011)

15. Lemaitre, J., Chaboche, J.-L.: Mechanics of Solid Materials. CUP, Cambridge (1990)
16. Lubarda, V.A.: Elastoplasticity Theory. CRC Press, Florida (2002)
17. Dunne, F., Petrinic, N.: Introduction to Computational Plasticity. Oxford University Press, Oxford (2005)

Weighted Eigenvalue Counts on Intervals for Spectrum Optimization

Anton Tkachuk[1(✉)] and Mykola Tkachuk[2]

[1] Department of Engineering and Physics, Karlstad University, 658 88 Karlstad, Sweden
`anton.tkachuk@kau.se`
[2] National Technical University "Kharkiv Polytechnical Insitute", 2, Kyrpychova Street, 61002 Kharkiv, Ukraine

Abstract. Power equipment is prone to vibrations. Removing eigenfrequencies of a structure from the interval of working frequencies reduces the probability of resonance during operation. In this contribution, a structural optimization problem is formulated whose objective at a minimum removes all eigenfrequencies from a given frequency interval. We consider systems without damping whose mass and stiffness matrices depend continuously on real parameters. The approach relies on the identity proposed by Futamura for eigenvalue count on intervals. The identity uses a contour integral in a complex plane of a trace of a specially constructed matrix. The contour integral is evaluated numerically using the trapezoidal rule over a circular path. The latter expression is differentiable. Present contribution extends the identity by adding a concave weighting function strictly positive in the interval. Furthermore, an explicit expression for the gradient of the objective and a simple optimization strategy are presented. Finally, a multi-degree of freedom example illustrates the performance of the approach.

Keywords: Eigenvalue counts on interval · Structural optimization · Eigenvalue spectrum

1 Introduction

The identity proposed recently by Futamura in [1] triggered the interest in eigenvalue counts on intervals in the context of numerical linear algebra. The identity computes the number of real eigenvalues in a given interval for a generalized eigenvalue problem of two symmetric matrices. It uses a contour integral in a complex plane of a trace of a specially constructed matrix. The contour should cross the endpoints of the interval, and a circle or an ellipse is the standard contour path. Furthermore, numerical quadrature of the contour integral with a moderate number of points provides valuable results even for large matrices. The algorithm can be significantly accelerated if a stochastic estimation of the trace is used.

Eigenvalue counts are currently used in numerical linear algebra. Information about eigenvalue distribution accelerates computations of electronic structure [2]. Eigenvalue counts are also included as preprocessors in the FEAST library for linear and non-linear eigenvalue problems since version 3.0 [3]. Efficient computation of the contour

integral in the Futurama identity may be carried out by trapezoidal, Gauss, or Zolotarev quadrature rules [1, 4, 5, 7]. In addition, standalone eigenvalue solvers may be derived from the high order moments computed with extensions of the identity [8].

The identity of Futamura distinguishes three features desired for an objective in structural optimization. First, the eigenvalue count is a differentiable function unless an eigenvalue belongs to the contour. Second, eigenvalues and eigenvectors are never explicitly computed. Third, avoiding a resonance would mean that the eigenvalue count on the interval of working frequencies is zero. Combining these features suggests a new class of heuristic objective functions for avoiding resonances in discrete mechanical systems without damping.

This contribution is organized into six Sections. A literature review on the topic of structural optimization of vibrating systems is given in Sect. 2. Problem statement for avoiding resonances of mechanical systems, the novel objective and optimization strategy are introduced in Sect. 3. Results for a numerical example and the general properties of the method are described in Sect. 4. Finally, the conclusion and direction of future work are given in Sect. 5.

2 Literature Review

Structural optimization of vibrating systems is a classical problem of mechanical design; see a detailed review on the topic [15]. This problem is usually considered by optimizing the natural frequencies (spectrum) or steady-state response under known harmonic loads at one or several frequencies. In this contribution, the focus is on the optimization of the spectrum. A typical spectrum optimization problem maximizes the first (base) eigenfrequency with a constraint on the total mass of the structure [9]. The common objective is the Rayleigh quotient, which requires explicit knowledge of the corresponding eigenvector. Alternatively, a dual formulation with a semi-definiteness constraint on dynamic stiffness is possible for the same problem [10]. However, the computational costs of the semi-definite programs is substantially higher than for the Rayleigh quotient. For optimization of higher eigenfrequencies, mode-tracking algorithms based on modal assurance criterion (MAC) are used [11, 12]. These algorithms allow reliable and accurate computation of objectives as weighted sums of eigenfrequencies or frequency gap between two consequent frequencies. These objectives are available in commercial optimization tools such as OptiStruct, Genesis, MSC Nastran or TOSCA. Application studies of this approach for power equipment and rotor dynamics show good performance [16, 17].

Special objectives are introduced for avoiding resonances in given frequency bands. For example, a normalized sum of eigenfrequency squares is used in [13, 18] and a sum of smoothed Heaviside functions computed for each eigenfrequency is used in [14]. The efficient implementation combines these objectives with the solid isotropic material with penalization (SIMP) approach for geometry description and a gradient-based optimization algorithm as a method of moving asymptotes (MMA). However, this combination requires the explicit computation of the eigenfrequencies and their sensitivities, which is computationally expensive. The identified gap of the work is to propose an objective for resonance avoidance that avoids explicit computation or ordering of eigenvalues and has the potential of cheap computation for large problems.

3 Research Methodology

3.1 Problem Statement

Problem statement: Consider a linearized eigenvalue problem for a system without damping

$$\left(\mathbf{K}(\mathbf{s}) - \omega^2 \mathbf{M}(\mathbf{s})\right)\boldsymbol{\varphi} = 0 \tag{1}$$

$\mathbf{K}(\mathbf{s})$ and $\mathbf{M}(\mathbf{s})$ denote the stiffness and mass matrices of a system with n degrees of freedom depending on a vector of p real design parameters $\mathbf{s}$. Design parameters $\mathbf{s}$ belong to an admissible non-empty set Q. The generalized eigenvalue problem in Eq. (1) generates a spectrum of the structure $\{\omega_j\}_{j=1}^n$. Each eigenfrequency ω_j corresponds to the eigenvector $\boldsymbol{\varphi_j} \in \mathbb{R}^n$. There is a single interval of eigenfrequencies $[\omega_a, \omega_b]$ that eigenfrequencies of the system in Eq. (1) should avoid. *Find* values of design parameters $\mathbf{s}$ from an admissible set Q such that the spectrum of the system does not have any eigenfrequency in a given interval $[\omega_a, \omega_b]$.

3.2 Heuristic Objective Function and Optimization Strategy

The problem statement is not yet formalized as a computable and tractable expression. Below, we introduce the necessary mathematical apparatus and propose an appropriate objective function. For simplicity of the expressions, squares of angular eigenfrequencies are used below

$$\lambda_j = \omega_j^2 \tag{2}$$

and they are referred to as eigenvalues of the system Eq. (1). The endpoints of the interval a scaled similarly and this interval is called herein the forbidden zone. Eigenvalue count μ for spectrum $\{\lambda_j\}_{j=1}^n$ in an interval $[\lambda_a, \lambda_b]$ is denoted with

$$\mu_{[\lambda_a, \lambda_b]} = \sum_{j=1}^n h(\lambda_j), \tag{3}$$

where function h is defined

$$h(\lambda_j) = \begin{cases} 1, \lambda_a \leq \lambda_j \leq \lambda_b \\ 0, \text{otherwise} \end{cases}. \tag{4}$$

We propose a novel heuristic objective function that is a weighted eigenvalue count

$$J(\mathbf{s}) = \sum_{j=1}^n g(\lambda_j) h(\lambda_j), \tag{5}$$

where weighting function $g(\lambda)$ is a concave function for all real numbers that is strictly positive in the forbidden zone $[\lambda_a, \lambda_b]$. The objective function has a following valuable

property: it is strictly positive if at least one eigenvalue of the spectrum is in the forbidden zone and it is exactly zero if the spectrum does not have any eigenvalue in the forbidden zone. The role of the weighting function is twofold. The first role is to push the eigenvalues from the center of the forbidden zone to boundaries. The second role is to reduce the discontinuity of the objective when an eigenvalue passes an endpoint of the interval. Herein, a quadratic weighting function satisfying the requirement above

$$g(\lambda) = -(\lambda - ((1+\alpha)\lambda_a - \alpha\lambda_b))(\lambda - ((1+\alpha)\lambda_b - \alpha\lambda_a)). \qquad (6)$$

The positive parameter α is called the inflation parameter and it offsets the roots of the parabola away from the boundaries of the interval, as illustrated in Fig. 1.
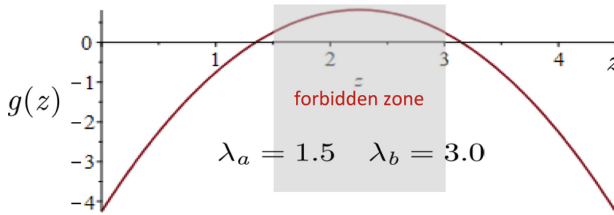

Fig. 1. The plot of the quadratic weighting function $g(z)$ with inflation parameter $\alpha = 0.1$ for the forbidden zone [1.5, 3.0].

The *formalization* of the problem statement yields the minimization prblem

$$\mathbf{s}^* = \arg\min_{\mathbf{s}\in\mathbf{Q}} J(\mathbf{s}) = \arg\min_{\mathbf{s}\in\mathbf{Q}} \sum_{j=1}^{n} g(\lambda_j)h(\lambda_j). \qquad (7)$$

The objective function is evaluated through identities by Futamuri [1]. First, we recall the main formulas for the evaluation of the eigenvalue count and later, we extend it to the case of the weighted eigenvalue count

$$\mathrm{tr}\left((z\mathbf{M} - \mathbf{K})^{-1}\mathbf{M}\right) = \sum_{j=1}^{n} \frac{1}{z - \lambda_j}, \qquad (8)$$

$$\mu_{[\lambda_a,\lambda_b]} = \frac{1}{2\pi i} \oint_C \mathrm{tr}\left((z\mathbf{M} - \mathbf{K})^{-1}\mathbf{M}\right) dz. \qquad (9)$$

The residue theorem is used to derive Eq. (9) from (8). i denotes in this contribution the imaginary unit and tr is the trace operator. The contour C must cross endpoints of the interval $[\lambda_a, \lambda_b]$. An efficient evaluation of the eigenvalue count is carried out by a numerical quadrature with m points

$$\frac{1}{2\pi i} \oint_C \mathrm{tr}\left((z\mathbf{M} - \mathbf{K})^{-1}\mathbf{M}\right) dz \approx \frac{1}{2\pi i} \sum_{j=1}^{m} \mathrm{tr}\left((z_j\mathbf{M} - \mathbf{K})^{-1}\mathbf{M}\right) w_j. \qquad (10)$$

The standard choice for the contour is a circle with a diameter aligned with the interval $[\lambda_a, \lambda_b]$. This contour has many quadrature rules [1], e.g. the trapezoidal rule has locations z_j and weights w_j for j$^{\text{th}}$ integration point with

$$z_j = \frac{\lambda_a + \lambda_b}{2} + \frac{\lambda_b - \lambda_a}{2} e^{2\pi i(j+0.5)/m}, \tag{11}$$

$$w_j = \frac{\lambda_b - \lambda_a}{2} e^{2\pi i(j+0.5)/m} = z_j - \frac{\lambda_a + \lambda_b}{2}. \tag{12}$$

Equation (10)–(12) describe the original approach for eigenvalue counts on intervals. An extension to high-order moments in the context of eigenvalue solvers can be found in [8]. An extension to the eigenvalue count with a concave weighting is used here for the objective function in Eq. (5). The product of the weighting function and the trace in Eq. (8) is still an analytic function. Thus, the residue theorem holds leading to the final expression for the objective

$$J(\mathbf{s}) = \frac{1}{2\pi i} \oint_C g(z)\text{tr}\left((z\mathbf{M} - \mathbf{K})^{-1}\mathbf{M}\right) dz, \tag{13}$$

$$J(\mathbf{s}) \approx \frac{1}{2\pi i} \sum_{j=1}^{m} g(z_j)\text{tr}\left((z_j\mathbf{M} - \mathbf{K})^{-1}\mathbf{M}\right) w_j. \tag{14}$$

The latter expression is differentiable w.r.t. the design parameters. The expression of the gradient requires only knowing the derivative of a matrix inverse. The final expressions read

$$\mathbf{C}_j = (z_j\mathbf{M} - \mathbf{K})^{-1}, \tag{15}$$

$$\frac{dJ(\mathbf{s})}{d\mathbf{s}} = \frac{1}{2\pi i} \sum_{j=1}^{m} g(z_j)\left[\text{tr}\left(\mathbf{C}_j\frac{d\mathbf{M}}{d\mathbf{s}}\right) - \text{tr}\left(\mathbf{M}\mathbf{C}_j\left(z_j\frac{d\mathbf{M}}{d\mathbf{s}} - z_j\frac{d\mathbf{K}}{d\mathbf{s}}\right)\mathbf{C}_j\right)\right] w_j. \tag{16}$$

The objective and the gradient are real; however, numerical computation with Eq. (14) and (16) usually lead to a small imaginary part due to round off errors. We neglect the imaginary part. Furthermore, the gradient in Eq. (16) is checked by finite differencing, which is standard in the structural optimization community. It should be mentioned that the matrix $\mathbf{C}_j$ is dense while $\frac{d\mathbf{M}}{d\mathbf{s}}$ and $\frac{d\mathbf{K}}{d\mathbf{s}}$ are usually sparse. Therefore, terms in Eq. (16) require computation of trace of products of dense and sparse matrices. Herein, this issue is not elaborated and all matrices are treated as dense. Finally, the gradient of the objective is computed explicitly. Using an equivalent adjoint approach should dramatically reduce the complexity of Eq. (16) in the context of large problems.

Now a minimization algorithm can be used to the objective and its gradient. Herein, the steepest descent algorithm with a constant step Δ, with a projection of the gradient to admissible directions and without rejection in case of increasing value is used. Iterations are stopped when the objective value drops below a given threshold. It is an easy and robust algorithm, which may need a large number of iteration, but it is robust w.r.t. discontinuity of the objective.

4   Results and Discussion

4.1   Numerical Example

The behavior of the proposed approach is illustrated with a 1D mass-spring example having ten degrees of freedom and three parameters, as shown in Fig. 2. Each node has one longitudinal degree of freedom. Only nodes have inertia, i.e. a diagonal mass governs the inertia properties of the system and springs are treated as massless. Lower and upper bounds of design parameters define the admissible set Q with

$$Q = \{\mathbf{s} : 0 \le s_1 \le 3, \ 0 \le s_2 \le 3, 0.75 \le s_3 \le 1.25\}. \tag{17}$$

Parameters s_1 and s_2 define the stiffness values of two groups of springs while the parameter s_3 define inertia of a group of nodes. Their initial values are given in Table 1. The forbidden interval for the frequencies is defined in the range [1.5,3.0]. The initial design has the fifth eigenvalue in the forbidden zone while the eigenvalues three and five are close to it. Therefore, the final design must double the gap between eigenfrequencies at that range. An expected change in the design achieves this by increasing the stiffness and decreasing the mass parameters of the system. Consequently, the number of eigenvalues below the forbidden zone should also decrease.
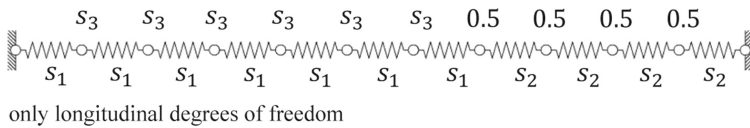

Fig. 2. Setup of the mass-spring example

The algorithm is implemented in the computer algebra system Maple [6] using double precision arithmetic. The base run uses the trapezoidal rule with 140 quadrature points for the contour integral and a constant step of the steepest descent method with $\Delta = 0.05$. The inflation parameter α is always 0.1. The threshold for the drop value for iterations is 0.5.

The results for the base run are demonstrated in Fig. 3 and Table 1. Convergence is achieved after iteration 54 with design parameters inside the admissible set Q. As expected, the stiffness parameters increased while the mass parameter changed insignificantly (by 2%). The forbidden zone lies between the eigenvalues three and four. Comparison of the weighted eigenvalue count with the standard eigenvalue count in Fig. 3 (right) shows that the former is a good surrogate of the latter while being a smoother function. It is also observed the influence of the steepest descent algorithm without rejection of the new solution in case of the increase of the objective.

The results for the run with 70 integration points are shown in Table 1. Evolutions of the spectrum and objective are omitted for space reasons. Convergence is achieved after iteration 67 with design parameters inside the admissible set Q. The design differs from the base run, meaning that the number of quadrature points is an important parameter of the algorithm.

The results for the run with smaller step $\Delta = 0.02$ are given in Fig. 4 and Table 1. This run converges after 328 iterations, which is significantly more than in the two previous runs. Furthermore, it converges to a different solution that is on the boundary of the admissible set Q. As in the previous run, both stiffness parameters increase while the mass parameter changes less, here by 14%. The evolution of the spectrum and the objective are similar to the base run.

Table 1. Eigenvalues close to the forbidden zone [1.5, 3.0], design parameters and the number of iteration to convergence. The violating frequency is marked in red.

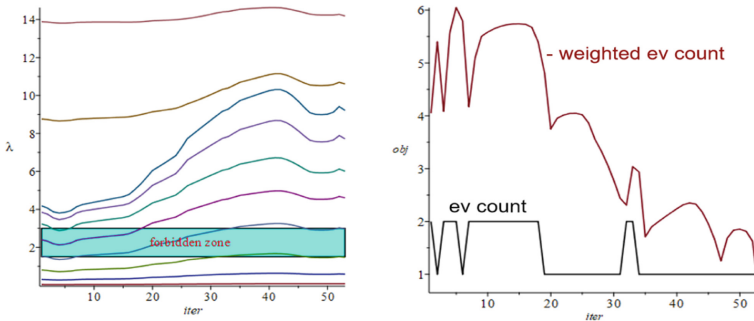| Design	j	λ_j	λ_{j+1}	λ_{j+2}	s_1	s_2	s_3	#iter
Initial design	4	1.44	2.25	3.05	1.00	2.00	1.00	-
Base run, $\Delta = 0.05$	3	1.50	3.02	4.67	2.41	1.92	0.98	54
Run with $m = 70$ and $\Delta = 0.05$	3	1.46	3.02	4.47	2.97	1.92	1.19	67
Run with smaller step, $\Delta = 0.02$	3	1.46	3.09	4.62	3.00	1.67	1.14	328

Fig. 3. Evolution of the spectrum (left) and of the weighted eigenvalue count objective (right) for the base run with step $\Delta = 0.05$

4.2 Discussion

A novel approach for resonance avoidance is presented in the contribution. Now, the features and properties of the algorithm are discussed. First, more than one solution is possible. It is explained by a multi-modal objective with a plateau at zero value for all correct solutions. Therefore, the algorithm exhibits dependency on the initial design (not shown here, but observed) and parameters of the algorithm as number quadrature points and inflation α. Second, the objective can be straightforwardly extended to two or more forbidden intervals in a manner similar to one presented in [13, 14]. Third, the algorithm is insensitive to the shape of eigenmode, i.e. it does not distinguish between longitudinal, bending, or torsional modes. That can be a disadvantage for various applications such as payload layout for space launchers, where forbidden intervals for longitudinal and

bending modes do not coincide. Also, local eigenmodes with small modal masses affect the objective in the same manner as the global eigenmodes with large modal masses. Therefore, this feature is a significant disadvantage. Fourth, the current approach does not include damping or gyroscopic matrix, which is important for many applications for power equipment. Finally, the current optimization strategy is suboptimal. Such a tiny example should not require the observed number of iterations. An alternative optimization strategy should be implemented. The proposed objective is a multi-modal function. Therefore, trust-region algorithms [19, 20], genetic algorithms [21, 22] and simulated annealing [23] may be considered in future work.
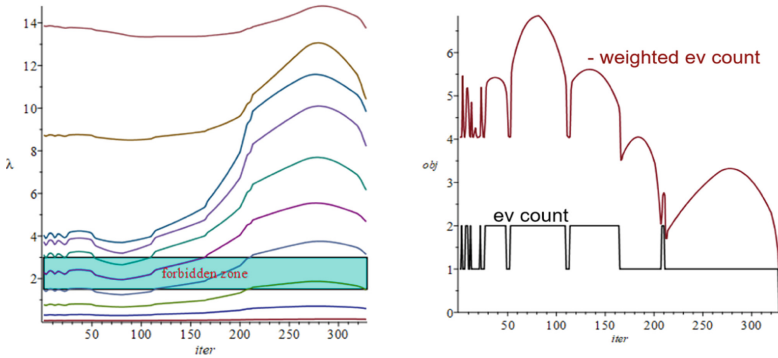

Fig. 4. Evolution of the spectrum (left) and of the weighted eigenvalue count objective (right) for the run with small step $\Delta = 0.02$

The importance of the contribution is in the transfer of recent ideas of numerical linear algebra to the field of structural optimization and dynamics. This enables modification of spectrum in contrast to current approaches that track and modify individual eigenfrequencies. Therefore, there is a great interest in overcoming several shortcomings and the creation of a new tool for optimization-based structural design.

5   Conclusion and Future Work

This contribution tackles the problem of finding a structural design without eigenfrequencies in a given frequency range. We propose a novel formalization of the problem via the minimization of weighted eigenfrequency counts. Computation of the weighted eigenfrequency counts avoids here explicit evaluation or ordering of the eigenfrequencies or Sylvester law of inertia (and any LDLT decompositions). Instead, we exploit the identity by Futamura [1], which provides a differentiable expression of eigenvalue count via a contour integral. The contour integral can be computed numerically using the trapezoidal rule. Furthermore, a special weighting is added to the eigenvalue count to push the eigenvalues from the center of the forbidden eigenfrequency range to boundaries. A simple minimization algorithm is implemented for the objective. A test example with ten degrees of freedom and three affine parameters validate the basic idea of the approach.

Three non-trivial feasible designs are obtained for different sets of numerical parameters. It showed that the number of quadrature points and the step size in the steepest descent algorithm influence the recovered design. Therefore, this approach illustrated the potential of solving the stated problem in practical applications and may be pursued in the future.

Several steps are envisaged at this stage. First, the approach is going to be tested for larger and more complex examples. Second, a more sophisticated and appropriate optimization algorithm should be, e.g., one from the family of trust-region algorithms [19, 20], genetic algorithms [21, 22] or simulated annealing [23]. Third, problems with several forbidden intervals can be solved. Fourth, the present algorithm requires improvement of numerical quadrature for the case of an eigenvalue close to the integration path. Finally, a combination of the Futamura identity with stochastic trace estimation should enable even larger problem sizes. Stochastic trace estimation is substantially cheaper than eigenvalue computation with common solvers. This is a core advantage over other approaches available now. At this stage, a comparison of the computational efficiency and robustness with other approaches as the nearest alternatives [13, 14] would be possible. That could also include design problems of power equipment subjected to vibration.

References

1. Futamura, Y., Tadano, H., Sakurai, T.: Parallel stochastic estimation method of eigenvalue distribution. JSIAM Lett. **2**, 127–130 (2010)
2. Iwata, J.I., et al.: A massively-parallel electronic-structure calculations based on real-space density functional theory. J. Comput. Phys. **229**(6), 2339–2363 (2010)
3. Polizzi, E.: FEAST eigenvalue solver v4.0 user guide. arXiv preprint. arXiv:2002.04807 (2020)
4. Guttel, S., Polizzi, E., Tang, P.T.P., Viaud, G.: Zolotarev quadrature rules and load balancing for the FEAST eigensolver. SIAM J. Sci. Comput. **37**(4), A2100–A2122 (2015)
5. Winkelmann, J., Di Napoli, E.: Non-linear least-squares optimization of rational filters for the solution of interior hermitian eigenvalue problems. Front. Appl. Math. Stat. **5**, 5 (2019)
6. Maple User Manual. Maplesoft, a division of Waterloo Maple Inc., 1996–2021
7. Di Napoli, E., Polizzi, E., Saad, Y.: Efficient estimation of eigenvalue counts in an interval. Numer. Linear Algebra Appl. **23**(4), 674–692 (2016)
8. Sakurai, T., Futamura, Y., Tadano, H.: Efficient parameter estimation and implementation of a contour integral-based eigensolver. J. Algorithms Comput. Technol. **7**(3), 249–269 (2013)
9. Zhang, Z., Chen, W.: An approach for maximizing the smallest eigenfrequency of structure vibration based on piecewise constant level set method. J. Comput. Phys. **361**, 377–390 (2018)
10. Achtziger, W., Kočvara, M.: Structural topology optimization with eigenvalues. SIAM J. Optim. **18**(4), 1129–1164 (2008)
11. Kim, T.S., Kim, Y.Y.: MAC-based mode-tracking in structural topology optimization. Comput. Struct. **74**(3), 375–383 (2000)

12. Du, J., Olhoff, N.: Topological design of freely vibrating continuum structures for maximum values of simple and multiple eigenfrequencies and frequency gaps. Struct. Multi. Optim. **34**(2), 91 (2007). https://doi.org/10.1007/s00158-007-0101-y

13. Maeda, Y., Nishiwaki, S., Izui, K., Yoshimura, M., Matsui, K., Terada, K.: Structural topology optimization of vibrating structures with specified eigenfrequencies and eigenmode shapes. Int. J. Numer. Meth. Eng. **67**(5), 597–628 (2006)

14. Li, Q., Wu, Q., Liu, J., He, J., Liu, S.: Topology optimization of vibrating structures with frequency band constraints. Struct. Multi. Optim. **63**(3), 1203–1218 (2020). https://doi.org/10.1007/s00158-020-02753-7

15. Zargham, S., Ward, T.A., Ramli, R., Badruddin, I.A.: Topology optimization: a review for structural designs under vibration problems. Struct. Multi. Optim. **53**(6), 1157–1177 (2015). https://doi.org/10.1007/s00158-015-1370-5

16. Rajagopal, A., Mandal, D.K.: An Evaluation of mode tracking methods for practical rotor dynamic analysis. In: ASME International Mechanical Engineering Congress and Exposition (vol. 84553, p. V07BT07A041). American Society of Mech. Engineers (2020)

17. Patnaik, U.K., Saiki, J., Arcos, I.: Tuning aircraft engines with optistruct rotor dynamics simulation (No. 2019-01-1366). SAE Technical paper (2019)

18. Wang, D., Zhang, W.H., Jiang, J.S.: Truss optimization on shape and sizing with frequency constraints. AIAA J. **42**(3), 622–630 (2004)

19. Sorensen, D.C.: Newton's method with a model trust region modification. SIAM J. Numer. Anal. **19**(2), 409–426 (1982)

20. Yuan, Y.-X.: Recent advances in trust region algorithms. Math. Program. **151**(1), 249–281 (2015). https://doi.org/10.1007/s10107-015-0893-2

21. Yang, J., Soh, C.K.: Structural optimization by genetic algorithms with tournament selection. J. Comput. Civ. Eng. **11**(3), 195–200 (1997)

22. Narayanan, S., Azarm, S.: On improving multiobjective genetic algorithms for design optimization. Struct. Optim. **18**(2), 146–155 (1999). https://doi.org/10.1007/BF01195989

23. Sonmez, F.O., Tan, C.M.: Structural optimization using simulated annealing. Simulated Annealing **2008**, 281–306 (2008)

Multi-scale Finite-Element Model for Numerical Prediction of Subcritical Damage and Limit State of Fiber-Reinforced Composites and Structures

Alexey Milenin[✉], Elena Velikoivanenko, Galina Rozynka, and Nina Pivtorak

E.O. Paton Electric Welding Institute of NAS of Ukraine, 11, K. Malevich Street, Kyiv 03150, Ukraine
asmilenin@ukr.net

Abstract. Specific problems of design, assessment of limit state and residual working life of critical structural elements made of composite materials demand the use of special analytical and numerical methods. However, mathematical description of spatially nonuniform materials and structures presupposes their resource-intensive computer implementation whereas anisotropic homogenous approximation does not make it possible to take into account the features of micro-scale composition of specific composite material. To overcome this issue the multi-scale finite-element methodology for predicting the stresses, strains, subcritical damage and limit state of typical fiber-reinforced composite materials and structures, made of them, has been proposed in this work. This methodology is based on a combination of macro-scale and meso-scale approaches for describing both the macro-deformation of actual structure under the operational load and subcritical damage of locally nonuniform brittle material. On the example of standard laboratory specimens as well as large cylindrical pressure vessels made of fiberglass-reinforced composite, the characteristic features of stress-strain, damaged and limit state under the external load were studied.

Keywords: Composite materials · Subcritical damage · State of stresses and strains · Limit state · Multi-scale model · Finite-element model

1 Introduction

The application of composite materials in the manufacture of structures for the needs of different industries is an effective way to obtain structural elements with unique operational properties. In particular, fiber-reinforced composites based on glass or carbon fibers have become widespread, which allow to achieve high strength of thin-walled structures at their relatively low weight [1, 2]. However, the spatial nonhomogeneity of such materials causes objective difficulties in the design, testing of technical condition and analysis of the residual working life of certain structural elements. The use of analytical approaches, which consist in assessing the effective properties of the material for further consideration as a homogeneous and anisotropic one, significantly limits the

range of practically significant problems to be solved. In particular, it is known that the process of nucleation and development of material defects is microscopic in scale. Thus, for correct consideration of the subcritical damage in analysis of the limit state of the structure under the design load, the specific structure of the material and its resistance to failure of certain type should be considered.

Possibilities of numerical description of composite structures in nonhomogeneous formulation are limited, so the development of analytical approaches those allow taking into account the microstructural state of the material in modeling along with consideration of the specific structural elements without significant simplification is actual and practically valuable one. All available methods for predicting the bearing capacity of structures made of composite materials can be divided into three classes - macrostructural, mesostructural and multi-scale. Thus, macrostructural approaches provide a homogeneous interpretation of the material, according to which all properties are defined explicitly and they are assigned certain effective values. The simplest method in this case is to use the mixture rule according to the partial contribution of each structural component [3] or formal averaging of the initial properties [4]. Further use of classical methods allows to implement relatively simple engineering algorithms that give a general idea of the bearing capacity of a particular structural element under a certain combination of external factors [5–7]. A common disadvantage of macrostructural approaches is the significant simplification of the behavior of materials, which significantly limits their applicability.

Mesostructural approaches consider the material as inhomogeneous ones, combining the principles of continuous mechanics, plasticity, fracture mechanics and physical materials science [8, 9]. Their advantages are the possibility of prediction the effective macroscopic properties of structurally inhomogeneous materials and analysis the material subcritical fracture, taking into account the distribution of structural components. But their applicability is limited for the analysis of large-scale structures because of considerable resource consumption of the corresponding issues.

Multiscale approaches use both homogeneous and inhomogeneous material descriptions, namely: at the mesolevel as a non-homogeneous material, at the macro level as a homogeneous material with properties through meso-macro link [10, 11]. Multi-scale methods are the most universal for analyzing the state of real structures, but for adequate prediction results and relevant expert conclusions they require substantiation of the links between meso- and macro-description of the material.

The main aim of this work is development of the methodology and numerical means for multi-scale prediction of stress-strain, damaged and limit states of structures made of typical fibrous composite materials.

2   Finite-Element Procedure for Prediction of Subcritical and Limit State of Fiber-Reinforced Composite Materials

2.1   Main Assumptions and Physical Model

The developed methodology is based on a finite-element implementation of tracing the state of the structure under loading in a macro-scale homogeneous anisotropic approximation and for each regular meso-scale region in an nonhomogeneous approximation. In

this case, the independence of the calculations for individual meso-scale areas makes it natural the use of algorithms for parallel calculation of the corresponding boundary value problems to reduce the time of numerical experiments [12]. The relationship between the levels is fulfilled by transition of a certain calculated data, namely the deformed state and subcritical damage (see Fig. 1). Components of composite are considered as elastic ones.

For the computer implementation of this approach, finite element modeling methods based on eight-node elements were used [13, 14], and each finite element of the macro task was considered as a regular meso-area, within which the corresponding meso-problem was set.
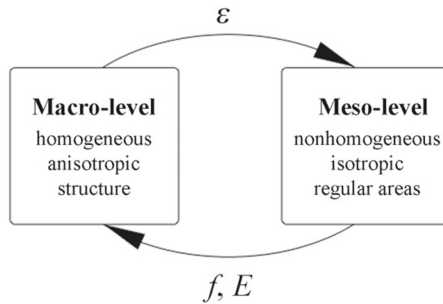

Fig. 1. Scheme of multi-scale problem of prediction the stress-strain, damaged and limit states of structures made of composite materials

2.2 Mathematical Description of Stress-Strain and Damage States of Spatially Nonhomogenious Material

The macro-scale approximation requires the averaged physical and mechanical properties of the material depending on the composition of the two-component composite (volume content of the matrix V_m and fiber V_f), direction and the properties of its individual components. The most common approaches are based on the rule of mixtures. In particular, if the fiber-reinforced composite is considered to be elastic orthotropic material, the value of Young's modulus along and across the fibers is calculated according to the next formula [15]:

$$\begin{cases} E_T = \dfrac{E_f \cdot E_m}{E_m \cdot V_f + E_f \cdot \left(1 - V_f\right)}; \\ E_L = E_f \cdot V_f + E_m \cdot \left(1 - V_f\right), \end{cases} \tag{1}$$

where E_m, E_f are Young's modules of the matrix material and fibers, respectively; E_T, E_L are Young's modules of conditionally homogeneous anisotropic composite along and across the fibers, respectively.

To determine averaged Poisson's ratio of orthotropic material, Whitney and Riley dependence in the following formulation was used [16]:

$$
\begin{cases}
v_{LT} = \dfrac{v_m - \left[2 \cdot \left(v_m - v_f\right) \cdot \left(1 - v_m^2\right) \cdot E_f \cdot V_f\right]}{E_m \cdot \left(1 - V_f\right) \cdot \left(1 - v_f - 2 \cdot v_f^2\right) + E_f \cdot \left[V_f \cdot \left(1 - v_m - 2 \cdot v_m^2\right) + \left(1 + v_m\right)\right]} \\
v_{TL} = v_m \cdot V_m + v_f \cdot V_f,
\end{cases}
\tag{2}
$$

where v_{LT}, v_{TL} are Poisson's ratios for directions along and across the fiber, respectively; v_m, v_f are Poisson's ratios of matrix material and fibers, respectively.

The limit state in a specific finite element of the macro-problem is achieved with an unfavorable combination of longitudinal (along the fibers) σ_{xx}, transverse σ_{yy} and tangential stresses σ_{xy}, which is mathematically determined, in particular, based on Hoffman's formula [17]:

$$
\left(\frac{\sigma_{xx}}{X_1}\right)^2 - \frac{\sigma_{xx} \cdot \sigma_{yy}}{X_1 \cdot X_2} + \left(\frac{\sigma_{yy}}{X_2}\right)^2 + \left(\frac{\sigma_{xy}}{S}\right)^2 > 1,
\tag{3}
$$

where X_1, X_2, S are material constants.

If the axes of the orthotropic composite do not coincide with the direction of the load, the constants in (3) were calculated as follows:

$$
\begin{cases}
X_1 = X_s \cdot \sin^2 \alpha + X_m \cdot \cos^2 \alpha \\
X_2 = X_m \cdot \sin^2 \alpha + X_s \cdot \cos^2 \alpha
\end{cases},
\tag{4}
$$

where α is the angle between the force vector and the direction of the fibers, X_m, X_s are the material constants characterizing the ultimate state of the material under load across and along the fibers, respectively.

The finite-element solution of the boundary problem of the stress-strain state of a particular structure made of composite material allows to assess the deformation field, that, in turn, is used in the analysis of the meso-state of each element as boundary conditions. The subcritical damage of the material (distributed damage of microcrack type) that affects the macroscopic stress-strain state, was estimated by calculating the meso-problem, which is formally taken into account by transferring the value of the volume concentration of damage to the macro-problem.

It is known that the characteristic feature of the failure of composite materials is a significant variance of the ultimate load due to local heterogeneity of properties, the natural deviation of the structure from the ideal, manufacture damage, etc. Therefore, description of subcritical damage development in the composite matrix was performed using a statistical approach based on the Weibull distribution function:

$$
df = \begin{cases}
A \cdot f_0 \cdot \varepsilon_{\max}^{\eta-1} \cdot \exp\left[-\left(\dfrac{\varepsilon_{\max}}{\varepsilon_0}\right)^{\eta}\right] d\varepsilon_{\max}, & \varepsilon_{\max} \geq 0; \\
0, & \varepsilon_{\max} < 0,
\end{cases}
\tag{5}
$$

where df is the increase in the damage volume concentration, $\varepsilon_{\max}$ is the maximum local deformation, $A = \eta / \varepsilon_0^{\eta}$, η, ε_0, f_0 are the constants.

If the damage volume concentration f exceeds a certain critical value of f_{cr} for a certain finite element, this element was considered to lose its bearing capacity. Thus, the total damage F is:

$$F = \frac{\sum\limits_{N} f + n_{st}}{N},$$ (6)

where n_{st} is the total number of elements that have lost their bearing capacity, N is the number of elements of the meso-area partition, $\sum\limits_{N}$ is the sum operator for all finite elements of the meso-area partition.

This value of F is used to adjust Young's modules in the macro-problem according to the following relationship:

$$E^f = \frac{E}{1 - F}.$$ (7)

In addition, the appearance and development of subcritical damage causes an additional component of the strain tensor, namely

$$\varepsilon^f = \Delta F / 3,$$ (8)

where ΔF is the increase in F at each step of the mechanical load.

2.3 Validation of the Developed Models and Means of Their Program Implementation

The proposed algorithm includes a number of material constants to be determined based on the results of appropriate laboratory tests. For this purpose, the literature data of experimental studies of the maximum load of fiberglass/epoxy composites ($V_m = V_f = 0.5$) with different direction of the fibers [18] has been used in this work. Based on the processing of these data, material constants were obtained, namely: $\eta = 3.2$; $\varepsilon_0 = 0.01$; $f_0 = 10^{-5}$; $X_m = 35$ MPa; $X_s = 350$ MPa; $S = 18$ MPa; $f_{cr} = 0.15$.

Figure 2 shows the results of comparing the calculated values of the ultimate load of the specimens with the experimental results. From these data it could be concluded that the accuracy of numerical technique for the specified material is satisfactory.
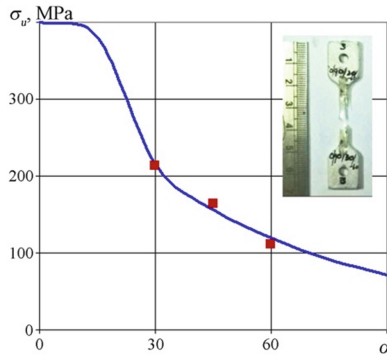
Fig. 2. Comparing the calculated values of the ultimate load of the fiberglass/epoxy composite specimens of different fiber orientation (solid line) with the experimental results (dots) [18]

3 Results and Discussion

One of the advantages of the developed approach is the possibility of numerical tracing of the development of subcritical damage of individual components of the composite and taking into account the influence of the nature of their meso-scale interaction on the limit state of large structures. Figure 3 shows the numerically assessed kinetics of accumulation of subcritical damage of the composite specimen under tensile load up to the limit state. The nonlinearity of this dependence is caused by the progressive weakening of the material and additional deformation of the material as a result of the appearance and growth of distributed damage.
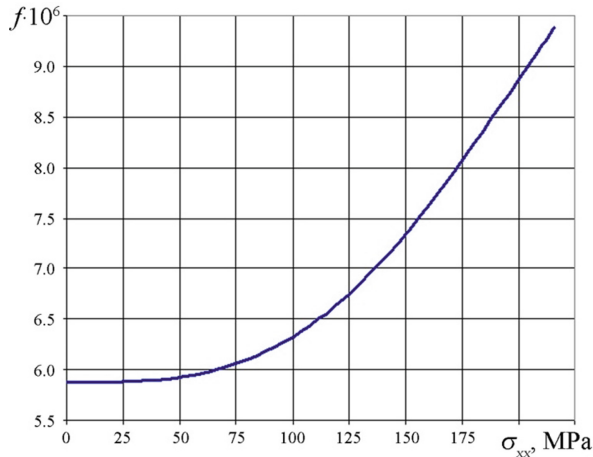

Fig. 3. Kinetics of accumulation of subcritical damage f of the composite specimen under tensile load σ_{xx} up to the limit state

Within the framework of the proposed methodology, the initial damaged state of the material is characterized by the constant f_0 from (5). In Fig. 4 the effect of a specific value of f_0 on the value of the maximum load of the sample of composite material ($V_f = V_m = 0.5$, $\alpha = 45°$) is shown. It is quasilinear because of inherent linearity of the influence of initial damaged state.
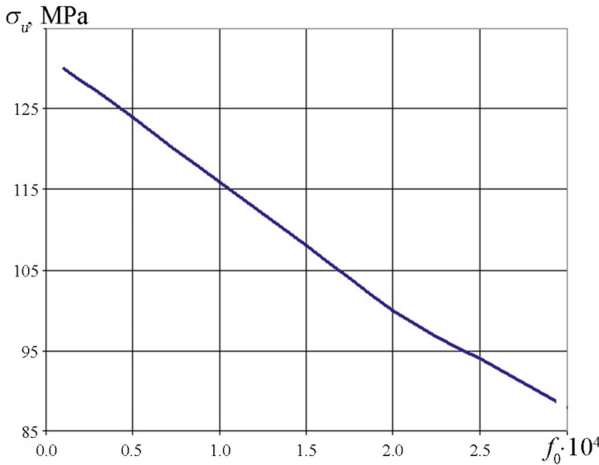

Fig. 4. Dependence of the ultimate strength σ_u of fiberglass-reinforced composite specimen ($V_f = V_m = 0.5$, $\alpha = 45°$) on the initial volume concentration of subcritical damage of material f_0

In respect to real structures, a cylindrical pressure vessel (that is made of fiber-glass/epoxy composite) with a diameter $D = 1200$ mm and a wall thickness $t = 3$ mm under the internal pressure P was considered. A characteristic feature of this example is the pronounced biaxial stress state in the circumferential and axial directions. This to a certain extent changes the dependence of the ultimate pressure in the structure on the angle of the fibers relative to the axis of the pressure vessel under consideration (Fig. 5), compared with the results of tension tests of specimens (see Fig. 2). However, since the circumferential stress prevails, its form is qualitatively similar.

4 Conclusions

1. The multi-scale model and corresponding program modules for prediction of stress-strain, damaged and limit states of structures made of typical fiber-reinforced composites have been developed. The proposed approach is based on a finite-element implementation of tracing the state of the entire structure in a homogeneous anisotropic approximation (macro-scale) and separately for each regular meso-scale area in an nonhomogeneous approximation (meso-scale). Comparison of the results of predicting the ultimate strength of fiberglass-reinforced composite specimens with the available literature data showed satisfactory accuracy of the developed approach.

2. Specific features of subcritical damage of fiber-reinforced composite standard specimens under uniaxial loading have been investigated. The characteristic nonlinearity of the damage volume concentration development in the cross section of the composite specimen, caused with gradual weakening and additional deformation of the material as a result of the appearance and growth of distributed damage, was shown. The influence of the initial damaged state of the material on its ultimate strength was demonstrated.

3. The characteristic features of the influence of biaxial stress on the ultimate load of the structure have been studied on the example of a cylindrical pressure vessel made of fiberglass/epoxy composite under internal pressure. In particular, it was shown that variation of fibers orientation to its axis changes the ultimate stress quantitatively in comparison with similar dependences obtained for standard tensile test specimens, but their forms remain qualitatively similar.
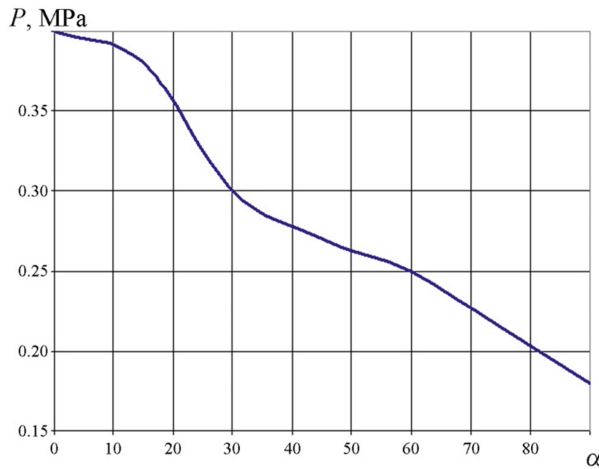

Fig. 5. Dependence of the ultimate pressure P in cylindrical pressure vessel (diameter 1200 mm, wall thickness 3 mm) on the angle of the fibers α relative to the axis of the structure

References

1. Nikbakt, S., Kamarian, S., Shakeri, M.: A review on optimization of composite structures part I: laminated composites. Compos. Struct. **195**, 158–185 (2018)
2. Das, M., Sahu, S., Parhi, D.R.: Composite materials and their damage detection using AI techniques for aerospace application: a brief review. Mater. Today: Proc. **44**, 955–960 (2021)
3. Feng, B., et al.: On the rule of mixtures for bimetal composites without bonding. J. Magnes. Alloy. **8**(4), 1253–1261 (2020)
4. Aboudi, J., Arnold, S.M., Bednarcyk, B.A.: Micromechanics of Composite Materials A Generalized Multiscale Analysis Approach. Butterworth-Heinemann, Oxford (2013)

5. Moss, D.R., Basic, M.: Pressure Vessel Design Manual. Butterworth-Heinemann, Oxford (2013)
6. Kollár, L.P., Springer, G.S.: Mechanics of Composite Structures. University Press, Cambridge (2003)
7. Sayyad, A.S., Ghugal, Y.M.: Bending, buckling and free vibration of laminated composite and sandwich beams: a critical review of literature. Compos. Struct. **171**, 486–504 (2017)
8. Ostoja-Starzewski, M.: Material spatial randomness: from statistical to representative volume element. Probab. Eng. Mech. **21**, 112–132 (2006)
9. Bargmann, S., et al.: Generation of 3D representative volume elements for heterogeneous materials: a review. Prog. Mater Sci. **96**, 322–384 (2018)
10. McDowell, D.L.: Simulation-based strategies for microstructure-sensitive fatigue modeling. Mater. Sci. Eng., A **468**, 4–14 (2007)
11. Wilson, D., Dunne, F.P.E.: A mechanistic modelling methodology for microstructure-sensitive fatigue crack growth. J. Mech. Phys. Solids **124**, 827–848 (2019)
12. Velikoivanenko, E.A., Milenin, A.S., Popov, A.V., Sidoruk, V.A., Khimich, A.N.: Methods of numerical forecasting of the working performance of welded structures on computers of hybrid architecture. Cybern. Syst. Anal. **55**(1), 117–127 (2019)
13. Makhnenko, V.: Problems of examination of modern critical welded structures. Paton Weld. J. **5**, 21–28 (2013)
14. Milenin, A., Velikoivanenko, E., Rozynka, G., Pivtorak, N.: Probabilistic procedure for numerical assessment of corroded pipeline strength and operability. Int. J. Press. Vessels Pip. **171C**, 60–68 (2019)
15. Abdel Ghafaar, M., Mazen, A.A.: Application of the rule of mixtures and Halpin-Tsai equations to woven fabric reinforced epoxy composites. J. Eng. Sci. **34**(1), 227–236 (2006)
16. Buragohain, M.K.: Micromechanics of a Lamina from: Composite Structures. Design, Mechanics, Analysis, Manufacturing, and Testing. CRC Press, USA (2017)
17. Nyambeni, N., Mabuza, B.R.: Considerations of failure analysis in a multi-layered composite structure under thermomechanical loading. In: Proceedings, vol. 2, no. 8, p. 447 (2018)
18. Naresh, K., Shankar, K., Velmurugan, R.: Reliability analysis of tensile strengths using Weibull distribution in glass/epoxy and carbon/epoxy composites. Compos. B Eng. **133**, 129–144 (2018)

Relaxation of the Technological Residual Stresses During the Thermal Exposure in Titanium Samples

Oleksiy Kachan , Dmytro Pavlenko[(✉)] , and Sergiy Ulanov

Zaporizhzhia Polytechnic National University, 64 Zhukovsky Street, Zaporizhzhia, Ukraine
dvp1977dvp@gmail.com

Abstract. The aim of the investigation is to establish regularities of influence of hardening time and temperature of thermoexposure on size and depth of distribution of the maximum compressive residual stresses after ultrasonic hardening by steel balls. The relaxation of technological residual stresses in the surface layer of samples made of high-temperature titanium alloy BT8, depending on the hardening time, temperature, and time of thermal exposure, has been studied. The surface layer of the pre-annealed samples was subjected to strain hardening with steel balls in an ultrasonic field for 5 and 15 min. After hardening, the samples were subjected to thermal exposure in a vacuum oven for 2 and 6 h at temperatures of 240 and 480 °C. The diagrams of the propagation of technological residual stresses in the surface layer of the samples were investigated by the method of layer-by-layer removal of thin metal layers by electrolytic polishing. The maximum values of residual stresses, the magnitude of stresses on the surface, and the depth of their propagation in the surface layer are determined. The main regularities of the relaxation of residual stresses are established depending on the initial state and modes of thermal exposure.

The practical significance of the work lies in the proposed new technology of surface plastic hardening of gas turbine engine parts made of titanium alloys in an ultrasonic field, taking into account thermal effects. This will ensure a stable level of safety margin during operation and increase the service life of their work. The established patterns can be used to assess the magnitude and depth of technological residual stresses in the parts of gas turbine engines after the operation.

Keywords: Titanium alloy · Surface work hardening · Residual stress · Surface layer · Relaxation · Thermal exposure

1 Introduction

Titanium alloys with special physical and mechanical properties that determine their performance are widely used in aircraft engine construction. Improving the quality and reliability of titanium alloy products is currently achieved by creating new alloys, improving product designs, as well as introducing advanced technological processes.

A perspective trend to increase the service life of titanium alloy parts is surface plastic deformation, carried out by various methods, including ultrasonic hardening.

The main performance properties of structural elements – wear resistance, strength, and fatigue resistance – significantly depend on the condition of the surface layer. Exhaustion of the time of failure of the part and its destruction begins, as a rule, with the surface layer. Therefore, in the manufacture of parts in the process of their machining or special strengthening technologies in the surface layer are compressed residual stresses that prevent the emergence of various kinds of dislocations.

Despite the fact that the role of residual stresses in increasing the service life of engine parts has been sufficiently proven, the question of their relaxation under the action of the thermal and mechanical load remains poorly understood. This, in turn, does not allow to reasonably determine the resource of their work and the time of re-strengthening. This issue becomes especially relevant when considering the service life of individual engine components in particular the compressor. Given the use of different materials and their operating conditions [1], the rate of relaxation of residual stresses can vary significantly. This can lead to a loss of strength of individual parts and the need to repair the compressor. The relevance of studying the patterns of relaxation of residual stresses is enhanced due to the possible change in the geometry of parts during operation. In [2] it is shown that one reason for the distortion of details is the relaxation of the initial residual stresses within the raw part. The residual initial stresses mainly depend on the manufacturing process of the raw part and the subsequent heat effects. In this regard, the study of the processes of relaxation of technological stresses in the surface layer of parts of gas turbine engines is relevant today in terms of ensuring their long-term coordinated work.

The research aimed to establish the patterns of relaxation of residual stresses in the surface layer of titanium specimens under the action of the thermal factor.

2   Literature Review

Technological residual stresses in the surface layer are one of the most important results of mechanical and finishing-hardening treatment of gas turbine engine parts. They have a significant impact on their durability. The authors of [3] emphasize the special role of residual stresses in the surface layer of parts made of titanium alloys. Where strict surface roughness constraints apply, such as aircraft engine components, finishing must be produced. Thus, the residual stresses arising during finishing are particularly important [4]. It is known that tensile stresses deteriorate the dynamic strength and chemical resistance of materials. Compressive stresses in the surface layer lead to an increase in the endurance limit. Rough surfaces and machining artifacts are also areas where compressive residual stresses are extremely effective. The influence of various stress concentrators, including material defects and inclusions, which also reduce the strength of parts [5], can be effectively eliminated due to technological compressive stresses. They also play a significant role in increasing the endurance of parts with structural stress concentrators [6] and in retardation of crack propagation rate [7].

Technological inheritance plays an important role in the performance properties of parts. Technological heredity means the phenomenon of transferring the properties of the workpiece from previous operations to the next, which further affects the performance of machine parts [8]. It is known that the use of deformation processing of the

surface layer of parts made of titanium alloys is also effective in combination with other processing methods. The authors [9] of the influence of the ultrasonic impact treatment on the structure and properties of the surface layer of α-titanium in a submicrocrystalline state was investigated. Was shown, combining the methods of bulk (twist extrusion) and superficial (ultrasonic impact treatment) severe plastic deformation, it is possible to provide increased strength, wear, and corrosion resistance of the surface layers of titanium alloys.

In this case, some properties and characteristics pass from one technological operation to another, that is, as if «inherited» from certain operations. Therefore, in the machining of parts, there is technological heredity. Therefore, when designing technological processes, it is necessary to introduce such operations that create more obstacles for the passage of negative factors to the finishing operation. Postoperative manifestation of technological heredity from the methods of obtaining the workpiece, to heat and machining, can reduce or increase the performance properties, which requires careful analysis of the elements in the development of new technological processes of machining parts [10].

There are known attempts to apply surface deformation treatment of specimens to achieve enhanced beneficial effects beyond shot peening conventional performance, at elevated temperatures, or under tensile stress loading with some success [11]. The authors note the need to search for an optimum in-situ warm peening condition after a trade-off between compressive residual stress relaxation and enhanced grain refinement, both of which are affected by thermal softening but to different degrees.

An important and insufficiently studied issue to date is the stability of the residual stresses formed in the surface layer. To date, there is a small number of studies in the literature devoted to the issue of stress relaxation.

In this study [12] it is emphasized that stress relaxation is an important characteristic of titanium alloys at elevated temperatures and loads, which is the theoretical basis for hot calibration and heat treatment. The results of a comprehensive analysis of stress relaxation in the titanium alloy Ti-6A1-4V in the range of average temperatures showed that the stress relaxation rate increases with temperature increasing. The residual stress in the Ti-6A1-4V alloy reaches the relaxation limit gradually after the relaxation period. In addition, the stress relaxation limits reach the same value for different initial stresses at the same temperature.

The results of studying the regularities of stress relaxation in parts made of the Ti-6A1-4V alloy are also given in [13]. Despite the results obtained by the authors, which make it possible to explain the mechanisms of creep and stress relaxation, they do not allow us to answer the question of the effect of time and temperature on the relaxation of technological residual stresses in the surface layer of parts made of BT8 alloy.

By analyzing the results of field tests, the authors of this study [14] concluded that the mechanisms of stress relaxation in the low, medium, and high-temperature regions were dislocations, return, and recrystallization, respectively. In addition, the authors of the study found that relaxation was more difficult in samples with an equiaxed microstructure, in comparison with samples that had a Widmanstätt structure at a temperature of 473 K, but easier at temperatures of 673 and 873 K. The significant effect on stress

relaxation mechanism of grain size and temperature range for titanium alloy Ti-6Al-4V in this study [15] was also established.

Thus, the analysis of the literature has shown that today no reliable regularities are describing the processes of relaxation of technological residual stresses in the surface layer of gas turbine engine parts due to the peculiarities of their operating modes. This makes it difficult to assess the effectiveness of the use of strain hardening for parts made of BT8 alloy operating in the range of elevated temperatures. Taking into account that, under the influence of the force factor, the structure and properties of the surface layer of hardened parts may differ from the structure of their core, as well as the special role of the surface layer, the study of the relaxation of surface residual stresses is an urgent task.

3   Research Methodology

The studies were performed on samples of two-phase ($\alpha + \beta$) titanium alloy BT8 (Ti-6,8Al-3,5Mo-0,32Si), which were subjected to preliminary heat treatment, namely – two-stage annealing in a vacuum according to the modes: I degree 930 ℃; holding time 1,5 h; II degree 590 ℃; exposure time 1 h.

After annealing, the samples were strengthened with steel balls in an ultrasonic field [14]. The working bodies were steel balls made of steel ШХ15 with a diameter of 1,6 mm according to OST 3722–81. The oscillation frequency of the wave concentrator was 17,5 kHz, which corresponded to the resonant frequency of the "concentrator – reinforcing bodies" system. The resonant frequency was determined by the maximum value of the kinetic energy of the balls using a sensor of the intensity of hardening and the amount of sound pressure generated by the walls of the concentrator. The amplitude of oscillations of the hub walls was 50–100 mkm.

The speed of impact of the balls with the reinforcing surface was in the range of 2–4 m/s. The samples were hardened for 5 and 15 min. After hardening, the samples were subjected to thermal exposure in a vacuum furnace. The time and temperature of thermal exposure were changed. The thermal exposure temperature was 240 °C and 480 °C, which corresponded to the average values of the operating temperature of the compressor parts of the gas turbine engine made of titanium alloys and close to the maximum operating temperature of the alloy BT8. Exposure time was 2 and 6 h. At least three samples were examined at each mode of hardening and thermal exposure.

Residual stresses were investigated on prismatic samples of $55 \times 10 \times 2$ mm. Used the method of removing thin layers of metal by electrolytic polishing.

4   Results and Discussion

In the samples after hardening for 5 min, the maximum of compressive residual stresses was −349 MPa and was observed at a depth of 20–40 mkm. On the surface of the samples, the compressive residual stresses were −250 MPa (Fig. 1, curve a).

After thermal exposure at a temperature of 240 °C with a holding time of 2 h, the maximum stress −349 MPa was at a depth of 5–10 mkm. On the surface of the samples, the stress was −320 MPa (Fig. 1, curve b).
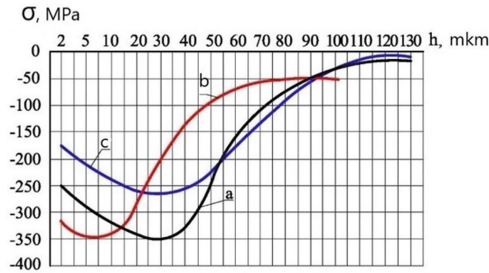
Fig. 1. Distribution of residual stresses in the surface layer after hardening for 5 min and thermal exposure at a temperature of 240 °C: a – after hardening for – 5 min (initial); b – after thermoexposure 240 °C, 2 h; c – after thermal exposure 240 °C, 6 h

Thermal exposure with a holding time of 6 h led to a decrease in the maximum value of residual stresses to −264 MPa with a propagation depth of 20–40 mkm. The surface tension was −175 MPa (Fig. 1, curve c).

At thermal exposure with a holding time of 2 h, the maximum residual stress did not change, but the depth of their propagation changed. With a holding time of 6 h, the residual stresses relaxed from −349 MPa to −264 MPa, means by 24.3%.

In the samples after hardening for 15 min, the maximum compressive residual stresses were −375 MPa and was observed at a depth of 20–40 mkm (Fig. 2, curve a). The compressive residual stresses on the surface of the samples were −230 MPa.
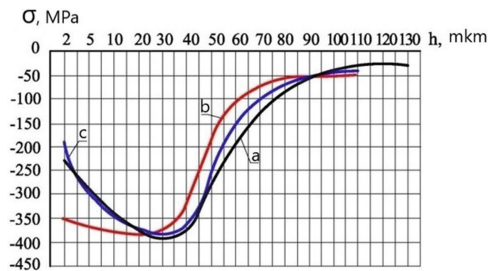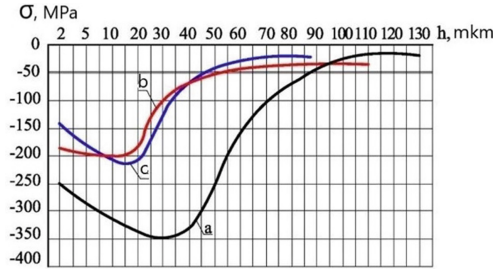

Fig. 2. Distribution of residual stresses in the surface layer after hardening for 15 min and thermal exposure at a temperature of 240 °C: a – after hardening for –15 min (initial); b – after thermal exposure 240 °C, 2 h; c – after thermal exposure 240 °C, 6 h

At thermal exposure with a holding time of 2 h, residual stresses were observed, the maximum value of which was −379 MPa with a propagation depth of up to 5–20 mkm. On the surface, the stress level was −350 MPa (Fig. 2, curve b). At thermal exposure with a holding time of 6 h, the maximum stress was −365 MPa and was at a depth of 20–40 mkm. On the surface, the residual stresses were −185 MPa (Fig. 2, curve c). The maximum stress has not changed. After thermal exposure at a temperature of 480 °C with a holding time of 2 h, in the samples hardened for 5 min, the maximum stress of −203 MPa was observed at a depth of 5–15 mkm. On the surface, the stress level was

−180 MPa (Fig. 3, curve b). The maximum residual stresses were relaxed by 41.8%, which is more than with thermal exposure with a holding temperature of 240 °C.

Thermal exposure with a holding time of 6 h leads to the formation of maximum stresses of −215 MPa with a depth of 10–20 mkm. On the surface of the sample compressive residual stresses were −140 MPa. The maximum residual stresses do not change, depending on the holding temperature. On the surface, the compressive residual stresses were relaxed, compared to the original sample, by 28% for thermal exposure with a holding time of 2 h and by 44% for a holding time of 6 h.

Fig. 3. Distribution of residual stresses in the surface layer after hardening for 5 min and thermal exposure at a temperature of 480 °C: a – after hardening (initial); b – after thermal exposure 480 °C, 2 h; c – after thermal exposure 480 °C, 6 h

For samples that were subjected to ultrasonic hardening for 15 min, the maximum compressive residual stresses of −375 MPa were observed at a depth of 20–40 mkm. On the surface, the compressive residual stresses were –350 MPa (Fig. 4, curve a).
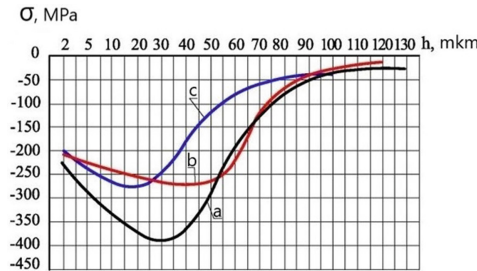

Fig. 4. Distribution of residual stresses in the surface layer after hardening for 15 min and thermal exposure at a temperature of 480 °C: a – after hardening (initial); b – after thermal exposure 480 °C, 2 h; c – after thermal exposure 480 °C, 6 h

After thermal exposure at a temperature of 480 °C with a holding time of 2 h, the maximum stress –264 MPa was at depths of 35–50 mkm, which means 29.6% less than in the initial state. On the surface, the stress was –210 MPa (Fig. 4, curve b).

At thermal exposure with a holding time of 6 h, the maximum compressive stresses were –270 MPa at a depth of 10–20 mkm (Fig. 4, curve c). The maximum residual stress decreased by 28%.

The results of the study showed that the stresses in the samples that were hardened for 15 min relaxed less than when hardened for 5 min. In General, at thermal exposure with a holding temperature of 240 °C, the stresses are relaxed in the samples with a holding time of 6 h and ultrasonic hardening of 5 min, and in other cases, they do not change. The depth of propagation changes. On the surface, the compressive residual stresses, with thermal exposure with a holding time of 2 h, increase. At thermal exposure with a holding temperature of 480 °C, the residual stresses relax a little more than at 240 °C. But when strengthened for 5 min, the amount of relaxation is greater than at 15 min. On the surface, when hardened for 15 min, the stresses do not change, regardless of temperature.

An analysis of the results of changes in the magnitude of residual stresses shows that they correlate with the hardening time and holding temperature. The established regularity of the effect of temperature is in good agreement with the results of most well-known studies, for example [16]. Stress relaxation is associated with the deformation of the surface layer material during term expansion. Also, stress relaxation at a high temperature can be caused by an acceleration of diffusion processes.

The influence of hardening time can be explained by the effect of strain hardening. It manifests itself in an increase in hardness and a change in some other mechanical characteristics of the material. In [17], an attempt was made to establish the relationship between the rate of relaxation of residual stresses and the characteristics of the surface layer of parts. The author of this, and other studies, relate the rate of stress relaxation to the degree of plastic deformation of the material. It is assumed that the relaxation rate is directly related to the degree of plastic deformation. The minimum relaxation rate will correspond to the material with the lowest plastic strain. Residual compressive stresses induced in the surface layer at a minimum level of plastic deformation will be more stable at elevated temperatures. However, this approach is not consistent with the currently widespread dislocation theory of strength.

The results of the study also refute the opinion about the stability of residual stresses at a minimum level of plastic deformation. The established regularities of relaxation can be used to optimize the mode of ultrasonic hardening of titanium alloy parts similar to BT8.

5   Conclusions

As a result of the study of the level and nature of technological residual stresses distribution in the surface layer of heat-resistant titanium alloy BT8 samples, which is caused by steel balls as a result of ultrasonic hardening regularities of influence of hardening time and temperature of thermoexposure on size and depth of distribution of the maximum compressive residual stresses are established.

It was found that at thermal exposure with a holding time of 2 h at a temperature of 240 °C after hardening for 5 min, the maximum stress does not change, but the depth of occurrence changes. With a holding time of 6 h, the residual stresses relaxed from –349 MPa to –264 MPa, which means about 24.3%.

In samples with a holding time of 2 h at a temperature of 480 °C after hardening for 5 min, the residual stresses at the point of maximum relaxed by 41.8%. On the surface,

the compressive residual stresses relax, in comparison with the original sample, by 28% - for thermal exposure with a holding time of 2 h and by 44% - for a holding time of 6 h.

In the samples after hardening for 15 min after thermal exposure at a temperature of 480 °C with a holding time of 2 h, the maximum residual stress was –264 MPa, which means 29.6% less than for the samples in the initial state. At thermal exposure with a holding time of 6 h, the maximum compressive stresses decreased by 28%.

Thus, it was found that the deformation hardening of the surface layer of parts of gas turbine engines made of titanium alloys BT8 for 15 min with the studied parameters is maintained at the operating temperature of the parts of the compressor rotor for a long time. This ensures a stable level of safety margin during operation.

References

1. Pavlenko, D., Dvirnyk, Y., Przysowa, R.: Advanced materials and technologies for compressor blades of small turbofan engines. Aerospace **8**(1), 1–16 (2021)
2. Landwehr, M., et al.: Influence of heat treatment on the residual stress-related machining distortion of ti-6Al-4V alloy monolithic parts. In: Paper Presented at the Procedia CIRP, vol., 104, pp, 13281333 (2021)
3. Abboud, E., Attia, H., Shi, B., Damir, A., Thomson, V., Mebrahtu, Y.: Residual stresses and surface integrity of Ti-alloys during finish turning - guidelines for compressive residual stresses. In: Paper Presented at the Procedia CIRP, vol. 45, pp. 5558 (2016)
4. Liang, H., Kan, Y., Chen, H., Zhan, R., Liu, X., Wang, D.: Effect of cutting process on the residual stress and fatigue life of the welded joint treated by ultrasonic impact treatment. Int. J. Fatigue **143**, 105998 (2021)
5. Shapoval, A., Savchenko, I., Markov, O.: Determination coefficient of stress concentration using a conformed display on a circle of a single radius. Solid State Phenom. **316**, 928–935 (2021)
6. Mcevily, A.J., Kasivitamnuay, J.: Metal Failures: Mechanisms, Analysis, Prevention, 2nd edn. Wiley, Somerset (2013)
7. Praveenkumar, K., Mylavarapu, P., Sarkar, A., Isaac Samuel, E., Nagesha, A., Swaroop, S.: Residual stress distribution and elevated temperature fatigue behaviour of laser peened Ti-6Al-4V with a curved surface. Int. J. Fatigue **156**, 106641 (2022)
8. Kusyi, Y.M., Stupnytskyy, V.V., Kuk, A.M., Topilnytskyy, V.G.: Development of the fundamental diagram of the formation and transformation of the products properties during their manufacturing. In: Paper Presented at the Journal of Physics: Conference Series, vol., 1781, no. 1 (2021)
9. Vasylyev, M.O., Mordyuk, B.M., Pavlenko, D.V., Yatsenko, L.F.: Ultrasonic impact processing of surface layer of the BT1-0 titanium in a submicrocrystalline state. Metallofiz. Noveishie Tekhnol. **37**(1), 121–134 (2015)
10. Xiao, J., Li, D., Li, X.: Modeling and simulation for the stress relaxation behavior of Ti-6Al-4V at medium temperature. Rare Metal Mater. Eng. **44**(5), 1046–1051 (2015)
11. Lim, S.H., et al.: In-situ warm shot peening on ti-6Al-4V alloy: effects of temperature on fatigue life, residual stress, microstructure and mechanical properties. J. Alloys Compound. **882**, 160701 (2021)
12. Bi, J., Cui, X., Zhang, Y., Zhang, Z., Wu, X.: Investigations on stress relaxation behavior of Ti-6Al-4V titanium alloy thin sheet. J. Mech. Eng **55**(18), 43–52 (2019)
13. Liu, Y., Yin, Z.D., Zhu, J.C., Li, M.W.: Stress relaxation behavior of Ti−6Al−4V alloy. Trans. Nonferrous Met. Soc. China **13**, 881–884 (2003)

14. Liu, Y., Yin, Z.D., Zhu, J.C.: Effects of temperature, stress and grain size on stress relaxation of the alloy TC4. Rare Metal Mat. Eng. **32**, 644–646 (2003). (in Chinese)
15. Peng, H., et al.: Effect of grain size on high-temperature stress relaxation behavior of fine-grained TC4 titanium alloy. Trans. Nonferrous Met. Soc. China (English Edition) **30**(3), 668–677 (2020)
16. Ivanov, S., Gushchina, M., Artinov, A., Khomutov, M., Zemlyakov, E.: Effect of elevated temperatures on the mechanical properties of a direct laser deposited Ti-6Al-4V. Materials **14**(21), 6432 (2021)
17. Prevey, P.S.: The effect of cold work on the thermal stability of residual compression in surface-enhanced IN718. Met. Finish. News **6**, 26–31 (2005)

Irregular Packing for Additive Manufacturing

Tatiana Romanova[1] , Andrii Chuhai[1]([✉]) , Georgiy Yaskov[1] , Igor Litvinchev[2] , and Yuriy Stoian[1]

[1] Department of Mathematical Modeling and Optimal Design, Institute for Mechanical Engineering Problems, National Academy of Sciences of Ukraine, Kharkiv, Ukraine
`chugay.andzey80@gmail.com`
[2] Faculty of Mechanical and Electrical Engineering, Nuevo Leon State University, San Nicolas de los Garza, Mexico

Abstract. In modern additive manufacturing technologies, parts are printed in a special container named the printer working chamber. The efficiency of volume filling with geometric objects is an important factor in the overall efficiency of the manufacturing process. To improve the efficiency of the production process, it is necessary to develop effective methods for packing objects in the working chamber of a 3D printer. The problem of filling the working chamber with parts is formulated as a three-dimensional irregular packing problem and presented as a nonlinear optimization problem. The article presents an origin optimization approach for tackling irregular packing problems for additive manufacturing. The approach involves construction of an exact mathematical model of irregular packing problem (using the phi-function technique) and development of a nonlinear optimization method based on state-of-arts solvers. The solution strategy uses the preliminary clustering of bodies to be packed and variable metric characteristics of bodies and a chamber. An exact mathematical model of the problem is constructed and a solution method is developed. Test results are shown.

Keywords: Additive manufacturing · Mathematical modeling · Irregular packing · Non-linear optimization

1 Introduction

Modern additive technologies cover all new areas of human activity. Designers, architects, archaeologists, paleontologists and other professions use 3D printers to implement various ideas and projects [1]. All these works are carried out with the active support of the state and business from various sources [2]. This technology is considered as one of the strategic technologies for development primarily in the aerospace and defense industries [3].

Nowadays many researches have studied technological issue of application of 3d printing in modern manufacturing. In paper [4] various modern additive manufacturing technologies are compared with real-life injection molding. The comparison is made in terms of lead time and total cost of production.

The paper [5] presents the results of research that help to determine the relationship between the parameters of the additive manufacturing process, its characteristic features and product quality.

Particular attention is paid to the development of SLS (Selective Laser Sintering). SLS is an additive production technology based on layer-by-layer sintering of powder materials (polyamides, plastics) using a laser beam [6]. The printing process using Selective Laser Sintering technology consists in layer-by-layer sintering of particles of powdered material before the formation of a physical object according to a given CAD model. The sintering of the material occurs under the influence of a beam of one or more lasers. Before starting the construction process, the consumables are heated almost to the melting point, which facilitates and accelerates the operation of the SLS installation. The article [7] estimates the costs incurred as a result of applying the technology using direct metal laser sintering.

The actual problem is to create automated information systems and technologies that will optimize the various technological stages of additive production [8]. To optimize the technological process of additive manufacturing, it is proposed to apply optimization geometric design.

3D packing problems arise in various applications, e.g., in nanophysics, production and aerospace engineering to mention a few. Some of the works [9, 10] deal with the packing of ellipsoids. Our preliminary results on 3D packing problems presented in [11, 12].

Today only a few works are dedicated to optimized packing problems in additive manufacturing [13, 14]. Analysis and a taxonomy of irregular three-dimensional packing problems in additive Manufacturing is presented in [14].

We consider a packing problem which relates to BVP (Build Volume Packing). The 3D printing process allows simultaneously producing parts in a the 3D-printer chamber. So, we deal with a 3D optimization irregular packing problem. A number of 3D parts should be packed into the container with a minimum metric characteristic. The parts have to be placed at given distances to avoid deformation when cooling.

Packing problems are known to be NP-complete. So, approximate solution methods are developed a major part of which are heuristic: special search rules, genetic, ant (bee) algorithms, simulated annealing, mathematical programming methods and hybrid/combined techniques.

Object arrangement is realized in a variety of ways which differ in: the path of object movement, rotation rules and allowing or avoiding overlapping during solution process.

This work is devoted to searching for a local minimum for the 3D irregular packing problem. A strategy proposed in this paper is based on construction of an exact mathematical model of the packing problem and application of modern methods of nonlinear programming.

2 Problem Definition

Irregular 3D-bodies are derived from following primary geometric objects:

- a polytope J_1 specified by vertices

$$p_{1t} = \left(p_{1t}^1, \; p_{1t}^2, \; p_{1t}^3 \right), \; t \in T_1 = \{1, 2, \ldots, \varrho_1\};$$

- a right cylinder $J_2 = \{X \in \mathbb{R}^3, \; x^2 + y^2 - R_2^2 \le 0, \; 0 \le z \le H_2\}$;
- a sphere $J_3 = \{X \in \mathbb{R}^3, \; x^2 + y^2 + z^2 - R_3^2 \le 0\}$;
- a right cone $J_4 = \{X \in \mathbb{R}^3, \; x^2 + y^2 - c_4^2(z - E_4)^2 \le 0, \; z \ge 0, E_4 > 0\}$;
- a truncated cone

$$J_5 = \{X \in \mathbb{R}^3, \; x^2 + y^2 - c_5^2(z - E_5)^2 \le 0, \; E_5 \ge H_5 \ge 0, \; 0 \le z \le H_5\};$$

- a segment of a sphere

$$J_6 = \{X \in \mathbb{R}^3, \; x^2 + y^2 + (z + H_6)^2 - R_6^2 \le 0, \; z - H_6 \le 0, \; 0 < H_6 < R_6\};$$

a half-space $J_7 = \{X \in \mathbb{R}^3, \; z \le 0\}$.

Let each irregular 3D-body Q_i, $i \in I = \{1, 2, \ldots, n\}$, be a union of a set of convex geometric bodies $O_i = \overset{\kappa_i}{\underset{k=1}{\cup}} O_{ik}$, where O_{ik} is one of the objects J_r, $r = 1, 2, \ldots, 7$. A placement of O_{ik} is given with a vector $u_{ik} = (v_{ik}, \theta_{ik})$, $k \in K_i = \{1, 2, \ldots, \kappa_i\}$.

A chamber $\mathbb{C}$ is a right rectangular parallelepiped $\mathbb{C}_1 = \{X \in \mathbb{R}^3, \; w_1 \le x \le w_2, \; l_1 \le x \le l_2, \; \eta_1 \le x \le \eta_2\}$, where $w_1 \ge 0$, $l_1 \ge 0$, $\eta_1 \ge 0$.

One should pack the bodies O_j, $i \in I$, into the chamber $\mathbb{C}$ with account of shortest distances between parts reaching the minimal value of the chamber volume.

Let $\hbar = (w_1, w_2, l_1, l_2, \eta_1, \eta_2) \in \mathbb{R}^6$. The body O_i can be simultaneously translate on a vector $v_i = (x_i, y_i, z_i)$ and rotated by a vector $\theta_i = (\varphi_i, \psi_i, \omega_i)$. So, a vector $u_i = (v_i, \theta_i) = (x_i, y_i, z_i, \varphi_i, \psi_i, \omega_i)$ defines a placement of the body O_i in the space $\mathbb{R}^3$ and a vector $u = (u_1, u_2, \ldots, u_n) \in \mathbb{R}^{6n}$ gives the placement of all bodies O_i, $i \in I$, in $\mathbb{R}^3$.

The body O_i translated by the vector v_i and rotated by the angles φ_i, ψ_i and ω_i is denoted by $O_i(u_i)$ and the chamber $\mathbb{C}$ with the size $\hbar$ is denoted as $\mathbb{C}(\hbar)$.

3 Mathematical Modeling

Using phi-function technique [15] a mathematical model of the problem stated can be presented as follows

$$\left(u^*, \hbar^*, Z^*\right) = \operatorname{argmin} H(\hbar) \quad \text{s.t. } (u, \hbar, Z) \in \Lambda \subset \mathbb{R}^N \tag{1}$$

$$\Lambda = \{(u, \hbar, Z) \in \mathbb{R}^N : \Phi_{ij}\left(u_i, u_j, \mathbb{Z}_{ij}\right) - d \ge 0, i < j \in I, \tag{2}$$

$$\Phi_i(u_i, \hbar) \geq 0, \ i \in I, L(\hbar) \geq 0\}$$

where $H(\hbar) = (w_2 - w_1)(l_2 - l_1)(\eta_2 - \eta_1)$, $L(\hbar) = w_1 \geq 0, l_1 \geq 0, \eta_1 \geq 0, w_2 - w_1 \geq 0, l_2 - l_1 \geq 0, \eta_2 - \eta_1 \geq 0$.

In the model (1)–(2) the inequality $\Phi_{ij}(u_i, u_j, \mathbb{Z}_{ij}) - d \geq 0$ ensures the distance condition for the bodies O_i and O_j and the inequality $\Phi_i(u_i, \hbar) \geq 0$ specifies a placement of the body O_i in the chamber $\mathbb{C}(\hbar)$.

We consider main characteristics of the mathematical model.

1. Due to $O_i = \overset{\epsilon_i}{\underset{s=1}{\cup}} O_{is}$ and $O_j = \overset{\epsilon_j}{\underset{p=1}{\cup}} O_{jp}$ we have $O_i \cap O_j = \varnothing$ if $O_{is} \cap O_{jp} = \varnothing$, $s \in K_i, p \in K_j$. Then $\Phi_{ij}(u_i, u_j, \mathbb{Z}_{ij}) = \min\{\Phi_{ij}^{sp}(u_i, u_j, \mathbb{Z}_{ij}^{sp}), s \in K_i, p \in K_j\}$ where $\Phi_{ij}^{sp}(u_i, u_j, \mathbb{Z}_{ij}^{sp})$ is either a phi-function or a quasi-phi-function for the bodies O_{is} and O_{jp}. So, if $\min\{\Phi_{ij}^{sp}(u_i, u_j, \mathbb{Z}_{ij}^{sp}), s \in K_i, p \in K_j\} \geq 0$, then $\Phi_{ij}(u_i, u_j\mathbb{Z}_{ij}) \geq 0$.

2. The quasi-phi-function $\Phi_{ij}^{sp}(u_i, u_j, \mathbb{Z}_{ij}^{sp})$ can be in general presented as $\Phi_{ij}^{sp}(u_i, u_j, \mathbb{Z}_{ij}^{sp}) = \max\{\Psi_{ij}^{spa}(u_i, u_j, \mathbb{Z}_{ij}^{sp}), \ a \in A_{ij}^{sp} = B_{ij}^{sp} \cup C_{ij}^{sp} = \{1, 2, \ldots, a_{ij}^{sp} + 1, a_{ij}^{sp} + 2, \ldots, \chi_{ij}^{sp}\}\}$. Then, $\Phi_{ij}^{sp}(u_i, u_j, \mathbb{Z}_{ij}^{sp}) \geq 0$ is valid if at least one of the inequality systems $\{\Psi_{ij}^{spa}(u_i, u_j, \mathbb{Z}_{ij}^{sp}) \geq 0, \ a \in A_{ij}^{sp}$, is satisfied. It is obvious that $\Phi_{ij}(u_i, u_j, \mathbb{Z}_{ij}) \geq 0$ when an inequality system $\{\Psi_{ij}^{spa}(u_i, u_j, \mathbb{Z}_{ij}^{sp}) \geq 0, \ s \in K_i, p \in K_j$, where $a \in A_{ij}^{sp}$, is fulfilled. Thus, the number of the systems is $\varsigma_{ij} = \prod_{s=1}^{\kappa_i} \prod_{p=1}^{\kappa_j} \chi_{ij}^{sp}$. The inequality systems are denoted as

$$\left\{\Psi_{ij}^t(u_i, u_j, \mathbb{Z}_{ij}^t) \geq 0, t \in T_{ij} = \{1, 2, ..., \varsigma_{ij}\}.$$

3. The inequality $\Phi_{ij}(u_i, u_j, \mathbb{Z}_{ij}) \geq 0, \ i < j \in I$, hold true if at least one of the inequality systems $\left\{\Psi_{ij}^t(u_i, u_j, \mathbb{Z}_{ij}^t) \geq 0, i < j \in I,$ Where $t \in T_{ij}$, is satisfied. The inequality systems are denoted as

$$G_\tau(u, \mathbb{Z}) \geq 0, \tau \in \Upsilon = \{1, 2, ..., \vartheta\}$$

where $\vartheta = \prod_{i=1}^n \prod_j^n \varsigma_{ij}$.

4. Functions $\Psi_{ij}^{spa}(u_i, u_j, \mathbb{Z}_{ij}^{sp}), a \in C_{ij}^{sp}$ contain auxiliary components $\mathbb{Z}_{ij}^{sp}$. The number of all variables is at most $\prod_{i=1}^{\kappa_i} \prod_{j=1}^{\kappa_i} \kappa_i \kappa_j$.

5. The function $\Phi_i(u_i, \hbar)$ can be written as

$$\Phi_i(u_i, \hbar) = \min\{\Phi_{is}(u_i, \hbar), \ s \in K_i = \{1, 2, ..., \kappa_i\}\}$$

where $\Phi_{is}(u_i, \hbar)$ is the phi-function for bodies O_{is} and $C(\hbar) = \mathbb{R}^3 \backslash int\mathbb{C}(\hbar)$.

6. Because of the items 3 and 4 the feasible region Λ can be presented as follows

$$\Lambda = \overset{\vartheta}{\underset{\tau=1}{\cup}} \Lambda_\tau,$$

where Λ_τ is specified by the inequality system

$$F_\tau(u, \hbar, \mathbb{Z}_\tau) = \begin{cases} G_\tau(u, \mathbb{Z}_\tau) \geq 0 \\ \Phi_i(u_i, \hbar) \geq 0, i \in I, \\ L(\hbar) \geq 0 \end{cases} = \begin{cases} f_{\tau 1}(\xi_{\tau 1}) \geq 0 \\ f_{\tau 2}(\xi_{\tau 2}) \geq 0 \\ \dots\dots \\ f_{\tau\epsilon}(\xi_{\tau\epsilon}) \geq 0 \end{cases}.$$

It is obvious that $f_{\tau j}(\xi_{\tau j})$, $j = 1, 2, \dots, \epsilon$, are smooth functions.

We reduce solving the main problem (1)–(2) the following subproblems

$$\left(u^{*\tau}, \hbar^{*\tau}\right) = \mathrm{argmin} H(\hbar) \quad \text{s.t.} \quad (u, \hbar) \in \Lambda_\tau \subset \mathbb{R}^N, \tau \in \Upsilon.$$

4 Solution Approach

Taking into account high problem dimensionality the following solution strategy which reduces computational cost significantly.

1. Generation of feasible starting points.

    a) Enclose bodies O_i to spheres S_i with minimum radii r_i^0, $i \in I$.
    b) Pack bodies O_i, $i \in I$, pairwise into clusters Q_t, $t \in T$, being rectangular parallelepipeds or spheres with minimum volumes.
    c) Tackle the problem of packing the clusters Q_t, $t \in T$, into the chamber $\mathbb{C}$ with minimum volume.
    d) Considering the placement parameters of the clusters Q_t, $t \in T$, the bodies O_i, $i \in I$, are packed into the chamber $\mathbb{C}$. In so doing we obtain a feasible starting point for the problem (1)–(2).

2. Local optimization.

    e) Fix the rotation angles of the bodies O_i, $i \in I$, a local minimum point of the problem (1)–(2) is computed.
    f) Considering θ_i and u_i, $i \in I$, as variables a local minimum point of the problem (1)–(2) is found.

5 Construction of Starting Points

To enclose bodies O_i to $S_i = \{X \in \mathbb{R}^3, x^2 + y^2 + z^2 - r_i^2 \leq 0\}$ the following problems:

$$r_i^0 = \min \quad r_i \text{ s.t. } (r_i, v_i) \in D_i \subset \mathbb{R}^4, \ i \in I, \tag{3}$$

$$D_i = \left\{ \left(r_i^0, v_i^0 \right) \in \mathbb{R}^4, \ \Phi_i(r_i, v_i) \geq 0 \right\} \tag{4}$$

are solved.

The inequality $\Phi_i(r_i, v_i) \geq 0$ ensures containment of the body O_i into the set $C_i = \{X \in \mathbb{R}^3, \ -(x - x_i)^2 - (y - y_i)^2 - (z - z_i)^2 + r_i^2 \geq 0\}$.

As a result of solving the problem a point $\left(r_i^0, v_i^0 \right)$ is calculated. Then the origins of the eigen coordinate systems $v_i = (x_i, y_i, z_i)$ of O_i are moved to coincide with centers of S_i, $i \in I$.

Now a problem of packing the spheres S_i, $i \in I$, into $\mathbb{C}$ of minimum volume. The problem is solved as described in [18]. So, a point (v^*, R^*) being an approximation to a global minimum point of the problem (3)–(4) is defined. Considering arbitrary rotation angles $\varphi_i = \varphi_i^0$, $\psi_i = \psi_i^0$ and $\omega_i = \omega_i^0$ of O_i, $i \in I$, we calculate a feasible starting point $\left(u^0, \theta^0 \right) = \left(v^*, \varphi^0, \psi^0, \omega^0 \right) \in \Lambda$ for the problem (1)–(2).

5.1 Packing Bodies Pairwise into Rectangular Parallelepipeds and Spheres

Let O_i, $i \in I$, consist of k groups each from which contains l_k identical bodies. We pack pairwise O_i, $i \in I$, into rectangular parallelepipeds Q_{ij} of minimum volumes V_{ij}^C, $i < j \in K = \{1, 2, ...k\}$. The problems

$$V_{ij}^C = F_{ij}\left(\hbar^\diamond \right) = \min F_{ij}(\hbar) \quad \text{s.t.} \ \left(u_i, u_j, \hbar \right) \in \Omega_{ij} \subset \mathbb{R}^{18}, \ i < j \in I, \tag{5}$$

where

$$F_{ij}(\hbar) = \left(w_2^{ij} - w_1^{ij} \right) \left(l_2^{ij} - l_1^{ij} \right) \left(\eta_2^{ij} - \eta_1^{ij} \right),$$

$$\Omega_{ij} = \{ \left(u_i, u_j, \hbar \right) \in \mathbb{R}^{18} : \Phi_{ij}\left(u_i, u_j \right) \geq 0, \Phi_i(u_i, \hbar) \geq 0,$$

$$\Phi_j\left(u_j, \hbar \right) \geq 0, L_{ij}(\hbar) \geq 0 \},$$

$$L_{ij}(\hbar) = (w_1^{ij} \geq 0, l_1^{ij} \geq 0, \eta_1^{ij} \geq 0, w_2^{ij} - w_1^{ij} \geq 0,$$

$$l_2^{ij} - l_1^{ij} \geq 0, \eta_2^{ij} - \eta_1^{ij} \geq 0),$$

are solved.

The inequality $\Phi_{ij}\left(u_i, u_j \right) \geq 0$ provides $int O_i \cap int O_j = \varnothing$ and the inequality $\Phi_i(u_i, \hbar) \geq 0$ ensures placement of O_i in Q_{ij}.

A local minimum point $\left(u_i^*, u_j^*, \hbar^* \right)$ of the problem (5) being close to a global minimum point is found.

Pairs of the bodies O_i, $i \in I$, are packed into spheres S_{ij} of the minimum radii R_{ij}^*, $i < j \in K = \{1, 2, ...k\}$. To this end we solve the following problems:

$$V_{ij}^S = \frac{4}{3}\pi \min \ R_{ij}^3 \quad \text{s.t.} \ \left(u_i, u_j, R_{ij} \right) \in \Omega_{ij} \subset \mathbb{R}^{13}, \ i < j \in I, \tag{6}$$

where

$$\Omega_{ij} = \{(u_i, u_j, R_{ij}) \in \mathbb{R}^{16} : \Phi_{ij}(u_i, u_j) \geq 0, \Phi_i(u_i, R_{ij}) \geq 0, \quad (7)$$

$$\Phi_j(u_j, R_{ij}) \geq 0, R_{ij} \geq 0\}.$$

Let point $\left(u_i^*, u_j^*, R_{ij}^*\right)$ be a solution of the problem (6)–(7).

Considering variable homothetic coefficients h_i of the bodies O_i and O_j we calculate a starting point from Ω_{ij}. The phi-functions now depends on homothetic coefficients h_i, $0 < h_i < \infty$. The homothetic coefficients h_i, $i \in T$, form a vector $h = (h_i, h_j) \in \mathbb{R}^2$.

Firstly, sizes $\hbar'$ of container $\mathbb{C}_{ij}(\hbar')$ are selected to ensure packing of the bodies O_i and O_j into $\mathbb{C}_{ij}(\hbar')$. We formulate the following auxiliary problem

$$\sum_{i=1}^{g} h_i^* = \max \ \sum_{i=1}^{g} h_i \quad \text{s.t.} (u, h) \in \Delta \subset \mathbb{R}^{14}, \quad (8)$$

where

$$\Delta = \{(u, h) \in \mathbb{R}^{14}, \ \Phi_{ij}(u_i, u_j, h_i, h_j) \geq 0, \Phi_k(u_k, h_k) \geq 0,$$

$$h_k \geq 0, \ h_k - 1 \geq 0, k = i, j\}.$$

A starting point $\left(u_i', u_j', h'\right)$ for the problem is constructed as follows. We take $h_k' = 0.01$, $k = i, j$, and give a random value of $u', v_k' \in \mathbb{C}_{ij}(\hbar')$, $k = i, j$.

If $h_k^* = 1$, $k = i, j$, then $\left(u_i^*, u_j^*, h^*\right)$ is a global maximum solution of the problem (8) and the bodies O_i and O_j are packed into the chamber $\mathbb{C}_{ij}(\hbar')$.

Considering the starting point $\left(u_i', u_j', h'\right)$ we solve the problem (8) and calculate a global maximum point $\left(u_i^*, u_j^*, 1\right)$.

A local optimization procedure is in detail described in paper [16].

6 Numerical Results

In this section we give a benchmark examples to show effectiveness of our approach. Figure 1 shows the results of packing 100 spherocylinders, 150 discuses and 200 spherocones. We use Intel Core I5 750 computer. To solve nonlinear optimization problems the IPOPT solver (https://projects.coin-or.org/Ipopt) is applied.
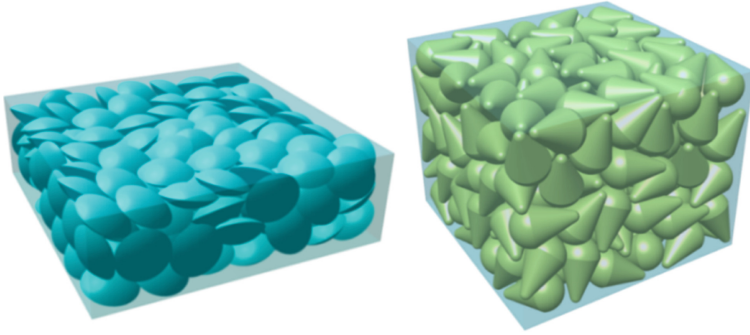
Fig. 1. Results of packing bodies

7   Conclusions

In modern additive manufacturing efficiency of the manufacturing process depends on dense 3-D printer chamber volume filling with parts.

The article presents an origin optimization approach for tackling irregular packing problems for additive manufacturing. The approach involves construction of an exact mathematical model of irregular packing problem (using the phi-function technique) and development of a nonlinear optimization method based on state-of-arts solvers.

The solution strategy uses the preliminary clustering of bodies to be packed and variable metric characteristics of bodies and a chamber. We reduce the computational cost due to constructing starting points making use of the clustering method which allows to consider convex bodies with a simpler geometry. Using the phi-function technique enables to apply non-linear programming methods for all stages of the solution process (construction of the feasible starting points, calculation of local optimal points).

References

1. Gebhardt, A., Kessler, J., Thurn, L.: 3D Printing: Understanding Additive Manufacturing. Hanser (2019)
2. Gardan, J.: Additive manufacturing technologies: state of the art and trends. Int. J. Prod. Res. **54**(10), 3118 (2016)
3. Charisios, A., Tzetzis, D., Raimondo, M.: Alternative production strategies based on the comparison of additive and traditional manufacturing technologies. Int. J. Prod. Res. **55**(12), 3497–3509 (2017)
4. Fasano, G., Pinter, J.D. (eds.): Modeling and Optimization in Space Engineering - State of the Art and New Challenges. Springer, Cham (2019). https://doi.org/10.1007/978-3-030-10501-3
5. Baumers, M., Beltrametti, L., Gasparre, A., Hague, R.: Informing additive manufacturing technology adoption: total cost and the impact of capacity utilisation. Int. J. Prod. Res. 1–14 (2017)

6. Mani, M., Lane, B., Donmez, M.A., Feng, S.C., Moylan, S.P.: A review on measurement science needs for real-time control of additive manufacturing metal powder bed fusion processes. Int. J. Prod. Res. **55**(5), 1400–1418 (2017)
7. Lupone, F., Padovano, E., Casamento, F., Badini, C.: Process phenomena and material properties in selective laser sintering of polymers: a review. Materials **15**, 183 (2022)
8. Mehrpouya, M., Dehghanghadikolaei, A., Fotovvati, B., Vosooghnia, A., et al.: The potential of additive manufacturing in the smart factory industrial 4.0: a review. Appl. Sci. **9**(18), 3865 (2019)
9. Leao, A., Toledo, F., Oliveira, J., Carravilla, M., et al.: Irregular packing problems: a review of mathematical models. Eur. J. Oper. Res. **282**(3), 803–822 (2020)
10. Kallrath, J.: Packing ellipsoids into volume-minimizing rectangular boxes. J. Global Optim. **67**(1–2), 151–185 (2015). https://doi.org/10.1007/s10898-015-0348-6
11. Birgin, E., Lobato, R.: Amatheuristic approach with nonlinear subproblems for large-scale packing of ellipsoids. Eur. J. Oper. Res. **272**(2), 447 (2019)
12. Lee, M., Fang, Q., Cho, Y., Ryu, J., et al.: Support-free hollowing for 3D printing via Voronoi diagram of ellipses. Comput. Aided Des. **101**, 23 (2018)
13. Araújo, L., Özcan, E., Atkin, J., Baumers, M.: Analysis of irregular three-dimensional packing problems in additive manufacturing: a new taxonomy and dataset. Int. J. Prod. Res. **57**(18), 5920 (2019)
14. Stoyan, Y.G., Semkin, V.V., Chugay, A.M.: Modeling close packing of 3D objects. Cybern. Syst. Anal. **52**(2), 296–304 (2016). https://doi.org/10.1007/s10559-016-9826-1
15. Romanova, T., Litvinchev, I., Pankratov, A.: Packing ellipsoids in an optimized cylinder. Eur. J. Oper. Res. **285**(2), 429–443 (2020)
16. Stoian, Y.E., Chugay, A.M., Pankratov, A.V., Romanova, T.E.: Two approaches to modeling and solving the packing problem for convex polytopes. Cybern. Syst. Anal. **54**(4), 585–593 (2018). https://doi.org/10.1007/s10559-018-0059-3

Porosity Measurement in Carbon-Fiber-Reinforced Polymer Composite Through Optical Microscopy Using ImageJ Software

Francisco Monticeli[(✉)] , Herman Voorwald, and Maria Odila Cioffi

Department of Materials and Technology, São Paulo State University, Guaratinguetá, SP, Brazil
f.monticeli@unesp.br

Abstract. Void morphology affects the mechanical behavior of carbon-fiber-reinforced polymer (CFRP) composites since void shape results in different stress concentration levels. Concerning of the importance of higher porosity characterization, this study proposes an automated methodology to measure the void content, morphology, and size of CFRP composites using ImageJ software (image processing) without generating toxic residues (sustainable void measurement). The results show that the variations in the threshold level strongly influence void measurement such that inappropriate levels can underestimate or overestimate the void content, highlight incorrect pixels, and prevent the measurement of the hole pore size. The most appropriate threshold level for CFRP composites was selected as 40 to ensure appropriate void content and size measurements. The proposed technique to measure the void content was validated by comparative analysis with a standard method. This study presents a careful analysis of porosity measurement parameters to quantify the void content, morphology, and size, and provides an automated methodology to configure the ImageJ software.

Keywords: Polymer composite · Void · Sustainable measurement · Optical microscopy

1 Introduction

The application of carbon-fiber-reinforced polymer (CFRP) composites in the aeronautics industry has reduced the weight of structural components and fossil fuel consumption [1]. The recent development of urban air mobility also aims to utilize 100% CFRPs in vehicle structures for low fuel consumption and sustainable CO_2 emissions [1, 2]. However, care is required in the manufacturing process to minimize defects because porosity (i.e., voids or pores) acts as stress concentrators that impair the mechanical strength of materials [3, 4].

Recent studies have demonstrated the negative impact of void content and morphology on mechanical and thermal analyses, indicating the importance of void shape on material properties [5, 6]. Hamidi et al. [7] highlighted that the pore morphology and

void position could significantly influence mechanical behavior because the pore shape leads to different stress concentration levels, while void position contributes to crack initiation and growth.

Different porosity measurement methods have been proposed the literature. These include acid digestion [8] and the Archimedes principle [9] based on the density of each composite component; mercury porosimetry [10] based on mercury intrusion into a high-pressure system; optical microscopy and scanning electric microscopy [7, 11] based on two-dimensional (2D) image analysis; and X-ray microtomography [12, 13] based on three-dimensional (3D) image analysis. Acid digestion, the Archimedes principle, and mercury porosimetry are the most widely used methods in the science and technology sector. However, acid digestion and the Archimedes principle provide insufficient information on porosity because these quantify only the void fraction. Acid digestion and mercury porosimetry usually detect high specific volumes of toxic residues, acid/oxygen peroxide solution, and high mercury concentrations, respectively [10, 14, 15]. The microscopy technique is a recent method that provides a large amount of void information by measuring and quantifying voids in images, and conducts analyses without toxic residue formation (sustainable method) [16, 17].

Saenz–Castillo [18] performed image analysis to characterize void formation and determine the appropriate manufacturing parameters for the project design step. Images allow micropore measurements (not possible with other techniques) to evaluate and determine the influence of micro voids on mechanical performance [19]. In addition, the application of the microscopy technique for measuring and analyzing porosity helps in the understanding of porosity formation mechanisms by infusion processes and in the characterization of physical damage mechanisms to enable the design of mechanical properties by prediction models [20, 21].

One of the main concerns found in the literature is the variations in measurement methods and the lack of a standardized procedure for the comparative analysis of pore measurements. No study has reported the use of free image processing software for void characterization in polymer composites. The main advantage of applying microscopy methods to measure porosity is the reduced waste/residue generated compared with conventional methods (acid digestion and mercury porosimetry), and the increased the amount of information obtained from the measurements, such as void content, morphology, and location [11, 12, 15].

Considering the importance of void characterization in CFRP composites for structural applications, this study aims to determine the optimal void measurement procedure and threshold effect using ImageJ software. For comparison, the porosity of CFRP composites was also quantified by acid digestion and optical microscopy. The optimization method was applied to ensure the appropriate image processing parameters. The results were validated by comparative analysis. This paper provides an automated method for measuring the void content and morphology of CRFP composites using the ImageJ software.

2   Experimental Procedure

2.1   Materials and Processing

The experimental analysis was performed for a CRFP composite. The matrix used was the epoxy PRISM EP2400 (Solvay SA, Belgium), while the carbon fiber was IM7 12k (Hexcel, USA) with a specific mass of 1.79 g/cm^3. The carbon fiber fabric used was a plain weave pattern (1 × 1) with a fiber diameter of 7.1 μm and a fabric weight of 200 g/m^2. The fiber volume fraction used in the composites was 54%. These processes can also be applied to other types of reinforcement (e.g., glass fiber or Kevlar) and distinct polymer matrices.

The composite was processed by resin transfer molding at an injection pressure of 120 °C to achieve a resin viscosity of 100 mPa·s. For all injection processes, the injection and vacuum pressure were 0.25 MPa and 0.05 MPa, respectively. The curing procedure was performed at 180 °C for 240 min. After cooling, the composite laminate was extracted from the mold.

Acid digestion was performed to determine the composite void volume content, calculated as the difference between the reinforcement and matrix volume fraction. The procedure and specimen dimensions followed the ASTM 3171 standard. The equipment used was a Marconi digestor. The specimens were first weighed, their density was measured, and then immersed in sulfuric acid at 190 °C for 120 min. A solution of 50% hydrogen peroxide and 50% distilled water (v/v) was added to perform bleaching. The resulting fibers were washed and dried at 100 °C for 60 min, and the void fraction (Vf) was calculated by Eq. (1). Where, m_f is the fiber mass after the digestion procedure, m_i is the initial CFRP mass, ρ_c is the CFRP density, ρ_r is the fiber density, and ρ_m is the epoxy matrix density.

$$V_f = 100 - \left[\left(\frac{m_i - m_f}{m_i} \right) \frac{\rho_c}{\rho_m} \cdot 100 \right] + \left[\left(\frac{m_f}{m_i} \right) \frac{\rho_c}{\rho_r} \cdot 100 \right] \tag{1}$$

2.2   Image Processing Procedure

The images were obtained from the cross-sectional area of the composite (thickness section). Polishing was conducted with a 9, 6, 3, and 1 μm diamond suspension using a DIAMT polishing cloth and 0.05 μm alumina suspension. The microscope used was an Axio Imager Z2m (Carl Zeiss AG, Germany) with a magnification appliance of 200× to ensure the high definition of porosity and voids larger than one pixel. The images were captured through the laminate thickness. Over 300 images of the laminate cross-section area of 30 × 3 mm^2 were obtained.

The images were processed by ImageJ software. The images were first transformed into an 8-bit type. The scale was set according to the magnification (image scale), and then a threshold adjustment was made in the range of 0–255 to determine the influence on void measurement and set the appropriate threshold.

3   Results and Discussion

3.1   Image Processing

The image processing method is shown in Fig. 1. The image of the CFRP composite (Fig. 1a) is used to measure the porosity (Fig. 1b) after the threshold level is selected. Figure 1c shows the threshold range (0–255). The porosity is determined by choosing appropriate values, which return from the boundary pore. The other parameters in Fig. 1c are for modifying the color scale after applying the threshold, i.e., the color chosen to highlight the pore and change the background color. According to the Abbe concept [22] and the applied magnification (neofluar epiplan –200 × with numerical aperture of 0.9), the theoretical lateral resolution is 490 nm, which ensures a smaller pixel than the lowest porosity.
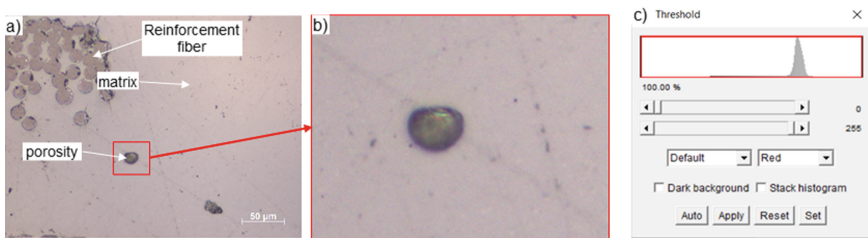
Fig. 1.   Surface image illustration: a) polymer composite, b) porosity highlighted, and c) threshold set.

Figure 2 shows the porosity measurements through threshold variations. Figure 2a shows the target measurement, i.e., pore diameter of 11 µm. Figure 2 also shows the variations in the visual aspect threshold values, in which the threshold level directly affects the pore fraction and size measurement. A value below the threshold leads to the underestimation of the void fraction (measuring only some pixels inside the pore). The same occurs for the size measurement, in which vales lower than the threshold only highlight single pixels and do not account for the hole pore size. Meanwhile, a higher threshold value than required overestimates the error in the pore fraction and size values and measures other defects in pore accounting. Over the threshold level of 40, an overestimation of the values is shown, and there is no need to continue to levels higher than those in Fig. 2n (i.e., 60).

Image quantification was performed by measuring the highlighted areas in Fig. 2 (red areas) to optimize the porosity measurement methodology using the ImageJ software. Figure 3 shows the threshold level versus the individual values of the pore fraction and size. For the sequence of images presented in Fig. 2, the optimal threshold level was chosen as 40, at which the total void (content and size) was measured. This threshold level ensures the appropriate measurements of the pore fraction and size of all the specimens tested. Figure 3 also shows the measured diameters using the appropriate threshold (i.e., 40).
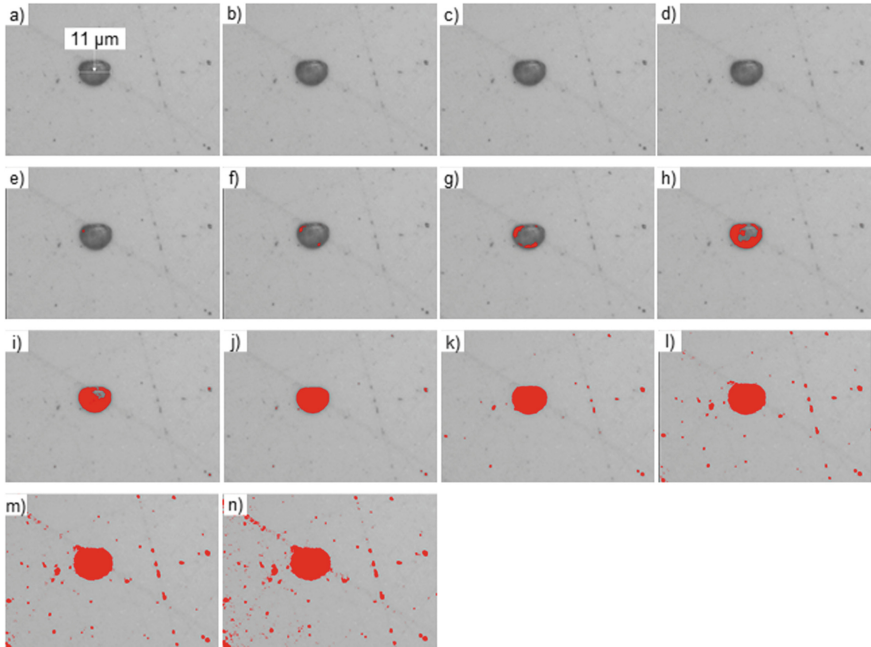
Fig. 2. Data on threshold level variations: a) diameter size; b) 0; c) 5; d) 10; e) 15; f) 20; g) 25; h) 30; i) 35; j) 40; k) 45; l) 50; m) 55; and n) 60.
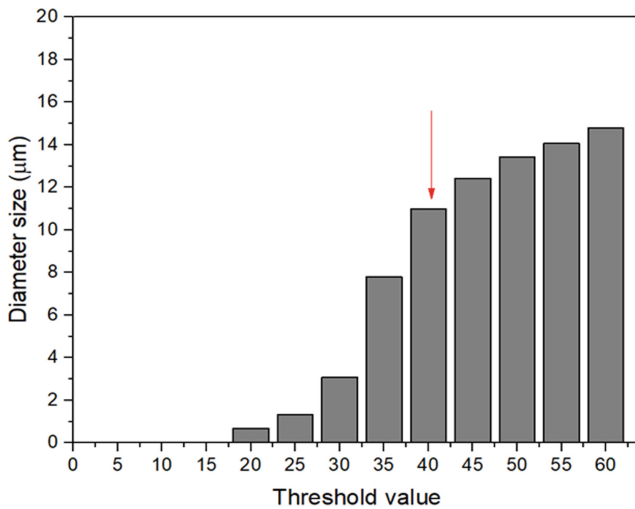

Fig. 3. Diameter size considering threshold value variation.

Following the threshold procedure, porosity measurements were performed for the entire laminated composite at the thickness surface to quantify the void content and void diameter size distribution (Fig. 4). Acid digestion (ASTM D371-15) was also carried out,

which showed that the composite has a void content of $2.42\% \pm 1.26$. Figure 4a shows the void content variations at different threshold levels. The average void fraction obtained using the appropriate threshold was $2.19\% \pm 1.27\%$. The void content values were similar to those found in the literature for similar composite manufacturing parameters [23].

The processing parameters used followed the V-shaped predictions of the porosity model proposed by Patel et al. [24] and Ruiz et al. [25]. This model considered both the viscous drag force and capillary effect to control the pore fraction, size, and position in the laminated composite manufactured by the infusion process. The appropriate capillary number and flow front velocity [24, 25] were applied to reduce the void content. The void measured with the proposed method also corresponded with the theoretical model, confirming the feasibility of the void measurement approach proposed in this study.

Considering the pore size measurement in Fig. 2 and the void content compared with that of acid digestion, it is possible to validate the pore fraction methodology by applying the proposed technique using 40 as the threshold value. The void content of the optical microscopy method is close to that measured by acid digestion. The error is negligible considering the standard deviation.
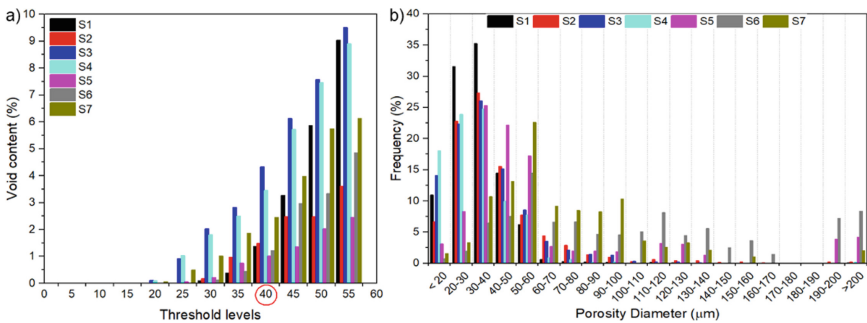
Fig. 4. Porosity measurement: a) void content versus threshold levels and b) diameter size distribution.

Using the selected threshold level (i.e., 40), the void diameter distribution was measured in the seven specimens, as shown in Fig. 4b. All the specimens showed the same results, with the highest frequency observed for small pores ($<50\,\mu m$), a frequency reduction for medium pores (50–$100\,\mu m$), and the lowest frequency for larger pores ($>100\,\mu m$). Higher average porosity results were obtained for void diameters ranging from $30\,\mu m$ to $40\,\mu m$; approximately 30% higher than in the other void diameter ranges. The large amount of reinforcement hinders the growth and coalescence of porosity, limiting its size to smaller pores. The histogram shape was similar to those obtained by Hamidi et al. [3] and Bodaghi et al. [11], confirming the feasibility of the proposed void measurement approach. However, the proposed method has limitations in the measurement of voids smaller than $5\,\mu m$, which can be resolved with higher magnification.

The 2D image analysis provides limited diversity with regard to the real porosity shape. For instance, a circular void in 2D images could be a 3D cylindrical or elliptical

image reflection in a 2D plane [26]. Nonetheless, void images still yield lower measurement errors and provide more information compared with conventional methods, which can reduce project costs. It also provides better information to simulate mechanical trends and is a clean methodology (with no residue formation of during analysis).

3.2 Automated Image Processing Procedure

Table 1 presents the automated configuration method of the ImageJ software, which can be used for image processing in porosity measurements. The first part requests the opening of an image sequence (images with exact dimensions and magnification), which can be applied to one or more images. Applying an 8-bit image ensures that more accessible image processing is carried out. If necessary, the scale ("distance = 1.4493 known = 1") can be changed by different magnifications. The threshold can also be changed to analyze different types of materials or magnifications.

The circularity result represents the void morphology (circular, elliptical, cylindrical, and irregular). Circularity can be used to measure the void morphology and content. A circularity close to 1 indicates perfect spherical pores; a lower value is associated with an irregular void shape [3]. In the results, a table summarizes the average porosity (%), total void area, morphology size (diameter distribution), etc.

Table 1. Automated method configuration for the ImageJ software.

```
run("Image Sequence...", "open=[] sort");
run("8-bit");
run("Set Scale...", "distance=1.4493 known=1 pixel=1 unit=µm global");
setAutoThreshold("Default");
//run("Threshold...");
//setThreshold(0, 40);
setOption("BlackBackground", false);
run("Convert to Mask", "method=Default background=Light");
run("Set Measurements...", "area perimeter bounding fit shape feret's redirect=None
decimal=2");
run("Analyze Particles...", "size=3-Infinity pixel circularity=0.00-1.00 show=Out-
lines display exclude clear include summarize stack");
run("Summarize");
```

4 Conclusions

This study is the first to report on image processing parameters to measure the porosity of advanced composites through 2D images. The data provides a valuable understanding of the methodology used by the ImageJ software for more precise and increased information on the porosity (defects) of polymer composites, such as the void content, area, and morphology, along with the composite laminate thickness. The experimental images

show the most appropriate method and how the changes in threshold levels may cause variations in the measured void morphology and size. The most appropriate threshold level was selected as 40 to ensure complete and precise void measurements. The void measurement based on optical microscopy technique was validated by the results of the comparative analysis with a standard method and literature analysis, presenting similar results for the same composite, i.e., 2.42, 2.19, and 1.98, respectively. The void size distribution showed a higher porosity concentration in smaller pores ($<50\,\mu m$).

In conclusion, this work presents a detailed study of porosity measurement parameters to quantify the void content, morphology, and size of CFRP composites, providing an automated methodology to configure the ImageJ software.

References

1. Donateo, T., Ficarella, A.: A modeling approach for the effect of battery aging on the performance of a hybrid electric rotorcraft for urban air-mobility. Aerospace (2020). https://doi.org/10.3390/AEROSPACE7050056
2. Clarke, M., Smart, J., Botero, E., Maier, W., Alonso, J.J.: Strategies for posing a well-defined problem for urban air mobility vehicles. In: AIAA Scitech 2019 Forum, pp. 1–14 (2019)
3. Hamidi, Y.K., Aktas, L., Altan, M.C.: Effect of packing on void morphology in resin transfer molded E-glass/epoxy composites. Polym. Compos. **26**, 614–627 (2005)
4. Monticeli, F.M., Almeida, J.H.S., Neves, R.M., Ornaghi, F.G., Ornaghi, H.L.: On the 3D void formation of hybrid carbon/glass fiber composite laminates: a statistical approach. Compos. Part A Appl. Sci. Manuf. **137**, 106036 (2020)
5. Zhu, B., Ma, J., Wang, J., Wu, J., Peng, D.: Thermal, dielectric and compressive properties of hollow glass microsphere filled epoxy-matrix composites. J. Reinf. Plast. Compos. **31**, 1311–1326 (2012)
6. Alves, F.C., Monticeli, F.M., Neves, R.M., Voorwald, H.J.C., Cioffi, M.O.H., Ornaghi, H.L.: Influence of void content and morphology on the creep behavior on glass/epoxy composites. Compos. Commun. **25**, 100712 (2021)
7. Hamidi, Y.K., Aktas, L., Altan, M.C.: Three-dimensional features of void morphology in resin transfer molded composites. Compos. Sci. Technol. **65**, 1306–1320 (2005)
8. Garschke, C., Weimer, C., Parlevliet, P.P., Fox, B.L.: Out-of-autoclave cure cycle study of a resin film infusion process using in situ process monitoring. Compos. Part A Appl. Sci. Manuf. **43**, 935–944 (2012)
9. Meier, R., Kahraman, I., Seyhan, A.T., Zaremba, S., Drechsler, K.: Evaluating vibration assisted vacuum infusion processing of hexagonal boron nitride sheet modified carbon fabric/epoxy composites in terms of interlaminar shear strength and void content. Compos. Sci. Technol. **128**, 94–103 (2016)
10. Giesche, H.: Mercury porosimetry: a general (practical) overview. Part. Part. Syst. Charact. **23**, 9–19 (2006)
11. Bodaghi, M., Cristóvão, C., Gomes, R., Correia, N.C.: Experimental characterization of voids in high fibre volume fraction composites processed by high injection pressure RTM. Compos. Part A Appl. Sci. Manuf. **82**, 88–99 (2016)

12. Cheon, J.H., Shin, E.S.: Assessment of the ablation characteristics of carbon/phenolic composites using X-ray microtomography. Compos. Sci. Technol. **182**, 107740 (2019)

13. Joffre, T., Segerholm, K., Persson, C., Bardage, S.L., Hendriks, C.L.L., Isaksson, P.: Characterization of interfacial stress transfer ability in acetylation-treated wood fibre composites using X-ray microtomography **95**, 43–49 (2017)

14. Mao, C., Feng, Y., Wang, X., Ren, G.: Review on research achievements of biogas from anaerobic digestion. Renew. Sustain. Energy Rev. **45**, 540–555 (2015)

15. Seraji, M., Ghafoorian, N., Bahramian, A.: Investigation of microstructure and mechanical properties of novolac/silica and C/SiO2/SiC aerogels using mercury porosimetry method. J. Non Cryst. Solids **435**, 1–7 (2016)

16. Francesconi, L., Taylor, M., Baldi, A.: An investigation of stress concentration, crack nucleation, and fatigue life of thin low porosity metallic auxetic structures. Conf. Proc. Soc. Exp. Mech. Ser. **6**, 65–71 (2019)

17. Boccaccini, A.R., Ondracek, G., Mombello, E.: Determination of stress concentration factors in porous materials. J. Mater. Sci. Lett. **15**(6), 534–536 (1996). https://doi.org/10.1007/BF00275423

18. Saenz-Castillo, D., Martín, M.I., Calvo, S., Rodriguez-Lence, F., Güemes, A.: Effect of processing parameters and void content on mechanical properties and NDI of thermoplastic composites. Compos. Part A Appl. Sci. Manuf. **121**, 308–320 (2019)

19. He, Q., Wang, H., Fu, K., Ye, L.: 3D printed continuous CF/PA6 composites: effect of microscopic voids on mechanical performance. Compos. Sci. Technol. **191**, 108077 (2020)

20. Mehdikhani, M., Steensels, E., Standaert, A., Vallons, K.A.M., Gorbatikh, L., Lomov, S.V.: Multi-scale digital image correlation for detection and quantification of matrix cracks in carbon fiber composite laminates in the absence and presence of voids controlled by the cure cycle. Compos. Part B Eng. **154**, 138–147 (2018)

21. Mehdikhani, M., Gorbatikh, L., Verpoest, I., Lomov, S.V.: Voids in fiber-reinforced polymer composites: a review on their formation, characteristics, and effects on mechanical performance. J. Compos. Mater. **53**, 1579–1669 (2019)

22. Hell, S.W., Dyba, M., Jakobs, S.: Concepts for nanoscale resolution in fluorescence microscopy. Curr. Opin. Neurobiol. **14**, 599–609 (2004)

23. Di Landro, L., Montalto, A., Bettini, P., Guerra, S., Montagnoli, F., Rigamonti, M.: Detection of voids in carbon/epoxy laminates and their influence on mechanical properties. Polym. Polym. Compos. **25**, 371–380 (2017)

24. Patel, N., Rohatgi, V., Lee, L.J.: Micro scale flow behavior and void formation mechanism during impregnation through a unidirectional stitched fiberglass mat. Polym. Eng. Sci. **35**, 837–851 (1995)

25. Ruiz, E., Achim, V., Soukane, S., Trochu, F., Bréard, J.: Optimization of injection flow rate to minimize micro/macro-voids formation in resin transfer molded composites. Compos. Sci. Technol. **66**, 475–486 (2006)

26. Ali, M.A., Umer, R., Khan, K.A., Cantwell, W.J.: In-plane virtual permeability characterization of 3D woven fabrics using a hybrid experimental and numerical approach. Compos. Sci. Technol. **173**, 99–109 (2019)

Special Functions in Heat Transfer Problems

Viktor Lyashenko[1] , Michail D. Todorov[2] , Elena Kobilskaya[1(✉)] ,
Olga Demyanchenko[3] , and Tetiana Hryhorova[1]

[1] Kremenchuk Mykhailo Ostrohradskyi National University, Kremenchuk, Ukraine
`kobilskaya1983@gmail.com`
[2] Technical University of Sofia, Sofia, Bulgaria
[3] Azov Maritime Institute of National University "Odessa Maritime Academy", Mariupol, Ukraine

Abstract. The paper investigates the temperature distribution in an infinite cylinder, which is heated by a point heat source or a moving heat source concentrated on a finite segment. The paper's objective is to construct a mathematical model of the temperature field of an long-length products (infinite cylinder, wire, filament) during 3D printing. For the first time, a mathematical model of the temperature field of an infinite cylinder with a constantly or periodically operating moving heat source has been constructed. Unlike existing models, the resulting model allows you to analyze the temperature field in the heating zone of the cylinder (wire, filament) before and after the heating zone. This becomes possible due to the introduction of a moving coordinate system and the involvement in the mathematical model of special functions. This model allows you to describe the temperature distributions during 3D printing of products and during heat treatment of moving wire (filament). The proposed mathematical model can be used to develop a temperature control system and control the temperature field during the manufacture of products on a 3D printer. The paper considers cases of heating a cylinder (wire, filament) both by a point heat source and by a heat source dispersed over a finite segment, which move at a constant speed. Analytical solutions for simplified problems are obtained. To solve boundary value problems, temperature averaging over one of the coordinates, dimensionless coordinates and parameters are entered, the problem is solved in a moving coordinate system.

Keywords: Dirac delta function · Heaviside step function · Heat treatment · Mathematical modeling

1 Introduction

In many problems of the heat conduction theory, it is assumed that the release or absorption of heat occurs in a small volume. The paper's objective is to construct a mathematical model of the temperature field of an long-length products (infinite cylinder) during 3D printing. Mathematical modeling of heat treatment processes for long-length products such as wire or filament during 3D printing of products is presented in [1]. Heating of the wire or filament is carried out by external or internal heat sources. Heating by passing an

electric current through a limited area of a wire or a thermal explosion can be attributed to internal heat sources. In [2] a two-dimensional Finite Difference (FD) model of the thermal history of parts manufactured in powder bed fusion Additive Manufacturing processes is presented. But in [2] the thermal analysis starts at the point, when the first layer of powder is laid upon the machine table and the laser head begins to offer energy to the powder. In [3] demonstrates the effects the thermal processing and heat treatment conditions on the accuracy and mechanical properties of long-length products. However, there is no mathematical model that allows you to calculate the required temperature of the filament. In [4] developed a novel three-dimensional heat transfer and fluid flow model by considering the effect of wire feeding. The model is static and does not allow you to control the temperature field, in contrast to the model considered in this paper. Electric current is supplied to the product using movable contacts or inductively in a limited area of finite length. The processing of a product with a hot gas jet or laser can be attributed to external sources of heat [5]. To ensure stable physical and mechanical properties of a metal or product during printing on a 3-D printer, it is necessary to control the temperature in the heating zone and maintain it at the level set by the technological conditions. In [6] experiment results show temperature-control 3D printing method has tremendous potential to design, control and realize different degrees of crystallinity and mechanical properties for different PEEK parts. However, the work [6] does not present the model on the basis of which the temperature field control system was developed, the capabilities of the control system are only declared. There are methods determination of filament temperature are based on the measurement of electrical resistance, electrical power, or intensity of thermal radiation at one or more wave lengths λ. In [7] work discusses the errors due to assumptions in these methods. It is rather difficult to determine the temperature of a filament without using a mathematical model [7]. With the help of an appropriate mathematical model of the temperature field in the heating zone and a temperature control system or the degree of heating of a moving wire or filament, built on the basis of such a model, it is possible to control the temperature [8]. A mathematical model is an idealized representation of the heating process of a physical object. From a mathematical point of view, such an idealization of the thermal effect during the heating process is often represented using special functions of the Dirac delta function and the Heaviside step function. Mathematical models in the works discussed above, in particular and in [9] make it possible to study the temperature distribution in the heating zone of a moving wire or filament, and does not allow to study the temperature field in its vicinity, before and after it. In many cases, knowledge of such a distribution is of significant scientific and practical interest [10]. Temperature field control systems that are not focused on mathematical models of the heating process do not allow high-precision control of the temperature in the heating zone, before and after it. This, in turn, reduces the efficiency of control of the heating process and reduces the quality of products.

2   Methodology

Let us consider a moving filament in the form of an infinite cylinder. To calculate the temperature distribution $T(P, t)$, it is assumed that an infinite cylinder [11] with constant thermophysical characteristics λ, c, ρ_n is heated in a heating zone with a length $l = z_2 -$

z_1, of a source $W(P, T) = W(P, t, T)[\eta(z - z_1(t)) - \eta(z - z_2(t))]$, that moves along the axis Oz in a positive direction with speed $v(t)$. Simultaneously with the temperature distribution in the heating zone, the temperature distribution before and after the heating zone is calculated. Thus, we build a mathematical model of the temperature field in three zones: in the heating zone, before and after the heating zone. The temperature at the boundaries of the region is equal to $\lim\limits_{z \to \pm\infty} T = T_0$. Heat exchange of the cylinder surface with the environment outside the heating zone is carried out according to the Newton and Stefan-Boltzmann laws [12]. In the initial stage, a transient heating process takes place, i.e. the speed and density of heat sources are variable, and the temperature at the end of the heating zone must be constant. In a steady state, the speed $v(t)$ of movement is constant, and the density of heat sources W is constant or depends on time. If the moving cylinder is heated by a single-turn inductor or an electron beam of a laser [13], then the heating zone can be as small as desired. Assuming in the physical model that $l \to 0$, and replacing the dispersed heating with a concentrated one with the same total power $W = wl$, we proceed to study the temperature field of a cylindrical region that is heated by a moving concentrated heat source. Obviously, in this case, its density increases indefinitely and in the limit is the Dirac delta function [14]. Indeed, when $l \to 0$, $z_1(t), z_2(t) \to v(t)t$, replacing the Heaviside step function with Dirac delta function the right-hand side of the relation $W(P, T) = W(P, t, T)[\eta(z - z_1(t)) - \eta(z - z_2(t))]$ can be rewritten as

$$\lim_{z_1 \to z_2} W(P, t, T)[\eta(z - z_1(t)) - \eta(z - z_2(t))] = W(P, t, T)\delta(z - v(t)t), \quad (1)$$

where $\eta(z - z_i)$ is the Heaviside step function. When solving problems, we use the following properties of the Dirac delta function $\delta(t)$ and the Heaviside step function $\eta(z - z_i)$.

1. $\delta(t) = 0$, $t \neq 0$, $\int\limits_{-\infty}^{\infty} \delta(t)dt = 1$, $\int\limits_{-\infty}^{\infty} f(t)\delta(t - t_0)dt = f(t_0)$,

2. $\eta(t) = \int\limits_{-\infty}^{t} \delta(x)dx = \begin{cases} 0, & \forall t < 0 \\ 1, & \forall t > 0 \end{cases}$.

The right-hand side of expression (1) is the product of $W(P, t, T)$ and Dirac delta function, which means that the source is concentrated at a moving point. P is the current coordinate of the point

$$\lim_{\Delta l \to 0} \frac{W(P, t, T)}{z_1(t) - z_2(t)}[\eta(z - z_1(t)) - \eta(z - z_2(t))] = W(P, t, T)\delta(z - v(t)t). \quad (2)$$

Consequently, in the case of concentrated heating, the density of heat sources is equal to $W(P, t, T)\delta(z - v(t)t)$, where

$$W(P, t, T) = w(T)f(t), w(T) = \frac{I^2\rho_0(1 + \beta T)}{\pi^2 r_0^4},$$

$f(t)$ is a piecewise monotonic function that reflects impulse heating.

In this case, the temperature distribution in a moving cylindrical region can be represented by solving the following initial-boundary value problem in the region $\Omega \times t = \{0 < r < r_0, z < \infty, t > 0\}$

$$\lambda \frac{1}{r} \frac{\partial}{\partial r} \left(r \frac{\partial T}{\partial r} \right) + \lambda \frac{\partial}{\partial z} \left(\frac{\partial T}{\partial z} \right) - c\rho_n \frac{\partial T}{\partial t} = -w(T)f(t)\delta(z - v(t)t), \tag{3}$$

$$T(r, z, 0) = T_0, \tag{4}$$

$$\lambda \frac{\partial T(r_0, z, 0)}{\partial r} = f(t)\left[\alpha(T_0 - T) + \varepsilon\sigma \left(T_0^4 - T^4 \right) \right], \qquad \frac{\partial T(0, z, 0)}{\partial r} = 0, \tag{5}$$

$$\lim_{z \to \pm\infty} T = T_0. \tag{6}$$

The function $f(t)$, depending on the technological features of the heat treatment process has the form

$$f(t) = 0,5\left(1 - \cos\frac{t}{t_0} \right),\ f(t) = \left| \sin\left(\frac{t}{t_0} \right) \right|,$$

$$f(t) = \begin{cases} \frac{t}{t_0} - 2n, & 2nt_0 < t < (2n+1)t_0 \\ -\frac{t}{t_0} + 2(n+1) & (2n+1)t_0 < t < (2n+2)t_0 \end{cases}.$$

Problem (3)–(6) is nonlinear. Nonlinearity is caused by the presence in condition (5) of the Stefan – Boltzmann $\varepsilon\sigma \left(T_0^4 - T^4 \right)$ boundary condition and piecewise nonlinear function $f(t)$. The solution to such a problem can be obtained only by numerical methods. In some cases, at low heating temperatures, the influence of the nonlinear component in condition (5) can be neglected and the linear problem can be considered.

By using the relation

$$u(z, t) = \frac{2}{r_0^2} \int\limits_0^{r_0} T(r, z, t)r\,dr$$

and the boundary condition (5), we obtain a problem for the determination of the average temperature along the radius in the area $\Omega_1 \times t = \{z < \infty, t > 0\}$

$$\lambda \frac{\partial^2 u}{\partial z^2} - c\rho_n \frac{\partial u}{\partial t} + \left[\frac{I^2 \rho_0 \beta}{\pi^2 r_0^4} f(t)\delta(z - v(t)t) - \frac{2\alpha}{r_0} \right]u - 2\varepsilon\sigma r_0^{-1}u^4$$
$$= -\frac{I^2 \rho_0}{\pi^2 r_0^4}f(t)\delta(z - v(t)t) - \frac{2\alpha T_0}{r_0} - 2\varepsilon\sigma r_0^{-1}T_0^4, \tag{7}$$

$$u(z, 0) = T_0, \qquad \lim_{z \to \pm\infty} u(z, 0) = T_0. \tag{8}$$

In problem (7)–(8), we pass to dimensionless quantities and criteria of Biot, Stark, Pomerantsev.

$$x = \frac{z}{l},\ \tau = \frac{a^2 t}{l^2},\ \mu = \frac{l}{r_0},\ W = \frac{I^2 \rho_0}{\pi^2 r_0^4},\ \nu = \beta T_0,\ Bi = 2\alpha l/\lambda,\ S = 2\varepsilon\sigma l^2 T_0^3/(\lambda r_0),$$
$$Po = wl^2/(\lambda T_0),\ a^2 = \lambda/(c\rho_n),\ \theta_0 = 0,\ \psi(\tau) = \frac{l}{a^2}v\left(\frac{l}{a^2}\tau \right),\ \theta = \frac{u - T_0}{T_0}. \tag{9}$$

After substituting (9) into Eq. (7), into the initial condition and the regularity condition (8), problem (7)–(8) becomes homogeneous in the domain $\Omega \times \tau = \{x < \infty, \ \tau > 0\}$

$$
\frac{\partial^2 \theta}{\partial x^2} - \frac{\partial \theta}{\partial \tau} + \{\nu Po f(t)\delta(x - \psi(t)t) - \mu Bi\}\theta - S(1 + \theta^4) \\
= -(1 - \nu)Po f(t)\delta(x - \psi(t)t) - S,
\tag{10}
$$

$$
\theta(x, 0) = 0, \quad \lim_{x \to \infty} \theta(x, \tau) = 0.
\tag{11}
$$

1. If heat loss by radiation from the surface is a small fraction of all losses, i. e. convective heat transfer prevails, then the nonlinear component in Eq. (10) can be neglected and proceed to the consideration of the linear initial-boundary value problem, which for $S \to 0$ takes the form

$$
\frac{\partial^2 \theta}{\partial x^2} - \frac{\partial \theta}{\partial \tau} - \mu Bi\theta = -Po f(t)\delta(x - \psi(t)t), \\
\theta(x, 0) = 0, \quad \lim_{x \to \pm\infty} \theta(x, \tau) = 0.
\tag{12}
$$

Next, we apply the Fourier transform to Eq. (12).

To do this, we multiply the differential equation by $\frac{1}{\sqrt{2\pi}}e^{-ix\kappa}$ and integrate over the variable x in the range from $-\infty$ to $+\infty$

$$
\frac{1}{\sqrt{2\pi}} \int_{-\infty}^{\infty} \frac{\partial^2 \theta}{\partial x^2} e^{-ix\kappa} dx - \frac{1}{\sqrt{2\pi}} \frac{\partial}{\partial \tau} \int_{-\infty}^{\infty} e^{-ix\kappa}\theta dx - \frac{\mu Bi}{\sqrt{2\pi}} \int_{-\infty}^{\infty} \theta e^{-ix\kappa} dx \\
= -\frac{Po f(t)}{\sqrt{2\pi}} \int_{-\infty}^{\infty} \theta e^{-ix\kappa}\delta(x - \psi(t)t)dx.
\tag{13}
$$

After integrating (13), taking into account condition (11), and also taking into account the relation

$$
\overline{\theta}(\kappa, \tau) = \frac{1}{\sqrt{2\pi}} \int_{-\infty}^{\infty} \theta(x, \tau)e^{-i\kappa x}dx,
\tag{14}
$$

we obtain the Cauchy problem for a first-order linear differential equation

$$
\frac{d\overline{\theta}}{d\tau} + \left(\kappa^2 + \mu Bi\right)\overline{\theta} = Po \times f(\tau)e^{-i\kappa x}dx, \ \tau > 0,
\tag{15}
$$

$$
\overline{\theta}(\kappa, 0) = 0.
\tag{16}
$$

The solution to this problem is written out in the form

$$
\overline{\theta}\left(\kappa, \tau\right) = Po \times e^{-\left(\kappa^2 + \mu Bi\right)\tau} \int_{0}^{\tau} f\left(\tau\right) e^{\left(-i\kappa\psi(\tau) + \kappa^2 + \mu Bi\right)\tau} d\tau.
\tag{17}
$$

2. Consider the case when a concentrated heat source moves at a constant speed v and $f(t) = 1$. Then, after averaging and changing variables $\zeta = z - vt$, problem (3)–(6) can be written in the form

$$\frac{d^2u}{d\zeta^2} + \frac{vc\rho_p}{\lambda}\frac{du}{d\zeta} + \left[\frac{I^2\rho_0\beta}{\pi^2 r_0^4\lambda}\delta(\zeta) - \frac{2\alpha}{\lambda r_0}\right]u - \frac{2\varepsilon\sigma}{\lambda r_0}u^4$$

$$= -\frac{I^2\rho_0}{\pi^2 r_0^4\lambda}\delta(\zeta) - \frac{2\alpha T_0}{\lambda r_0} - \frac{2\varepsilon\sigma}{\lambda r_0}T_0^4, \zeta < \infty \qquad (18)$$

$$\lim_{\zeta \to \pm\infty} u(\zeta) = T_0. \qquad (19)$$

In the linear case, when heat loss by radiation can be ignored, problem (18)–(19) is simplified and an analytical solution can be obtained

$$\frac{d^2u}{d\zeta^2} + \frac{vc\rho_p}{\lambda}\frac{du}{d\zeta} + \left[\frac{I^2\rho_0\beta}{\pi^2 r_0^4\lambda}\delta(\zeta) - \frac{2\alpha}{\lambda r_0}\right]u$$

$$= -\frac{I^2\rho_0}{\pi^2 r_0^4\lambda}\delta(\zeta) - \frac{2\alpha T_0}{\lambda r_0}, \zeta < \infty, \qquad \lim_{\zeta \to \pm\infty} u(\zeta) = T_0. \qquad (20)$$

For $\zeta < 0$ or $\zeta > 0$, problem (20) has the form

$$\frac{d^2u}{d\zeta^2} + \frac{vc\rho_p}{\lambda}\frac{du}{d\zeta} - \frac{2\alpha}{\lambda r_0}u = -\frac{2\alpha T_0}{\lambda r_0}, \qquad \lim_{\zeta \to \pm\infty} u(\zeta) = T_0. \qquad (21)$$

Its solution is written as follows

$$u(\zeta) = T_0 + C_1 e^{k_1\zeta} + C_2 e^{k_2\zeta}, \ \zeta < 0, \ \zeta > 0, \quad k_{1,2} = -\frac{vc\rho_p}{2\lambda} \pm \sqrt{\left(\frac{vc\rho_p}{2\lambda}\right)^2 + \frac{2\alpha}{\lambda r_0}}. \qquad (22)$$

To determine the constants C_1, C_2, we use the property of the Dirac delta function – the jump condition

$$\left[\frac{du}{d\zeta}\right]_{\zeta=0} + \frac{I^2\rho_0\beta}{\pi^2 r_0^4 vc\rho_p}u(0) = -\frac{I^2\rho_0}{\pi^2 r_0^4 vc\rho_p}. \qquad (23)$$

Whence, after substituting (22) in (23) and taking into account the properties of the Dirac delta function we obtain

$$C_{1,2} = \frac{I^2\rho_0(1 + \beta T_0)}{\pi^2 r_0^4 vc\rho_n(k_1 - k_2) - I^2\rho_0\beta}. \qquad (24)$$

Substituting (24) into (22), we obtain

$$u(\zeta) = T_0 + \frac{I^2\rho_0(1 + \beta T_0)}{\pi^2 r_0^4 vc\rho_n(k_1 - k_2) - I^2\rho_0\beta}\begin{cases} e^{k_1\zeta}, \zeta \leq 0 \\ e^{k_2\zeta}, \zeta > 0 \end{cases}. \qquad (25)$$

Since $|k_2| > k_1$, the curve characterizing the solution has a different slope at the intervals $(-\infty, 0]$, $(0, \infty)$.

3 Results

At high speeds of movement of the heat source, the different character of the slope of the curve will be even more pronounced. The graph (see Fig. 1) shows the curves calculated by the formula (25) and corresponding to different speeds of the heat source. Calculations are made for the following parameters:

$$r_0 = 10^{-6} \text{ m}, \quad T_0 = 300 \text{ K}, \quad \alpha = 0,001 \; \frac{\text{W}}{\text{m}^2\text{K}}, \quad I = 10 \text{ A}, \quad v = 0,001 \; \frac{\text{m}}{\text{s}}.$$
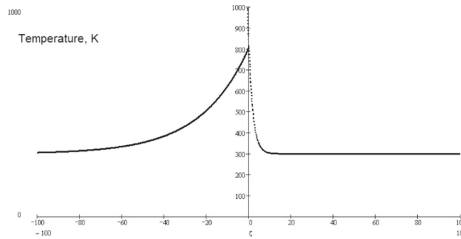

Fig. 1. Temperature distribution obtained from (25).

The analysis of the numerical experiment showed that the nature of the temperature field of the wire or filament most sensitively changes with a change in such parameters as the heat transfer coefficient α, current strength I, and speed v of the source.

a)   b)
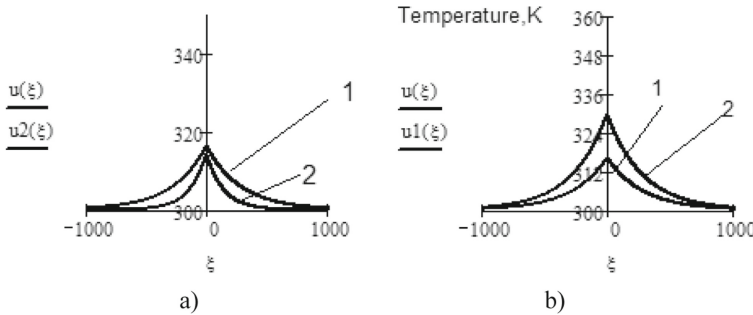
Fig. 2. Temperature distributions, which are obtained from (25) for various values of the heat transfer coefficient and current strength

a) curve 1–$\alpha = 10^{-3} \; \frac{\text{W}}{\text{m}^2\text{K}}$, curve 2–$\alpha = 2 \times 10^{-3} \; \frac{\text{W}}{\text{m}^2\text{K}}$; b) curve 1–$I = 3 \cdot 10^{-2}$ A, curve 2–$I = 4 \cdot 10^{-2}$ A.

Figure 2 shows the temperature distributions constructed from (25) for PLA filament during 3D printing in the extruder area and beyond, Fig. 2a) shows two curves constructed for different values of the heat transfer coefficient, Fig. 2 b) for different values of current strength. Calculations show that increasing the value of the current leads to an increase

in the temperature of the filament, and increasing the value of the heat transfer coefficient leads to a decrease in temperature. The structure of the program is built on a modular basis. This made it possible to combine the solutions of problems for the equations of heat conduction and, taking into account the technological features of the processes, to carry out calculations by changing the boundary conditions. To solve the two-dimensional nonlinear heat equation, the alternating directions method was applied, which made it possible to restrict ourselves to one module for solving tape systems of equations.

4   Conclusion

The processes of heat treatment of long-length products such as wire or filament are considered. Filament is presented as an infinite cylinder. The paper discusses the possibility of using special functions of mathematical physics to build mathematical models. For the first time, a mathematical model of the temperature field of an infinite cylinder with a constantly or periodically operating moving heat source has been constructed. Mathematical models of the temperature field of an infinite cylinder (wire, filament) are constructed in the form of boundary value problems for the heat equation with the involvement of special functions – the Dirac delta function and the Heaviside step function. Unlike existing models, the resulting model allows analyzing the temperature field both in the heating zone of the cylinder (wire) and outside it. This model allows describing the temperature distribution during 3D printing of products in the extruder zone and beyond, as well as the temperature field during the heat treatment of an endless wire (filament). The mathematical model proposed in the work can be used to create control systems for the heat treatment process in the production of wire and tape from non-ferrous and refractory metals. The numerical analysis carried out showed, that the nature of the temperature distribution in the wire changes most sensitively with a change in such parameters as the heat transfer coefficient, the current strength, and the speed of the source. By changing these parameters it is possible to control and manage the temperature distribution.

References

1. Zagirnyak, M., Kobilskaya, E., Lyashenko, V., Salenko, A.: Mathematical models of the temperature field in the filament-extruder system during 3D printing. AIP Conf. Proc. **2302**, 100008–110001 (2020)
2. Foteinopoulos, P., Papacharalampopoulos, A., Stavropoulos, P.: On thermal modeling of additive manufacturing processes. CIRP J. Manuf. Sci. Technol. **20**, 66–83 (2018)
3. Geng, P., et al.: Polymers **10**, 875–887 (2018)
4. Hu, R., et al.: Thermal fluid dynamics of liquid bridge transfer in laser wire deposition 3D printing. Sci. Technol. Weld. Join. 1–11(2019). https://doi.org/10.1080/13621718.2019.1591039
5. Fuchs, J., Schneider, C., Enzinger, N.: Wire-based additive manufacturing using an electron beam as heat source. Weld. World **62**(2), 267–275 (2018). https://doi.org/10.1007/s40194-017-0537-7
6. Yang, C., Tian, X., Cao, Y., Zhao, F., Shi, C.: Influence of thermal processing conditions in 3D printing on the crystallinity and mechanical properties of PEEK material. J. Mater. Process. Technol. 18–29 (2017)

7. Onnink, A.J., Schmitz, J., Kovalgin, A.Y.: How hot is the wire: optical, electrical, and combined methods to determine filament temperature. Thin Solid Films **674**, 22–32 (2019)
8. Kobilskaya, E., Lyashenko, V., Hryhorova, T.: Integral conditions in the inverse heat conduction problems. Math. Model. Comput. **7**(2), 219–227 (2020)
9. Bhalodi, D., Zalavadiya, K., Gurrala, P.K.: Influence of temperature on polymer parts manufactured by fused deposition modeling process. J. Braz. Soc. Mech. Sci. Eng. **41**(3), 1–11 (2019). https://doi.org/10.1007/s40430-019-1616-z
10. Enescu, D., Colella, P., Russo, A.: Thermal assessment of power cables and impacts on cable current rating: an overview. Energies **13**, 5319 (2020). https://doi.org/10.3390/en13205319
11. Chen, X., Xia, H.: Flow and surface heat transfer analysis of a square cylinder in turbulent cross-flow. Numer. Heat Transf. Part A: Appl. **75**(12), 795–823 (2019)
12. Zaika, A., Hrytsiuk, O., Kobilskaya, E., Lyashenko, V.: Generalized mathematical model of heat conduction in a complex multi-layered area. AIP Conf. Proc. **1895**, 090004-1–090004-9 (2017)
13. Bailly-Grandvaux, M., Santos, J.J., Bellei, C., et al.: Guiding of relativistic electron beams in dense matter by laser-driven magnetostatic fields. Nat. Commun. **9**, 102–109 (2018)
14. Tomasz, K.: Heat source models in numerical simulations of laser welding. Materials **13**, 2653 (2020)
15. Amaku, M., Coutinho, F.A.B., Eboli, O.J.P., Massad, E.: Some problems with the Dirac delta function: divergent series in physics. Braz. J. Phys **51**, 1324–1332 (2021)

Coupled Finite and Boundary Element Methods in Fluid-Structure Interaction Problems for Power Machine Units

Vasyl Gnitko[1]([✉]) [iD], Oleksandr Martynenko[2] [iD], Ivan Vierushkin[1] [iD],
Yehor Kononenko[1] [iD], and Kyrylo Degtyarev[1] [iD]

[1] A. Podgorny Institute of Mechanical Engineering Problems NASU, vul. Pozharskogo, 2/10,
Kharkiv 61046, Ukraine
`gnitkovi@gmail.com`

[2] Stuttgart Centre for Simulation Sciences (SC SimTech), University of Stuttgart, Nobelstr. 15,
70569 Stuttgart, Germany

Abstract. New computational techniques are developed to study fluid-structure interaction problems for elements of the structure. The approach is based on coupled finite and boundary element methods involving hypersingular integral equations. Thin shells and plates are considered as structural elements interacting with ideal and incompressible liquids. The fundamental relations of the continuous mechanics are incorporated to describe the motion of structural elements and fluid. The fluid motion is supposed to be irrotational. The Laplace equation with respect to the liquid pressure on the wetted surfaces of the structural elements is obtained, and the corresponding boundary conditions for unilateral and bilateral contact of the structural element with the liquid are formulated. A hypersingular integral equation is obtained for bilateral contact of the structural element with liquid. The finite element method coupled with the boundary element method for the hypersingular integral equation is implemented to find the fluid pressure on the plate. The frequencies and modes of structure vibrations taking into account the added masses of the liquid are obtained. The accuracy and reliability of the proposed method are ascertained.

Keywords: Fluid-structure interaction · Hypersingular integral · Finite and boundary element methods · Modes of Kaplan turbine blade · Vibrations

1 Introduction

The objective of this paper is to elaborate a new effective method for solving hypersingular integral equations and apply it for determining frequencies and modes of free vibrations of structure elements immersed in a liquid. Different engineering areas such as the aerospace industry, chemical industry, wind power engineering, transport, and power machine building extensively use thin-wall structural elements that function under excess process loads and interact with different liquids. The current issues are the problems of calculating this equipment's strength and dynamic characteristics in order to clarify the residual life and ensure the reliability and safety of structures during the operation.

2 Literature Review

One of the tasks that needs to be solved is to determine the frequencies and modes of free vibrations of structural elements, taking into account the interaction with the water or air environment [1, 2]. It should be noted that consideration of the hydro-elastic influence leads to a significant effect on the vibration frequencies. Therefore, it is difficult to adjust to unwanted resonances if these phenomena are not accounted for [1, 3]. Elements of structures operating in the presence of a liquid medium are either fully immersed in the liquid or have a surface in contact with it. Thus, there are two classes of problems of hydro-elastic interaction. The first one includes the problems of studying the dynamic behaviour of structures in unilateral contact with a liquid or gas. Such designs include hydraulic turbine covers [1], high-pressure vessels [3], liquid storage tanks [4, 5]. Second class concerns with determining the dynamic characteristics of thin elastic structures when the bearing surfaces are in bilateral contact with the liquid. This class includes the blades of Kaplan and Francis turbines [6–8], powerful wind units [9, 10], aircraft wings [11], etc. Effective computational methods have been developed for numerical solutions to such problems. One can name methods of finite differences, finite and boundary elements among them [10, 12, 13]. Nevertheless, each new structure, operating at intense loads, requires careful analysis of strength and dynamic characteristics in interaction with the environment. This leads to the necessity of elaborating the computational methods that will consider specific features of the structure under analysis.

3 Problem Statement

3.1 Main Relations of Elastic Body Motion

The fundamental relations of continuous mechanics are used to describe the motion of both an elastic structure and a fluid. Suppose there is an elastic body occupying the region Ω with boundary Γ. Suppose furthermore that the given volume and surface forces act on the body. In addition, part of the body surface is in contact with the liquid. All models of the continuous medium [14] provide methods of estimating stress fields σ_{ij}, strains ε_{ij}, displacements u_i, pressure p, and density ρ, depending on the time. To determine these fields, the following fundamental relations [14] are used:

Equations of motion formulated in stresses

$$\sigma_{ij,j} + X_i = \rho \frac{\partial^2 u_i}{\partial t^2} 0; \quad i, j = 1, 2, 3, \tag{1}$$

Cauchy's relationship for small deformations

$$\varepsilon_{ij} = \frac{1}{2}(u_{ij} + u_{ij}), \tag{2}$$

as well as the conditions of deformation compatibility, boundary and initial conditions, and equations of state that relate the pressure, density and temperature of the medium.

Equations (1)–(2) are not sufficient for the unambiguous definition of σ_{ij}, ε_{ij}, u_i ($i, j = 1, 2, 3$). Therefore, we need to set additional relationships between stresses

and strains, or between stresses and strain rates. If the elastic body is studied, then the relationship between strains and stresses is described by Hooke's law. Assume that the body displacements are given on the boundary part Γ_1, and the tensions are given on the part Γ_2; $\Gamma = \Gamma_1 - \Gamma_2$. The initial conditions are also needed to be set, if the dynamic state is considered. Taking into account Hooke's law, Eqs. (1) take the form

$$\mu \Delta u_j^e + (\lambda + \mu) \frac{\partial \vartheta^e}{\partial x_j} + X_j = \rho \frac{\partial^2 u_j^e}{\partial t^2}, \quad j = 1, 2, 3. \tag{3}$$

where $\Delta = \frac{\partial^2}{\partial x_1^2} + \frac{\partial^2}{\partial x_2^2} + \frac{\partial^2}{\partial x_3^2}$, $\vartheta^e = \mathrm{div}\mathbf{u}^e = \frac{\partial u_1^e}{\partial x_1} + \frac{\partial u_2^e}{\partial x_2} + \frac{\partial u_3^e}{\partial x_3}$.

To solve equations of motion (3) we use the weighted residual method, where the unknowns are given in the form of the series based on the finite functions $\{\psi_n\}|_{n=1}^{N_1}$. As trial ones, we use functions from the same basis. After integration of the received relation on volume and reduction of some of the volume integrals to surface ones we receive finite-element formulation of the problem as follows

$$[\mathbf{M}_S]\ddot{\mathbf{u}}^e + [\mathbf{K}_S]\mathbf{u}^e = \{\mathbf{f}_S\} + \{\mathbf{f}_{pr}\}, \tag{4}$$

where $[\mathbf{M}_S]$, $[\mathbf{K}_S]$ are mass and stiffness matrices, respectively, $\{\mathbf{f}_S\}$ is the vector of given forces acting on the elastic body, $\{\mathbf{f}_{pr}\}$ is the vector characterizing the liquid pressure on the wetted surfaces of the elastic body.

3.2 Main Relations of Liquid Motion

To determine the vector $\{\mathbf{f}_{pr}\}$, we turn to the formulation of the initial-boundary value problem in fluid mechanics. To describe the fluid, we also use relations (1)–(2). The relationship between stresses and strain rates is also specified. Let us make the following assumptions about a liquid medium. We suppose that the liquid is compressible and viscous, and its movement is vortex-free. We assume that the perturbations of fluid pressure due to the motion of an elastic body are small, i.e. we solve the problem in a linear formulation. The general laws of fluid mechanics are in use, namely: the mass conservation law (the continuity equation) and momentum conservation law

$$\frac{\partial \rho}{\partial t} = -\mathrm{div}(\rho \mathbf{V}_f) + Q, \quad \rho \frac{d\mathbf{V}_f}{dt} = \rho \mathbf{b} + \mathrm{div}(\sigma_f),$$

where $\mathbf{V}_f$ is the velocity vector, ρ is liquid density, Q is for mass sources, t is time. To determine the components of the stress tensor, the following hypothesis is accepted:

$$\sigma_f = -p\mathbf{I} + \mathbf{T}; \quad \mathbf{T} = 2\mu \left(\dot{\mathbf{S}} - \frac{1}{3}(\mathrm{div}\mathbf{V}_f) \right),$$

where $\dot{\mathbf{S}}$ is the strain-rate deviator.

Using the equation of state we have the following approximate relations:

$$\mathrm{div}\mathbf{V}_f = -\frac{1}{\rho_0 c^2} \frac{\partial p}{\partial t} + \frac{Q}{\rho_0}, \quad \frac{\partial \mathbf{V}_f}{\partial t} = -\frac{1}{\rho_0} \nabla p + \frac{4\mu}{3\rho_0} \left(-\frac{1}{\rho_0 c^2} \frac{\partial p}{\partial t} + \frac{Q}{\rho_0} \right).$$

In what follows, let suppose that the liquid is incompressible and non-viscous, and there are no mass sources. Then

$$\mathrm{div}\mathbf{V}_f = 0, \quad \rho_0 \frac{\partial \mathbf{V}_f}{\partial t} = -\nabla p. \tag{5}$$

Calculating divergence from the second relation in (5), we obtain that the pressure p is a harmonic function, i.e. it satisfies the Laplace equation, namely

$$\frac{\partial^2 p}{\partial x^2} + \frac{\partial^2 p}{\partial y^2} + \frac{\partial^2 p}{\partial z^2} = 0. \tag{6}$$

The pressure, or its overfall, is included in the right-hand side of Eqs. (4).

Suppose that there is such expansion for unknown displacements

$$\mathbf{u}^e(x, y, z, t) = \sum_{k=1}^{N} c_k(t)\mathbf{u}_k(x, y, z), \tag{7}$$

where $c_k(t)$ are unknown coefficients, and functions $\mathbf{u}_k(x, y, z)$ are given ones. Time functions $c_k(t)$ are usually considered as generalized coordinates. With (7), Eq. (4) takes the following form

$$\sum_{k=1}^{N} \{\ddot{c}_k(t)[\mathbf{Mu}_k] + c_k(t)[\mathbf{Ku}_k]\} = \{\mathbf{f}_S\} + \{\mathbf{f}_{pr}\}. \tag{8}$$

Hereinafter we use the weighted residual method [15], that is equivalent to performing the dot product of Eqs. (8) sequentially on the functions $u_l(x,y,z)$.

The following equations are received

$$[\mathbf{M}][\ddot{\mathbf{c}}] + [\mathbf{K}][\mathbf{c}] = \{\tilde{\mathbf{f}}_S\} + \{\tilde{\mathbf{f}}_{pr}\}, \tag{9}$$

where $[\mathbf{M}] = \{\mathbf{Mu}_k, \ \mathbf{u}_l\}, \quad [\mathbf{K}] = \{\mathbf{Ku}_k, \ \mathbf{u}_l\}$.

If $\{\tilde{\mathbf{f}}_S\} = \{\tilde{\mathbf{f}}_{pr}\} = 0$, then we define the frequencies and modes of structural element free vibrations without the liquid added masses; when $\{\tilde{\mathbf{f}}_S\} = 0$, we determine the frequencies and modes of the structural element with added liquid masses.

3.3 Pressure on the Surfaces of Structural Elements in Bilateral Contact with Liquid

We need to find the right part in equations

$$[\mathbf{M}][\ddot{\mathbf{c}}] + [\mathbf{K}][\mathbf{c}] = \{\tilde{\mathbf{f}}_{pr}\} \tag{10}$$

If the bilateral contact of the structural element with the liquid is studied, then the pressure overfall must be considered on the wetted surfaces. As mentioned above, the pressure satisfies the Laplace Eq. (6). To unambiguously solve this equation, it

is necessary to formulate boundary conditions. Suppose that the structural element is relatively thin, so that the boundary conditions can be set on the middle surface of the element under consideration. We formulate the boundary condition of non-penetration, that for the inviscid fluid is the equality of the normal components of the velocities of the fluid and the structural element

$$\left(\dot{\mathbf{u}}^e, \mathbf{n}\right) = \left(\mathbf{V}_f, \mathbf{n}\right), \quad \frac{\partial p}{\partial \mathbf{n}}^{\pm} = -\rho_l\left(\ddot{\mathbf{u}}^e, \mathbf{n}\right) = -\rho_l \sum_{k=1}^{N} \ddot{c}_k(t)(\mathbf{u}_k, \mathbf{n}). \tag{11}$$

The normal derivative of pressure has to be continuous, but the pressure has the overfall on the element surface, and the function describing the pressure is harmonic. In addition, this harmonic function must satisfy Sommerfeld's condition at infinity. As it is known, the double layer potential has such properties

$$p(\mathbf{P}_0) = \frac{1}{4\pi} \iint\limits_{S} \Gamma(\mathbf{P}) \frac{\partial}{\partial \mathbf{n}} \frac{1}{|\mathbf{P} - \mathbf{P}_0|} dS, \quad \mathbf{P} \in S, \tag{12}$$

where S is the area occupied by the structural element; $\mathbf{n}$ is the unit normal to the surface S; $\mathbf{P}$ and $\mathbf{P}_0$ are points of three-dimensional space with coordinates (x, y, z) and (x_0, y_0, z_0), $\Gamma(\mathbf{P})$ is the potential density, and

$$|\mathbf{P} - \mathbf{P}_0| = \sqrt{(x - x_0)^2 + (y - y_0)^2 + (z - z_0)^2}.$$

The function defined by the formula (12), satisfies the Laplace Eq. (6), has a continuous normal derivative, and at the intersection of the surface S along the normal has a finite gap, namely

$$p^+(\mathbf{P}_0) - p^-(\mathbf{P}_0) = \Gamma(\mathbf{P}_0), \quad \mathbf{P} \in S$$

Note that to determine the pressure overfall, it is necessary to find an unknown density $\Gamma(\mathbf{P})$ on the surface. The boundary condition (11) has to be satisfied. This leads to an integral equation in the form

$$\frac{\partial}{\partial \mathbf{n}_0} \frac{1}{4\pi} \iint\limits_{S} \Gamma(\mathbf{P}) \frac{\partial}{\partial \mathbf{n}} \frac{1}{|\mathbf{P} - \mathbf{P}_0|} = -\rho_l\left(\mathbf{u}^e, \mathbf{n}\right), \quad \mathbf{P}, \mathbf{P}_0 \in S. \tag{13}$$

From (12) one can received that

$$\Gamma(\mathbf{P}) = \sum_{k=1}^{N} \ddot{c}_k(t)\Gamma_k(\mathbf{P}), \tag{14}$$

where functions $\Gamma_k(\mathbf{P})$ are satisfying the following integral equations

$$..\frac{\partial}{\partial \mathbf{n}_0} \frac{1}{4\pi} \iint\limits_{S} \Gamma_k(\mathbf{P}) \frac{\partial}{\partial \mathbf{n}} \frac{1}{|\mathbf{P} - \mathbf{P}_0|} = -\rho_l(\mathbf{u}_k, \mathbf{n}), \quad \mathbf{P}, \mathbf{P}_0 \in S.$$

If we introduce the following operator $\mathbf{H}$ in the form

$$\Gamma_k(\mathbf{P}) = -\rho_l \mathbf{H}_k(\mathbf{u}_k),$$

then for added masses in (10) the next relation is received

$$\left\{ \tilde{\mathbf{f}}_{pr} \right\} = -\rho_l[\mathbf{H}][\ddot{\mathbf{c}}], \quad [\mathbf{H}] = \{\mathbf{H}\mathbf{u}_k, \mathbf{u}_l\} \tag{15}$$

Thus, the obtained equations for determining the frequencies and modes of the free vibrations in bilateral contact with the liquid are differential Eqs. (10), where $\left\{ \tilde{\mathbf{f}}_{pr} \right\}$ is calculated by the formula (15). It would be noted that the indirect formulation of the boundary element method [15] is used here to calculate the fluid pressure.

4 Numerical Simulation

4.1 Finite Element Method in Problems of Free Vibrations

As an example of numerical implementation of the proposed approach, consider the problem of determining the frequencies and modes of a circular plate immersed in a liquid. The circular plate is considered with the following parameters: modulus of elasticity $E = 2.06 \cdot 10^8$ kPa, Poisson's ratio $\nu = 0.3$, material density $\rho = 7850$ kg/m^3, plate thickness $h = 0.01$ m, plate radius $R = 1.0$ m. The plate is considered under different conditions fixing, namely, clamped boundary conditions

$$w|_{\rho=R} = 0, \quad \left. \frac{dw}{dr} \right|_{\rho=R} \tag{16}$$

and simply supported conditions $w|_{\rho=R} = 0, \quad M|_{\rho=R}$, where M is the bending moment, w is the plate deflection.

The frequencies and modes of the plate vibrations are determined using the finite element method (FEM). ANSYS software was used with **Shell181** finite elements applied. Different numbers of finite elements (FE) were chosen to validate the accuracy of FEM. In Fig. 1 the finite element mesh is shown. Consequently, Table 1 shows the vibration frequencies of the circular plates.
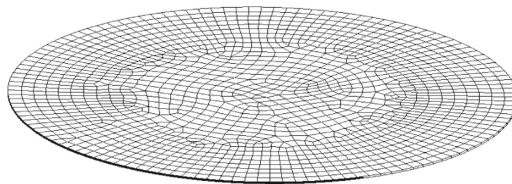
Fig. 1. Finite element mesh

Calculations have shown that the results obtained by the proposed method are well correlated with the analytical solution [16]. The first modes of clamped plate are shown in Fig. 2.

Table 1. Vibration frequencies of circular plates under different fixation conditions, Hz

Mode number m	Clamped plate		Simply supported	
	Analytical solution	Numerical solution	Analytical solution	Numerical solution
1	25.2047	25.20	100.8186	100.74
2,3	52.4540	52.44	209.8161	209.52
4,5	86.0492	86.00	344.1970	343.37
6	98.1241	98.07	392.4964	391.67
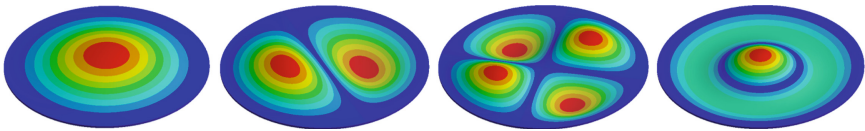
Fig. 2. Vibration modes of circular plate

The vibration modes of the circular plate are presented hereinafter in the form

$$u_{nm}(\rho, \theta) = w_{nm}(\rho) \cos n\theta,$$

where n is the wave number, m is the mode number corresponded to the nth harmonic.

4.2 Numerical Solution of the Hypersingular Equation

To find the matrix of added masses, the numerical solution of the hypersingular integral Eq. (13) is performed. This equation was reduced to a one-dimensional hypersingular equation in the form

$$\frac{1}{\pi} \int_0^R \Gamma_{mn}(\rho) \frac{\rho E_n(k) d\rho}{(\rho + \rho_0)(\rho - \rho_0)^2} = -w_{mn}(\rho_0), \tag{17}$$

where

$$E_n(k) = (-1)^n \left(1 - 4n^2\right) \int_0^{\pi/2} \cos 2n\psi \sqrt{1 - k^2 \sin^2 \psi}\, d\psi, \quad k'^2 = 1 - k^2$$

is the generalized elliptic integral of the second kind [12], $w_{nm}(\rho)$ are plate own modes. Numerical solutions of Eq. (17) with given right-hand sides are obtained using the method developed in [12, 17].

Figure 3 shows the functions $w_{m1}(\rho)$ and corresponding to them solutions $\Gamma_{m1}(\rho)$, $m = 0, 1, 2$, of hypersingular integral Eqs. (17). Here, the numbers 1–3 correspond to
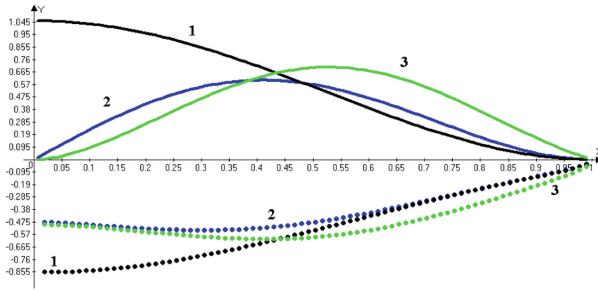
Fig. 3. Vibration modes and solutions of hypersingular equations

numbers $m = 0, 1, 2$, the dashed lines represent the right parts $w_{m1}(\rho)$, and the solid lines correspond to the functions. $\Gamma_{m1}(\rho)$.

According to the properties of the hypersingular operator, the functions $\Gamma_{m1}(\rho)$ restore the nature of the functions $w_{m1}(\rho)$.

After solving hypersingular Eqs. (17), the matrix of added masses is obtained.

4.3   Free Vibrations of the Round Plate with Liquid Added Masses

Since the preliminary analysis revealed that the lowest frequencies correspond to the vibration modes $w_{01}, w_{02}, w_{11}, w_{21}$ of the "dry" plate, the vibration modes of the plate, with the liquid added masse are represented as

$$w(\rho, \theta, t) = c_1(t)w_{01}(\rho) + c_2(t)w_{11}(\rho)\cos\theta + c_3(t)w_{11}(\rho)\sin\theta + c_4(t)w_{21}(\rho)\cos 2\theta + c_5(t)w_{21}(\rho)\sin 2\theta$$

According to the properties of the operator **H** and considering (14), the similar representation for the potential density of the double layer is received

$$\Gamma(\rho, \theta, t) = \ddot{c}_1(t)\Gamma_{01}(\rho) + \ddot{c}_2(t)\Gamma_{11}(\rho)\cos\theta + \ddot{c}_3(t)\Gamma_{11}(\rho)\sin\theta + \ddot{c}_4(t)\Gamma_{21}(\rho)\cos 2\theta + \ddot{c}_5(t)\Gamma_{21}(\rho)\sin 2\theta$$

It would be noted that both in the case of "dry" plate, and when taking into account the added masses of the liquid there are multiple frequencies corresponding to the modes $w_{11}(\rho)\cos\theta$, $w_{11}(\rho)\sin\theta$ and $w_{21}(\rho)\cos 2\theta$, $w_{21}(\rho)\sin 2\theta$.

Table 2 below presents the frequency values for these modes for the "dry" plate Ω_{i1} and ω_{i1} for the plate immersed in the liquid, under rigid fixation (17).

Table 2. Frequencies of round plate vibrations, Hz

i	0	1	2
Ω_{i1}	25.20	52.44	86.00
ω_{i1}	7.241	12.69	16.80

Note that the vibration modes of the plate immersed in the liquid, almost coincide with the ones of the "dry" plate. Hence consideration of a liquid presence leads to a significant reduction in the frequencies of free vibrations.

4.4   Free Vibrations of the Kaplan Turbine Blade Models

The developed coupled finite-boundary element method was applied to the frequency estimations of the blade models for the Kaplan turbine.

The sectorial cantilevered plate is considered ($R_1 = 0.115$ m, $R_2 = 0.230$ m, $\varphi_1 = 0$, $\varphi_2 = \pi/2$), the thickness varies along the radius according to the linear law, $\nu = 0.3$, h (R_1) = 0.006 m, h (R_2) = 0.002 m); $E = 2.1 \cdot 10^6$ N/m^2, $\rho_1 = 7900$ kg/m^3, Fig. 4a).

Table 3. Frequencies of sectorial cantilevered plate vibrations, Hz

Mode number, m	Frequencies of sectorial plate vibrations, Hz			
	Air		Liquid	
	Experiment	Simulation	Experiment	Simulation
1	402	398.2	159	171
2	416	425.0	–	242
3	514	549.7	277	300
4	714	791.0	420	480

Table 3 demonstrates a comparison of numerical results obtained by the proposed method and experimental data [18]. The results are in good agreement.

The vibration modes are shown in Fig. 4c) and Fig. 4d).
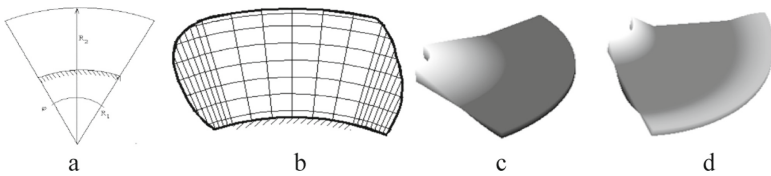
Fig. 4. Vibration modes of sectorial cantilever plates

The model of the original Kaplan turbine blade is shown in Fig. 4b). The geometrical and physical characteristics here are from [19]. In Table 4 the comparison of numerical and experimental results [19] is provided.

The results are in good agreement especially for the lowest frequencies.

Table 4. Frequencies Caplan turbine blade vibrations, Hz

Mode number, m	Air		Liquid	
	Experiment	Simulation	Experiment	Simulation
1	434	425	220	221
2	542	540	340	358
3	869	754	567	560
4	1107	1132	711	670

5   Conclusions

The developed method makes it possible to find the frequencies and modes of vibrations of the hydraulic turbine blades with high accuracy with and without taking into account the added masses of liquids. It has been proven that there is a more than twofold decrease in the lower frequencies when interacting with liquid compared to the frequencies of a dry blade. Comparison with experimental data gives an error of less than 1%.

References

1. Misura, S., Smetankina, N., Misiura, I.: Optimal design of the cyclically symmetrical structure under static load. In: Nechyporuk, M., Pavlikov, V., Kritskiy, D. (eds.) ICTM 2020. LNNS, vol. 188, pp. 256–266. Springer, Cham (2021). https://doi.org/10.1007/978-3-030-66717-7_21
2. Strelnikova, E., Kriutchenko, D., Gnitko, V., Degtyarev, K.: Nonlinear sloshing analysis for shells of revolution under longitudinal excitations. Eng. Anal. Bound. Elem. **111**, 78–87 (2020). https://doi.org/10.1016/j.enganabound.2019.10.008
3. Strelnikova, E., Choudhary, N., Kriutchenko, D., Gnitko, V., Tonkonozhenko, A.: Liquid vibrations in circular cylindrical tanks with and without baffles under horizontal and vertical excitations. Eng. Anal. Bound. Elem. **120**, 13–27 (2020). https://doi.org/10.1016/j.enganabound.2020.07.024
4. Karaiev, A., Strelnikova, E.: Singular integrals in axisymmetric problems of elastostatics. Int. J. Model. Simul. Sci. Comput. **11**(1), 2050003 (2020). https://doi.org/10.1142/S1793962320500038
5. Behshad, A., Shekari, M.: A boundary element study for evaluation of the effects of the rigid baffles on liquid sloshing in rigid containers. Int. J. Marit. Technol. **10**, 45–54 (2018). https://doi.org/10.29252/ijmt.10.45
6. Rusanov, A., Shubenko, A., Senetskyi, O., Babenko, O., Rusanov, R.: Healing modes and design optimization of cogeneration steam turbines of powerful units of combined heat and power plant. Energetika **65**(1), 39–50 (2019). https://doi.org/10.6001/energetika.v65i1.3974
7. Atroshenko, O., Tkachuk, M., Martynenko, O., Saverska, M., Hrechka, I., Khovanskyi, S.: The study of multicomponent loading effect on thin-walled structures with bolted connections. East.-Eur. J. Enterp. Technol. **1**(7), 15–25 (2019). https://doi.org/10.15587/1729-4061.2019.154378

8. Peczkis, G., Wiśniewski, P., Zahorulko, A.: Experimental and numerical studies on the influence of blade number in a small water turbine. Energies **14**(9), 1–15 (2021). https://doi.org/10.3390/en14092604

9. Tarfaoui, M., Nachtane, M., Khadimallah, H., Saifaoui, D.: Simulation of mechanical behavior and damage of a large composite wind turbine blade under critical loads. Appl. Compos. Mater. **25**(2), 237–254 (2017). https://doi.org/10.1007/s10443-017-9612-x

10. Navadeh, N., Goroshko, I., Zhuk, Y., Moghadam, F., Fallah, A.: Finite element analysis of wind turbine blade vibrations. Vibration **4**(2), 310–322 (2021). https://doi.org/10.3390/vibration4020020

11. Iemma, U., Vitagliano, F.P., Centracchio, F.: A multi-objective design optimization of eco-friendly aircraft: the impact of noise fees on airplanes sustainable development. Int. J. Sustain. Eng. **11**, 122–134 (2018). https://doi.org/10.1080/19397038.2017.1420109

12. Griffith, B., Patankar, N.: Immersed methods for fluid-structure interaction. Ann. Rev. Fluid Mech. **52**, 421–448 (2020). https://doi.org/10.1146/annurev-fluid-010719-06022

13. Gnitko, V., Degtyariov, K., Karaiev, A., Strelnikova, E.: Multi-domain boundary element method for axisymmetric problems in potential theory and linear isotropic elasticity. WIT Trans. Eng. Sci. **122**, 13–25 (2019). https://doi.org/10.2495/BE410021

14. Shabana, A.: Computational Continuum Mechanics. Springer, Berlin (2020)

15. Brebbia, C.: The birth of the boundary element method from conception to application. Eng. Anal. Bound. Elem. **77**, iii–x (2017). https://doi.org/10.1016/j.enganabound.2016.12.001

16. Naumenko, K., Altenbach, H.: Plates and shells. In: Modeling High Temperature Materials Behavior for Structural Analysis. STRUCTMAT, vol. 112, pp. 169–206. Springer, Cham (2019). https://doi.org/10.1007/978-3-030-20381-8_5

17. Karaiev, A., Strelnikova, E.: Axisymmetric polyharmonic spline approximation in the dual reciprocity method. Z. Angew. Math. Mech. **101**, e201800339 (2021). https://doi.org/10.1002/zamm.201800339

18. Sardjono, J.A., Darmawan, S., Tanujaya, H.: IOP Conf. Ser.: Mater. Sci. Eng. **1007**(1) (2020). Art. no. 012035. https://doi.org/10.1088/1757-899X/1007/1/012035

19. Ghenaiet, A., Bakour, M.: Simulation of steady and unsteady flows through a small-size Kaplan turbine. Eng. Rep. **2**(2), e12112 (2020). https://doi.org/10.1002/eng2.12112

Mathematical Model of Additive Mixing During RH Process Using Elliptic Cylindrical Coordinates

Kyrylo Krasnikov$^{(\boxtimes)}$

Dniprovskyi State Technical University, Kamianske, Ukraine
`kir_kras@ukr.net`

Abstract. The RH process is used in the ferrous metallurgy to reach the lowest level of dissolved gases, which positively influences quality of product. At a specified time after beginning of the process, additive is added to modify contents of melt. Additive is mixed by argon-stirred melt especially in vessel. Duration of additive homogenization and other unknowns are estimated using mathematical model based on elliptic coordinates. They fit geometry of immersed vessel with two snorkels. It is assumed that melt is incompressible viscous Newtonian fluid, which consists of inert gas and additive. Speed of gas floatation is constant. Navier-Stokes equations define dynamics of the fluid and are solved using central difference scheme. Such results of numerical modeling as velocity distribution and mixing behavior are compared to the measured data presented in scientific literature. Pictures show developed velocity field with vortex near melt surface in vessel. The model takes into account diameter of snorkels, vessel, ladle, gas injection rate and others. It can be used to optimize real process in different conditions. Also the proposed model can predict similar processes in power engineering and hydraulic equipment.

Keywords: Mathematical model · RH process · Hydrodynamics · Mixing · Responsible consumption and production

1 Introduction

To achieve the lowest level of gas concentration in melt metallurgical plants utilize Ruhrstahl-Heraeus (RH) process. The process begins after a long vessel (also named as "RH reactor" [1] or more general "vacuum chamber" [2]) with two snorkels is inserted into ladle with melt. While the process is going some amount of additive is added. It is homogenized by flowing melt, which is stirred by inert gas. The gas exits from injection nozzles at the up-snorkel wall, enters melt and floats up at RH reactor. After lifting up the melt moves in the reactor, and then, goes down through the second snorkel back to the ladle – there is recirculation.

The aim of the article is to present mathematical model of the process based on elliptic cylindrical coordinates, which fits the geometry of ladle and immersed vessel. The model will be used for the numerical experiments to investigate the process and to get additive variation dependency on the time and on the gas consumption rates.

2 Literature Review

There are papers devoted to modeling of RH process. In paper [1] it is considered melting of aluminum particles added in vessel. Authors present figures which illustrate spread of dissolved aluminum from vessel to ladle. Authors of paper [2] take into account bubble expansion. They used DMP method for bubbles and FOV – for estimating free surface of melt. They conclude significant influence of bubble expansion. In [3] authors use water-oil physical model to calculate flow pattern and predict lining erosion of vessel. The figures show the highest erosion rate at the snorkel, where inert gas is injected. Also speed of fluid in vessel and snorkel is measured – the highest one is in up-snorkel. In paper [4] authors investigate phenomenon of mixing effectiveness changing in vessel, when depth of its immersion varies from 400 mm to 720 mm. The experimental water model is used to measure velocity profiles. Authors compare average speed in mixing horizontal layer (about 100 mm) of melt in ladle just under snorkels. Figure shows that speed under up-snorkel is few times lower than it is under down-snorkel.

In paper [5] author presents another way of momentum and mass conservation formulation for Navier-Stokes. He compares his formulation to stream function-vorticity and finds them analogous. The paper [6] is devoted to Crank-Nicholson scheme for solution of Navier-Stokes equation in 2D rectangular domain and incompressible fluid. Authors use MATLAB to check the consistence of the scheme. The further investigations can be taking into account external forces, as well as compressibility. In [7] elliptic cylindrical coordinates are applied to Navier–Stokes equations, which are used in the present paper, to predict flow induced by an applied potential. Authors compare velocity profiles with various times and find that oscillatory pressure can prevail. Authors of the paper [8] present novel solution to 2D problem of non-isothermal flows of incompressible fluid. The peculiarity of the method is the usage of unstructured geometries and different kinds of convection. In the paper [9] authors presents solution of linear Navier-Stokes equations using Picard method. The solution is obtained for a range of Reynolds number. Illustrations show stream function for variety of flows, which is a good adequacy examination. The paper [10] contains expressions for a fundamental tensor, gradient, divergence, and Laplace operator of vector field, which are needed in present research. The expressions for elliptic cylindrical coordinates can be compared to results in [11], where authors consider scale factors, velocities, and accelerations in mentioned coordinates.

There are papers devoted to investigation of flow behavior of melt in RH degasser. In [12] authors used coupled DMP–VOF method. The feature of [13] is sampling rod inserted near up-snorkel. Authors conduct physical and numerical modeling with different location of rod. The paper [14] devoted to physical modeling of RH process with comparison of regular and oval-shaped snorkels considering treatment time and effectiveness in terms of carbon concentration variation. The oval snorkels show better effectiveness (by 50%). In the paper [15] authors also consider oval-shaped snorkels and investigate velocity field and its influence on lining of ladle. The proposed geometry decreases lining erosion, thanks to smaller speeds near bottom and wall of ladle.

3   Methodology

3.1   Assumptions

RH reactor has two snorkels equally distanced from the axis. Axis of snorkel is located at foci of elliptic cylindrical coordinate system by adjusting corresponding parameter. List of assumptions to simplify problem is following:

1. Geometry of ladle and vessel is cylindrical (see Fig. 1 and 2).
2. Axis of vessel coincides with axis of ladle.
3. The top surface of melt is flat.
4. The melt is incompressible viscous Newtonian fluid, which density is constant. It includes inert gas and additive field.
5. Speed of the melt at the beginning of experiment is zero.
6. Gas floats up at a constant speed and accelerates vertical component of melt's velocity.
7. All phases are interpenetrating continuums. Additive phase doesn't influence hydrodynamics.
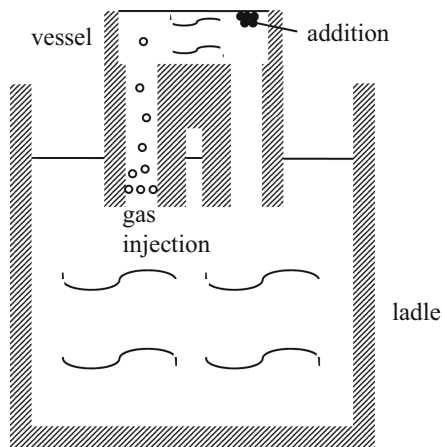
Fig. 1. Schematic axial cross-section of teeming ladle with RH reactor inside. Lines represent top surface of melt. The solid surfaces are shaded.

The complex geometrical configuration leads to the mathematical model with problem formulation in three spatial dimensions, because there is no axial symmetry for simplification. It is planned to get computed fields at different moments of time for further analysis and for level tracking of additive homogenization to create dependency chart. The complexity of hydrodynamics and mass transfer equations requires numerical solution.
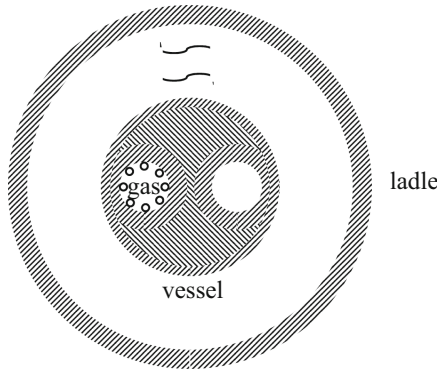
Fig. 2. Schematic top view of teeming ladle with RH vessel inside. The solid surfaces are shaded.

3.2 Equations

Dynamics of the process is defined by following partial differential equations, which represent conservation laws for fluid momentum and mass:

$$\frac{\partial \vec{v}}{\partial t} + \vec{v} \cdot \nabla \vec{v} = -\frac{\nabla p}{\rho} + \nabla^2 \vec{v} - \alpha \vec{g} \tag{1}$$

$$\nabla \cdot \vec{v} = 0 \tag{2}$$

$$\frac{\partial \alpha}{\partial t} + \nabla \cdot \left[\alpha (\vec{v} + \vec{v}_f) \right] = D_\alpha \nabla^2 \alpha + S_\alpha \tag{3}$$

$$S_\alpha = \frac{q}{V} \frac{300}{T_m} \tag{4}$$

$$\frac{\partial c}{\partial t} + \nabla \cdot (\vec{v} c) = D_c \nabla^2 c + S_c \tag{5}$$

where $\bar{v}_f$ – floatation speed of gas; S_α, S_c – source rates for gas and additive concentration.

The fact that elliptic cylindrical coordinates (d, φ, z) are orthogonal simplifies formulation of gradient, divergence, rotor and Laplacian for scalar and vector fields using scale factors. After simplification of expressions, for elliptic cylindrical coordinates one obtains:

$$h = a\sqrt{\frac{1}{2}(\cosh 2d - \cos 2\varphi)} \tag{6}$$

$$\nabla c = \frac{\hat{e}_1}{h} \frac{\partial c}{\partial d} + \frac{\hat{e}_2}{h} \frac{\partial c}{\partial \varphi} + \hat{e}_3 \frac{\partial c}{\partial z} \tag{7}$$

$$\nabla \cdot \vec{v} = \frac{1}{h^2} \left[\frac{\partial (hu)}{\partial d} + \frac{\partial (hv)}{\partial \varphi} \right] + \frac{\partial w}{\partial z} \tag{8}$$

$$\nabla \times \vec{v} = \frac{\hat{e}_1}{h} \left[\frac{\partial w}{\partial \varphi} - h \frac{\partial v}{\partial z} \right] + \frac{\hat{e}_2}{h} \left[h \frac{\partial u}{\partial z} - \frac{\partial w}{\partial d} \right] + \frac{\hat{e}_3}{h^2} \left[\frac{\partial (hv)}{\partial d} - \frac{\partial (hu)}{\partial \varphi} \right] \tag{9}$$

$$\nabla^2 c = \frac{2}{a^2(\cosh 2d - \cos 2\varphi)}\left[\frac{\partial^2 c}{\partial^2 d} + \frac{\partial^2 c}{\partial^2 \varphi}\right] + \frac{\partial^2 c}{\partial^2 z} \tag{10}$$

where d – positive number coordinate, φ – angle coordinate $[0, 2\pi]$, z – vertical coordinate. The material derivative has the convection term:

$$\vec{v}\cdot\nabla\vec{v} = \hat{e}_1\left[\frac{u}{f}\frac{\partial u}{\partial r} + \frac{v}{f}\frac{\partial u}{\partial \varphi} + \frac{v}{f^2}\left(u\frac{\partial f}{\partial \varphi} - v\frac{\partial f}{\partial r}\right) + w\frac{\partial u}{\partial z}\right] \tag{11}$$

$$+\hat{e}_2\left[\frac{u}{f}\frac{\partial v}{\partial r} - \frac{u}{f^2}\left(u\frac{\partial f}{\partial \varphi} - v\frac{\partial f}{\partial r}\right) + \frac{v}{f}\frac{\partial v}{\partial \varphi} + w\frac{\partial v}{\partial z}\right] \tag{12}$$

$$+\hat{e}_3\left[\frac{u}{f}\frac{\partial w}{\partial r} + \frac{v}{f}\frac{\partial w}{\partial \varphi} + w\frac{\partial w}{\partial z}\right] \tag{13}$$

Laplacian of velocity field is expressed using famous expression with curl of curl of vector field [5, 6]:

$$\nabla^2\vec{v} = \nabla(\nabla\cdot\vec{v}) - \nabla\times\nabla\times\vec{v} \tag{14}$$

$$\nabla(\nabla\cdot\vec{v}) = \frac{\hat{e}_1}{h}\frac{\partial\left[\frac{1}{h^2}\left[\frac{\partial(hu)}{\partial d} + \frac{\partial(hv)}{\partial \varphi} + h^2\frac{\partial w}{\partial z}\right]\right]}{\partial d} \tag{15}$$

$$+\frac{\hat{e}_2}{h}\frac{\partial\left[\frac{1}{h^2}\left[\frac{\partial(hu)}{\partial d} + \frac{\partial(hv)}{\partial \varphi}\right] + \frac{\partial w}{\partial z}\right]}{\partial \varphi} + \hat{e}_3\frac{\partial\left[\frac{1}{h^2}\left[\frac{\partial(hu)}{\partial d} + \frac{\partial(hv)}{\partial \varphi}\right] + \frac{\partial w}{\partial z}\right]}{\partial z} \tag{16}$$

$$\nabla\times\nabla\times\vec{v} = \frac{\hat{e}_1}{h}\frac{\partial\left(\frac{1}{h^2}\left[\frac{\partial(hv)}{\partial d} - \frac{\partial(hu)}{\partial \varphi}\right]\right)}{\partial \varphi} - \frac{\hat{e}_1}{h}\frac{\partial\left(h\frac{\partial u}{\partial z} - \frac{\partial w}{\partial d}\right)}{\partial z} \tag{17}$$

$$+\frac{\hat{e}_2}{h}\frac{\partial\left(\frac{\partial w}{\partial \varphi} - h\frac{\partial v}{\partial z}\right)}{\partial z} - \frac{\hat{e}_2}{h}\frac{\partial\left(\frac{1}{h^2}\left[\frac{\partial(hv)}{\partial d} - \frac{\partial(hu)}{\partial \varphi}\right]\right)}{\partial d} \tag{18}$$

$$+\frac{\hat{e}_3}{h^2}\frac{\partial\left(h\frac{\partial u}{\partial z} - \frac{\partial w}{\partial d}\right)}{\partial d} - \frac{\hat{e}_3}{h^2}\frac{\partial\left(\frac{\partial w}{\partial \varphi} - h\frac{\partial v}{\partial z}\right)}{\partial \varphi} \tag{19}$$

where u, v, w – components of velocity in elliptic cylindrical coordinates.

Using defined above expressions vector Laplacian of velocity field gets following expression:

$$\hat{e}_1\left(\nabla^2\vec{v}\right) = \frac{1}{h}\frac{\partial\left[\frac{1}{h^2}\left[\frac{\partial(hu)}{\partial d} + \frac{\partial(hv)}{\partial \varphi}\right]\right]}{\partial d} - \frac{1}{h}\frac{\partial\left(\frac{1}{h^2}\left[\frac{\partial(hv)}{\partial d} - \frac{\partial(hu)}{\partial \varphi}\right]\right)}{\partial \varphi} + \frac{\partial u}{\partial^2 z} \tag{20}$$

$$\hat{e}_2\left(\nabla^2\vec{v}\right) = \frac{1}{h}\frac{\partial\left[\frac{1}{h^2}\left[\frac{\partial(hu)}{\partial d} + \frac{\partial(hv)}{\partial \varphi}\right]\right]}{\partial \varphi} + \frac{1}{h}\frac{\partial\left(\frac{1}{h^2}\left[\frac{\partial(hv)}{\partial d} - \frac{\partial(hu)}{\partial \varphi}\right]\right)}{\partial d} + \frac{\partial v}{\partial^2 z} \tag{21}$$

$$\hat{\mathbf{e}}_3\left(\nabla^2\vec{\mathbf{v}}\right) = \frac{1}{h^2}\left(\frac{\partial w}{\partial^2 d} + \frac{\partial w}{\partial^2 \varphi}\right) + \frac{\partial w}{\partial^2 z} \tag{22}$$

Derivation of equations for regular cylindrical coordinates is verified using presented results in paper [5, 10].

Boundary condition for normal and parallel velocity at a solid surface is:

$$\left.\frac{\partial \vec{\mathbf{v}}^{\|}}{\partial n}\right|_w = 0 \tag{23}$$

$$\left.\vec{\mathbf{v}}^{\perp}\right|_w = 0 \tag{24}$$

where n – normal to wall.

Boundary conditions for gas and concentration are: impermeability at solid surfaces, constant outlet speed for gas at the top surfaces of melt.

4   Results and Discussion

The central difference scheme is used to approximate terms in equations. The software is developed to calculate and visualize of modeling results. The Table 1 lists technological parameters used for numerical experiment.

Table 1. Experiment parameters.

Object	Parameters	Values
Ladle	Inner radius	1.11 m
	Depth of melt	2.25 m
Immersed vessel	Inner radius	0.4 m
	Depth of immersion	0.4 m
Snorkel	Inner radius	0.1 m
	Gas injection rate	30/60/120 l/min
Additives	Mass	20 kg
Computational domain	Number of layers for d coordinate	32
	Number of layers for φ	38
	Number of layers for z	32
	Timestep	0.0001

In the case of elliptic cylindrical coordinates deviation of ladle walls geometry from perfect circle is about 3.6%.

Figure 3 depicts the axial cross-section of the velocity – the arrows show its direction and the colors represent its magnitude (white correspond to the speed more than 0.2 m/s). There are zones without arrows – they represent a solid body and are not included in the calculations.

The figure shows vortex in RH vessel, created by floating gas. This vortex transfers the additive from one snorkel to another one, intensifying its mixing. The melt goes down in the second snorkel with speed about 0.18 m/s and enters ladle, where moves to the up-snorkel.

The two speedy zones are formed. The first one, at the center of the ladle, transfers additive under the up-snorkel. The second zone, at the bottom of ladle, is directed at the opposite side.

Figure 4 shows almost the same decrease of additive concentration variation before the 90 s for 30 l/min and 60 l/min. After that, there is deviation the maximum gas rate gives the best homogenization.

Experiments show, that there is a nonlinear dependency of gas injection rate on the maximum vertical speed in the down-snorkel of RH vessel. The speed is about 0.12 m/s for the rate of 30 l/min, about 0.15 m/s – for the rate of 60 l/min, and about 0.18 m/s – for the rate of 120 l/min.
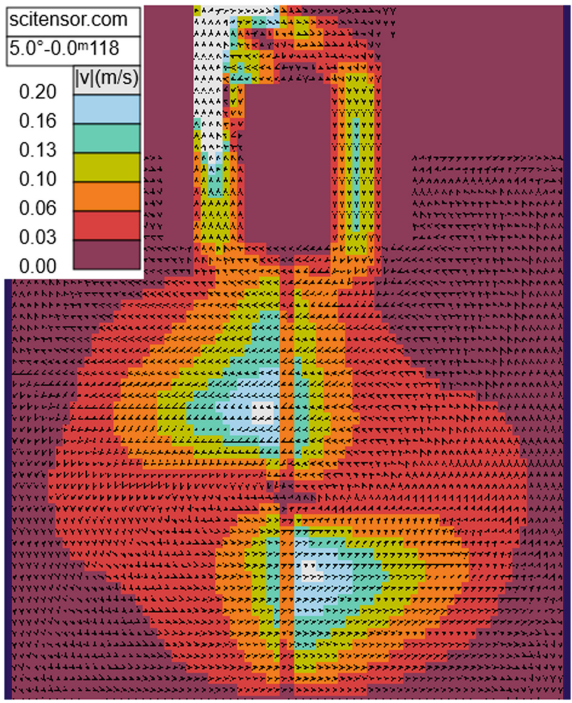
Fig. 3. Developed velocity profile at $\varphi = 5°$ on the 118th second (60 l/min).

Time, s	40	60	80	100	120
····· 30 l/min	593	326	245	212	170
− − 60 l/min	590	324	242	198	161
—— 120 l/min	659	420	278	192	143
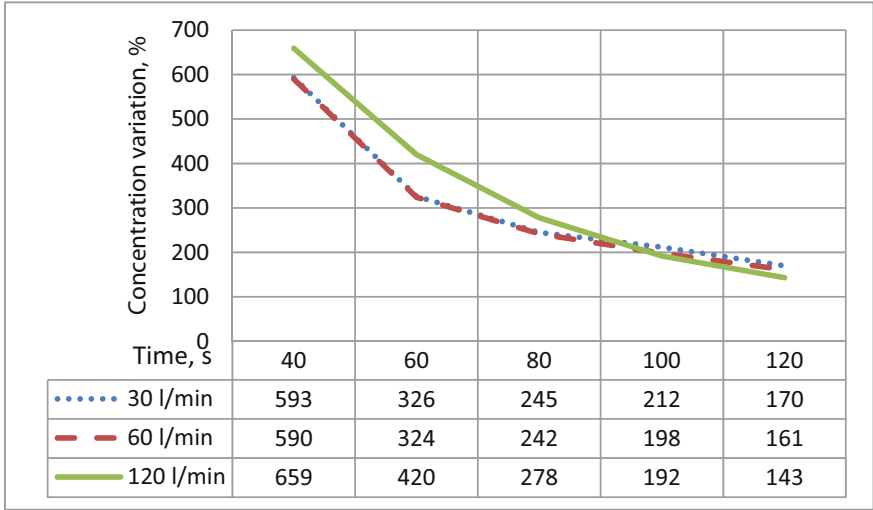
Fig. 4. Variation dependency on time for three rates of gas injection (lower percent is better).

A special numerical experiment was conducted to compare achieved results with the data in other research – both experiments are conducted in the same conditions. For the comparison, it have been chosen nine spots, laying on the line parallel to the x-axis, in RH-reactor: four – above the up-snorkel (negative x), one – on the ladle's axis and the other four – above the down-snorkel (positive x). Figure 5 shows melt's speed at these nine distances from the ladle's axis. Comparison shows a difference of no more than 20%. As seen on the figure, the difference in speeds above the up-snorkel is larger than the one above the down-snorkel – this can be explained by turbulence caused by bubbles and high speed vortex (top part of Fig. 3).

x, m	-0.35	-0.26	-0.17	-0.08	0	0.08	0.17	0.26	0.35
····· our	0.22	0.16	0.12	0.05	0.01	0.02	0.05	0.08	0.12
− − other	0.2	0.19	0.16	0.04	0.02	0.01	0.07	0.1	0.13
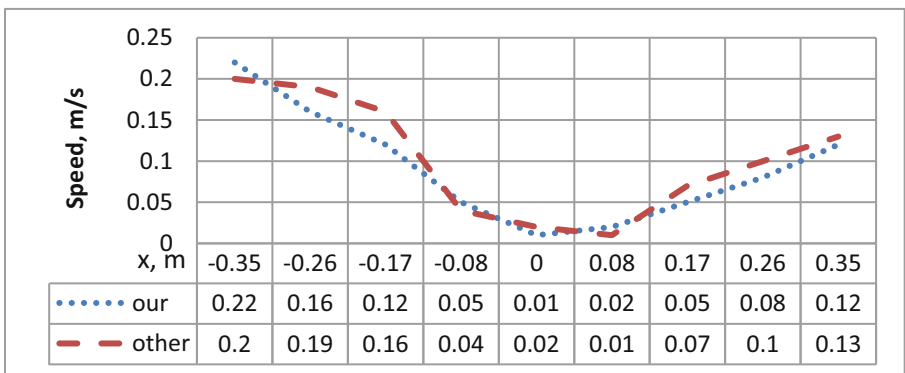
Fig. 5. Comparison of calculated speed with one in literature [2] (on horizontal plane near the snorkels inside the RH reactor).

5   Conclusions

The paper presents mathematical model of melt hydrodynamics and additive mixing during RH process. The model utilizes elliptic cylindrical coordinates to fit problem geometry. The results of numerical experiment are compared to the data in the papers [1] and [2]. The comparison (Fig. 5) shows difference of no more than 20%, which is small enough to conclude that the model is adequate. The developed velocity field mixes additive mainly under up-leg, where argon is injected. And only after about 90 s significant amount of additive reaches the bottom part of the ladle, where another speed zone is formed. As experiments show, growing gas consumption rate by 4 times increases melt's speed in down-snorkel by 1.5 times. That influences intensification of additive mixing in the ladle – increasing gas consumption from 30 l/min up to 120 l/min contributes to the improvement of additive homogenization by 1.18 times.

The model has many adjustable parameters and recommended to predict mixing time in RH-vessel using different industrial conditions.

References

1. Chang, L., Haojian, D., Lifeng, Z.: Modeling of the melting of aluminum particles during the RH refining process. Metals **9**(442), 1–13 (2019). https://doi.org/10.3390/met9040442
2. Chang, L., Shusen, L., Lifeng, Z.: Simulation of gas-liquid two-phase flow and mixing phenomena during RH refining process. Acta Metall. Sin. **2**(54), 347–356 (2018). https://doi.org/10.11900/0412.1961.2017.00429
3. Qiang, W., et al.: A CFD study on refractory wear in RH degassing process. ISIJ Int. 1–10 (2019). https://doi.org/10.2355/isijinternational.ISIJINT-2019-768
4. Kaitian, Z., Heng, C., Rudong, W., Yang, L.: Mixing phenomenon and flow field in ladle of RH process. Metals **9**(886), 1–13 (2019). https://doi.org/10.3390/met9080886
5. Dimitriou, I.: Planar incompressible Navier-Stokes, Euler, and Laplace equations: the angle-function formulation. Phys. Fluids **12**(30) (2018). https://doi.org/10.1063/1.5051542
6. Charles, S., John, R., Daniel, A.: Numerical solution of the Navier-Stokes equations for incompressible fluid flow by Crank-Nicolson implicit scheme. Appl. Comput. Math. **1**(10), 10–18 (2021). https://doi.org/10.11648/j.acm.20211001.12
7. Chuchard, P., Orankitjaroen, S., Wiwatanapataphee, B.: Study of pulsatile pressure-driven electroosmotic flows through an elliptic cylindrical microchannel with the Navier slip condition. Adv. Differ. Equ. **2017**(1), 1–13 (2017). https://doi.org/10.1186/s13662-017-1209-z
8. Aricò, C., Sinagra, M., Driss, Z., Tucciarelli, T.: A new solver for incompressible non-isothermal flows in natural and mixed convection over unstructured grids. Appl. Math. Model. **103**, 445–474 (2022). https://doi.org/10.1016/j.apm.2021.10.042
9. Mohammadein, S.A., Gad El-Rab, R.A., Ali, M.S.: The simplest analytical solution of Navier-Stokes equations. Inf. Sci. Lett. **10**(2), 159–165 (2021). https://doi.org/10.18576/isl/100201
10. Sungnul, S.: Transformation of the Navier-Stokes equations in curvilinear coordinate systems with maple **4**(12), 3315–3325 (2016)
11. Omaghali, N.E.J., Obagboye, L.F., Howusu, S.X.K.: Velocity and acceleration in elliptic cylindrical coordinates. Arch. Appl. Sci. Res. **8**(3), 72–74 (2016)
12. Gujun, C., Qiangqiang, W., Shengping, H.: Assessment of an Eulerian multi-fluid VOF model for simulation of multiphase flow in an industrial Ruhrstahl-Heraeus degasser. Metall. Res. Technol. **116**, 6 (2019). https://doi.org/10.1051/metal/2019049

13. Zhu, B.H., Chattopadhyay, K., Hu, X.P., Zhang, B., Liu, Q.C.: Optimization of sampling location in the ladle during RH vacuum refining process. Vacuum **152**, 30–39 (2018). https://doi.org/10.1016/j.vacuum.2018.02.033
14. Ling, H.T., Guo, C.B., Conejo, A.N., Li, F., Zhang, L.F.: Effect of snorkel shape and number of nozzles on mixing phenomena in the RH process by physical modeling. Metall. Res. Technol. **114**, 111–123 (2017). https://doi.org/10.1051/metal/2016058
15. Luo, Y., Liu, C., Ren, Y., Zhang, L.: Modeling on the fluid flow and mixing phenomena in a RH steel degasser with oval down-leg snorkel. Steel Res. Int. **89**, 1800048 (2018). https://doi.org/10.1002/srin.201800048

A Study of the Dynamic Response of Materials and Multilayer Structures to Shock Loads

Sergey Ugrimov[1](✉) , Natalia Smetankina[1] , Oleg Kravchenko[1] ,
Vladimir Yareshchenko[1] , and Leopold Kruszka[2]

[1] A. Pidhornyi Institute of Mechanical Engineering Problems of the National Academy of
Sciences of Ukraine, vul. Pozharskogo, 2/10, Kharkiv 61046, Ukraine
`sugrimov@ipmach.kharkov.ua`
[2] Military University of Technology, ul. gen. Sylwestra Kaliskiego 2, 00-908 Warsaw, Poland

Abstract. The paper deals with investigating the behaviour of multilayer struc-
tures subjected to a low-velocity transverse impact, as well as determining the
properties of materials under high-velocity dynamic loading. The impact response
of multilayer structures is simulated using the equations of the generalized two-
dimensional discrete structure theory. It is based on expanding all the components
of the displacement vector of each layer into power series for the transverse coor-
dinate. This theory takes into account all the components of the strain tensor in
the layers and the spatial character of the strain of the multilayer structure close
to the impact point. The impact of a ball with a homogeneous steel plate and a
sandwich with a soft filler is considered. The paper also describes the experimen-
tal method for investigating the properties of materials under high deformation
rate conditions. The specimens were investigated experimentally with a constant
deformation rate. A pneumatic gun launches the projectile to cause tension of the
specimen and dynamometer bar. The wideband strain gauge method is used to
register their deformation. The true tension diagram of the material investigated is
found from the equality of longitudinal forces in the specimen and dynamometer
bar. The data obtained on the dynamometer bar are definitive ones for building this
diagram, whereas the data obtained on the specimen are used for controlling the
constancy of the specimen deformation rate. The strength properties of steel flat
specimens were investigated under conditions of static and high-velocity loading.
The strength parameters of the material are found to increase substantially with
an increasing deformation rate.

Keywords: Multilayer plate · Impact · High-rate deformation · Experiment

1 Introduction

Investigating the behaviour of structures and materials under conditions of the action
of intense short-time loading is a topical and challenging problem in mechanics [1–
3]. When investigating transient deformation processes, it is necessary to account for
the structure's natural frequencies, the process of propagation of strain waves, and the
dependence of material strength characteristics on the deformation rate.

One of the most challenging problems in dynamics is investigating the response of multilayer shell structures to an impact with a solid [4–6]. When solving such problems, known mathematical difficulties related to an adequate description of the behaviour of the shell itself under the impact of a localised dynamic load are aggravated because the contact force and the loading domain are unknown a priori and depend on the strain properties of the interacting bodies [7–10]. Numerical approaches based on applying the finite element method [11] are widely used to solve such problems. Studies dedicated to analytical methods of solving such problems are very few [5, 12, 13]. Threat, low-order theories are used, as a rule, to describe the response of multilayer shell structures [5, 12], whereas the process of contact interaction is described based on the Hertz law [4, 14].

When analysing the response of a structure to transient loads, it is necessary to consider the dependence of the material properties on the loading velocity [15, 16]. Such dependencies can be derived easily by analysing tension diagrams obtained for different deformation rates. To obtain the tension diagrams, the dynamic parameters of materials are investigated at either a steady deformation rate or a constant load action amplitude. One of the most common methods of dynamic testing is the Kolsky method using the Hopkinson split bar, as well as its various modifications [15, 17, 18]. Other experimental techniques for investigating material properties are used less often, though some of them are quite straightforward and effective. Nowadays there is a significant interest in investigating the static and dynamic properties of metals and alloys [19], polymer [20, 21] and composite materials [22, 23], as well as materials obtained using additive technologies [24]. The problems of experimental investigation of material properties under high-rate deformation conditions have been poorly studied so far [20–22, 25].

The paper presents the results of theoretical research of the response of single-layer and three-layer plates to transverse impact, as well as the technique and the results of studying material properties under dynamic loading.

2 Response of Multilayer Plates to Low-Velocity Impact

2.1 Problem Statement

A low-velocity transverse impact of a ball with the mass M and the radius R with a horizontally arranged multilayer plate is considered (Fig. 1). The plate layers are made of isotropic materials, and the mechanical properties of the layers can differ significantly. The number of layers in the package is I, with the contact between the layers assumed to be ideal. The ball is dropped from the height H to point $C(x_{10}, x_{20}, 0)$ and the ball's velocity at the instance of contact with the plate's first layer is V_0.

Figure 2 is the experimental setup diagram (1 – indentor, 2 – dropping device; 3 – multilayer plate, 4 – support plate, 5 – strain gauges, 6 – registering devices). In the experiment provided conditions close to a simply supported plate. The plate strains were measured using the dynamic wideband strain gauge method. A three-component rosette strain gauge is bonded to the middle of the outer surface of the I-layer.
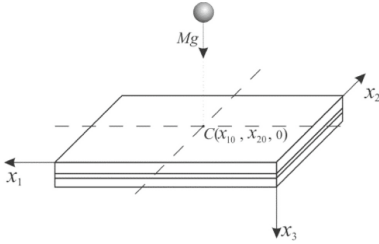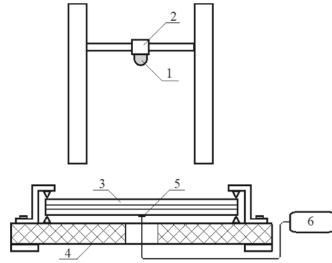
Fig. 1. Impact problem

Fig. 2. Experimental setup diagram

The strains were measured using the "Tenzodin" measurement complex developed by the A. Pidhornyi Institute of Mechanical Engineering Problems. The bridge circuit setup is used to measure the strains. The characteristics of strain gauge amplifier that is used in experiment are given in Table 1.

Table 1. Characteristics of strain gauge amplifier

Number of measurement channels	8
Carrier frequency, kHz	1,000
Working frequency range, kHz	0.04 to 200
Dynamic range, dB	80
Calibration range, relative strain unit	$30 \cdot 10^{-6}$ to $2.4 \cdot 10^{-3}$
Resistance of strain gauges used, Ω	50 to 200

2.2 Mathematical Models. Governing Equation

To find the plate response to an impact with a solid, the character of motion of the plate and the ball, and the conditions of their contact interaction should be taken into account. This problem is challenging to solve because neither the contact area nor the characteristics of the contact force (distribution and magnitude) are known initially. These parameters must be found for each time instance during the problem solution. The area of contact of the ball with the plate can be described approximately by a circle of radius $r(t)$. Similar to the Hertz solution, we shall neglect the tangent stresses in the contact area. Hence, the character of the pressure distribution across the contact area can be described by the following law.

$$q_3(x_1,\ x_2,\ t) = P_0(t)\left[1 - \frac{(x_1 - x_{10})^2 + (x_2 - x_{20})^2}{r^2}\right]^{0.5},$$

$$q_1(x_1,\ x_2,\ t) = q_2(x_1,\ x_2,\ t) = 0.$$

The process of multilayer plate strain at impact is described using the generalized two-dimensional model [4, 8] based on the kinematic hypotheses. The displacements of a point on the i-th layer in the direction of coordinate axes Ox_α have the form [8].

$$u_\alpha^i(x_1, \ x_2, \ x_3, t) = u_\alpha + \sum_{k=1}^{K_\alpha} \left[\sum_{j=1}^{i-1} h_j^k u_{\alpha k}^j + (x_3 - \delta_{i-1})^k u_{\alpha k}^i \right], \qquad (1)$$

where $h_j^k = (h_j)^k$, $\delta_i = \sum_{j=1}^{i} h_j$, $\delta_{i-1} \le x_3 \le \delta_i$, $i = \overline{1, I}$; u_α, $u_{\alpha k}^i$ are the coefficients of expanding the displacements into power series, which are sought functions of the arguments x_1, x_2, t; K_α are the parameters determining the number of retained power series terms for displacements.

The parameters K_1 and K_2, which describe the number of retained power series terms for plane displacements, will be the same and equal to K. Since the plate thickness is less than its plan form dimensions, parameter K_3, which specifies the number of retained power series terms in the transverse direction, is chosen to be equal to another value equal to L. Hence, these parameters specify the chosen level of approximation of the displacement field. Earlier it was shown that [8], under the conditions of localised action, the character of the distribution of the plane stresses and the strains over the thickness close to the loading area is essentially nonlinear. High-order theories are required to describe this distribution [8]. Therefore, the paper in the following will use the generalized theory with $K = 3$, $L = 2$ to analyse the impact response of multilayer plates.

Plate deformations are assumed to be small and described by Cauchy relationships in each layer. The relationship between the stresses $p_{\alpha\beta}^i$ and the strains $\varepsilon_{\alpha\beta}^i$ in the i-th layer is established by Hooke's law.

For forces and moments, the plate motion equations have the form [8]

$$\sum_{i=1}^{I} \left[L_\alpha^i - I_{\alpha1}^i \right] + q_\alpha^1 = 0, N_{1\alpha,1}^{ik_\alpha} + N_{\alpha2,2}^{ik_\alpha} - k_\alpha N_{\alpha3}^{ik_\alpha-1} + h_i^{k_\alpha} \sum_{j=i}^{I-1} \left[L_\alpha^{j+1} - I_{\alpha1}^{j+1} \right] - I_{\alpha k_\alpha+1}^i = 0, \quad (2)$$

where $L_1^i = N_{11,1}^{i0} + N_{12,2}^{i0}$, $L_2^i = N_{22,2}^{i0} + N_{12,1}^{i0}$, $L_3^i = N_{13,1}^{i0} + N_{23,2}^{i0}$; $N_{\alpha\beta}^{ik} = N_{\beta\alpha}^{ik} = \int_{\delta_{i-1}}^{\delta_i} (x_3 - \delta_{i-1})^k p_{\alpha\beta}^i \mathrm{d}x_3$, $\alpha, \beta = \overline{1, \ 3}$, $k = \overline{1, K}$, $i = \overline{1, I}$;

$$I_{\alpha r}^i = \frac{\rho_i h_i^r}{r} \left(u_{\alpha 0, tt} + \sum_{k=1}^{K_\alpha} \left[\sum_{j=1}^{i-1} h_j^k u_{\alpha k, tt}^j + \frac{r h_i^k}{k+r} u_{\alpha k, tt}^i \right] \right), \ K_\alpha = \overline{1, K_\alpha}, \ i = \overline{1, I},$$

These equations are solved using the analytical-numerical approach. The sought-for components of the displacements vector are expanded into a series for functions satisfying support conditions. As a result, for the simply supported plate, the initial system of partial differential equations is reduced to solving a system of ordinary second-order equations. By introducing a new variable, this system is reduced to a system of first-order equations, which are integrated by expanding the solution expansion into a Taylor series.

The equation describing the motion of the ball's centre of mass has the form [4, 5]

$$Mz_{,tt} = Mg - P, \; z(0) = 0, \; z_{,t}(0) = V_0, \tag{3}$$

where $z = z(t)$ is the indentor displacement, P is the contact force, and g is the gravity acceleration. Equation (3) is solved using the Laplace integral transform.

The condition of the joint displacement of the indentor and plate is

$$u_3^1(x_{10}, \; x_{20}, \; 0, \; t) + a(t) - z(t) \geq 0, \tag{4}$$

where $a(t)$ is the contact approach of the ball and plate in the contact point.

The amount of the contact approach and the contact area radius depend on the magnitude of the applied force, and they are found from the solution of the Hertz problem [4, 9, 14]:

$$a = k \, P^{2/3}; \; k = \left[\frac{9}{256} \frac{(\theta_1 + \theta)}{R} \right]^{1/3}; \; r(t) = \left[\frac{3}{16} \cdot P(t) \; \cdot R \cdot (\theta + \theta_1) \right]^{1/3},$$

$$\theta_1 = 4(1 - v_1^2)/E_1, \quad \theta = 4(1 - v^2)/E.$$

Here E, v, E_1, v_1 are the Young's modulus and the Poisson ratio for the ball material and for the plate first layer correspondingly.

Hence, the problem of determining the response of a multilayer plate to an impact is reduced to the joint integration of a system of differential equations for the plate (2) and the ball motion Eq. (3) simultaneously with analysing the condition of displacement compatibility (4).

2.3 Numerical and Experimental Results

To test the potentials of the suggested approach, a test problem was solved for a steel ball ($R = 3$ cm, $V_0 = 1$ m/s) striking a three-layer plate with a thick core ($A = B = 30$ cm, $h_1 = h_3 = 0.15$ cm, $h_2 = 1.5$ cm). The material of the casing of the three-layer plate is aluminium ($E_1 = E_3 = 71$ GPa, $v_1 = v_3 = 0.3$, $\rho_1 = \rho_3 = 2{,}500$ kg/m^3); the core material is an epoxy compound ($E_2 = 2.5$ GPa, $v_2 = 0.4$, $\rho_2 = 1{,}500$ kg/m^3).

Figure 3 shows the comparison of results obtained using the suggested theory with numerical data given in [10] (solid line – suggested theory; dash line — Timoshenko-type theory with account for the approach of casings; dot-dash line — Timoshenko theory without account for the approach of casings). Figure 3 shows the graphs for the contact force P and the deflection of the plate third layer $u_3{}^3$.

The Fig. 3 illustrates that the theories accounting for the approach of casings yield close results and that considering the approach of casings produces a pressure reduction and increases the contact time.

Also considered was the problem of ball impact with a steel plate with and without account for local plastic deformations in the contact zone.

The response of a single-layer steel plate ($A = 0.675$ m, $B = 0.18$ m, $h = 0.005$ m) to an impact with a steel ball ($R = 3$ cm) dropped from the height $H = 2.3$ m is investigated.

Figure 4 shows the time-dependent change of strain ε_{22}^1 on the plate bottom surface (solid line – generalized theory; dash line – experiment; dots – Timoshenko theory).
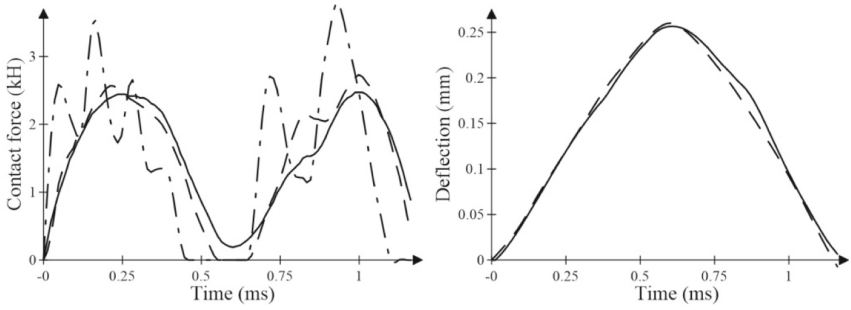
Fig. 3. Impact response of the three-layer plate

The strains calculated using the suggested theory differ from both experimental and calculated data. This is because local elastoplastic strains occur in the zone of contact of the indentor and the plate. Contact approach in this case can be represented as a sum of the elastic component defined by the Hertz law and the plastic component.

$$
a = \begin{cases} kP^{2/3} + \kappa P, & P \le P_{\max} \\ kP^{2/3} + a^*, & P > P_{\max} \end{cases}.
$$

Here, the first term corresponds to the elastic component and the second term, to the plastic one (constant κ is found experimentally); a^* are residual displacements equal to $a^* = \kappa P_{\max}$; $P_{\max}$ is the maximum contact force.

Computational results according to the suggested theory with account for elastoplastic local strains ($\kappa = 6.63 \times 10^{-7}$ m/N) are shown in Fig. 5 (solid line – computational results, dash line − experimental data). The figure shows that with account for the local elastic-plastic deformations in the zone of contact interaction, the computation results according to the suggested method and experimental data are in good agreement. The minor differences in the results are attributed to the complexity of implementing exactly the simple supporting condition for the plate (see Fig. 2) in the experiment.
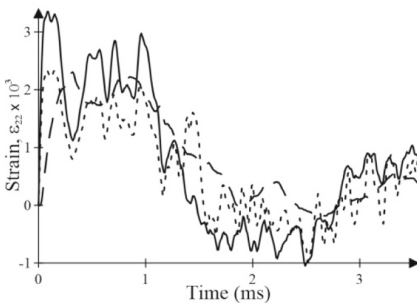
Fig. 4. Elastic impact with the plate
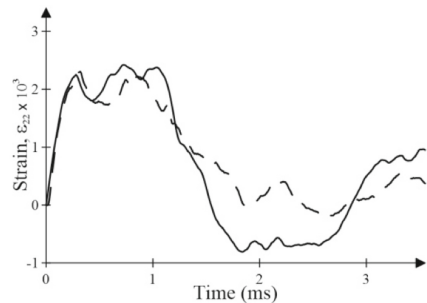
Fig. 5. Elastoplastic impact with the plate

3 Investigating Material Properties at High-Rate Deformation

The experimental investigation of the material properties under dynamic loading used a vertical pneumatic gun (Fig. 6). The diagram of the experimental setup for studying the dynamic tension properties of the material is shown in Fig. 7 (1 – support frame, 2 – case, 3 – solenoid valve, 4 – diaphragm, 5 – dynamometer bar, 6 – protective tube, 7 – projectile, 8 – centering washer, 9 – anvil, 10 – centering ring, 11 – specimen, 12 – protective casing) [16].

Fig. 6. Vertical pneumatic gun
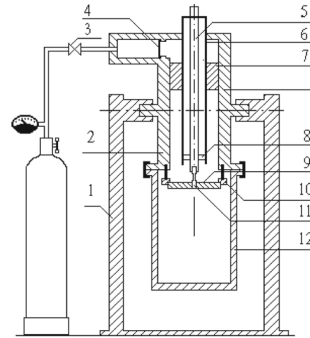
Fig. 7. Diagram of the experimental setup

The gun tube diameter is 125 mm and the length is 1,500 mm. The gun can accelerate a body with a mass of up to 4 kg to 150 m/s. This makes it possible to provide the deformation rate of the specimens $d\varepsilon/dt = 10^2 \times 10^4$ s^{-1}. The launch velocity is registered by fixing the time of rupture of two wires spaced 100 mm from each other along the projectile's path of travel.

The mechanical properties of flat steel specimens were investigated under static and high-rate deformation. The static tests were conducted on the "Instron-20" installation using specimens with a working zone length of $l_0 = 25$ mm, width $b = 5$ mm and thickness $h = 2$ mm. Static loading showed that the yield and ultimate tensile material strength values are $\sigma_{0.2}^{st} = 285$ MPa and $\sigma_{uts}^{st} = 416$ MPa, correspondingly. Dynamic tests were conducted using a pneumatic gun on specimens 10 mm long and with a working zone width of $b = 3.0$ mm. The technique of conducting dynamic tests of specimens consists in simultaneously registering the deformation of the tested specimen and the bar dynamometer at a known velocity of the projectile-indentor when it exits the tube (V_0 is the indentor velocity at impact with the anvil). These data help obtain the specimen tension diagram from the condition of equality of longitudinal forces in the specimen and bar. Specimen (11) is secured in centering clamps that are attached with the help of screw joints to the bar dynamometer (5) and the anvil (9). The bar dynamometer registers the longitudinal and circumferential deformations, and in the specimen, the longitudinal ones. The launched projectile strikes the anvil and propels it into motion, causing the tension of the specimen and bar dynamometer. The experimental investigation of specimens was conducted at a constant deformation rate $d\varepsilon/dt =$ const [16]. The deformation rates are determined as $d\varepsilon/dt = V_0/l_0$, where l_0 is the length of the

specimen working part. The rate constancy is ensured by a substantially greater kinetic energy of the projectile as compared to the energy needed for specimen deformation and destruction. The deformations of the bar dynamometer and the specimen working part were registered with the "Tenzodin" measurement complex. In this case, the specimen deformation tensogram is an indicator diagram because specimen elongation changes linearly with time ($\Delta l = (d\varepsilon/dt) \times t$) up to failure. The sought-for dependence $\sigma = \sigma(t)$ for the specimen working part is found from the results of measuring the strains $\varepsilon_{dyn} = \varepsilon_{dyn}(t)$ of the dynamometer elastic element. A simple recomputation based on the equality of longitudinal forces in the dynamometer and specimen was used for this. The longitudinal force N_x in the specimen in section x_1 under conditions of a uniform field of stresses across the section is found from the known dependence.

$$N_x = \sigma(x, t) \cdot S(x, t).$$

where $\sigma_x(x, t)$ is the axial component of the stress tensor, $S(x, t)$ is the specimen area in the section x_1.

The force in the bar dynamometer in the section at a distance of x_2 from the free end of the bar can be written down as

$$N_x = \sigma_x(x_2, t - t_2) \cdot S_{dyn}(x_2, t - t_2) = \frac{E}{1 - \nu} \cdot \left(\varepsilon_x^e(x_2, t - t_2) + \nu \varepsilon_\theta^e(x_2, t - t_2)\right) \cdot S_{dyn}(x_2, t - t_2),$$

where $\sigma_x(x, t)$ is the axial component of the stress tensor in the bar; $S_{dyn}(x, t)$ is the area of the bar cross-section in section x_2; E, ν are the elastic characteristics of the bar dynamometer; ε_x^e, ε_θ^e are the components of elastic strains in section x_2 in the longitudinal and circumferential directions; t_2 is the time lag between the start of the process of bar deformation and the specimen deformation process. The time lag is found based on the known wave propagation speeds in the bar and specimen.

The equality of longitudinal forces in the dynamometer bar and specimen yields the sought-for dynamic diagram of material deformation [16].

$$\sigma(t) = E\varepsilon_{dyn}\chi,$$

where χ is the ratio of the areas of the transverse sections of the dynamometer and working parts of the specimen; E is the elasticity modulus whose value is independent of the deformation rate.

Table 2 shows the results of investigating the dynamic deformation-strength characteristics of specimens for different deformation rates. It gives the ratios of ultimate strength characteristics for specimens under dynamic and static loading $\sigma_{0.2}^d/\sigma_{0.2}^{st}$ and $\sigma_{uts}^d/\sigma_{uts}^{st}$. With an increasing deformation rate, the material tension strength grows and at the deformation rate of 53.6×10^2 s^{-1} it practically exceeds by a factor of three the similar values obtained under static loading.

Ultimate strength ratio	Deformation rate $d\varepsilon/dt \times 10^{-2}$, s^{-1}						
	3.25	5.53	10.8	12.8	17.4	43.4	53.6
$\sigma_{0.2}{}^{d}/\sigma_{0.2}{}^{st}$	1.50	1.66	1.83	1.98	2.12	2.71	3.06
$\sigma_{uts}{}^{d}/\sigma_{uts}{}^{st}$	1.71	1.82	1.96	1.98	2.08	2.29	3.00

4   Conclusions

An approach is suggested to investigate the response of multilayer plates to a low-velocity transverse impact. A method is also proposed for investigating material properties, and the results of determining the strength properties of steel subjected to high-velocity loading are given.

The multilayer plate impact response is described using the generalized model of a layer structure. This allows taking into account the spatial nature of the deformation near the point of impact. The potentials of the proposed theoretical approach are shown using a test example of calculating the impact response of the sandwich plate and the homogeneous steel plate. The computational results by the theory suggested are compared against known theoretical solutions and experimental data obtained by the authors. It was shown that, the suggested approach has demonstrated its high effectiveness when analysing the impact response of the considered structures.

The properties of steel specimens for the case of high-rate deformation were investigated experimentally. The static and dynamic properties of flat steel specimens during tension were investigated. It was shown that, with increasing deformation rates, the strength parameters (yield and ultimate strength) of the material grow substantially. This is indicative of the need to take into account the dependence of material mechanical properties on the deformation rate to conduct a refined analysis of the strength of structures working under high-velocity loading conditions.

References

1. Smirnov, I.V., Lamzin, D.A., Konstantinov, A., Lomunov, A.K.: A unified experimental-theoretical approach to predict the critical stress characteristics of failure and yielding under quasi-static and dynamic loading. Eng. Fracture Mech. **225**, 106197 (2020)
2. Jemielita, G., Kozyra, Z., Kruszka, L.: Experimental analysis of elastic-plastic free vibrations of beam models caused by impact. Key Eng. Mater. **715**, 254–260 (2016)
3. Patil, S., Reddy, D.M., Reddy, M.: Low-velocity impact analysis on composite structures – a review. In: AIP Conference Proceedings, vol. 1943, 020009 (2018)
4. Ugrimov, S., Smetankina, N., Kravchenko, O., Yareshchenko, V.: Analysis of laminated composites subjected to impact. In: Nechyporuk, M., Pavlikov, V., Kritskiy, D. (eds.) Integrated Computer Technologies in Mechanical Engineering, vol. 188, pp. 234–246. Springer, Cham (2021). https://doi.org/10.1007/978-3-030-66717-7_19
5. Smetankina, N.V., Shupikov, A.N., Sotrikhin, S.Y., Yareschenko, V.G.: Dynamic response of an elliptic plate to impact loading: theory and experiment. Int. J. Impact Eng. **34**(2), 264–276 (2007)

6. Zhang, J., Liu, K., Ye, Y., Qin, Q.: Low-velocity impact of rectangular multilayer sandwich plates. Thin-walled Struct. **141**, 308–318 (2019)
7. Liu, H., Liu, J., Ding, Y., et al.: Effects of impactor geometry on the low-velocity impact behaviour of fibre-reinforced composites: an experimental and theoretical investigation. Appl. Compos. Mater. **27**, 533–553 (2020). https://doi.org/10.1007/s10443-020-09812-8
8. Ugrimov, S.V., Shupikov, A.N.: Layered orthotropic plates generalized theory. Compos. Struct. **129**(1), 224–235 (2015)
9. Dinnik, A.N.: Selected Works. Academy of Sciences of the Ukrainian SSR Publishers, Kiev (1952)
10. Kan, S.N.: Calculation of Metal and Reinforced Concrete Shells. Kharkiv University Press, Kharkiv (1972)
11. Bhuarya, M.K., Rajput, M.S., Gupta, A.: Finite element simulation of impact on a metal plate. J. Non-Cryst. Solids **432**, Part B, 432–439 (2016)
12. Pierson, M.O., Vaziri, R.: Analytical solution for low-velocity impact response of composite plates. AIAA J. **34**(8), 1633–1640 (1996)
13. Correas, A.C., Crespo, A.C., Ghasemnejad, H., et al.: Analytical solutions to predict impact behaviour of stringer stiffened composite aircraft panels. Appl. Compos. Mater. (2021). https://doi.org/10.1007/s10443-021-09909-8
14. Zukas, J.A., Nicholas, T., Swift, H.F., et al.: Impact Dynamics. Wiley, New York (1982)
15. Bragov, A.M., Lomunov, A.K., Konstantinov, A., Lamzin, D.A.: Modified Kolsky method for determining the shear strength of brittle materials. Tech. Phys. Lett. **43**, 130–132 (2017). https://doi.org/10.1134/S1063785017010175
16. Vorobiev, Yu.S., Kolodiazhny, A.V., Sevryukov, V.I., Yanyutin, E.G.: High-velocity deformation of structural elements. Naukovadumka, Kiev (1989)
17. Chen, W., Song, B.: Split Hopkinson (Kolsky) Bar. Springer, New York (2011). https://doi.org/10.1007/978-1-4419-7982-7
18. Shin, H., Kim, J.-B.: Evolution of specimen strain rate in split Hopkinson bar test. Proc. Inst. Mech. Eng. Part C: J. Mech. Eng. Sci. **233**(13), 4667–4687 (2019)
19. Armstrong, R.W., Walley, S.M.: High strain rate properties of metals and alloys. Int. Mater. Rev. **53**(3), 105–128 (2008)
20. Siviour, C.R., Jordan, J.L.: High strain rate mechanics of polymers: a review. J. Dyn. Behav. Mater. **2**(1), 15–32 (2016). https://doi.org/10.1007/s40870-016-0052-8
21. Miao, Y.-G., Li, Y.-L., Liu, H.-Y., et al.: Determination of dynamic elastic modulus of polymeric materials using vertical split Hopkinson pressure bar. Int. J. Mech. Sci. **108–109**, 188–196 (2016)
22. Acosta-Flores, M., Jiménez-López, E., Chávez-Castillo, M., et al.: Experimental method for obtaining the elastic properties of components of a laminated composite. Result Phys. **12**, 1500–1505 (2019)
23. Kondratiev, A., Gaidachuk, V., Nabokina, T., Tsaritsynskyi, A.: New possibilities of creating the efficient dimensionally stable composite honeycomb structures for space applications. In: Nechyporuk, M., Pavlikov, V., Kritskiy, D. (eds.) Integrated Computer Technologies in Mechanical Engineering, vol. 1113, pp. 45–59. Springer, Cham (2020). https://doi.org/10.1007/978-3-030-37618-5_5
24. Utzeri, M., Farotti, E., Coccia, M., Mancini, E., Sasso, M.: High strain rate compression behaviour of 3D printed Carbon-PA. J. Mater. Res. **36**(10), 2083–2093 (2021). https://doi.org/10.1557/s43578-021-00248-9
25. Thang, T.Q., Kuznetsova, E.L.: Effect of high-velocity deformation on the strength of armored composite materials. Turk. J. Comput. Math. Educ. **12**(2), 2709–2713 (2021)

Rotation of the Layer with the Cylindrical Pipe Around the Rigid Cylinder

Miroshnikov Vitaly[(⊠)] [iD]

National Aerospace University "KHAI", Chkalova Street 17, Kharkiv 61000, Ukraine
`v.miroshnikov@khai.edu`

Abstract. This article presents the solution to the layer spatial problem of elasticity for a containing a longitudinally thick long-walled cylindrical pipe rigidly connected to it. Stresses are specified on the layer boundary, while displacements are set on the pipe internal surface. The off-center compressive stresses at the layer surfaces cause the layer and its rigidly connected pipe to rotate. The problem is solved using the analytic-numerical generalized Fourier method, which is applied to Lamé equations in pipe-associated cylindrical coordinates and layer-associated Cartesian coordinates. When the boundary conditions are satisfied, a system of infinite linear algebraic equations is formed suitable to apply the method of reduction. As a result, the stresses and displacements at different points of the composite body are obtained. The accuracy of the boundary conditions approaches 10^{-4} for zero to one values. The stress state at the layer-pipe interface, as well as on the inner surface of the pipe depending on the thickness of the pipe and the location of the load has been analyzed. The load shift from the pipe center along the layer surface, as well as a decrease in the inner radius of the pipe cause a significant increase in tangential stresses at the pipe interfaces. Areas of maximum stresses are shown.

Keywords: Layer with cylindrical inclusions · Lame's equation · Generalized Fourier method

1 Introduction

The design of structures and mechanisms exposed to various loads must consider the distribution of the stress state in their various parts. This is especially true of the interfaces of different bodies or space around cavities.

The medium presented in this paper is a composite material and, thus, shows a non-linear mechanical behavior. Different approaches are used to determine the stress state of such structures. If we consider the given composite body as an integral object, its nonlinear stress state should be factor in: the paper [1] reviews tension-compression asymmetry behavior, unloading characteristics, viscous behavior, interaction between stress tensor components and effects of environmental factors on mechanical characteristics. In the manuscript [2], the analysis of progressive fracture was used to predict the notched final failure of woven glass/epoxy composite laminates. In the present manuscript [3], an deep

numerical analysis has been performed in order to study the influence of material non-linearity on the stress behavior and stress concentration factors in laminated composite materials. In this manuscript [4], a detailed numerical analysis is performed to estimate the error of the Tan's model of derive the concentration factor of stress, for a plate with finite dimensions containing an open hole. The influence of plate length on the stress distribution around the hole is studied.

In [5], the mechanical characteristics of a composite structure were obtained experimentally. Another approach is numerical-experimental. Thus, in [6] the reaction of layered composite to impact load was analyzed, in [7] the strength of multilayer cabin windows was calculated under the influence of various operating factors, in [8] a model was developed to simulate the process of bird strikes on a steel plate, in [9] the method of analysis of the strength of laminated glazing of the aircraft and the method of analysis of excess pressure are presented.

Many papers with a perpendicular cylindrical cavity are devoted to half-space [10], layer [11], elliptical [12] and rectangular [13] plate, as well as with perpendicular to half-space [14] or layer [15] located inclusion. However, the methods proposed in these proceedings do not allow to analyze the problem when the solid inclusion is orientated parallel to boundaries of the layer.

The present paper applies an analytical-numerical approach and generalized Fourier method is used [16]. The substantiation of this method for a half space with cylindrical voids is treated in [17].

Using the generalized Fourier method, the problems of half space with cylindrical voids [18] and for a layer with one cylindrical cavity [19] are solved. The problem for a plate with a cylindrical inclusion was considered in [20], with a cylindrical pipe at given displacements in [21]. This method solves problems for a cylinder with four cylindrical cavities [22], with N cylindrical voids [23], with cylindrical voids in the form of hexagonal structure [24] and with four cylindrical inclusions [25].

This paper provides the analysis of the layer with a axial cylindrical pipe under stresses set on the layer interfaces and with displacements set on the inner surface of the pipe. Such a problem has not been studied before, but similar calculation schemes are found in the design of parts and components in engineering and aircraft construction, as well as in power equipment.

2 Problem Statement

In the rectangular coordinate system *(x, y, z)* there is an elastic homogeneous layer of thickness $h + \tilde{h}$. The layer contains a circular cylindrical tube with an outer and inner radii R_1 and R_2, which will be treated in a cylindrical coordinate system (ρ, φ, z). The boundary surfaces of the layer and the pipe do not intersect.

The top and bottom boundaries of the layer are located at a distance $y = h$ and $y = -\tilde{h}$, respectively. Stresses $F\vec{U}(x, z)|_{y=h} = \vec{F}_h^0(x, z)$, $F\vec{U}(x, z)\big|_{y=-\tilde{h}} = \vec{F}_{\tilde{h}}^0(x, z)$ are set at the boundaries of the layer, and $\vec{U}(\varphi, z)|_{\rho=R_2} = \vec{U}_p^0(\varphi, z)$ is set at the inner surface of the displacement pipe.

where

$$\vec{F}_h^0(x, z) = \tau_{yx}^{(h)}\vec{e}_x + \sigma_y^{(h)}\vec{e}_y + \tau_{yz}^{(h)}\vec{e}_z ,$$

$$\vec{F}_{\tilde{h}}^0(x, z) = \tau_{yx}^{(\tilde{h})}\vec{e}_x + \sigma_y^{(\tilde{h})}\vec{e}_y + \tau_{yz}^{(\tilde{h})}\vec{e}_z , \tag{1}$$

$$\vec{U}_p^0(\varphi, z) = U_\rho^{(p)}\vec{e}_\rho + U_\varphi^{(p)}\vec{e}_\varphi + U_z^{(p)}\vec{e}_z$$

are known functions.

The pipe-layer boundary has the preset interface conditions.

$$\vec{U}_0(\varphi, z)_{|\rho=R_1} = \vec{U}_p(\varphi, z)_{|\rho=R_1} , \tag{2}$$

$$F\vec{U}_0(\varphi, z)_{|\rho=R_1} = F\vec{U}_p(\varphi, z)_{|\rho=R_1} , \tag{3}$$

where $F\vec{U} = 2 \cdot G \cdot \left[\frac{\sigma}{1-2\cdot\sigma}\vec{n} \cdot div\vec{U} + \frac{\partial}{\partial n}\vec{U} + \frac{1}{2}\left(\vec{n} \times rot\vec{U}\right)\right]$ – stress operator.

3 Problem Solution

The basic solutions of the Lamé equation are taken as follows [16]:

$$\vec{u}_k^\pm(x, y, z; \lambda, \mu) = N_k^{(d)}e^{i(\lambda z+\mu x)\pm\gamma y};$$

$$\vec{R}_{k,m}(\rho, \varphi, z; \lambda) = N_k^{(p)}I_m(\lambda\rho)e^{i(\lambda z+m\varphi)}; \tag{4}$$

$$\vec{S}_{k,m}(\rho, \varphi, z; \lambda) = N_k^{(p)}\left[(sign\lambda)^m K_m(|\lambda|\rho) \cdot e^{i(\lambda z+m\varphi)}\right]; k = 1, 2, 3;$$

$N_1^{(d)} = \frac{1}{\lambda}\nabla; N_2^{(d)} = \frac{4}{\lambda}(\sigma - 1)\vec{e}_2^{(1)} + \frac{1}{\lambda}\nabla(y\cdot); N_3^{(d)} = \frac{i}{\lambda}rot\left(\vec{e}_3^{(1)}\cdot\right); N_1^{(p)} = \frac{1}{\lambda}\nabla; N_2^{(p)} = \frac{1}{\lambda}\left[\nabla\left(\rho\frac{\partial}{\partial\rho}\right) + 4(\sigma - 1)\left(\nabla - \vec{e}_3^{(2)}\frac{\partial}{\partial z}\right)\right]; N_3^{(p)} = \frac{i}{\lambda}rot\left(\vec{e}_3^{(2)}\cdot\right); \gamma = \sqrt{\lambda^2 + \mu^2}, -\infty < \lambda, \mu < \infty$, where σ is the Poisson's ratio; $I_m(x), K_m(x)$ - modified Bessel functions; $\vec{R}_{k,m}, \vec{S}_{k,m}, k = 1, 2, 3$ are the Lame equation internal and external solutions for the cylinder, respectively; $\vec{u}_k^{(-)}, \vec{u}_k^{(+)}$ are the Lamé equation solutions for a plate.

The solution to the problem is as follows [22]:

$$\vec{U}_0 = \sum_{k=1}^{3} \int_{-\infty}^{\infty} \sum_{m=-\infty}^{\infty} B_{k,m}(\lambda) \cdot \vec{S}_{k,m}(\rho, \varphi, z; \lambda)d\lambda+$$

$$+\sum_{k=1}^{3} \int_{-\infty}^{\infty} \int_{-\infty}^{\infty} \left(H_k(\lambda, \mu) \cdot \vec{u}_k^{(+)}(x, y, z; \lambda, \mu) + \tilde{H}_k(\lambda, \mu) \cdot \vec{u}_k^{(-)}(x, y, z; \lambda, \mu)\right)d\mu d\lambda,$$

$$\tag{5}$$

$$\vec{U}_1 = \sum_{k=1}^{3} \int_{-\infty}^{\infty} \sum_{m=-\infty}^{\infty} A_{k,m}(\lambda) \cdot \vec{R}_{k,m}(\rho, \varphi, z; \lambda) + \tilde{A}_{k,m}(\lambda) \cdot \vec{S}_{k,m}(\rho, \varphi, z; \lambda)d\lambda, \tag{6}$$

where $\vec{S}_{k,m}(\rho_p,\varphi_p,z;\lambda)$, $\vec{R}_{k,m}(\rho_p,\varphi_p,z;\lambda)$, $\vec{u}_k^{(+)}(x,y,z;\lambda,\mu)$, and $\vec{u}_k^{(-)}(x,y,z;\lambda,\mu)$ are the basic solutions, which are described by the formulas (4), and the unknown functions $H_k(\lambda,\mu)$, $\tilde{H}_k(\lambda,\mu)$, $B_{k,m}(\lambda)$, and $\tilde{A}_{k,m}(\lambda)$ must be found from the boundary conditions (1) and the interface conditions (2), (3).

Analytical solutions (4)–(6) allow to obtain the result at any point of the solid exactly taking into account the infinite boundaries of this solid [16].

The formulas [16] must be used to transition the basic solutions between the coordinate systems:

– to transfer from the solutions $\vec{S}_{k,m}$ of the cylindrical coordinate system to the solutions of the layer $\vec{u}_k^{(-)}$ (at $y>0$) and $\vec{u}_k^{(+)}$ (at $y<0$)

$$\vec{S}_{k,m}(\rho,\varphi,z;\lambda)=\frac{(-i)^m}{2}\int_{-\infty}^{\infty}\omega_{\mp}^m\cdot\vec{u}_k^{(\mp)}\cdot\frac{d\mu}{\gamma},\ k=1,3;$$

$$\vec{S}_{2,m}(\rho,\varphi,z;\lambda)=\frac{(-i)^m}{2}\int_{-\infty}^{\infty}\omega_{\mp}^m\cdot\left(\left(\pm m\cdot\mu-\frac{\lambda^2}{\gamma}\right)\vec{u}_1^{(\mp)}-\lambda^2\vec{u}_2^{(\mp)}+\right.\qquad(7)$$

$$\left.\pm 4\mu(1-\sigma)\vec{u}_3^{(\mp)}\right)\frac{d\mu}{\gamma^2},$$

where $\gamma=\sqrt{\lambda^2+\mu^2}$, $\omega_{\mp}(\lambda,\mu)=\frac{\mu\mp\gamma}{\lambda}$, $m=0,\pm 1,\pm 2,\ldots$;

– to transfer from the solutions $\vec{u}_k^{(+)}$ and $\vec{u}_k^{(-)}$ of the layer to the solutions $\vec{R}_{k,m}$ of the cylindrical coordinate system

$$\vec{u}_k^{(\pm)}(x,y,z)=\sum_{m=-\infty}^{\infty}(i\cdot\omega_{\mp})^m\vec{R}_{k,m},\ (k=1,3);$$

$$\vec{u}_2^{(\pm)}(x,y,z)=\sum_{m=-\infty}^{\infty}\left[(i\cdot\omega_{\mp})^m\cdot\lambda^{-2}\left((m\cdot\mu)\cdot\vec{R}_{1,m}\pm\ \gamma\cdot\vec{R}_{2,m}+4\mu(1-\sigma)\vec{R}_{3,m}\right)\right],$$

$$(8)$$

where $\vec{R}_{k,m}=\vec{b}_{k,m}(\rho,\lambda)\cdot e^{i(m\varphi+\lambda z)}$;

$$\vec{b}_{1,n}(\rho,\lambda)=\vec{e}_{\rho}\cdot I_n'(\lambda\rho)+i\cdot I_n(\lambda\rho)\cdot\left(\vec{e}_{\varphi}\frac{n}{\lambda\rho}+\vec{e}_z\right);$$

$$\vec{b}_{2,n}(\rho,\lambda)=\vec{e}_{\rho}\cdot\left[(4\sigma-3)\cdot I_n'(\lambda\rho)+\lambda\rho_p I_n''(\lambda\rho)\right]+$$

$$+\vec{e}_{\varphi}i\cdot m\left(I_n'(\lambda\rho)+\frac{4(\sigma-1)}{\lambda\rho}I_n(\lambda\rho)\right)+\vec{e}_z i\lambda\rho I_n'(\lambda\rho);$$

$$\vec{b}_{3,n}(\rho,\lambda)=-\left[\vec{e}_{\rho}\cdot I_n(\lambda\rho)\frac{n}{\lambda\rho}+\vec{e}_{\varphi}\cdot i\cdot I_n'(\lambda\rho)\right],$$

$\vec{e}_{\rho},\vec{e}_{\varphi},\vec{e}_z$ are unit vectors of the cylindrical coordinate system;

To meet the boundary conditions at the top and bottom boundaries of the layer, in the right part (5) we rewrite the basic solutions $\vec{S}_{k,m}$ through $\vec{u}_k^{(-)}$ at $y=h$, and $\vec{u}_k^{(+)}$ at y

$= -\tilde{h}$. To do this, use the transition formulas (7). To the obtained vectors we apply the stress operator and equate at $y = h$ given $\vec{u}_k^{(-)}$, at $y = -\tilde{h}$ given $\vec{u}_k^{(+)}$, represented by the double Fourier integral.

Following from these equations need to find the functions $H_k(\lambda, \mu)$ and $\tilde{H}_k(\lambda, \mu)$ through $B_{k,m}(\lambda)$.

To fulfill the conditions of conjugation (2) of the pipe with a layer, in the right part (5) we will rewrite the basic solutions through $\check{R}_{k,m}, \check{S}_{k,m}$. To do this, use the transition formulas (8). The obtained vector, at $\rho = R_1$, is equated to the right side of (6).

If the stress operator is applied to the obtained equations, three more equations will be created for the coupling conditions (3).

To satisfy the boundary conditions on the inner surface of the pipe, need to equate the right-side part (6), $\rho = R_2$, to the preset $\bar{U}_R^0(\varphi, z)$.

From the resulting system of equations, need to exclude the previous functions $H_k(\lambda, \mu)$ and $\tilde{H}_k(\lambda, \mu)$ through $B_{k,m}(\lambda)$ and freed from series by m and integrals by λ.

As a result, we have nine infinite systems of linear algebraic equations to determine the unknowns $B_{k,m}(\lambda)$, $A_{k,m}(\lambda)$ and $\tilde{A}_{k,m}(\lambda)$.

The functions $B_{k,m}(\lambda)$ found are substituted into the expressions for $H_k(\lambda, \mu)$ and $\tilde{H}_k(\lambda, \mu)$. Once these unknowns are found, the problem will be solved.

4   Numerical Studies of the Stress State

We have an elastic isotropic layer and a cylindrical pipe (Fig. 1). Layer: $\sigma_0 = 0.38$, $E_0 = 1700$ MPa. Pipe: $\sigma_1 = 0.21$, $E_1 = 2 \cdot 10^5$ MPa. Section geometry: $h = \tilde{h}$, $R_1/h = 2/3$, the inner radius of the pipe was calculated in two versions $R_2/R_1 = 0.7$ and $R_2/R_1 = 0.5$.
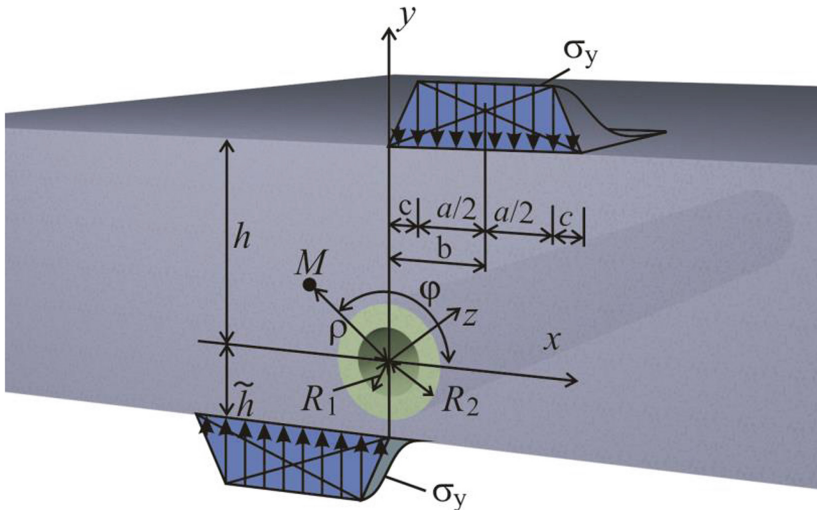
Fig. 1. A layer with the cylindrical pipe

The upper interface of the layer has the preset stresses $\sigma_y^{(h)} = -F \cdot \sigma_1(z) \cdot \sigma_2(x)$, where F is the load intensity,

$$\sigma_1(z) = 10^8 \cdot (z^2 + 10^2)^{-2}, \ \sigma_2(x) =$$

$$|x| \geq a/2 + c + b, \ \sigma_2(x) = 0$$
$$a/2 + b|x| \leq a/2 + c + b, \ \sigma_2(x) = \frac{a/2 + c - |x|}{c},$$
$$|x| \leq a/2 + b, \ \sigma_2(x) = 1$$

$\sigma_y^{(h)} = \tau_{yz}^{(h)} = 0$, $a = R_1 \cdot 2$, $b = a/2 + c$. The lower interface of the layer has the preset stresses $\sigma_y^{(\tilde{h})} = -F \cdot \sigma_1(z) \cdot \sigma_2(x)$, $a = R_1 \cdot 2$, $b = -a/2 - c$.

The infinite system of equations was reduced to m = 8. The accuracy of the boundary conditions at the specified values of geometric parameters 10^{-2}.

Figure 2 presents a comparison of the stress $\tau_{\rho\varphi}$ at the layer-pipe interface under both centrifugal and off-center load in MPa.
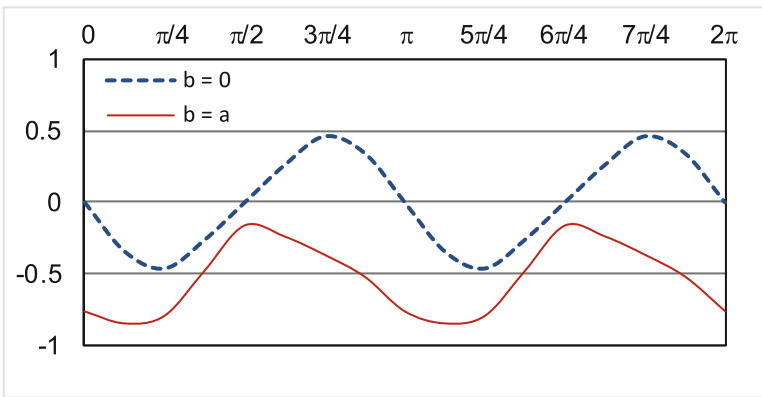
Fig. 2. Stress $\tau_{\rho\varphi}/F$ at the pipe and layer interface in cross-section, $z = 0$

Figure 2 shows an increase in stresses $\tau_{\rho\varphi}$, if $\varphi = 0$ and $\varphi = \pi$, when the load is shifted from the center of the pipe. However, the maximum stresses occur at $\varphi = \pi/8$ and $\varphi = 9\pi/8$. A significant increase in tangential stresses is logical, given the occurrence of torque during load shear. The tangential stresses do not exceed the set ones but can exceed the maximum allowable interface stresses, which can lead to the loss of the hard connection.

Figure 3 presents a comparison of the stress $\tau_{\rho\varphi}$ at the inner surface of the pipe under both centrifugal and off-center load, in MPa.

Figure 3 shows that the graph of stress $\tau_{\rho\varphi}$ at the pipe-and-rigid fixed cylinder interface has the same character as at the pipe-layer interface, but has greater values.

When the radius R_2 decreases up to $R_2/R_1 = 0.5$, the stresses $\tau_{\rho\varphi}$ at the pipe-layer interface do not change. However, due to the increase in torque, the tangential stresses $\tau_{\rho\varphi}$ at the inner surface of the cylinder increase significantly (see Fig. 4).

Thus, the reduction of the inner radius of the pipe leads to a significant increase in tangential stresses.
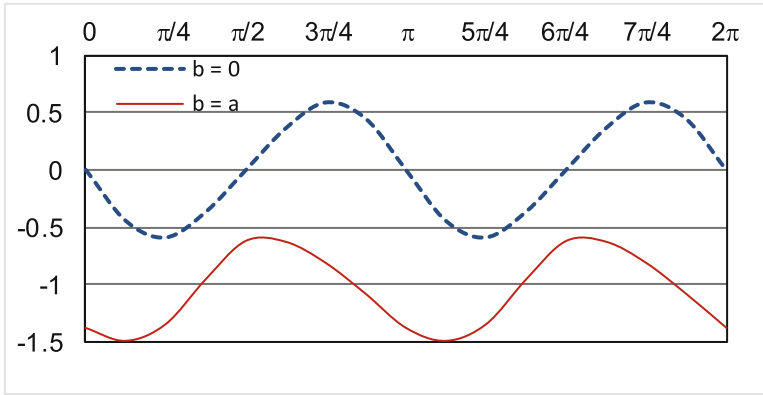
Fig. 3. Stress $\tau_{\rho\varphi}/F$ at the inner surface of the pipe in cross-section, $z = 0$
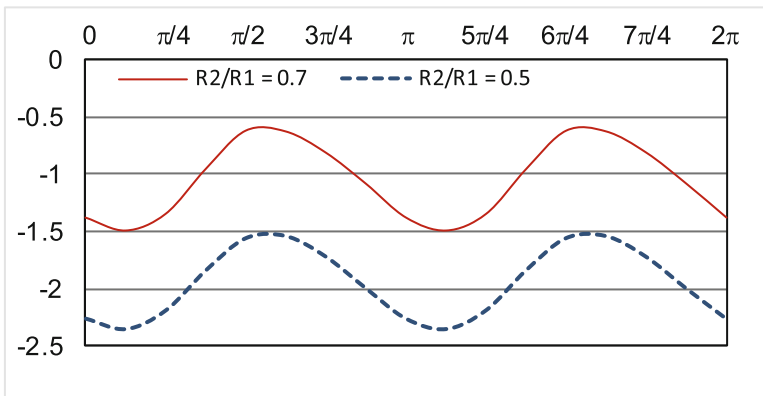
Fig. 4. Stress $\tau_{\rho\varphi}/F$ at the inner surface of the pipe in cross-section, $z = 0$, based on its inner radius.

5 Summary

The problem of the theory of elasticity is solved for a layer that has a longitudinal thick-walled cylindrical pipe. Stresses are set on the layer interfaces, while displacements are set on the inner surface of the cylinder. The problem is reduced to an infinite linear algebraic equations the reduction method is applied to. This provides the result with a predetermined accuracy.

Numerical analysis indicates the dependence of the values of tangential stresses on the amount of shear load (relative to the center of the pipe), as well as on the radius of interface. The points of the maximum stresses are also determined.

Comparison of the results obtained with the article [21] showed the similarity of the stress state in them, which confirms the authenticity of the algorithm and the calculations performed.

References

1. Fallahi, H., Taheri-Behrooz, F., Asadi, A.: Nonlinear mechanical response of polymer matrix composites: a review. Polym. Rev. **60**(1), 42–85 (2020)
2. Taheri-Behrooz, F., Bakhshan, H.: Characteristic length determination of notched woven composites. Adv. Compos. Mater. **27**(1), 67–83 (2018)
3. Taheri-Behrooz, F., Bakhshi, N.: Neuber's rule accounting for the material nonlinearity influence on the stress concentration of the laminated composites. J. Reinf. Plast. Compos. **36**(3), 214–225 (2017)
4. Bakhshi, N., Taheri-Behrooz, F.: Length effect on the stress concentration factor of a perforated orthotropic composite plate under in-plane loading. Int. J. Compos. Mater. **1**, 71–90 (2019)
5. Aitharaju, V., Aashat, S., Kia, H., Satyanarayana, A., Bogert, P.: Progressive damage modeling of notched composites. NASA Technical Reports Server. https://ntrs.nasa.gov/archive/nasa/casi.ntrs.nasa.gov/20160012242.pdf. Accessed 30 May 2021
6. Ugrimov, S., Smetankina, N., Kravchenko, O., Yareshchenko, V.: Analysis of laminated composites subjected to impact. In: Nechyporuk, M., Pavlikov, V., Kritskiy, D. (eds.) Integrated Computer Technologies in Mechanical Engineering, vol. 188, pp. 234–246. Springer, Cham (2021). https://doi.org/10.1007/978-3-030-66717-7_19
7. Rodichev, Y.M., Smetankina, N.V., Shupikov, O.M., Ugrimov, S.V.: Stress-strain assessment for laminated aircraft cockpit windows at static and dynamic load. Strength Mater. **50**(6), 868–873 (2018). https://doi.org/10.1007/s11223-019-00033-4
8. Smetankina, N., Ugrimov, S., Kravchenko, I., Ivchenko, D.: Simulating the process of a bird striking a rigid target. In: Ivanov, V., et al. (eds.) Advances in Design, Simulation and Manufacturing II, pp. 711–721. Springer, Cham (2020). https://doi.org/10.1007/978-3-030-22365-6_71
9. Smetankina, N., Kravchenko, I., Merculov, V., Ivchenko, D., Malykhina, A.: Modelling of bird strike on an aircraft glazing. In: Nechyporuk, M., Pavlikov, V., Kritskiy, D. (eds.) Integrated Computer Technologies in Mechanical Engineering. AISC, vol. 1113, pp. 289–297. Springer, Cham (2020). https://doi.org/10.1007/978-3-030-37618-5_25
10. Jiang, G., Yang, Z., Sun, C., Li, X., Yang, Y.: Dynamic stress concentration of a cylindrical cavity in vertical exponentially inhomogeneous half space under SH wave. Meccanica **54**(15), 2411–2420 (2019). https://doi.org/10.1007/s11012-019-01076-2
11. Jafari, M., Bayati Chaleshtari, M.H., Ardalani, E.: Determination of optimal parameters for finite plates with a quasi-square hole. J. Solid Mech. **10**(2), 300–314 (2018)
12. Dastjerdi, S., Yazdanparast, L.: New method for large deflection analysis of an elliptic plate weakened by an eccentric circular hole. J. Solid Mech. **10**(3), 561–570 (2018)
13. Abolghasemi, S., Eipakchi, H.R., Shariati, M.: Investigation of pre-buckling stress effect on buckling load determination of finite rectangular plates with circular cutout. J. Solid Mech. **10**(4), 816–830 (2018)
14. Ardeshir-Behrestaghi, A., Eskandari-Ghadi, M.: Analytical investigation of a two-layered elastic half-space containing a cylindrical elastic inhomogeneity under forced torsional rotation. Int. J. Solids Struct. **163**, 220–241 (2019)
15. Fesenko, A.A., Moyseenok, A.P.: Exact solution of a nonstationary problem for the elastic layer with rigid cylindrical inclusion. J. Math. Sci. **249**(3), 478–495 (2020). https://doi.org/10.1007/s10958-020-04954-3
16. Nikolayev, A.G., Protsenko, V.S.: Obobshchennyy metod Fur'ye v prostranstvennykh zadachakh teorii uprugosti. Nats. aerokosm. universitet im. N.Ye. Zhukovskogo «KHAI», Khar'kov (2011)
17. Ukrayinets, N., Murahovska, O, Prokhorova, O.: Solving a one mixed problem in elastici-ty theory for half-space with a cylindrical cavity by the generalized Fourier method. East.-Eur. J. Enterp. Technol. **2**(7(110)), 48–57 (2021)

18. Protsenko, V., Miroshnikov, V.: Investigating a problem from the theory of elasticity for a half-space with cylindrical cavities for which boundary conditions of contact type are assigned. East.-Eur. J. Enterp. Technol. **4**(7), 43–50 (2018)

19. Miroshnikov, V.Y.: Stress state of an elastic layer with a cylindrical cavity on a rigid foundation. Int. Appl. Mech. **56**(3), 372–381 (2020). https://doi.org/10.1007/s10778-020-01021-x

20. Miroshnikov, V., Medvedeva, A.V., Oleshkevich, S.V.: Determination of the stress state of the layer with a cylindrical elastic inclusion. Mater. Sci. Forum **968**, 413–420 (2019)

21. Miroshnikov, V.: Investigation of the stress strain state of the layer with a longitudinal cylindrical thick-walled tube and the displacements given at the boundaries of the layer. J. Mech. Eng. **22**(2), 44–52 (2019)

22. Nikolaev, O.G., Tanchik, E.A.: Stresses in an infinite circular cylinder with four cylindrical cavities. J. Math. Sci. **217**(3), 299–311 (2016). https://doi.org/10.1007/s10958-016-2974-z

23. Nikolaev, A.G., Tanchik, E.A.: The first boundary-value problem of the elasticity theory for a cylinder with N cylindrical cavities. Numer. Anal. Appl. **8**, 148–158 (2015). https://doi.org/10.1134/S1995423915020068

24. Nikolaev, A.G., Tanchik, E.A.: Stresses in an elastic cylinder with cylindrical cavities forming a hexagonal structure. J. Appl. Mech. Tech. Phys. **57**(6), 1141–1149 (2016). https://doi.org/10.1134/S0021894416060237

25. Nikolaev, A.G., Tanchik, E.A.: Model of the stress state of a unidirectional composite with cylindrical fibers forming a tetragonal structure. Mech. Compos. Mater. **52**(2), 177–188 (2016). https://doi.org/10.1007/s11029-016-9571-6

Reduction of Dynamic Stresses and Overloads Using Dampers in the Rocket Fairing Separation System

Borys Zaitsev[1] , Tetiana Protasova[1(✉)] , Natalia Smetankina[1] ,
Dmytro Klymenko[2] , and Dmytro Akimov[2]

[1] A. Pidhornyi Institute of Mechanical Engineering Problems of the National Academy of
Sciences of Ukraine, 2/10 Pozharsky Street, Kharkiv 61046, Ukraine
tatyprotasova@gmail.com
[2] Yuzhnoye State Design Office, 3, Krivorizka Street, Dnipro 49008, Ukraine

Abstract. A method is presented for the design of the rocket fairing elastic elements that contact via a damper with nonlinear properties– plasticity and a unilateral linkage. The finite element method and the Wilson finite-difference method are used. The damper is simulated as a one-dimensional element. Its nonlinearity is taken into account using the proposed method of introducing boundary forces on the damper ends. The boundary forces are found by iterations at each integration step. These forces depend on the damper state and contact conditions. Exploratory research into the characteristics of effective dampers was conducted. The research aimed at reducing the dynamic stresses and vibrational overloads during the different operational phases of the fairing separation system. With impulse perturbation from pyrotechnic devices, an effective damper is an elastic one with reduced stiffness (E≈200–400 MPa) between the instrument compartment casing and the support. Vibrational overload characteristics and the shock spectra of the instrument compartment casing in the frequency range up to 10 kHz were reduced significantly.

Keywords: Stresses · Contact · Plasticity

1 Introduction

Rocket fairing designs can be conventionally classified into two groups: composite fairings with separating shells and integral design fairings that separate from the rocket. The first designs are the most widespread, whereas the second ones are not so common in rocket building and are used in small rockets. Fairing ejection, i.e. its separation from the rocket and deflection from the rocket's flight path is a critical and multistage operation with several requirements imposed on it [1, 2]. They are as follows: to be shock-free with the relative motion of separating units; the selection of energy characteristics of pyrotechnical devices, and the spring and pneumatic pushers. When the fairing is separated by the impulse-shock action of the actuators, transient oscillatory processes occur. Thereat the dynamic stresses in the fairing elements or linked thereto

rocket airframe elements can reach high values. This presents a problem for the functioning of the entire fairing separation system. Besides, a significant factor is the level of vibrational action transferred to the overload-sensitive airborne equipment. Hence, among the mechanical-related rocket fairing separation issues, the significant ones are those of ensuring dynamic strength and reducing vibration overloads.

As a rule, the designs of fairings of different types and their separation systems have distinctive features [3, 4]. Respectively, the approaches to solving strength and vibration problems also differ and are represented by few publications. Paper [5] investigates the dynamics of the hinged payload fairing separation system. The researchers use a finite-element approach and the explicit nonlinear analysis method in their study. They underline the significant effect of the dynamic factor and the presence of plastic strain. Paper [6] considers the fairing separation from the launch rocket with the help of pyrotechnic means in the separation junctions. These means initiate the occurrence of a high-pressure gas medium. The flexible fairing dynamics under the action of expanding gases were investigated based on the gas medium – the fairing design coupled model. Publications [7, 8] study the so-called breathing vibrations of fairing shells and the impact thereon of different factors. Paper [7] analyses the effect of the air resistance and axial overload on the fairing separation and deformation characteristics. Air resistance reduces the breathing vibration frequencies of the rocket fairing and, jointly with the axial overload, it increases their amplitude. Paper [8] takes into account the contact between the elastic elements of a large-size fairing. The authors use the explicit nonlinear dynamics method to analyse the contact effect on the fairing rotation speed increase and the reduction of deformations during breathing vibrations. Some papers consider the issues of reducing vibrations by placing dampers and evaluating their effect using mathematical modelling methods. For instance, papers [9, 10] deal with the application of shock absorbers to reduce the vibration levels during the transfer of shock action via support structures to the payload when the fairing separates. Paper [11] presents a scheme of vibration isolation of the satellite and rocket to provide the required dynamic gap between the satellite and fairing. The finite-element model is used to analyse vibration transmission at resonance frequencies and its reduction with changing damping characteristics. Paper [12] deals with the transmission of vibration overloads from the fairing base to the payload. Disturbances from the aerodynamic load on the fairing and the excitation from rocket engines are considered. The finite-element method (FEM) is used to determine the accelerations at the fairing base when the payload changes.

The researchers [13] use the FEM for modelling the dynamic stress in the pyrotechnic system for separating the fairing from the rocket. The dynamic response is reduced using a plastic crasher. Its characteristics are chosen to minimise the maximal dynamic stresses. In paper [14], the FEM and the composite structure model are used for investigating the dynamic zone of the large-size fairing during its separation from the rocket. The fairing oscillation amplitudes are reduced by changing the shape of the force impulse from the pneumopushers, with the values of these amplitudes being kept. On the whole, inadequate attention has been paid to research in vibration control problems during fairing separation. In this paper, the problem of mitigating the adverse impact of dynamic actions is investigated by the example of a pyrotechnic fairing separation system (PFSS).

The general schematic diagram of such a system with its basic components is shown in Fig. 1. Some components comprise the movable part (MP) – cylinder and fairing casing, and the other ones comprise the fixed part (FP) – the support, rod and instrument compartment casing (ICC). The PFSS is activated by the pyrotechnically created impulse pressure in the space between the cylinder and rod. In the process, the impulse is transmitted to the ICC to cause vibrational overloads, which are subject to regulation. The impulse action activates the MP until the required velocity is attained. Upon completion of the cylinder travel relative to the rod shock contact of FP and MP occurs. It is followed by "picking up", the linking of the FP and the MP into a single system and the separation from the rocket. At the point of contact, big dynamic stresses occur in PFSS components.

Hence, the operability of the PFSS being considered depends on two factors – dynamic stress during shock contact and ICC vibrational overloads during an impulse load. To address these problems, it is practical to use dampers (crashers) in the form of annular elements with reduced stiffness parameters. The location of dampers is shown in Fig. 1. The transmission of motion from the movable element to the fixed one causes an intense reduction of the thin ring (damper) and involves severe plastic strain. Thereat the ring's resistance to reduction, i.e. its stiffness changes with its contraction. The damper's variable stiffness is a critical characteristic that affects the dynamics of the contact interaction of colliding structures.
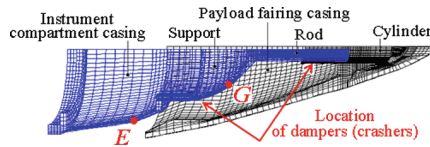
Fig. 1. General arrangement schematic of the PFSS

The plastic strain of dampers and the disturbance of unilateral links during shock contact are the cause of the nonlinearity of the occurring mechanical processes. The problem posed is that of simulating the dynamic processes in PFSS elements with the use of dampers, and of determining their characteristics to reduce vibration stresses and overloads. Unlike paper [13], this study, apart from investigating dynamic strength, also considers vibration overload problems stemming from kinematic excitation. This factor is critical in maintaining the functionality of the rocket payload.

2   Simulation. Accounting for Damper Nonlinearity

The PFSS composite construction is simulated as a three-dimensional piecewise-homogeneous body. Due to the axial symmetry of the PFSS structure, the computational models are presented as quarter shapes with the introduction of appropriate fastenings. The materials of various PFSS elements are as follows: alloy VNS-5 (steel 13Kh15N4AM3) – cylinder and rod; titanium alloy VT6S – support and instrument compartment casing. The FEM model with program implementation is used [13, 14].

It employs a solid poly- linear finite element with a topologically regular discretisation system. The FEM oscillation and motion equations in matrix form are presented as a mathematical model $[M]\ddot{u} + [D]\dot{u} + [K]u = F_e$, where u, $\dot{u}$, $\ddot{u}$ are the vectors of nodal displacements, the velocities and accelerations; $[M]$, $[D]$, $[K]$ are the matrices of masses, the damping and stiffness; F_e is the external load vector. The initial problem is solved using the Wilson finite-difference θ-method [15] – an unconditionally stable one with second-order accuracy. The discretisation in the computational model was chosen based on numerical experiments with regard for achieving an acceptable accuracy and reducing the computational burden.

The construction is considered as a mechanical system wherein the basic power components are linearly elastic ones and the damper is a nonlinear element. Its nonlinearity is associated with plasticity and resistance only to compression, i.e. due to a unilateral linkage. The damper is simulated as a one-dimensional element characterised by the relative displacement of its ends $\lambda = u_y(A) - u_y(B)$ and the force N transmitted via the element. The plastic stiffness $N(\lambda)$ is the damper's characteristic and it depends on its design and material. The damper stiffness can be found approximately by considering its stress state at small strains and by simulating shape changes at big reductions. Irrespective of the damper's design features (presence of holes, etc.), the elastic-plastic compression rigidity is characterised and defined by diagram $N(\lambda)$. The method used to obtain diagram $N(\lambda)$ is very approximate. A much more accurate and consistent determination of diagram $N(\lambda)$ is associated with solving the elastic-plastic problem with big strains with accounting for the contact between the boundaries of holes. Since implementing such an approach is challenging, it is unfeasible.

The damper can be in the following states: active plastic strain, elastic unloading and separation, i.e. the disturbance of contact. With elastic-plastic strain, the overall relative displacement is presented as $\lambda = \lambda_e + \lambda_p$, where λ_e, λ_p are the elastic and plastic components. The plastic strain is considered as an additional one according to the method of additional strains in the theory of plasticity. Based on the method, the additional strains are taken into account by "fictitious" volumetric forces. In this case, they are reduced to the boundary forces P at the damper ends (Fig. 2), whereas the computational model treats the damper as an elastic element.
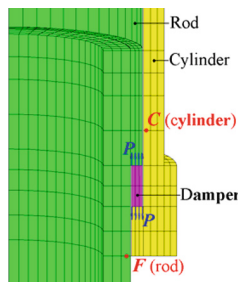

Fig. 2. Schematic diagram of introducing boundary forces

The boundary forces P are external ones and are recalculated at each time integration step. Their purpose is to compensate for the elastic forces developed in the model of

the damper as an elastic component of the design. With the plastic compression strain, the forces P should increase the strain suppressed by the elastic forces. When contact is disturbed, i.e. the separation of components from each other, the boundary forces should completely compensate the stresses in the damper model by nullifying them.

The boundary forces are proportional to the plastic component λ_p: $P = E \cdot \lambda_p \cdot L^{-1}$, where L is the damper height. The boundary forces P at each equation of motion integration step are found by iterations. The schematic diagram of their determination is shown in Fig. 3.
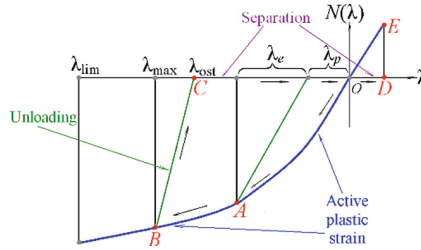
Fig. 3. Schematic diagram of determining boundary forces

The quantity λ_e is a known function of the current value of the relative displacement $\lambda_e = \lambda_e(\lambda)$. In view of the relationship $\lambda_p = \lambda - \lambda_e$, we obtain $P = E \cdot L^{-1}[\lambda - \lambda_e(\lambda)]$. At the time integration step, the displacement with regard for the boundary forces is expressed as $\lambda = \lambda_0 + \alpha P$, where λ_0 is the displacement regardless of boundary forces; α is the displacement at the step due to an impulse of unit boundary forces.

The equations derived are a system with respect to λ, P. Excluding P, we obtain a nonlinear equation with respect to λ: $\lambda = \frac{\lambda_o + \alpha \cdot E \cdot L^{-1} \cdot \lambda_e(\lambda)}{1 - \alpha \cdot E \cdot L^{-1}}$.

The denominator in the formula is non-zero because the term $\alpha E L^{-1} < 1$. It is the ratio of the compliances resulting from the action of the boundary forces under the dynamic (α) and static ($E^{-1} L$) loadings. Obviously, with dynamic loading, when the system inertia acts, the compliance is less.

With active plastic strain, $\Delta \lambda_p = \lambda_p^{i+1} - \lambda_p^i > 0$, where λ_p^i, λ_p^{i+1} are the plastic components of the displacement at steps i, $i + 1$, respectively. Here, the point in the plane λ, N is on the curve $N(\lambda)$, and the boundary forces are determined by the relationship $P = \frac{[\lambda_0 - \lambda_e(\lambda)] \cdot L^{-1} \cdot E}{1 - \alpha \cdot E \cdot L^{-1}}$.

With $\Delta \lambda_p < 0$, an elastic unloading state occurs. The plastic component λ_p is fixed and equals its achieved maximum value. Accordingly, the boundary forces are also fixed $P = E \cdot L^{-1}[\lambda_{\max} - \lambda_e(\lambda_{\max})]$.

Unloading occurs when $\lambda > \lambda_{ost}$ (Fig. 3), where $\lambda_{ost} = \lambda_{\max} - \lambda_e(\lambda_{\max})$. When this condition is violated, the state is determined as separation, and force interaction of elements via the damper is absent. The condition $\lambda_e = 0$ serves to determine the value of the boundary forces $P = \frac{\lambda_0 \cdot L^{-1} \cdot E}{1 - \alpha \cdot E \cdot L^{-1}}$. At the separation state, with the negative λ, the boundary forces $P < 0$, and at positive ones, $P > 0$.

The technique was tested, in particular, for the shock contact of solids through an elastic-plastic component, and the results were confirmed qualitatively and quantitatively. Definite requirements are put forward to the accuracy of specifying unit boundary forces. These requirements concern the strict compliance of forces with the specified value and balance. With contact strain, this is not critical, though without contact and with free motion this has an effect and introduces errors.

3   Reducing Vibration Stress During Shock Contact

At shock interaction of MP and FP at the PFSS "pick up" phase, the ICC is not included in the computational model, and the fairing casing is represented as a mock-up model with the same mass. Fastenings were introduced on the support bottom flange. The MP and FP impact is simulated with account for the discontinuous initial conditions at $t = 0$: $V_{FP} = 0$; $V_{MP} = V_0$ ($V_0 = 60$ m/s). The damper is placed between the parts of the cylinder and rod that contact during "pick up" (Fig. 1). Several options of using dampers are considered: a starting one with a mild characteristic $N(\lambda)$; an elastic steel one with a high stiffness parameter; an efficient one with a fitting ultimate stiffness N_p.

To analyze MP and FP contact interaction, the following computational data are information-bearing: the changes in the relative displacement of the ends of the damper $\lambda(t)$, and the velocities of the points in FP (point A) and MP (point B). They are shown in Fig. 4, where 1 is the elastic damper, 2 is the source damper, and 3 is the efficient damper. The initial approach of the ends with plastic strain is representative. It is followed by unloading and the subsequent disturbance of the contact and the free motion of the separated bodies. For an elastic steel damper, the approach of the ends is small, whereas when the plastic properties of the source and the efficient dampers are taken into account, it is big – up to the limit value λ_{lim}. For an efficient damper, the maximum values of λ were close to λ_{lim} or reached them for a short time. This is because the maximum stress reduction should occur over a bigger time interval at a big λ value. The exhaustion of the strain capability ($\lambda = \lambda_{lim}$) should not be protracted, otherwise, an additional shock action can occur.
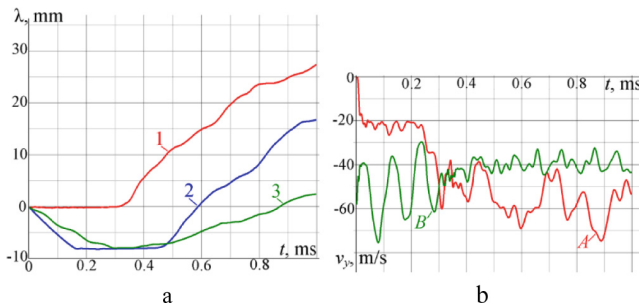

Fig. 4. The change of the relative displacement (a) of the ends and the velocities (b) of the points on the damper ends (points A, B)

The dynamic stresses in the different PFSS elements: the cylinder (point C), the rod (point F), and the support (point G) for different damper design options are shown

in Fig. 5. The basic differences in the dynamic response value are associated with the impulse action interval ($\approx$0.4 ms) until a maximum pressure from the powder gases is achieved.

The maximum stress intensities are achieved during dynamic contact, following which the stresses decrease sharply with free vibrations of the separated components.

The data on the maximum values of the dynamic stresses expressed as relative quantities $\sigma_i^{*\max} = \sigma_i^{\max}/\sigma_p$, where σ_p is the yield strength, are tabulated in Table 1. They belong to different PFSS components (points: C – the cylinder, F – the rod, G – the support) and for different dampers. The calculations show that changing the stresses for the variants of the source and elastic steel dampers are identical in magnitude and law. The source damper with the mild characteristic $N(\lambda)$ offers little resistance and only delays the point of rigid impact of parts. This is typical for an elastic steel damper. A focused search for the limiting value N_p of an efficient damper significantly reduced the maximum dynamic stresses (by about 1.7 times).
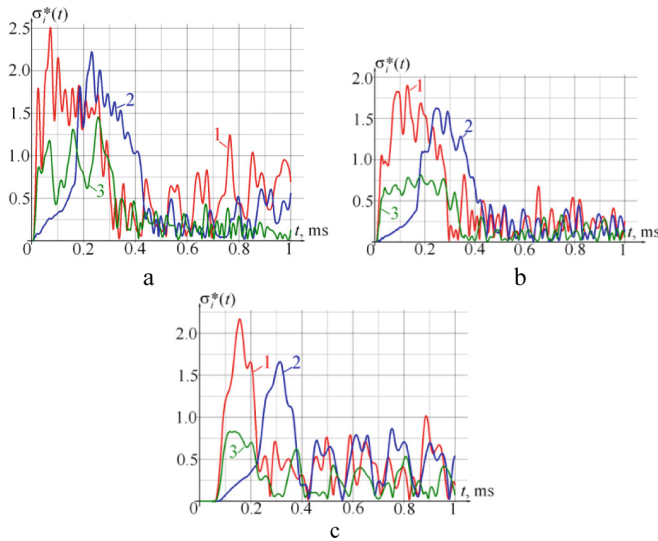
Fig. 5. Relative value of stress intensities: a – point C; b – point F; c– point G

Table 1. Maximum values of the stress intensities in the PFSS components

Damper	$\sigma_i^{*}{}_{\max}(C)$	$\sigma_i^{*}{}_{\max}(F)$	$\sigma_i^{*}{}_{\max}(G)$
Elastic	2.51	1.91	2.17
Source	2.23	1.63	1.66
Efficient	1.45	0.81	0.83

4   Reducing the Vibrational Overloads

The computational model includes the ICC with axial bearing on the bottom flange (the rocket body), a support and a simulator rod of the same mass. The impulse load from the pyrotechnic device is applied to the support upper flange. Overloads in the ICC occur during the MP motion phase; hence, the MP is not included in the computational model. The damper is placed between the support and the ICC. The following dampers are considered: a high-stiffness elastic steel one, a plastic one, and an elastic one with reduced stiffness.

The problem posed is to choose the characteristics of the material of the damping elements to evaluate their impact on the emergence of vibrational overloads. Shock spectra are used to evaluate the overloads under the effect of impulse loads. The spectra are calculated with a specially developed program. The input data are the kinematic parameters: the displacements, the velocities and the accelerations as the functions of time obtained during the computation of the dynamic response of the structure to an impulse action. Since the parameters differ in each point of the design model, the shock spectra are computed point by point. In this case, the reference point E was chosen, with its location shown in Fig. 1.

The initial variant (variant 1), for which the correlations are done, is the case when the damper characteristics are identical to those of the support and the ICC ($E = 1.99 \cdot 10^5$ MPa; steel 28Cr3CNiMnWPAl). This variant actually corresponds to the absence of a damper. The kinematic parameters of the reference point E in the ICC for this case are shown in Figs. 6, 7 and 8. Note that the prevailing component in the axial displacement is the periodic one. It is very close to the third natural frequency of the entire system ($\omega_3 = 1,477$ Hz), to which the axisymmetrical vibration mode corresponds. Higher frequencies occur for velocity and acceleration. Note also that during the active impulse (about 4 ms) the vibrations in the system repeat many times (with the account for a changing amplitude because the action magnitude changes). This means that one-time, i.e. during one period, vibration damping due to the plastic strain (the crusher) is ineffective. This is because it is followed by continuing elastic vibrations of the entire system, which are transmitted through the plastic-strained damper. This was found in the calculations, in which the damper plastic strain and a unilateral linkage were allowed, i.e. the possibility of separation with subsequent "micro shocks" with contact restoration.
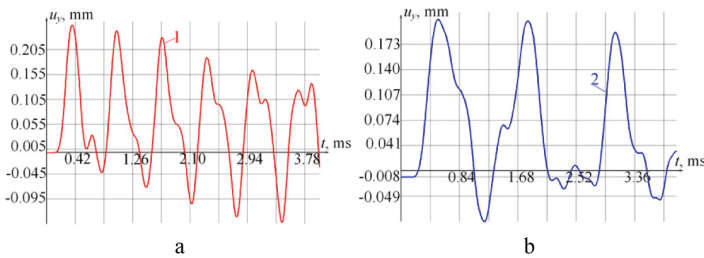

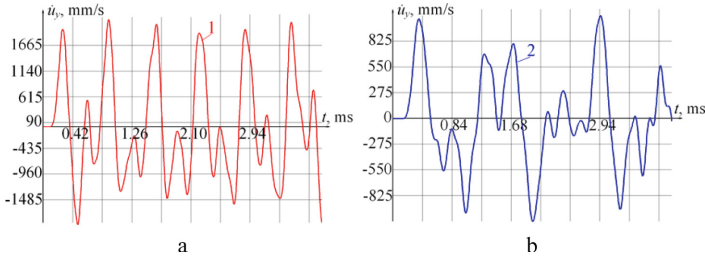**Fig. 6.** Axial displacements in the ICC point *E*: a – variant 1, b – variant 2

Fig. 7. Axial velocities in the ICC point *E*: a – variant 1; b – variant 2
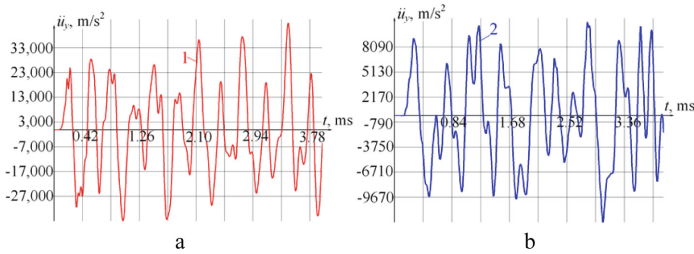

Fig. 8. Axial accelerations for different dampers: a – variant 1; b – variant 2

Shock spectra data for the variants considered (variants 1–3) are shown in Fig. 9.

It follows that using an elastic damper with reduced stiffness characteristics dramatically reduces the vibrational overloads in the ICC. The peaks on the shock spectra graphs, especially for variant 1 (absence of a damper) indicate that the initial signal (the kinematic characteristics) has pronounced period components with corresponding frequencies.
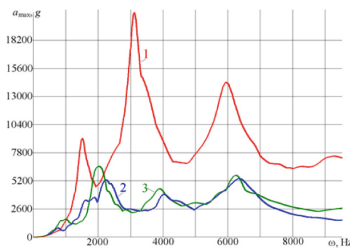
Fig. 9. Shock spectra for different dampers: 1, 2, 3 – variant numbers

Hence, numerical research has shown that using dampers with reduced elastic stiffness characteristics can be effective. The overload value defined by a_{max} is reduced by more than 1.5 times for the frequency range up to 10 kHz. The stiffness can be reduced not by material selection, but rather by design solutions.

Threat, the damper need not be an elastic solid spacer. It can have a more complex shape, e.g., a corrugated plastic ring.

5   Conclusions

The developed method was applied to reduce the dynamic stress and the vibrational overloads for different phases of the PFSS operation by installing different dampers and selecting their characteristics. For the "pick up" – the shock contact phase, the limit stiffness of the plastic damper between the cylinder and rod was found. At this stiffness value the maximum dynamic stresses in the contacting components were reduced by 1.5–1.7 times. With impulse perturbation from pyrotechnic devices, an effective damper is an elastic one with a reduced stiffness ($E \approx 200$–400 MPa) between the ICC and the support. The vibrational overload characteristics – the ICC shock spectra in the frequency range up to 10 kHz were reduced significantly.

References

1. Kokushkin, V.V., Petrov, N.K., Borzykh, S.V., Yaskov, V.V.: Development and simulation of large space rocket stages separation processes. Space Eng. Technol. **1**, 44–55 (2013)
2. Kolesnikov, K.S., Kokushkin, V.V., Borzykh, S.V., Pankova, N.V.: Calculation and design of missile stage separation systems: a tutorial. N. E. Bauman Moscow State Technical University Publications, Moscow (2006)
3. Potapov, A.M., Kovalenko, V.A., Kondratiev, A.V.: Payload fairings comparison of existing and prospective launch vehicles and their foreign counterparts. Aerosp. Tech. Technol. **1**(118), 35–43 (2015)
4. Rusin, M., Romashin, A.G., Kamnev, P.I.: Experience in the development of aircraft head fairings. Aerosp. Tech. Technol. **5**(13), 63–69 (2004)
5. Tang, X.-H., Li, B., Li, G., Hao, P., Chen, C., Ren, M.-F.: Self-impact analysis of the fairing hinge system based on dynamic constitutive models. Chin. J. Comput. Mech. **34**(4), 403–410 (2017). https://doi.org/10.7511/jslx201704001
6. Cheng, S.-C.: Payload fairing separation dynamics. J. Spacecr. Rocket. **36**(4), 511–515 (1999). https://doi.org/10.2514/3.27193
7. Cheng, X.-Y., Fan, B.-C., Rong, J.-L., Zhang, T., Xiang, D.-L.: Simulation and analysis on the ground separation test of a flexible fairing and its flying mode prediction. Acta Armamentarii **39**(3), 608–617 (2018). https://doi.org/10.3969/j.issn.1000-1093.2018.03.024
8. Li, G., et al.: Effects of spring component on the separation dynamics of a large-scale elastic payload fairing. J. Solid Rocket Technol. **38**(3), 326–331 (2015). https://doi.org/10.7673/j.issn.1006-2793.201503.005
9. Johnson, M., Batton, B., Osman, H., Fuller, C.: Controlling shock propagation in struts using cylindrical distributed vibration absorbers. In: 13th International Congress on Sound and Vibration 2006, ICSV 2006, vol. 1, pp. 249–256 (2006)
10. Cao, X., Wei, C., Liang, J., Wang, L.: Design and dynamic analysis of metal rubber isolators between satellite and carrier rocket system. Mech. Sci. **10**(1), 71–78 (2019). https://doi.org/10.5194/ms-10-71-2019
11. Pan, Z., Xing, J., Wang, L., Chen, S.: Research on whole-spacecraft vibration isolation based on parallel load-bearing and damping system. Lixue Xuebao / Chin. J. Theor. Appl. Mech. **51**(2), 364–370 (2019). https://doi.org/10.6052/0459-1879-18-285
12. Guthrie, M., Ross, M.R., Pulling, E.: Deriving transmissibility functions from finite elements for specifications. AIAA Scitech 2021 Forum, pp. 1–16 (2021)
13. Zaytsev, B., Asayenok, A., Protasova, T., Klimenko, D., Akimov, D., Sirenko, V.: Dynamic processes during the through plastic-damper shock interaction of rocket fairing separation system components. J. Mech. Eng. **21**(3), 19–30 (2018). https://doi.org/10.15407/pmach2018.03.019

14. Zaitsev, B.P., Protasova, T.V., Smetankina, N.V., Klymenko, D.V., Larionov, I.F., Akimov, D.V.: Oscillations of the payload fairing body of the cyclone-4M launch vehicle during separation. Strength Mater. **52**(6), 849–863 (2021). https://doi.org/10.1007/s11223-021-00239-5
15. Bathe, K.-J.: Finite Element Procedures. Prentice Hall, Hoboken (1996)

Numerical Modeling of Dynamic Processes of Elastic-Plastic Deformation of Axisymmetric Structures

Pavlo Gontarovskyi [ID], Nataliia Garmash[(✉)] [ID], and Iryna Melezhyk [ID]

A. Pidhornyi Institute of Mechanical Engineering Problems of the National Academy of Sciences of Ukraine, 2/10 Pozharsky Street, Kharkiv 61046, Ukraine
garm.nataly@gmail.com

Abstract. A technique and software for numerically modeling the dynamic processes of the elastic-plastic deformation of axisymmetric structures with using the finite element method are proposed. To integrate the equilibrium equations of the dynamic theory of plasticity, Newmark's and Wilson's algorithms of implicit incremental procedures are used. In solving the dynamic problem of the theory of plasticity at each time increment and iteration, it is necessary to both calculate and triangulate the matrix of the system of resolving finite element method. Dynamic processes of the elastic-plastic deformation of axisymmetric structures under short-term pulsed loading, as well as upon their impact against a rigid stationary barrier, were simulated. The distributions of stresses, plastic deformations, and also of the velocities and accelerations of structural elements at different times are obtained. At high impact velocities, the problem of divergence of the incremental time integration process arises. This problem can be overcome by reducing time increments at the initial moment of structural deformation. The calculation method can be used in the analysis of the dynamic processes in space-rocket hardware components.

Keywords: Dynamic loading · Stress-strain state · Finite element method

1 Introduction

The study of the behavior of structures under dynamic loading is one of the urgent problems associated with a wide class of theoretical [1] and practical problems [2]. In these problems significant dynamic loads often occur [3]. These loads act on different structural elements [4, 5], and often the intensity of the loads is so high [6] that plastic deformations can occur in the structural elements [7]. This leads to the necessity of solving the elastoplastic problem [8]. At high loading rates, it is necessary to set an appropriate deformation diagram of the material, taking into account the increase of the yield strength [9].

The solution of elastic-plastic problems was carried out by the finite element method (FEM) [10], which is widely used for solving different difficult problems [11, 12]. In solving the dynamic problem of the theory of plasticity at each time increment and iteration, it is necessary to both calculate and triangulate the matrix of the system of resolving FEM equations, which makes changes to the algorithms of implicit incremental integration procedures by Newmark's and Wilson's methods [13].

2   The Main Relationships of the Analysis of Transient Processes in Axisymmetric Structures with Plastic Deformations Taken into Account

In solving the axisymmetric dynamic boundary value problem with using FEM [14] for the numerical time integration of equilibrium equations, Newmark's and Wilson's implicit incremental procedures are used.

The FEM equilibrium equation in the state of motion has the form:

$$M\ddot{u}_{t+\Delta t} + C\dot{u}_{t+\Delta t} + Ku_{t+\Delta t} = R_{t+\Delta t}, \tag{1}$$

where M, K, C are the mass, stiffness and damping matrices; R is the vector of nodal loading; $u_{t+\Delta t}$, $\dot{u}_{t+\Delta t}$, $\ddot{u}_{t+\Delta t}$ are the vectors of nodal displacements, velocities, and accelerations of the ensemble of finite elements. The region of a plane or an axisymmetric problem consists of quadrangular subregions whose sides can be either rectangular or curvilinear (in the form of arcs of circles), forming a topologically regular grid [15]. Each subregion has its own material properties depending on temperature, and, based on the given information, is divided into simple quadrangular elements [16, 17].

$$u_{t+\Delta t} = u_t + \Delta t\dot{u}_t + \frac{\Delta t^2}{6}(\ddot{u}_{t+\Delta t} + 2\ddot{u}_t).$$

To solve the problem of plasticity theory, the flow theory with isotropic hardening is used. The increments of the components of plastic deformations $\Delta\varepsilon_{ij}^p$ are calculated from relations [18]:

$$\Delta\varepsilon_{ij}^p = \left(\frac{3}{2^1\sigma_i}\right)^2\left(\frac{1}{E_t} - \frac{1}{E}\right){}^1S_{ij}{}^1S_{km}\Delta\sigma_{km} + \frac{3}{2^1\sigma_i}\left(\frac{1}{E_t} - \frac{1}{E}\right)\left({}^1\sigma_i - {}^1\sigma_s\right), \tag{2}$$

where E is Young's modulus; E_t is the tangent modulus, which is determined by the material deformation diagram; ${}^1\sigma_i$ is the stress intensity at the beginning of the increment, $\sigma_i = \sqrt{\frac{2}{3}S_{ij}\delta_{ij}}$; ${}^1\sigma_s$ is the yield strength corresponding to the beginning of the increment; S_{ij} is the deviator part of the stress tensor, $S_{ij} = \sigma_{ij} - \sigma_{ij}\delta_{ij}$; δ_{ij} are Kronecker symbols; $\Delta\sigma_{km}$ are the increments of the stress tensor components [19].

In solving the problem of plasticity theory, at each time increment, an iterative process occurs during which the FEM stiffness matrix changes. In contrast to the dynamic problem of elasticity theory, at each increment and iteration, the stiffness matrix is calculated and triangulated. Moreover, the algorithms of Newmark's and Wilson's methods [13] undergo changes.

Expressing $\ddot{u}_{t+\Delta t}$ and $\dot{u}_{t+\Delta t}$ through the displacement increment vector $\Delta u_{t+\Delta t} = u_{t+\Delta t} - u_t$

$$
\begin{aligned}
\ddot{u}_{t+\Delta t} &= -\ddot{u}_t + \Delta u_{t+\Delta t}\frac{4}{\Delta t^2} - \dot{u}_t\frac{4}{\Delta t}, \\
\dot{u}_{t+\Delta t} &= -\dot{u}_t + \Delta u_{t+\Delta t}\frac{2}{\Delta t},
\end{aligned}
\tag{3}
$$

substituting them into (1) and using (1) for the previous time t, we obtain:

$$
\hat{K}\Delta u_{t+\Delta t} = \Delta\hat{R}_{t+\Delta t},
\tag{4}
$$

where $\hat{K} = K_{t+\Delta t} + C\frac{2}{\Delta t} + M\frac{4}{\Delta t^2}$;

$$
\Delta\hat{R} = R_{t+\Delta t} - R_t + M\left(2\ddot{u}_t + \dot{u}_t\frac{4}{\Delta t}\right) + 2C\dot{u}_t + \left(K_t - K_{t+\Delta t}\right)u_t.
$$

After solving the system of FEM Eqs. (4), using (2), we determine the displacements, velocities, and accelerations of nodes for time $t + \Delta t$:

$$
\begin{aligned}
u_{t+\Delta t} &= u_t + \Delta u_{t+\Delta t}, \\
\ddot{u}_{t+\Delta t} &= -\ddot{u}_t - \frac{4}{\Delta t}\dot{u}_t + \frac{4}{\Delta t^2}\Delta u_{t+\Delta t}, \\
\dot{u}_{t+\Delta t} &= \dot{u}_t + (\ddot{u}_t + \ddot{u}_{t+\Delta t})\frac{\Delta t}{2}
\end{aligned}
\tag{5}
$$

Similarly, we obtain relations for integrating the equations of motion when solving the nonlinear dynamic problem of the theory of plasticity by the Wilson method [12]:

$$
\begin{aligned}
\ddot{u}_{t+\theta\Delta t} &= \frac{6}{\theta^2\Delta t^2}(u_{t+\theta\Delta t} - u_t) - \frac{6}{\theta\Delta t}\dot{u}_t - 2\ddot{u}_t, \\
\dot{u}_{t+\theta\Delta t} &= \frac{3}{\theta\Delta t}(u_{t+\theta\Delta t} - u_t) - 2\dot{u}_t - \frac{\theta\Delta t}{2}\ddot{u}_t
\end{aligned}
\tag{6}
$$

After substituting relations (6) into equilibrium Eq. (1) for time $t + \theta\Delta t$ and taking θ equal to 1.4, we obtain:

$$
\hat{K}_{t+\theta\Delta t}\Delta u_{t+\Delta t} = \theta(R_{t+\Delta t} - R_t) + M\left(\frac{6}{\theta\Delta t}\dot{u}_t + 3\ddot{u}_t\right) + C\left(3\dot{u}_t + \frac{\theta\Delta t}{2}\ddot{u}_t\right) + \left(K_t - K_{t+\theta\Delta t}\right)u_t
\tag{7}
$$

where $\hat{K}_{t+\theta\Delta t} = K_{t+\theta\Delta t} + \frac{6}{(\theta\Delta t)^2}M + \frac{3}{\theta\Delta t}C$.

After solving the system of FEM Eqs. (7), we calculate the displacements, velocities, and accelerations for time $t + \Delta t$

$$\ddot{u}_{t+\Delta t} = \frac{6}{\theta^3 \Delta t^2}(u_{t+\theta \Delta t} - u_t) - \frac{6}{\theta^2 \Delta t}\dot{u}_t + \left(1 - \frac{3}{\theta}\right)\ddot{u}_t,$$

$$\dot{u}_{t+\Delta t} = \dot{u}_t + \frac{\Delta t}{2}(\ddot{u}_{t+\Delta t} + \ddot{u}_t),$$

$$u_{t+\Delta t} = u_t + \Delta t \dot{u}_t + \frac{\Delta t^2}{6}(\ddot{u}_{t+\Delta t} + 2\ddot{u}_t).$$

In calculating the mass and stiffness matrices, numerical integration over the area of finite elements is carried out in both directions with using two-node Gaussian formulas. At the same time, the finite element region is mapped onto a square with a side of one. Elements of the mass matrix are calculated once and stored in the array $(ku + 1)*5$, where ku is the number of the nodes of finite structural elements.

After determining the displacements, velocities, and accelerations for time $t + \Delta t$, at each iteration, both the stress-strain state of the structure and the accumulated plastic strains e_{ip} are calculated. They are compared with their e_{ip} values for the previous iteration. In the case of convergence of the process $(e_{ip} - e_{ipp})/e_{ip} < \varepsilon$, where ε is a given accuracy, the last iteration is performed with the output of results and proceeding to the next increment.

3 Modeling Dynamic Processes of Elastic-Plastic Deformation of Axially Symmetric FEM Structures

Let us consider the solution of test examples for the elastoplastic deformation of continuous cylinders loaded with a short-term axial pulse in the form of a sinusoidal half-wave with an amplitude of 800 MPa and a duration of 12 μs. The second end of the cylinder rests on a fixed barrier.

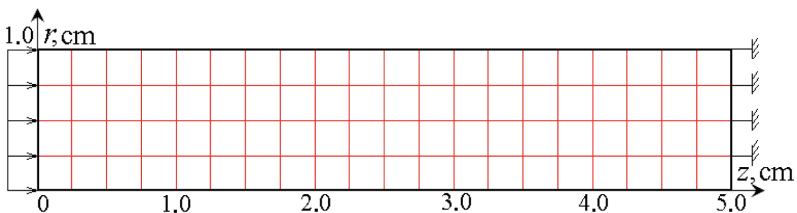The meridional section of the cylinder with its discretization into finite elements is shown in Fig. 1.

Fig. 1. The design scheme of the cylinder

The elastic properties of the material were taken equal to $E = 2 \times 10^5$ MPa, $\nu = 0$. The deformation diagram is shown in Fig. 2. The time integration was carried out by the Newmark method with a time increment of 2 μs.
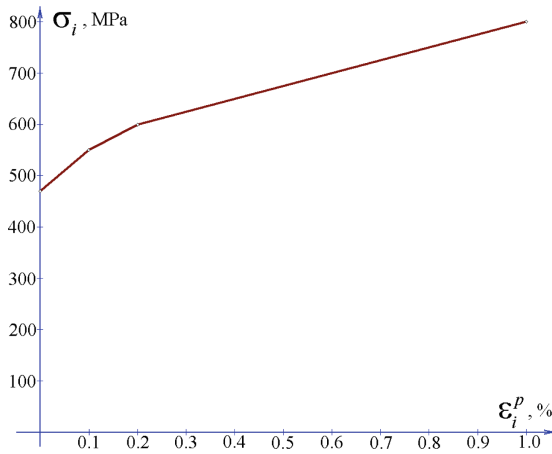
Fig. 2. Material deformation diagram

The distribution of axial stresses along the cylinder length at the outer surface for different times t is shown in Fig. 3, and that of plastic deformations, in Fig. 4. During plastic deformations, the material is incompressible, which is why a 3D stress-strain state is realized in the cylinder. After the time increment reaches 8 μs, elastic unloading begins where the pulse acts, and the plastic deformation zone continues to develop due to inertia forces, reaching the opposite end in 14 μs. Before the time increment reaches 16 μs, half of the cylinder becomes unloaded, and in its second part, the plastic deformations continue to increase.
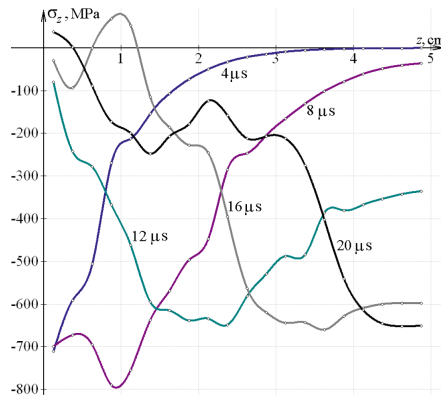
Fig. 3. The distribution of axial stresses along the cylinder length

Consider the cylinder impact (Fig. 1), at a speed of 100 m/s, against a fixed barrier. Material properties were taken $E = 2 \times 10^5$ MPa, $\nu = 0.3$. To solve the problem by the Newmark method, the following temporal discretization is adopted: 5×10^{-8}; 1×10^{-7}; 3×10^{-7}; 7×10^{-7}; 1×10^{-6}; 1.5×10^{-6}; 2×10^{-6} s and further with an increment of
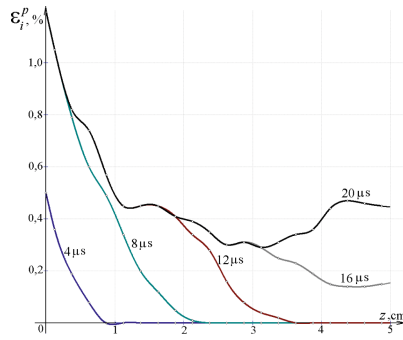
Fig. 4. The distribution of plastic deformations

1 μs to 20 μs. The first increment should be so small that the deformations are elastic. Further, the increments need to be constantly increased. Otherwise, due to large errors in the description of the wave processes of deformation from the opposite end, there occurs an additional unreal loading of the cylinder.

Figures 5 and 6 show the results of the distribution of axial stresses and equivalent plastic deformations along the cylinder length at different times t, at $r = 1.25$ mm (Fig. 5, a and Fig. 6, a) and $r = 8.75$ mm (Fig. 5, b and Fig. 6, b). Before the time increment reaches 20 μs, the plastic deformation of the cylinder becomes almost complete.

a

b

a $- r$=1.25 mm; b $- r$=8.75 mm
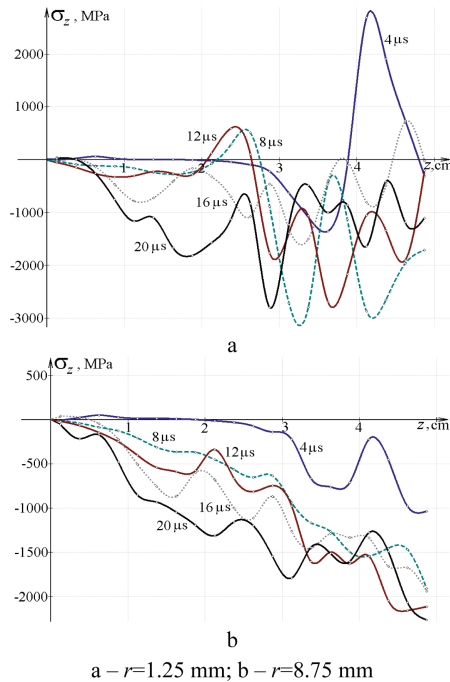
Fig. 5. The distribution of axial stresses along the cylinder length
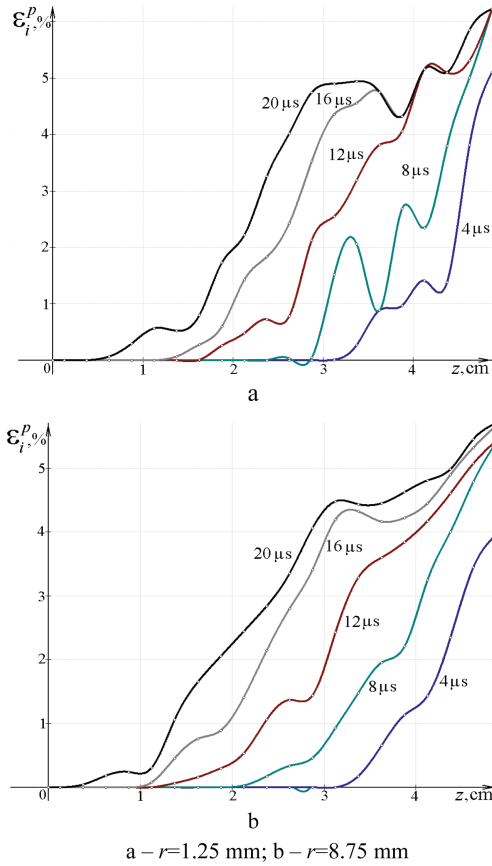
Fig. 6. The distribution of plastic deformations

The maximum equivalent plastic deformations at the point where the cylinder impacts against the barrier reach 6% and, at a time of 20 μs, propagate practically over the entire cylinder.

At an impact velocity of 20 μs, the maximum plastic deformations of 0.9% occur at a time of 20 μs on the cylinder axis at a distance of about 10 mm from the point where the cylinder impacts against the barrier, and propagate to a distance of up to 3.5 mm from the impact point, with the time increment being 2 μs.

4   Conclusions

Dynamic loading of structures is very often accompanied by the plastic deformation of material, which requires the solution to an elastic-plastic problem. A calculation method was developed and dynamic processes of the elastic-plastic deformation of axisymmetric structures under short-term pulsed loading, as well as upon their impact against a rigid stationary barrier, were simulated. The distributions of stresses, plastic deformations,

and also of the velocities and accelerations of structural elements at different times t are obtained. At high impact velocities, the problem of divergence of the incremental time integration process arises. This problem can be overcome by reducing time increments at the initial moment of structural deformation. At high loading rates, it is necessary to set an appropriate deformation diagram of the material, taking into account the increase of the yield strength.

Both the calculation methodology and software can be used in the analysis of dynamic processes when undocking space-rocket hardware elements.

References

1. Hatami, H., Shokri Rad, M., Ghodsbin Jahromi, A.: A theoretical analysis of the energy absorption response of expanded metal tubes under impact loads. Int. J. Impact Eng. **109**, 224–239 (2017). https://doi.org/10.1016/j.ijimpeng.2017.06.009

2. Sun, Z., Kasbergen, C., Skarpas, A., Anupam, K., Dalen, K.N., Erkens, S.M.J.G.: Dynamic analysis of layered systems under a moving harmonic rectangular load based on the spectral element method. Int. J. Solids Struct. **180–181**, 45–61 (2019). https://doi.org/10.1016/j.ijsolstr.2019.06.022

3. Shul'zhenko, N.G., Gontarovskii, P.P., Garmash, N.G., Grishin, N.N.: Torsional vibrations and damageability of turboset shaftings under extraordinary generator loading. Strength. Mater. **47**(2), 227–234 (2015)

4. Ugrimov, S.V., Shupikov, A.N.: Layered orthotropic plates generalized theory. Compos. Struct. **129**(1), 224–235 (2015)

5. Dastjerdi, S., Akgöz, B., Civalek, O., Malikan, M., Eremeyev, V.A.: On the non-linear dynamics of torus-shaped and cylindrical shell structures. Int. J. Eng. Sci. **156** (2020). https://doi.org/10.1016/j.ijengsci.2020.103371

6. Yuan, Y., Tan, P.J.: On large deformation, damage and failure of ductile plates to blast loading. Int. J. Impact Eng. **132**, 134–143 (2019). https://doi.org/10.1016/j.ijimpeng.2019.103330

7. Mehreganian, N., Fallah, A.S., Louca, L.A.: Plastic dynamic response of simply supported thick square plates subject to localised blast loading. Int. J. Impact Eng. **126**, 85–100 (2019). https://doi.org/10.1016/j.ijimpeng.2018.12.010

8. Peng, Q., Jin, Y., Liu, X., Wei, Y.G.: Effect of plasticity on the coefficient of restitution of an elastoplastic sphere impacting an elastic plate. Int. J. Solids Struct. 222–223 (2021). https://doi.org/10.1016/j.ijsolstr.2021.03.023

9. Voyiadjis, G.Z., Song, Y.: Strain gradient continuum plasticity theories: theoretical, numerical and experimental investigations. Int. J. Plast. **121**, 21–75 (2019). https://doi.org/10.1016/j.ijplas.2019.03.002

10. Sakharov, A.S., et al.: Finite Element Method in Mechanics of Solids. Vishcha shkola, Kiev (1982)

11. Zhidkov, A.V., Krutova, K.A., Mironov, A.A., Chekmarev, D.T.: Numerical solution of 3D elastic-plastic dynamical using rare mesh FEM scheme. Probl. Strength Plast. **79**(3), 327–337 (2017)

12. Sanchez-Rivadeneira, A.G., Duarte, C.A.: A high-order generalized finite element method for multiscale structural dynamics and wave propagation. Comput. Methods Appl. Mech. Eng. **384** (2021). https://doi.org/10.1016/j.cma.2021.113934

13. Bate, K., Vilson, E.: Numerical Methods of Analysis and Finite Element Method. Stroyizdat, Moscow (1982)

14. Sarkar, P., Chakraborty, P.: An asynchronous integration method for accelerated finite element analysis. Finite Elem. Anal. Des. **163**, 44–54 (2019). https://doi.org/10.1016/j.finel.2019.06.002

15. Hontarovskyi, P., Smetankina, N., Garmash, N., Melezhyk, I.: Analysis of crack growth in the wall of an electrolyser compartment. J. Mech. Eng. **23**(4), 38–44 (2020). https://doi.org/10.15407/pmach2020.04.038

16. Gontarovskyi, P., Smetankina, N., Garmash, N., Melezhyk, I.: Numerical analysis of stress-strain state of fuel tanks of launch vehicles in 3D formulation. In: Nechyporuk, M., Pavlikov, V., Kritskiy, D. (eds.) Integrated Computer Technologies in Mechanical Engineering - 2020, vol. 188, pp. 609–619. Springer, Cham (2021). https://doi.org/10.1007/978-3-030-66717-7_52

17. Shul'zhenko, N.G., Gontarovskii, P.P., Matyukhin, Y.I., Garmash, N.G.: Numerical analysis of the long-term strength of the rotor disks of steam turbines. Strength Mater. **42**, 418–425 (2010). https://doi.org/10.1007/s11223-010-9232-2

18. Birger, I.A., Schorr, B.F., Demyanushko, I.V., Dulnev, R.A., Sizova, R.N.: Thermal Strength of Machine Parts. Mechanical Engineering, Moscow (1975)

19. Washizu, K.: Variational Methods in Elasticity and Plasticity, 3rd edn. Pergamon Press, New York (1982)

Cross-Line Method for Solving Heat Conduction Problems

Xiao-Wei Gao[✉]

Dalian University of Technology, Dalian 116024, China
`xwgao@dlut.edu.cn`

Abstract. In this paper, a new collocation type numerical method, Cross-Line Method (CLM), is proposed for solving general engineering problems governed by second order partial differential equations with proper boundary conditions. The method is based on the use of a finite number of lines crossing the collocation node under consideration and therefore it is also called the Finite Line Method (FLM). In the method, the Lagrange interpolation formulation is used to construct the shape functions over each line. By differentiating the shape functions, a set of equations are established along each line and the Least-Square technique is applied to all lines' equations to form an equation set to solve the first and second orders of partial derivatives of any physical variables with respect to the global coordinates. The distinct feature of the proposed method is that the derived spatial partial derivatives are directly substituted into the governing partial differential equations and related boundary conditions to set up the system of equations with physical variables, temperatures, at all collocation nodes as unknowns. As an application, the proposed method is used to solve the heat conduction problems and two numerical examples are given to verify the correctness of the proposed method.

Keywords: Cross line element · Cross Line Method · Finite Line Method · Heat transfer

1 Introduction

As development of super computers, numerical analysis has become more and more important in modern engineering problems such as the heat conduction problem. The finite element method (FEM) is the most frequently used numerical method in science and engineering problems [1, 2], including heat conduction problems. This is attributed to the use of well-developed isoparametric elements which can make the computational results very stable. Besides, the finite elements have fixed nodes distribution, which not only can make different material properties easily imposed, but also can result in high computational efficiency. FEM is a type of weak-form methods [3], which requires a variational principle or energy equation to set up the solution algorithm. In addition, the numerical integration is needed over each element, which makes FEM not as flexible as strong-form methods, such as the collocation type of methods [4–12].

In collocation methods, the free element method (FrEM) [13] is a very flexible method in forming elements and setting up the system of equations. FrEM is a novel method absorbing the advantages of FEM [4] and mesh free methods [10] and has been successfully used to solve advanced heat conduction [14], solid mechanics [15], fluid mechanics problems [16], and others [17]. To improve the computational efficiency of FrEM, a family of cross-line elements (CLEs) are constructed in [18], which can use extremely few nodes to discretize problems' geometries, since the first order spatial derivatives are only related to the nodes over lines crossing the collocation node and the second ones are only related to the nodes over plates crossing the collocation node. CLEs are very easy to be used and have high computational efficiency. However, only quadratic CLEs are constructed in [18]. It has been demonstrated that for collocation type methods, high-order elements are needed to obtain accurate results [19]. Thus, to improve the accuracy of CLEs, a completely new construction method of any high order CLEs is proposed in the paper and a related new numerical method, called the Cross-Line Method (CLM), is presented, which can be used for any number of cross lines. Since CLM is based on the use of a finite number of straight or curved lines, it is also called the Finite Line Method (FLM) [20].

CLM is based on equations from all chosen lines crossing the collocation node. Since the number of lines crossing a node is usually more than the number of components of the first and second orders spatial partial derivatives, the Lest-Square technique is employed to form the equation set to solve for the spatial partial derivatives which are used to collocate the system of equations by the governing equations and related proper boundary conditions. To demonstrate the correctness of the newly proposed CLM, two numerical examples will be given for heat conduction problems over two-dimensional (2D) and three-dimensional (3D) configurations, respectively.

2 Methodology

2.1 Cross Lines and Their Spatial Partial Derivatives Used in Cross-Line Method

2.1.1 Formulations for Computing the First Order Partial Derivatives

Most engineering problems are governed by the second order partial derivatives with respect to the global coordinates and the related Neumann boundary conditions are related to the first order partial derivatives [3–18]. To compute these derivatives, let's consider lines crossing a collocation node. For 2D problems, three types of line distributions can be identified as shown in Fig. 1. At a collocation node located on the smooth boundary, 2 lines can be defined; for a corner node, 3 lines can be used; and for a node located inside the problem, 4 lines may be formed. For an easy view, Fig. 1 shows three-noded straight lines for the three types of cases. In fact, cross lines can be curved and the number of each line's nodes can be more than 3 for high order line elements.
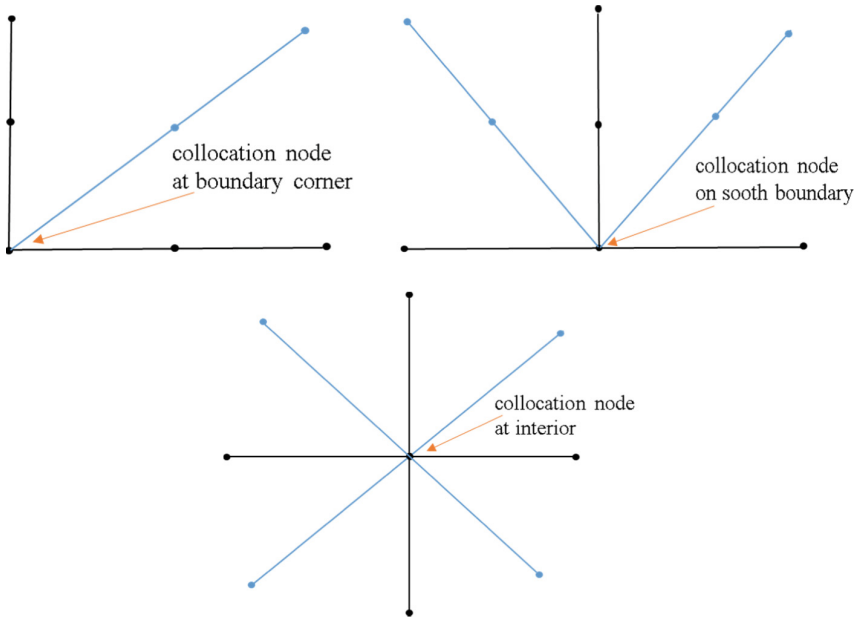
Fig. 1. Lines crossing three types of collocation nodes in 2D problems

Taking the 3D problem as the derivation background, let's denote the first order partial derivatives of a function $f(x)$ with respect to the global coordinates $x = \{x_1, x_2, x_3\}$ using $\partial f / \partial x_i$, $i = 1,2,3$, and thus the directional derivative of $f(x)$ along the length l of a line can be expresses as

$$\frac{\partial f}{\partial l} = \sum_i \frac{\partial f}{\partial x_i} \frac{\partial x_i}{\partial l} = [\frac{\partial x_1}{\partial l}, \frac{\partial x_2}{\partial l}, \frac{\partial x_3}{\partial l}] \begin{Bmatrix} \dfrac{\partial f}{\partial x_1} \\ \dfrac{\partial f}{\partial x_2} \\ \dfrac{\partial f}{\partial x_3} \end{Bmatrix} \tag{1}$$

where the length l of a line is accounted from one of the two ends of the line. For each line crossing the collocation node, we can write up an equation like Eq. (1) and thus after considering all crossed lines, the following matrix equation can be written:

$$[J]\begin{Bmatrix} \dfrac{\partial f}{\partial x} \end{Bmatrix} = \begin{Bmatrix} \dfrac{\partial f}{\partial l} \end{Bmatrix} \tag{2}$$

where

$$[J] = \begin{bmatrix} \dfrac{\partial x_1}{\partial l_1}, & \dfrac{\partial x_2}{\partial l_1}, & \dfrac{\partial x_3}{\partial l_1} \\[2mm] \dfrac{\partial x_1}{\partial l_2}, & \dfrac{\partial x_2}{\partial l_2}, & \dfrac{\partial x_3}{\partial l_2} \\[2mm] \vdots & \vdots & \vdots \\[2mm] \dfrac{\partial x_1}{\partial l_n}, & \dfrac{\partial x_2}{\partial l_n}, & \dfrac{\partial x_3}{\partial l_n} \end{bmatrix}, \quad \left\{ \dfrac{\partial f}{\partial x} \right\} = \left\{ \begin{array}{c} \dfrac{\partial f}{\partial x_1} \\[2mm] \dfrac{\partial f}{\partial x_2} \\[2mm] \dfrac{\partial f}{\partial x_3} \end{array} \right\}, \quad \left\{ \dfrac{\partial f}{\partial l} \right\} = \left\{ \begin{array}{c} \dfrac{\partial f}{\partial l_1} \\[2mm] \dfrac{\partial f}{\partial l_2} \\[2mm] \vdots \\[2mm] \dfrac{\partial f}{\partial l_n} \end{array} \right\}, \tag{3}$$

in which n is the number of lines crossing the collocation node, and l_J represents the J-th line.

If the number of selected cross lines are equal to the number of components of $\partial f / \partial x_i$ which is 2 for 2D and 3 for 3D problems, we can directly solve Eq. (2) for the values of $\partial f / \partial x_i$ and this means that only 2 or 3 cross lines are needed for 2D and 3D problems, respectively, as marked lines in black color in Fig. 1.

For the case that more cross lines are considered, as shown in Fig. 1 for lines marked in both black and blue colors, n in Eq. (3) is more than the components of $\partial f / \partial x_i$. In this case, to make Eq. (2) solvable, we apply the Least-Square technique to Eq. (2), which can result in the following matrix equation:

$$[J]^T [J] \left\{ \dfrac{\partial f}{\partial x} \right\} = [J]^T \left\{ \dfrac{\partial f}{\partial l} \right\} \tag{4}$$

where $[J]^T$ represents the transpose matrix of $[J]$.

Now, $[J]^T [J]$ is invertible, and thus we can easily obtain the following equations:

$$\left\{ \dfrac{\partial f}{\partial x} \right\} = [Q] \left\{ \dfrac{\partial f}{\partial l} \right\} \tag{5}$$

where

$$[Q] = \left([J]^T [J] \right)^{-1} [J]^T \tag{6}$$

Let's characterize a line using a number of nodes as in FEM, then the derivative $\partial f / \partial l_J$ for line J can be approximated using the following equation:

$$\dfrac{\partial f}{\partial l_J} = \sum_{\alpha=1}^{m_J} \dfrac{\partial L_\alpha^J(l)}{\partial l} f^\alpha \tag{7}$$

where m_J is the number of nodes defined over line J, f^α is the value of f at node α, and L_α^J is the shape functions of line J. The Lagrange interpolation formulation [7] can be used to easily form the shape functions, which can be expressed as

$$L_\alpha^J(l) = \prod_{\beta=1,\ \beta \neq \alpha}^{m_J} \dfrac{l - l_\beta}{l_\alpha - l_\beta} \quad \alpha = 1 \sim mJ \tag{8}$$

Similarly, the derivatives of coordinates in $[J]$ of Eq. (3) can also be computed by

$$\frac{\partial x_i}{\partial l_J} = \sum_{\alpha=1}^{m_J} \frac{\partial L_\alpha^J(l)}{\partial l} x_i^\alpha \qquad (9)$$

Noticing Eq. (7), Eq. (5) can be written as

$$\frac{\partial f}{\partial x_i} = \sum_{\alpha=1}^{M_1} N_{i\alpha}' f^\alpha \qquad (10)$$

where M_1 is the number of all nodes defined over the selected lines for the 1st order partial derivative, and

$$N_{i\alpha}' = \sum_{J=1}^{n} Q_{iJ} \frac{\partial L_\alpha^J(l)}{\partial l_J} \qquad (11)$$

in which, Q_{iJ} is the elements computed by Eq. (6).

2.1.2 Formulations for Computing the Second Order Partial Derivatives

From Eqs. (10) and (11), we can easily derived that

$$\frac{\partial^2 f}{\partial x_i \partial x_j} = \sum_{J=1}^{n} \sum_{\alpha=1}^{M_1} \left(Q_{iJ} \frac{\partial l_J}{\partial x_j} \frac{\partial^2 L_\alpha^J(l)}{\partial l_J^2} + \frac{\partial Q_{iJ}}{\partial x_j} \frac{\partial L_\alpha^J(l)}{\partial l_J} \right) f^\alpha \qquad (12)$$

in which, $\partial l_J / \partial x_j = 1/(\partial x_j / \partial l_J)$ and

$$\frac{\partial Q_{iJ}}{\partial x_j} = \sum_{k=1}^{d} ([J]^T[J])_{ik}^{-1} \left(\frac{\partial J_{Jk}}{\partial x_j} - \sum_{I=1}^{n} \sum_{p=1}^{d} \frac{\partial J_{Ik}}{\partial x_j} J_{Ip} Q_{pJ} \right)$$
$$- \sum_{I=1}^{n} \sum_{p=1}^{d} Q_{iI} \frac{\partial J_{Ip}}{\partial x_j} Q_{pJ} \qquad (13)$$

with $d = 2$ for 2D and $d = 3$ for 3D problems.

For easier use, Eq. (12) can be expressed as the following form:

$$\frac{\partial^2 f}{\partial x_i \partial x_j} = \sum_{\alpha=1}^{M_2} N_{ij\alpha}'' f^\alpha \qquad (14)$$

where M_2 is the number of all nodes defined over the selected lines for the 2nd order partial derivative, and

$$N_{ij\alpha}'' = \sum_{J=1}^{n} \left(Q_{iJ} \frac{\partial l_J}{\partial x_j} \frac{\partial^2 L_\alpha^J(l)}{\partial l_J^2} + \frac{\partial Q_{iJ}}{\partial x_j} \frac{\partial L_\alpha^J(l)}{\partial l_J} \right) \qquad (15)$$

Using Eqs. (14) and (10), we can establish the system of equations by collocating the governing differential equations and related boundary conditions at internal and boundary nodes, respectively, as shown in the following for the heat conduction problems.

2.2 Cross-Line Method for Solving Heat Conduction Problems

2.2.1 Govern Equation and Boundary Conditions in Heat Conduction

The governing equation for steady state heat conduction problems with a spatially varying thermal conductivity and heat source can be expressed as [3]

$$\lambda_{ij}(x)\frac{\partial^2 T(x)}{\partial x_i \partial x_j} + \frac{\partial \lambda_{ij}(x)}{\partial x_i}\frac{\partial T(x)}{\partial x_j} + S(x) = 0 \tag{16}$$

and three commonly used boundary conditions are as follows:

$$T(x) = \overline{T} \qquad x \in \Gamma_1 \tag{17}$$

$$-\lambda_{ij}(x)\frac{\partial T(x)}{\partial x_j}n_i = \overline{q} \qquad x \in \Gamma_2 \tag{18}$$

$$-\lambda_{ij}(x)\frac{\partial T(x)}{\partial x_j}n_i = h(T(x) - T_\infty) \qquad x \in \Gamma_3 \tag{19}$$

in which, $\Gamma_1 \cup \Gamma_2 \cup \Gamma_3 = \Gamma$, $\Gamma = \partial\Omega$, $\boldsymbol{n}$ is the outward normal to the boundary Γ, h is the heat transfer coefficient; $\overline{T}$, $\overline{q}$ and T_∞ are the prescribed temperature, heat flux and environmental temperature on the boundary, respectively; λ_{ij} is the thermal conductivity, and S the source of heat-generation rate. The repeated subscripts i and j represent the summation through its range which is 2 for 2D and 3 for 3D problems.

2.2.2 Generation of the System of Equations Using CLM for Heat Conduction

As in the mesh free method [8–10], in CLM the computational domain is discretized into a series of nodes. At each node, a number of cross lines are formed with surrounding nodes, as shown in Fig. 1. For internal nodes, substituting Eqs. (14) and (10) into Eq. (16) results in

$$\left(\lambda_{ij}N''_{ij\alpha} + \frac{\partial \lambda_{ij}}{\partial x_i}N'_{j\alpha}\right)T^\alpha + S = 0 \tag{20}$$

And for boundary nodes at which the heat fluxes are given, substituting Eq. (10) into Eq. (18) yields

$$-\lambda_{ij}N'_{j\alpha}n_iT^\alpha = \overline{q} \tag{21}$$

$$-\lambda_{ij}N'_{j\alpha}n_iT^\alpha = h(T^c - T_\infty) \tag{22}$$

where T^c is the temperature at the collocation node, which is one of T^α, $\alpha = 1,...,M$ with M being the number of total nodes over all the crossed lines at the collocation node. As for the boundary nodes at which the temperature is specified, Eq. (17) is directly served as one of the system equations.

After apply the specified boundary conditions to Eqs. (20)–(22), the final system of equations can be formed and can be written as the matrix form as follows

$$[A]\{T\} = \{b\} \tag{23}$$

where $[A]$ is the coefficient matrix, $\{b\}$ is a known vector formed by specified temperatures and fluxes as well as the heat source S. It is noted that $[A]$ is a sparse matrix, since for each collocation node, only surrounding nodes are related.

By solving Eq. (23) for $\{T\}$, we can obtain the temperature values at all nodes.

3 Results and Discussion

A computer code has been developed based on the above described CLM. To validate the proposed method and show its ability of solving complicated problems, two numerical examples are given in the following for these purposes.

3.1 Heat Conduction Over a Plate

The demonstrated first example is a plate of 100 mm × 60 mm. The left side of the plate is imposed with a temperature of $\overline{T} = 200$K and the right side with heat flux of $\overline{q} = 10\text{J}/(\text{m}^2 \cdot \text{s})$. Upper and lower sides are adiabatic. The heat conductivity of the plate is $\lambda = 10$ W/m/K.

Obviously, the exact solution to this simple example can be easily obtained, that is, the temperature on the right side is 100K and linearly increased to the left side. To examine the stability of the proposed method, four different nodes distributions are modeled as shown in Fig. 2, among which the left side two meshes have regularly distributed nodes, while right side two have irregularly distributed nodes. In computation, 3-noded lines are used for boundary and internal nodes, as shown in Fig. 1. The contour plots of the computed temperatures based on the four models are shown in Fig. 2. From Fig. 2 it can be seen that the computed results are almost the same, and all are in excellent agreement with the exact solution. This indicates that the proposed method has good stability even for highly irregularly distributed nodes.

3.2 Heat Conduction over a Heat Radiator

The second example demonstrated in the paper is a heat radiator as shown in Fig. 3. The dimensions and material property are also shown in Fig. 3. The square area on the bottom is subjected to a temperature of T = 85 °C and other surfaces are in the heat convection condition of $h = 5W/m^2K$, $T_\infty = 20$ °C.

(a) 3×3 regular nodes

(b) 3×3 irregular nodes

(c) 30×20 Regular nodes
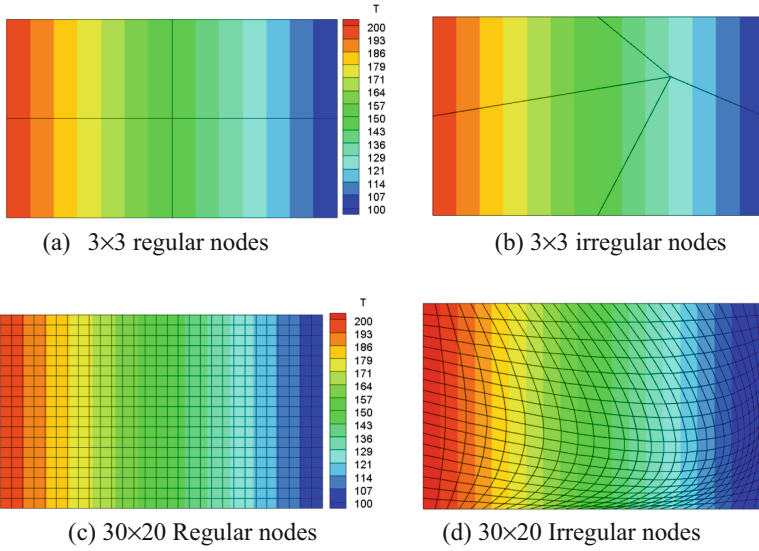
(d) 30×20 Irregular nodes

Fig. 2. Four models with different nodes distributions and contour plots of computed temperatures using CLM

The radiator is discretized as 122,791 collocation nodes. At each node, 3 cross lines are formed and 3 nodes are used over each line. Figure 4 shows the mesh formed by connecting all cross lines.
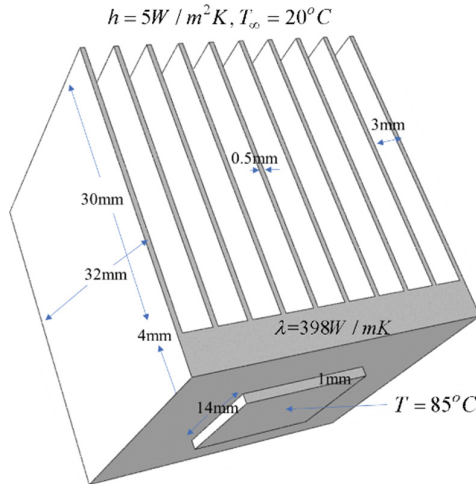

$$h = 5W \ / \ m^2 K, T_\infty = 20^o C$$

3mm

0.5mm

30mm

32mm

$$\lambda = 398W \ / \ mK$$

4mm

1mm

14mm

$$T = 85^o C$$

Fig. 3. Dimensions, material and boundary conditions of a heat radiator

Figure 5 is the contour plot of computed temperature and Table 1 lists the computed temperature at a few nodes along the central line of the middle blade of the radiator. For
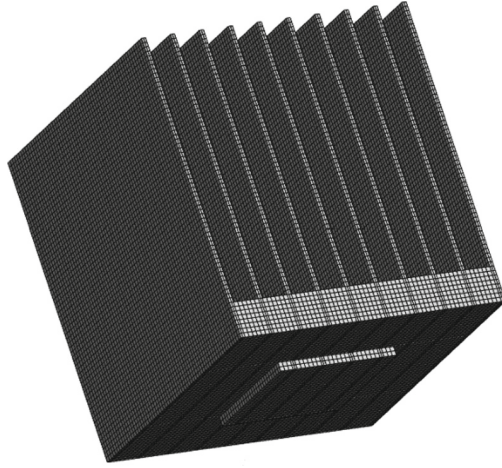
Fig. 4. Mesh connected by cross lines in CLM computation

comparison, the commercial software ABAQUS is also used to compute this problem with the same nodes as shown in Fig. 4.

From Fig. 5, it can be seen that the contour lines are very smooth over the whole radiator. This indicates that the computed results are stable. And from Table 1 it can be seen that the CLM results are in good agreement with ABAQUS. The maximum relative error is 1.32%. These indicate that the proposed method is correct and can simulate complicated 3D problems.
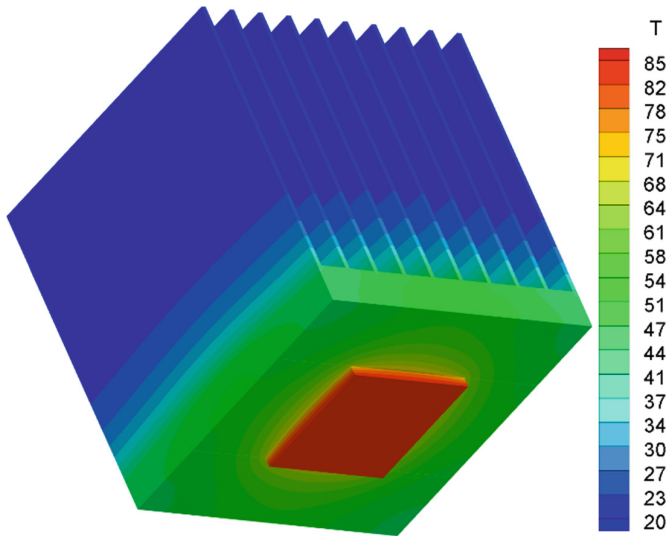
Fig. 5. Contour plot of computed temperature (°C)

Table 1. Comparison of temperatures

z	ABAQUS	CLM	Relative error (%)
−1	85.0000	85.0000	0.0000
2.5	73.0770	74.0396	1.3173
6	49.6425	49.2711	−0.7481
9.5	33.0269	32.8995	−0.3858
13	25.7559	25.7181	−0.1468
16.5	22.5575	22.5463	−0.0498
20	21.1427	21.1409	−0.0087
23.5	20.5149	20.5151	0.0009
27	20.2381	20.2388	0.0036
30.5	20.1222	20.1228	0.0032
34	20.0884	20.0889	0.0026

4   Conclusions

The following conclusions can be drawn for the proposed Cross-Line Method (CLM):

(1)   The use of CLM is similar to the mesh free method (MFM). The difference is that CLM works on crossed lines even for 2D and 3D problems, but MFM uses a cluster of scatter points.
(2)   High order cross lines used in CLM can be easily formed by surrounding nodes, and its shape functions can be directly constructed using the Lagrange interpolation formulation.
(3)   In this paper, only the first and second order spatial partial derivatives are derived analytically. However, higher order derivatives, if required, can be evaluated by recursively using the first-order one.
(4)   In CLM, all nodes surrounding the collocation node can have contribution to the final system of equations, while in the Lagrange elements of FEM as well as the algorithm in finite difference method, nodes only over two lines (in 2D) or 3 lines (in 3D) have contributions.
(5)   Although the heat conduction problem is taken as a research background in the paper, other engineering problems such as the mechanical and fluid mechanics problems can also be solved using CLM in the straightforward way, and with the help of using the zonal technique as in [17, 19], complicated large-scale problems can be easily simulated.

References

1. He, P.Q., Sun, Q., Liang, K.: Generalized modal element method: part-I—theory and its application to eight-node asymmetric and symmetric solid elements in linear analysis. Comput. Mech. **63**(4), 755–781 (2018). https://doi.org/10.1007/s00466-018-1618-1

2. He, P.Q., Sun, Q., Liang, K.: Generalized modal element method: part II—application to eight-node asymmetric and symmetric solid-shell elements in linear analysis. Comput. Mech. **63**(4), 783–804 (2018). https://doi.org/10.1007/s00466-018-1622-5

3. Gao, X.W., et al.: Element differential method for solving general heat conduction problems. Int. J. Heat Mass Transf. **115**, 882–894 (2017)

4. Lv, J., et al.: A new strong form technique for thermo-electro-mechanical behaviors of piezoelectric solids. Coatings **11**, 687 (2021). https://doi.org/10.3390/coatings11060687

5. Wen, P.H., Li, Y., Li, J.: Finite and infinite block Petrov-Galerkin method for cracks in functionally graded materials. Appl. Math. Model. **68**, 306–326 (2018)

6. Yang, J.J., Zheng, J.L., Wen, P.H.: Generalized method of fundamental solutions (GMFS) for boundary value problems. Eng. Anal. Bound. Elem. **94**, 25–33 (2018)

7. Gao, X.W., et al.: Element differential method and its application in thermal-mechanical problems. Int. J. Numer. Methods Eng. **113**(1), 82–108 (2018)

8. Wang, Z., et al.: Grinding temperature field prediction by meshless finite block method with double infinite element. Int. J. Mech. Sci. **153–154**, 131–142 (2019)

9. Wang, D.D., Wang, J.R., Wu, J.C.: Super convergent gradient smoothing meshfree collocation method. Comput. Methods Appl. Mech. Eng. **340**, 728–766 (2018)

10. Wang, L.H., Qian, Z.H.: A meshfree stabilized collocation method (SCM) based on reproducing kernel approximation. Comput. Methods Appl. Mech. Eng. **371**, 113303 (2020)

11. Qian, Z.H., et al.: An efficient meshfree gradient smoothing collocation method (GSCM) using reproducing kernel approximation. Comput. Methods Appl. Mech. Eng. **374**, 113573 (2021)

12. Wang, L.H.: Radial basis functions methods for boundary value problems: performance comparison. Eng. Anal. Bound. Elem. **84**, 191–205 (2017)

13. Gao, X.W., Gao, L.F., Zhang, Y.: Free element collocation method: a new method combining advantages of finite element and mesh free methods. Comput. Struct. **215**, 10–26 (2019)

14. Xu, B.B., Gao, X.W., Cui, M.: High precision simulation and analysis of non-Fourier heat transfer during laser processing. Int. J. Heat Mass Transf. **178**, 121574 (2021)

15. Lv, J., et al.: Fracture mechanics analysis of functionally graded materials using a mixed collocation element differential method. Eng. Fract. Mech. **244**(1), 107510 (2021)

16. Liu, H.Y., Gao, X.W.: An implicit free element method for simulation of compressible flow. Comput. Fluids **192**, 104276 (2019)

17. Jiang, W.W., Gao, X.W., Xu, B.B., Lv, J.: Analysis of piezoelectric problems using zonal free element method. Eng. Anal. Bound. Elem. **127**, 40–52 (2021)

18. Gao, X.W., Liang, Y., Xu, B.B.: Cross-line elements for free element method in thermal and mechanical analyses of functionally gradient materials. Eng. Anal. Bound. Elem. **108**(11), 422–437 (2019)

19. Gao, X.W., Liu, H.Y., Ruan, B.: Discontinuous zone free element method with variable condensation and applications in thermal-stress analysis of functionally graded material structures with cracks. Comput. Struct. **243**(15), 106411 (2021)

20. Gao, X.W.: Finite line method for solving general high-order partial differential equations. In: 2021 International Conference on Applied Mathematics, Modeling and Computer Simulation (AMMCS 2021), 13–14 November 2021, Wuhan, China (2021)

Vibration Analysis of Curved Panels and Shell Using Approximate Methods and Determination of Optimum Periodic Angle

Chitaranjan Pany[✉] [ORCID]

Vikram Sarabhai Space Centre, Trivandrum 695022, India
chitaranjan.pany@gmail.com

Abstract. The goal of this paper is to deduce the lowest free vibration frequency of a curved panel (cylindrical) simply supported edges (SSSS) correspondent to a range of circumferential subtended angles at the center and arriving at optimum angle. Beam functions modes and arbitrary triangular shallow shell finite element (FE) shape functions are used here as displacement functions. Thin shell theory used. Rayleigh-Ritz's approach is applied to get the solution. It is noticed that in a curved panel there is a distinct subtended angle, where the frequency is lowest. The same frequency is also the lowest in a full shell with axially simply supported ends. This distinct subtended angle is the optimum angle of the curved panel. Panel is called an optimum curved panel. The optimum angle for a curved SSSS panel is determined as well as the lowest frequencies for various a / R and h / R ratios. Optimal angles obtained for curved SSSS panels for a particular geometry are considered to find frequencies for various edge boundary conditions. Further, considering subtended angle of curved panel available in literature which is not optimum for a given geometry, natural frequencies are computed for different edge constraints and different modes (axial and circumferential). Frequencies from present FEM and beam functions modes are compared well with published data. These optimum curved panel (periodic/repeating cells of a complete cylindrical shell) frequencies are useful for comparing the bounding or cutoff frequencies and modes of the periodic shell structure (alike curved panels or cells joined an end-to-end or side-by-side) analysis.

Keywords: Optimum periodic angle · Optimum curved panel · Cylindrical shell · Free vibration · Lowest natural frequencies (LNF) · FEM · Beam function

1 Introduction

The structural module of aerospace, marine, and missile structures can be idealized as curved panels (single and multi-supported). Vibration and noise are key problems, which are experienced in various engineering structures. A periodic structure com-prises basically of a number of the alike structural module (repeating cells) that are joined together in one or two-dimensional array to form the complete/full structure [1, 2]. For a circular cylindrical shell, every repeating cell is a section of the shell between two consecutive nodal positions (Fig. 1).
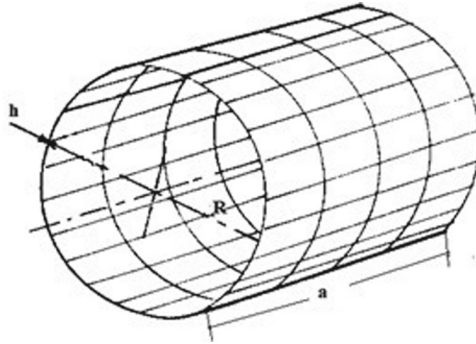
Fig. 1. Axial and circumferential nodal lines of a circular cylindrical shell

In [1], free vibration of two axially stiffened (forty four and sixty six stiffeners) cylindrically shells was performed using the exact solution of the differential equation, considering the structure as an assembly of curved panels as repeating cells. One of them, with forty four stiffeners, has been idealized as an assemblage of forty four curved panels, each subtending an angle at the center of any cross-section of $2\pi/44$ radians and the other with sixty six stiffeners idealized with cells subtending an angle of $2\pi/66$ radians. However, in each case, the geometry of the shell is identical. Shell vibration problem using the hierarchical finite element method(FEM)studied [2] for obtaining the dynamic characteristics with forty-four line-stiffened with identical shell dimension [1]. Fuzhen et al. [3] contributed vibration evaluation using the Jacobi-Ritz approach of sealed cylindrical containers. Zuocai et al. [4] studied frequency features, and responsiveness evaluation of a size-reliant laminated cylindrical nanoshell. Ghasemi and Mohandes [5] provided the differences in frequencies of the rotating fiber metallic laminated cylindrical shell due to different axial and circumferential wave numbers, a/R ratios, thicknesses, and volume fractions of metal. Laurent et al.[6] proposed a semi-analytical approach to analyze the dynamic (vibro-acoustic) conduct of submerged repeating (axisymmetric frames) stiffened cylindrical shells via the circumferential admittances technique and FEM. The impact of Bloch-Floquet conditions on waves and the support distance at the noise transmission is brought out. Hirwani et al. [7] studied the frequency responses considering nonlinearities of the laminated curved panels CFRP composite each numerically and experimentally. From the above research, it's determined that in past literature, the selection of the repeating cells has been random [1, 2] and lacks the optimum curved panel approach [1–7].

Free wave propagation in an unstiffened shell [8] and ring [9] studied using periodic structure concept considering an assembly of curved panel and curved beam respectively. Syed and Bishay [10] presented FE-based design method for periodic beam with geometry and material discontinuity, to aim at a particular wanted attenuation frequency band. Jisu et al. [11] presented the analytic method to envisage the wave transmission at joints linking two semi-infinite periodic reinforced plates subjected to an applied point external harmonic force using the Bloch-Floquet theory and fourier transform. In periodic supported beams, the lowest natural frequency (LNF) resembles to the lowest mode (m = 1) between any two supports vibrating with simply-supported ends. Similarly in

multi-span flat rectangular panels the LNF resembles to the minimum mode (m = 1 in length direction and $n_c = 1$ in the width direction) of any repeating cells vibrating with all sides simply supported (SSSS) [8]. Hence it emerges judicious for shell analysis to take the repeating cells that would correspond to the LNF with SSSS boundary conditions. An attempt has been made in earlier work to determine the optimum repeating or periodic cells [8, 9].

For a circular cylindrical shell with simply supported ends, the minimum radial vibration frequency resembles to the minimum axial mode (m = 1) but the circumferential mode number depends on the axial length (a) to radius (R) ratio and thickness (h) to radius (R) ratios of the shell [12]. Therefore, in this article, free vibration of a single curved panel, with SSSS boundary conditions for different (a/R) and (h/R) ratios are examined. Following Warburton's full-shell method [12], SSSS curved panels were analyzed in a range of circumferential subtended angles θ at center. Note that in a curved panel, there is a distinct subtended angle, where the frequency is lowest. The same frequency is also the lowest in a full shell with axially simply supported ends. This angle is called the optimal angle(θ_0) for the curved panel geometry. The curved panel is named as optimum curved panel (periodic curved panels/ repeating cells) for a given a/R and h/R ratios. This optimum or optimally curved panel should be used in case of periodic shell vibration. This aspect has not been discussed in the studies previously published by other researchers. This is a noteworthy observation of this paper and is very important for periodic shell vibration analysis. Fortran programs have been developed for the free vibration of curved plates/panels with various edge constraints for both (i) using characteristic beam function (BF) mode [12], and (ii) an arbitrary triangular shallow shell FE shape functions [14]. Frequencies are obtained from both programs are compared well with [1, 2]. These results are useful for comparing the cutoff frequencies of the propagation planes of periodic shell structures [1, 2].

2 Methodology

2.1 Free Vibration of Cylindrical shell WARBURTON'S [12] and Curved Panel

Cylindrical Shell:
Free vibration analysis of a cylindrical shell (Fig. 1) that simply supports the ends. The circumferential full waves and axial modes are N and m, respectively. The possible displacement functions in axial (u), circumferential (v), and radial (w) vibrations are:

$$u = \overline{A}_{mn} \quad \cos(N\theta)\cos\left(\frac{m\pi x}{a}\right) \quad e^{i\omega t}$$
$$v = \overline{B}_{mn} \quad \sin(N\theta)\sin\left(\frac{m\pi x}{a}\right) \quad e^{i\omega t} \tag{1}$$
$$w = \overline{C}_{mn} \quad \cos(N\theta)\sin\left(\frac{m\pi x}{a}\right) \quad e^{i\omega t}$$

The natural frequency of a cylindrical shell is a function of shell variables (a/R and h/R) and modes m and N. Using the displacement function of the Eq. (1) in the strain and kinetic energy expressions of Love-Timoshenko thin shell theory obtainable in [1]

in x, θ coordinates, a cubic equation of Δ derived [12] for natural frequency(Ω)in a Rayleigh-Ritz principle.The lowest root is for radial vibration.

Curved Panels

Figure 2 shows a cylindrical plate/panel that represents the length (a) in axial direction, radius (R),and subtended angle (θ₀). The displacement or deflection functions which meet the SSSS conditions exactly are:

$$u = \overline{A}_{mn} sin\,(\lambda_c\,\theta)\ cos(m\,\pi\,x/a)e^{i\omega t}$$
$$v = \overline{B}_{mn} cos(\lambda_c\,\theta)\ sin(m\,\pi\,x/a)e^{i\omega t} \qquad (2)$$
$$w = \overline{C}_{mn} sin(\lambda_c\,\theta)\ sin(m\,\pi\,x/a)e^{i\omega t}$$

where $\lambda_c = n_c\pi/\theta_0$; θ₀ is circumferential subtended angle of curved panel (Fig. 2); n_c and m are number of circumferential half waves and axial half waves respectively; b = Rθ₀ is curved length of panel. The deflection functions of Eq. (2) are used in the strain and kinetic energy expressions [1] and integrated with a limit from 0 to θ on curved panels instead of 0 to 2π in full shell [12]. Rayleigh-Ritz's principle is applied to get a cubic frequency equation in Δ. The lowest root corresponds to radial vibration. The natural frequencies are function of the shell parameters (a/R and h/R) and the modes (m,n_c). The frequency equation for curved panel is similar to shell of [12] as follows (Eq. 3).

$$\Delta^3 - P_2\Delta^2 + P_1\Delta - P_0 = 0 \qquad (3)$$

where P_0,P_1,and P_2 are constants. Dimensionless frequency equation is
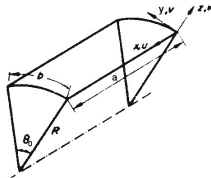
Fig. 2. Curved panel.

$$\Delta = \Omega^2 = \frac{\rho R^2\omega^2(1-\upsilon^2)}{E}$$

2.2   Free Vibration of Curved Panel in Dimensionless Co-ordinates

The strain and kinetic energy equations based on the Love Timoshenko theory of the cylindrical shell can be described in dimensionless (ξ = x/a, η = y/ Rθ) coordinates as follows.

$$
U = \frac{Ehab}{2R^2(1-v^2)} \int_0^1 \int_0^1
\begin{bmatrix}
C_1 u_{,\xi\xi}^2 + C_2 v_{,\eta\eta}^2 + C_3(2wv_{,\eta}) + w^2 + C_4(2u_{,\xi}v_\eta) + C_5(2wu_{,\xi}) + \\
C_6 v_{,\xi}^2 + C_7(2v_{,\xi}u_{,\eta}) + C_8 u_\eta^2 + C_9 w_{,\xi\xi}^2 + C_{10}w_{,\eta\eta}^2 - C_{11}(2w_{,\eta\eta}^2 v_\eta) \\
+ C_{12}v_{,\eta\eta}^2 + C_{13}(2w_{,\xi\xi}^2 w_{,\eta\eta}^2) - C_{14}(2w_{,\xi\xi}^2 v_\eta) + C_{15}w_{,\xi\eta}^2 \\
- C_{16}(2w_{,\xi\eta}^2 v_{,\xi}) + C_{17}v_{,\xi\xi}^2
\end{bmatrix} d\xi d\eta
\quad (4)
$$

$$
T = \frac{\rho hab}{2} \int_0^1 \int_0^1 (u_{,t}^2 + v_{,t}^2 + w_{,t}^2) d\xi \, d\eta
$$

where,

$$
C_1 = \frac{R^2}{a^2}, \quad C_2 = \frac{R^2}{b^2}, \quad C_3 = \frac{R}{b}, C_4 = v\frac{R^2}{ab}, \quad C_5 = v\frac{R}{a}, \quad C_6 = (1-v)\frac{R^2}{2a^2}
$$

$$
C_7 = (1-v)\frac{R^2}{2ab}; \quad C_8 = (1-v)\frac{R^2}{2b^2}; \quad C_9 = \beta\frac{R^4}{a^4}; \quad C_{10} = \beta\frac{R^4}{b^4}
$$

$$
C_1 = \beta\frac{R^3}{b^3}; \quad C_{12} = \beta\frac{R^2}{b^2}; C_{13} = v\frac{R^4}{a^2b^2}; C_{14} = v\beta\frac{R^3}{a^2b}; \quad C_{15} = 2(1-v)\beta\frac{R^4}{a^2b^2}
$$

$$
C_{16} = 2(1-v)\frac{R^3}{a^2b}; C_{17} = 2(1-v)\beta\frac{R^2}{a^2}; \beta = \frac{h^2}{12R^2}
$$

(A) Displacement Functions for a Curved Panel with SSSS Conditions

$$
U(\xi, \eta, t) = u(\xi, \eta)_e^{i\omega t}; \quad u = \sum_m \sum_n u_{mn} \cos(m\pi\xi)\sin(n\pi\eta)
$$

$$
V(\xi, \eta, t) = v(\xi, \eta)_e^{i\omega t}; \quad v = \sum_m \sum_n v_{mn} \sin(m\pi\xi)\cos n\pi\eta
\quad (5)
$$

$$
W(\xi, \eta, t) = w(\xi, \eta)_e^{i\omega t}; \quad w = \sum_m \sum_n w_{mn} \sin(m\pi\xi)\sin n\pi\eta
$$

(B) Displacement Functions for a Curved Panel with Curved Sides Clamped and Straight Sides Simple Supported(SCSC)

$$
U(\xi, \eta, t) = u(\xi, \eta)_e^{i\omega t}; \quad u = \sum_m \sum_n u_{mn}(\phi_{m,n})_{,\xi}\sin(n\pi\eta)
$$

$$
V(\xi, \eta, t) = v(\xi, \eta)_e^{i\omega t}; \quad v = \sum_m \sum_n v_{mn}\phi_{m,n}\cos n\pi\eta
\quad (6)
$$

$$
W(\xi, \eta, t) = w(\xi, \eta)_e^{i\omega t}; \quad w = \sum_m \sum_n w_{mn}\phi_{m,n}\sin n\pi\eta
$$

Using the displacement functions Eqs. (5 and 6) in the strain and kinetic energy expressions the stiffness and mass matrices of the curved panel have been derived using Rayleigh Ritz's method as follows.
$\frac{\partial\Omega^2}{\partial q} = 0$; $(q = u, v, w)$, one finds an eigenvalue problem(Eq. 7)

$$
\left([K] - \Omega^2[M]\right)\{q\} = \{0\}
\quad (7)
$$

The following equation of motion is obtained for non-trivial solutions of the coefficients qi (i = 1....3)

$$\det | [K] - \Omega^2 [M] | = \{0\} \tag{8}$$

Here (3 × 3) stiffness & mass matrices are obtained. The stiffness matrix and mass matrices are presented explicitly below for a four edges simply supported curved panel (SSSS) is:

$K_{11} = C_1 m^2 \pi^2 + C_8 n^2 \pi^2; \quad K_{12} = (C_4 + C_7) mn\pi^2; \quad K_{13} = C_5(-m\pi)$

$K_{22} = (C_2 + C_{12})n^2 \pi^2 + (C_6 + C_{17}) m^2 \pi^2; \quad K_{23} = C_3(-n\pi) - C_{11}(n\pi)^3 - (C_{14} + C_{16})nm^2 \pi^3$

$K_{33} = 1 + C_9 m^4 \pi^4 + C_{10} n^4 \pi^4 + 2(C_{13} + C_{15}) m^2 n^2 \pi^4$

$M_{11} = M_{22} = M_{33} = 1.0$

Similarly the stiffness and mass matrices for SCSC curved panel are as follows:

$K_{11} = C_1 F_4 + C_8 n^2 \pi^2 F_2; \quad K_{12} = (C_7 F_2 C_4 F_3) n\pi; \quad K_{13} = C_5 F_3$

$K_{22} = (C_2 + C_{12})n^2 \pi^2 F_1 + (C_6 + C_{17}) F_2; \quad K_{23} = C_3(n\pi) C_{11}(n\pi)^3 (C_{14}F_3 + C_{16}F_2)n\pi$

$K_{33} = (1 + C_{10} n^4 \pi^4) F_1 + C_9 F_4 + 2(C_{15}F_2 C_{13}F_3) n^2 \pi^2$

$M_{11} = F_2; \quad M_{22} = M_{33} = F_1$

$$F_1 = \int_0^1 \varphi_m \varphi_n d\xi; \quad F_2 = \int_0^1 (\varphi_m)_{,\xi} (\varphi_n)_{,\xi} d\xi; \quad F_3 = \int_0^1 (\varphi_m)_{,\xi\xi} (\varphi_n)_{,\xi} d\xi; \quad F_4 = \int_0^1 (\varphi_m)_{,\xi\xi} (\varphi_n)_{,\xi\xi} d\xi;$$

The functions ϕ_m, ϕ_n are given by [13]. Using values of m (axial half wave),$n = n_c$ (circumferential half wave) the dimensionless frequencies Ω are obtained from Eq. 8.

3   Finite Element Formulation for Free Vibration Analysis

3.1   Present Finite Element(FE) for Curved Panel

The basic shallow shell element used here is Cowper et al. [14]. The shallow shell finite element is the conforming higher order arbitrary triangular shaped with 12 degrees of freedom per node. The shallow shell is defined as a slightly curved plate/panel with a large minimum radius at any point compared to the maximum length measured along the central surface of the shell.

3.2   Equation of Motion

The governing equation of motion for undamped free vibrations in a small displacement elastic structural system can be expressed as:

$$[M] \left\{ \ddot{q} \right\} + [K] \{q\} = \{0\} \tag{9}$$

where, [K] is global stiffness matrices of the cylindrically curved panel
    [M] is global mass matrices of the cylindrically curved panel.

$\{\ddot{q}\}$ is global acceleration vectors and $\{q\}$ is the displacement vectors.

$$\{q\} = \{\overline{q}\}e^{i\omega t} \tag{10}$$

Putting Eq. (10) in Eq. (9), one can get

$$[\, [K] - \Omega^2 \, [M] \,]\{\overline{q}\} = \{0\} \tag{11}$$

$$\textit{Where, } \ \Omega^2 = \frac{\rho R^2 \omega^2 (1 - \upsilon^2)}{E} \tag{12}$$

Elements of the overall matrix of the expression shell structure Eq. 11 can be created by assembling the corresponding element matrix of shell elements. Details of the element stiffness matrix [14] and mass matrix [15] of the shell element are available elsewhere.

4   Results and Discussions

4.1   Free Vibration of Full Circular Cylindrical Shell, Single Curved Panel and Determination of Optimum Periodic Angle and Repeating Cells

Material properties and geometric data used to generate numerical results are taken from [1].The material is aluminum and has the following properties: E (Young's modulus) = 70 GPa, ν (Poisson's ratio) = 0.3, ρ(material density) = 2700 kg / m3.The geometric properties of curved panels and fully circular shells are axial length a = 0.135 m, shell and panel radius R = 0.381 m, and thickness h = 0.559 mm. For a cylindrical shell (Fig. 1), the minimum Ω corresponds to the minimum axial mode (m = 1), while the number of circumferential full-wave modes (N) depends on ratio of the axial length and shell radius [12]. Here following Warburton's [12] approach and taking the dimension of [1], showed the lowest Ω corresponds to m = 1, and N = 18 for radial vibration(Fig. 3). Next, a curved panel having the same a/R and h/R ratios with SSSS condition is taken. In Fig. 4, the natural Ω of this panel for a range of subtended angle is shown. This curve reveals that for a given a/R and h/R ratios, there prevails one subtended angle for which the natural Ω is lowest. The LNF of this curved panel is Ω = 0.2516 and it is the same as that of a full shell of the same (a/R, h/R) ratios. The corresponding subtended angle is π/18 rad (optimum periodic angle θ_0) and oscillating in first axial mode(m = 1) and circumferential modes(n_c = 1). This panel will be called the optimum periodic curved panel.This confirmed that θ_0 = π/18 rad is the periodic angle where the natural(fundamental) Ω is minimum. However, in reference [1, 2], the periodic subtended angles of curved plate are assumed to be (random) as π/22 radians and π/33 radians without logic.

Table 1 shows the different θ_0 of the curved SSSS panel or plate, for different m and n_c, where same lowest Ω should occur. Ω are determined for the various dimensionless circumferential angles (Fig. 5) of the curved plate using SSSS conditions for a range of axial half waves and circumferential half waves (n_c = 1 to 5).

Note that the natural Ω of a curved panel in a given set (a / R, h / R, m, and n_c) depends on the subtended angle θ_0 and has a minimum Ω where θ_0 is a minimum. The corresponding natural Ω is equal to the full shell LNF under radial vibration.
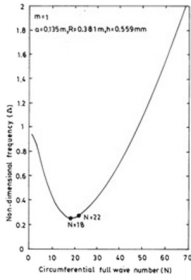
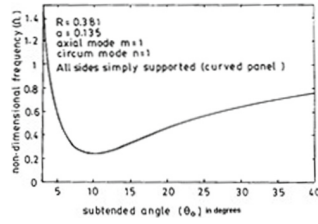**Fig. 3.** Free vibration (radial)Warburton curve

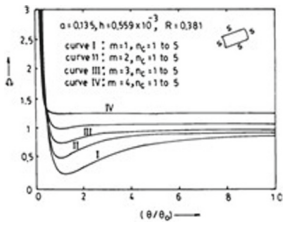**Fig. 4.** Dimensionless frequency versus sub-tended angle plot

Fig. 5. Dimensionless frequency (Ω) vs. dimensionless angle (θ/θ_0) for a range of m and n_c for a SSSS curved panel.

Table 1. The situation of identical lowest frequencies for different optimum subtended angle (θ_0) of curved SSSS panel, for different m and n_c.

m	n_c					Ω
	1	2	3	4	5	
1	10	20	30	40	50	0.2516
2	8	16	24	32	40	0.5036
3	8	16	24	32	40	0.7565
4	9	18	27	36	45	1.0078
5	15	30	45	60	75	1.2600

Figure 6a and 6b show the natural Ω for a range of a/R ratio for two values of (h/R) ratio. The Ω of the θ_0 at the center of a cross-section of SSSS curved panels for different a/R and h/R ratios are shown in Table 2. From this plot, it can be seen that as the a/R ratio increases, the lowest Ω decreases. And as h/R ratios increase the Ω and corresponding subtended angle (θ_0) increases for a given a/R ratio (Table 2). Also, for a particular pair of a / R and h / R ratios, the LNF corresponds to the lowest axial mode number m = 1, but the n_c is dependent on the a/R and h/R ratios.

Table 2. The optimum angle (θ_0 in degrees) and dimensionless frequencies (Ω) of curved panel with SSSS conditions with different h/R ratios and a range of a/R ratios.

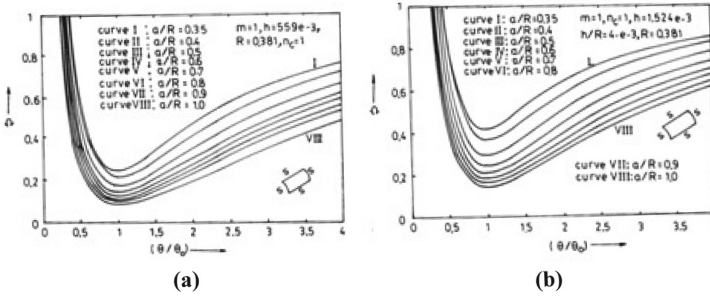| a/R→ h/R↓	0.354	0.5	0.6	0.7	0.8	0.9	1.0
1.467e-3	$\theta_0\rightarrow$ 10	11	12	13	14	15	15
	$\Omega\rightarrow$0.2516	0.1780	0.1481	0.1268	0.111	0.0988	0.0887
4.000e-3	$\theta_0\rightarrow$ 14	15	16	17	18	19	20
	$\Omega\rightarrow$0.414	0.292	0.243	0.208	0.182	0.161	0.145

Fig. 6. Dimensionless Ω-subtended angle of curved panel(a)h/R = 4.e-3 (b) h/R = 1.467e-3

4.2   Single Curved Panel Finite Element

To validate the finite element code of the current arbitrary triangular element with 12 degrees of freedom per node, the dimensions [1, 2] of the Mead and Bardell curved panels (repeating unit) are considered in the periodic subtended angle of $\pi/22$ radians. Convergence studies consider (4x4) meshes (Fig. 7).
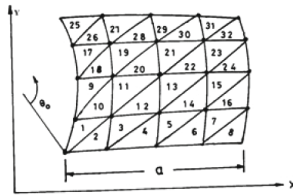

Fig. 7. Triangular element with 4×4 mesh

Free vibration frequencies of curved panel (Table 3), of various types of edge constraints such as SSSS, four edges clamped(CCCC), curved sides clamped with straight sides simply support(SCSC) and curved sides simply support with straight sides clamped(CSCS), are compared well with the [1, 2] for different m and n_c. The lowest Ω with this periodic angle $\pi/22$ rad is obtained of 0.2724. Then, the results of the free vibration Ω for different edge conditions of the same curved plate with the optimum periodic angle of $\pi/18$ are shown (Table 4). It turns out that the fundamental Ω is 0.2526, which corresponds to the SSSS condition. Therefore, there is a clear difference in Ω is seen of 0.2724 ($\pi/22$ rad, arbitrary selection of periodic angle) against 0.2526 ($\pi/18$ rad, optimum periodic angle). From the above discussion, it can conclude that the correct minimum $\Omega = 0.2526$ is missing if the selected θ_0 of the curved plate/panel is equal to $\pi/22$ rad [1].

Top values no parenthesis,current FEM;Top values in parenthesis,current BF; lower values [1, 2].

The frequencies values are shown in Table 3 are bounding or cutoff frequencies(different m and n_c) [8] of periodic shell structure [1, 2] corresponding to assume periodic angle of $\pi/22$ rad(not optimum).

Table 3. Curved panel frequencies with subtended angle θ (π/22)[1].

(m,n_c)	SSSS	SCSC	CSCS	CCCC
1,1	0.2724(0.2724)	0.3268(0.3318)	0.9521	0.9590
	0.2724	0.3238	0.9517	0.9574
2,1	0.5021(0.5046)	0.5538(0.5779)	0.9912	1.019
	0.5039	0.5575	0.9887	1.008
3,1	0.7560(0.7572)	0.8223(0.8283)	1.0785	1.1515
	0.7569	0.8229	1.0712	1.1164
1,2	0.8548(0.8534)	0.8676(0.8664)	1.3164	1.3718
	0.8556	0.8648	1.3164	1.3229
2,2	0.9661(0.9616)	1.012(1.0008)	1.4257	1.4606
	0.9636	0.9944	1.4164	1.4381

Table 4. Curved panel frequencies for optimum subtended angle θ_0 (π/18).

(m, n_c)	SSSS	SCSC	CSCS	CCCC
1,1	0.2526 (0.2516)	0.3340(0.3290)	0.8715	0.8788
2,1	0.5402(0.5412)	0.5891(0.5914)	0.9108	0.9388
1,2	0.5880(0.5854)	0.6023(0.6035)	0.9027	0.9164
2,2	0.7089(0.7062)	0.7622(0.7563)	1.0345	1.0764
3,1	0.7519(0.7864)	0.8296(0.8565)	0.9962	1.0642

Top values no parenthesis, current FEM; Top values in parenthesis, current BF.

The frequencies values are shown in Table 4 are bounding or cutoff frequencies [8] (different m and n_c) of periodic shell structure corresponding to optimum periodic angle of π/18 rad.

5   Conclusion

Free vibration of a full circular cylindrical shell with axially simply supported ends is performed using beam functions modes. Free vibration of a cylindrically curved panel is carried out using present beam functions modes [13] and FEM of [14] for different edge constraint. The frequencies of the curved panels are evaluated and found that the SSSS condition is the lowest and vibrating in the first axial and first circumferential mode. The natural frequency (Ω) of the full shell with axially simply supported ends are correlated with the frequency (Ω) of SSSS condition single curved panel with the various subtended angles at the center of cross-section and considering same geometry as that of the full shell (a/R and h/R ratios). Note that the natural frequency(Ω)of a curved panel depend on the subtended angle θ for a given set (a/R, h/R, m, and n_c) and has the lowest value of θ_0 (optimum angle) for which the natural Ω is lowest for SSSS condition. The θ_0 is equal to π/18 radians and oscillating in m = 1 and n_c = 1(Ω = 0.2516). The same natural Ω is also the lowest of the full shell with the same a/R and h/R ratio vibrating radially (m = 1 and N = 18). The curved panel corresponding to θ_0 optimum periodic angle is called the optimum periodic curved panel(optimum curved panel). The lowest Ω for the optimum curved panel is found out for a range of a/R and h/R ratios. It is seen that as the a/R ratio increases, the lowest Ω decreases. And as h/R ratios increase the Ω

and θ_0 increases for a given a/R ratio. It is also visualized that for a given pair of a/R and h/R ratios the LNF has axial mode m = 1 but the n_c depends on a/R, h/R. In earlier published works by other researchers, this aspect is not discussed. Because the periodic angle of curved panel is considered random of $\pi/22$ and $\pi/33$ radians [1, 2] in place of $\pi/18$ for the same geometry. This is the noteworthy finding of this article which is essential for periodic shell vibration study.

The natural frequency (Ω) for the curved panels using the current FEM code and beam functions with different edge boundary conditions is presented. The bounding modes (different m and n_c) and frequencies (Ω) obtained for the periodic shell structure [1, 2] with assumed periodic curved panel angle $\pi/22$ rad[1, 2] are compared closely. The minimum frequency (Ω) using this periodic angle $\pi/22$ rad is 0.2724. Finally, the natural Ω results for different edge boundary conditions of a curved panel with the optimum periodic angle θ_0 of $\pi/18$ are presented. The minimum (first mode of m and n_c) Ω is found of 0.2526 corresponding to SSSS conditions. So there is a distinct difference in Ω is seen of $\Omega = 0.2724$ ($\pi/22$ rad, random) against $\Omega = 0.2526$ ($\pi/18$ rad, optimum). From the above discussion, it can conclude that the correct lowest (fundamental) Ω of 0.2526 is missing if the selected periodic angle of the curved plate or panel is equal to $\pi/22$ rad[1] for this particular geometry. This is the significant outcome of this paper.

References

1. Mead, D.J., Bardell, N.S.: Free vibration of thin cylindrical shells with discrete axial stiffeners. J. Sound Vib. **111**(2), 229–250 (1986)
2. Bardell, N.S., Mead, D.J.: Free vibration of an orthogonally stiffened cylindrical shell. Part I: discrete line simple supports. J. Sound Vibr. **134**(1), 29–54(1989)
3. Fuzhen, P., et al.: Free and forced vibration analysis of airtight cylindrical vessels with doubly curved shells of revolution by using Jacobi-Ritz method. Shock. Vib. **20**, 4538540 (2017)
4. Zuocai, D.: Frequency characteristics and sensitivity analysis of a size-dependent laminated nanoshell. Adv. Nano Res. **10**(2), 175–189 (2021)
5. Ghasemi, A.R., Mohandes, M.: Free vibration analysis of rotating fiber–metal laminate circular cylindrical shells. J. Sandwich Struct. Mater. **21**(3), 1009–1031 (2019)
6. Laurent, M., et al.: Noise radiated from a periodically stiffened cylindrical shell excited by a turbulent boundary layer. J. Sound Vibr. **466**(3), 115016(2020)
7. Hirwani, C.K., et al.: Nonlinear free vibration analysis of laminated carbon/epoxy curved panels. Def. Sci. J. **67**(2), 207–218 (2017)
8. Pany, C., et al.: Study of circumferential wave propagation in an unstiffened circular cylindrical shell using periodic structure theory. J. Inst. Eng. India, IE (I)-AS, **80**, 18–24(1999). Scopus Paper ID (EID:2-s2.0–0012562212)
9. Pany, C., Parthan, S.: Free vibration analysis of multi-span curved beam and circular ring using periodic structure concept. J. Inst. Eng. India, IE (I)-AS,83, 18–24 (2002). Scopus paper ID (EID: 2-s2.0–0036589014)
10. Syed, M., Bishay, P.L.: Analysis and design of periodic beams for vibration attenuation. J. Vib. Control **25**(1), 228–239 (2019)
11. Jisu, J., et al.: Wave transmission and vibration response in periodically stiffened plates using a free wave approach. J. Acoust. Soc. Am. **149**, 3694 (2021)
12. Warburton, G.B.: Dynamical Behaviour of Structures, 2nd edn. Pergamon Press, Great Britain (1976)

13. Bishop, R.E.D., Johnson, D.C.: The Mechanics of Vibration. Cambridge University Press, Cambridge (1966)
14. Cowper, G.R., et al.: A shallow shell finite element of triangular shape. Int. J. Solids Struct. **6**, 1133–1156 (1970)
15. Sinha, G., Mukhopadhyay, M.: Finite element free vibration analysis of stiffened shells. J. Sound Vib. **171**(4), 529–548 (1994)

Fast Fracture of Conic Shell Under the Action of Belt Explosive Charge

Holm Altenbach[1], Dmytro Breslavsky[2(✉)], Marina Chernobryvko[2,3], Alyona Senko[2], and Oksana Tatarinova[2]

[1] Otto-von-Guericke-University, Magdeburg, Germany
[2] National Technical University "Kharkiv Polytechnic Institute", Kharkiv, Ukraine
`Dmytro.Breslavsky@kpi.kharkov.ua`
[3] National Academy of Science of Ukraine, Podgorny Institute for Mechanical Engineering, Kharkiv, Ukraine

Abstract. Fracture of a thin-walled conic aluminium shell under the action of the belt explosive charge is analyzed numerically. Initial stress-strain state of the shell is determined by using shell finite elements. This state is used as initial conditions of the band, which is cut from the shell along generating lines. 2D initial-boundary value problem of the band plastic deformation is solved by FEM. Constitutive equations include flow rule with respect to the rates of inelastic deformation as well as kinetic equation for a damage parameter. The finite element simulation determines the place and time of the macrodefect onset. Refining of the finite element mesh with extraction of the fractured parts was performed in order to calculate the time of the crack growth. A new mathematical model and the developed software for the crack growth description are presented. The verification of the suggested method is performed via comparison of the numerical results with the experimental curves of explosive deformation and the results obtained by the simulations in ANSYS software.

Keywords: Thin-walled conic aluminum shell · Belt explosive charge · Damage kinetic equation · Stress-strain state of the shell · Finite element method

1 Introduction

Mathematical modeling of the structural fracture under the action of the explosive loads is the complex part of the nonlinear continuum mechanics. Studies devoted to these problems are reviewed in [1, 2] among others. These problems differ essentially from the traditional formulations of the elastic-plastic structure behavior. They are formulated as initial-boundary value problems, describing the crack growth and the structure stress redistribution in time. Joint application of viscoplasticity theory [2] and fracture mechanics [3] is effective tool to describe time-dependent nonlinear deformation at complex stress-strain state. The formulation of the initial value problem allows obtaining the time dependence of the plastic deformation and fracture.

Numerical methods, among which are finite difference methods (FDM) and finite element method (FEM), are used to solve the above-mentioned nonlinear problems [2].

Deformation of thin-walled structures under the action of the explosive loads is studied in [4, 5]. The elastoplastic strains in shells were analyzed by use both analytical methods and FEM. The constitutive equations for the description of time-dependent plasticity, which can be used in finite element analysis, were discussed by Cristescu [1].

Inelastic deformation with high stresses at short time can result the fracture of structures. Analysis of fracture under the action of impact and explosive loading using FEM is implemented in LS DYNA software [6]. FEM is applied effectively to predict strains growth in containment vessels [4]. In order to simulate the fast fracture processes, the simplified models, which are based on the deformation criterion, are used in the LS DYNA software. The continuum damage mechanics (CDM), which is based on the papers of L. Kachanov and Y. Rabotnov discussed in [7–9], is developed intensively in last decades. The CDM approaches can be applied effectively to solve the problems of an explosive and an impact loading, in which damage accumulation is preferably ductile. A reviews of computational models and constitutive equations for ductile damage and fracture are presented in [8, 10, 11].

However, the time and location of macrodefect nucleation, determined by CDM use, cannot be considered as final fracture in many cases. In this moment, the macrodefect (crack) is initiated. Initially, CDM approaches and fracture mechanics were combined with finite element simulations in creep theory. An approach, in which the destroyed element is excluded from the model, is presented in [12]. This approach allow representing the changes both in the stiffness and in the boundary conditions. The elimination of the finite elements having critical values of the damage parameters is performed. Afterwards, the solution of the considered problem with new geometry is continued.

In the present paper, the above-treated approach is applied to determine time and fracture pattern of the launcher fairing under the action of the belt explosive charge. The initial stress state in the conic shell under the action of the explosive pressure is calculated. The obtained stress state is used for the boundary conditions of the shell segment. Therefore, 2D inelastic stress state is computed with subsequent elimination of the fractured elements and the fracture time of the shell is determined. The obtained results are compared with 3D ANSYS LS Dyna modelling with Cowper-Symonds strain rate model [13]. The approach and details of such simulation are presented in [14]. The presented approach permits to reduce the time of the numerical calculations due to use of 2D finite elements as well as applying the simplified quasi-static model with damage consideration.

2 Numerical Simulation of Stress-Strain State Localization in Conic Shell

The fairing is used to protect a spacecraft from a flow. It is thrown down, when atmosphere has been passed through. The division of the fairing into two parts along the longitudinal direction is performed by the belt explosive charge operation. This division is necessary due to the technical specification to safety of the launcher equipment. The shape of this macrodefect and its localization are imposed.

The truncated cone, which is the central part of the fairing, is considered. The length of the generating line and diameters of the cone are l = 1.6 m, d_1 = 0.68 m and d_2 =

0.4 m. The shell thickness is h = 0.004 m. Internal pressure is applied on the narrow band with width 0.003 m along the generating line. The material of the shell is aluminum alloy closest to 24ST4 with the yield stress $\sigma_y = 240$ MPa, ultimate tensile strength σ_U = 345 MPa. The loading program was implemented with linear rising of pressure during 10 μs up to 231 MPa. This value were kept up during rest 90 μs.

The simulation of the shell plastic deformation up to fracture is performed by FE software ANSYS. The shell is meshed on four layers of the finite elements SOLID164 across the thickness (Fig. 1 a, arrow 1). The belt charge is arranged along the cone generating line, which is shown here by arrow 2.

The Cowper-Symonds model [6, 13] describes high rate plastic behavior. The shell fracture is simulated by removing elements, in which von Mises plastic strains reach their limiting value $\varepsilon_{lim} = 0.08$. The choice of the fracture criterion based on the maximal plastic strains is determined by the results of experimental analysis [14]. It was suggested, that fracture of the shell occurs, when all elements across thickness and along the generatrix are destroyed.

FEM data are presented in Fig. 1b, where the strain-fracture map is shown at t = 75 μs. This time can be considered as the instant of full fracture of the shell.

As follows from 3D simulation, it is possible to use 2D formulation of the problem in the local region close to the stressed part of the shell. Its remaining part deforms elastically. Let us note, that 3D calculation for thin long shell are time-consuming due to the large number of finite elements in the mesh. Furthermore, the dynamic calculations use small time step for solution convergence. The technique, which use 2D problem formulation, is considered below in order to perform the calculations during the design of the launcher fairing.

a)   b)
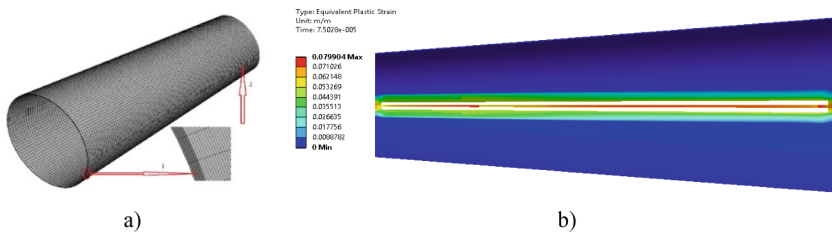
Fig. 1. 3D modelling of a shell. a) FE mesh; arrow 1: mesh across the thickness; arrow 2: the place of the belt charge, b) equivalent plastic strains at t = 75 μs

3   Stress-Strain State of Conic Shell Under the Action of Impact Pressure

In order to consider the launcher fairing a thin conic shell model, which is a approximation of the nonlinear theory of thin shells (see, for example, [15–18], is used. The Donnel-Mushtari-Vlasov shell theory [19] is used for moderate deflections. The strains and the displacements for conic shell satisfy the following equations:

$$\varepsilon_{ij} = e^l_{ij} + e^n_{ij} + z\chi_{ij}; \; e^l_{11} = \frac{\partial u}{\partial s}; \; e^l_{22} = \frac{\partial v}{r\partial s} + \frac{u}{r}\cos\alpha + \frac{w}{r}\sin\alpha; \; e^l_{12} = \frac{\partial u}{r\partial\beta} + \frac{\partial v}{\partial s} - \frac{v}{r}\cos\alpha$$

$$e^n_{11} = \frac{1}{2}\left(\frac{\partial w}{\partial s}\right)^2; \; e^n_{22} = \frac{1}{2r^2}\left(\frac{\partial w}{\partial\beta}\right)^2; \; e^n_{12} = \frac{1}{2r}\left(\frac{\partial w}{\partial s}\frac{\partial w}{\partial\beta}\right); \; \chi_{11} = -\frac{\partial^2 w}{\partial s^2}; \; \chi_{22} = -\frac{\partial^2 w}{r^2\partial\beta^2} \quad (1)$$

$$-\frac{\cos\alpha}{r}\frac{\partial w}{\partial s} + \frac{\sin\alpha}{r^2}\frac{\partial v}{\partial\alpha}; \; \chi_{12} = -2\frac{\partial^2 w}{r\partial s\partial\beta} + 2\frac{\partial w}{r^2\partial\beta}\cos\alpha - 2\frac{v}{r^2}\sin\alpha\cos\alpha + \frac{\partial v}{\partial s}\frac{\sin\alpha}{r},$$

where u, v, w are components of the middle surface displacement vector; e^l, e^n are linear and nonlinear components of the middle surface strains, this decomposition is necessary for use in numerical method; χ consists of curvature deviations and torsion components; β and s are coordinates of the middle surface and z is normal to it.

The variational formulation is used. The variation of the strain energy and variation of the forces satisfy the equation:

$$\int_S \left(b_{ijkl}\varepsilon^m_{kl}\delta\varepsilon^m_{ij} - d_{ijkl}\chi^m_{kl}\delta\chi^m_{ij}\right)dS - \int_S \left(P + \rho\frac{\partial^2 w}{\partial t^2}\right)\delta w\, dS = 0; \; \varepsilon^m_{ij} = e^l_{ij} + e^n_{ij} \quad (2)$$

where P is normal pressure; b_{ijkl}, d_{ijkl} are elastic constants; S is middle surface area. Elasto-plastic material is described by the Prandtl-Reuss equations [7, 20]:

$$\sigma_{ij} = b_{ijkl}\left(\varepsilon_{ij} - \varepsilon^p_{ij}\right); \; f(\sigma_{ij}) = \frac{3}{2}s_{ij}s_{ij} - \left(\varepsilon^p_{vM}\right)^2; \; \varepsilon^p_{vM} = \Phi\left(\int d\overline{p}\right); \; d\varepsilon_{ij} = \frac{3}{2}\frac{d\overline{p}}{\sigma_{vM}}s_{ij} \quad (3)$$

where $\varepsilon^p_{ij\,j}$ are components of plastic strain tensor; ε_{vM} and σ_{vM} are von Mises equivalent strain and stress; s_{ij} are components of stress tensor deviator; $\overline{p}$ is Odqvist parameter.

The finite element method (FEM) is applied. The quadnode element of thin conic shell with 7 degrees-of-freedom (three displacements and four their derivatives) is used. The method described in [21, 22] is used.

The initial stress-strain state calculations are performed for the quasi-static formulation. The shell calculations were done for different values of the pressure acting on the narrow band with the width 0.003 m. Figure 2 shows the field of the von Mises stress on the middle surface (internal pressure 31.25 MPa). As follows from this figure, the maximum values of stresses take place in the loaded part of the band and the region adjacent to this part. This conclusion coincides with the results of 3D modelling.

4 Flow Rule and Damage Equation

The data of the experimental analysis of the explosive expansion of thin rings, which are made from duralumin 24ST4, are presented in [23]. The experimental dependences of the rings hoop strains on time are studied for different values of the strain rate.

The approach, which account the dependence of the irreversible plastic strains on time, is used to obtain the constitutive equation [1, 2]. The deformation process of

isotropic solid is considered, so the curves from [23] are described by the flow rule with strain hardening law (4) [7].

$$\dot{\varepsilon}_{ij}^{p}\left(\varepsilon_{vM}^{p}\right)^{\alpha} = \frac{3}{2}B\sigma_{vM}^{m-1}s_{ij} \tag{4}$$

where ε_{vM}^{p} is von Mises equivalent strain; B, m, α are constants, which are calculated from experiments. The obtained strains are limited by the maximal rupture strain ε_{lim}.
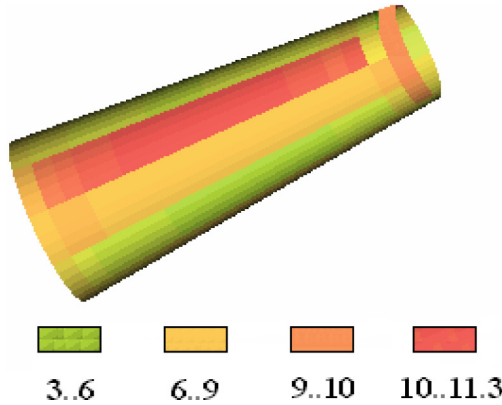

Fig. 2. Von Mises equivalent stress in the conic shell, MPa

The results of the experimental analysis from [23] are used to obtain the constants including in Eq. (4). The time dependences of strains for the rings with the radiuses 81.5; 54.5 mm and the strains rates 3400, 2300 and 1680 1/s are used. The time interval 50 μs, when the strains of the ring are increased, is considered. The results of the ring explosive deformation are shown in Fig. 3 by dots. Curve 1 (▲) conforms to $R = 81.5$ mm and initial stain rate $\dot{\varepsilon}_{ij}^{n} = 3400$ 1/s. Curve 2 (♦): $R = 54.5$ mm, $\dot{\varepsilon}_{ij}^{n} = 2300$ 1/s.

The stress state of the ring is determined in [23] from the ordinary differential equation describes the symmetric expansion of the ring. Obtained solutions are used to calculate the hoop stresses at different time instants. The following values of constants for Eq. (4) were obtained: B = 9.67605·10⁻¹⁷ (MPa)⁻¹/μ s, m = 8.89657, α = 0.125. The calculated by use of Eq. (4) strain curves are shown in Fig. 3 by small squares. As follows from this Figure, the obtained results and the experimental data are close, the maximal relative difference does not exceed 14%.

The loading of the structure results in accumulation of the hidden damage. Jermolaj [24] obtains the experimental data on the fracture of the aluminum alloy with the similar composition at biaxial stress state. These data allow to simulate the mechanism of damage accumulation by use of the following kinetic equation:

$$\frac{d\omega}{dt} = \frac{1}{(k+1)}\exp(p_1\sigma_e + p_2)\left(1-\omega\right)^{-k}, \quad \omega(0) = 0, \ \omega(t_*) = \omega_{lim}, \tag{5}$$

where t_* is time of hidden damage finishing and macrodefect's initiation; ω, ω_{lim} is damage parameter and its critical value for finishing the hidden damage, $\omega_{lim} \leq 1$.

Following Jermolaj [24], $\sigma_e = \chi(\tau_{okt} - \sigma_1) + \sigma_1$, [7], where τ_{oct} is octahedral shear stress; σ_1 is maximal principal stress. The parameters of the Eq. (5) take the following values: $p_1 = -0.121$, $p_2 = 397.5$ MPa, $\chi = 0.086$; $k = 16.67$. The obtained results were compared with the experimental data of combined loaded pipes.

Therefore, two processes in solid (the strain increase up to ε_{lim} and the damage accumulation up to its critical value ω_{lim}) are treated in the problem of the shell fracture.

5   Solution of Damage-Fracture Plane Stress Problem

The nonstationary stress-strain state near the place of action of the belt explosive charge is analyzed. For this aim, the shallow shell is cut out from the structure along its generatix. The length of this shallow band is equal to the length of the generating line and the width is varied in order to analyze its influence on the stress-strain state. Small curvature of this shallow shell is neglected. As a result, the rectangle is obtained (Fig. 4). Here, for clarity, we present the net with small number of finite elements.
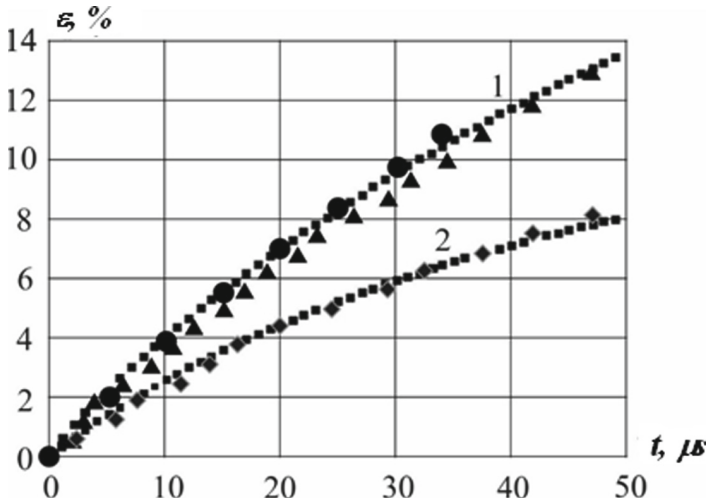
Fig. 3. The dependences of strains on time at explosive loading

The method for analysis of the band fracture is presented in this Section 2D problem is solved numerically. The constitutive Eqs. (4) and (5) are included to the system (1)-(3). The combination of FEM and prediction-corrector difference method for the time integration is used. This approach is implemented in the developed software [12, 21].

The problem is solved in quasi-static formulation. The FE mesh with a large number of nodes is chosen after studying of data convergence. If the damage parameter reaches critical value $\omega = \omega_{lim}$ in some finite element, then the element is eliminated and the new configuration of the solid is obtained. The fractured finite element and its nodes are removed from the mesh. The reconstructions of the stiffness matrix and vector of nodal forces are performed. If it is necessary, the new formulation of the boundary conditions
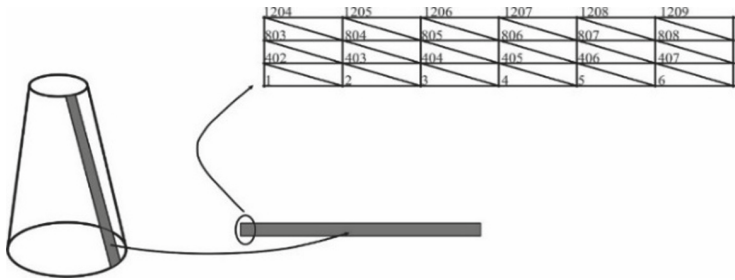
Fig. 4. Maximally loaded part of shell

with respect to the stresses and the displacements is performed. The numerical simulation of deformation with accounting for damage is continued up to the finishing of hidden damage of another element. The process stops, when damage parameters reach their critical value in all finite elements on the generating line of the shell. Thus, the cutting of the shell is observed.

6 Numerical Simulation of Damage and Fracture in Rectangular Area. Results and Discussion

The verification analysis in order to determine the possibility of the use of constitutive equations and software for simulation of the structure fracture is performed at first. The deformation of the planar specimen made from duralumin 24ST4 with length 50 mm and width 5 mm is considered. Its left edge is clamped, the constant tensile stress is applied to the second. The dependences of the strains on time are obtained using the Eq. (4) based on the experimental data. The same data are obtained by the 2D calculations. The results are close, the differences do not exceed 8%. The symbols "•" (Fig. 3) show the data of the FE simulations with the conditions described by the curve 1 and $\dot{\varepsilon}_{ij}^{n} = 3400$ 1/s.

The deformation and fracture of the rectangular band, which is cut along the shell generating line (Fig. 4), are considered further. The half of the band is analyzed due to its symmetry and the boundary conditions. The length of the region is equal to 1600 mm and its width is varied. The tensile loads are set on three edges of the region. Their numerical values are determined from the stress-strain state of the shell, which is discussed in Sect. 2. In the beginning, the width of the region and its finite element mesh are selected. The choice of mesh was done according to the character of stress varying in the band in consideration. The following values of width were analyzed: 5, 7 and 9 mm. The width of the region is equal to 7 mm and mesh with 6000 elements were chosen.

Six cases are solved numerically. The cases 1–4 are solved with the constant pressure acting on the band. The cases 5 and 6 are defined by the linear increase of the pressure from the initial value 31.25 MPa during 10 and 1 μ s. Then this pressure remains constant up to fracture. The stopping criterion of the analysis is the complete fracture of the shell band along its length or absence of fracture during preset time. Figure 5 shows the dependence of the loading on time for the cases 1–6. The curves 1–4 correlate with the constant pressures P_i (i = 1...4), which has the values 31.25, 62.5, 93.75 and 125 MPa,

respectively. Curve 5 describes increase of the pressure P_5 during 10 μs up to 231 MPa. Curve 6 describes the increase of the pressure P_6 during 1 μs up to 231 MPa. The points show the fracture times. As follows from the calculation, the band pressures 31.25 MPa and 62.5 MPa (curves 1 and 2) do not result in fracture during 20 μs. If P_2 acts on the structure, the accumulation of the hidden damage is finished at 11 μs. The crack is increased on 22.3 μs. The structure is fractured at $t_2 = 206.81$ μs. If $P_3 = 93.75$ MPa acts on the structure, it is fractured at $t_3 = 6.38$ μs. If $P_4 = 125$ MPa acts on the structure, it is fractured at $t_4 = 3.95$ μs. The applications of the pressures P_5 and P_6 result in fractures at times instants $t_5 = 9.38$ μs and $t_6 = 5.35$ μs, respectively.

In all considered cases, the finishing of the hidden damage accumulation and crack growth are observed in the regions of the maximum equivalent stresses, which is spaced close to the shell less diameter. The loading of the structure in the cases 3–6 results in fracture along the shell generating line. Let us note that the character of the fractures differs in different cases. Figure 6 shows the view of the band under the action of P_4 before finishing the fracture at $t_4 = 3.95$ μs. The distribution of the damage parameter, which is localized near the crack, is shown in Fig. 6, a. Moreover, two small transverse cracks are arisen besides this longitudinal one (Fig. 6, b). If the pressure P_3 acts on structure, such transverse cracks are not arisen. In this case, only longitudinal crack is expanded.
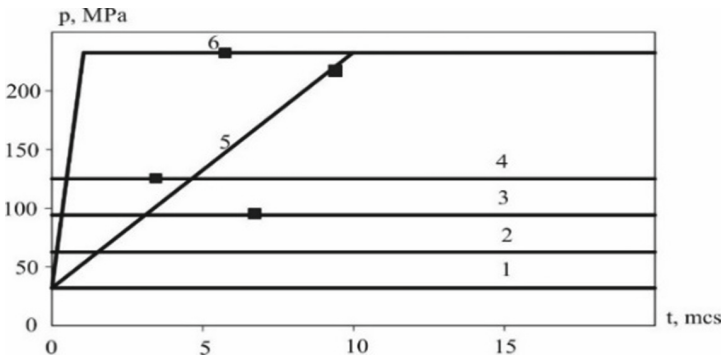
Fig. 5. The dependences of the explosive pressure on time and fracture times

Let us analyze the fracture under the action of P_5 and P_6, when the values of pressure are increased linearly in time at the first stage. Then the values remain constant. As follows from the comparison of the simulations under the action of P_3, P_4, P_5, if the pressures increase linearly, the fracture time is higher in comparison with the cases with constant pressures. This can be explained by different rates of the damage accumulation. As follows from the damage Eq. (5), this rate is determined by the values of the stresses.

As follows from Fig. 5 the final fracture under the action of P_5 is observed at time $t_5 = 9.38$ μs. In this case, the maximum value of the pressure 231 MPa is not reached. If the increase of the pressure P_6 is gone during 1 μs, the final fracture is observed faster, then in the structure under the action of P_5.
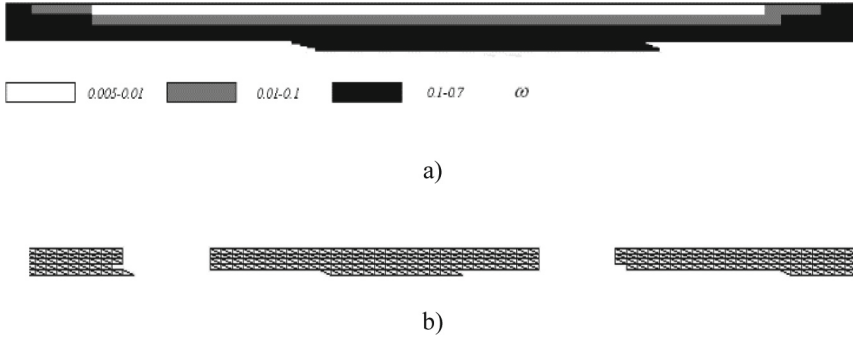
Fig. 6. The band fracture under the action of P_4 at t = 3.95 μs; a) distribution of the damage parameter ω near the crack; b) FE mesh after fracture of band

The shape of the band is analyzed at the time prior to the final fracture at the whole length. As an example, the shape of the shell detail under the action of P_6 *is* shown in Fig. 7. Due to significantly higher values of the pressure (P_4 and P_6), the growth of the damage is observed not only in the middle of the band. Therefore, the new directions of macrodefect growth are induced.

Fig. 7. The detail of shape of macrodefect before fracture of the structure under the action of P_6

In spite of high value of the pressure acting on the structure, the strains do not have time to growth and they remain small due to small time of the loading and fast accumulation of damage. The von Mises strains do not exceed 1% at all considered cases. This allow us to use approach with small strains.

Comparison of results, which were obtained by use of ANSYS and developed software, shows their qualitative agreement. The action of analyzed in two simulations pressure P_5 leads to total fracture of the band in both cases at necessary time. Additional use of damage equation allows us to consider the influence of the hidden damage accumulation that is neglected in ANSYS simulations. That is why the time of finishing the crack growth process is much faster in the case of the damage consideration.

7 Conclusions

The new approach for calculation the time of the crack propagation and its shape is presented. The crack is initiated due to the operation of the belt explosive charge along the generating line of the shell. The main idea of the suggested approach is the following. The parameters of the state equations are identified from the experimental data of the explosive high rate deformation of rings and pipes at complex stress-strain state. Then the numerical simulations of the damage accumulation and crack growth are performed.

Classical formulation of long-term deformation with account of material damage is supplemented by the algorithms of mesh refining and reformulation the boundary problem after exclusion of finite elements from the FE model. The first stage of a method is numerical simulation of the stress-strain state of the conic shell under the action of the belt explosive charge using FEM. On the second stage, the band, which is cutout from the conic shell, is analyzed by using 2D stress-strain state formulation. The small curvature of the band is not accounted. The stresses, which are obtained on the first stage from the shell model, are considered as a band traction.

The following conclusion can be made from the calculations. The difference between the time of the final fracture and the time of the hidden damage accumulation is in inverse proportion to the equivalent stresses. For example, the time of the hidden damage under the action of P_2 is $10.64\,\mu$s and the time of final fracture is $t_2 = 206.81\,\mu$s. If P_4 acts, the time of the hidden damage is $3.76\,\mu$s and the time of the final fracture is $t_4 = 3.91\,\mu$s. Thus, in the case of large values of pressure, which are widespread in practice, and if there is no need to analyze the shape of the macrodefect, the approximate time of the final fracture can be equated to the time of the hidden damage. The calculation of the time of the damage accumulation does not require complex algorithms and huge time for the simulation.

The suggested approach allows analyzing the fracture of the conic shell in time and the shape of the obtained crack. Because of the numerical simulations, it is obtained, that some cases the meridian crack is kinked in the circumferential direction of the conic shell.

References

1. Cristescu, N.: Dynamic Plasticity. North Holland, Amsterdam (2004)
2. Simo, J.C., Hughes, T.J.R.: Computational inelasticity. In: Interdisciplinary Applied Mathematics 7. Springer, Cham (1998). https://doi.org/10.1007/0-387-22763-6_8
3. Erdogan, E.: Fracture mechanics. Int. J. Solids Struct. **37**, 171–183 (2000)
4. Duffey, T.A., Romero, C.: Strain growth in spherical explosive chambers subjected to internal blast loading. Int J Imp Eng **28**, 967–983 (2003)
5. Ma, L., Hu, Y., Zheng, J.Y., Deng, G.D., Chen, Y.: Failure analysis for cylindrical explosion containment vessels. Eng Fail Anal **17**, 1221–1229 (2010)
6. Hallquist, J.: LS–Dyna theory manual: LSTC (Livermore Software Technology Corporation) (2018)
7. Lemaitre, J., Chaboche, J.L.: Mechanics of Solid Materials. Cambridge University Press, Cambridge (1994)
8. Naumenko, K., Altenbach, H.: Modeling high temperature materials behavior for structural analysis. Part I: continuum mechanics foundations and constitutive models. Adv. Struct. Mater. **28.** Springer, Cham (2016) https://doi.org/10.1007/978-3-319-31629-1
9. Altenbach, H., Eisenträger, J.: Introduction to creep mechanics. In: Encyclopedia of Continuum Mechanics. Altenbach, H., Öchsner, A., (Eds.) Springer, Heidelberg, pp.1337–1344 (2020)
10. Naumenko, K., Altenbach, H.: Modeling high temperature materials behavior for structural analysis. Part II: solution procedures and structural analysis examples, Cham: Springer (2020) https://doi.org/10.1007/978-3-319-31629-1
11. Besson, J.: Continuum models for ductile fracture: a review. Int J Dam Mech **19**, 3–52 (2010)

376 H. Altenbach et al.

12. Breslavsky, D., Kozlyuk, A., Tatarinova, O.: Numerical simulation of two–dimensional problems of creep crack growth with material damage consideration. East-Eur J Ent Techn Appl Mech **92**, 27–33 (2018)
13. Cowper, G. R., Symonds, P. S.: Strain-hardening and strain-rate effects in the impact loading of cantilever beams. Brown Univ Providence Ri (1957)
14. Martynenko, G., et al.: Numerical simulation of missile warhead operation. Adv Eng Soft **123**, 93–103 (2018)
15. Sanders, J.L.: Nonlinear theories for thin shells. Q. Appl. Math. **21**(1), 21–36 (1963)
16. Donnell, L.H.: Beams, Plates, and Shells. USA, McGraw-Hill, New York (1976)
17. Vlasov, V.Z.: General theory of shells and its applications in engineering. NASA Technical Translation F-99: Washington, DC, USA (1964)
18. Mushtari, K.M.: Certain generalizations of the theory of thin shells. Izv. Fiz. Mat. Ob-Va. Pri Kaz. Un-Te 11, 28–56 (1938). (in Russia)
19. Amabili, M.: Nonlinear Vibrations and Stability of Shells and Plates. Cambridge University Press, Cambridge (2008)
20. Bruhns, O.T.: The Prandtl-Reuss equations revisited. Z. Angew. Math. Mech. **94**(3), 187–202 (2014)
21. Breslavskii, D.V., Morachkovskii, O.K.: Nonlinear creep and the collapse of flat bodies subjected to high-frequency cyclic loads. Int. Appl. Mech. **34**(3), 287–292 (1998)
22. Breslavsky, D.V., Morachkovs'kyi, O.K., Tatarinova, O.A.: High-temperature creep and long-term strength of structural elements under cyclic loading. Strength of Materials. **40** (5), 531–537 (2008)
23. Ryzhansky, V.A., Mineev, V.N., Tsypkin, V.I., Ivanov, A.G., Kleshchevnikov, O.A.: Experimental investigation of explosive extension of thin rings made from annealed aluminum alloy. Phys. Combust. Explosion **12**, 120–124 (1976). (in Russia)
24. Jermolaj, W.: Influence of loading asymmetrical cycle on behaviour of metal alloys under fatigue in biaxial stress states. Creep and coupled processes. Sel. and rev. papers presented on 5th International Symp. on Creep and Coupled Processes, pp. 157–160. Bialystok, Bialystok Technical University Publication (1996)

Author Index